Physics of Atomic Nuclei, Vol. 64, No. 4, 2001, pp. 585–587. Translated from Yadernaya Fizika, Vol. 64, No. 4, 2001, pp. 643–645.

90th ANNIVERSARY OF A.B. MIGDAL'S BIRTHDAY
NUCLEI

Surface Heating of Deuterium Clusters by the Field of a Superintense Ultrashort Laser Pulse for Implementing the Nuclear Reaction $d + d \longrightarrow {}^3\mathrm{He} + n$

V. P. Krainov* and M. B. Smirnov, 1)**

Moscow Institute for Physics and Technology, Institutskiĭ pr. 9, Dolgoprudnyĭ, Moscow oblast, 141700 Russia

Received July 17, 2000

Abstract—A new mechanism for heating the electron component of plasmas formed upon the application of a superintense ultrashort laser pulse to atomic clusters is proposed. Clusters considered here consist of deuterium atoms. Upon the emission of a large number of electrons, an irradiated cluster, which acquires a positive charge, explodes (Coulomb explosion). Deuterons that are ejected as the result of this possess high kinetic energies, so that collisions between them can result in ^{3}He formation accompanied by neutron emission. The new mechanism of the heating of the electron plasma from clusters is based on the conjecture that, when an ionization electron is reflected from the inner surface of the cluster ion in the presence of a laser field, it predominantly absorbs (rather than emits) laser photons. © *2001 MAIK "Nauka/Interperiodica".*

The nuclear reaction $d + d \longrightarrow {}^3\mathrm{He} + n$ requires high kinetic energies of the deuterons involved for their Coulomb repulsion to be overcome. This energy can be estimated as $1/4R_d$, where $R_d = 1.96$ fm is the deuteron radius (hereafter, we use the system of atomic units, where $e = m_e = \hbar = 1$), so that it amounts to 180 keV. The cross section for the reaction in question depends only slightly on the deuteron kinetic energy, its value in the energy region around 200 keV being 0.01 b. The energy of the emitted neutron is 2.45 MeV.

Deuterons of such high kinetic energies can be produced in the explosion of deuterium clusters exposed to an ultrashort laser pulse of intensity in excess of 10^{15}–10^{16} W/cm^2. Deuterium clusters have a spherical shape and consist of a few hundred deuterium atoms bound together by weak attractive Van der Waals forces. Therefore, their density is much lower than typical densities of solids.

When such clusters are irradiated with an intense laser pulse, deuterium atoms in a cluster are ionized. Since the intensity of the laser pulse exceeds the corresponding quantities for atomic fields and since the laser field penetrates freely in the cluster interior (the thickness of the skin layer is much greater than cluster dimensions), almost all deuterium atoms are ionized before the termination of the laser pulse. Part of free electrons generated in this way begin to escape from the cluster through its surface. This continues until the positive charge of the cluster ion formed attains a value so large that the kinetic energy of electrons is insufficient for overcoming the Coulomb field of this cluster ion. This Coulomb field tends to pull the electrons in the cluster again. All this occurs within the laser-pulse duration of $\tau = 30$–50 fs. Because of Coulomb repulsion, deuterons in the charged cluster ion fly apart over this time interval for a distance of about the cluster diameter. After the termination of the laser pulse, the divergence of the deuterons continues. This is the explosion of a cluster, and it can generate deuterons with energies in excess of the above value of 200 keV. As a result, there can occur the fusion of two deuterons emitted from different cluster ions (in addition to the aforementioned channel, there is also the channel $d + d \longrightarrow t + p$), which was observed experimentally in [1]. For a cluster ion of charge $Z = 1000$ and initial radius $R = 25$ A (it is precisely this mean radius of deuterium clusters that was recorded in [1]), the mean kinetic energy of emitted deuterons can be estimated at $Z/R \sim 2.5$ keV. This value complies with the data from the earlier experiment reported in [2]. However, the energies of individual deuterons can take values that substantially exceed the above mean value and which are sufficient for overcoming the Coulomb barrier for the fusion of two deuterons. In the deuterium plasma formed, deuterons undergo multiple collisions with one another, which results in thermalization (the concentration of deuterons in the experiment reported in [1] was 1.5×10^{19} cm^{-3}).

Of course, there are only few deuterons with energies $E \simeq 200$ keV. According to the Maxwell distribution, their fraction at temperature $T_d = 2.5$ keV is as small as $\exp(-E/T_d) \sim 10^{-35}$. However, deuterons with subbarrier energies of 50 to 100 keV can fuse successfully by means of quantum tunneling through a Coulomb barrier, which is low in this case. For example,

* e-mail: krainov@cyberax.ru
** e-mail: smirnov@imp.kiae.ru
1) Russian Research Centre Kurchatov Institute, pl. Kurchatova 1, Moscow, 123182 Russia.

Ditmire *et al.* [1] observed about 10^4 neutrons from the reaction $d + d \longrightarrow {}^3\mathrm{He} + n$ per laser pulse.

From the aforesaid, it follows that, in order to implement the fusion of deuterons, it is necessary that the kinetic energy of electrons formed within a cluster as the result of ionization by the field of a laser pulse be as high as possible, since this ensures a higher charge of the resulting cluster ion. The most popular mechanism for increasing the kinetic energy of ionization electrons is the following. At the instant of ionization, the kinetic energy of electrons does not exceed a few eV. An electron that escapes from a deuterium atom collides with positively charged deuterons. In the field of laser radiation, it acquires energy—this is the so-called inverse bremsstrahlung effect [3]: an electron can either absorb or emit a laser-field photon, but the probability of absorption is somewhat higher than the probability of emission. For slow electrons, the probability of the inverse bremsstrahlung effect was calculated in [4]. Of course, electron–electron collisions also occur, but they do not change the electron energy. The electron temperature increases adiabatically with time.

The probability of an elastic electron–deuteron collision is given by the expression

$$w_{ed} = \frac{4\sqrt{2\pi}N\ln\Lambda}{3T^{3/2}}, \qquad (1)$$

[T is the electron temperature, N is the concentration of deuterons in a cluster, and $\ln\Lambda$ is the Coulomb logarithm (equal to about 10 in the problem being considered)], which is well known from physical kinetics [5]. At temperature $T = 1$ keV, which was recorded experimentally in [1], and the deuteron concentration of $N = 10^{21}$ cm^{-3}, this probability is about 0.001 1/fs. Thus, no electron–deuteron collision occurs over the duration of the applied laser pulse; that is, the above mechanism for enhancing the electron temperature is inoperative for deuterium clusters. However, it is a dominant mechanism for metal clusters, where the concentration of atoms is much higher (close to concentrations in solids) and where the nuclear charge Z' is much greater than unity [the probability in Eq. (1) is proportional to $(Z')^2$] [6].

In a deuterium cluster ion, ionization electrons fly freely from one cluster surface to another (they can hardly escape from the cluster because of a large positive charge that the cluster has acquired owing to the emission of preceding electrons). For the probability of electron–electron collisions, we have the same estimate given by (1) as for electron–nucleus collisions. Under the above conditions, the inner surface of a cluster ion is an ideally reflecting surface for free electrons within the cluster. In the absence of a laser field, the energy of the reflected electron would obviously be equal to the energy of an incident electron. In the presence of a laser field, however, the electron can absorb or emit a laser-radiation photon. On average, the probability of absorption is higher than the probability of emission [3], the mean energy increment per collision being equal to the ponderomotive (vibrational) energy $F^2/4\omega^2$ of an electron in the laser-radiation field [7, 8]; here, F is the amplitude of the electric-field strength in a laser pulse, while ω is the laser-radiation frequency. Of course, this energy is small in relation to the above thermal energy of electrons; that is, the energy is enhanced in small portions. For the intensity of 10^{15} W/cm^2 and a typical laser-photon energy of $\omega \sim 1.5$ eV (the laser-radiation wavelength was 820 nm in the experiment reported in [1]), we find that the ponderomotive energy is about 50 eV.

The rate at which the thermal energy $3T/2$ of an electron grows is determined from the balance equation

$$\frac{3}{2}\frac{dT}{dt} = \eta\frac{F^2}{4\omega^2}\frac{v}{2R}, \qquad (2)$$

where $2R$ is the cluster diameter (the distance that a free electron travels between two opposite points of the cluster surface), while $v = (3T)^{1/2}$ is the thermal velocity of electrons. The phenomenological coefficient η, which is much less than unity, considers that, in fact, the collision between an electron and the cluster-ion surface is not elastic and that the direction of the strength of the electric field in the laser wave does not coincide with the direction of electron motion. In the following, we set $\eta = 0.1$.

Integrating Eq. (2) with respect to time, we find that the temperature of electrons upon the termination of the laser pulse is

$$T = \eta^2\frac{F^4\tau_{\mathrm{eff}}^2}{192\omega^4}, \qquad (3)$$

where τ_{eff} is the effective time over which the field strength F in the laser pulse is close to the amplitude (maximum) value. In deriving Eq. (3), it was also assumed that the initial energy of an ionization electron is small in relation to its final energy. The distribution of the laser-pulse intensity in time is close to a Gaussian distribution, but we retain only the quasiplanar segment of this distribution at its top and denote by τ_{eff} the width of this moderately narrow segment. For metal clusters, similar estimates obtained by considering collisions between electrons and atomic ions within a cluster can be found in our review article [9].

Substituting the laser-radiation-intensity amplitude of 10^{15} W/cm^2, the frequency of $\omega = 2$ eV, and the effective pulse duration of $\tau_{\mathrm{eff}} = 10$ fs into (3), we obtain the final electron temperature of $T = 5$ keV. This value complies with the experimental estimates of the electron temperature for various cluster ions [10, 11] and is on the same order of magnitude as the potential barrier Z/R, which opposes the escape of an electron from the cluster ion. Of course, the assumption that electrons are reflected elastically from the inner surface of the cluster is based on the inequality $T \ll Z/R$. Therefore, the above estimates are quite rough.

Atomic ions with energies up to 1 MeV [12, 13] and electrons with energies up to 3 keV were observed in experiments where argon and xenon clusters exploded under the effect of ultrashort laser pulses of intensity about 10^{16} W/cm^2. Such high ion energies (much higher than deuteron energies) were due to large charges of xenon and argon atomic ions (xenon ions of charge as large as +40 were observed). We note that, in cluster explosions caused by Coulomb repulsion, the hydrodynamic expansion of the cluster plasma also contributes to the generation of high-energy atomic ions, but its role is less significant than the role of Coulomb repulsion.

Clusters of deuterium atoms should be preferred to polyethylene targets containing deuterium, because only some 100 neutrons from deuteron fusion were observed in the second case per laser pulse [14].

In summary, we can conclude that the induced absorption of laser-radiation photons at the instant of free-electron reflection from the inner surface of a cluster ion is a dominant mechanism for the enhancement of the electron temperature in experiments where deuterium clusters are exposed to an ultrashort laser pulse.

ACKNOWLEDGMENTS

This work was supported in part by the Russian Foundation for Basic Research (project no. 99-02-17810).

REFERENCES

1. T. Ditmire *et al.*, Nature (London) **398**, 489 (1999).
2. T. Ditmire *et al.*, Nature (London) **386**, 54 (1997).
3. M. V. Fedorov, *Atomic and Free Electrons in a Strong Light Field* (World Sci., Singapore, 1997).
4. V. P. Krainov, J. Phys. B **33**, 1585 (2000).
5. V. P. Silin, *An Introduction to the Kinetic Theory of Gases* (Nauka, Moscow, 1971).
6. B. M. Smirnov, Usp. Fiz. Nauk **170**, 495 (2000).
7. Yu. P. Raizer, *Laser-Induced Discharge Phenomena* (Nauka, Moscow, 1974; Consultants Bureau, New York, 1977).
8. N. B. Delone and V. P. Krainov, *Multiphoton Processes in Atoms*, 2nd ed. (Springer-Verlag, Berlin, 2000).
9. V. P. Kraĭnov and M. B. Smirnov, Usp. Fiz. Nauk **170**, 969 (2000).
10. T. Ditmire *et al.*, Phys. Rev. A **53**, 3379 (1996).
11. Y. L. Shao *et al.*, Phys. Rev. Lett. **77**, 3343 (1996).
12. M. Lezius *et al.*, Phys. Rev. Lett. **80**, 261 (1998).
13. T. Ditmire *et al.*, Phys. Rev. A **57**, 369 (1998).
14. G. Pretzler *et al.*, Phys. Rev. E **58**, 1165 (1998).

Translated by A. Isaakyan

Physics of Atomic Nuclei, Vol. 64, No. 4, 2001, pp. 588–594. From Yadernaya Fizika, Vol. 64, No. 4, 2001, pp. 646–652.

90th ANNIVERSARY OF A.B. MIGDAL'S BIRTHDAY
NUCLEI

Mean-Field Theory for Global Binding Systematics*

G. F. Bertsch and K. Hagino

Institute for Nuclear Theory, Department of Physics, University of Washington, Seattle, WA 98195, USA

Received July 5, 2000

Abstract—We review some possible improvements of mean-field theory for application to nuclear-binding systematics. Up to now, microscopic theory has been less successful than models starting from the liquid drop in accurately describing the global binding systematics. We believe that there are good prospects for developing a better global theory, using modern forms of energy-density functionals and treating correlation energies systematically by the RPA. © *2001 MAIK "Nauka/Interperiodica".*

1. INTRODUCTION

An important goal of nuclear theory is to predict nuclear-binding energies. While mean-field theory offers the most fundamental basis to understanding nuclear structure, paradoxically it has not been as successful as other approaches in making a global fit to nuclear-binding energies. The most accurate theory of nuclear-binding systematics [1] starts from the liquid-drop model and treats shell effects perturbatively. It fits the binding energies with an RMS deviation of 0.67 MeV, taking 15 free parameters and a similar number of fixed parameters to achieve the fit. No such systematic study with so many parameters has been attempted in a purely microscopic approach, but there are a number of partial studies, beginning with the pioneering work of Vautherin and Brink [2], using an energy functional based on the Skyrme interaction. Noteworthy recent papers using Skyrme interactions are by Patyk *et al.* [3] and by Brown [4]. Patyk *et al.* found that Skyrme interactions taken from the literature give RMS errors greater than 2 MeV. This level is also found for the Gogny interaction, which unlike the Skyrme has a finite range. Brown recently made a new Skyrme fit to closed-shell nuclei, including radii and spectroscopic properties in the fitting [4]. He found an RMS deviation of 0.8 MeV for the 10 nuclei he considered, encouraging the hope that deviations below 1 MeV might be reached microscopically. Of course, open-shell nuclei have significant correlation energies, which must be included. We discuss how this might be done in Section 3 below. Another problem is the choice of energy-density functional, and there may be reason to use other forms than the Skyrme or finite-range generalizations. This is discussed in the next section.

* This article was submitted by the authors in English.

2. NEW FORMS FOR THE ENERGY FUNCTIONAL

Some perspective on the energy functional can be obtained from the analogous problem in condensed-matter physics. Correlation effects are rather mild in the many-electron problem, and the mean-field approach is very successful. The energy functional analogous to the Skyrme is called the local-density approximation (LDA), and it is widely used to calculate structures of many-atom systems. Its accuracy for chemical purposes is inadequate, however. For example, in a comparison of different functionals, Perdew *et al.* [5] noted that the LDA had a mean absolute error of 1.4 eV in a sample of small molecules with binding energies in the range 5–20 eV.[1)] Two refinements of the energy functional, going beyond the LDA, make a dramatic improvement in the quality of agreement. The first refinement is to include a term in the energy functional that depends on the gradient of the density. Gradient terms are already present in the Skyrme interaction, but, in the electron system, improvement only appears with a nonlinear functional form of the gradient term,

$$e(n, \nabla n) \sim \frac{f(n)}{1 + a(\nabla n/n)^2}. \qquad (1)$$

The mean absolute error decreases by a factor of 4, to 0.35 eV, when this term is added.[2)] The other improvement is to allow the functional to depend on the kinetic-energy density τ, as well as on the local density $n(r)$. This also is a familiar feature of the Skyrme interaction, but for the electron case, τ is combined with the ∇n dependence in Eq. (1). The resulting mean absolute error is reduced by almost a factor of 3, which gives a final mean absolute error of 0.13 eV.

[1)] It should be mentioned, however, that the LDA energy functional is constructed ab initio without fitting binding data.

[2)] Again, no free parameters are added with this term; the functional form and dependences on ∇n and τ are constructed to simulate the nonlocality of the exchange.

1063-7788/01/6404-0588$21.00

The nuclear problem is different from the electron problem in one important respect. In the latter, much of the loss of accuracy is due to the exchange potential, which is intrinsically nonlocal, but which must be treated in a nearly local approximation for computational reasons. In contrast, in the nuclear problem the strong interaction is short-range, implying that the exchange is also short-range and thus suited to local approximations. Nevertheless, it might be that more complicated functional forms such as Eq. (1) could be useful in the nuclear problem. Indeed, this kind of generalization was examined by Fayans [6]. He used such terms in an energy functional that was fit to 100 spherical nuclei. He obtained an RMS binding error of 1.2 MeV, a factor of 2 better than the Gogny or the published Skyrme functionals.

3. CORRELATION ENERGY

As mentioned earlier, in open-shell nuclei the correlation energy associated with nearly degenerate configurations can be of the order of several MeV, so the single-configuration mean-field approximation is not accurate enough for global energy systematics.

We believe that the following correlations should be considered explicitly in the theory:

center-of-mass delocalization,

quadrupole deformations,

pairing.

These are obvious correlations associated with symmetry breaking in the mean-field Hamiltonian. Translational invariance is always broken in finite systems, and rotational invariance is often broken as well. Pairing treated by BCS theory violates particle-number conservation.

How important are these correlations to the energetics? For the center of mass, the correlation energy can be estimated in the harmonic-oscillator model (but see below) as $3\hbar\omega_0/4 \approx 30/A^{1/3}$ MeV. The resulting magnitude of several MeV is certainly much larger than the allowable error in a global mass theory. However, the energy varies very smoothly and one could question whether it needs to be treated explicitly as a correlation energy or whether its effect can be absorbed in the parameters of the mean-field energy functional. The latter might not be the case because the mean-field functional determines most directly the leading terms in the liquid-drop expansion, varying as A and $A^{-1/3}$. One should not use it to simulate a completely different A dependence. This argument, and some mean-field calculations to support, were given recently by Bender *et al.* [7].

The correlation energy associated with the deformations may be thought of as the energy gained by projecting the states of good angular momentum out of the deformed intrinsic state that contains many angular momenta. Its magnitude can be quite large on our accuracy scale of hundreds of keV. For example, the nucleus ^{20}Ne has a Hartree–Fock ground state close in structure to the [8, 0] $SU(3)$ state of the harmonic oscillator. Combining probabilities of different angular states with the energies of the states derived from the experimental spectrum, one can easily show that the energy gained by the projection is of the order of 4 MeV. A similar number was obtained recently in the projected mean-field calculations of ^{24}Mg by [8]. Thus, this correlation energy should be included with an accuracy of 10% or better to achieve the desired accuracy of the mass theory.

The situation with pairing is less severe. It is certainly necessary to include pairing in a theory of masses just to get realistic odd–even mass differences, but the need to include correlation effects beyond the Hartree–Fock–Bogolyubov theory is less clear. With certain simplified pairing interactions, the pairing Hamiltonian can be solved exactly, without making the BCS approximation [9]. The error in the BCS energy due to the number nonconservation is of the order of 0.5 MeV ([10], Table 11.1). This might be significant in the global mass theory, and we shall include it in our discussion.

There are many ways in which correlation energies can be calculated. The most popular one seems to be the obvious method in which the eigenstates of the symmetry are projected out of the mean-field wave function. If the energy minimization is carried out after the projection, this method is rather costly to use and probably not suitable for a global mass theory. For a global theory, it is important that the method be simple computationally and also that it be systematic, applicable in principle to all possible mean-field solutions. Particularly important is that it does not introduce a discontinuity when the mean-field solution changes its character. In the systematic development of many-particle perturbation theory, the leading term beyond the mean-field approximation gives the correlation energy as an integral over the RPA excitation modes. In a finite system, the RPA correlation formula is given by [10, 11]

$$E_{\rm corr} = \frac{1}{2}\left(\sum_i \hbar\omega_i - {\rm tr}(A)\right), \qquad (2)$$

where ω_i is the (positive) frequency of the RPA phonon and A is the A matrix in the RPA equations. This approach was first proposed by Friedrich and Reinhard [12]. It seems to us that this formula is well suited to the requirements we need for a systematic mass theory. We shall first argue that the formula is adequate in principle and then take up the issue of computational feasibility. In the next section, we summarize experience with simple model Hamiltonians that show that Eq. (2) is more accurate than commonly used projection techniques or is easier to calculate. In the section following, we examine specific algorithms for calculating nuclear-binding energies efficiently.

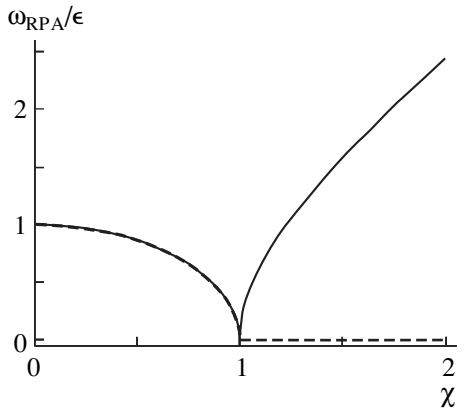

Fig. 1. RPA frequencies in the three-level Lipkin model versus $\chi \equiv V(N-1)/\epsilon$. The number of particles N is chosen to be 20.

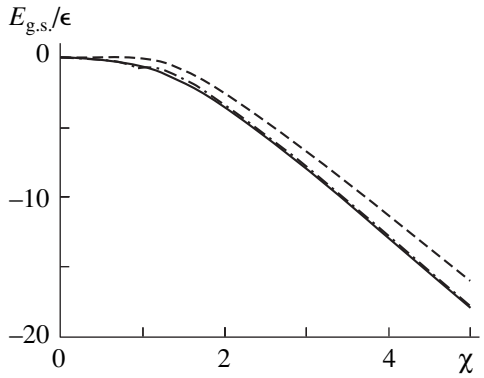

Fig. 2. Comparison of the ground-state energies in the three-level Lipkin model that were obtained by several methods. The solid line is the exact numerical solution. The ground-state energy in the Hartree–Fock approximation is denoted by the dashed line, while the dot-dashed line takes into account the RPA correlation energy in addition to that.

4. EXPERIENCE FROM SIMPLE MODELS

A. Center-of-Mass Localization

The Hamiltonian of two particles interacting through a quadratic potential $V(r_{12}) = m\omega_0^2 r_{12}^2/2$ is solvable exactly and also has an analytic mean-field approximate solution. One might guess that the RPA correlation energy might give the correction exactly, because one can derive the RPA by considering quadratic approximations in a path integral formulation of the problem. This is indeed the case [13]. The RPA spectrum has two states, a zero-frequency mode and a finite-frequency mode. Substituting these frequencies into Eq. (2), one finds that the correction to the mean-field energy $\hbar\omega_0$ is just what is needed to give the exact energy for the total, $\hbar\omega_0/\sqrt{2}$.

It is interesting to compare the RPA approach with other ways of dealing with correlation energies associated with broken symmetries. In the case of center-of-mass motion, a recipe that is often used is to subtract the expectation value of the center-of-mass operator from the mean-field energy (e.g., in [7]). With our Hamiltonian, this prescription gives

$$E_{\rm cm} = -\left\langle \mathrm{MF}\left|\frac{1}{2}\frac{(p_1+p_2)^2}{2m}\right|\mathrm{MF}\right\rangle = -\frac{1}{4}\hbar\omega_0. \qquad (3)$$

The total $E_{\rm MF} + E_{\rm cm} = 3\hbar\omega_0/4$ is not exact, although it is close to the exact energy, $\hbar\omega_0/\sqrt{2}$. This study shows that, for this first kind of correlation, the RPA formula provides a better method to calculate the associated energy.

B. Deformations

When the mean-field solution is deformed, a continuous symmetry is broken. As in the above example, a signature of the broken continuous symmetry is a zero-frequency RPA mode. A model to test theories of the correlation energy should thus have a corresponding continuous symmetry. We constructed a model with those properties in [13], making a generalization of the Lipkin model. In the original Lipkin model, which has been studied for 40 years, one considers many distinguishable particles, each of which can be in one of two states. For that model, the ground-state correlation was studied by Parikh and Rowe [14]. They compared various methods for treating the correlation energy, finding that the RPA formula worked best. In [13], we extended the Lipkin model to a three-state wave function to get sufficient degrees of freedom for a continuously broken symmetry. The symmetry is imposed on the Hamiltonian by requiring it to be invariant under transformations within two of the three states. The two degenerate upper states could be thought of as the first excited states of a two-dimensional harmonic oscillator, thus allowing deformed wave functions in two dimensions. As expected, when the mean-field solutions and their RPA excitations are calculated, one sees zero frequency when the mean-field solution is deformed. There is also another mode at a finite frequency. In this case, the first mode corresponds to rotational motion perpendicular to the symmetry axis, while the second mode corresponds to a beta vibration. In the "spherical" phase, the RPA frequencies for the modes are identical and have a finite frequency. Figure 1 shows the RPA frequencies versus $\chi \equiv V(N-1)/\epsilon$ for the particle number $N = 20$, where V and ϵ are the strength of the interaction and the single-particle energy, respectively. One can clearly see the discontinuity at the critical point $\chi = 1$.

Figure 2 compares the ground-state energies χ that were obtained by several methods. The number of particles N is set to 20. The solid line is the exact solution obtained by numerically diagonalizing the Hamiltonian. The dashed line is the ground-state energy in the Hartree–Fock (HF) approximation. It considerably deviates from the exact solution through the entire range of χ shown in the figure. The dot-dashed line

takes into account the RPA correlation energy in addition to the HF energy. Clearly, the RPA significantly improves the results. The corresponding energy as a function of the number of particles is shown in Fig. 3. One sees that the RPA correlation energy is reliable for large N, but it may be problematic when there are only a few valence particles. That situation is further complicated by the pairing interaction, which may dominate the mean-field solution for $N = 2$.

C. Pairing

Pairing is the final example of a long-range correlation that significantly affects the energy. The mean-field approach leads to BCS theory, whose ground state has an indefinite particle number. An early study by Bang and Krumlinde [15] showed that the RPA formula reproduces the exact correlation energy rather well in a schematic model. The RPA method has in fact been used in realistic models of deformed nuclei [16]. The RPA correlation in the normal phase was studied in [17] by using the self-consistent version of RPA.

Kyotoku *et al.* [18] derived an analytic solution for the model first proposed in [19], fermions in a space of two nondegenerate j shells interacting with a pairing Hamiltonian. They were able to solve the model exactly and then compared the energy with several approximate methods to calculate the correlation corrections to the BCS energy. They found that the ground-state energy in the BCS + quasiparticle RPA (QRPA) coincides with the exact solution at the leading order of an expansion in $1/N$, N being the number of particles in the system. None of the other methods obtained the correct coefficient of the leading-order contribution. For example, the well-known method of Lipkin and Nogami [20] gave a result that is only correct in the limit of a strong pairing force (see Table I in [18]).

In [21], we specifically compared the RPA with the computationally attractive alternative methods, testing the behavior across shell closures and considering both even- and odd-N systems. Taking, as a test case, the two-level problem with a level degeneracy of $\Omega = 8$ and a Fermi energy half-way between the levels, we found that the RPA was much superior to the Lipkin–Nogami method over most of the range of pairing strengths. This behavior is consistent with the result of [18], as we discussed above. However, right at the phase-transition point, the two methods had comparable errors of opposite sign.

We therefore also looked at a more realistic situation, varying the particle number N rather than the interaction strength G. We consider the pairing energy in oxygen isotopes, taking the neutron $1p$ and $2s$–$1d$ shells as the lower and higher levels of the two-level model. The pair degeneracy Ω thus reads $\Omega_1 = 3$ and $\Omega_2 = 6$ for the lower and the upper levels, respectively. The number of particles in a system is given by $N = A - 8 - 2$ for the ^{A}O nucleus. We assume that the energy difference between the two levels ϵ is given by $\epsilon = 41A^{-1/3}$ and the pairing strength is $G = 23/A$. The upper panel of Fig. 4 shows the ground-state energy as a function of A. In order to match with the experimental data for the ^{16}O nucleus, we have added a constant –72.8 MeV to the Hamiltonian for all the isotopes. The exact solutions are denoted by the filled circles. The deviation from the BCS approximation (the dashed line) is around 2 MeV

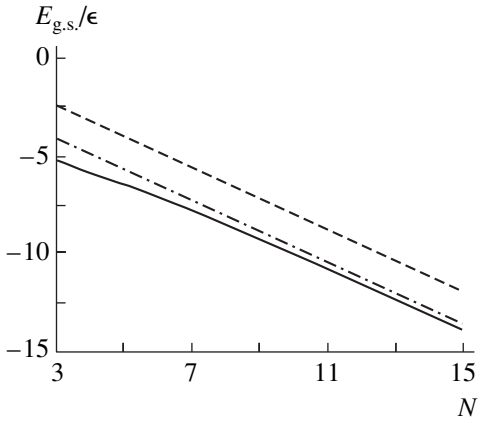

Fig. 3. The ground-state energy of the three-level Lipkin model as a function of N for $\chi = 5$. The meaning of each line is the same as in Fig. 2.

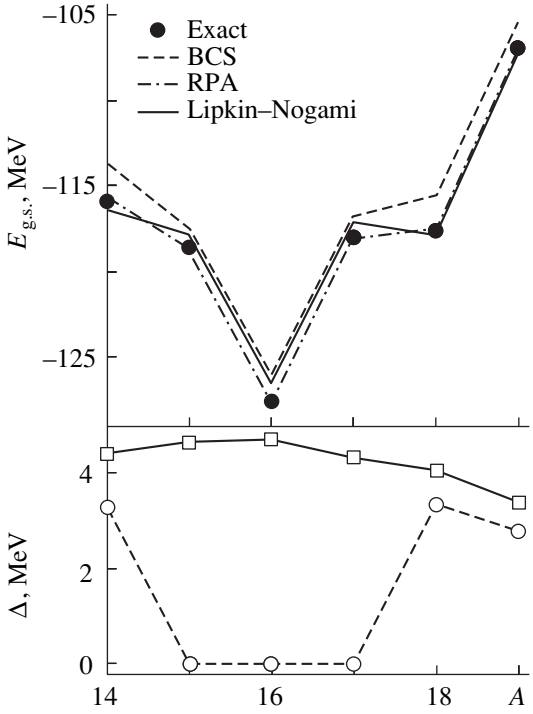

Fig. 4. The ground-state energy $E_{g.s.}$ (the upper panel) and the pairing gap (the lower panel) for oxygen isotopes estimated with the two-level model versus the mass number. The exact results are denoted by the filled circles. For the pairing gap in the Lipkin–Nogami method, λ_2 is added to the pairing gap Δ.

for even-A systems and is around 1.2 MeV for odd-A systems. This value varies within about 0.5 MeV along the isotopes and shows relatively strong A dependence. One can notice that the RPA approach (the dot-dashed line) reproduces the exact solutions quite well. In contrast, the Lipkin–Nogami approach (the solid line) is much less satisfactory and shows an A dependence different from the exact results. The pairing gap Δ in the BCS approximation and in the Lipkin–Nogami method is shown separately in the lower panel of Fig. 4. For the Lipkin–Nogami method, we show $\Delta + \lambda_2$, which is to be compared with experimental data [20]. Here, the Lipkin–Nogami Routhian is defined as $\hat{H} - \lambda\hat{N} - \lambda_2\hat{N}^2$, $\hat{H}$ and $\hat{N}$ being the nuclear Hamiltonian and the particle-number operator, respectively. The closed-shell nucleus ^{16}O and its neighbor nuclei ^{15,17}O have zero pairing gap in the BCS approximation, and the Lipkin–Nogami method does not work well for these nuclei. On the other hand, the RPA approach reproduces the correct A dependence of the binding energy. Evidently, the RPA formula provides a better method to compute correlation energies than the Lipkin–Nogami method, especially for shell closures.

5. IS RPA COMPUTATIONALLY FEASIBLE?

We now discuss the practicality of using Eq. (2) to calculate the correlation energy. In general, the RPA is computationally more demanding than the mean-field minimization for the ground state by an order of magnitude or more. One must diagonalize an RPA matrix whose dimensions are $2D \times 2D$, where D is the number of particle–hole configurations. This number can be huge if one is interested in deformed nuclei or heavy spherical nuclei. A widely used way around this is to take a residual interaction of a separable form. Then, the matrix equation to be solved has the dimension of the rank of the separable interaction; with a single term, it is just the well-known algebraic dispersion relation.

Given a separable interaction, there are several efficient ways to get the RPA correlation energy (2) without explicitly calculating all the roots of the dispersion relation. One method was recently proposed by Dönau *et al.* [22] and also by Shimizu *et al.* [23]. Instead of directly calculating the RPA correlation energy according to Eq. (2), one carries out an integration of a function that depends on a free-response function and its first derivative in the complex energy plane. An advantage of this method is that one can choose the integration path so that the integrand is smooth enough, and thus the mesh of the numerical integration along this path can be much larger than the actual energy intervals of the RPA solutions ω_α. This method is particularly useful when a separable interaction is used so that the free-response function and its first derivative are analytically evaluated.

Alternatively, one can also use the Lanczos-type method proposed in [24] to evaluate the RPA correlation energy. As we show below, this method quickly converges when the interaction is separable. The idea is to define at the outset a characteristic operator associated with each kind of correlation. That operator applied to the mean-field ground state gives an excited state, which is taken as the first vector in a space built up by applications of the Hamiltonian to existing states. Equation (2) is then evaluated in the restricted spaces, and the method would be computationally feasible if the convergence is rapid enough.

Suppose the matrices A and B in the RPA equation are given by

$$A_{ij} = \epsilon_i\delta_{i,j} + \kappa f_i f_j, \tag{4}$$

$$B_{ij} = \kappa f_i f_j, \tag{5}$$

where i and j label particle–hole configurations and f_i is normalized as $\sum_i f_i^2 = 1$. For such an interaction, the collective operator can be chosen as $\psi_i = f_i$. Notice that f is an eigenvector of the matrix B with the eigenvalue κ and also that $B\phi = 0$ for any vector ϕ that is orthogonal to f. Starting from the initial vectors $|X_1\rangle = |\psi\rangle$ and $|Y_1\rangle = 0$, the Lanczos manipulation [24] transforms the matrices A and B into the form

$$A' = \begin{pmatrix} e_1 & a_1 & 0 & \\ a_1 & e_2 & a_2 & \\ 0 & a_2 & e_3 & \\ & & & \ddots \end{pmatrix}, \quad B' = \begin{pmatrix} \kappa & 0 & 0 & \\ 0 & 0 & 0 & \\ 0 & 0 & 0 & \\ & & & \ddots \end{pmatrix}. \tag{6}$$

The Lanczos basis for the backward-scattering amplitude $|Y_i\rangle$ remains all zero in the manipulation, and thus the transformed matrix B' has only one element that is not equal to zero. This is not generally the case for nonseparable interaction. Note that the matrix B' measures the degree of correlation in the transformed space. Since it has a very simple form, the correlation energy evaluated in the restricted space converges very rapidly.

We have tested the method with RPA matrices given by Eq. (5) with $\epsilon_i = e_0 + (i-1)\Delta e$. The method works very well when there is a gap in the particle–hole spectrum. For example, if we take a model with $D = 20$ particle–hole states and other parameters $f_i = 1$, $\Delta e = e_0/D$, and $\kappa = -0.035e_0$, the RPA spectrum has a collective state at $\omega_1 = 0.145e_0$. The correlation energy from Eq. (2) with all eigenvalues is $E_{\rm corr} = -0.542e_0$. The single-state approximation starting from the state $\psi_i = f_i/\sqrt{D}$ is only off by 20%. The two-state approximation has an accuracy of 1%. The calculational effort to get these numbers is essentially that of three applications of the Hamiltonian to the ground-state single-particle wave function, much less than the effort to get the con-

verged wave functions in the Hartree–Fock minimization (see table).

From our point of view, the problem is then to define a reliable separable interaction that can be used globally in RPA calculations. For particle–hole residual interactions, a few possible ways to construct a separable interaction have been proposed on the basis of the self-consistency argument [25–31]. The basic argument is that the collective motions primarily result in the displacement of the nuclear surface; thus, the transition potential can be generated by displacing the self-consistency potential associated with the ground-state density. In equations, the transition density has a form locally given by the gradient of the static density, and the transition potential is the corresponding gradient of the static potential:

$$\delta\rho = a(\Omega)\frac{d\rho_0}{dr}, \tag{7}$$

$$\delta V = a(\Omega)\frac{dU_0}{dr}, \tag{8}$$

where Ω is an angle giving the direction to an element of the nuclear surface. The separable residual interaction then has the shape of (8) and the required magnitude to satisfy (7). Thus, we have

$$v(\mathbf{r}_1, \mathbf{r}_2) = \delta V(\Omega_1, r_1)\delta V(\Omega_2, r_2)/\int d\mathbf{r}\delta V\delta\rho. \tag{9}$$

It is amusing to compare the above self-consistent definition with the microscopic particle–hole interaction proposed by Migdal [32]. For the above transition density, his transition potential would be given by

$$\delta V(\mathbf{r}) = V_0\left(f^{\mathrm{ex}} + (f^{\mathrm{in}} - f^{\mathrm{ex}})\frac{\rho_0(\mathbf{r})}{\rho_0(0)}\right)\delta\rho(\mathbf{r}). \tag{10}$$

The two transition potentials for ^{208}Pb are compared in Fig. 5. We generate the static potential U_0 using the velocity-independent part of the Skyrme interaction with *S*III parametrization, and we use a Fermi distribution for a static density $\rho_0(r)$. The parameters of the Migdal interaction are given in [33]. We see that the two transition potentials have a similar surface-peaked radial dependence.

The above self-consistency argument can be applied very easily to the translation mode, where $a(\Omega) = \cos\theta$ for translations in the z direction. For the rotational degrees of freedom, we would use the displacement fields associated with the five components of the quadrupole operator, i.e., $a_\mu(\Omega) = Y_{2\mu}(\Omega)$, $\mu = -2, -1, 0, 1, 2$. Note that the RPA correlations are to be evaluated for spherical and for deformed nuclei; a major point of the approach is that the theory applies to all cases.

It is not so simple to construct a global, separable pairing interaction. The commonly used forms for the pairing interaction give divergent results without a cutoff in the space of states included in the BCS calculation. Here, we propose a nonlocal surface-peaked separable form:

Convergence characteristics of the Lanczos algorithm

Iteration number	E_{corr}/e_0	ω_1/e_0
1	−0.2211	0.3326
2	−0.2688	0.1539
3	−0.2710	0.1454
Exact	−0.2711	0.1451

$$v(\mathbf{r}_1\mathbf{r}_2, \mathbf{r}'_1\mathbf{r}'_2) = \delta(\mathbf{r}_1 - \mathbf{r}_2)\delta(\mathbf{r}'_1 - \mathbf{r}'_2) \times\left[-\frac{\chi}{2}\frac{dU_0}{dr_1}\frac{dU_0}{dr'_1}\sum_{\lambda\mu}Y_{\lambda\mu}(\hat{\mathbf{r}}_1)Y^*_{\lambda\mu}(\hat{\mathbf{r}}'_1)\right]. \tag{11}$$

The pairing matrix elements of this interaction are to be evaluated as

$$\langle p_1\bar{p}_1|v|p_2\bar{p}_2\rangle = -\frac{\chi}{2}\sum_{\lambda\mu}\left\langle p_1\left|\frac{dU_0}{dr}Y_{\lambda\mu}(\hat{\mathbf{r}})\right|p_1\right\rangle\left\langle p_2\left|\frac{dU_0}{dr'}Y^*_{\lambda\mu}(\hat{\mathbf{r}}')\right|p_2\right\rangle. \tag{12}$$

This form is inspired by recent observations that the pairing is essentially a surface phenomenon [34–36]. A similar surface-peaked separable interaction was used for the particle–hole channel in [37]. We have tested the surface-peaked separable pairing interaction (11) by comparing it with the density-dependent delta interaction proposed in [38]. The problem of the cutoff is much less severe with this interaction than with a contact interaction, because the smoothness of dU_0/dr cuts off the radial integrals. Our preliminary calculations show that the separable pairing interaction can reproduce results of the density-dependent pairing interaction reasonably well once the strength χ is adjusted. For

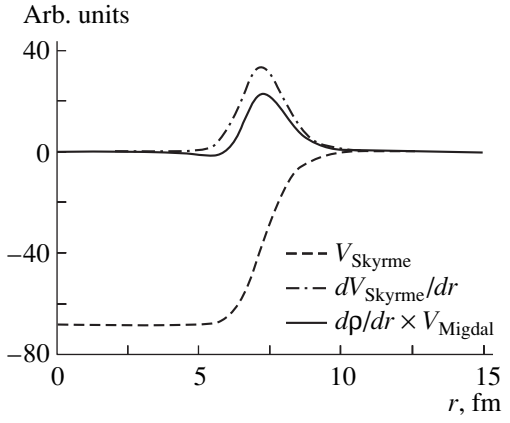

Fig. 5. Comparison between transition potentials obtained with the Skyrme and Migdal interactions.

the purpose of the global binding systematics, the A dependence of the strength has yet to be sorted out.

6. SUMMARY

Our goal is to develop a better microscopic theory for the nuclear-binding systematics. In this paper, we argued that the RPA approach provides a promising and computationally tractable way to include correlation effects in a global model, going beyond the mean-field approximation. We have shown that the HF + RPA approach indeed works well using simple Hamiltonian models for the correlation associated with broken mean-field symmetries, namely, the center-of-mass localization, rotation, and pairing. The RPA equation can be easily solved for a separable residual interaction. For example, the Lanczos method is quite efficient to solve the RPA equation for a separable interaction. This contrasts to other popular computational methods such as the generator-coordinate method and the variation-with-projection method, which are rather complicated to apply. A work is now in progress to tackle the nuclear masses by using the HF + RPA approach discussed in this paper.

ACKNOWLEDGMENTS

We thank P.-G. Reinhard, W. Nazarewicz, B.A. Brown, and A. Bulgac for discussions.

This work was supported by the U.S. Department of Energy under Grant no. DE-FG03-00-ER41132.

REFERENCES

1. P. Möller, J. R. Nix, W. D. Myers, and W. J. Swiátecki, At. Data Nucl. Data Tables **59**, 185 (1995).
2. D. Vautherin and D. M. Brink, Phys. Rev. C **5**, 626 (1972).
3. Z. Patyk, A. Baran, J. F. Berger, *et al.*, Phys. Rev. C **59**, 704 (1999).
4. B. A. Brown, Phys. Rev. C **58**, 220 (1998).
5. J. P. Perdew, K. Burke, and M. Ernzerhof, Phys. Rev. Lett. **77**, 3865 (1996); J. P. Perdew, S. Kurth, A. Zupan, and P. Blaha, Phys. Rev. Lett. **82**, 2544 (1999).
6. S. A. Fayans, Pis'ma Zh. Éksp. Teor. Fiz. **68**, 161 (1998) [JETP Lett. **68**, 169 (1998)].
7. M. Bender, K. Rutz, P.-G. Reinhard, and J. A. Maruhn, Eur. Phys. J. A **7**, 467 (2000).
8. A. Valor, P.-H. Heenen, and P. Bonche, Nucl. Phys. A **671**, 145 (2000).
9. R. W. Richardson and N. Sherman, Nucl. Phys. **52**, 221 (1964).
10. P. Ring and P. Schuck, *The Nuclear Many Body Problem* (Springer-Verlag, New York, 1980).
11. D. J. Rowe, Phys. Rev. **175**, 1283 (1968).
12. J. Friedrich and P.-G. Reinhard, Phys. Rev. C **33**, 335 (1986).
13. K. Hagino and G. F. Bertsch, Phys. Rev. C **61**, 024307 (2000).
14. J. C. Parikh and D. J. Rowe, Phys. Rev. **175**, 1293 (1968).
15. J. Bang and J. Krumlinde, Nucl. Phys. A **141**, 18 (1970).
16. Y. R. Shimizu, J. D. Garrett, R. A. Broglia, *et al.*, Rev. Mod. Phys. **61**, 131 (1989).
17. J. Dukelsky, G. Röpke, and P. Schuck, Nucl. Phys. A **628**, 17 (1998); J. Dukelsky and P. Schuck, Phys. Lett. B **464**, 164 (1999).
18. M. Kyotoku, C. L. Lima, and Hsi-Tseng Chen, Phys. Rev. C **53**, 2243 (1996).
19. J. Högaasen-Feldman, Nucl. Phys. **28**, 258 (1961).
20. H. J. Lipkin, Ann. Phys. (N.Y.) **9**, 272 (1960); Y. Nogami, Phys. Rev. **134**, B313 (1964); H. C. Pradhan, Y. Nogami, and J. Law, Nucl. Phys. A **201**, 357 (1973).
21. K. Hagino and G. F. Bertsch, Nucl. Phys. A **679**, 163 (2000).
22. F. Dönau, D. Almehed, and R. G. Nazmitdinov, Phys. Rev. Lett. **83**, 280 (1999).
23. Y. R. Shimizu, P. Donati, and R. A. Broglia, Phys. Rev. Lett. **85**, 2260 (2000).
24. C. W. Johnson, G. F. Bertsch, and W. D. Hazelton, Comput. Phys. Commun. **120**, 155 (1999).
25. A. Bohr and B. R. Mottelson, *Nuclear Structure* (Benjamin, New York, 1975; Mir, Moscow, 1981), Vol. 2.
26. J. Babst and P.-G. Reinhard, Z. Phys. D **42**, 209 (1997).
27. V. O. Nesterenko, W. Kleinig, V. V. Gudkov, *et al.*, Phys. Rev. A **56**, 607 (1997).
28. V. O. Nesterenko, W. Kleinig, V. V. Gudkov, and J. Kvasil, Phys. Rev. C **53**, 1632 (1996).
29. T. Suzuki and H. Sagawa, Prog. Theor. Phys. **65**, 565 (1981).
30. V. V. Pal'chik, N. I. Pyatov, and S. A. Fayans, Yad. Fiz. **34**, 903 (1981) [Sov. J. Nucl. Phys. **34**, 504 (1981)].
31. D. J. Rowe, Phys. Rev. **162**, 866 (1967).
32. A. B. Migdal, *Theory of Finite Fermi Systems and Applications to Atomic Nuclei* (Nauka, Moscow, 1965; Interscience, New York, 1967).
33. P. Ring and J. Speth, Nucl. Phys. A **235**, 315 (1974).
34. F. Barranco, R. A. Broglia, G. Gori, *et al.*, Phys. Rev. Lett. **83**, 2147 (1999).
35. M. Baldo, U. Lombardo, E. Saperstein, and M. Zverev, Phys. Lett. B **459**, 437 (1999).
36. M. Farine and P. Schuck, Phys. Lett. B **459**, 444 (1999).
37. Y. Alhassid, G.F. Bertsch, D. J. Dean, and S. E. Koonin, Phys. Rev. Lett. *77*, 1444 (1996).
38. G. F. Bertsch and H. Esbensen, Ann. Phys. (N.Y.) **209**, 327 (1991); H. Esbensen, G. F. Bertsch, and K. Hencken, Phys. Rev. C **56**, 3054 (1997).

Physics of Atomic Nuclei, Vol. 64, No. 4, 2001, pp. 595–610. From Yadernaya Fizika, Vol. 64, No. 4, 2001, pp. 653–668.

90th ANNIVERSARY OF A.B. MIGDAL'S BIRTHDAY
NUCLEI

Microscopic Approach to Transition-Energy Staggering in Superdeformed Bands*

I. M. Pavlichenkov and A. A. Shchurenkov

Russian Research Centre Kurchatov Institute, pl. Kurchatova 1, Moscow, 123128 Russia

Received July 27, 2000

Abstract—The current status of the $\Delta I = 4$ bifurcation in superdeformed bands is reviewed by making use of a theoretical model based on the interaction of rotation and single-particle nucleon motion in nuclei with an axial deformation. It is shown that the hexadecapole-type distortion of a nuclear shape by rotation is especially important for explaining the phenomenon. The necessary condition for staggering is obtained from an analysis of the nonadiabatic effect of rotation. This criterion is applied to 30 superdeformed bands in the mass region around $A \sim 150$. An analysis confirms the configuration-dependence effect and allows us to discriminate between single-particle states active and inactive for staggering. The consideration is based on the additivity of the nonaxial hexadecapole moment, which plays a key role in the staggering phenomenon. © *2001 MAIK "Nauka/Interperiodica".*

1. INTRODUCTION

The $\Delta I = 4$ bifurcation, or the $\Delta I = 2$ staggering, is a well-known mysterious phenomenon in the physics of superdeformed (SD) bands. It is observed as regular oscillations of the gamma-ray energy differences against a smooth behavior. The amplitude of oscillations is approximately 100 eV (to be compared to a transition energy of about 1 MeV), and the observation of these oscillations is a good example of the experimental potential of third-generation gamma-ray detector arrays, such as Eurogam and Gammasphere. Although the phenomenon is of a small energy scale, it has been of considerable interest, and much experimental and theoretical work has been devoted to it. The motivation was furnished by a period of oscillations, $\Delta I = 4$, that was unusual for nuclear physics and by their long and regular character.

The first experimental indication of the staggering phenomenon in the octupole vibrational band of ^{236}U was reported by Peker *et al.* [1], who observed oscillations of the differences

$$\Delta E_\gamma(I) = E_\gamma(I+2) - E_\gamma(I), \tag{1}$$

where $E_\gamma(I)$ is the transition energy between the $I + 2$ and I levels, with I being the level spin. It was proposed to describe the rotational energy in a band by the formula

$$E(I) = \mathcal{A}I(I+1) + \mathcal{B}I^2(I+1)^2 + \ldots + (-1)^{(I+2)/2}B_0, \tag{2}$$

where $\mathcal{A}$ and $\mathcal{B}$ are the inertial parameters representing the regular part of the energy. The last term splits the normal $\Delta I = 2$ rotational band into two $\Delta I = 4$ subbands of spins I_0, $I_0 + 4$, $I_0 + 8$, … and $I_0 + 2$, $I_0 + 6$, $I_0 + 10$, … by shifting them in opposite directions. Ten years later, the phenomenon was discovered in the yrast SD band of ^{149}Gd by Flibotte *et al.* [2]. They found it more convenient to represent the effect by comparing the $\Delta E_\gamma(I)$ values with a smooth reference calculated by the expression

$$\Delta E_\gamma^{\mathrm{ref}}(I) = \frac{1}{4}[\Delta E_\gamma(I+2) + 2\Delta E_\gamma(I) + \Delta E_\gamma(I-2)]. \tag{3}$$

Afterward, other examples of staggering [3–8] were identified, but no examples have been found that would exhibit the $\Delta I = 2$ staggering as regular and over so large region of spins as the ^{149}Gd(1) band.[1)]

Several theoretical explanation of the phenomenon were proposed [9–15]. It seems natural to explain the $\Delta I = 4$ bifurcation by fourfold symmetry, whose role was already mentioned in [1]. Hamamoto and Mottelson [9] and Macchiavelli *et al.* [10] postulated the existence of such symmetry with respect to the 3-axis (the axis of symmetry). The nonadiabatic nature of nuclear rotation requires an effective rotational Hamiltonian as a power series in the body-fixed components (I_β with $\beta = 1, 2, 3$) of the spin operator. The symmetry of a system imposes certain restrictions on the terms of this series. For the C_{4v} symmetry axis, the lowest order nonaxial operator in the Hamiltonian is proportional to $I_+^4 + I_-^4$ ($I_\pm = I_1 \pm iI_2$). This operator means that there are four preferred directions for the spin **I** (which cor-

* This article was submitted by the authors in English.

[1)] As a rule, multiple SD bands in a nucleus are numbered according to their intensities. Thus, the most intense yrast band is labeled with 1.

respond to four minima of the rotational energy) in the body-fixed frame (or four preferred orientations of the nuclear shape with respect to the direction **I** in the space-fixed frame). The tunneling of the spin between these directions produces four almost degenerate states, known as cluster states in molecular rotational spectra [16]. The C_{4v} cluster involves four states labeled with the quantum numbers of this point-symmetry group. The fact that the intrinsic shape has C_{4v} symmetry implies that the C_{4v} quantum number of a cluster state is determined by the intrinsic configuration. Of the four states, only a single C_{4v} eigenstate is therefore appropriate for the rotational band based on a given intrinsic state. Because the position of a state in a cluster is alternated with the quantum number I, the level energy of a band has the regular $\Delta I = 4$ oscillatory behavior in accordance with Eq. (2).

Fourfold symmetry implies the existence of a nonaxial hexadecapole deformation of the nuclear surface. However, calculations of the equilibrium shape for nuclei exhibiting staggering within the Strutinsky [17, 18] and the Hartree–Fock–Bogolyubov [19] method showed that the static deformation ε_{44} is too small to generate $\Delta I = 2$ staggering with an amplitude of experimental value [20]. Another inherent difficulty of the theory based on this tunneling mechanism was revealed by one of the present authors (I.M. Pavlichenkov) and Flibotte [11]. It is well known that, because of an increase in the tunneling path, the splitting of cluster levels decreases with increasing angular momentum [16]. Therefore, it is difficult to fit the parameters of the Hamamoto and Mottelson Hamiltonian to avoid a fast damping of the staggering amplitude with increasing I, but such damping has not been observed experimentally. Important advances in testing this Hamiltonian were made owing to the discovery [21] of the $\Delta I = 4$ bifurcation in the SD bands ^{148}Eu(1) and ^{148}Gd(6),[2)] two bands identical to ^{149}Gd(1). The aforementioned three bands in different nuclei show a striking similarity in the staggering behavior; this immediately rules out the explanation [15] of the phenomenon by band crossing. Further, the high degree of correlation (about 0.1 keV over 12 MeV in excitation energy) between the staggering patterns in these bands of three different nuclei give sufficient grounds to conjecture that the Hamiltonian parameters are independent of both spin and nucleus. This observation was used in [23] to constrain the parameters that turned out to be inappropriate for SD nuclei. The result indicated that a tunneling mechanism of the Hamamoto and Mottelson type could not explain the $\Delta I = 4$ bifurcation. Another important observation of [23] is the second triplet of bands ^{147}Eu(1), ^{147}Gd(4), and ^{148}Gd(1) having the same single-particle structures as the bands quoted above, except that they lack a neutron in the positive-signature $N = 6$ Nilsson orbital. Such a seemingly insignificant change in the structures of these bands completely destroys their staggering patterns. This experimental fact is an excellent demonstration of the configuration dependence, which offers the possibility of studying the microscopic origin of the staggering phenomenon.

There is a more general cause of the $\Delta I = 4$ bifurcation. According to the approach proposed first in [2] and confirmed later by the phenomenological treatment in [11], a C_4-symmetry perturbation may have a dynamical origin. In [24, 25], this idea was formulated at the microscopic level. In this theory, the operator $I_+^4 + I_-^4$ of the rotational Hamiltonian is explained by the coupling of rotation to the single-particle motion of nucleons in an axisymmetric nucleus. The essential ingredients of this coupling are two-body hexadecapole interaction and nucleons occupying active orbitals, which generate, due to rotation, a large nonaxial hexadecapole moment. The coupling distorts rotational motion and may lead to staggering, provided that some conditions depending, in particular, on the occupation of the active orbitals are satisfied. The contribution of the high-j intruder states to active orbitals is dominant. For this reason, active orbitals were approximated in [26] by the states of isolated intruder subshells. It was shown that the staggering behavior of the SD bands in $A \sim 150$ nuclei depends on the intruder configuration $\pi 6^m \nu 7^n$ with m protons (π) and n neutrons (ν) in the subshells with principal quantum numbers 6 and 7, respectively. This result explains the experimental observation that the staggering is not a universal characteristic of SD bands. However, the simplified model being used is not reliable for the SD bands because the intruder subshells cannot be treated as isolated ones. It cannot explain, for example, the aforementioned triplet of the nonstaggering bands.

Interest in the staggering problem has been revived upon the versatile analysis of experimental data that was undertaken in [27, 28]. In particular, Haslip *et al.* [28] presented a systematic survey and a statistical analysis of the $\Delta I = 2$ staggering in 19 SD bands of Eu and Gd nuclei. This rendered an improvement of the theory highly desirable. Here, the rotation-single-particle coupling model of the $\Delta I = 4$ bifurcation is reformulated in the context of a realistic shell-model potential. The perturbation method developed in the theory of nonadiabatic effects in nuclear rotational spectra [29–31] is modified in Section 2 to derive the effective rotational Hamiltonian featuring a C_{4v}-symmetry term. It is shown in Section 3 that the simple rotational regime of this Hamiltonian may involve staggering. The necessary condition of the staggering behavior is also obtained. Orbitals that are active and inactive for staggering and which are involved in the configurations of the SD bands in the mass region around $A \sim 150$ are discussed in Section 4. There, we also estimate the parameters of the effective Hamiltonian. In Section 5, the simple criterion found in Section 3 for the $\Delta I = 4$ bifurcation is applied to 30 superdeformed bands of

[2)]The SD bands in ^{148}Gd are numbered according to the scheme proposed in [22].

$A \sim 150$ nuclei. Our results are discussed and summarized in Section 6.

2. EFFECTIVE ROTATIONAL HAMILTONIAN WITHIN THE CRANKING HARTREE–FOCK FORMALISM

Our consideration is based on the second quantized Routhian

$$H' = \sum_{i,k} \epsilon_{ik} a_i^+ a_k - \frac{1}{2} \sum_{\lambda = 2,4} \chi_\lambda \hat{\mathcal{Q}}_\lambda \cdot \hat{\mathcal{Q}}_\lambda - \omega_1 J_1 - \omega_2 J_2, \quad (4)$$

with the quadrupole and hexadecapole two-body interactions of strengths χ_2 and χ_4, respectively. The centered-dot symbol denotes the scalar product $\hat{\mathcal{Q}}_\lambda \cdot \hat{\mathcal{Q}}_\lambda = \sum_\mu \mathcal{Q}^*_{\lambda\mu} \mathcal{Q}_{\lambda\mu}$ of the multipole-moment operators

$$\mathcal{Q}_{\lambda\mu} = \sum_{i,k} \langle i | q_{\lambda\mu} | k \rangle a_i^+ a_k, \quad (5)$$

where a^+ and a are the particle creation and annihilation operators. The first term in Eq. (4) is the single-particle energy. The last two terms are cranking with the angular-momentum projections

$$J_\beta = \sum_{i,k} \langle i | j_\beta | k \rangle a_i^+ a_k. \quad (6)$$

They correspond to rotation about an arbitrary axis perpendicular to the 3-axis. For the sake of simplicity, we ignore pairing interaction, whose role will be discussed later.

Since all the numerical calculations performed so far show the absence of a noticeable triaxial superdeformation, it is reasonable to confine ourselves to the axial case. Accordingly, we perform the canonical transformation to the new single-particle functions $|s\rangle$, which satisfy the self-consistent Schrödinger equation

$$(H_0 - \omega_+ j_- - \omega_- j_+)|s\rangle = \varepsilon_s |s\rangle, \quad (7)$$

where

$$H_0 = \hat{\epsilon} - \sum_{\lambda = 2,4} \chi_\lambda \alpha_{\lambda 0} \hat{q}_{\lambda 0} \quad (8)$$

is the shell-model Hamiltonian with the quadrupole and hexadecapole deformed potentials, which are proportional to the axial collective coordinates $\alpha_{\lambda 0} = \sum_s q_{ss}(\lambda 0) n_s$ (n_s are the nucleon occupation numbers of the given rotational band); $j_\pm = j_1 \pm i j_2$; and $\omega_\pm = (\omega_1 \pm i\omega_2)/2$. The energy in the rotating frame as a function of frequencies ω_+ and ω_- is given by

$$\mathcal{E}' = \sum_s \varepsilon_s n_s + \frac{1}{2} \sum_\lambda \chi_\lambda \alpha_{\lambda 0}^2 - \frac{1}{2} \sum_{\lambda, \mu \neq 0} \chi_\lambda \alpha_{\lambda\mu} \alpha_{\lambda, -\mu}. \quad (9)$$

The last term of this equation contains the nonaxial collective coordinates

$$\alpha_{\lambda\mu} = \mathrm{tr}(q_{\lambda\mu}\rho), \quad \mu = \pm 2, \pm 4, \quad (10)$$

which are nonvanishing because the system density matrix ρ in the representation of Eq. (7) is not axial due to the cranking terms. Let us decompose these quantities into two parts

$$\alpha_{\lambda\mu} = \tilde{\alpha}_{\lambda\mu} + Q_{\lambda\mu}, \quad (11)$$

where $\tilde{\alpha}_{\lambda\mu}$ and $Q_{\lambda\mu}$ are, respectively, the perturbative and nonperturbative nonaxial multipole moments induced by rotation. The separation of multipole moments is explained by the two types of the single-particle states generating nonaxial moments: inactive and active orbitals. The former are responsible for the regular ω dependence of $\alpha_{\lambda\mu}$. It is possible to use perturbation theory to obtain this dependence for the first quantity:

$$\tilde{\alpha}_{\lambda\mu} = \mathrm{tr}(q_{\lambda\mu}\tilde{\rho}^{(2)}) + \mathrm{tr}(q_{\lambda\mu}\tilde{\rho}^{(4)}) + \ldots, \quad (12)$$

where $\tilde{\rho}^{(n)}$ is the nth order correction to the density matrix of the perturbative states resulting from the cranking term of Eq. (7):

$$V = -\omega_+ j_- - \omega_- j_+. \quad (13)$$

In performing corresponding calculations, we will utilize the representation of nonrotating axially deformed nuclei with the eigenfunctions satisfying the equation

$$\left(\hat{\epsilon} - \sum_{\lambda = 2,4} \chi_\lambda \alpha_{\lambda 0}^{(0)} \hat{q}_{\lambda 0} \right) |1\rangle = \varepsilon_1 |1\rangle. \quad (14)$$

It is important to note that the perturbation series for the axial collective coordinates, $\alpha_{\lambda 0}$, begins with the ω-independent quantity $\alpha_{\lambda 0}^{(0)}$, which is equal to the multipole moment of nonrotating nucleus,

$$\alpha_{\lambda 0}^{(0)} = \mathrm{tr}(q_{\lambda 0}\rho^{(0)}). \quad (15)$$

The active orbitals generate the nonaxial moments $Q_{\lambda\mu}$, which cannot be treated by perturbation theory and should be evaluated with the wave functions of Eq. (7).

Due to the extreme regularity of the SD-band spectra, the first two terms in Eq. (9) can be approximated by the Harris formula

$$\sum_s \varepsilon_s n_s + \frac{1}{2} \sum_\lambda \chi_\lambda \alpha_{\lambda 0}^2 \approx \mathcal{E}_0 - 2\omega_+\omega_- \mathcal{J} - 4\omega_+^2 \omega_-^2 \beta, \quad (16)$$

where $\mathcal{E}_0$ is the energy of nonrotating nucleus and

$$\mathcal{J} = \frac{1}{\omega} \mathrm{tr}(j_1 \rho^{(1)}), \quad \beta = \frac{1}{\omega^3} \mathrm{tr}(j_1 \rho^{(3)}) \quad (17)$$

are the well-known coefficients of cranking expansion. They depend on corrections to the density matrix of the

whole system. The decomposition in (11) and Eqs. (12) and (16) allow us to obtain the expansion of the energy (9) in the powers of the rotational frequencies ω_+ and ω_- with the same accuracy as in Eq. (16),

$$\mathcal{E}' \approx \mathcal{E}_0 - 2\omega_+\omega_-\mathcal{J} - (\omega_+^2 + \omega_-^2)\Gamma_2^{(2)} - 4\omega_+^2\omega_-^2\beta - (\omega_+^3\omega_- + \omega_+\omega_-^3)\Gamma_2^{(4)} - (\omega_+^4 + \omega_-^4)\Gamma_4^{(4)}. \quad (18)$$

Here, the coefficients $\mathcal{J}$ and β are modified by the centrifugal distortion of the axial collective coordinates $\alpha_{\lambda 0}$. They are expressed in terms of the inertial parameters of Eq. (2) as (we assume $\hbar = 1$)

$$\mathcal{J} = \frac{1}{2\mathcal{A}}, \quad \beta = -\frac{\mathcal{B}}{4\mathcal{A}^4}, \quad (19)$$

where $\mathcal{J}$ is the kinematical moment of inertia. The nonaxial terms of Eq. (18) arise from the quadrupole and hexadecapole coupling of the active states with the nonaxial distortion of the nuclear mean field. They are proportional to the parameters

$$\Gamma_2^{(n)} = \sum_\lambda \chi_\lambda Q_{\lambda 2}\tilde{\alpha}_{\lambda 2}^{(n)}, \quad \Gamma_4^{(4)} = \chi_4 Q_{44}\tilde{\alpha}_{44}^{(4)}, \quad (20)$$

where the ω-independent quantities $\tilde{\alpha}_{\lambda\mu}^{(n)}$ are given by

$$\tilde{\alpha}_{\lambda\mu}^{(n)} = \tilde{\alpha}_{\lambda,-\mu}^{(n)} = \omega_+^{-(n+\mu)/2}\omega_-^{-(n-\mu)/2}\mathrm{tr}(q_{\lambda\mu}\tilde{\rho}^{(n)}). \quad (21)$$

It is important to emphasize that Eq. (18) is not a usual low-ω expansion. Perturbation theory is used only for part of orbitals, while an exact diagonalization is employed for other. Thus, the method we have developed allows us to find correctly the nonaxial terms generating, as will be shown below, the staggering.

The next step is the transformation of the Routhian (18) to the space-fixed-frame energy in terms of the angular momentum by using the obvious expressions

$$\mathcal{E} = \mathcal{E}' - \omega_+\frac{\partial\mathcal{E}'}{\partial\omega_+} - \omega_-\frac{\partial\mathcal{E}'}{\partial\omega_-}, \quad I_\pm = -\frac{\partial\mathcal{E}'}{\partial\omega_\mp}. \quad (22)$$

For our purposes, we need only the rotational energy with accuracy to within quartic terms in the angular momentum. We start with the rotational frequencies ω_+ and ω_-, which can be obtained from the last of Eqs. (22) as power series in $I_\pm/\mathcal{J}$. The small parameter $\Gamma_2^{(2)}/\mathcal{J}$ simplifies calculations. The result with a reasonable accuracy is

$$\omega_\pm = \frac{I_\pm}{2\mathcal{J}} - \frac{I_+^2 + I_-^2}{8\mathcal{J}^3}\frac{\partial\Gamma_2^{(2)}}{\partial\omega_\mp} + 2I_\pm^2 I_\mp\mathcal{B} - \frac{I_\pm}{16\mathcal{J}^4}(I_\pm^2 + 3I_\mp^2)\Gamma_2^{(4)} - \frac{I_\mp^3}{4\mathcal{J}^4}\Gamma_4^{(4)}, \quad (23)$$

where the term with the partial derivative is caused by the ω dependence of the nonperturbative quantities $Q_{\lambda\mu}$. These values and the first of Eqs. (22) allow us to obtain the energy $\mathcal{E}$ as a power series in the angular momentum components I_+ and I_-. Finally, we have to quantize these components. The cranking approach allows us to do this with an accuracy of their commutators. In order to obtain correctly the term proportional to $\Gamma_2^{(4)}$, we use the time-reversal invariance and the D_2-group symmetry of the effective Hamiltonian (see [32]). The result for an isolated rotational band is

$$H_{\mathrm{eff}} = \mathcal{A}(\mathbf{I}^2 - I_3^2) + \mathcal{B}(\mathbf{I}^2 - I_3^2)^2 - \frac{\Gamma_2^{(2)}}{4\mathcal{J}^2}(I_+^2 + I_-^2) - \frac{\Gamma_2^{(4)}}{32\mathcal{J}^4}[I_+^2 + I_-^2; \mathbf{I}^2 - I_3^2]_+ - \frac{\Gamma_4^{(4)}}{16\mathcal{J}^2}(I_+^4 + I_-^4), \quad (24)$$

where $[\ldots]_+$ means an anticommutator and the parameters $\Gamma_\mu^{(n)}$ are the functions of $I/\mathcal{J}$.

The effective rotational Hamiltonian (24) is obtained by a $SU(2)$ mapping from the original fermion space to the rotor one. This method allows us to separate the rotational and the single-particle motion at the cost of nonadiabatic terms. For small spin I, when the values $Q_{\lambda\mu}$ are close to zero, Eq. (24) is reduced to the standard rotational Hamiltonian of axially symmetric nuclei, which is a power series of the operator $\mathbf{I}^2 - I_3^2$. It is easy to show that such a Hamiltonian does not lead to staggering. If a nucleus has a stable nonaxial deformation ε_{22}, the collective coordinates α_{22}, α_{42}, and α_{44} have ω-independent parts by analogy with $\alpha_{\lambda 0}^{(0)}$ [see Eq. (15)]. The rotational Hamiltonian then has the form of Eq. (24), but its nonaxial terms are greater than the ones for axial nuclei. A similar Hamiltonian was considered in [13], where it was shown that it generates the irregular $\Delta I = 2$ staggering. For the ε_{44} deformation, α_{44} is the only coordinate that involves an ω-independent part. Accordingly, the Hamiltonian has the C_{4v}-symmetric form used in [9].

3. SIMPLE ROTATIONAL REGIME WITH THE $\Delta I = 2$ STAGGERING

The Hamiltonian (24) is not fourfold-invariant. The terms with the operator $I_+^2 + I_-^2$ violate the C_{4v} symmetry. In order to prove that the nonaxial terms of the effective Hamiltonian are responsible for the $\Delta I = 2$ staggering, we consider the rotational regime with rotation about an axis perpendicular to the symmetry axis. Then, the terms proportional to I_3^2 and I_3^4 in Eq. (24) are smaller than the nonaxial ones and the rotational Hamiltonian takes the simplest form,

$$H_{\mathrm{eff}} = \mathcal{A}\mathbf{I}^2 + \mathcal{B}\mathbf{I}^4 + d(I_+^2 + I_-^2) + c(I_+^4 + I_-^4), \quad (25)$$

with the inertial parameters $\mathscr{A}$ and $\mathscr{B}$ of its regular part and the parameters of nonaxial terms

$$d = -\frac{1}{4\mathscr{I}^2}\left[\Gamma_2^{(2)} + I(I+1)\frac{\Gamma_2^{(4)}}{4\mathscr{I}^2}\right], \quad c = -\frac{\chi_4}{8\mathscr{I}^4}Q_{44}\alpha_{44}^{(4)}. \tag{26}$$

The nonaxial terms split a single band characteristic of an axial nucleus in a series of bands that correspond to different directions of the vector **I**. The Hamiltonian (25) is adequate only for the description of the yrast band, for which the angular momentum **I** is perpendicular to the symmetry axis. All other bands are separated from the yrast one by a large energy gap caused by the small nonaxial deformation induced by rotation. They are beyond the scope of our interest. The Hamiltonian is invariant under the D_2 point-symmetry group and under the transformation $d \longrightarrow -d$ with the simultaneous rotation through 90° about the 3-axis. The latter invariance allows us to consider only the negative values of d. The transformation $c \longrightarrow -c$ results in the inversion of multiplet levels (or bands). In order to investigate the staggering in the yrast band, we will consider the positive values of c.

We begin with the study of the rotational energy surface defined by the spin projections in the body-fixed frame,

$$I_1 = I\sin\theta\cos\varphi, \quad I_2 = I\sin\theta\sin\varphi. \tag{27}$$

Substituting these projections into the Hamiltonian (25), we obtain the energy surface

$$E(I,\theta,\varphi) = \mathscr{A}I^2 + \mathscr{B}I^4 + 2dI^2\sin^2\theta\cos 2\varphi + 2cI^4\sin^4\theta\cos 4\varphi \tag{28}$$

as a function of the spherical angles θ and φ and spin I. Depending on I, there are three possibilities for the arrangement of maxima, minima, and saddle points on this surface. They are shown in Fig. 1 for $d < 0$ and $c > 0$. Two or four equivalent minima in the equatorial plane provide the angular momentum **I** in the yrast band to be localized in the plane normal to the symmetry axis. As I increases, the quartic nonaxial term becomes comparable with the quadratic one and the stationary state with **I** directed along the 1-axis bifurcates at

$$I_c = \sqrt{\frac{|d|}{4c}} \tag{29}$$

to the C_{2v} symmetrical state, which has four minima and two saddle points. In turn, as I increases further, the saddle points are doubled at $I_{c1} = \sqrt{2}I_c$ and move off the equatorial plane. For higher I, when the last term of Eq. (28) becomes greater than the term proportional to $I_+^2 + I_-^2$, the four equivalent minima tend to form the C_{4v}-symmetric configuration. We are not interested in this high-I limit; instead, we consider the low-spin region $I < I_c$, where the C_4-symmetric term is small in relation to the C_2 one.

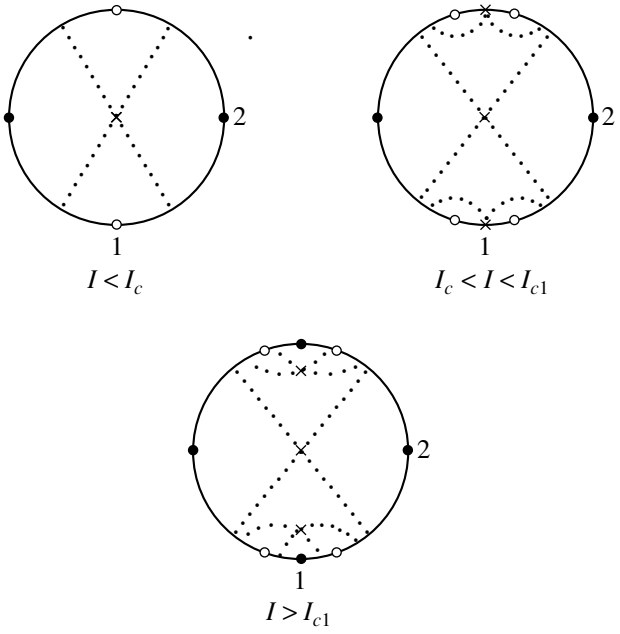

Fig. 1. Phase space of the Hamiltonian (25) for $c > 0$ and $d < 0$. Depending on the spin I, the rotational surface of the Hamiltonian has three possibilities for the arrangement of stationary points [maximum (●), minimum (○), and saddle point (×)]. In all cases, the minima corresponding to the yrast band lie on the equator. Only one view of the phase sphere is shown: we look from the direction of the 3-axis, and the positive 1- and 2-axes are labeled. The separatrices passing through saddle points are indicated by dotted lines.

Two sets of the equivalent classical trajectories surrounding the 1-axis inside the separatrices (see Fig. 1) correspond to the quantum states of a yrast band. The energy $E_0(I)$ of these states is determined by the Bohr quantization condition [33]

$$S_1(E) = \int_0^{2\pi} I_1(\phi, E)d\phi = 2\pi I, \tag{30}$$

where the ϕ-conjugate variable I_1 is the angular-momentum projection onto the quantization axis, i.e., the 1-axis. The energy levels of the band occur in degenerate pairs. The angular-momentum tunneling removes the degeneracy and leads to the C_{2v} doublets. Only a single totally symmetric state of the doublet is appropriate for the yrast SD band of even–even nuclei. Its energy is given by

$$E(I) = E_0(I) - 2|T|\cos\{\mathrm{Re}\,S_2(E_0)\}, \tag{31}$$

where

$$T = \left(\frac{\partial E}{\partial S_1}\right)_{E_0} e^{iS_2(E_0)}, \quad S_2(E) = \int_\gamma I_2(\phi, E)d\phi, \tag{32}$$

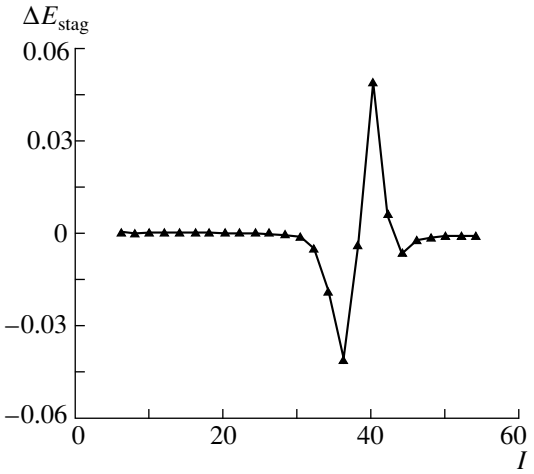

Fig. 2. Staggering plot for the yrast band of Hamiltonian (25) with the parameters $d/\mathcal{A} = -0.01$, $\mathcal{B}/\mathcal{A} = -4 \times 10^{-6}$, and $c/\mathcal{A} = 2 \times 10^{-6}$. The staggering-amplitude-independent reference is used (see main body of the text). Note that ΔE_{stag} is given in units of $\mathcal{A}$. The staggering begins from the spin $I_0 = 27$, where the tunneling amplitude (32) acquires a real part.

is the tunneling amplitude for the angular momentum precessing on one trajectory to leak over on another. The tunneling path γ, connecting the points on the equivalent trajectories where $I_2 = 0$, is a part of the great circle, which passes through the saddle point at the 3-axis. Since the angle ϕ is taken around the 2-axis, the representation of the Hamiltonian (25) should be used with the 2-axis as the axis of quantization. Transforming the Hamiltonian to new axes, we can estimate $S_2(E)$ for the classical minimum $E_{\min} = (\mathcal{A} + 2d)I^2 + (\tilde{\mathcal{B}} + 2c)I^4$. The action S_2 calculated in this way acquires a real part at $I_0 < I < I_c$, where

$$I_0 = (2-\sqrt{2})^{1/2} I_c = \left[(2-\sqrt{2})\frac{|d|}{4c}\right]^{1/2}. \qquad (33)$$

As spin I increases in this region, the second term of Eq. (31) changes its sign whenever the $\mathrm{Re}S_2$ value increases by π. Thus, we have irregular staggering with the phase inversion.

Figure 2 shows the staggering pattern obtained by the direct diagonalization of the Hamiltonian (25) for the I-independent parameters c and d. We use the reference found in [34] by analogy with the extraction of the pairing energy from nuclear masses:

$$\Delta E_{\text{stag}} = \frac{1}{2}[\Delta^3 E_\gamma(I-2) + 4\Delta^3 E_\gamma(I-4) + \Delta^3 E_\gamma(I-6)], \qquad (34)$$

where $\Delta^3 E_\gamma$ means the third derivative of $E_\gamma(I)$.

The above analysis shows that the staggering phenomenon is connected with the wave-function oscillations in the classically forbidden regions of the rotational-motion phase space. This effect is unusual for the Schrödinger equation and is the characteristic of a fourth-order wave equation. That is why the parameter c appears in the condition for the staggering behavior, which has the form

$$I > I_0, \quad c > 0. \qquad (35)$$

On the other hand, the term with the operator $I_+^2 + I_-^2$ breaks a fourfold symmetry and makes the staggering pattern irregular (see also [13]). In other words, the nonaxial terms of the Hamiltonian (25) crimp the rotational energy surface. The short-wave crimps near the stationary point (i.e., the axis of rotation) are important for staggering. However, the crimped surface does not yet solve the problem. The staggering may exist if the stationary point is a minimum, which happens for $c > 0$. For the negative value of this parameter, the staggering is absent in the yrast band but exists in the uppermost one. The sign of d is not important for staggering.

4. PARAMETERS OF THE EFFECTIVE HAMILTONIAN: ACTIVE AND INACTIVE ORBITALS

As was shown in the preceding section, the staggering effect depends strongly on the parameters of the Hamiltonian (25). Now, we consider these parameters, which are functions of the spin I and the occupation of single-particle states. At first, we address a more realistic model of a nucleus with Z protons and N neutrons. Assuming that the mean square radius and deformation are identical for neutrons and protons [35], we obtain the inequality

$$c = -\chi_4\left[\left(\frac{2Z}{A}\right)^{2/3} Q_{44}(\pi) + \left(\frac{2N}{A}\right)^{2/3} Q_{44}(\nu)\right] \times \left[\left(\frac{2Z}{A}\right)^{2/3} \tilde{\alpha}_{44}^{(4)}(\pi) + \left(\frac{2N}{A}\right)^{2/3} \tilde{\alpha}_{44}^{(4)}(\nu)\right] > 0, \qquad (36)$$

which will be used for the staggering analysis of SD bands in the next section.

The parameter c involves the perturbative, $\tilde{\alpha}_{44}^{(4)}$, and the nonperturbative, Q_{44}, factors. The latter has the form

$$Q_{44}(\tau) = \sum_s \langle s\tau | q_{44} | s\tau \rangle, \quad \tau = \pi, \nu, \qquad (37)$$

where the summation is performed over all occupied active single-particle states. In calculating these values, we use the eigenfunctions of Eq. (7), which, after performing the rotation of the intrinsic coordinate system through the angle η about the 3-axis ($\cos\eta = \omega_1/\omega$, $\omega = \sqrt{\omega_1^2 + \omega_2^2}$), take the form of a cranked shell-model potential:

$$(H_0 - \omega j_1)|s\tau\rangle = \varepsilon_{s\tau}|s\tau\rangle. \qquad (38)$$

We employ the realistic modified oscillator (MO) potential by using the GAMPN code [36]. The state s is

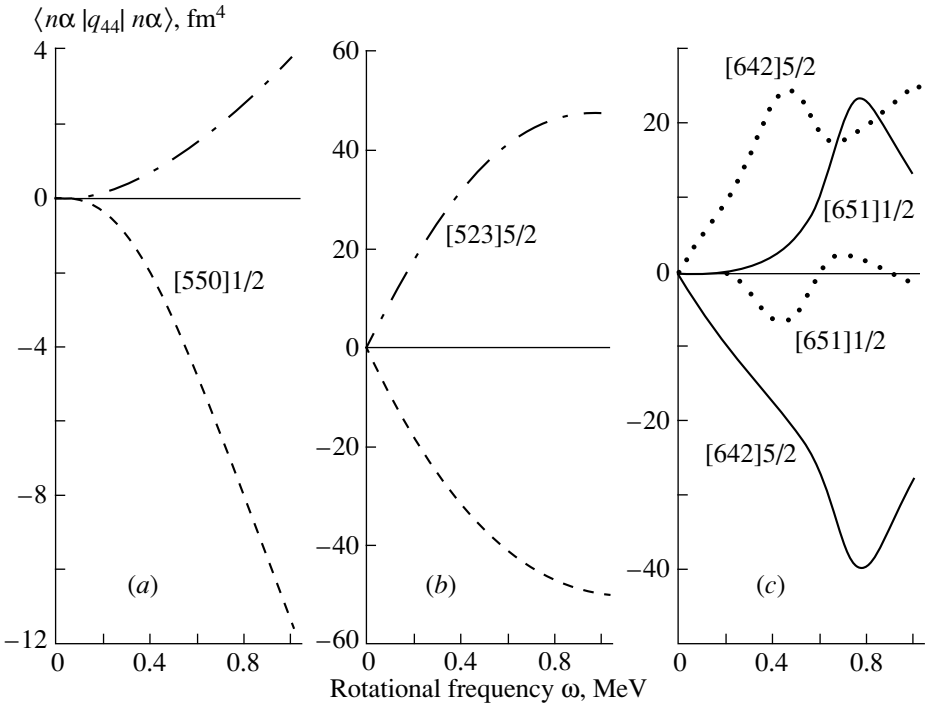

Fig. 3. Expectation values of the multipole moment $q_{44}(\mathbf{r})$ versus the rotational frequency ω for various single-neutron orbitals. The deformation parameters of $\varepsilon_2 = 0.555$ and $\varepsilon_4 = 0.026$ correspond to the calculated minimum energy of ^{149}Gd(1) at $I \approx 40$. The orbitals are labeled with the asymptotic quantum numbers $n = [Nn_3\Lambda]\Omega$. Their parity and signature α (+, +1/2), (+, –1/2), (–, +1/2), and (–, –1/2) are represented by solid, dotted, dashed, and dash-dotted lines, respectively.

characterized by the quantum numbers n and the signature α. For n, we will use the asymptotic quantum numbers $[Nn_3\Lambda]\Omega$ of a nonrotating nucleus. The κ and μ parameters of the MO potential have been taken from [37]. The expectation values $q_{44}(n\alpha\tau) = \langle n\alpha\tau|q_{44}|n\alpha\tau\rangle$ involved in Eq. (37) are calculated with the wave functions

$$\psi_{n\alpha} = \sum_{lj\Omega} a_{lj\Omega}^{n\alpha} |N_{\rm rot} lj\Omega\rangle \qquad (39)$$

of the cranking potential, where $N_{\rm rot}$ is the principal quantum number in the stretched rotating basis. The small coupling between different $N_{\rm rot}$ shells is neglected.

In order to single out the active orbitals, we have investigated how the expectation values $q_{44}(n\alpha)$ depend on the rotational frequency ω. All the single-particle states occupied by neutrons and protons in the $A \sim 150$ nuclei have been considered. The following conclusions can be drawn. (i) There are three different patterns of the ω dependence, which are shown in Fig. 3. Each of the patterns is associated with the specific types of orbitals. (ii) The perturbative (Fig. 3*a*) and nonperturbative (Fig. 3*b*) dependences are associated with orbitals inactive and active for staggering, respectively. These orbitals are the same for neutrons and protons. (iii) The set of active orbitals is supplemented with the inactive states interacting with the active ones. The orbitals [642]5/2 and [651]1/2 placed above the neutron gap at $N = 80$ represent a classical example of an avoided level crossing [38]. Figure 3*c* shows q_{44} as a function of ω for the two signature branches of these orbitals. According to the Strutinsky prescription, we use a renormalization factor of 1.27 to have the possibility of a comparison with the observed rotational frequencies. At a low frequency, the [651]1/2 orbitals are inactive, whereas, at a high frequency, they involve a large admixture of the active, [642]5/2, orbitals and have the nonperturbative dependence for q_{44}.[3)] These interacting orbitals with the positive signature carry considerable hexadecapole moment. Thus, the removal or addition of a neutron in these states may change the sign of the left part in inequality (36). Other active states induced by an avoided crossing make a moderate contribution to the quantity $Q_{44}(\pi)$ or $Q_{44}(\nu)$. Let us note the orbitals π[402]1/2 and π[301]1/2 with both signatures, which are active for virtually all frequencies because their avoided crossings with the orbitals ν[422]3/2 and ν[303]5/2, respectively, occur at low frequencies. All the considered pairs of interacting states belong to the same $N_{\rm rot}$ shell. The coupling between different $N_{\rm rot}$ shells generates the avoided crossings, which change the moments q_{44} only slightly due to a small interaction.

The set of states active for staggering is shown in Fig. 4. These are not necessarily intruder orbitals but all

[3)]The orbitals are followed adiabatically.

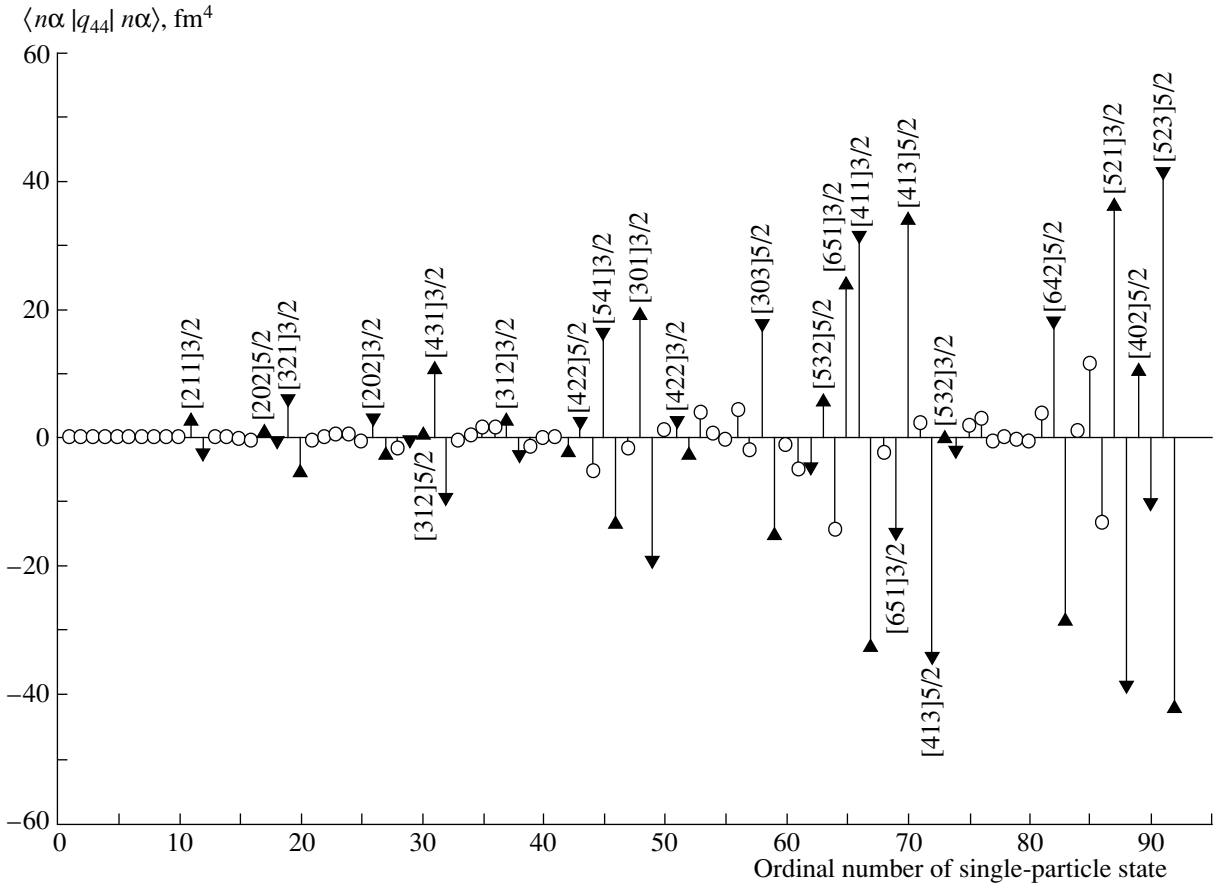

Fig. 4. Nonaxial hexadecapole moments of active (filled triangles) and inactive (empty circles) neutron orbitals versus the ordinal number of a single-particle state in the cranking modified oscillator potential for the rotational frequency of ω = 0.8 MeV. The asymptotic quantum numbers $[Nn_3\Lambda]\Omega$ label the active states with the signature α = +1/2 (upward-oriented triangles) and –1/2 (downward-oriented triangles). The deformation-parameter values are identical to those in Fig. 3.

have the asymptotic quantum numbers Ω = 3/2 and 5/2. Compared to inactive orbitals, active ones carry large q_{44} values, which are nevertheless smaller than the hexadecapole q_{40} moment of the single-particle states around the SD core of ^{152}Dy [39]. As a rule, the moments of the states with the same asymptotic quantum numbers have close absolute values and opposite signs for different signatures. They almost offset each other. Thus, the contribution of the active orbitals to the total nonaxial hexadecapole moment has the same order of magnitude as that of inactive ones. Consequently, the equilibrium deformation ε_{44} at high rotational frequencies is small [17–19].

To explain these findings, let us consider a cranking isolated j shell with the Hamiltonian

$$H_j = H_{j0} + \kappa_0 j_3^2 - \omega j_1, \tag{40}$$

where H_{j0} is the spherical part and κ_0 is proportional to an axial quadrupole deformation. Assuming the small rotational frequency ω, we shall use perturbation theory with the unperturbed function in the signature representation

$$u_{j\Omega\alpha} = (|j\Omega\rangle + e^{i\pi(j-\alpha)}|j-\Omega\rangle)/\sqrt{2}. \tag{41}$$

There are the two types of states in the limit of small rotational frequencies ω. Those with Ω = 3/2 and 5/2 generate q_{44}, which are proportional to ω,

$$q_{44}(j\,3/2\,\alpha) = -q_{44}(j\,5/2\,\alpha) = \frac{\omega}{\kappa_0}\langle\|q_4\|\rangle f(j)e^{i\pi(j-\alpha)}, \tag{42}$$

where the form of the positive definite function f is immaterial for us. For states with other Ω, the first nonvanishing contribution to $q_{44}(j\Omega\alpha)$ is proportional to higher powers of ω and, consequently, is small. Figures 3*a* and 3*b* show this distinction in the ω dependence, which becomes more obvious at high frequencies. The equality (42) also explains the signature dependence of the values q_{44} for almost all active orbitals shown in Fig. 4 because they are mostly high-j intruder or high-j ones with a rather good quantum number j. An anomalous signature dependence is observed for the five states with small j.

The second factors, $\tilde{\alpha}_{44}^{(4)}(\tau)$, depend smoothly on the number and the configuration of nonperturbative orbitals. This allows us to adopt the approximation

Table 1. Parameters of the Hamiltonian (25) that were calculated with an axially deformed oscillator potential for superdeformed and normal deformed bands [in obtaining numerical data, we have used the following estimates for the pairing gap Δ and the moment of inertia $\mathcal{J}$: $\Delta/\omega_0 \sim A^{-1/3}$ and $\omega_0\mathcal{J} \sim A^{4/3}$, where $\omega_0 = 41A^{-1/3}$ MeV is the deformation-independent oscillator frequency and $A \sim 150$ is the number of nucleons; the function $f(\omega_0/\Delta)$ is characteristic of SD nuclei with pairing correlations, $f(x) = x^{-2}\ln x$]

Parameters	$\mathcal{B}/\mathcal{A}$	$d/\mathcal{A}$	$c/\mathcal{A}$
SD band without pairing	$A^{8/3}/(\omega_0\mathcal{J})^4 \sim 10^{-6}$	$A^{5/3}/(\omega_0\mathcal{J})^2 \sim 10^{-2}$	$A^{5/3}/(\omega_0\mathcal{J})^4 \sim 10^{-8}$
SD band with pairing	$fA^{10/3}/(\omega_0\mathcal{J})^4 \sim 10^{-6}$	$fA^{5/3}/(\omega_0\mathcal{J})^2 \sim 10^{-4}$	$fA^{7/3}/(\omega_0\mathcal{J})^4 \sim 10^{-8}$
ND band with pairing	$A^{8/3}/(\Delta\mathcal{J})^4 \sim 10^{-3}$	$A^{4/3}/(\Delta\mathcal{J})^2 \sim 10^{-2}$	$A^{2}/(\Delta\mathcal{J})^4 \sim 10^{-5}$

$\tilde{\alpha}^{(4)}_{44}(\tau) \approx \xi_\tau \alpha^{(4)}_{44}(\tau)$[4], where ξ_τ is the fraction of the filled inactive states. The same estimations remain true for the perturbative values $\tilde{\alpha}^{(n)}_{\lambda 2}(\tau)$ entering into the parameter d. Thus, the problem is reduced to obtaining the corrections to the nuclear density matrix of the second and the fourth orders in the perturbation V (13). In order to simplify the calculations, the Green's function method is used. For independent nucleons, we have the following expressions for these values in the representation of Eq. (14):

$$\rho^{(2)}_{13} = \sum_2 \int_C \frac{d\varepsilon}{2\pi i} G_1(\varepsilon) V_{12} G_2(\varepsilon) V_{23} G_3(\varepsilon),$$
$$\rho^{(4)}_{15} = \sum_{2,3,4} \int_C \frac{d\varepsilon}{2\pi i} G_1 V_{12} G_2 V_{23} G_3 V_{34} G_4 V_{45} G_5, \quad (43)$$

where the unperturbed Green's function is

$$G_1(\varepsilon) = \frac{1}{\varepsilon - \varepsilon_1 + i\delta(1-2n_1)}, \quad \delta \longrightarrow +0, \quad (44)$$

and the contour C is located in the upper half-plane of the complex ε plane. The occupation numbers n_1 refer to a nonrotating nucleus. The Green's function in the presence of pairing correlations is more complicated than that in (44), but Eqs. (43) remain valid (see [29, 30]).

The estimation of the quantities $\alpha^{(n)}_{\lambda\mu}$ is based on modeling the real self-consistent nuclear field of Eq. (14) with the axially deformed harmonic-oscillator potential with the frequencies ω_3 along the symmetry axis and $\omega_\perp$ in the perpendicular plane. Being tested by evaluating macroscopic quantities such as the rotational constants $\mathcal{A}$ [40] and $\mathcal{B}$ [29] for normally deformed (ND) bands, the oscillator potential has the advantage that $\alpha^{(n)}_{\lambda\mu}$ can be expressed analytically in terms of the quantities $\sum(n_\perp + 1)$, $\sum(n_3 + 1/2)$, $\sum(n_\perp + 1)^2$, etc., where $n_\perp = N - n_3$, and n_3 are the quantum numbers (we use the representation $[Nn_3\Lambda]$) and the summation is performed over all occupied states. It also allows us to use the self-consistent doubly-stretched multipole interaction for the determination of the strength constants χ_2 and χ_4 [41]. The semiclassical summation of the above quantities makes it possible to find their A dependences.

First of all, it is interesting to study the expression for the perturbative factor of the parameter c. Using the small ratio $(\omega_\perp - \omega_3)/(\omega_\perp + \omega_3)$, one obtains

$$\alpha^{(4)}_{44} = \sqrt{\frac{35}{32\pi}} \frac{9}{64M^2\omega_\perp^4\omega_3^2}\left(\frac{\omega_\perp + \omega_3}{\omega_\perp - \omega_3}\right)^4 \times (3\Sigma_{33} - 12\Sigma_{\perp 3} + 3\Sigma_{\perp\perp} - \Sigma_{\Lambda\Lambda}), \quad (45)$$

where M is the nucleon mass and Σ_{ik} are the sums of the bilinear combinations of the oscillator quantum numbers $n_\perp$, n_3, and Λ over occupied orbitals. In the semiclassical approximation, we have

$$4\Sigma_{\perp\perp} = 3\Sigma_{33}, \quad 2\Sigma_{\perp 3} = \Sigma_{33}, \quad 4\Sigma_{\Lambda\Lambda} = \Sigma_{33} \text{ for SD bands;}$$
$$\Sigma_{\perp\perp} = 3\Sigma_{33}, \quad \Sigma_{\perp 3} = \Sigma_{\Lambda\Lambda} = \Sigma_{33} \text{ for ND bands.} \quad (46)$$

Thus, the quantity $\tilde{\alpha}^{(4)}_{44}$ is negative for both ND and SD bands.

The perturbative factors of the parameter d are calculated analogously. Table 1 shows the results of the calculations for the parameters $\mathcal{B}$, c, and d in units of $\mathcal{A} = \varepsilon_F A^{-5/3}$, where ε_F is the Fermi energy. The second inertial parameter $\mathcal{B}$ representing the axial part of the Hamiltonian (25) does not affect the staggering. We need it only as a reference point in the calculation of c and d. It is well known that the interaction of rotation with quasiparticle motion and attenuation of pairing correlations make the main contributions to $\mathcal{B}$ for the ND bands [30]. The quenching of the pairing gap leads to the decrease in $\mathcal{B}$ by a factor of $A^{2/3}$ [42]. On the other hand, the static pairing plays a limiting role in the SD bands [43]. Thus, the estimates of the parameters c and d shown in the first line of Table 1 seem to be more relevant to SD bands.

[4] There is no difference between active and inactive states in the quantity $\alpha^{(4)}_{44}(\tau)$.

Table 2. Total moment Q_{44} of the neutron and proton active orbitals, sign of the coefficient c, and staggering significance Y for the SD bands with the known equilibrium deformation for three rotational frequencies ω (MeV) (the subscripts + and – denote the sign of the signature $\alpha = \pm 1/2$; the standard notation is used for intruder orbitals)

Band	Configuration (relative to ^{149}Gd(1))	Q_{44}, $(\hbar/M\omega_0)^2$			Sign of c	Y
		ω = 0.4	ω = 0.6	ω = 0.8		
^{147}Gd(2)	$\nu\left[642\frac{5}{2}\right]_+^{-1}\nu\left[651\frac{1}{2}\right]_+^{-1}$	0.891	1.161	1.194	>0	0.05
^{147}Gd(3)	$\nu\left[651\frac{1}{2}\right]_+^{-1}\nu 7_1^{-1}$	0.389	0.485	0.443	>0	0.15
^{147}Gd(4)	$\nu\left[411\frac{1}{2}\right]_+^{-1}\nu\left[651\frac{1}{2}\right]_+^{-1}$	0.284	0.195	–0.341	<0	0.16
^{148}Gd(1)	$\nu\left[651\frac{1}{2}\right]_+^{-1}$	0.235	0.199	–0.264	<0	0.23
^{148}Gd(3)	$\nu 7_1^{-1}$	0.197	0.361	0.270	>0	0.1
^{148}Gd(4)	$\nu\left[642\frac{5}{2}\right]_+^{-1}$	1.011	1.131	2.059	>0	0.98
^{148}Gd(6)	$\nu\left[411\frac{1}{2}\right]_+^{-1}$	0.337	0.369	0.683	>0	3.1
^{149}Gd(1)		0.321	0.227	0.505	>0	2.3
^{149}Gd(5)	$\nu\left[402\frac{5}{2}\right]_+\nu\left[651\frac{1}{2}\right]_+^{-1}$	0.344	0.456	0.600	>0	
^{149}Gd(6)	$\nu\left[402\frac{5}{2}\right]_-\nu\left[651\frac{1}{2}\right]_+^{-1}$	–0.112	–0.297	–0.516	<0	
^{150}Gd(1)	$\nu 7_2$	–0.079	0.112	0.625	>0	0.5
^{150}Gd(4a)	$\nu\left[402\frac{5}{2}\right]_+$	0.485	0.316	0.864	>0	
^{150}Gd(4b)	$\nu\left[402\frac{5}{2}\right]_-$	0.025	–0.442	–0.265	<0	1.0
^{151}Tb(1)	$\pi 6_3\nu 7_2$	0.776	1.320	1.477	>0	
^{152}Dy(1)	$\pi 6_3\pi 6_4\nu 7_2$	–0.040	0.618	0.784	>0	
^{153}Dy(1)	$\pi 6_3\pi 6_4\nu 7_2\nu 7_3$	0.915	1.317	1.382	>0	

The parameters obtained allow us to find the critical spin with which the $\Delta I = 2$ staggering starts. In the context of the rotational regime of the Hamiltonian (25), we have the following values in the $A \sim 150$ mass region: $I_0 \sim 400$ for the SD nuclei without pairing, $I_0 \sim 40$ for the SD nuclei with pairing, and $I_0 \sim 10$ for the ND nuclei with pairing.

5. ANALYSIS OF $\Delta I = 4$ BIFURCATION IN $A \sim 150$ SUPERDEFORMED NUCLEI

In a similar way as in [26], we now check the criterion (36), bearing in mind that this condition is necessary but insufficient. The estimations of the preceding section show that the third multiplier on the left-hand side of Eq. (36) is negative. The straightforward calculation of the perturbative quantity $\tilde{\alpha}_{44}^{(4)}$ in the MO model confirms this result. Thus, we will be interested only in the sign of the second multiplier

$$Q_{44} = \left(\frac{2Z}{A}\right)^{2/3} Q_{44}(\pi) + \left(\frac{2N}{A}\right)^{2/3} Q_{44}(\nu), \qquad (47)$$

where the moments $Q_{44}(\pi)$ and $Q_{44}(\nu)$ are calculated by using additivity of contributions from individual orbitals according to Eq. (37). The main difficulty in this

Table 3. As in Table 2, but for the SD bands whose deformations ε and ε_4 were estimated by using the additivity principle

Band	Configuration (relative to ^{149}Gd(1))	ω, MeV	ε	ε_4	Q_{44}, $(\hbar/M\omega_0)^2$	Sign of c	Y
^{147}Eu(1)	$\pi\left[301\frac{1}{2}\right]_-^{-1}\nu\left[651\frac{1}{2}\right]_+^{-1}$	0.8	0.554	0.043	−0.117	<0	0.95
^{147}Eu(3)	$\pi\left[301\frac{1}{2}\right]^{-2}\pi 6_3\nu\left[651\frac{1}{2}\right]_-^{-1}$	0.8	0.573	0.047	1.191	>0	0.58
^{148}Eu(1)	$\pi\left[301\frac{1}{2}\right]_-^{-1}$	0.8	0.564	0.042	0.617	>0	2.3
^{148}Gd(5)	$\pi\left[301\frac{1}{2}\right]^{-2}\pi 6_3\pi 6_4\nu\left[411\frac{1}{2}\right]^{-2}\nu 7_2$	0.8	0.619*	0.037*	0.010	>0	2.8
^{150}Gd(2)	$\pi\left[301\frac{1}{2}\right]^{-2}\pi 6_3\pi 6_4\nu 7_2$	0.8	0.608	0.042	0.743	>0	0.14
^{150}Gd(8a)	$\pi\left[301\frac{1}{2}\right]_-^{-1}\pi 6_3\nu\left[402\frac{5}{2}\right]_-$	0.8	0.553	0.029	0.549	>0	0.13
^{150}Gd(8b)	$\pi\left[301\frac{1}{2}\right]_-^{-1}\pi 6_3\nu\left[402\frac{5}{2}\right]_+$	0.8	0.553	0.029	1.719	>0	
^{151}Gd(1a)	$\nu 7_2\nu\left[402\frac{5}{2}\right]_+$	0.6	0.545	0.012	0.480	>0	1.8
^{151}Gd(1b)	$\nu 7_2\nu\left[402\frac{5}{2}\right]_-$	0.6	0.545	0.012	−0.280	<0	0.25
^{152}Tb(1)	$\pi 6_3\nu 7_2\nu\left[402\frac{5}{2}\right]_+$	0.6	0.554	0.012	1.051	>0	
^{152}Tb(2)	$\pi 6_3\nu 7_2\nu\left[402\frac{5}{2}\right]_-$	0.6	0.554	0.012	0.276	>0	
^{152}Dy(4)	$\pi 6_3\pi 6_4\nu\left[402\frac{5}{2}\right]_-$	0.6	0.551	0.015	−0.387	<0	
^{152}Dy(5)	$\pi 6_3\pi 6_4\nu\left[402\frac{5}{2}\right]_+$	0.6	0.551	0.015	0.394	>0	
^{153}Dy(2)	$\pi 6_3\pi 6_4\nu 7_2\nu\left[402\frac{5}{2}\right]_-$	0.6	0.562	0.009	−0.362	<0	
^{153}Dy(3)	$\pi 6_3\pi 6_4\nu 7_2\nu\left[402\frac{5}{2}\right]_+$	0.6	0.562	0.009	0.421	>0	

* The deformation parameters were taken from [45].

calculation is the nuclear equilibrium deformation since the shape trajectories in the $(\varepsilon, \varepsilon_4)$ plane are known for a limited number of SD bands. Starting with these bands, we give, in Table 2, the estimated values of Q_{44} for three rotational frequencies. The corresponding parameters ε and ε_4 have been taken from [44] (^{147}Gd), [45, 46] (^{148}Gd), [47] (^{149}Gd), [48] (^{150}Gd, ^{151}Tb, $^{152, 153}$Dy), and [49] (^{150}Gd (4a, 4b)). The present analysis has an advantage because the sign of c can be compared with the staggering significance Y found in [28]. According to that study, the significance is equal to the mean staggering amplitude divided by its uncertainty. It is highly unlikely that all the bands with the significance $Y > 2$ exhibit the $\Delta I = 4$ bifurcation only because of statistical fluctuations in the γ-ray energy measurements. In particular, the independent measurements of

Table 4. Deformation changes induced by a nucleon in a fixed single-particle state (only these orbitals are necessary to estimate the deformation parameters of the SD bands presented in Table 3; with the exception of the state π[301]1/2, all values have been extracted from pairs of bands in adjacent nuclei with an extra nucleon in the indicated orbital)

Orbital	ω = 0.6 MeV		ω = 0.8 MeV		Source
	δε	$\delta\varepsilon_4$	δε	$\delta\varepsilon_4$	
$\pi\left[301\frac{1}{2}\right]_+$	−0.013	−0.008	−0.014	−0.009	^{149}Gd(4) vs ^{150}Gd(1)
$\pi\left[301\frac{1}{2}\right]_-$	−0.012	−0.007	−0.013	−0.008	^{149}Gd(3) vs ^{149}Gd(1)
$\pi\left[651\frac{3}{2}\right]_+$	0.009	−0.001	0.009	0.000	^{151}Tb(1) vs ^{150}Gd(1)
$\pi\left[651\frac{3}{2}\right]_-$	0.008	−0.003	0.009	−0.004	^{152}Dy(1) vs ^{151}Tb(1)
$\nu\left[651\frac{1}{2}\right]_-$	0.010	0.002	0.009	0.003	^{149}Gd(1) vs ^{148}Gd(2)
	0.011	−0.001	0.009	0.001	^{148}Gd(1) vs ^{147}Gd(1)
$\nu\left[770\frac{1}{2}\right]_+$	0.011	−0.006	0.012	−0.004	^{150}Gd(1) vs ^{149}Gd(1)

the ^{149}Gd(1) staggering conclusively demonstrate the existence of the effect. We use this band as a reference for the single-particle structures of all the bands studied in this work.

Table 3 presents the bands without calculated deformation. In their analysis, we have used the observation of [37] that the filling of any particular orbital always induces the same deformation change in different nuclei. Subsequently, this feature has been explained by the additivity of quadrupole and hexadecapole moments for SD bands in the $A \sim 150$ mass region [39, 50]. In a similar way as in the cited works, we find the deformation changes δε and $\delta\varepsilon_4$ induced by a nucleon in the given state. The corresponding values are presented in Table 4 for the two rotational frequencies. They are used to evaluate the parameters ε and ε_4 of the bands collected in Table 3. The bands ^{150}Gd(6a, 6b) are omitted in this table because the deformation changes induced by the orbital ν[514]9/2 are not known.

Tables 2 and 3 help to understand which property of the single-particle structure is responsible for the $\Delta I = 4$ bifurcation. First of all, we emphasize that the necessary condition (36) is not violated in either of the bands with the known staggering significance. This is not a trivial fact because of the double cancellations in the expression Q_{44}: the partial cancellation of the $q_{44}(n\alpha)$ values with different signatures and the partial cancellation of the quantities $Q_{44}(\pi)$ and $Q_{44}(\nu)$ for almost all these bands. As a direct consequence of these cancellations, the value Q_{44} for some bands with the small significance Y changes sign and becomes negative for high rotational frequencies. The zero point of Q_{44} depends not only on the deformed shell-model potential but also on the frequency renormalization factor, for which we take the conventional value of 1.27. With such scaling, the criterion (36) seems unreliable for small frequencies. Thus, we use the high frequencies (ω = 0.6 and 0.8 MeV) to compare the staggering criterion with the experimental significance.

While Tables 2 and 3 exhibit definitely the correlations between the sign of the parameter c and the significance Y, they also show some discrepancies. The high positive value of Q_{44} in the bands ^{147}Gd(2) and ^{148}Gd(4) is the consequence of the neutron hole in the state ν[642]5/2 (α = 1/2), which has, according to Table 5, the large negative q_{44}. The same effect is produced by the orbital $\pi 6_3$ in the bands ^{147}Eu(3) and ^{150}Gd(8a). The discrepancies observed in the bands ^{147}Gd(3) and ^{148}Gd(3) are less evident. Among the bands under study, only these bands have the empty state $\nu 7_1$. It is possible that the first intruder plays the crucial role in the phenomenon (let us recall that the criterion (36) is only necessary). This tentative conclusion is confirmed by the nonstaggering bands ^{150}Gd(1, 2), ^{151}Tb(1), and ^{152}Dy(1), but it disagrees with the staggering bands ^{148}Gd(5) and ^{151}Gd(1a). The first intruder is blocked up by the second one, $\nu 7_2$, in these bands (see also [2]). Let us also note that the first proton intruder $\pi 6_1$ is blocked up in all the bands under study.

From a strictly logical point of view, a better test of the inequality (36) is provided by the pairs of the bands with configurations that differ by a single nucleon

Table 5. Expectation values $\langle\tau|q_{44}|\tau\rangle$ (in $(\hbar/M\omega_{0\tau})^2$, $\tau = \pi, \nu$) of the active states involved in the configurations of the bands with a known staggering significance Y (all the quantities were calculated for the fixed rotational frequency of $\omega = 0.8$ MeV; a blank space means that the corresponding orbital is inactive in a given band)

Band	Proton states				Neutron states						
	$\pi\left[301\frac{1}{2}\right]_+$	$\pi\left[541\frac{1}{2}\right]_-$	$\pi\left[651\frac{3}{2}\right]_+$	$\pi\left[651\frac{3}{2}\right]_-$	$\nu\left[541\frac{1}{2}\right]_-$	$\nu\left[523\frac{7}{2}\right]_+$	$\nu\left[651\frac{1}{2}\right]_+$	$\nu\left[651\frac{1}{2}\right]_-$	$\nu\left[642\frac{5}{2}\right]_+$	$\nu\left[402\frac{5}{2}\right]_+$	$\nu\left[402\frac{5}{2}\right]_-$
^{147}Eu(1)	0.153		0.817	−0.204			0.731	−0.022	−1.394	0.609	−0.583
^{147}Eu(3)			0.824	−0.341			0.837	0.041	−1.494	0.623	−0.597
^{148}Eu(1)	0.166		0.834	−0.353			0.856	0.028	−1.521	0.614	−0.588
^{147}Gd(2)	−0.012		0.848	−0.183			0.765	−0.070	−1.442	0.588	−0.561
^{147}Gd(3)	0.081		0.767	0.175*	0.143	−0.402		−0.159	−1.180	0.597	−0.570
^{147}Gd(4)	0.064		0.859	−0.321			0.872	−0.007	−1.549	0.560	−0.573
^{148}Gd(1)	0.044		0.842	−0.231			0.790	−0.042	−1.463	0.597	−0.570
^{148}Gd(3)	0.091		0.801	−0.038				−0.090	−1.303	0.602	−0.575
^{148}Gd(4)	0.006		0.865	−0.334			0.888	−0.015	−1.570	0.594	−0.567
^{148}Gd(5)			0.877	−0.673			−0.664		0.071	0.639	−0.613
^{148}Gd(6)	0.080	0.290	0.873	−0.449			0.976	0.042	−1.652	0.605	−0.578
^{149}Gd(1)	0.061		0.858	−0.376			0.914	0.011	−1.591	0.603	−0.576
^{150}Gd(1)	0.058	0.726	0.886	−0.558			0.947	0.084	−1.620	0.606	−0.579
^{150}Gd(2)			0.862	−0.637			0.372	0.167	−0.991	0.640	−0.613
^{150}Gd(4b)	−0.157		0.892	−0.422			0.986	−0.012	−1.683	0.578	−0.551
^{150}Gd(8a)	0.008	0.401	0.881	−0.491			1.004	0.045	−1.685	0.599	−0.572
^{151}Gd(1a, 1b)	−0.165	0.769	0.919	−0.587			0.989	0.065	−1.684	0.582	−0.554
^{151}Tb(1)	0.089		0.892	−0.606			0.764	0.113	−1.427	0.615	−0.588
^{152}Dy(1)	0.077	−0.356	0.908	−0.666			0.408	0.149	−1.057	0.620	−0.592

* Strongly disturbed orbital.

Table 6. Test of the staggering criterion for the fixed rotational frequency $\omega = 0.8$ MeV by employing the relative moment ΔQ_{44} of the band A with respect to the reference band B [the symbol + or – is used to show whether the staggering significance of the band A agrees or disagrees with the sign of Q_{44}(A) obtained from Eqs. (48) and (51); a blank space means that such a comparison is impossible; it is assumed that the sign of Q_{44}(B) is unchanged if $|\Delta Q_{44}| < 0.5$]

A \ B	^{148}Eu(1)	^{148}Gd(6)	^{149}Gd(1)	^{151}Gd(1a)	^{147}Gd(2)	^{147}Gd(3)	^{148}Gd(3)	^{150}Gd(2)	^{150}Gd(8a)	^{147}Gd(4)	^{148}Gd(1)	^{151}Gd(1b)
^{148}Eu(1)		+	+		–	–	–	–	–			
^{148}Gd(6)	+		+	+	–	–	–	–	–			
^{149}Gd(1)	+	+			–	–	–	–	–			
^{151}Gd(1a)	+	+	+		–			–				
^{147}Gd(2)	–	–	–	–				+				
^{147}Gd(3)	–	–	–		+		+	+	+			+
^{148}Gd(3)	–	–	–		+	+		+	+			+
^{150}Gd(2)	–	–	–	–	+	+	+		+			
^{150}Gd(8a)	–	–	–		+	+	+	+				
^{147}Gd(4)					+	+	+	+	+		+	+
^{148}Gd(1)					+	+	+	+	+	+		+
^{151}Gd(1b)					+	+	+	+	+	+	+	

occupying an active or an inactive orbital. The filling of the inactive orbital $\pi[301]1/2$ ($\alpha = -1/2$) does not change Q_{44}. Therefore, any pair of the identical bands ^{147}Eu(1)/^{148}Gd(1), ^{148}Eu(1)/^{149}Gd(1) has identical staggering properties. The same is true for the identical bands ^{147}Gd(4)/^{148}Gd(1) and ^{148}Gd(6)/^{149}Gd(1), whose configurations are distinguished by a neutron in the state [411]1/2 ($\alpha = -1/2$). This finding explains the observation of the staggering effect in identical SD bands [21]. Similarly, the two identical bands ^{150}Gd(2)/^{152}Dy(1), whose configurations differ by the two [301]1/2 protons, do not stagger. An exception is the band ^{148}Gd(5) exhibiting clear evidence for staggering. Its configuration is the same as those for the bands ^{150}Gd(2) or ^{152}Dy(1) apart from two neutron holes in the state [411]1/2 or the two [411]1/2 neutron and two [301]1/2 proton holes, respectively. Nevertheless, statistically significant staggering has not been observed in the latter bands. One would suppose that the superposition principle does not work in this case. This suggestion is confirmed by the large nonaxial deformation of ^{148}Gd(5) found in the calculations performed in [51].

The active orbitals give us a more rigorous verification of the theory. A nucleon occupying this state contributes significantly to the quantity Q_{44} and may change its sign. Table 5 shows the estimated values q_{44} for some active orbitals involved in the configurations of almost all the studied bands. The orbital $\nu[651]1/2$ ($\alpha = 1/2$) is one such example. Starting with the staggering bands ^{148}Eu(1), ^{148}Gd (6), and ^{149}Gd(1) and removing a neutron from this orbital, we get the bands, respectively, ^{147}Eu(1), ^{147}Gd(4), and ^{148}Gd(1), which do not stagger. Thus, this active orbital explains the remarkable property of the $\Delta I = 4$ bifurcation observed in [23].

At the next step, we consider the signature partner bands based on the state $\nu[402]5/2$, which is associated with the generation of identical bands. The corresponding active orbitals have reasonably large values of the moment q_{44} to modify the inequality in (36). Consequently, a pair of identical bands may have different staggering properties. The example is the band ^{150}Gd(4b), which is identical to ^{149}Gd(1), but which does not exhibit staggering because the state $\nu[402]5/2$ ($\alpha = -1/2$) has the large negative value q_{44}. Its signature partner, ^{150}Gd(4a), should stagger. Other examples of the signature partner bands involving this state are shown in Tables 2 and 3.

We now extend this procedure to the two bands with the configurations that differ by an arbitrary number of particles and holes in active and inactive orbitals. For a fixed rotational frequency, the Q_{44} values of the two bands A and B are related by the equality

$$Q_{44}(\mathrm{A}) = Q_{44}(\mathrm{B}) + \delta Q_{44} + \delta Q_{44}^{\mathrm{def}}, \qquad (48)$$

where δQ_{44} is the contribution resulting from the difference in active orbitals, while $\delta Q_{44}^{\mathrm{def}}$ represents the contribution due to the deformation change induced by both active and inactive orbitals. According to the additivity of multipole moments, the former quantity can be written as

$$\delta Q_{44} = \sum_a q_{44}(a), \qquad (49)$$

where a runs over the active particle and/or hole states, which define the intrinsic configuration of the band A with respect to the band B (the reference band). Since the contributions δQ_{44} and $\delta Q_{44}^{\mathrm{def}}$ may be comparable, we have used the values Q_{44} listed in Tables 2 and 3 to evaluate the relative nonaxial moment of active orbitals,

$$\Delta Q_{44} = \delta Q_{44} + \delta Q_{44}^{\mathrm{def}} = Q_{44}(\mathrm{A}) - Q_{44}(\mathrm{B}). \qquad (50)$$

These quantities, along with the staggering significances Y_{A} and Y_{B}, allow us to obtain a more sophisticated test of the staggering criterion.

We have first selected 12 bands having the proper staggering significances to deal with the sample involving staggering ($Y \geq 1.8$) and nonstaggering ($Y \leq 0.25$) bands with a reasonably high likelihood. According to Eqs. (36) and (47), the former are characterized by the value $Q_{44} > 0$ and the latter have $Q_{44} < 0$. To compare the staggering properties of the bands A and B, we consider the two strong inequalities

$$Q_{44}(\mathrm{B}) + \Delta Q_{44} > 0 \ \text{ if } \ Y_\mathrm{B} \geq 1.8 \ \text{ and } \ \Delta Q_{44} > 0,$$
$$Q_{44}(\mathrm{B}) + \Delta Q_{44} < 0 \ \text{ if } \ Y_\mathrm{B} \leq 0.25 \ \text{ and } \ \Delta Q_{44} < 0. \quad (51)$$

For other combinations of the values Y_B and ΔQ_{44}, the sign of the sum $Q_{44}(\mathrm{B}) + \Delta Q_{44}$ becomes indefinite unless $|\Delta Q_{44}| < |Q_{44}|$. Let us consider, for example, the bands ^{148}Gd(1) with $Y_\mathrm{A} = 0.23$ and ^{147}Gd(3) with $Y_\mathrm{B} = 0.25$, for which $\Delta Q_{44} = -0.71$. According to Eq. (48) and to the second inequality (51), we have $Q_{44}(\mathrm{A}) < 0$, which is in agreement with the absence of staggering in the band ^{148}Gd(1). On the other hand, considering ^{148}Gd(1) as a reference band, we cannot find the staggering behavior of the band ^{147}Gd(3) because the sign of the right-hand side of Eq. (48) is indefinite.

The result of such a comparison for 132 pairs of bands is presented in Table 6. The columns of this table involve the reference bands B, whereas the lines represent the bands A. The symbol + (–) means that Eq. (48) and the inequalities (51) determine the staggering behavior of the band A correctly (incorrectly). A blank space is used when the sign of $Q_{44}(\mathrm{A})$ is indefinite and its comparison with the significance Y_A is impossible. Three groups of bands are clearly visible in Table 6. (i) The nonstaggering bands ^{147}Gd(4), ^{148}Gd(1), and ^{151}Gd(1b). There is no contradiction in the staggering behavior inside this group of bands. Such a contradiction has not been found between these bands and the bands of other groups either. (ii) The four bands ^{148}Eu(1), ^{148}Gd(6), ^{149}Gd(1), and ^{151}Gd(1a) with clear evidence of staggering. Whether or not the staggering behavior of the last band contradicts that of the band ^{148}Eu(1) or ^{149}Gd(1) is not clear. (iii) The most striking feature of Table 6 is the third group of bands, whose behavior is found to contradict that of all the bands of the second group. The bands ^{147}Gd(3) and ^{148}Gd(3) with the empty first intruder $\nu 7_1$ and the band ^{150}Gd(2) with the blocked first intruder belong to this group. It should be noted that the band ^{148}Gd(5) being included in the sample contradicts the bands of the first and third groups.

6. CONCLUSION

In rapidly rotating nuclei, the Coriolis force produces a variety of nonadiabatic effects, including the $\Delta I = 4$ bifurcation, which appeared as a new and unexpected event. The analogy with molecular cluster states allowed us to find the phenomenological background of the phenomenon: the term proportional to the nonaxial operator $I_+^4 + I_-^4$ in the rotational Hamiltonian. Its microscopic origin is described in this article.

The Coriolis force in a rotating nucleus is the cause of rotation-single-particle interaction, which leads to a nonaxial distortion of the hexadecapole component of the nuclear mean field. This dynamical mechanism involves two kinds of the single-particle states generating a nonaxial hexadecapole moment: active and inactive orbitals. The proper sign of the Q_{44} moment of all active orbitals is the necessary condition for the existence of the $\Delta I = 4$ bifurcation. The fluctuating dependence of this quantity on the number of nucleons occupying active orbitals explains the configuration dependence of the staggering phenomenon. One can observe the effect of filling each of the active orbitals near the Fermi surface upon the staggering behavior of a band. We have used this simple criterion to test the microscopic theory.

A systematic study of the $\Delta I = 4$ bifurcation in 30 SD bands of the mass region around $A \sim 150$ shows that the criterion of staggering behavior works surprisingly well and is in reasonable agreement with the statistical analysis of Haslip *et al.* [28]. We have explained the triplet of the identical staggering bands ^{148}Eu(1), ^{148}Gd(6), and ^{149}Gd(1) and the related triplet of the nonstaggering bands ^{147}Eu(1), ^{147}Gd(4), and ^{148}Gd(1). Another important result is the fact that the necessary condition is violated in none of the 18 bands with known staggering significance. Discrepancies between the theory and experiment may be attributed to other requirements necessary for staggering, which are not met in some bands. For example, the discrepancies observed in the bands with the empty [^{147}Gd(3), ^{148}Gd(3)] or the blocked [^{150}Gd(1, 2), ^{151}Tb(1), ^{152}Dy(1)] first intruder $\nu 7_1$ may indicate that this state is an essential ingredient of the $\Delta I = 4$ bifurcation. The role of the first proton intruder is not clear because all the bands analyzed in [28] have the intruder proton configuration $\pi 6^2$. The analysis also reveals contradictions in the staggering behavior of some bands, whose configurations differ in inactive orbitals. In these cases, we cannot rule out the violation of the additivity principle, which is a basic assumption of our theory. The band ^{148}Gd(5) is a fine example of such a violation. These contradictions may also be due to some inconsistencies in experimental data.

The theory is not intended for reproducing the pattern of staggering, because it relies on a rather general form of rotation-single-particle interaction. As a consequence, we can only analyze the simplest rotational regime and obtain the necessary condition. The simplified approach used is a first step in dealing with so complicated a phenomenon as the $\Delta I = 4$ bifurcation. A further study is required for obtaining a sufficient condition and for reproducing staggering patterns.

ACKNOWLEDGMENTS

We are grateful to A. Afanasjev and I. Ragnarsson for placing information about the structure and deformations of some bands at our disposal and to D. Appelbe for giving the configurations of the $^{150, 151}$Gd bands.

This work was supported in part by the Russian Foundation for Basic Research (project no. 00-15-96590).

REFERENCES

1. L. K. Peker, S. Pearlstein, J. O. Rasmussen, and J. H. Hamilton, Phys. Rev. Lett. **50**, 1749 (1983).
2. S. Flibotte *et al.*, Phys. Rev. Lett. **71**, 4299 (1993).
3. B. Cederwall *et al.*, Phys. Rev. Lett. **72**, 3150 (1994).
4. B. Cederwall *et al.*, Phys. Lett. B **346**, 244 (1995).
5. L. A. Bernstein *et al.*, Phys. Rev. C **52**, R1171 (1995).
6. A. T. Semple *et al.*, Phys. Rev. Lett. **76**, 3671 (1996).
7. G. de Angelis *et al.*, Phys. Rev. C **53**, 679 (1996).
8. S. M. Fischer *et al.*, Phys. Rev. C **53**, 2126 (1996).
9. I. Hamamoto and B. Mottelson, Phys. Lett. B **333**, 294 (1994); Phys. Scr. **T56**, 27 (1995).
10. A. O. Macchiavelli *et al.*, Phys. Rev. C **51**, R1 (1995).
11. I. M. Pavlichenkov and S. Flibotte, Phys. Rev. C **51**, R460 (1995).
12. K. Burzyński, P. Magierski, J. Dobaczewski, and W. Nazarewicz, Phys. Scr. **T56**, 228 (1995).
13. P. Magierski, K. Burzyński, and J. Dobaczewski, Acta Phys. Pol. B **26**, 291 (1995).
14. I. N. Mikhailov and P. Quentin, Phys. Rev. Lett. **74**, 3336 (1995).
15. Yang Sun, Jing-ye Zhang, and Mike Guidry, Phys. Rev. Lett. **75**, 3398 (1995).
16. W. G. Harter, Comput. Phys. Rep. **8**, 319 (1988).
17. I. Ragnarsson, Poster of the Conference on Physics from Large γ-Ray Detector Arrays, Berkeley, 1994.
18. W. D. Luo, A. Bouguettoucha, J. Dobaczewski, *et al.*, Phys. Rev. C **52**, 2989 (1995).
19. P. Magierski, P.-H. Heenen, and W. Nazarewicz, Phys. Rev. C **51**, R2880 (1995).
20. F. Dönau, S. Frauendorf, and J. Meng, Phys. Lett. B **387**, 667 (1996).
21. D. S. Haslip *et al.*, Phys. Rev. Lett. **78**, 3447 (1997).
22. B. Singh, R. B. Firestone, and S. Y. Frank Chu, Nucl. Data Sheets **78**, 1 (1996).
23. D. S. Haslip, S. Flibotte, C. E. Svensson, and J. C. Waddington, Phys. Rev. C **58**, R1893 (1998).
24. I. M. Pavlichenkov, Pis'ma Zh. Éksp. Teor. Fiz. **64**, 231 (1996) [JETP Lett. **64**, 252 (1996)].
25. I. M. Pavlichenkov, Phys. Rev. C **55**, 1275 (1997).
26. I. M. Pavlichenkov, Pis'ma Zh. Éksp. Teor. Fiz. **66**, 759 (1997) [JETP Lett. **66**, 796 (1997)].
27. G. A. Lalazissis and K. Hara, Phys. Rev. C **58**, 243 (1998).
28. D. S. Haslip *et al.*, Phys. Rev. C **58**, R2649 (1998).
29. Yu. T. Grin' and I. M. Pavlichenkov, Zh. Éksp. Teor. Fiz. **43**, 465 (1962) [Sov. Phys. JETP **16**, 333 (1963)].
30. I. M. Pavlichenkov, Nucl. Phys. **55**, 225 (1964).
31. E. R. Marshalek, Phys. Rev. B **139**, 770 (1965); **158**, 993 (1967).
32. I. M. Pavlichenkov, Phys. Rep. **226**, 175 (1993).
33. W. G. Harter and C. W. Patterson, J. Chem. Phys. **80**, 4241 (1984).
34. I. M. Pavlichenkov, in *Proceedings of the Conference on Physics from Large γ-Ray Detector Arrays, Berkeley, 1994*, p. 14.
35. M. Baranger and K. Kumar, Nucl. Phys. A **110**, 490 (1968).
36. I. Ragnarsson and P. B. Semmes, Hyperfine Interact. **43**, 425 (1988).
37. B. Haas *et al.*, Nucl. Phys. A **561**, 251 (1993).
38. G. Hebbinghaus *et al.*, Phys. Lett. B **240**, 311 (1990).
39. W. Satula, J. Dobaczewski, J. Dudek, and W. Nazarewicz, Phys. Rev. Lett. **77**, 5182 (1996).
40. A. B. Migdal, Nucl. Phys. **13**, 655 (1959).
41. H. Sakamoto and T. Kishimoto, Nucl. Phys. A **501**, 205 (1989).
42. I. M. Pavlichenkov, Pis'ma Zh. Éksp. Teor. Fiz. **71**, 8 (2000) [JETP Lett. **71**, 4 (2000)].
43. Y. R. Shimizu, Nucl. Phys. A **520**, 477c (1990).
44. Ch. Theiseh *et al.*, Phys. Rev. C **54**, 2910 (1996).
45. H. Savajols *et al.*, Phys. Rev. Lett. **76**, 4480 (1996).
46. I. Ragnarsson, private communication.
47. S. Flibotte *et al.*, Nucl. Phys. A **584**, 373 (1995).
48. W. Nazarewicz and I. Ragnarsson, in *Handbook of Nuclear Properties*, Ed. by D. Poenaru and W. Greiner (Clarendon Press, Oxford, 1996), p. 80.
49. G. de France *et al.*, Phys. Lett. B **331**, 290 (1994).
50. L. B. Karlsson, I. Ragnarsson, and S. Åberg, Nucl. Phys. A **639**, 654 (1998).
51. L. B. Karlsson, Doctoral Dissertation (Lund Univ., 1999).

Physics of Atomic Nuclei, Vol. 64, No. 4, 2001, pp. 611–618. From Yadernaya Fizika, Vol. 64, No. 4, 2001, pp. 669–676.

90th ANNIVERSARY OF A.B. MIGDAL'S BIRTHDAY
NUCLEI

Microscopic Theory of Strong Superfluidity*

M. Baldo[1] and A. Grasso[2]

Received August 11, 2000

Abstract—Various forms of superfluidity in nuclei and nuclear and neutron matter are characterized by the relevance of strong nucleon–nucleon correlations, as well as by gap values, which can be a substantial fraction of the Fermi energy. We present a microscopic many-body theory of nuclear superfluidity. The influence of various physical effects is analyzed within the Green's function formalism and the Bethe–Brueckner–Goldstone expansion. In particular, dispersive effects are discussed in detail. We point out open problems that must be solved before a full understanding of nuclear superfluidity can be achieved. © *2001 MAIK "Nauka/Interperiodica".*

1. INTRODUCTION

The pairing phenomenon in nuclei and nuclear matter is one of the fundamental issues in nuclear physics that received invaluable contributions from the work of Migdal [1]. Within the Green's function formalism, he showed the way in which nucleon–nucleon correlations affect the pairing phenomenon in the case of weak superfluidity—namely, when one can introduce an effective pairing interaction concentrated around the Fermi momentum. He also proposed, as the most convenient attitude, to handle the effective pairing interaction and the quasiparticle strength as phenomenological parameters, to be used in fitting the experimental data or to be taken anyhow from other sets of experiments. Nowadays, in view of the more recent developments in many-body theory and the rapid progress in computer power, it appears challenging to try to understand nuclear superfluidity merely on the basis of bare nucleon–nucleon interaction and nucleon correlations without the introduction of any free parameters. In particular, this is mandatory in the case of neutron-star superfluidity. In this case, in fact, since the observational data are only indirectly related to superfluidity or need explicit models for their interpretation, a firm theoretical prediction of the superfluidity strength, based on microscopic ab initio calculations, appears to be highly required. Indeed, neutron and nuclear-matter superfluidity is one of the main issues in the physics of neutron stars. Superfluidity is expected to play a major role in some of the most striking phenomena occurring in neutron stars, like glitches and postglitch transients [2], vortex pinning [3], neutron-star cooling, and maybe strong magnetic-field penetration [4]. Since neutron and nuclear matter are strongly correlated systems, where short-range correlations dominate the overall interaction energy even at densities well below the saturation value, the superfluidity problem turns out to be a complex many-body problem, where a delicate balance between short-range interactions and the long-range pairing correlations needs an accurate treatment. Many authors have tried to predict the pairing strength in neutron matter within a definite microscopic many-body theory, like the variational Jastrow method [5], the Babu–Brown approach [6] and its generalizations [7, 8], and Landau theory [9]. In general, these microscopic approaches seem to indicate a reduction of the pairing gap due to the medium, with respect to the BCS [10] approximation with bare interaction. The use [11] in the BCS scheme of realistic bare nucleon–nucleon interactions, which reproduce the experimental phase shifts, can be a good starting point for a more sophisticated many-body treatment, and the connection between the pairing gap value and the phase shifts was elucidated, in general, in [12].

Dispersive effects, due to the energy dependence of the single-particle self-energy, are usually neglected or considered in the weak-coupling limit. Only in [13] was a self-consistent scheme developed where the short-range correlations and the pairing problem are treated on the same footing. The method is numerically complex, and it was solved only for a schematic interaction [13]. More recently [14], a scheme to treat dispersive effects has been proposed that is supposed to be valid whenever the pairing gap is not too large with respect to the Fermi energy and the quasiparticle width is small with respect to the quasiparticle energy. Both conditions are indeed satisfied in the case of neutron matter [14].

In this paper, we discuss the general scheme of treating strong superfluidity within the Green's function formalism and the Bethe–Brueckner–Goldstone method for the inclusion of short-range correlations. The Green's function formalism, generalized to the pairing problem, was extensively developed long ago in [15, 16] and, of course, in [1]. The formalism will be reviewed, for definiteness, in Section 2, and different effects and mechanisms that can contribute to the

* This article was submitted by the authors in English.

[1] ECT*, Strada delle Tabarelle 286, I-38050 Villazzano (TN), Italy, and INFN, Sez. Catania, Corso Italia 57, I-95129 Catania, Italy.
[2] Dipartimento di Fisica, Università di Catania, Corso Italia 57, I-95129 Catania, Italy.

1063-7788/01/6404-0611$21.00

development of the superfluid phase are shortly discussed. In Sections 3 and 4, dispersive effects are discussed in detail. Section 5 is devoted to the application to neutron-star superfluidity. The medium renormalization of the nucleon–nucleon interaction is discussed in Section 6. A short conclusion is drawn in Section 7.

2. GENERAL FORMULATION OF THE GAP EQUATION

The Green's function (GF) formalism for the pairing problem can be extended to generalize the Gorkov's method beyond the BCS approximation [15, 16]. The single-particle Green's function $\mathcal{G}$ has a 2×2 matrix structure, with normal diagonal components F_1 and abnormal off-diagonal components F_2:

$$\mathcal{G}(k, \omega) = \begin{pmatrix} F_1(k, \omega) & F_2(k, \omega) \\ F_2(k, \omega) & -F_1(k, -\omega) \end{pmatrix}, \tag{1}$$

$$\mathcal{G}^{-1}(k, \omega) = \begin{pmatrix} \tilde{\epsilon}_k - \omega + M(k, \omega) & \Delta(k, \omega) \\ \Delta(k, \omega) & -(\tilde{\epsilon}_k + \omega + M(k, -\omega)) \end{pmatrix}.$$

In the expression for the inverse Green's function $\mathcal{G}^{-1}$, we have introduced the quantity $\tilde{\epsilon}_k = \hbar^2 k^2/2m - \mu$ as the single-particle kinetic energy, with respect to the chemical potential μ, the diagonal single-particle self-energy $M(k, \omega)$, and the momentum- and energy-dependent gap function $\Delta(k, \omega)$. Here, we assume S-wave singlet pairing; therefore, we omit spin indices. They simply express the coupling between the time-reversal states $(k, \uparrow)$ and $(-k, \downarrow)$.

The constituent equation for the pairing problem is the generalized gap equation, which expresses the condition that the gap function $\Delta(k, \omega)$ is solution of the homogeneous Bethe–Salpeter equation [1, 15]. The inhomogeneous Bethe–Salpeter equation is the general equation for the two-body scattering matrix in the medium [1]; therefore, the existence of a solution for the corresponding homogeneous Bethe–Salpeter equation physically indicates the formation of bound Cooper pairs and the onset of the superfluid phase. The generalized gap equation [1, 15] can be written as

$$\Delta(k, \omega) = \sum_{k'} \int d\omega' \times \frac{I(k\omega, k'\omega')\Delta(k', \omega')}{(\tilde{\epsilon}_{k'} - \omega' + M(k', \omega'))(\tilde{\epsilon}_{k'} + \omega' + M(k', -\omega')) + \Delta(k', \omega')^2}, \tag{2}$$

where $I(k\omega, k'\omega')$ is the irreducible *NN* interaction at zero total energy and momentum.

Since both $M(k, \omega)$ and $\Delta(k, \omega)$ can be expanded in terms of the *NN* interaction and the full GF itself, Eqs. (1) and (2) in general imply a self-consistent procedure for both the self-energy and the gap function. Alternatively, one can introduce the single-particle spectral function as the quantity to be determined self-consistently [13]. In general, of course, one has to introduce a suitable approximation for the irreducible interaction I and the self-energy M, and then solve the resulting gap Eq. (2). If one takes the bare *NN* interaction for the interaction I, and the Hartree–Fock approximation for the diagonal self-energy $M(k, \omega)$, the standard BCS approximation is recovered. The same result holds true if one introduces an energy-independent effective interaction, to be determined phenomenologically or within a microscopic many-body scheme. Since we take the microscopic point of view here, our first choice will be the bare *NN* interaction, but later we will discuss possible improvement.

It has to be noticed that the energy dependence of the gap function $\Delta(k, \omega)$ originates only from the energy dependence of the irreducible interaction I. In fact, if the interaction is taken as energy independent, the gap function is also energy independent, despite the possible energy dependence of the self-energy $M(k, \omega)$. This indicates that dispersive effects, which are present as soon as one goes beyond the Hartree–Fock approximation for the diagonal self-energy $M(k, \omega)$, are well distinct from the medium renormalization effects on the *NN* interaction.

According to the so-called "conserving approximations" [17], a well-defined relation between self-energy and irreducible interaction should be used. If one considers the self-energy as a functional of the corresponding Green's function, then the irreducible interaction should be taken as the functional derivative of M with respect to $\mathcal{G}$. However, it has to be noticed that this type of many-body theory is mainly devised for describing transport properties and ensure that conservation laws are then fulfilled. The relevance of such a prescription in describing the ground state properties, where conservation laws play no role, is not clear. It appears, therefore, that an approximation scheme has to be devised for both the self-energy and the irreducible *NN* interaction.

The medium modifications of the irreducible *NN* interactions were considered by few authors in the case of pure neutron superfluidity. In general, a "screening" of the interaction was found, namely, a reduction of the pairing strength [5, 7]. In [8], these findings were essentially confirmed; however, at the highest densities the attraction due to spin-density fluctuations was found to overcome the repulsion due to density fluctuations and an enhancement of the pairing gap was predicted near the gap closure. Indeed, in [9], it was pointed out the crucial role of the delicate balance between density and spin-density fluctuations in determining the overall medium effect on the renormalized *NN* interaction. At present, no firm microscopic prediction of the medium modifications of the *NN* interaction is available. This point is further discussed in Section 5.

3. DISPERSIVE EFFECTS

In order to single out dispersive effects, let us assume that the irreducible *NN* interaction is energy independent. Then the energy integration appearing in the gap Eq. (2) can be formally performed, since the gap function Δ is also energy independent, as was already noticed above. The denominator is an even function of the energy ω (we recall again that single-particle energies are measured with respect to μ). This is a feature typical of the superconducting phase. Furthermore, the propagation kernel is then proportional to the anomalous Green's function F_2 of (1), as can be explicitly checked. As such, the kernel satisfies the general dispersion relation fulfilled by the superfluid Green's functions. If we define

$$D(k,\omega) = (\tilde{\epsilon}_k - \omega + M(k,\omega)) \times (\tilde{\epsilon}_k + \omega + M(k,-\omega)) + \Delta(k,\omega)^2, \tag{3}$$

then the kernel $1/D(k,\omega)$ satisfies the (exact) dispersion relation

$$\frac{1}{D(k,\omega)} = \int_0^\infty \frac{d\omega'}{\pi}\mathrm{Im}\left(\frac{1}{D(k,\omega')}\right) \times \left[\frac{1}{\omega'-\omega-i\epsilon}+\frac{1}{\omega'+\omega-i\epsilon}\right]. \tag{4}$$

Equation (4) allows us to rewrite the general gap Eq. (2) in a form that resembles the usual BCS gap equation. Indeed, upon inserting (4) into (2), the ω' integration can be performed and one gets

$$\Delta(k) = -\sum_{k'} I(k,k')\frac{\Delta(k')}{2\mathscr{E}(k')}, \tag{5}$$

where the following definition has been introduced:

$$\frac{1}{2\mathscr{E}(k)} = \frac{1}{\pi}\int d\omega' \mathrm{Im}\left(\frac{1}{D(k,\omega')}\right), \tag{6}$$

where Im(…) indicates the imaginary part of the complex number in the parenthesis. For a given approximation scheme for the self-energy $M(k,\omega)$, Eq. (5) gives the corresponding gap equation with the inclusion of dispersive effects. In general, the ω integration in (6) can be easily done numerically for each value of the momentum k. It has to be noticed that the kernel of the integral (5) is a real function and, therefore, the gap function $\Delta(k)$ can also still be taken as real.

Of course, dispersive effects are easily included in the gap equation, once the weak coupling limit is adopted [1]. Equations (5) and (6) generalize the treatment to the strong coupling case, where the momentum and energy integration cannot be restricted around the Fermi surface, as it will be discussed in detail in the next section.

4. POLE APPROXIMATION

If the imaginary part of the self-energy is small with respect to the single-particle energy, it is possible to approximate the energy integration of (2) in a simple way (still assuming the *NN* interaction as energy independent). This will allow us to get a closer connection with the weak coupling limit. In this case, in fact, the main contribution is expected to come from the poles close to the real axis. The denominator is an even function of the energy ω (we again recall that single-particle energies are measured with respect to μ); therefore, the kernel has two poles symmetric with respect to the origin in the complex ω plane. Formally, the pole energies $\pm E_k$ are the solutions of the implicit equation

$$\pm E_k = \frac{1}{2}(M(k,\pm E_k) - M(k,\mp E_k)) \pm \sqrt{\left[\tilde{\epsilon}_k + \frac{1}{2}(M(k,-E_k)+M(k,E_k))\right]^2 + \Delta(k)^2}. \tag{7}$$

If the energy dependence of $M(k,\omega)$ is neglected, then (7) reduces to the usual square root expression for the quasiparticle excitation energy of the BCS approximation. On the other hand, in the nonsuperconducting limit $\Delta \longrightarrow 0$ and neglecting the imaginary part of $M(k,\omega)$, one can verify that Eq. (7) reduces to the usual self-consistent equation, e.g., Brueckner [18], for the single-particle energy e_k:

$$e_k = \tilde{\epsilon}_k + M(k,e_k). \tag{8}$$

Equation (8) is valid whenever Δ is negligible, in particular for momenta far away from the Fermi surface, since then $|\Delta_k| \ll |\tilde{\epsilon}_k|$. Taking the corresponding residue of the kernel at the pole, we can write the gap Eq. (2) as

$$\Delta(k) = -\sum_{k'} I(k,k')Z_{k'} \times \frac{\Delta_{k'}}{2\sqrt{\left[\tilde{\epsilon}_k + \frac{1}{2}(M(k,-E_k)+M(k,E_k))\right]^2 + \Delta(k)^2}}, \tag{9}$$

where Z_k is a factor that is related to the quasiparticle strength (see below). The pole approximation is exact in the limit of vanishing imaginary part of the self-energy, as can be checked from Eqs. (5) and (6). It has to be noticed that in the generalized gap Eq. (9) the square root in the denominator does not coincide with the quasiparticle energy, implicitly defined by Eq. (7), in contrast with the usual BCS approximation, where the full pairing quasiparticle energy appears.

Let us discuss Eq. (9) in the extreme weak-coupling limit, where one assumes that the main contribution to the momentum integral is concentrated around the Fermi surface and one neglects pairing in the diagonal self-energy, which is then identified with the one in the normal phase. In this limit, following the standard pro-

cedure of expanding the integrand of Eq. (9) around k_F, one gets [19]

$$\Delta_F = 8\frac{E_F}{m_F}\exp\left(-\frac{1}{m_F Z_F \pi^2 n_0 I(k_F)}\right), \quad (10)$$

where n_0 is the density of state for the free Fermi gas and m_F is the so-called k mass (in units of the bare mass) [20]. The interaction $I(k_F)$ is the diagonal matrix element of the *NN* potential in the considered channel (e.g., $^1S_0$ for neutron matter), in the plane-wave representation. The self-energy effects are, therefore, contained mainly in the factor $m_F Z_F$, which can be written also as $m^* Z_F^2$, since the full effective mass $m^* = m_F/Z_F$ [20]. This is the standard result for the weak coupling limit [1]. Equation (9) generalizes the treatment to the case where the contribution from momenta far from the Fermi surface is relevant, within the adopted pole approximation. The appearance of the k mass is a peculiar feature of the pairing phenomenon, and it is a direct consequence of the coupling between time-reversal states. In Eq. (9), the combination $M(k, -\omega) + M(k, \omega)$ gives rise to the combined density of state of the pair $\{(k, \omega); (-k, -\omega)\}$, which is mainly determined by the k mass.

The weak coupling limit is not valid in general for neutron or nuclear matter [18], if one starts from the bare *NN* interaction. This can be seen directly from the observation that the gap equation often has a well-defined solution even when the interaction matrix element $I(k_F)$ is positive. This is due to the dominant role of the off-diagonal matrix elements $I(k, k')$. Therefore, in this case one must solve the more general Eqs. (9) or (5).

In the case of neutron matter, a further approximation is viable. Short-range correlations are dominant in this case, and the size of the normal-phase self-energy is expected to be much larger than the pairing gap. It is indeed of the same order of the Fermi kinetic energy E_F, and Eq. (8) will then be valid to the order of $\Delta(k_F)/E_F$, which is expected to be small.

In the superfluid phase, in principle, the diagonal self-energy $M(k, \omega)$ differs from the self-energy in the normal phase. The main contribution not present in the normal phase originates from the coupling of the single-particle motion with the superfluid collective modes. The latter correspond mainly to the center-of-mass motion of the Cooper pairs and their possible "vibrations" [21, 22]. The branch starting at zero energy, in the long wave-length limit, is the branch of the Goldstone boson [21], corresponding to the gauge invariance symmetry breaking at the superfluid phase transition. This contribution to the diagonal single-particle self-energy is expected to be at most on the order of the superfluid condensation energy per particle and is therefore negligible with respect to the typical short-range correlation energy, as calculated, e.g., in Brueckner theory, at least to the extent that $\Delta/E_F \ll 1$. For the same reason, the deviation of the occupation number from the free-gas value and the presence of a forbidden energy region, of the order of Δ, around the Fermi energy, typical of the pairing phenomenon, seem to play no relevant role in determining the size of the self-energy. It therefore appears to be justified to adopt, for $M(k, \omega)$, its normal phase value.

Therefore, on the right-hand side of (7), we can replace E_k with e_k, solution of (8), to get

$$E_k \approx \frac{1}{2}(M(k, |e_k|) - M(k, -|e_k|)) + \sqrt{\left[\tilde{\epsilon}_k + \frac{1}{2}(M(k, -e_k) + M(k, e_k))\right]^2 + \Delta(k)^2}. \quad (11)$$

The procedure is justified, provided $M(k, \omega)$ is a smooth function of ω. Along the same lines, one can approximate the factor Z_k of the kernel at the pole. The general expression of the factor Z_k at each one of the poles can be easily calculated:

$$Z_k = \left[1 - \frac{1}{2}((1 - \Theta_k)a_k + (1 + \Theta_k)b_k)\right]^{-1},$$

$$\Theta_k = \frac{\tilde{\epsilon}_k + \frac{1}{2}(M(k, -E_k) + M(k, E_k))}{S_k}, \quad (12)$$

$$a_k = \left(\frac{\partial M}{\partial \omega}\right)_{\omega = E_k}, \quad b_k = \left(\frac{\partial M}{\partial \omega}\right)_{\omega = -E_k},$$

where S_k is the square root appearing in Eq. (11). In the limit $\Delta \longrightarrow 0$, this is the usual expression for the quasiparticle strength, provided the momentum k is close enough to k_F. The corrections to the normal phase value of $1 - Z_k^{-1}$ are of the order $\Delta(k_F)/E_F$; therefore, the factor can be identified with the quasiparticle strength, at least in the vicinity of the Fermi surface. Far away from the Fermi momentum, the factor Z_k still has this expression (with $E_k \sim e_k$) in the limit of a small imaginary part, although the quasiparticle concept becomes less meaningful, since its width can be large (but it can be still much smaller than the real part of the energy). In this case, the procedure is just an approximate method of calculating the energy integral (i.e., within the pole approximation) of (6).

5. APPLICATION TO NEUTRON-MATTER SUPERFLUIDITY

In a set of calculations for neutron matter, we focused the analysis on the dispersive effects. The calculations were restricted to the $^1S_0$ channel, which appears to be the strongest pairing channel. The irreducible *NN* interaction was taken to coincide with the bare Argonne v_{14} potential [23], according to the con-

siderations developed in the Introduction and in Section 2. Consistently, we calculated the normal self-energy within the Brueckner approximation with the same interaction. The choice of the bare interaction for $I(k, k')$ is suggested by the observation that no ladder summation should be included in the irreducible interaction kernel $I(k, k')$ [1, 18]. Of course, other terms like polarization diagrams should be included [8], as mentioned in the Introduction. However, calculations with the bare Argonne v_{14} potential, and no dispersive effects, in nuclear matter are well reproduced [24] by calculations which adopt phenomenological pairing forces. It seems, therefore, that the medium renormalization of the *NN* interaction is not too strong, at least to a first approximation. The deep reason for that is not at all clear. Some comments on this point are reported in the next section, but surely the issue requires further investigations.

The neutron self-energy has been calculated from the sum of the two diagrams depicted in Fig. 1. The continuous choice [18] for the self-consistent single-particle potential was used. It turns out that the second-order diagram (in the Brueckner G matrix) is at least one order of magnitude smaller than the first one, which is the standard Brueckner diagram, in the considered density range. This gives confidence on the accuracy of the expansion in this case.

Once the normal self-energy is calculated in an energy grid, for a given momentum k, the integral of (6) can be performed numerically. In the pole approximation discussed in the previous section, this energy integral produces the Z_k factor of (9), together with the corresponding square root in the denominator. The latter can be evaluated once the quasiparticle energy is obtained from Eqs. (7) or (11).

It is possible to write down the gap Eq. (5) in the same form of Eq. (9) if we introduce the "effective" factor Z_k^{eff} defined as

$$Z_k^{\text{eff}} = \sqrt{\left[\tilde{\epsilon}_k + \frac{1}{2}(M(k,-E_k) + M(k,E_k))\right]^2 + \Delta(k)^2}/\mathscr{E}(k)$$

$$= \sqrt{\left[\tilde{\epsilon}_k + \frac{1}{2}(M(k,-E_k) + M(k,E_k))\right]^2 + \Delta(k)^2} \qquad (13)$$

$$\times \frac{2}{\pi}\int_0^\infty d\omega\,\mathrm{Im}\left(\frac{1}{D(k,\omega)}\right).$$

Then, Eq. (5) has the same form of Eq. (9), with Z_k^{eff} replacing Z_k. In principle, the factor Z_k^{eff} depends on the value of the gap $\Delta(k)$. Because of the smallness of $\Delta(k)$, it turns out that Z_k^{eff} is actually independent of the gap value with great accuracy. Even for momenta very close to k_F, where $Z_k^{\text{eff}} \approx Z_k$, the gap dependence can be neglected, as can be seen from (12). The closeness of Z_k to Z_k^{eff} indicates the accuracy of the pole approximation. In Fig. 2, these two quantities are reported as functions of k for $k_F = 1.3$ fm^{-1}. As one can see, the pole approximation introduces a systematic overestimation of the factor Z_k, but it appears to be an overall fair approximation. The factor can even slightly exceed unity in the pole approximation for intermediate values of k. This is not surprising, since the regular (nonpolar) contribution to the integral can be negative. Of course, close to the Fermi momentum, Z_k is smaller than unity, since then it acquires the meaning of quasiparticle strength. According to Migdal–Luttinger theorem [1], in fact, the value Z_F of Z_k at $k = k_F$ is the discontinuity of the momentum distribution at the Fermi momentum (in the normal phase). One must have, therefore, $0 < Z_F < 1$. For higher momentum values, Z_k tends to unity, since then the self-energy becomes energy independent [25]. Also, Z_k^{eff} tends smoothly to unity but from values smaller than one. The asymptotic value of Z_k^{eff} can be expected from the fact that, for large enough k, the self-energy around the peak of the function $\mathrm{Im}(1/D(k, \omega))$ becomes negligible with respect to the kinetic energy, and the energy dependence of the kernel is then the same as for free particle. In the case of Fig. 2, for $k >$

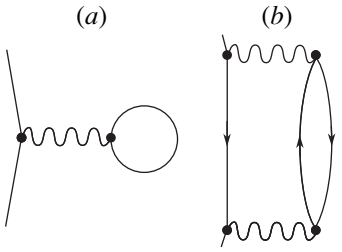

Fig. 1. Self-energy diagrams in the Bethe–Brueckner–Goldstone expansion. A wavy line indicates a Brueckner G matrix.

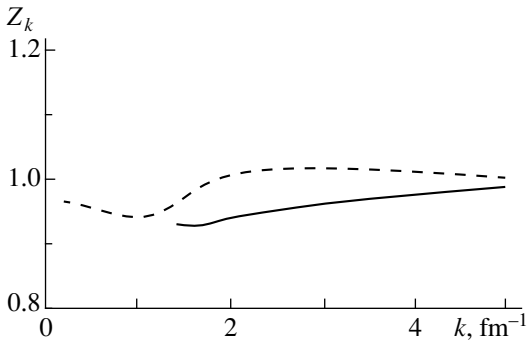

Fig. 2. The renormalization factor Z in the pole approximation (dashed line) and in the exact procedure (solid line). For details, see the text.

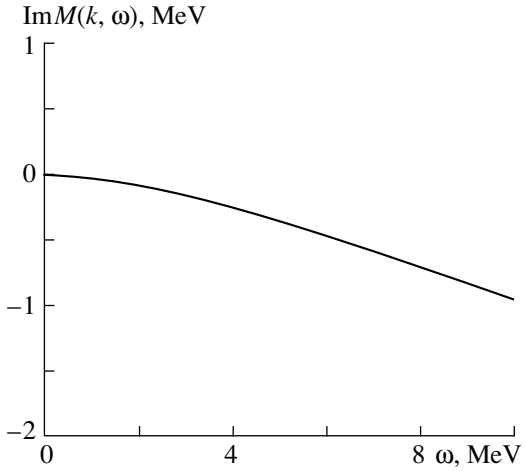

Fig. 3. The imaginary part of the self-energy as a function of the single-particle energy ω (calculated with respect to the chemical potential) for the Fermi momentum $k_F = 1.1$ fm^{-1} and the momentum $k = 1.2$ fm^{-1}.

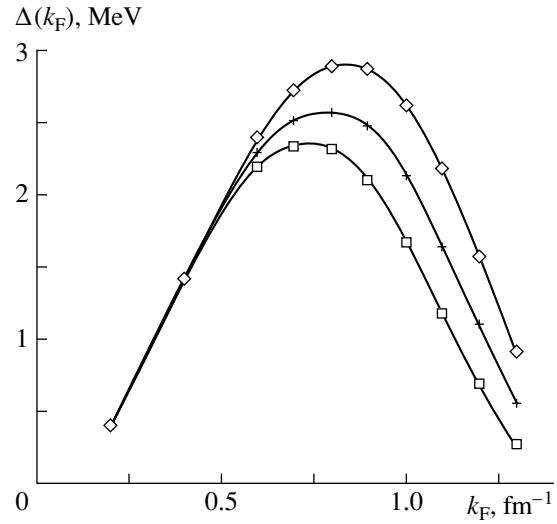

Fig. 4. The superfluid gap value, at the Fermi momentum, as a function of density, in the case of free single-particle spectrum (◇), with the inclusion of the factor Z_k^{eff} (+) and with the inclusion of both Z_k^{eff} factor and the self-energy in the single-particle spectrum (□).

6 fm^{-1}, the value of Z_k^{eff} can be safely taken as equal to one.

On the other hand, the numerical comparison between Z_k and Z_k^{eff} cannot be done exactly at k_F. There, in fact, the imaginary part of the self-energy is vanishingly small and the integral in (6) cannot be done numerically, since the integrand is too sharply peaked. Indeed, for $k \longrightarrow k_F$, it becomes a delta function, which, of course, cannot be integrated numerically. However, the pole approximation close to the Fermi momentum is expected to become accurate; therefore, one should have $Z_k^{\text{eff}} \approx Z_k$. From our calculations, the region around k_F where this happens is quite small; therefore, we could check this result numerically only to a certain extent, namely, at distance not too small from the Fermi surface. Still, at the shortest distance allowed by the numerical accuracy, some discrepancies between Z_k and Z_k^{eff} persist, despite their clear tendency to be closer. Looking at the self-energy near the Fermi momentum, one indeed notices that the ratio between the imaginary part and the quasiparticle energy remains small but almost constant down to values close to k_F. Only at even closer values of k does the imaginary part appear to display the expected quadratic dependence on ω [1] and to become vanishingly small with respect to the quasiparticle energy (which has linear dependence), see Fig. 3. It is found that, for $k < k_F$, the imaginary part of the self-energy is quite small throughout the whole energy range; therefore, we use the pole approximation in any case there. Fortunately, it turns out that the values of Z_k^{eff} just above k_F and the values of Z_k at and just below k_F look to join quite smoothly; therefore, a simple interpolation for Z_k^{eff} across the Fermi surface appears quite reliable.

Similar results are obtained for the other considered values of k_F.

Once the values of Z_k^{eff} are evaluated as functions of k, the gap equation can be numerically solved. In Fig. 4, the gap value at the Fermi momentum as a function of neutron density is reported. For comparison, three different cases are plotted: (i) the results with free single-particle spectrum, i.e., without any self-energy [11]; (ii) including only the Z_k^{eff} factor in the numerator of the gap Eq. (9); (iii) with both the self-energy in the denominator and the Z_k^{eff} factor. The reduction of the pairing gap is substantial at the highest densities, near the gap closure. The gap values in cases (ii) and (iii) are slightly smaller than in [14], as expected, since there the pole approximation was adopted. The comparison with [14], however, indicates that the pole approximation is a fairly good approximation, at least in neutron matter. The results appear in line with the work of [13], where the self-consistent treatment of pairing and short range correlations seems indeed to reduce strongly the gap value mainly because of these two factors [13, 26]. Dispersive effects seem, therefore, to be well established with good accuracy in neutron matter.

6. RENORMALIZATION OF THE NUCLEON–NUCLEON INTERACTION

The problem of medium renormalization of the nucleon–nucleon interaction has been considered by several authors. The main effect which has been con-

sidered is the "screening" of the interaction due to the coupling with particle–hole excitation of the Fermi liquid. In neutron matter, the particle–hole excitations are the density and spin-density fluctuations. As already noticed by Brown (see [6] for a review), the main difference between the particle–hole and particle–particle irreducible interactions is just due to this coupling with particle–hole excitations (see Fig. 5). Since at the Fermi momentum the particle–hole irreducible interaction can be identified with the relevant set of Landau–Migdal parameters, it has been suggested [5] to estimate the pairing particle–particle irreducible interaction just by correcting the parameters with the inclusion of the particle–hole ring-diagram series. This amounts to neglecting the momentum dependence of the particle–hole interaction. It turns out that, if one uses a reasonable estimate of the Landau–Migdal parameters in neutron matter the spin-density fluctuations produce a strong additional repulsion to overcome the attractive contribution coming from the density fluctuations [5, 18]. As a result, the pairing gap in neutron matter appears strongly reduced by medium effects on the pairing particle–particle interaction. This result was somehow confirmed in [7–9], where more refined treatments were adopted. The full-momentum dependence of the particle–hole interaction was, however, never considered, and it was included only within some crude approximate scheme. As we have already noticed, the weak-coupling limit is not applicable in a microscopic treatment of neutron- and nuclear-matter superfluidity.

The problem of the interaction renormalization is still an open problem, and it is surely the only main source of uncertainty in the microscopic theory of neutron- and nuclear-matter superfluidity. The main difficulty, besides the obvious numerical complexity of the calculation, is the inclusion of the relevant set of diagrams in evaluating the particle–hole irreducible interactions, keeping the full-momentum dependence. If the irreducible particle–hole interaction is identified with the Brueckner G matrix, then the problem is well defined and numerically viable. However, in neutron and nuclear matter, the situation is probably more complex, since it is known that the Brueckner G matrix is not a sufficient approximation, and at least the so-called "rearrangement term" has to be included, see, e.g., [27, 28].

Moreover, if one follows the expansion scheme suggested by the "conserving approximation" [17], one gets a well-defined prescription for the irreducible particle–particle interaction consistent with the adopted self-energy—namely, the former is obtained by a functional derivative of the latter (Φ-derivable theory, in the terminology of [17]). In neutron matter, where it appears to be an excellent approximation to calculate the self-energy from the diagrams in Fig. 1, one finds that one should include only one bubble in the ring series in Fig. 5 (second diagram) instead of the full RPA series. As already noticed, it is not at all clear whether this prescription has any relevance to ground-state properties; therefore, the role of the higher order terms of the series should be checked.

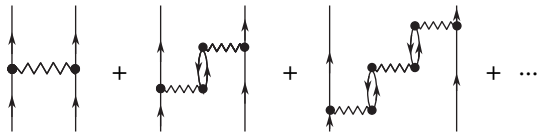

Fig. 5. Diagrams defining the screened nucleon–nucleon interaction.

In conclusion, it appears difficult, but numerically feasible, to include in the pairing microscopic theory the medium renormalization of the nucleon–nucleon interaction, still keeping the momentum dependence of the resulting effective interaction. Much work has to be done in this direction, but the solution of this still unsolved problem will open the possibility of predicting on a firm theoretical basis the strength of the pairing gap in neutron and nuclear matter.

7. CONCLUSIONS

We have discussed a general scheme for treating strong superfluidity in neutron and nuclear matter, where short-range correlations dominate the normal single-particle self-energy. Dispersive effects can be treated on a firm theoretical basis, and the corresponding modification of the pairing gap has been calculated in the case of pure neutron matter. In this case, it turns out that dispersive effects are relevant mainly near the gap closure, where the pairing strength is considerably reduced.

The theoretical uncertainties in the theoretical evaluation of the gap values are mainly concentrated in the estimate of the medium modification of the nucleon–nucleon interaction. Still, much work has to be done before this problem can be clarified.

REFERENCES

1. A. B. Migdal, *Theory of Finite Fermi Systems and Applications to Atomic Nuclei* (Nauka, Moscow, 1965; Interscience, London, 1967).
2. S. L. Shapiro and S. A. Teukolsky, *Black Holes, White Dwarfs, and Neutron Stars* (Wiley, New York, 1983; Mir, Moscow, 1985).
3. D. Pines and M. A. Alpar, Nature **316**, 27 (1985).
4. D. A. Baiko and D. G. Yakolev, astro-ph/9812071.
5. J. M. C. Chen, J. W. Clark, R. D. Davé, and V. V. Khodel, Nucl. Phys. A **555**, 59 (1993).
6. S.-O. Bäckman, G.E. Brown, and J.A. Niskanen, Phys. Rep. **124**, 1 (1985).
7. T. L. Ainsworth, J. Wambach, and D. Pines, Phys. Lett. B **222**, 173 (1989); J. Wambach, T. L. Ainsworth, and D. Pines, Nucl. Phys. A **555**, 128 (1993).
8. H.-J. Schulze, J. Cugnon, A. Lejeune, *et al.*, Phys. Lett. B **375**, 1 (1996).

9. J. W. Clark, C.-G. Källman, C.-H. Yang, and D. A. Chakkalakal, Phys. Lett. B **61B**, 331 (1976).
10. J. Bardeen, L. N. Cooper, and J. R. Schrieffer, Phys. Rev. **108**, 1175 (1957).
11. M. Baldo, J. Cugnon, A. Lejeune, and U. Lombardo, Nucl. Phys. A **515**, 409 (1990); **536**, 349 (1991).
12. M. Baldo, Ø. Elgarøy, L. Engvik, *et al.*, Phys. Rev. C **58**, 1921 (1998).
13. P. Bozek, Nucl. Phys. A **657**, 187 (1999).
14. M. Baldo and A. Grasso, Phys. Lett. B (in press).
15. P. Nozières, *Theory of Interacting Fermi Systems* (Benjamin, New York, 1966).
16. A. A. Abrikosov, L. P. Gor'kov, and I. E. Dzyaloshinskii, *Methods of Quantum Field Theory in Statistical Physics* (Fizmatgiz, Moscow, 1962; Prentice-Hall, London, 1963).
17. G. Baym, Phys. Rev. **127**, 1391 (1962).
18. For a pedagogical introduction, see *International Review of Nuclear Physics*, Vol. 9: *Nuclear Methods and the Nuclear Equation of State*, Ed. by M. Baldo (World Sci., Singapore, 1999).
19. A. L. Fetter and J. D. Walecka, *Quantum Theory of Many-Particle Systems* (McGraw-Hill, New York, 1971).
20. See, e.g., J. W. Negele and H. Orland, *Quantum Many-Particle Systems*, *Frontiers in Physics* (Addison-Wesley, Reading, 1987), Vol. 68.
21. M. Baldo, G. Giansiracusa, U. Lombardo, and R. Pucci, Nuovo Cimento B **58**, 301 (1980).
22. P. Wölfle, Physica B (Amsterdam) **90**, 96 (1977).
23. R. B. Wiringa, R. A. Smith, and T. L. Ainsworth, Phys. Rev. C **29**, 1207 (1984).
24. E. Garrido, P. Sarriguren, E. Moya de Guerra, and P. Schuck, nucl-th/9909026.
25. M. Baldo, G. Giansiracusa, U. Lombardo, *et al.*, Nucl. Phys. A **545**, 741 (1992).
26. P. Bozek, nucl-th/0003048.
27. M. Baldo and L.S. Ferreira, Phys. Rev. C **50**, 1887 (1994).
28. S.-O. Bäckman, Nucl. Phys. A **130**, 427 (1969).

Physics of Atomic Nuclei, Vol. 64, No. 4, 2001, pp. 619–626. From Yadernaya Fizika, Vol. 64, No. 4, 2001, pp. 677–685.

90th ANNIVERSARY OF A.B. MIGDAL'S BIRTHDAY
NUCLEI

Impact of Spin–Isospin Fluctuations on Single-Particle Degrees of Freedom in Dense Neutron Matter*

J. W. Clark,[1)] V. A. Khodel,[1), 2)] and M. V. Zverev[2), **]

Received August 26, 2000

Abstract—The Fermi surface of dense neutron matter may experience a rearrangement near the onset of pion condensation, due to a strong momentum dependence of the effective interaction by spin–isospin fluctuations. For example, a second (inner) Fermi surface may arise as high-momentum single-particle states are filled and low-momentum states are vacated. The influence of this phenomenon on the superfluid-transition temperature is investigated with the aid of a separation transformation of the BCS gap equation. Attention is also given to modifications of the specific-heat discontinuity at the transition temperature and the relation between the transition temperature and the zero-temperature energy gap. © *2001 MAIK "Nauka/Interperiodica".*

Understanding the properties of strongly correlated Fermi systems that may exist beyond the domain of applicability of Fermi liquid theory presents a continuing challenge for theorists. The study of such systems promises valuable insights into exotic materials ranging from high-T_c superconductors to the matter inside neutron stars.

Key aspects of behavior beyond Fermi liquid theory hinge on the rearrangement of the characteristic Landau quasiparticle distribution $n_F(\mathbf{p})$. For the sake of simplicity, we shall restrict the discussion to homogeneous systems, for which the Fermi liquid distribution $n_F(p)$ coincides with the momentum distribution of an ideal Fermi gas. The actual quasiparticle distribution $n(p)$ inevitably departs from $n_F(p) = \theta(p_F - p)$ if the necessary condition for its stability is violated. At $T = 0$, this condition requires that the change in the ground-state energy E_0 remain positive for any admissible variation $\delta n(p)$ away from $n_F(p)$. More explicitly, stability of a given quasiparticle distribution implies

$$\delta E_0 = \int \xi(p, n(p))\delta n(p)\frac{d^3p}{(2\pi)^3} > 0, \qquad (1)$$

where $\xi(p, n(p)) \equiv \varepsilon(p, n(p)) - \mu$ is the quasiparticle energy measured relative to the chemical potential μ. In the case of $n(p) = n_F(p)$, condition (1) is violated if $\varepsilon(p)$ rises above μ at $p < p_F$, or if $\varepsilon(p)$ drops below μ at $p > p_F$. A rearrangement of quasiparticle occupancies is precipitated when the density ρ attains a critical value ρ_{cF} at which the relation

$$\xi(p, n_F(p); \rho_{cF}) = 0 \qquad (2)$$

exhibits a bifurcation leading to a new root $p = p_0$. This relation usually serves only to determine the Fermi momentum p_F.

In homogeneous systems, the simplest type of rearrangement of the momentum distribution $n(p)$ of quasiparticles of given spin and isospin maintains the property that its values are restricted to 0 and 1, but the Fermi sea becomes doubly or multiply connected [1]. In particular, we may suppose that, at densities exceeding the critical value ρ_{cF}, the normal-state distribution $\theta(p_F - p)$ is altered by the formation of a "bubble," or particle void, over a range $p_i < p < p_I < p_F$, with the Fermi momentum p_F readjusted to maintain the prescribed density. As shown in Fig. 1, one then has three Fermi surfaces, namely, two inner surfaces located at p_i and p_I, along with the usual outer surface at p_F. However, a more dramatic rearrangement can also occur, resulting in a distribution with a partial occupation of quasiparticle states that lacks the distinctive trademark of Fermi liquid theory, namely, the discontinuity of $n(p)$ at the Fermi surface. In this scenario, called fermion condensation, there exists a finite momentum range over which the quasiparticle energy coincides with the chemical potential, corresponding to the creation of a "fermion condensate" [2–4].

Any change in $n(p)$ from the normal-state distribution $n_F(p)$ must entail an increase in the kinetic energy of the quasiparticle system. Accordingly, the anticipated rearrangement only becomes possible if it is accompanied by a counterbalancing reduction of the potential energy, which implies that the effective interaction between quasiparticles has acquired a substantial momentum dependence. The emergence of such a strong momentum dependence is exactly what one expects to occur as the density is increased toward the critical value ρ_c for a second-order phase transition in which a branch of the spectrum $\omega_s(k)$ of collective excitations of the Fermi system collapses at a nonzero value k_c of the wave vector k.

* This article was submitted by the authors in English.

[1)] McDonnell Center for the Space Sciences and Department of Physics, Washington University, St. Louis, USA.
[2)] Russian Research Centre Kurchatov Institute, pl. Kurchatova 1, Moscow, 123182 Russia.
** e-mail: zverev@mbslab.kiae.ru

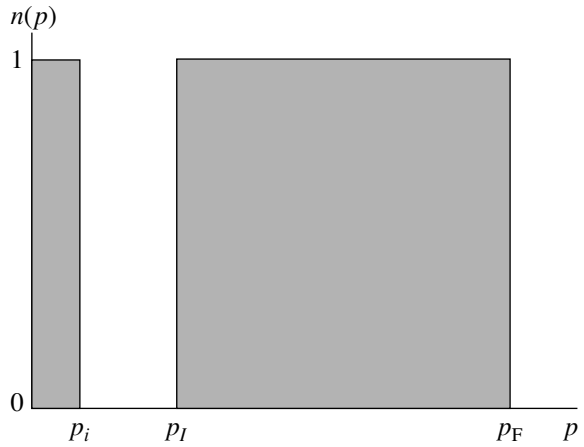

Fig. 1. The bubble-type rearrangement of the quasiparticle occupation $n(p)$.

To justify the latter assertion, we follow the lead of Dyugaev [5] and consider the behavior of the quasiparticle scattering amplitude $F(\mathbf{p}_1, \mathbf{p}_2, \mathbf{k}) \equiv z^2\Gamma(\mathbf{p}_1, \mathbf{p}_2; \mathbf{k}, \omega = 0)M^*/M$ in the vicinity of the phase-transition point. In this construction, $\Gamma(\mathbf{p}_1, \mathbf{p}_2; \mathbf{k}, \omega)$ is the ordinary (in-medium) scattering amplitude, M^* is the effective mass, and z is the renormalization factor determining the weight of the quasiparticle pole. The amplitude F can be written as the sum $F^r + F^s$ of a regular part F^r and a singular part F^s, with the latter taking the universal form

$$\begin{aligned} &F^s_{\alpha\delta;\,\beta\gamma}(\mathbf{p}_1, \mathbf{p}_2, \mathbf{k};\, \rho \longrightarrow \rho_c) \\ &= -O_{\alpha\delta}O_{\beta\gamma}D(k) + O_{\alpha\gamma}O_{\beta\delta}D(|\mathbf{p}_1 - \mathbf{p}_2 + \mathbf{k}|) \end{aligned} \tag{3}$$

in terms of the propagator $D(k)$ of the collective excitation. This form has been derived with due attention to the antisymmetry of the two-particle wave function under exchange of the particle coordinates (spatial, spin, isospin). The collective propagator is conveniently parameterized according to [5]

$$D^{-1}(k) = \beta^2 + \gamma^2(k^2/k_c^2 - 1)^2, \tag{4}$$

where the parameter $\beta(\rho)$, with $\beta(\rho_c) = 0$, measures the proximity to the phase-transition point. The vertex O appearing in (3) determines the structure of the collective-mode operator and is normalized by $\mathrm{Tr}(OO^+) = 1$. Specifically, the choice $O = 1$ is made in treating the rearrangement of the quasiparticle distribution due to collapse of density oscillations [6], while $O = \boldsymbol{\sigma}$ is appropriate when studying the rearrangement of $n_F(p)$ triggered by the softening of the spin collective mode [7]. In the present investigation, we will be concerned with dense, homogeneous neutron matter in which abnormal occupation is induced by spin–isospin fluctuations; thus the pertinent operator is $O = (\boldsymbol{\sigma} \cdot \mathbf{k})\boldsymbol{\tau}$.

Details aside, the most essential features of the model defined by Eqs. (3) and (4) are that the function $F^s(\mathbf{p}_1, \mathbf{p}_2, \mathbf{k} = 0) \simeq D(\mathbf{p}_1 - \mathbf{p}_2)$ depends on the difference $\mathbf{p}_1 - \mathbf{p}_2$ and that, in the neighborhood of the soft-mode phase-transition point, this dependence becomes very strong.

Equations (3) and (4) provide suitable raw material for an efficient evaluation of the single-particle spectrum $\xi(p)$ in the vicinity of the second-order phase transition. We implement a straightforward connection between $\xi(p)$ and the scattering amplitude $F(\mathbf{p}_1, \mathbf{p}_2, \mathbf{k} = 0)$, thereby avoiding the awkward frequency integration that would be encountered in an RPA approach. The connection is made through the relation

$$\frac{\partial\xi(p)}{\partial\mathbf{p}} = \frac{\mathbf{p}}{M} + \frac{1}{2}\int F_{\alpha\beta;\,\alpha\beta}(\mathbf{p}, \mathbf{p}_1)\frac{\partial n(p_1)}{\partial\mathbf{p}_1}\frac{d^3p_1}{(2\pi)^3}, \tag{5}$$

which we derive in the Appendix using the Landau–Pitaevskiĭ identities [8]. The contribution to (5) from the singular part (3) of F can be easily integrated over the momentum $\mathbf{p}$ to obtain

$$\xi(p) = \frac{p^2}{2M_r^*} + \frac{1}{2}\int D(\mathbf{p} - \mathbf{p}_1)n(p_1)\frac{d^3p_1}{(2\pi)^3}. \tag{6}$$

In writing this result, we assume that the contributions to the single-particle spectrum from the regular part of F are accounted for by the replacement of the bare mass M appearing in Eq. (5) by an effective mass M_r^*. (We note that the generally accepted values for this effective mass due to the nonsingular interactions lie in the range 0.7–0.8 for the relevant densities in the neutron-star interior.)

In his pioneering works reviewed in [9, 10] (see also [11]), A.B. Migdal revealed to us that if the density ρ of neutron matter in the liquid core of a neutron star attains a critical density $\rho_{c\pi}$ of some 2–3 times the equilibrium density ρ_0 of ordinary nuclear matter, the spin–isospin collective mode collapses at a finite wave vector $k = k_c \sim p_F$ and a phase transition identified as pion condensation sets in. A conspicuous feature of the ground state of the system beyond the phase-transition point is the presence of a condensate of spin–isospin density waves. As shown in Eqs. (3) and (4), spin–isospin fluctuations with $k \sim k_c$ are significantly enhanced in the vicinity of the transition as a consequence of the divergence of the propagator $D(k \longrightarrow k_c, \rho_c)$.

Let us now apply Eq. (6) to dense neutron matter near the onset of neutral pion condensation. Insertion of the parametrization (4) into (6) yields the working formula

$$\begin{aligned} \xi(p) &= \frac{p^2}{2M_r^*} \\ &+ \frac{1}{2}\int\frac{1}{\beta^2 + \gamma^2((\mathbf{p} - \mathbf{p}_1)^2 - k_c^2)^2/k_c^4}n(p_1)\frac{d^3p_1}{(2\pi)^3}. \end{aligned} \tag{7}$$

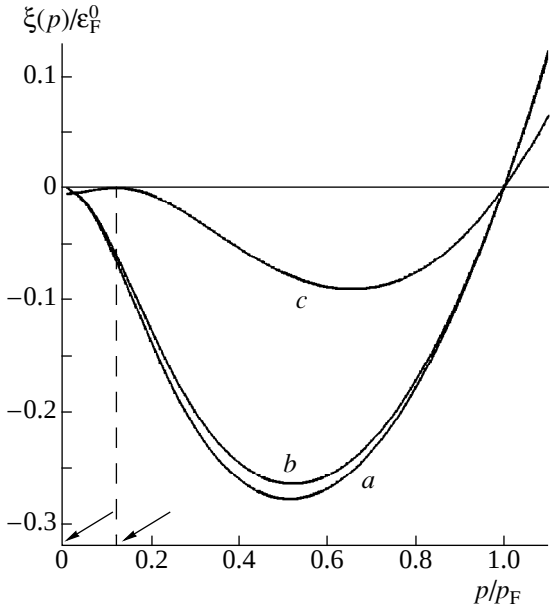

Fig. 2. The neutron spectrum $\xi(p)$ (measured in $\varepsilon_F^0 = p_F^2/2M$) at the critical densities ρ_{cF} corresponding to three different sets of model parameters: (*a*) $\gamma = 1.25m_\pi$, $k_c = 0.9p_F$, $\beta^2 = 0.22m_\pi^2$ ($\rho_{cF} \simeq 1.19\rho_0$), (*b*) $\gamma = 1.25m_\pi$, $k_c = 0.9p_F$, $\beta^2 = 0.25m_\pi^2$ ($\rho_{cF} \simeq 1.76\rho_0$), and (*c*) $\gamma = 1.25m_\pi$, $k_c = p_F$, $\beta^2 = 0.13m_\pi^2$ ($\rho_{cF} \simeq 1.88\rho_0$), where m_π is the pion mass. Two different positions of the bifurcation point, namely, $p_0 = 0$ (for parameter sets (*a*) and (*b*)) and $p_0 \simeq 0.12p_F$ (for set (*c*)), are indicated by arrows.

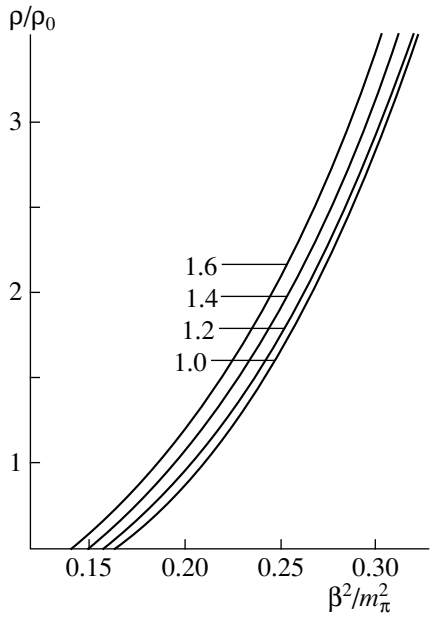

Fig. 3. Phase diagram of neutron matter in the variables ρ (measured in ρ_0) and β^2 (measured in m_π^2), as calculated for $k_c = 0.9p_F$ and four different values of γ, which (in m_π units) label the corresponding phase boundaries separating the bubble phase (upper left) from the normal phase (lower right).

Unfortunately, there is as yet no definitive microscopic treatment of neutron-star matter from which one can extract or derive quantitatively reliable values for the input parameters β, γ, and k_c. Moreover, the predicted values of the critical density $\rho_{c\pi}$ range from 0.2 to 0.5 fm^{-3} (corresponding to 1–3 times ρ_0), depending on a number of theoretical assumptions [9–11].

We have little recourse but to perform calculations based on the formula (7) for several choices (or "guesses") of the parameters of the microscopic model. Substituting expression (7) into (2), one finds the critical density ρ_{cF} at which the solution of the latter equation bifurcates. For $\rho > \rho_{cF}$, this equation then determines two new momenta p_i and p_I where $\xi(p)$ vanishes and between which $\xi(p)$ is positive. The bubble region evidently lies between these two momenta. Representative numerical results for the spectrum $\xi(p)$ are displayed in Fig. 2. Results for the phase diagram of dense neutron matter, plotted in the ρ/ρ_0 versus β^2/m_π^2 plane, are presented in Fig. 3. Different values of γ are considered while keeping the parameter k_c fixed at the value $0.9p_F$ suggested by earlier numerical calculations [10].

It is quite clear that variation of the parameters β, γ, and k_c within sensible bounds can have strong effects on the phase diagram and therefore on the extent, in density, of the phase with rearranged quasiparticle occupation. Nevertheless, our numerical study has documented four characteristic and generic features of the bubble rearrangement.

(i) The critical density ρ_{cF} for the rearrangement is less than the critical density $\rho_{c\pi}$ for pion condensation. Since both phenomena are linked with the strong momentum dependence of the amplitude $F(\mathbf{p}_1, \mathbf{p}_2; \mathbf{k} \longrightarrow 0)$, rearrangement of the quasiparticle distribution may be viewed as a precursor of pion condensation.

(ii) The bifurcation point associated with formation of a bubble in the neutron momentum distribution is located at small momenta, $p_0 < 0.2p_F$, regardless of the applicable value of $\rho_{c\pi}$.

(iii) The spectrum $\xi(p)$ exhibits a deep depression for $p \sim (0.5–0.6)p_F$.

(iv) The ratios $\rho_{cF}/\rho_{c\pi}$ and p_0/p_F are insensitive to the actual value taken by $\rho_{c\pi}$ within the range of plausible theoretical predictions.

The emergence in neutron matter of one or more new Fermi surfaces positioned at low momentum values would provide a new avenue for rapid direct-Urca neutrino cooling of neutron stars [12]. More broadly, the creation of new Fermi surfaces by the mechanism

we have described, as well as the more profound rearrangement involved in fermion condensation, would call for revision of many of the conclusions that have been developed within Fermi liquid theory. Here, we shall focus on some elementary properties of pairing in the reconfigured system.

For simplicity, we shall assume that, beyond the instability point, there exist only two Fermi surfaces, an outer one defined by the usual Fermi momentum p_F and an additional inner one at p_I lying close to the origin in momentum space. (Thus, we consider the limiting case $p_i = 0$ in our original specification of the "bubble" rearrangement.) Also in the interests of simplicity, we restrict the analysis to the $^1S_0$ pairing problem, for which the BCS gap equation has the simple form

$$\Delta(p) = -\int \mathcal{V}(p, p_1)\mathcal{G}^{-1}(p; T)\Delta(p_1)d\tau_1, \qquad (8)$$

where $\mathcal{V}$ is the effective particle–particle interaction. For economy of expression, we have adopted the notation $d\tau = p^2dp/2\pi^2$ for the volume element and

$$\mathcal{G}^{-1}(p; T) = \frac{\tanh[E(p)/2T]}{2E(p)} \qquad (9)$$

for the usual combination of tanh-temperature factor and energy denominator $2E(p)$. The form of the superfluid quasiparticle energy $E(p) = [\xi^2(p) + \Delta^2(p)]^{1/2}$ is of course responsible for the nonlinearity of the gap problem. The quantity $\xi(p)$ is to be interpreted as the single-particle spectrum in the system with pairing turned off.

Implementing the strategy for solving gap equations that was introduced in [13] and elaborated in [14, 15], we write the block $\mathcal{V}$, identically, as a separable part plus a remainder that automatically vanishes on the outer Fermi surface. Thus, we write

$$\mathcal{V}(p_1, p_2) \equiv V_F\phi_F(p_1)\phi_F(p_2) + W(p_1, p_2) \qquad (10)$$

and choose $\phi_F(p) = \mathcal{V}(p, p_F)/V_F$, where $V_F \equiv \mathcal{V}(p_F, p_F)$. It follows directly that $W(p, p_F) \equiv W(p_F, p) = 0$, as required. In the ordinary case where there is only one Fermi surface, this decomposition allows us to replace the singular nonlinear integral equation (8) by two equivalent equations, namely, a nonsingular quasilinear integral equation for a T-independent shape factor $\chi(p) = \Delta(p)/\Delta_F$ and a nonlinear "algebraic" equation for the T-dependent gap value $\Delta_F(T) \equiv \Delta(p_F, T)$. In the present case involving two Fermi surfaces, we must extend the procedure of [13] to deal consistently with the inner Fermi surface as well as the outer one. This is achieved by decomposing the block W appearing in (10) in the same manner as before, setting

$$W(p_1, p_2) \equiv W_I\phi_I(p_1)\phi_I(p_2) + Y(p_1, p_2) \qquad (11)$$

with $\phi_I(p) = W(p, p_I)/W_I$ and $W_I = W(p_I, p_I) \equiv \mathcal{V}(p_I, p_I) - \mathcal{V}^2(p_F, p_I)/\mathcal{V}(p_F, p_F)$, so that $Y(p, p_I) \equiv Y(p_I, p) \equiv Y(p_F, p) \equiv Y(p, p_F) = 0$. The above relations imply the boundary values

$$\phi_F(p_F) = 1, \quad \phi_I(p_I) = 1, \quad \phi_I(p_F) = 0, \qquad (12)$$

whereas the key quantity $\phi_F(p_I) \sim \mathcal{V}(p_I, p_F)$ characterizes the connection between the quasiparticles of the two Fermi surfaces in the particle-particle channel. If $\phi_F(p_I)$ vanishes, these surfaces are disconnected and the problem is obviated.

In the general case where $\mathcal{V}(p_I, p_F) \neq 0$, insertion of Eqs. (10) and (11) into the BCS gap equation (8) yields

$$\begin{aligned}\Delta(p) &= -V_F\phi_F(p)\int \phi_F(p_1)\mathcal{G}^{-1}(p_1; T)\Delta(p_1)d\tau_1 \\ &- W_I\phi_I(p)\int \phi_I(p_1)\mathcal{G}^{-1}(p_1; T)\Delta(p_1)d\tau_1 \\ &- \int Y(p, p_1)\mathcal{G}^{-1}(p_1; T)\Delta(p_1)d\tau_1.\end{aligned} \qquad (13)$$

This equation is conveniently recast as

$$\begin{aligned}\Delta(p) &= -V_F\chi_F(p)\int \phi_F(p_1)\mathcal{G}^{-1}(p_1; T)\Delta(p_1)d\tau_1 \\ &- W_I\chi_I(p)\int \phi_I(p_1)\mathcal{G}^{-1}(p_1; T)\Delta(p_1)d\tau_1\end{aligned} \qquad (14)$$

or, equivalently,

$$\Delta(p) = B_F\chi_F(p) + B_I\chi_I(p), \qquad (15)$$

with

$$\begin{aligned}B_F &= -V_F\int \phi_F(p)\mathcal{G}^{-1}(p; T)\Delta(p)d\tau, \\ B_I &= -W_I\int \phi_I(p)\mathcal{G}^{-1}(p; T)\Delta(p)d\tau\end{aligned} \qquad (16)$$

and

$$\begin{aligned}\chi_F(p) &= \phi_F(p) - \int Y(p, p_1)\mathcal{G}^{-1}(p_1; T)\chi_F(p_1)d\tau_1, \\ \chi_I(p) &= \phi_I(p) - \int Y(p, p_1)\mathcal{G}^{-1}(p_1; T)\chi_I(p_1)d\tau_1.\end{aligned} \qquad (17)$$

Appealing to Eqs. (12), we observe that

$$\begin{aligned}\chi_I(p_I) &= \chi_F(p_F) = 1, \quad \chi_I(p_F) = 0, \\ \chi_F(p_I) &= \phi_F(p_I) = \mathcal{V}(p_I, p_F)/\mathcal{V}(p_F, p_F)\end{aligned} \qquad (18)$$

because the block Y vanishes when either of its arguments lies on a Fermi surface. By this same property, it is permissible, within the quantity $\mathcal{G}^{-1}$ appearing in the integral equations (17), to replace the superfluid quasiparticle energy $E(p_1)$ by $|\xi(p_1)|$ and the temperature factor $\tanh[E(p_1)/2T]$ by unity. Because the energy gaps involved are generally very small compared to the Fermi energy, these replacements are valid to an excellent approximation. We are then left with the linear integral equations

$$\begin{aligned}\chi_F(p) &= \phi_F(p) - \int Y(p, p_1)\frac{1}{2|\xi(p_1)|}\chi_F(p_1)d\tau_1, \\ \chi_I(p) &= \phi_I(p) - \int Y(p, p_1)\frac{1}{2|\xi(p_1)|}\chi_I(p_1)d\tau_1\end{aligned} \qquad (19)$$

for the two shape functions needed to assemble the gap function $\Delta(p)$ via Eq. (15). Since there remains no trace

of the temperature T in these equations, we are free to regard the solutions $\chi_I(p)$ and $\chi_F(p)$ as T-independent quantities.

Using the properties (18), Eq. (15) yields

$$\begin{aligned}\Delta_F \equiv \Delta(p_F) &= B_F,\\ \Delta_I \equiv \Delta(p_I) &= B_I + B_F\phi_F(p_I).\end{aligned} \tag{20}$$

Upon introducing the decomposition (15) in (16), we arrive at the system of two equations

$$\begin{aligned}B_F &= -V_F L_{FF} B_F - V_F L_{FI} B_I,\\ B_I &= -W_I L_{IF} B_F - W_I L_{II} B_I\end{aligned} \tag{21}$$

for determining the amplitudes B_F and B_I entering into the construction (15), with

$$\begin{aligned}L_{FF} &= \int \phi_F(p)\mathscr{E}^{-1}(p;T)\chi_F(p)d\tau,\\ L_{II} &= \int \phi_I(p)\mathscr{E}^{-1}(p;T)\chi_I(p)d\tau,\\ L_{IF} \equiv L_{FI} &= \int \phi_I(p)\mathscr{E}^{-1}(p;T)\chi_F(p)d\tau\\ &\equiv \int \phi_F(p)\mathscr{E}^{-1}(p;T)\chi_I(p)d\tau.\end{aligned} \tag{22}$$

In practice, it is advantageous to rewrite the system of Eqs. (21) in the equivalent form

$$\begin{aligned}&[1 + V_F L_{FF}(T) - V_F\phi_F(p_I)L_{FI}(T)]\Delta_F\\ &\quad + V_F L_{FI}(T)\Delta_I = 0,\\ &[W_I L_{IF}(T) - (1 + W_I L_{II}(T))\phi_F(p_I)]\Delta_F\\ &\quad + [1 + W_I L_{II}(T)]\Delta_I = 0.\end{aligned} \tag{23}$$

For a solution to exist, the determinant $\mathscr{D}(T)$ of (21) or (23) must equal zero for any T. Together with either of the two equations (21) [or either of (23)], the dispersion relation $\mathscr{D}(T) = 0$ forms a closed system that allows one to determine all characteristics of the superfluid system feeding upon the two Fermi surfaces located at p_I and p_F.

We begin to explore the implications of the formalism we have developed by examining the influence of the additional (inner) Fermi surface on the superfluid-transition temperature T_c and on the behavior of the pairing gap near T_c. As shown earlier, Eqs. (21) [or (23)] become decoupled if $L_{IF} = 0$. Let us assume, as a first case, that *both* of the interaction parameters V_F and W_I are negative, so that Cooper pairing could exist at *both* Fermi surfaces when they are disconnected. The pairing effect is naturally more intensive at the main (outer) surface due to a greater density of states. From the two solutions of the problem as stated, we therefore choose $\Delta(p) = \Delta_F\chi_F(p)$ with $\Delta_I = \phi_F(p_I)\Delta_F$, implying that the individual critical temperatures T_c^F and T_c^I satisfy $T_c^F > T_c^I$. It is worth noting that, in spite of this inequality, the magnitude of the ratio $\Delta_I/\Delta_F \sim \phi_F(p_I)$ is not necessarily less than unity (see below).

Working in the vicinity of the transition temperature T_c, standard calculations in the spirit of BCS theory establish the behaviors

$$\begin{aligned}&L_{FF}(T \longrightarrow T_c)\\ &\longrightarrow N_F(0)\{(1 + g_{IF}^2)(L + \alpha\tau) - \beta[D_F^2 + g_{IF}^2 D_I^2]\},\\ &L_{II}(T \longrightarrow T_c) \longrightarrow N_I(0)[L + \alpha\tau - \beta D_I^2],\\ &L_{IF}(T \longrightarrow T_c) \longrightarrow N_I(0)\phi_F(p_I)[L + \alpha\tau - \beta D_I^2]\end{aligned} \tag{24}$$

in terms of the dimensionless parameters $\tau = (T_c - T)/T_c$, $D_F = \Delta_F/T_c$, and $D_I = \Delta_I/T_c$. In Eqs. (24), $N_F(0)$ and $N_I(0)$ are the densities of states at the indicated Fermi surfaces; $g_{IF}^2 = \phi_F^2(p_I)N_I(0)/N_F(0)$ is an effective coupling constant; and $L = \ln(\varepsilon_F^0/\pi T_c) + C$ measures the transition temperature, where ε_F^0 is the free Fermi energy and the value of Euler's constant is $C = 0.577$. Certain irrelevant constants entering the derivation of the limiting behaviors of $L_{II}(T)$, $L_{IF}(T)$, and $L_{FF}(T)$ reduce in effect to a renormalization of the critical temperatures T_c^F and T_c^I and may hence be omitted in forming Eqs. (24). The temperature dependence of the relevant quantities is determined entirely by the ratio $\alpha/\beta = (8\pi^2/7)\zeta(3)$, where $\zeta(x)$ is the Riemann zeta function.

Upon substituting the results (24) into (23), we are led to

$$\begin{aligned}&[1 + V_F N_F(0)(L + \alpha\tau - \beta D_F^2)]D_F\\ &\quad + V_F N_I(0)\phi_F(p_I)(L + \alpha\tau - \beta D_I^2)D_I = 0,\\ &-\phi_F(p_I)D_F + [1 + W_I N_I(0)](L + \alpha\tau - \beta D_I^2)D_I = 0.\end{aligned} \tag{25}$$

Putting $T = T_c$ and evaluating the determinant $\mathscr{D}(T_c)$ of this system, we arrive at a closed formula giving the new critical temperature T_c in terms of the individual critical temperatures T_c^F and T_c^I for the uncoupled system:

$$(L - l_I)(L - l_F) - g_{IF}^2 l_I L = 0. \tag{26}$$

Here, we have introduced the definitions $l_F \equiv \ln(\varepsilon_F^0/\pi T_c^F) + C = -1/V_F N_F(0)$ and $l_I \equiv \ln(\varepsilon_F^0/\pi T_c^I) + C = -1/W_I N_I(0)$. Evidently, the inequality $T_c^F > T_c^I$ implies $l_I > l_F$.

The situation for small coupling, $g_{IF}^2 \ll 1$, is especially transparent. In this case, the value of L (which measures T_c) differs little from the value of l_F (which measures T_c^F), permitting us to replace L by l_F in the last term of the determinantal condition (26). The solution of Eq. (26) is then given by

$$L_\pm = \frac{l_I + l_F}{2} \pm \left[\frac{(l_I - l_F)^2}{4} + g_{IF}^2 l_I l_F\right]^{1/2}. \tag{27}$$

This formula resembles the familiar textbook solution of the two-level problem. If, in that problem, the off-diagonal interaction is switched on, the two energy levels repel each other. The lower level moves downward and the upper level moves upward. Correspondingly, in the current problem, the greater logarithm (in this case, L_+) increases while the smaller logarithm (L_-) decreases; in particular,

$$L_- - l_\mathrm{F} \simeq -g_{IF}^2 \frac{l_I l_\mathrm{F}}{l_I - l_\mathrm{F}}. \tag{28}$$

Since l_I and l_F are both positive in the case under consideration, with $l_I > l_\mathrm{F}$, we conclude that the emergence of the second Fermi surface increases the critical temperature T_c relative to T_c^F.

The picture changes nontrivially when we turn to the more interesting case in which pairing is absent at the new Fermi surface when the two surfaces are disconnected, though still present at the original surface. Upon restoration of the coupling, a pairing gap is found to exist on the new Fermi surface as well as the old one, a feature which is directly seen from either of Eq. (23). The result (27) remains valid. However, in contrast to the preceding case, the value of l_I becomes negative while l_F stays positive. Consequently, the single acceptable value of L derived from Eq. (27) increases relative to l_F, implying a decrease of T_c with respect to T_c^F. This finding should not come as a surprise: the value of the pairing gap depends on the shape of the single-particle spectrum, and if the spectrum becomes flatter in a region where the interaction is repulsive, there must be a suppression of the gap value and a corresponding suppression of T_c. We should emphasize that the situation is now quite different from that of perturbation theory, where the gap increases independently of the sign of the perturbating interaction. The distinctive behavior we have described is indicative of a failure of perturbation theory in this second case. We should also point out the close resemblance between the predicted behavior and the proximity effect observed in junctions between a superconductor and a normal metal: the superconductor tends to induce superconditivity on the normal side of the junction, at the expense of a suppression of its intensity on the superconducting side.

Let us now turn to the matter of the jump in the superfluid specific heat C_s at $T = T_c$ triggered by the branch point in $\Delta_\mathrm{F}^2(T)$ at the critical temperature T_c. In BCS theory, there is a universal relation

$$\Delta_\mathrm{F}^2 \simeq 3.06 T_c (T_c - T) \tag{29}$$

whose origin is clarified if we set $L_{IF} = 0$ in Eq. (23). Subtracting from the general equation its special case for $T = T_c$, several cancellations leave us with the result

$$L_{\mathrm{FF}}(T) - L_{\mathrm{FF}}(T_c) = 0, \tag{30}$$

which is completely independent of the choice of the interaction between the particles. The relation (29) follows directly.

In the general case where $L_{IF} \neq 0$, the same subtraction procedure yields

$$\begin{aligned} &\alpha[2L - l_I - l_\mathrm{F} - g_{IF}^2 l_I]\tau \\ &-\beta[(L - l_I)D_\mathrm{F}^2 + (L - l_\mathrm{F} - g_{IF}^2 l_I)D_I^2] = 0, \end{aligned} \tag{31}$$

from which we learn that Δ_F^2 and Δ_I^2 are linear in $T_c - T$. Consequently, the specific-heat jump at $T = T_c$ persists in the presence of the two Fermi surfaces.

To determine the gap values and the magnitude of the specific-heat jump, another relation between Δ_F and Δ_I is needed. With the help of the second of Eqs. (25), we obtain

$$D_I = \phi_\mathrm{F}(p_I)(1 - l_\mathrm{F}/l_I)^{-1} D_\mathrm{F} \equiv d_I D_\mathrm{F}. \tag{32}$$

Together with Eq. (31), this relation permits us to evaluate both $\Delta_\mathrm{F}(T \longrightarrow T_c)$ and $\Delta_I(T \longrightarrow T_c)$.

The result (32) is readily applied to the evaluation of the specific-heat jump ΔC at $T = T_c$ in the system with the two Fermi surfaces. One has

$$\begin{aligned} \Delta C &= -T\frac{dS}{dT} \\ &= \frac{1}{T_c}\int\left[\frac{d\Delta^2(p)}{dT}\right]_{T=T_c} n(p)[1 - n(p)]\frac{d^3p}{(2\pi)^3}, \end{aligned} \tag{33}$$

with $n(p) = \{1 + \exp[\xi(p)/T]\}^{-1}$. Simple algebra produces the result

$$\frac{\Delta C}{C_n} = (1 + R)\left(\frac{\Delta C}{C_n}\right)_{\mathrm{BCS}}, \tag{34}$$

where C_n is the specific heat of the system just above the transition temperature and the excess R, again assuming $g_{IF}^2 \ll 1$, is given by

$$R \simeq \frac{N_I}{N_\mathrm{F}}\left[\frac{\partial D_I^2/\partial T}{\partial D_\mathrm{F}^2/\partial T} - 1\right]. \tag{35}$$

It is instructive to analyze the excess R in more detail. On the one hand, its value is proportional to the ratio $N_I(0)/N_\mathrm{F}(0)$, which is seen to be small by phase-space arguments. On the other hand, R also depends on the departure of the quantity

$$\frac{\partial D_I^2/\partial T}{\partial D_\mathrm{F}^2/\partial T} \simeq \frac{\phi_\mathrm{F}^2(p_I)}{(1 - l_\mathrm{F}/l_I)^2}$$

from unity. This quantity, being positive and proportional to the ratio $\mathcal{V}(p_I, p_\mathrm{F})/\mathcal{V}(p_\mathrm{F}, p_\mathrm{F})$, can in fact have a value considerably in excess of 1. Indeed, the singular interaction represented by (3) should be present in both the particle–hole and particle–particle channels. If the

ratio of $\mathcal{V}$'s is evaluated for the amplitude F^s of Eq. (3), we immediately infer that for k_c close to p_F the factor $1 + R$ appearing in (34) does exceed unity.

In view of the above findings, it may be expected that the touchstone formula

$$\Delta_{BCS}(T = 0) = 1.57T_c \tag{36}$$

of BCS theory fails for a system having two or more Fermi surfaces. To verify this prediction, we (i) observe that the vanishing of the determinant $\mathcal{D}(T = 0)$ gives the relation

$$[L_0(\Delta_F) - l_F][L_0(\Delta_I) - l_I] - g_{IF}^2 L_0(\Delta_I) l_I = 0, \tag{37}$$

where $L_0(\Delta_F) = \ln(\varepsilon_F^0/\Delta_F)$ and $L_0(\Delta_I) = \ln(\varepsilon_F^0/\Delta_I)$; (ii) insert Eq. (32) into this relation; and (iii) compare the result with (26). After straightforward algebra, one obtains

$$\begin{aligned} L_0(\Delta_F) - L &\equiv \ln\left[\frac{1.57T_c}{\Delta_F(T = 0)}\right] \\ &= g_{IF}^2 \frac{\ln d_I}{1 - (l_F/l_I)[1 - (l_F/l_I) - \ln d_I]}. \end{aligned} \tag{38}$$

The ratio in the last member of Eq. (38) should be positive for positive $\ln d_I$. Further, if the value of this logarithm is of order unity, the connection

$$\ln\left[\frac{1.57T_c}{\Delta_F(T = 0)}\right] = R \ln d_I \tag{39}$$

can be established between the excess in the specific-heat jump and the deviation of the ratio $T_c/\Delta_F(T = 0)$ from its BCS value.

In summary, we have studied the rearrangement of single-particle degrees of freedom that precedes the phenomenon of pion condensation, the phase transition in nuclear and neutron matter that was predicted by A.B. Migdal more than 25 years ago. We have found that this rearrangement may express itself in the emergence of a bubble in the quasiparticle momentum distribution. As a consequence, the Fermi surface becomes doubly connected. We have examined some of the repercussions of such a rearrangement for the superfluid properties of dense neutron matter, specifically the ensuing modifications of the standard BCS results for the specific-heat jump at the transition temperature and for the relation between this critical temperature and the gap value at zero temperature. The formalism we have developed and the results we have obtained can be applied more widely in the theory of strongly correlated Fermi systems. In this spirit, it will be of special interest to revisit the case of superfluid ^{3}He, which offers a realistic example of a Fermi liquid existing near an antiferromagnetic phase transition.

ACKNOWLEDGMENTS

This research was supported in part by the US National Science Foundation under grant no. PHY-9900713 (J.W.C. and V.A.K.); by the McDonnell Center for the Space Sciences (V.A.K.); and by Russian Foundation for Basic Research, grant no. 00-15-96590 (V.A.K. and M.V.Z.). M.V.Z. acknowledges the hospitality of the INFN (Sezione di Catania) during a visit in which some of this work was carried out.

APPENDIX

The key relation (5) between the spectrum $\xi(p)$, the static limit Γ^k of the Landau scattering amplitude, and the quasiparticle momentum distribution $n(p)$ can be derived from the following two formulas (19.2) and (19.3) of [16]:

$$\begin{aligned} -\frac{\partial G^{-1}(\mathbf{p}, \varepsilon)}{\partial \mathbf{p}} &= \frac{\mathbf{p}}{M} + \frac{1}{2}\int \Gamma^k_{\alpha\beta,\alpha\beta}(\mathbf{p}, \mathbf{p}; \varepsilon, \varepsilon_1) \\ &\times G(\mathbf{p}_1, \varepsilon_1)\frac{\mathbf{p}_1}{M} G(\mathbf{p}_1 + \mathbf{k}, \varepsilon_1; k \longrightarrow 0)\frac{d^4 p_1}{(2\pi)^4 i} \end{aligned} \tag{A.1}$$

and

$$\begin{aligned} \frac{\partial G^{-1}(p, \varepsilon)}{\partial \varepsilon}\frac{\mathbf{p}}{M} &= \frac{\mathbf{p}}{M} + \frac{1}{2}\int \Gamma^\omega_{\alpha\beta,\alpha\beta}(\mathbf{p}, \mathbf{p}_1; \varepsilon, \varepsilon_1) \\ &\times G(\mathbf{p}_1, \varepsilon_1)\frac{\mathbf{p}_1}{M} G(\mathbf{p}_1, \varepsilon_1 + \omega;\ \omega \longrightarrow 0)\frac{d^4 p_1}{(2\pi)^4 i}. \end{aligned} \tag{A.2}$$

The single-particle Green's function

$$G(\mathbf{p}, \varepsilon) = zG^q(\mathbf{p}, \varepsilon) + G^r(\mathbf{p}, \varepsilon) \tag{A.3}$$

is made up of the pole term, namely $G^q(\mathbf{p}, \varepsilon) = [\varepsilon - \xi(p)]^{-1}$ multiplied by the quasiparticle weight factor z, together with the regular term $G^r(\mathbf{p}, \varepsilon)$. The symbol Γ^k entering (A.1) denotes the static limit $\Gamma(\mathbf{p}_1, \mathbf{p}_2, \varepsilon_1, \varepsilon_2, \mathbf{k} \longrightarrow 0, \omega \longrightarrow 0)$ of the scattering amplitude, with the limits taken so that $\omega/k \longrightarrow 0$. Similarly, Γ^ω denotes the static limit evaluated under the opposite constraint, $k/\omega \longrightarrow 0$. The amplitudes Γ^k and Γ^ω are linked to one another by

$$\begin{aligned} \Gamma^k_{\alpha\beta,\gamma\delta}(\mathbf{p}_1, \mathbf{p}_2; \varepsilon_1, \varepsilon_2) &= \Gamma^\omega_{\alpha\beta,\gamma\delta}(\mathbf{p}_1, \mathbf{p}_2; \varepsilon_1, \varepsilon_2) \\ &+ \int \Gamma^k_{\alpha\xi,\gamma\eta}(\mathbf{p}_1, \mathbf{p}; \varepsilon_1, \varepsilon) A(\mathbf{p}, \varepsilon) \\ &\times \Gamma^\omega_{\eta\beta,\xi\delta}(\mathbf{p}, \mathbf{p}_2; \varepsilon, \varepsilon_2)\frac{d^4 p_1}{(2\pi)^4 i}, \end{aligned} \tag{A.4}$$

where

$$\begin{aligned} A(\mathbf{p}, \varepsilon) &\equiv G(\mathbf{p}, \varepsilon) G(\mathbf{p} + \mathbf{k}, \varepsilon; k \longrightarrow 0) \\ - G(\mathbf{p}, \varepsilon) G(\mathbf{p}, \varepsilon + \omega;\ \omega \longrightarrow 0) &= 2\pi z^2 \delta(\varepsilon)\frac{dn(p)}{d\xi(p)}. \end{aligned} \tag{A.5}$$

Our objective is to recast (A.2) into a form containing only quasiparticle contributions. To this end, let us multiply both members of Eq. (A.2) from the left by the product $\Gamma^k A$ and integrate. Rewriting the result for the first term on the right-hand side with the aid of (A.4), we find

$$\frac{1}{2}\int \Gamma^k_{\alpha\beta,\,\alpha\beta}(\mathbf{p},\mathbf{p}_1;\,\varepsilon,\varepsilon_1)A(\mathbf{p}_1,\varepsilon_1)\frac{\partial G^{-1}(\mathbf{p}_1,\varepsilon_1)}{\partial\varepsilon_1}\frac{\mathbf{p}_1}{M}\frac{d^4p_1}{(2\pi)^4 i}$$

$$= \frac{1}{2}\int \Gamma^k_{\alpha\beta,\,\alpha\beta}(\mathbf{p},\mathbf{p}_1;\,\varepsilon,\varepsilon_1)A(\mathbf{p}_1,\varepsilon_1)\frac{\mathbf{p}_1}{M}\frac{d^4p_1}{(2\pi)^4 i} \qquad \text{(A.6)}$$

$$+\frac{1}{2}\int [\Gamma^k_{\alpha\beta,\,\alpha\beta}(\mathbf{p},\mathbf{p}_1;\,\varepsilon,\varepsilon_1) - \Gamma^\omega_{\alpha\beta,\,\alpha\beta}(\mathbf{p},\mathbf{p}_1;\,\varepsilon,\varepsilon_1)]$$

$$\times G(\mathbf{p}_1,\varepsilon_1)\frac{\mathbf{p}_1}{M}G(\mathbf{p}_1,\varepsilon_1+\omega;\,\omega\longrightarrow 0)\frac{d^4p_1}{(2\pi)^4 i}.$$

Collecting, on the right-hand side of the equation, similar terms containing Γ^k and using (A.1), we are led to

$$\frac{1}{2}\int \Gamma^k_{\alpha\beta,\,\alpha\beta}(\mathbf{p},\mathbf{p}_1;\,\varepsilon,\varepsilon_1)A(\mathbf{p}_1,\varepsilon_1)\frac{\partial G^{-1}(\mathbf{p}_1,\varepsilon_1)}{\partial\varepsilon_1}\frac{\mathbf{p}_1}{M}\frac{d^4p_1}{(2\pi)^4 i}$$

$$=\frac{1}{2}\int \Gamma^k_{\alpha\beta,\,\alpha\beta}(\mathbf{p},\mathbf{p}_1;\,\varepsilon,\varepsilon_1)G(\mathbf{p}_1,\varepsilon_1)\frac{\mathbf{p}_1}{M}G(\mathbf{p}_1+\mathbf{k},\varepsilon_1;\,k\longrightarrow 0) \qquad \text{(A.7)}$$

$$\times\frac{d^4p_1}{(2\pi)^4 i} - \frac{1}{2}\int \Gamma^\omega_{\alpha\beta,\,\alpha\beta}(\mathbf{p},\mathbf{p}_1;\,\varepsilon,\varepsilon_1)G(\mathbf{p}_1,\varepsilon_1)\frac{\mathbf{p}_1}{M}$$

$$\times G(\mathbf{p}_1,\varepsilon_1+\omega;\,\omega\longrightarrow 0)\frac{d^4p_1}{(2\pi)^4 i}.$$

Next, we subtract (A.1) and (A.2) from one another and observe that the difference coincides (in magnitude) with the right-hand side of Eq. (A.7). The latter equation may then be rewritten as

$$-\frac{\partial G^{-1}(\mathbf{p},\varepsilon)}{\partial\mathbf{p}} = \frac{\partial G^{-1}(\mathbf{p},\varepsilon)}{\partial\varepsilon}\frac{\mathbf{p}}{M}$$

$$+z^2\frac{1}{2}\int \Gamma^k_{\alpha\beta,\,\alpha\beta}(\mathbf{p},\mathbf{p}_1;\,\varepsilon,\varepsilon_1=0) \qquad \text{(A.8)}$$

$$\times\left(\frac{\partial G^{-1}(\mathbf{p}_1,\varepsilon_1)}{\partial\varepsilon_1}\right)_0\frac{\mathbf{p}_1}{M}\frac{dn(p_1)}{d\xi(p_1)}\frac{d^3p_1}{(2\pi)^3}.$$

We now set $\varepsilon = 0$ and replace $\partial G^{-1}(\mathbf{p},\varepsilon)/\partial\mathbf{p}$ by the derivative of the quasiparticle factor $(G^q)^{-1}(\mathbf{p},\varepsilon)$, which is reduced to $z^{-1}\partial\xi(p)/\partial\mathbf{p}$. Analogous transformations of the first term on the right-hand side of Eq. (A.8) yield $z^{-1}\mathbf{p}/M$. Since $(\mathbf{p}/M)dn/d\xi = (dn/d\mathbf{p})(M^*/M)$, we arrive at

$$\frac{\partial\xi}{\partial\mathbf{p}} = \frac{\mathbf{p}}{M}$$

$$+\frac{1}{2}\int F_{\alpha\beta,\,\alpha\beta}(\mathbf{p},\mathbf{p}_1;\,\varepsilon,\varepsilon_1=0)\frac{\partial n(p_1)}{\partial\mathbf{p}_1}\frac{d^3p_1}{(2\pi)^3}, \qquad \text{(A.9)}$$

where $F = z^2(M^*/M)\Gamma^k$. This is exactly the connection formula (5) that has been applied in the main text of the article.

REFERENCES

1. M. de Llano and J.P. Vary, Phys. Rev. C **19**, 1083 (1979).
2. V. A. Khodel and V. R. Shaginyan, Pis'ma Zh. Éksp. Teor. Fiz. **51**, 488 (1990) [JETP Lett. **51**, 553 (1990)]; Condens. Matter Theor. **12**, 222 (1997).
3. P. Nozieres, J. Phys. (Paris) **2**, 443 (1992).
4. M. V. Zverev, V. A. Khodel, and M. Baldo, Pis'ma Zh. Éksp. Teor. Fiz. **72**, 183 (2000) [JETP Lett. **72**, 126 (2000)].
5. A. M. Dyugaev, Zh. Éksp. Teor. Fiz. **70**, 2390 (1976) [Sov. Phys. JETP **43**, 1247 (1976)].
6. V. A. Khodel, V. R. Shaginyan, and M. V. Zverev, Pis'ma Zh. Éksp. Teor. Fiz. **65**, 242 (1997) [JETP Lett. **65**, 253 (1997)].
7. M. V. Zverev and V. A. Khodel, cond-mat/9907061.
8. L. P. Pitaevskiĭ, Zh. Éksp. Teor. Fiz. **37**, 1794 (1960) [Sov. Phys. JETP **10**, 1267 (1960)].
9. A. B. Migdal, Rev. Mod. Phys. **50**, 107 (1978).
10. A. B. Migdal, E. E. Saperstein, M. A. Troitsky, and D. N. Voskresensky, Phys. Rep. **192**, 179 (1990).
11. A. Akmal, V. R. Pandharipande, and D. G. Ravenhall, Phys. Rev. C **58**, 1804 (1998).
12. D. N. Voskresensky, V. A. Khodel, M. V. Zverev, and J. W. Clark, Astrophys. J. Lett. **533**, L127 (2000).
13. V. V. Khodel, V. A. Khodel, and J. W. Clark, Nucl. Phys. A **598**, 390 (1996).
14. V. V. Khodel, V. A. Khodel, and J. W. Clark, Phys. Rev. Lett. **81**, 3828 (1998).
15. V. A. Khodel, V. V. Khodel, and J. W. Clark, Nucl. Phys. A (in press).
16. A. A. Abrikosov, L. P. Gor'kov, and I. E. Dzialoshinskii, *Methods of Quantum Field Theory in Statistical Physics* (Fizmatgiz, Moscow, 1962; Prentice-Hall, Englewood Cliffs, 1963).

Physics of Atomic Nuclei, Vol. 64, No. 4, 2001, pp. 627–636. Translated from Yadernaya Fizika, Vol. 64, No. 4, 2001, pp. 686–695.

90th ANNIVERSARY OF A.B. MIGDAL'S BIRTHDAY
NUCLEI

Some Problems in the Generalized Theory of Finite Fermi Systems

S. P. Kamerdzhiev and E. V. Litvinova

Institute of Physics and Power Engineering, pl. Bondarenko 1, Obninsk, Kaluga oblast, 249020 Russia

Received July 18, 2000

Abstract—A realistic version of the generalization of the theory of finite Fermi systems to the case where some complex configurations involving phonons are explicitly taken into account is proposed. Secular equations describing the fragmentation of simple states in odd and even–even nuclei over complex configurations that belong to, respectively, the *quasiparticle* ⊗ *phonon* + *quasiparticle* ⊗ *phonon* ⊗ *phonon* and the *two quasiparticles* ⊗ *phonon* type and which are presently of greatest interest are derived on the basis of general relations for nuclei that involve pairing (nonmagic nuclei). These equations take into account effects associated with ground-state correlations due to complex configurations and with the additional quasiparticle–phonon mechanism of Cooper pairing in nuclei. The effects in question were disregarded previously, but they are of interest since they can be observed in present-day experiments. © *2001 MAIK "Nauka/Interperiodica".*

1. INTRODUCTION

It is well known that the conventional theory of finite Fermi systems was developed by A.B. Migdal [1] as a generalization of the Landau microscopic theory of Fermi liquids to the case of a finite nucleus—that is, to the case of a Fermi system consisting of two types of nucleons, possessing the property of superfluidity, and having finite dimensions. From the point of view of a comparison with available alternative approaches to studying even–even nuclei, the equations of the conventional theory of finite Fermi systems appear to be the equations of the random-phase approximation (RPA) for magic nuclei or the equations of the quasiparticle random-phase approximation (QRPA) for nonmagic nuclei as formulated in terms of the Green's function method. However, the use of consistent many-body theory in terms of the Green's function method proved to be seminal for a further development of the microscopic theory of the nucleus. The statement that the parameters of the theory have the same values for all nuclei (with the exception of light ones)—the universality principle advocated by Migdal and his disciples—is of paramount importance, especially at present, when much attention is being given to various unstable nuclei not yet investigated experimentally. In particular, this property of the theory of finite Fermi systems was largely responsible for its rapid and successful advancement to the fore as the underlying theory in the physics of giant multipole resonances immediately after their discovery in 1971 and 1972 (for an overview, see [2, 3]).

A further development of the theory of finite Fermi systems was associated primarily with taking into account self-consistency effects [4–6] and mesonic degrees of freedom [6]. Resorting to the coordinate representation, which made it possible to treat reliably the continuous single-particle spectrum in magic ([6]) and nonmagic ([7]) nuclei, was of paramount importance from the point of view of the computational technique. This circumstance was crucial for describing unstable nuclei whose binding energy is close to zero. Thus, the theory of finite Fermi systems basically remained a consistent microscopic theory that took into account relatively simple configurations, $1p1h$ within the RPA or $2qp$ within the QRPA; that is, an excited state was treated as a superposition of these configurations[1)] (more complex configurations were assumed to be effectively absorbed in the phenomenological constants of the theory of finite Fermi systems). For magic and odd near-magic nuclei, *particle* + *phonon* configurations were taken into account in order to compute the energies of the corresponding multiplets and some static effects (see the review articles [3–5]).

A microscopic theory that takes into account more complex configurations in nonmagic nuclei and which is based on the Green's function method has been developed since the study of Belyaev and Zelevinskiĭ [8], who considered pairing effects in odd nuclei. For even–even nuclei, it was the problem of describing the widths of giant multipole resonances (for an overview, see [2, 9–11]) that required generalizing the (Q)RPA. It turned out that, in order to solve this problem, it was sufficient, as a rule, to take into account the simplest of more complex configurations (that is, $1p1h \otimes$ *phonon* [9, 10] or $2qp \otimes$ *phonon* [11]). It should be emphasized that, in relation to the problem of taking into account

[1)]Of course, we also include ground-state correlations taken into account within the RPA or QRPA. For the sake of simplicity, we make use of the notation *qp* (quasiparticle), implying Bogolyubov quasiparticles and the full QRPA basis involving quasiparticle $1p1h$, $1h1p$, $1p1p$, and $1h1h$ channels.

simple configurations, that which incorporates more complex configurations is much more involved both theoretically and numerically, especially for nuclei where pairing effects are significant. A wide variety of approaches have been developed to tackle the last problem. Of these, the most advanced approach is that which is based on the quasiparticle–phonon model [11] relying on the Hamiltonian formulation and separable forces fitted to data on the energies of low-lying collective levels. However, this model takes no account of the single-particle continuous spectrum and, as a rule, of ground-state correlations associated with complex configurations.

In recent years, the need for refining and further developing a microscopic theory for taking into account complex configurations, especially in nuclei with pairing, has ever become more pressing, predominantly in connection with the emergence of new experimental results. By way of example, we list below some of the realms where advancements in experimental techniques have made it possible to obtain relevant information:

(i) Intensive development of modern germanium detectors and multidetector gamma spectrometers like those of the EUROBALL cluster and the EUROBALL type (see [12–14]) ensured an unprecedentedly high resolution and a high efficiency in recording gamma rays of energy up to 20 MeV. This furnished radically new information not only about deformed nuclei but also about multiplets of the $1qp \otimes phonon$ and the $1qp \otimes 2phonon$ type [13, 14]—that is, direct information about configurations involving phonons.

(ii) Results that have already been obtained—and even to a still greater extent, those that will be obtained—at radioactive-beam accelerators call for theoretical approaches that would take into account complex configurations for nuclei whose binding energy is close to zero, nuclei with a high neutron deficit, neutron-rich nuclei, and other unstable nuclear species.

In addition, there are many unresolved questions in the region of the neutron binding energy and above (region of giant resonances). These include those that are associated with the fine structure and decay properties of resonances, the origin of resonance-like structures, and the role of the odd nucleon [10, 11].

Experience gained in the first studies aimed at applying the theory of finite Fermi systems [6] to taking into account complex configurations in odd nuclei on the basis of this theory [3, 5] and on the basis of its generalization that incorporates $1p1h \otimes phonon$ configurations [9, 10] showed that the Green's function formalism makes it possible to consider the single-particle continuous spectrum, ground-state correlations associated with complex configurations [9, 15, 16], and complex configurations in the particle–particle channel (in particular, in the problem of Cooper pairing) [17, 18]. The majority of these effects can be observed in present-day experiments, and it is of prime importance that they can be incorporated in a theory that employs the Green's function formalism.

In order to formulate a viable approach—that is, an approach that would allow a sufficiently fast numerical implementation for a great number nuclei with pairing (it should be borne in mind that such nuclei present considerable computational difficulties) and which would be able, on the other hand, to describe present-day data—one can make use of two simplifying circumstances: the existence of the small parameter g^2 (g is the dimensionless amplitude for the production of a low-energy phonon) for semimagic nuclei [19] and the absence of self-consistency (in just the same way as in the conventional theory of finite Fermi systems) in our problem featuring complex configurations (this means that we will use two sets of input phenomenological parameters—parameters that describe the mean nuclear field and parameters that describe nucleon interactions in the particle–hole and the particle–particle channel).

On the basis of the Green's function formalism, we propose here viable methods for explicitly taking into account some complex configurations in odd and even–even nuclei. We will derive secular equations that describe the fragmentation of simple states over complex configurations in nonmagic nuclei. In order to avoid encumbering our presentation, some results will be presented, however, only for magic nuclei.

2. GENERAL RELATIONS FOR NUCLEI THAT INVOLVE PAIRING

In this section, we obtain general relations that will be specified in Sections 3 and 4. Here, we do not preset any concrete form of self-energy operators, only assuming that they involve quasiparticle–phonon interaction generating complex configurations.

Since there is no self-consistency, the phenomenological pairing gap Δ_λ and the phenomenological mean field that is described by the Woods–Saxon potential and which determines the relevant single-particle energies ϵ_λ and the corresponding wave functions appear as inputs in our problem. Since the self-energy operators contribute to the phenomenological quantities ϵ_λ and Δ_λ, special care should be taken here to avoid double counting. For this, the above phenomenological quantities must be refined by removing the contribution of quasiparticle–phonon interaction contained in the self-energy operators from these phenomenological quantities. The refining procedure—that is, a transition from $\{\epsilon_\lambda, \Delta_\lambda\}$ to their refined counterparts $\{\tilde{\epsilon}_\lambda, \tilde{\Delta}_\lambda\}$—is specified at the end of this section.

2.1. General Equations for Single-Particle Green's Functions

In [19, 20], general equations for single-particle Green's functions for a Fermi system that involves pairing were obtained in a form where known mean-field components described by Green's functions of the Gor'kov type were singled out explicitly. This was done by proceeding from the most general equations for the normal (causal) and anomalous Green's functions G and F in a Fermi system that involves pairing. In the symbolic notation used in the present section, they are given by

$$\begin{aligned} G &= G_0 + G_0\Sigma G - G_0\Sigma^{(1)}F^{(2)}, \\ F^{(2)} &= G_0^h\Sigma^h F^{(2)} + G_0^h\Sigma^{(2)}G, \end{aligned} \tag{1}$$

where Σ, Σ^h, $\Sigma^{(1)}$, and $\Sigma^{(2)}$ are the corresponding total self-energy operators, while G_0 and G_0^h are the Green's functions for a perfect gas. The set of Eqs. (1) must be supplemented with analogous equations for G^h and $F^{(1)}$, which describe the inverse process. In order to obtain realistic equations, each self-energy operator is represented as the sum of two terms,

$$\begin{aligned} &\Sigma(\epsilon) = \tilde{\Sigma} + M(\epsilon), \quad \Sigma^{(1)}(\epsilon) = \tilde{\Sigma}^{(1)} + M^{(1)}(\epsilon), \\ &\Sigma^h(\epsilon) = \tilde{\Sigma}^h + M^h(\epsilon), \quad \Sigma^{(2)}(\epsilon) = \tilde{\Sigma}^{(2)} + M^{(2)}(\epsilon). \end{aligned} \tag{2}$$

Here, the first terms are independent of energy and correspond to pairing described by a mechanism of the Bardeen–Cooper–Schrieffer (BCS) type for the self-energy operators $\Sigma^{(1)}$ and $\Sigma^{(2)}$ and to our mean field. The second terms (self-energy operators $M^{(i)}$) are not specified for the time being. It is assumed that they involve quasiparticle–phonon interaction, which generates complex configurations. The set of Eqs. (1) can then be recast into the form [20]

$$\begin{aligned} G &= \tilde{G} + \tilde{G}MG - \tilde{F}M^hF^{(2)} - \tilde{G}M^{(1)}F^{(2)} - \tilde{F}^{(1)}M^{(2)}G, \\ F^{(2)} &= \tilde{F}^{(2)} + \tilde{F}^{(2)}MG + \tilde{G}^hM^hF^{(2)} \\ &\quad - \tilde{F}^{(2)}M^{(1)}F^{(2)} + \tilde{G}^hM^{(2)}G. \end{aligned} \tag{3}$$

Here, the tilde-labeled Green's functions are the Gor'kov Green's functions

$$\begin{aligned} \tilde{G}_\lambda(\epsilon) &= \tilde{G}_\lambda^h(-\epsilon) = \frac{\tilde{u}_\lambda^2}{\epsilon - \tilde{E}_\lambda + i\delta} + \frac{\tilde{v}_\lambda^2}{\epsilon + \tilde{E}_\lambda - i\delta}, \\ \tilde{F}_\lambda^{(1)}(\epsilon) &= \tilde{F}_\lambda^{(2)}(\epsilon) \\ &= -\frac{\tilde{\Delta}_\lambda}{2\tilde{E}_\lambda}\left(\frac{1}{\epsilon - \tilde{E}_\lambda + i\delta} - \frac{1}{\epsilon + \tilde{E}_\lambda - i\delta}\right), \end{aligned} \tag{4}$$

where

$$\tilde{u}_\lambda^2 = 1 - \tilde{v}_\lambda^2 = \frac{\tilde{E}_\lambda + \tilde{\epsilon}_\lambda}{2\tilde{E}_\lambda}, \quad \tilde{E}_\lambda = \sqrt{\tilde{\epsilon}_\lambda^2 + \tilde{\Delta}_\lambda^2}.$$

It is important here that, by definition, the tilde-labeled quantities involve no contributions from the self-energy operators $M^{(i)}$. Since the input quantities $\{\epsilon_\lambda, \Delta_\lambda\}$ are determined from experimental data in our approach, the contribution of $M^{(i)}$ must be removed from them in order to obtain the refined quantities $\{\tilde{\epsilon}_\lambda, \tilde{\Delta}_\lambda\}$.

It is advisable to recast Eqs. (1) into an alternative form that would make it possible to single out more compactly that pairing mechanism which is different from the conventional BCS mechanism. For this, we represent Eqs. (1) as [19]

$$\begin{aligned} G &= \tilde{G}_0 + \tilde{G}_0MG - \tilde{G}_0\Sigma^{(1)}F^{(2)}, \\ F^{(2)} &= \tilde{G}_0^hM^hF^{(2)} + \tilde{G}_0^h\Sigma^{(2)}G, \end{aligned} \tag{5}$$

where the Green's functions $\tilde{G}_0$ and $\tilde{G}_0^h$ define refined quasiparticles (without pairing) in the mean field:

$$\begin{aligned} \tilde{G}_0 &= G_0 + G_0\tilde{\Sigma}\tilde{G}_0, \\ \tilde{G}_0^h &= G_0^h + G_0^h\tilde{\Sigma}^h\tilde{G}_0^h. \end{aligned} \tag{6}$$

Further, we introduce the Green's function $\overline{G}^h$ that satisfies the Dyson equation

$$\overline{G}^h = \tilde{G}_0^h + \tilde{G}_0^hM^h\overline{G}^h. \tag{7}$$

The second equation in (5) then reduces to the form

$$F^{(2)} = \overline{G}^h\Sigma^{(2)}G. \tag{8}$$

Substituting (8) into the first equation in (5), we find that the Green's function G satisfies the equation

$$G = \tilde{G}_0 + \tilde{G}_0MG - \tilde{G}_0\Sigma^{(1)}\overline{G}^h\Sigma^{(2)}G. \tag{9}$$

By using the refined Gor'kov Green's function (4), which satisfies the equation

$$\tilde{G} = \tilde{G}_0 - \tilde{G}_0(\tilde{\Sigma}^{(1)}\tilde{G}_0^h\tilde{\Sigma}^{(2)})\tilde{G}, \tag{10}$$

we eventually obtain

$$G = \tilde{G} + \tilde{G}MG + \tilde{G}M_{\text{el}}G, \tag{11}$$

where the self-energy operator

$$M_{\text{el}} = -(\Sigma^{(1)}\overline{G}^h\Sigma^{(2)} - \tilde{\Sigma}^{(1)}\tilde{G}_0^h\tilde{\Sigma}^{(2)}) \tag{12}$$

represents the general expression for that part of the self-energy operator in a Fermi system which is responsible for the pairing mechanism additional to the refined BCS mechanism {here, the last term in (12) [see Eq. (10)] corresponds to this mechanism}—that is, for the quasiparticle–phonon mechanism in our case.

By way of example, we indicate that, in the case where all $M^{(i)} = 0$, the above results coincide with the results known from the theory of finite Fermi systems if our refined quantities are replaced by their phenomenological analogs and if M_{el} is set to zero.

2.2. Secular Equation for the Excitation Energies of an Odd Nucleus

For the sake of simplicity, we will henceforth use the diagonal approximation in the single-particle indices λ. For a spherical nucleus, this approximation of $M_{\lambda\lambda'}$ is quite reasonable, since off-diagonal $M_{\lambda\lambda'}$ are nonzero only for transitions where the initial and the final state do not belong to the same shell or to neighboring shells. For the problem without pairing, the off-diagonal case was considered in [21]; the results obtained there can easily be generalized to the case where pairing is taken into account. In the diagonal approximation, the required solutions to the set of Eqs. (3) are given by [19, 22]

$$G_\lambda(\epsilon) = \frac{\epsilon + \tilde{\epsilon}_\lambda + M_\lambda^h(\epsilon)}{\theta_\lambda(\epsilon)}, \qquad F_\lambda^{(2)}(\epsilon) = \frac{\tilde{\Delta}_\lambda^{(2)} + M_\lambda^{(2)}(\epsilon)}{\theta_\lambda(\epsilon)}, \tag{13}$$

where

$$\theta_\lambda(\epsilon) = [\epsilon - \tilde{\epsilon}_\lambda - M_\lambda(\epsilon)][\epsilon + \tilde{\epsilon}_\lambda + M_\lambda^h(\epsilon)] - [\tilde{\Delta}_\lambda^{(2)} + M_\lambda^{(2)}(\epsilon)]^2. \tag{14}$$

By setting $\theta_\lambda(\epsilon)$ to zero, we therefore obtain a secular equation that determines the fragmentation of a single-particle state λ over complex configurations specified by the operators $M^{(i)}$ in an odd nucleus with pairing. Accordingly, we have

$$[\eta - \tilde{\epsilon}_\lambda - M_\lambda(\eta)][\eta + \tilde{\epsilon}_\lambda + M_\lambda^h(\eta)] - [\tilde{\Delta}_\lambda^{(2)} + M_\lambda^{(2)}(\eta)]^2 = 0, \tag{15}$$

where η is a solution to the equation $\theta_\lambda(\epsilon) = 0$; it must have two indices, λ and n (solution number). Since $M^h(\epsilon) = M(-\epsilon)$ and since $M^{(2)}(\epsilon)$ is an even function of ϵ, Eq. (15) is invariant under the substitution $\eta \longrightarrow -\eta$.

Following [22], we represent the operator M as the sum of the even and the odd component,

$$M(\epsilon) = M_{\rm ev}(\epsilon) + M_{\rm od}(\epsilon). \tag{16}$$

Equation (15) then takes the form

$$\eta^2 - \tilde{E}_\lambda^2 - 2\eta M_{\lambda\rm od}(\eta) - 2\tilde{\epsilon}_\lambda M_{\lambda\rm ev}(\eta) - 2\tilde{\Delta}_\lambda^{(2)} M_\lambda^{(2)}(\eta) - [M_{\lambda\rm ev}^2 - M_{\lambda\rm od}^2 + M_\lambda^{(2)2}](\eta) = 0, \tag{17}$$

where $\tilde{E}_\lambda = \sqrt{\tilde{\epsilon}_\lambda^2 + \tilde{\Delta}_\lambda^2}$.

From Eq. (3) or (15), we can also obtain the formal solution

$$\eta = \pm\sqrt{\epsilon_{\lambda n}^2 + \Delta_{\lambda n}^2}, \tag{18}$$

where

$$\epsilon_{\lambda n} = \frac{\tilde{\epsilon}_\lambda + M_{\lambda\rm ev}(\eta)}{1 + q_\lambda(\eta)}, \quad \Delta_{\lambda n}^{(2)} = \frac{\tilde{\Delta}_\lambda^{(2)} + M_\lambda^{(2)}(\eta)}{1 + q_\lambda(\eta)}, \tag{19}$$

with $q_\lambda = -M_{\lambda\rm od}(\eta)/\eta$. Equations that are similar in form to those in (18) and (19) were obtained in [17], but the terms $\tilde{\epsilon}_\lambda$ and $\tilde{\Delta}_\lambda$ were not singled out explicitly there.

2.3. Equations for the Refined Quantities $\tilde{\epsilon}_\lambda$ and $\tilde{\Delta}_\lambda$

By using Eqs. (18) and (19), we can obtain the refined quantities $\tilde{\epsilon}_\lambda$ and $\tilde{\Delta}_\lambda$ from their phenomenological counterparts ϵ_λ and Δ_λ. The experimental single-particle energies must correspond to dominant levels (that is, levels characterized by the largest spectroscopic factors) obtained as solutions to Eq. (17) or solutions to the set of Eqs. (18) and (19). Therefore, the refining procedure must be implemented in such a way that one of the solutions coincides with the experimental value and that this solution (we denote by E_λ the corresponding energy) would remain dominant. We denote the relevant quantities by ϵ_λ and Δ_λ. With the aid of Eqs. (18) and (19), we then find that the refined quantities $\tilde{\epsilon}_\lambda$ and $\tilde{\Delta}_\lambda$ are related to their phenomenological counterparts ϵ_λ and Δ_λ by the equations

$$\epsilon_\lambda = \frac{\tilde{\epsilon}_\lambda + M_{\lambda\rm ev}(E_\lambda)}{1 + q_\lambda(E_\lambda)}, \quad \Delta_\lambda^{(2)} = \frac{\tilde{\Delta}_\lambda^{(2)} + M_\lambda^{(2)}(E_\lambda)}{1 + q_\lambda(E_\lambda)}, \quad E_\lambda = \sqrt{\epsilon_\lambda^2 + \Delta_\lambda^2}, \tag{20}$$

where $q_\lambda = -M_{\lambda\rm od}(E_\lambda)/E_\lambda$. The nonlinear relations (20) determine the refined quantities $\tilde{\epsilon}_\lambda$ and $\tilde{\Delta}_\lambda$ if we know the phenomenological quantities ϵ_λ and Δ_λ. The latter can be found from experimental low-lying single-particle excitations in nonmagic nuclei (see, for example, [19]).

Expression (20) for the observed pairing gap receives contributions from two mechanisms of Cooper pairing in nuclei. These are the conventional BCS mechanism, which is concealed in the quantity $\tilde{\Delta}_\lambda$, and the quasiparticle–phonon mechanism, which is determined by the self-energy operators $M_\lambda^{(2)}$ and $M_{\lambda\rm od}$. The latter also contributes to $\tilde{\Delta}_\lambda$ [18, 19]. The first quantitative estimations of these mechanisms revealed [18] that, for the ^{120}Sn nucleus, the total contribution of the quasiparticle–phonon mechanism saturates 26% of the observed pairing gap, the difference $\Delta_\lambda - \tilde{\Delta}_\lambda$ being 31% (these values were obtained for the relevant quantities averaged over the states λ).

3. FRAGMENTATION OF SINGLE-QUASIPARTICLE STATES OVER COMPLEX CONFIGURATIONS

3.1. Complex Configurations 1qp ⊗ phonon

Let us derive the secular equation for the simplest case of $M^{(i)} \sim g^2$. The self-energy operator then has the form

$$\hat{M} = \quad , \qquad \hat{\tilde{G}}_2$$

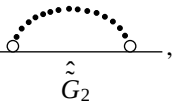

$$\hat{M} \equiv \hat{M}(g^2) = \begin{pmatrix} M & iM^{(1)} \\ -iM^{(2)} & -M^h \end{pmatrix} = -gD\hat{\tilde{G}}g, \quad (21)$$

where

$$\hat{\tilde{G}} = \begin{pmatrix} \tilde{G} & -i\tilde{F}^{(1)} \\ i\tilde{F}^{(2)} & -\tilde{G}^h \end{pmatrix}$$

is the matrix of the bare Green's functions specified by Eqs. (4); no account is taken here of pair phonons. Here and below, a dotted line represents the phonon Green's function.

From expression (21), we can see that, for the g^2 approximation to be realized, $\hat{M}$ must involve the refined Green's functions $\tilde{G}^i$ constructed from $\tilde{\epsilon}_\lambda$ and $\tilde{\Delta}_\lambda$. For the case of $M^{(i)}(g^2)$ considered here, it would not be absolutely erroneous to use the phenomenological quantities ϵ_λ and Δ_λ in (21). Partly, this issue was considered in [23] (difference $\epsilon_\lambda - \tilde{\epsilon}_\lambda$) and in [19], where it was shown that, in order to obtain quantitatively correct results, it is necessary to take into account the refinement of the gap. It would be interesting to find an experimental corroboration of this effect. But if it is necessary to include terms of order g^4 (see Subsection 3.2), as is required in the majority of cases, the use of the refined quantities is mandatory to avoid the double counting of the operators M (or quasiparticle–phonon interaction).

The expressions for the operators $M^{(i)}(g^2)$ are presented in the Appendix to [19]. Substituting these expressions into (17), we obtain the secular equation

$$E_{1n}^2 - \tilde{E}_1^2 - 2\sum_{2s} \left|g_{12}^s\right|^2 \frac{1}{E_{1n}^2 - \tilde{E}_{2s}^2}\left[E_{1n}^2 + \frac{\tilde{E}_{2s}}{\tilde{E}_2}(\tilde{\epsilon}_1\tilde{\epsilon}_2 - \tilde{\Delta}_1\tilde{\Delta}_2)\right]$$

$$+ \sum_{2s} \left|g_{12}^s\right|^2 \sum_{2's'} \left|g_{12'}^{s'}\right|^2 \frac{1}{(E_{1n}^2 - \tilde{E}_{2s}^2)(E_{1n}^2 - \tilde{E}_{2's'}^2)} \quad (22)$$

$$\times \left[E_{1n}^2 - \frac{\tilde{E}_{2s}\tilde{E}_{2's'}}{\tilde{E}_2\tilde{E}_{2'}}(\tilde{\epsilon}_2\tilde{\epsilon}_{2'} + \tilde{\Delta}_2\tilde{\Delta}_{2'})\right] = 0,$$

where $\lambda = \lambda_1 \equiv 1$ and $\tilde{E}_{2s} = \tilde{E}_2 + \omega_s$. The double sum over (2, s) and (2', s') involves g^4 terms obtained upon taking into account the bracketed expression in Eq. (17); note that there are no second-order poles in the double sum. For semimagic nuclei, where $g^2 < 1$, the contribution of this double sum can be quite modest, but this was not verified numerically. Without terms of order g^4, the above equation coincides with the corresponding equation in the quasiparticle–phonon model if we discard ground-state correlations, which ensure invariance under time reversal, and replace $\tilde{\epsilon}_\lambda$ and $\tilde{\Delta}_\lambda$ by, respectively, ϵ_λ and Δ_λ (for more details, see [19]).

3.2. Complex Configurations 1qp ⊗ phonon + 1qp ⊗ phonon ⊗ phonon

Since relevant expressions for nuclei where pairing occurs are very cumbersome, we will henceforth present the eventual analytic formulas only for magic nuclei. As to the general procedure for deducing results for odd and even–even nonmagic nuclei (present subsection and Section 4, respectively), it becomes clear upon following the analogous procedure for magic nuclei, which is modified by replacing, in the relevant diagrams and in the corresponding general formulas, the Green's functions G and $\tilde{G}$ and the self-energy operator M by, respectively, $\hat{G}$, $\hat{\tilde{G}}$, and $\hat{M}$ [see Eq. (21)] and by additionally replacing, if pair phonons are taken into account, the phonon amplitude g by the matrix $\hat{g}$.

It was mentioned above that, in order to describe available experimental data for odd nuclei, it is necessary to include, in addition to 1*qp* ⊗ *phonon* complex configurations, at least 1*qp* ⊗ *phonon* ⊗ *phonon* configurations [13, 14]. The main problem here is to formulate equations that do not involve second-order poles. In terms of Green's functions, the simplest 1*qp* ⊗ *phonon* ⊗ *phonon* terms in the self-energy operator have the graphic representation

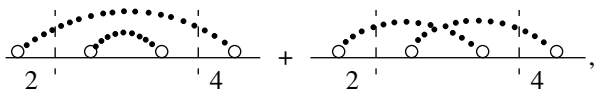

(23)

where thin lines stand for the refined Green's functions $\tilde{G}$. It can easily be seen, however, that these graphs involve unphysical second-order poles $[\eta - (\epsilon_\lambda + \omega_s)]^2$, which, at $\lambda_2 = \lambda_4$, correspond to cuts shown by dashed lines. That one aims here at describing individual low-lying levels renders this difficulty all the more serious. A general recipe for sidestepping such problems is well

known (see, for example, [23]): it is necessary to sum diagrams belonging to a specific class in all orders in g^2. For this reason, we will proceed from the general representation of the self-energy operator for the case of quasiparticle–phonon interaction [24]:

$M =$ 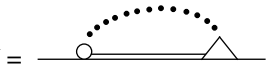 $\equiv -gDG\Gamma.$ (24)

Here, the double line represents the total Green's function G, while the triangle stands for the vertex operator. For phonons, we use the well-known Green's function with experimental features or features fitted to experimental data [8]. In the vertex Γ taken in the approximation adopted here, it is necessary to include, in addition to the bare expression, the simplest expression of order g^3,

$i\Gamma_{21} =$ 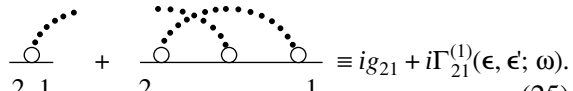 $\equiv ig_{21} + i\Gamma^{(1)}_{21}(\epsilon, \epsilon'; \omega).$ (25)

Here, the refined Green's functions $\tilde{G}$ appear in $\Gamma^{(1)}$. Taking into account (25), we then find from (24) that

$M =$ 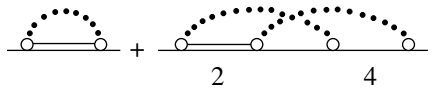 $\equiv M^r + M^v.$ (26)

If configurations that are more complex than $1qp \otimes phonon \otimes phonon$ are not needed, the total Green's function G in Eq. (26) must be taken with the self-energy operator involving only g^2 [see Eq. (17)]:

$G =$  ,

$$G = \tilde{G} + \tilde{G}M(g^2)G. \quad (27)$$

Thus, the representation of the self-energy operator in the form specified by Eqs. (26) and (27) conforms to the problem under consideration—as can be seen from (26), neither term now has second-order poles since the total Green's function in (26) represents, according to (27), an infinite sum of diagrams of order g^2 (see also below). Solutions to Eq. (27) can easily be obtained both for magic ([21, 25]) and for nonmagic ([19]) nuclei.

In order to derive the expression for the rainbow graph M^r, we make use of the general representation of the Green's function in the diagonal approximation [21]. We have

$$G_\lambda(\epsilon) = \sum_k \frac{a_{\lambda_k}}{\epsilon - \epsilon_{\lambda_k} + i\gamma \mathrm{sgn}\epsilon_{\lambda_k}}, \quad (28)$$

where

$$a_{\lambda_k} = \left(1 - \frac{\partial M_\lambda(g^2, \epsilon)}{\partial \epsilon}\right)^{-1}_{\epsilon = \epsilon_{\lambda_k}} \quad (29)$$

and ϵ_{λ_k} is a solution to Eq. (27). By explicitly singling out the dominant (phenomenological) term, we can recast expression (28) into the alternative form [21]

$$G_\lambda(\epsilon) = a_\lambda\left\{\frac{1-n_\lambda}{\epsilon - \epsilon_\lambda + i\gamma} + \frac{n_\lambda}{\epsilon - \epsilon_\lambda - i\gamma}\right\} + \sum_{k\neq 1}\left\{\frac{a^p_{\lambda_k}}{\epsilon - \epsilon_{\lambda_k} + i\gamma} + \frac{a^h_{\lambda_k}}{\epsilon - \epsilon_{\lambda_k} - i\gamma}\right\}. \quad (30)$$

For our purposes, it is important that, upon the substitution of (30) into (26), $\epsilon_2 \neq \tilde{\epsilon}_4$, which implies the absence of second-order poles. Substituting expression (28) into M^r, we obtain

$$M^r_1(\epsilon) = \sum_{2,s,k}\left|g^s_{12}\right|^2\left\{\frac{a^p_{2_k}}{\epsilon - \omega_s - \epsilon_{2_k} + i\delta} + \frac{a^h_{2_k}}{\epsilon + \omega_s - \epsilon_{2_k} - i\delta}\right\}. \quad (31)$$

The expressions derived for the vertex $\Gamma^{(1)}$ and for the crossed self-energy operator M^v with allowance for (28) are presented in the Appendix. Substituting $M = M^r + M^v$ from (31) and (A.2) into Eq. (15) (this is more convenient in the case of magic nuclei—that is, when $\tilde{\Delta} = M^{(2)} = 0$), we find that the secular equation that determines the fragmentation of the single-particle state λ over $1qp \otimes phonon$ and $1qp \otimes phonon \otimes phonon$ configurations has the form

$$\eta \mp \tilde{\epsilon}_1 \mp \sum_{2,s,k}\frac{\left|\langle 1\|g^s\|2\rangle\right|^2}{2j_1+1}\left\{\frac{a^p_{2_k}}{\pm\eta - \omega_s - \epsilon_{2_k}} + \frac{a^h_{2_k}}{\pm\eta + \omega_s - \epsilon_{2_k}}\right\} + \sum_{s,s'}\sum_{\tilde{3},\tilde{4},\tilde{5}}\frac{(-1)^{j_1+j_3+j_{\tilde{4}}+j_{\tilde{5}}}}{2j_1+1} \times \begin{Bmatrix} j_3 & L & j_1 \\ j_{\tilde{5}} & L' & j_{\tilde{4}} \end{Bmatrix}\langle 1\|g^s\|3\rangle\langle 3\|g^{s'}\|\tilde{4}\rangle\langle\tilde{4}\|g^s\|\tilde{5}\rangle \times \langle\tilde{5}\|g^{s'}\|1\rangle\mathcal{J}^{ss'}_{3\tilde{4}\tilde{5}}(\pm\eta) = 0, \quad (32)$$

where $\mathcal{J}^{ss'}_{3\tilde{4}\tilde{5}}(\eta)$ is given by expression (A.2) in the Appendix. It follows from (15) that Eq. (32) is invariant under the substitution of $-\eta$ for η. We retained here $k \neq 1$ terms, but it seems that of greatest importance are $k = 1$ terms—that is, the first two terms in Eq. (30).

There is every reason to hope that Eq. (32) describes quite accurately not only the energies of levels that appear to be superpositions of $1qp \otimes phonon$ configu-

rations but also the energies of levels that are determined by $1qp \otimes phonon \otimes phonon$ configurations. In stating the latter, we bore in mind that, on one hand, such levels, sufficiently pure ones indeed, were observed experimentally [13, 14] and that, on the other hand, the contributions of diagrams of order g^6, which correspond to taking into account three phonons, must be modest for semimagic nuclei, since $g^2 < 1$ for such nuclear species. Additional terms, at least part of them are already contained in the above equations, can be taken into account, if necessary, by analogy with the procedure outlined here.

Equation (32) differs noticeably from the corresponding equation in the quasiparticle–phonon model (see [11]). Our equations disregard g^6 and g^8 terms, which stem from the use of a more precise expression for the phonon Green's function in [11], but—what is more important—they take into account ground-state correlations. A second distinctive feature of our approach is that it relies on the refined quantities $\tilde{\epsilon}_\lambda$ and $\tilde{\Delta}_\lambda$ (in the sense clarified above), which must be found by formulas (20) with the aid of the above complicated expressions for our self-energy operators. These two distinctions may be of importance in describing individual low-lying levels in odd nuclei.

4. FRAGMENTATION OF PARTICLE–HOLE STATES OVER $1p1h \otimes phonon$ COMPLEX CONFIGURATIONS

Here, we will consider only magic nuclei and derive equations not featuring second-order poles. In this sense, our results emerge from a direct generalization of the approach formulated in [23]; for this reason, we discuss solely the most important point—namely, the modification of the propagators in the integral equation for the density matrix or for the vertex function (the remaining formulas retain the original form). By invoking the result obtained in [26], the idea being discussed can be straightforwardly generalized to nuclei where pairing occurs.

For the problem of taking into account complex configurations of the $1p1h \otimes phonon$ type within the Green's function formalism, an attempt at getting rid of second-order poles is not new. Previously, it was implemented numerically within a more complicated version that is referred to as the method of the chronological decomposition of diagrams and which is based on approximately summing, in the propagator, diagrams of order g^2 that feature self-energy inserts and a phonon in the transverse particle–hole channel (for detail, see [10]). This approach was successfully used to describe many giant multipole resonances in the doubly magic nuclei ^{40}Ca, ^{56}Ni, ^{48}Ca, ^{208}Pb, ^{78}Ni, ^{100}Sn, and ^{132}Sn, as well as in ^{58}Ni. In this way, it appeared to be possible to take simultaneously into account the single-particle continuous spectrum, ground-state correlations, and nonseparable effective interaction [10]. However, the problem of generalizing the method of the chronological decomposition of diagrams is very cumbersome. Anyway, it is instructive to consider an alternative approach that would be in a sense more natural and simpler in a numerical implementation, the latter being of prime importance for its generalization to the case of nonmagic nuclei.

The fragmentation of pure $1p1h$ configurations that is due to particle–hole interactions is taken into account within the theory of finite Fermi systems or within the RPA. Our task is to include more complex configurations—at least those of the $1p1h \otimes phonon$ type—in such a way as to avoid the emergence of second-order poles. The equation for the density matrix or for the vertex function is determined almost completely by the propagator

$$A(\omega) = \int K(\epsilon, \omega)\frac{d\epsilon}{2\pi i}, \tag{33}$$

where

$K =$ 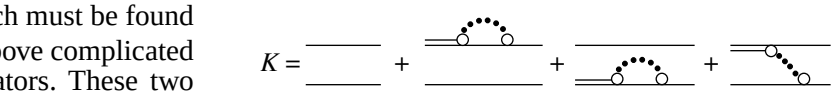 ,

$$K = \tilde{G}\tilde{G} + GM\tilde{G}\tilde{G} + \tilde{G}GM\tilde{G} - G\tilde{G}gDg\tilde{G}\tilde{G}. \tag{34}$$

Here, the total Green's function G satisfies Eq. (27). It seems that of greatest interest is the case of $k = 1$, which corresponds to taking into account the first term in expression (30) for the function K (34). In [23], use was made of the quantity K involving the Green's function $\tilde{G}$ instead of the total Green's function G, but this resulted in the emergence of second-order poles. Expression (34) can be recast into two alternative forms:

$$K = -\tilde{G}\tilde{G} + G\tilde{G} + \tilde{G}G - G\tilde{G}gDg\tilde{G}\tilde{G}, \tag{35}$$

$$K = GG - \tilde{G}MG\tilde{G}MG - G\tilde{G}gDg\tilde{G}\tilde{G}. \tag{36}$$

We must further specify the full Green's function G. Proceeding in just the same way as in the case of odd nuclei [see Eq. (26)], we can represent it in the form $G = [\tilde{G}^{-1} - M(g^2, \epsilon)]^{-1}$ or make use of the solution to equation $G^{-1} = 0$ in the form (28), where it is necessary to take into account the total sum over k in solving Eq. (27). With the aid of (28), we find for the propagator in (35) that

$$A_{12}(\omega) = -\frac{n_{\tilde{1}} - n_{\tilde{2}}}{\epsilon_{\tilde{1}\tilde{2}} + \omega} + \sum_k a_{1_k}\frac{n_{1_k} - n_{\tilde{2}}}{\epsilon_{1_k\tilde{2}} + \omega}$$

$$+ \sum_k a_{2_k}\frac{n_{\tilde{1}} - n_{2_k}}{\epsilon_{\tilde{1}2_k} + \omega} + \sum_{\tilde{3},\tilde{4},s}\sum_k \frac{a_{1_k}}{(\epsilon_{1_k\tilde{2}} + \omega)(\epsilon_{\tilde{3}\tilde{4}} + \omega)}$$

$$\times\left\{\frac{n_{1_k}(1-n_{\tilde{3}})}{\epsilon_{\tilde{3}1_k} + \omega_s} - \frac{(1-n_{1_k})n_{\tilde{3}}}{\epsilon_{\tilde{3}1_k} - \omega_s} - \frac{n_{\tilde{2}}(1-n_{\tilde{3}})}{\epsilon_{\tilde{3}\tilde{2}} + \omega_s + \omega}\right. \tag{37}$$

$$+\frac{(1-n_{\tilde{2}})n_{\tilde{3}}}{\epsilon_{\tilde{3}\tilde{2}}-\omega_s+\omega}-\frac{n_{1_k}(1-n_{\tilde{4}})}{\epsilon_{\tilde{4}1_k}+\omega_s-\omega}+\frac{(1-n_{1_k})n_{\tilde{4}}}{\epsilon_{\tilde{4}1_k}-\omega_s-\omega}$$

$$+\frac{n_{\tilde{2}}(1-n_{\tilde{4}})}{\epsilon_{\tilde{4}\tilde{2}}+\omega_s}-\frac{(1-n_{\tilde{2}})n_{\tilde{4}}}{\epsilon_{\tilde{4}\tilde{2}}-\omega_s}\Bigg\},$$

where $\epsilon_{\tilde{1}\tilde{2}}\equiv\tilde{\epsilon}_1-\tilde{\epsilon}_2$ and $\epsilon_{\tilde{1}2}\equiv\tilde{\epsilon}_1-\epsilon_2$ and where we have considered that $a^p_{1_k}=a_{1_k}(1-n_{1_k})$ and $a^h_{1_k}=a_{1_k}n_{1_k}$.

All the remaining formulas, including those that describe observables, are obtained from the corresponding formulas in [23] by substituting expression (37) for the propagator. This approach makes it possible to calculate much more straightforwardly all giant multipole resonances in magic nuclei (and not only $M1$ resonances as in [23]). Following a procedure similar to that outlined above and using the results presented in [26], one can easily generalize the results obtained in this section to the case of nonmagic nuclei.

5. CONCLUSION

A viable and, probably, the simplest possible procedure has been proposed for generalizing the theory of finite Fermi systems to the case where it is necessary to take explicitly into account more complex configurations. More specifically, we have derived secular equations for describing the fragmentation of single-particle (for odd nuclei) and particle–hole (for even–even nuclei) states over complex configurations of, respectively, the $1qp\otimes phonon+1qp\otimes phonon\otimes phonon$ and the $2qp\otimes phonon$ type, which are the most interesting ones at present. A more detailed analysis, including analysis of transition probabilities, and a numerical realization of the proposed versions call for much additional effort, but the latter seems quite feasible. A generalization to the case of nonmagic nuclei would require only algebraic complications. By using general relations presented in Section 2, one can extend, if necessary, the proposed scheme to the case of even more complex configurations and to the case where effects associated with a single-particle continuum are sizable (see, for example, [26]).

In just the same way as the conventional theory of finite Fermi systems, our approach is not self-consistent. Unfortunately, no self-consistent theory that would take into account complex configurations has been formulated conclusively so far for either nonmagic or magic nuclei, although the first attempts for the latter case have already been made [27] (in [28], self-consistency is satisfied only at the RPA level).

The equations obtained in the present study cover two effects that have hitherto been disregarded and which can be tested in experiments employing modern gamma detectors and gamma spectrometers. These are ground-state correlations associated with complex configurations and quasiparticle–phonon pairing mechanism in nuclei (an additional one with respect to the conventional BCS mechanism). It would be of great interest to study these effects both theoretically and experimentally. The proposed approach is advantageous is that it produces, as a final output, expressions employing solutions to Eq. (5), whereby the problem at hand is broken down into two parts, each being solved individually. This makes it possible to reduce computational difficulties.

ACKNOWLEDGMENTS

We are grateful to V.I. Tselyaev and A.V. Avdeenkov for enlightening discussions on the results of this study.

APPENDIX

Expressions for the Vertex $\Gamma^{(1)}$ and the Self-Energy Operator M^{ν}: Magic Nuclei

Presented immediately below are the expressions that we have used in Subsection 3.1 for the vertex $\Gamma^{(1)}$ (25) and the self-energy operator M^{ν} (26). For the vertex, we have

$$i\Gamma_{32}^{(1)s}(\epsilon',\epsilon,\omega)=$$

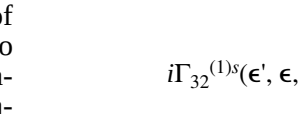

$$i\Gamma_{32}^{(1)s}(\epsilon',\epsilon,\omega)=i^3(-1)^{j_3-m_3+M}\delta(\epsilon'+\omega-\epsilon)$$

$$\times\sum_{\tilde{4},\tilde{5},s'}(-1)^{j_{\tilde{4}}+j_{\tilde{5}}}\langle 3\|g^{s'}\|\tilde{4}\rangle\langle\tilde{4}\|g^{s}\|\tilde{5}\rangle\langle\tilde{5}\|g^{s'}\|2\rangle$$

$$\times\begin{pmatrix} j_3 & L & j_2\\ -m_3 & -M & m_2\end{pmatrix}\begin{Bmatrix} j_3 & L & j_2\\ j_{\tilde{5}} & L' & j_{\tilde{4}}\end{Bmatrix}\mathcal{J}^{s'}_{\tilde{4}\tilde{5}}(\epsilon',\epsilon),$$

$$\mathcal{J}^{s'}_{\tilde{4}\tilde{5}}(\epsilon',\epsilon)=\frac{-(1-n_{\tilde{4}})(1-n_{\tilde{5}})}{(\epsilon'-\omega_{s'}-\epsilon_{\tilde{4}}+i\gamma)(\epsilon-\omega_{s'}-\epsilon_{\tilde{5}}+i\gamma)}$$

$$+\frac{-n_{\tilde{4}}n_{\tilde{5}}}{(\epsilon'+\omega_{s'}-\epsilon_{\tilde{4}}-i\gamma)(\epsilon+\omega_{s'}-\epsilon_{\tilde{5}}-i\gamma)}$$

$$+\frac{(1-n_{\tilde{4}})n_{\tilde{5}}}{\epsilon'-\epsilon-\epsilon_{\tilde{4}\tilde{5}}+i\gamma}\Bigg[\frac{1}{\epsilon'-\epsilon_{\tilde{4}}-\omega_{s'}+i\gamma}$$

$$-\frac{1}{\epsilon-\epsilon_{\tilde{5}}+\omega_{s'}-i\gamma}\Bigg]+\frac{n_{\tilde{4}}(1-n_{\tilde{5}})}{\epsilon'-\epsilon-\epsilon_{\tilde{4}\tilde{5}}-i\gamma}$$

$$\times\Bigg[\frac{1}{\epsilon'-\epsilon_{\tilde{4}}+\omega_{s'}-i\gamma}-\frac{1}{\epsilon-\epsilon_{\tilde{5}}-\omega_{s'}+i\gamma}\Bigg],\qquad(A.1)$$

Hereafter, $s \equiv (n, L, M)$ and $s' \equiv (n', L', M')$ are the phonon number and quantum numbers.

The self-energy operator has the form

$M^{v}_{12}(\varepsilon') =$ 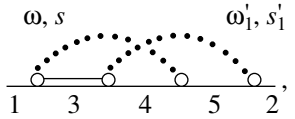

,

$$M^{v}_{12}(\epsilon) = -\frac{\delta_{12}}{2j_1+1}$$

$$\times \sum_{s,s'} \sum_{\tilde{3},\tilde{4},\tilde{5}} (-1)^{j_1+j_3+j_{\tilde{4}}+j_{\tilde{5}}} \left\{ \begin{array}{ccc} j_3 & L & j_1 \\ j_{\tilde{5}} & L' & j_{\tilde{4}} \end{array} \right\}$$

$$\times \langle 1 \| g^{s} \| 3 \rangle \langle 3 \| g^{s'} \| \tilde{4} \rangle \langle \tilde{4} \| g^{s} \| \tilde{5} \rangle \langle \tilde{5} \| g^{s'} \| 1 \rangle \mathcal{J}^{ss'}_{3\tilde{4}\tilde{5}}(\epsilon),$$

$$\mathcal{J}^{ss'}_{3\tilde{4}\tilde{5}}(\epsilon) = \mathcal{L}^{ss'}_{3\tilde{4}\tilde{5}}(\epsilon) + [\mathcal{L}^{ss'}_{3\tilde{4}\tilde{5}}(\epsilon)]^{**},$$

$$\mathcal{L}^{ss'}_{3\tilde{4}\tilde{5}}(\epsilon) = \sum_{k} \left\{ \frac{(1-n_{\tilde{4}})G_{3_k}(\epsilon-\omega_s)\tilde{G}_5(\epsilon-\omega_{s'})}{\epsilon-\omega_s-\omega_{s'}-\epsilon_{\tilde{4}}} \right. \quad \text{(A.2)}$$

$$- \frac{a^{p}_{3_k} n_{\tilde{4}} D_s(\epsilon-\epsilon_{3_k})\tilde{G}_5(\epsilon+\omega_{s'})}{\epsilon_{\tilde{4}3_k}-\omega_{s'}}$$

$$- \frac{n_{\tilde{4}}(1-n_{\tilde{5}})G_{3_k}(\epsilon+\omega_s)D_{s'}(\epsilon-\epsilon_{\tilde{5}})}{\epsilon_{\tilde{4}\tilde{5}}-\omega_s}$$

$$\left. - \frac{a^{p}_{3_k} n_{\tilde{4}}(1-n_{\tilde{5}})D_s(\epsilon-\epsilon_{3_k})D_{s'}(\epsilon-\epsilon_{\tilde{5}})}{\epsilon-\epsilon_{3_k}+\epsilon_{\tilde{4}\tilde{5}}} \right\},$$

where $\epsilon_{\tilde{1}\tilde{2}} = \epsilon_{\tilde{1}} - \epsilon_{\tilde{2}}$ and where the Green's functions $\tilde{G}_5(\epsilon)$, $G_{3_k}(\epsilon)$, and $D_s(\epsilon)$ are given by

$$\tilde{G}_5(\epsilon) = \frac{1-n_{\tilde{5}}}{\epsilon-\epsilon_{\tilde{5}}+i\gamma} + \frac{n_{\tilde{5}}}{\epsilon-\epsilon_{\tilde{5}}-i\gamma},$$

$$G_{3_k}(\epsilon) = \frac{a^{p}_{3_k}}{\epsilon-\epsilon_{3_k}+i\gamma} + \frac{a^{h}_{3_k}}{\epsilon-\epsilon_{3_k}-i\gamma},$$

$$D_s(\omega) = \frac{1}{\omega-\omega_s+i\gamma} - \frac{1}{\omega+\omega_s-i\gamma}.$$

In order to avoid encumbering expressions (A.2), we have introduced the following formal operation denoted by the symbol **:

$$\left\{ \begin{array}{l} n_{\tilde{4}} \longrightarrow 1-n_{\tilde{4}} \\ n_{\tilde{5}} \longrightarrow 1-n_{\tilde{5}} \\ a^{p}_{3_k} \longrightarrow a^{h}_{3_k} \\ \omega_s \longrightarrow -\omega_s \\ \omega_{s'} \longrightarrow -\omega_{s'} \\ \text{complex conjugation}. \end{array} \right.$$

REFERENCES

1. A. B. Migdal, *Theory of Finite Fermi Systems and Applications to Atomic Nuclei* (Nauka, Moscow, 1965; Interscience, New York, 1967).
2. I. N. Borzov and S. P. Kamerdzhiev, Preprint No. 580, FÉI (Institute of Physics and Power Engineering, Obninsk, 1975); Izv. Akad. Nauk SSSR, Ser. Fiz. **41**, 4 (1977); S. P. Kamerdzhiev, in *Proceedings of the 12th LNPI Winter School, 1977*, p. 122.
3. J. Speth, E. Werner, and W. Wild, Phys. Rep. **33**, 128 (1977).
4. É. E. Sapershteĭn, S. A. Fayans, and V. A. Khodel', Fiz. Élem. Chastits At. Yadra **9**, 221 (1978) [Sov. J. Part. Nucl. **9**, 91 (1978)].
5. V. A. Khodel and E. E. Saperstein, Phys. Rep. **92**, 183 (1982).
6. A. B. Migdal, *Theory of Finite Fermi Systems and Applications to Atomic Nuclei* (Nauka, Moscow, 1983, 2nd ed.).
7. A. P. Platonov and É. E. Sapershteĭn, Yad. Fiz. **46**, 437 (1987) [Sov. J. Nucl. Phys. **46**, 231 (1987)].
8. S. T. Belyaev, Yad. Fiz. **1**, 3 (1965) [Sov. J. Nucl. Phys. **1**, 1 (1965)]; S. T. Belyaev and V. G. Zelevinskiĭ, Yad. Fiz. **1**, 13 (1965) [Sov. J. Nucl. Phys. **1**, 10 (1965)]; **2**, 615 (1965) [**2**, 442 (1965)]; **2**, 51 (1965) [**2**, 35 (1965)].
9. S. P. Kamerdzhiev, G. Ya. Tertychnyĭ, and V. I. Tselyaev, Fiz. Élem. Chastits At. Yadra **28**, 333 (1997) [Phys. Part. Nucl. **28**, 134 (1997)].
10. S. P. Kamerdzhiev, Izv. Akad. Nauk, Ser. Fiz. **61**, 152 (1997).
11. V. G. Solov'ev, *Theory of Atomic Nuclei* (Énergoatomizdat, Moscow, 1989; Institute of Physics, Bristol, 1992).
12. *Progress in Particle and Nuclear Physics*, Vol. 38: *4π High Resolution Gamma Ray Spectroscopy and Nuclear Structure* (Proceedings of International School in Nuclear Physics, Erice, 1996), Ed. by A. Faessler (Pergamon, 1997).
13. J. Reif, P. von Bretano, J. Eberth, *et al.*, Nucl. Phys. A **620**, 1 (1997).
14. V. Yu. Ponomarev, J. Bryssinck, L. Govor, *et al.*, Phys. Rev. Lett. **83**, 4029 (1999).
15. S. Kamerdzhiev and J. Speth, Nucl. Phys. A **599**, 373c (1996).
16. A. Avdeenkov and S. Kamerdzhiev, Phys. Lett. B **459**, 423 (1999).
17. S. G. Kadmenskiĭ and P. A. Luk'yanovich, Yad. Fiz. **49**, 384 (1989) [Sov. J. Nucl. Phys. **49**, 238 (1989)].

18. A. V. Avdeenkov and S. P. Kamerdzhiev, Pis'ma Zh. Éksp. Teor. Fiz. **69**, 669 (1999) [JETP Lett. **69**, 715 (1999)].
19. A. V. Avdeenkov and S. P. Kamerdzhiev, Yad. Fiz. **62**, 610 (1999) [Phys. At. Nucl. **62**, 563 (1999)].
20. S. P. Kamerdzhiev, Yad. Fiz. **60**, 572 (1997) [Phys. At. Nucl. **60**, 497 (1997)].
21. S. P. Kamerdzhiev and V. I. Tselyaev, Izv. Akad. Nauk SSSR, Ser. Fiz. **47**, 917 (1983).
22. G. M. Éliashberg, Zh. Éksp. Teor. Fiz. **38**, 966 (1960) [Sov. Phys. JETP **11**, 696 (1960)].
23. V. N. Tkachev and S. P. Kamerdzhiev, Yad. Fiz. **42**, 832 (1985) [Sov. J. Nucl. Phys. **42**, 527 (1985)]; S. P. Kamerdzhiev and V. N. Tkachev, Z. Phys. A **334**, 19 (1989).
24. A. A. Abrikosov, L. P. Gor'kov, and I. E. Dzyaloshinskii, *Methods of Quantum Field Theory in Statistical Physics* (Fizmatgiz, Moscow, 1962; Prentice-Hall, Englewood Cliffs, 1963).
25. P. Ring and E. Werner, Nucl. Phys. A **211**, 198 (1973).
26. S. Kamerdzhiev, E. Litvinova, and D. Zawischa (in press).
27. V. I. Tselyaev, Yad. Fiz. **61**, 821 (1998) [Phys. At. Nucl. **61**, 739 (1998)].
28. G. Colo, P. F. Bortignon, Nguen Van Giai, *et al.*, Phys. Lett. B **276**, 279 (1992); G. Colo, Nguen Van Giai, P. F. Bortignon, *et al.*, Phys. Rev. C **50**, 1496 (1994).

Translated by A. Isaakyan

Physics of Atomic Nuclei, Vol. 64, No. 4, 2001, pp. 637–651. From Yadernaya Fizika, Vol. 64, No. 4, 2001, pp. 696–710.

90th ANNIVERSARY OF A.B. MIGDAL'S BIRTHDAY
NUCLEI

Effective Field Theories, Landau–Migdal Fermi Liquid Theory, and Effective Chiral Lagrangians for Nuclear Matter*

M. Rho[1), 2)]

Received August 10, 2000

Abstract—We reinterpret Landau–Migdal Fermi liquid theory of nuclear matter as an effective chiral field theory with a Fermi surface. The effective field theory is formulated in terms of a chiral Lagrangian with its mass and coupling parameters scaling à la Brown–Rho and with the Landau–Migdal parameters identified as the fixed points of the field theory. We show how this mapping works out for response functions to the EM vector current and, then using the same reasoning, make a prediction on nuclear axial current, in particular on the enhanced axial-charge transitions in heavy nuclei. We speculate on how to extrapolate the resulting theory, which appears to be sound both theoretically and empirically up to normal nuclear-matter density ρ_0, to hitherto unexplored higher density regime relevant to relativistic heavy-ion processes and to cold compact (neutron) stars. © *2001 MAIK "Nauka/Interperiodica".*

1. INTRODUCTION

In a recent beautiful development [1], Landau's Fermi liquid theory has been reformulated as a modern effective field theory with the Fermi liquid state identified as a stable fixed point. This theory represents an effective field theory, which is as beautiful as chiral Lagrangian field theory for low-energy pionic interactions. It is then most natural that Migdal's theory of nuclear matter [2], which is based on Landau's Fermi liquid theory, can also be formulated as an effective field theory. We dedicate this paper, which is based on recent work [3, 4], as a tribute to Migdal on the occasion of his 90th anniversary.

2. EFFECTIVE FIELD THEORY

Effective field theories enter the nuclear physics domain in two different ways. One is to make precise predictions for certain processes involving few-nucleon systems that are connected with fundamental issues of physics. This is often called for to answer questions of fundamental nature in other areas of physics such as astrophysics or particle physics [5]. The other—which is our objective here—is to be able to extrapolate the knowledge available in normal conditions beyond the normal nuclear-matter regime into a high-temperature or high-density regime that will be the focus of experimental efforts in the coming years. In making the extrapolation, the usual quantum-mechanical many-body approach lacks the necessary versatility, and field theoretical approaches anchored in quantum chromodynamics will be required. Migdal's formulation of Fermi liquid for nuclear matter has proven to be powerful at least up to normal nuclear-matter density and has even led to a variety of predictions of phenomena that might take place under extreme conditions [6]. In its original form, however, it is somewhat limited in its scope if one wishes to extrapolate to extreme conditions, where QCD phase changes may be induced. Such densities are expected in upcoming laboratories and probably exist in neutron-star interiors. In this paper, we wish to discuss our recent attempt to formulate the Landau–Migdal theory of nuclear matter in a modern effective-field-theory framework. Such a framework, which offers the possibility of extrapolation to extreme conditions, has been quite successful in such different fields as condensed matter and high-energy physics.

2.1. Effective Field Theory for Light Nuclei

Before going into our main topic of dense matter, we briefly summarize the status of effective field theories in few-nucleon systems. Here, the setting for an effective field theory (EFT) is straightforward.

The objectives there are essentially twofold. One is to derive the nucleon–nucleon interactions—which are fairly well understood from phenomenological approaches—from fundamental principles. The basic question is: Can all two-nucleon systems, viz, nucleon–nucleon scattering at low energy and bound states (e.g., the deuteron), be understood in the framework of an effective field theory? This old question, which was stimulated by the work of Weinberg [7], recently became the focus of intense activities in many theoretical communities. The status of the field is comprehensively summarized in the proceedings of two recent INT–Caltech workshops [8]. The original Weinberg approach had certain apparent inconsistency in the power counting invoked for a systematic calculation,

* This article was submitted by the author in English.

[1)] School of Physics, Korea Institute for Advanced Study, Seoul, Korea.
[2)] Service de Physique Théorique, CE Saclay, Gif-sur-Yvette, France.

but this problem can be readily resolved as shown by the INT–Caltech collaboration [9]. In that work, the notion of power-divergence subtraction was introduced into the dimensional regularization. This enables one to handle the anomalous length scale that appears when a quasibound state is nearby in a more straightforward manner. We now know that when done correctly, the two schemes (i.e., Weinberg's and the INT/Seattle–Caltech scheme) are essentially equivalent in the treatment of low-energy two-nucleon interactions. Although they may differ in specific details, the two schemes reproduce the low-energy observables thus far studied with equal quality.

The other objective is to exploit the power of effective field theories in making *bona fide* predictions for processes which cannot be accessed by standard nuclear physics methods. Examples that have been discussed recently are the asymmetry observables in the polarized *np* capture [10]

$$\vec{n} + \vec{p} \longrightarrow d + \gamma \tag{1}$$

and the solar *hep* process [11]

$$p + {}^3\mathrm{He} \longrightarrow {}^4\mathrm{He} + e^+ + \nu_e. \tag{2}$$

The first process (1) has been studied theoretically in a variety of different methods [10, 12] and is being measured [13]. The second process (2) has been recently measured in the SuperKamiokande experiment [14] and has generated a lot of excitement among theorists [15]. It turns out rather remarkably that these two processes complement each other in providing a theoretical strategy to overcome a nontrivial obstacle on the way to a parameter-free calculation.

Now, in order to increase the predictive power in general and to facilitate accurate calculations of the above processes, a hybrid version of EFT (called MEEFT or "more effective EFT") was launched by Park, Kubodera, Min, and Rho [11, 16, 17]. This approach, which combines the sophisticated standard nuclear physics approach with chiral perturbation theory, turns out to be far more powerful and robust than naively expected. Within this scheme, one can actually make reliable calculations of observables that cannot be obtained by other methods. Of equal importance is the fact that such predictions can be confronted with data. Thus, the validity of this approach will be settled by experiment in the near future. The accuracy with which such predictions can be made is assessed in [11].

2.2 EFT for Heavy Nuclei and Nuclear Matter

In both cases mentioned above addressing low-density systems, the effective Lagrangians are defined at zero density and the relevant fluctuations are made on top of the zero-density vacuum which is accessible by various QCD analyses, treating the matter density as an external perturbation. In a dense medium, the situation is expected to be quite different. While in the light systems the parameters that figure in the effective Lagrangian are in principle derivable from QCD (perhaps on a lattice) or more often from experimental data, this is not the case in a dense medium. Deriving an EFT for dense matter from QCD is probably of similar difficulty as deriving the Hubbard model from QED. The best one can do is to start with a Lagrangian defined at zero density and go up in density. Unfortunately, this will be limited to low density and cannot be pushed to high enough density to be useful in the regime we would like to explore.

In this note, we circumvent the difficulty of deriving such a theory directly. Rather, we construct an effective chiral Lagrangian field theory that maps onto an established many-body theory, specifically Landau–Migdal Fermi liquid theory, and then extrapolate that field theory to the regime of higher density. This is certainly in accordance with the original spirit of Landau–Migdal theory, though it is not clear if such a scheme will work in all density regimes. We can only say that up to now there is no evidence against the scheme. For a recent review, see [4].

3. NUCLEAR MATTER AS A FERMI LIQUID FIXED POINT

3.1. Chiral Liquid

How to obtain a realistic description of nuclear matter from an effective Lagrangian anchored in the fundamentals of QCD is very much an open problem at the moment. There are, however, several models available. One of them, the skyrmion with an infinite baryon number, is yet to be confronted in nature. The skyrmion is a soliton solution of a Skyrme-type Lagrangian, which is an approximate Lagrangian for QCD at an infinite number of colors, $N_c = \infty$. Because the mathematical structure of this model is not very well known at the moment, only very little information can be extracted from it.

Another model is the nontopological soliton picture proposed in an embryonic form sometime ago by Lynn [18]. This description has recently been given a more realistic structure by Lutz, Friman, and Appel [19]. The idea here is that one writes down an effective potential or energy calculated to the highest order feasible in practice in chiral perturbation theory, suitably taking into account all relevant scales involved, and then looks for the minimum of the effective potential to be identified with the nuclear matter ground state. The state so obtained may be identified with Lynn's chiral liquid state. The connection between the skyrmion with an infinite winding number and the chiral liquid matter—which must exist in large N_c limit—is presently not understood.

The starting point of our consideration is the assumption that we have a chiral-liquid solution of the type described in [19] that represents the ground state (vacuum), on top of which fluctuations can be calculated. The discussion of [19] does not specify how these

fluctuations are to be made. To proceed, we propose that the parameters of the Lagrangian (such as masses, coupling constants, etc.) of the fields representing the relevant degrees of freedom are determined at this ground state, not at the zero-density vacuum which gives the starting point of the Lynn strategy and hence run with density.[3)] The Lagrangian so defined is assumed to satisfy the same symmetry constraints—such as chiral symmetry and scale anomaly—as those intrinsic to QCD at zero density.

3.2. Effective Chiral Lagrangian

Let us denote the parameters so defined at a density ρ with a star. The mass of a nucleon in the system will be denoted as M^*, the pion decay constant f_π^*, etc. The simplest chiral Lagrangian for the nuclear system so defined takes the form

$$\mathcal{L} = \bar{N}[i\gamma_\mu(\partial^\mu + iV^\mu + g_A^*\gamma_5 a^\mu) - M^*]N - \sum_i C_i^*(\bar{N}\Gamma_i N)^2 + \ldots, \tag{3}$$

where the ellipsis denotes higher dimensional nucleon operators and the Γ_i's Dirac and flavor matrices as well as derivatives consistent with chiral symmetry. Furthermore,

$$\xi^2 = U = e^{i\pi\tau/f_\pi^*},$$
$$V_\mu = -\frac{i}{2}(\xi^\dagger\partial_\mu\xi + \xi\partial_\mu\xi^\dagger), \tag{4}$$
$$a_\mu = -\frac{i}{2}(\xi^\dagger\partial_\mu\xi - \xi\partial_\mu\xi^\dagger).$$

In (3), only the pion (π) and nucleon (N) fields appear explicitly; all other fields have been integrated out. The effect of massive degrees of freedom will be lodged in higher dimensional and/or higher derivative interactions. The external electroweak fields that we will consider below are straightforwardly incorporated by suitable gauging.

If one considers symmetric nuclear matter and restricts oneself to the mean-field approximation, one can write, following [20], an equivalent Lagrangian that contains just the degrees of freedom that appear in a linear model of the Walecka-type [21],

$$\mathcal{L} = \bar{N}(i\gamma_\mu(\partial^\mu + ig_v^*\omega^\mu) - M^* + h^*\phi)N - \frac{1}{4}F_{\mu\nu}^2 + \frac{1}{2}(\partial_\mu\phi)^2 + \frac{m_\omega^{*2}}{2}\omega^2 - \frac{m_\phi^{*2}}{2}\phi^2 + \ldots, \tag{5}$$

where the ellipsis denotes higher dimension operators. This Lagrangian is totally equivalent to (3) in the mean-field approximation [20, 22]. Unless otherwise noted, we will be using (3).

3.3. Interpreting the Density Dependence of the Parameters

From a field theory point of view, it is unclear what density dependence of various constants of the Lagrangian means. This is because the number density ρ is defined as the expectation value of the number density operator $\bar{N}\gamma_0 N$ with respect to the state vector one is considering. Thus, the density ρ is defined only when the state is determined. The only way that such a quantity can be introduced into the Lagrangian is to assume that the parameters of the Lagrangian such as coupling constants and masses are functions of the fields involved. The constraint that the Lagrangian be invariant under chiral-symmetry transformation then limits the field dependence. One may choose a chiral singlet scalar field or a chiral invariant bilinear in the nucleon fields. In what follows, we shall choose the latter.

For this purpose, we define the chirally invariant operator

$$\check{\rho}u^\mu \equiv \bar{N}\gamma^\mu N, \tag{6}$$

where

$$u^\mu = \frac{1}{\sqrt{1-\mathbf{v}^2}}(1, \mathbf{v}) = \frac{1}{\sqrt{\rho^2 - \mathbf{j}^2}}(\rho, \mathbf{j}) \tag{7}$$

is the fluid 4-velocity. Here,

$$\mathbf{j} = \langle\bar{N}\boldsymbol{\gamma}N\rangle \tag{8}$$

is the baryon current density, and

$$\rho = \langle N^\dagger N\rangle = \sum_i n_i \tag{9}$$

is the baryon number density. The expectation value of $\check{\rho}$ yields the baryon density in the restframe of the fluid. Using $\check{\rho}$ it is easy to construct a Lorentz-invariant, chirally invariant Lagrangian with density dependent parameters. However, here we shall not use the relativistic formulation.

Now, a density-dependent mass parameter in the Lagrangian should be interpreted as

$$m^* = m^*(\check{\rho}). \tag{10}$$

This means that the model (5) is no longer linear, but highly nonlinear even at the mean-field level. We shall illustrate this using the Lagrangian (5) in the mean-field approximation and show that our interpretation is thermodynamically consistent.

The Euler–Lagrange equations of motion for the bosonic fields are the usual ones, but the nucleon equa-

[3)] The meaning of density dependence in the parameters in an effective Lagrangian we shall study will be precisely defined later. There is a subtlety due to the requirement of chiral symmetry that needs to be addressed.

tion of motion is not. This is because of the functional dependence of the masses and coupling constants on the nucleon field:

$$\frac{\delta\mathcal{L}}{\delta\bar{N}} = \frac{\partial\mathcal{L}}{\partial\bar{N}} + \frac{\partial\mathcal{L}}{\partial\check{\rho}}\frac{\partial\check{\rho}}{\partial\bar{N}} \tag{11}$$

$$= [i\gamma^{\mu}(\partial_{\mu} + ig_{v}^{*}\omega_{\mu} - iu_{\mu}\check{\Sigma}) - M^{*} + h^{*}\phi]N = 0$$

with

$$\check{\Sigma} = \frac{\partial\mathcal{L}}{\partial\check{\rho}} = m_{\omega}^{*}\omega^{2}\frac{\partial m_{\omega}^{*}}{\partial\check{\rho}} - m_{\phi}^{*}\phi^{2}\frac{\partial m_{\phi}^{*}}{\partial\check{\rho}} \tag{12}$$

$$- \bar{N}\omega^{\mu}\gamma_{\mu}N\frac{\partial g_{v}^{*}}{\partial\check{\rho}} - \bar{N}N\frac{\partial M^{*}}{\partial\check{\rho}}.$$

Here, we assume that $(\partial/\partial\check{\rho})h^{*} \approx 0$. It may be possible to justify this but we shall not attempt it here. The additional term $\check{\Sigma}$, which may be related to what is referred to in many-body theory as rearrangement terms, is essential in making the theory consistent. This point has been overlooked in the literature.

Here we shall briefly summarize the results. Details can be found in [4, 23]. When one computes the energy-momentum tensor with (5), one finds the canonical term, which is obtained when the parameters are treated as constants, as well as a new term proportional to $\check{\Sigma}$:

$$T^{\mu\nu} = T^{\mu\nu}_{\rm can} + \check{\Sigma}(\bar{N}u\cdot\gamma N)g^{\mu\nu}. \tag{13}$$

The pressure is then given by $\frac{1}{3}\langle T_{ii}\rangle_{\mathbf{v}=0}$. The additional term in (7) matches precisely the terms that arise when the derivative with respect to ρ acts on the density-dependent masses and coupling constants in the formula derived from T_{00}:

$$p = -\frac{\partial E}{\partial V} = \rho^{2}\frac{\partial\mathcal{E}/\rho}{\partial\rho} = \mu\rho - \mathcal{E}, \tag{14}$$

where

$$\mathcal{E} = \langle T^{00}\rangle. \tag{15}$$

This matching assures energy–momentum conservation and thermodynamic consistency.

Once the interpretation of the density dependence is specified, the derivation of the Landau–Migdal parameters, thermodynamic quantities etc. from (5) is completely analogous to the procedure used by Matsui [24] for Walecka's linear σ–ω model.

3.4. Nuclear Matter with Brown–Rho Scaling

We saw above that the masses and coupling constants in (5) (or equivalently (3)) are to be treated as functionals of $\check{\rho}$ given by Eq. (6). When treated at the mean-field level, $\check{\rho}$ is just the number density, so the parameters become density dependent. The dependence of the parameters in the Lagrangian on the fields rather than on the density is essential for thermodynamic consistency. Note, however, that these considerations do not require the parameters to satisfy scaling relations. It is the chiral symmetry and scale symmetry that suggest that the masses satisfy Brown–Rho (BR) scaling at the mean-field level [25]

$$\Phi(\rho) \approx \frac{f_{\pi}^{*}(\rho)}{f_{\pi}} \approx \frac{m_{\phi}^{*}(\rho)}{m_{\phi}} \approx \frac{m_{V}^{*}(\rho)}{m_{V}} \approx \frac{M^{*}(\rho)}{M}. \tag{16}$$

Here, V stands for the light-quark vector mesons ρ and ω. The quantity $\Phi(\rho)$ is the scaling factor that needs to be determined from theory or experiments. For concreteness, we shall assume

$$\Phi(\rho) = (1 + y\rho/\rho_{0})^{-1}. \tag{17}$$

The value of y will be determined below by a global fit of the ground-state properties of nuclear matter. Now taking the free-space values,

$$M = 938\ \text{MeV},\ m_{\omega} = 783\ \text{MeV},\ m_{\phi} = 700\ \text{MeV}, \tag{18}$$

and

$$g_{v} = 15.8, \quad h = 6.62, \tag{19}$$

with one additional assumption that the vector coupling g_{v}^{*} scales like the mass m_{ω}^{*} and h^{*} is almost constant, one finds the following properties for the ground state of nuclear matter

$$m_{N}^{*}/M = 0.62, \quad E/A - M = -16.0\ \text{MeV}, \tag{20}$$
$$k_{\rm F} = 257\ \text{MeV}, \quad K = 296\ \text{MeV}.$$

Here, $k_{\rm F}$ is the Fermi momentum at the saturation point and K is the corresponding compression modulus. The best values favored by nature that are "well determined" and that "can be associated with an equal number of nuclear properties and general features of RMF (relativistic mean field) models" [24][4] are

$$m_{N}^{*}/M = 0.61 \pm 0.03, \ E/A - M = -16.0 \pm 0.1\ \text{MeV}, \tag{21}$$
$$k_{\rm F} = 256 \pm 2\ \text{MeV}, \quad K = 250 \pm 50\ \text{MeV}.$$

To arrive at (20), we need $y = 0.28$ which implies that $\Phi(\rho_{0}) \approx 0.78$. The scaling of g_{v}, which is needed to obtain a good fit, was not incorporated in the original BR scaling [25] but it does not invalidate the scaling relation (16) which is a mean-field relation. The scaling of the coupling constant is a fluctuation effect on top of the BR scaling ground state, that is, a running as in the

[4] It is worth pointing out that the RMF that has been successful so far involves nonlinear terms deemed natural in the terminology of EFT. These terms can be interpreted as representing high-dimension Fermi operators.

renormalization group as discussed in [27]. A caveat here is that at this level, the Kawarabayashi–Suzuki–Riazuddin–Fyazuddin (KSRF) relation that holds in free space between the vector mass m_V and $f_\pi g_V$ must have a density-dependent correction in order for the scaling of g_V^* to make sense. To date the possible validity of the KSRF relation or some generalization of it in medium is not yet unraveled.

Another observation of interest is the in-medium mass of the scalar ϕ.[5)] In the analysis of [26], the scalar mass does not have a simple scaling since it is a complicated nonlinear theory. See [4] for a detailed discussion on this matter. In the present theory, we in fact have the relation

$$m_\phi^*(\rho_0) = m_\phi \Phi(\rho_0) \tag{22}$$

which for $\Phi(\rho_0) \approx 0.78$ gives the mass of the scalar in nuclear matter to be 546 MeV which should be compared with the value 500 ± 20 MeV favored by [26].

It should be stressed that, given the simplicity of the model considered here, the agreement between the simple BR scaling model and the sophisticated nonlinear mean-field model [26] is most remarkable. Whether there is something deep here or it is just a coincidence is an issue to be resolved.

4. DERIVING MIGDAL'S FORMULAS FROM EFFECTIVE CHIRAL LAGRANGIANS

Here, we sketch Migdal's derivation of nuclear orbital gyromagnetic ratio and then write an analogous expression for the nuclear axial charge operator following the same steps taken for the vector current. We have no rigorous proof that the axial charge that results is a unique one that follows from the premise of Fermi liquid theory but we are offering it here as a possible one.

4.1. Landau–Migdal Formulation

4.1.1. Vector currents. Consider the response of a heavy nucleus to a slowly varying electromagnetic field. We wish to calculate the gyromagnetic ratio g_l of a nucleon sitting on top of the Fermi sea. There are several ways for doing this calculation [29]. Here we shall use the simplest which turns out to be straightforwardly applicable to the axial current, in particular to its time component, i.e., the axial charge.

We are interested in the response of a homogeneous quasiparticle excitation to the convection current. This corresponds to the limit $q/\omega \longrightarrow 0$, where $(\omega, \mathbf{q})$ is the four-momentum transfer induced by the electromagnetic field. The first step is to compute the total current carried by the wave packet of a localized quasiparticle

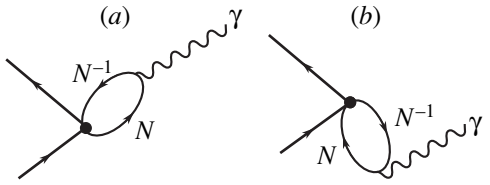

Fig. 1. Particle–hole contributions to the convection current involving the full particle–hole interaction (solid circle) given by Eq. (24). Here, the backward-going nucleon line N^{-1} denotes a hole and the wiggly line the photon. These graphs vanish in the $q/\omega \longrightarrow 0$ limit.

with group velocity $\mathbf{v}_F = \dfrac{\mathbf{k}}{m_N^*}$ where m_N^* is the Landau effective mass of the quasiparticle and $\mathbf{k}$ is the momentum carried by the quasiparticle.[6)] The convection current for a localized quasiparticle is

$$\mathbf{J}_{\rm LQP} = \frac{\mathbf{k}}{m_N^*}\left(\frac{1+\tau_3}{2}\right). \tag{23}$$

However, this is not really what we want. Among other things, it does not conserve the charge. This is because the quasiparticle interacts with the surrounding medium generating what is known as back-flow. Consequently, we have to incorporate the back-flow to restore gauge invariance. A simple way to account for the back-flow is to compute the particle–hole contributions of the type given in Fig. 1 with the full particle–hole interaction—represented in the figure by the solid circle given by Eq. (24) (see below)—in the limit that $\omega/q \longrightarrow 0$. (Note that this contribution vanishes in the other limit $q/\omega \longrightarrow 0$.) The full interaction between two quasiparticles $\mathbf{p}_1$ and $\mathbf{p}_2$ at the Fermi surface of symmetric nuclear matter written in terms of a few spin and isospin invariants is [30]

$$\begin{aligned} f_{\mathbf{p}_1\sigma_1\tau_1,\,\mathbf{p}_2\sigma_2\tau_2} = \frac{1}{N(0)}\Big[& F(\cos\theta_{12}) + F'(\cos\theta_{12})\boldsymbol{\tau}_1\cdot\boldsymbol{\tau}_2 \\ & + G(\cos\theta_{12})\boldsymbol{\sigma}_1\cdot\boldsymbol{\sigma}_2 + G'(\cos\theta_{12})(\boldsymbol{\sigma}_1\cdot\boldsymbol{\sigma}_2)(\boldsymbol{\tau}_1\cdot\boldsymbol{\tau}_2) \\ & + \frac{\mathbf{q}^2}{k_F^2}H(\cos\theta_{12})S_{12}(\hat{\mathbf{q}}) + \frac{\mathbf{q}^2}{k_F^2}H'(\cos\theta_{12})S_{12}(\hat{\mathbf{q}})\boldsymbol{\tau}_1\cdot\boldsymbol{\tau}_2\Big], \end{aligned} \tag{24}$$

where θ_{12} is the angle between $\mathbf{p}_1$ and $\mathbf{p}_2$ and $N(0) = \dfrac{\gamma k_F^2}{2\pi^2}\left(\dfrac{dp}{d\varepsilon}\right)_F$ is the density of states at the Fermi surface. We use natural units with $\hbar = 1$. The spin and isospin degeneracy factor γ is equal to 4 in symmetric nuclear matter. Furthermore, $\mathbf{q} = \mathbf{p}_1 - \mathbf{p}_2$ and

$$S_{12}(\hat{\mathbf{q}}) = 3(\boldsymbol{\sigma}_1\cdot\hat{\mathbf{q}})(\boldsymbol{\sigma}_2\cdot\hat{\mathbf{q}}) - \boldsymbol{\sigma}_1\cdot\boldsymbol{\sigma}_2, \tag{25}$$

[5)]The scalar that figures here is an effective degree of freedom which need not be identified with a particle in the Particle Data booklet. From our point of view, it is closer to the dilaton discussed by Beane and van Kolck [28].

[6)]This should be distinguished from the BR-scaling effective mass M^* that appears in (3) and (5) and will be defined more precisely later.

where $\hat{\mathbf{q}} = \mathbf{q}/|\mathbf{q}|$. The tensor interactions H and H' are important for the axial charge which we will consider later. The functions F, F', … are expanded in Legendre polynomials,

$$F(\cos\theta_{12}) = \sum_{\ell} F_\ell P_\ell(\cos\theta_{12}), \tag{26}$$

with analogous expansion for the spin- and isospin-dependent interactions.

In terms of (24), the quasiparticle–quasihole graphs of Fig. 1, suitably generalized to the full interaction, yield

$$\begin{aligned}\mathbf{J}_{ph} &= -\frac{1}{3\pi^2}\hat{\mathbf{k}}k_{\mathrm{F}}^2(f_1 + f_1'\tau_3)\\ &= -\frac{\mathbf{k}}{M}\left(\frac{\tilde{F}_1 + \tilde{F}_1'\tau_3}{6}\right),\end{aligned} \tag{27}$$

where M denotes the free-space mass of the nucleon and

$$\tilde{F}_i \equiv (M/m_N^*)F_i. \tag{28}$$

In order to obtain the desired current, we have to add the back-flow term (i.e., $-\mathbf{J}_{ph}$) to the localized quasiparticle term (23),

$$\begin{aligned}\mathbf{J}_{\mathrm{Migdal}} &= \mathbf{J}_{\mathrm{LQP}} - \mathbf{J}_{ph} = \frac{\mathbf{k}}{M}g_l\\ &= \frac{\mathbf{k}}{M}\left(\frac{1+\tau_3}{2} + \frac{1}{6}(\tilde{F}_1' - \tilde{F}_1)\tau_3\right),\end{aligned} \tag{29}$$

where

$$g_l = \frac{1+\tau_3}{2} + \delta g_l \tag{30}$$

is the orbital gyromagnetic ratio and

$$\delta g_l = \frac{1}{6}(\tilde{F}_1' - \tilde{F}_1)\tau_3. \tag{31}$$

In arriving at (29), we have used the relation between the Landau effective mass and the quasiparticle interaction

$$\frac{m_N^*}{M} = 1 + \frac{1}{3}F_1 = \left(1 - \frac{1}{3}\tilde{F}_1\right)^{-1}. \tag{32}$$

It is important to note that, as a consequence of charge conservation and Galilei invariance, the isoscalar term in (29) is not renormalized by the interaction. Thus, the renormalization of g_l is purely isovector. It is also important to note that it is the free-space mass M, not the Landau mass m_N^*, that appears in (29). This is an analog to the Kohn theorem for the cyclotron frequency of an electron in an external magnetic field [31, 32],[7] and constitutes a strong constraint for a consistent theory to satisfy. The effective Lagrangian theory discussed below does satisfy this condition.

4.1.2. Axial currents. Next we turn to the axial-charge operator A_0^a (where the superscript a is an isospin index). In deriving the "Migdal formula" for this operator,[8] we assume that we can follow exactly the same reasoning as above for the vector current. This assumption needs still to be justified.

In matter-free space, the axial-charge operator for a nonrelativistic nucleon with mass M is

$$A_0^a = g_A\frac{\tau^a}{2}\frac{\boldsymbol{\sigma}\cdot\mathbf{k}}{M}, \tag{33}$$

while, in dense matter, a localized quasiparticle with a Landau effective mass m_N^* has the axial charge

$$A_{0\mathrm{LQP}}^a = g_A\frac{\tau^a}{2}\frac{\boldsymbol{\sigma}\cdot\mathbf{k}}{m_N^*}. \tag{34}$$

Next we calculate the particle–hole contribution—which is minus the back-flow contribution—in the same way as for the vector current (i.e., Fig. 1 with the photon vertex replaced by the axial-charge vertex). The result [29] is

$$A_{0ph}^a = -g_A\frac{\tau^a}{2}\frac{\boldsymbol{\sigma}\cdot\mathbf{k}}{m_N^*}\Delta \tag{35}$$

with

$$\Delta = \frac{1}{3}G_1' - \frac{10}{3}H_0' + \frac{4}{3}H_1' - \frac{2}{15}H_2', \tag{36}$$

where G' and H' are the spin–isospin-dependent components of the force given in Eq. (24). Therefore, the total is

$$A_{0\mathrm{Migdal}}^a = A_{0\mathrm{LQP}}^a - A_{0ph}^a = g_A\frac{\tau^a}{2}\frac{\boldsymbol{\sigma}\cdot\mathbf{k}}{m_N^*}(1+\Delta). \tag{37}$$

It will become clearer when we calculate the same quantity based on chiral Lagrangian, but at this point it should be noted that, unlike the vector current, here there is no analog of the Kohn theorem. This is because chiral symmetry is realized, not in the Wigner mode, but rather in the Goldstone mode for which the meaning of a conserved charge is different from that of the vector charge. Another point to be noted is that while

[7] The cyclotron frequency of an electron with a Landau effective mass m_e^* in an external magnetic field of magnitude $B = 2\pi n_f\phi/e$, where n_f is the electron number density and ϕ is the flux integer (=2 for fermions), is *not* $\omega_0 = 2\pi n_f\phi/m_e^*$, as one would naively expect for a localized quasiparticle but $\omega_0 = 2\pi n_f\phi/m_e$ due to the back-flow effect.

[8] We put quotation marks since Migdal did not derive formulas for the axial charge.

for the convection current only F_1 and F_1' appear, it is a lot more complicated for the axial charge. It involves spin–isospin dependent interactions as well as tensor forces. These two features will show up nontrivially when we compute the δg_l and the Δ with the effective chiral Lagrangian.

4.2. Calculation with Effective Chiral Lagrangian

We will now compute δg_l and Δ using a BR-scaling chiral Lagrangian. One can use either the Lagrangian (3) or the Lagrangian (5) with BR scaling [25] incorporated. We shall use (3) as we did for the vector current. We need only the two terms of the four-Fermi interactions that correspond to the ω and ρ channels:

$$-\frac{C_\omega^{*2}}{2}(\bar{N}\gamma_\mu N)^2 - \frac{C_\rho^{*2}}{2}(\bar{N}\gamma_\mu \tau N)^2 + \ldots, \qquad (38)$$

i.e., what remains when the vectors ω and ρ are integrated out. The subscripts represent not only the vector mesons ω and ρ nuclear physicists are familiar with but also all vector mesons of the same quantum numbers, so the two "counter terms" subsume the full short-distance physics of the same chiral order.

4.2.1. Landau mass from the chiral Lagrangian. We first calculate the single-particle energy with (3). In the nonrelativistic approximation, we have

$$\varepsilon_p = \frac{p^2}{2M^*} + C_\omega^{*2}\langle N^\dagger N\rangle + \Sigma_\pi(p), \qquad (39)$$

where $M^* = \Phi M$ is the BR-scaling nucleon mass and $\Sigma_\pi(p)$ is the nucleon self-energy due to the pion Fock term. The Landau effective mass is defined [33] by

$$\frac{m_N^*}{M} = \frac{k_F}{M}\left(\frac{d}{dp}\varepsilon_p\Big|_{p=k_F}\right)^{-1} = \left(\Phi^{-1} - \frac{1}{3}\tilde{F}_1(\pi)\right)^{-1}, \qquad (40)$$

where we have used the fact that the second term of (39) does not contribute and

$$\tilde{F}_1(\pi) = -\frac{3M}{k_F}\frac{d\Sigma_\pi(p)}{dp}\Big|_{p=k_F} = -\frac{3f^2M}{8\pi^2 k_F}I_1, \qquad (41)$$

where $f = g_A m_\pi/(2f_\pi) \simeq 1$ and

$$I_1 = \int_{-1}^{1} dx \frac{x}{1 - x + m_\pi^2/(2k_F^2)} = -2 + \left(1 + \frac{m_\pi^2}{2k_F^2}\right)\ln\left(1 + \frac{4k_F^2}{m_\pi^2}\right). \qquad (42)$$

Now using the Landau mass formula (32) and

$$\tilde{F}_1 = \tilde{F}_1(\omega) + \tilde{F}_1(\pi), \qquad (43)$$

we find

$$\tilde{F}_1(\omega) = 3(1 - \Phi^{-1}). \qquad (44)$$

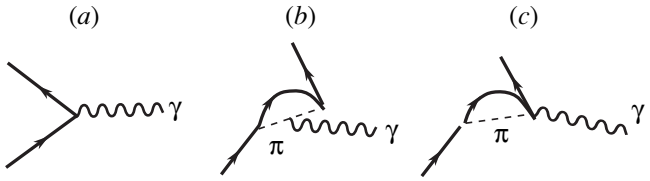

Fig. 2. Feynman diagrams contributing to the EM convection current in effective chiral Lagrangian field theory. Diagram (*a*) is the single-particle term, (*b*) and (*c*) the next-to-leading chiral order pion-exchange current term. Diagram (*c*) does not contribute to the convection current; it renormalizes the spin gyromagnetic ratio.

4.2.2. Convection current. In the chiral Lagrangian approach, the isovector magnetic multipole operator to which the convection current belongs is chiral-filter-protected [34], which means that the one-soft-pion exchange should dominate in the correction to the leading single-particle term. The single-particle term for a nucleon with the BR-scaling mass M^* on the Fermi surface with momentum $\mathbf{k}$ corresponding to Fig. 2*a* is

$$\mathbf{J}_{1\text{-body}} = \frac{\mathbf{k}}{M^*}\frac{1+\tau_3}{2}. \qquad (45)$$

Note that the nucleon mass appearing in (45) is the BR scaling mass M^* as it appears in the Lagrangian, not the (Landau) effective mass m_N^* that appears in the Fermi liquid approach for the localized quasiparticle current. To the next-to-leading order, we have two soft-pion terms Figs. 2*b* and 2*c* as discussed in [7]. To the convection current, only Fig. 2*b* contributes

$$\mathbf{J}^\pi_{2\text{-body}} = \frac{\mathbf{k}}{k_F}\frac{f^2}{4\pi^2}I_1\tau_3 = \frac{\mathbf{k}}{M}\cdot\frac{1}{6}(\tilde{F}_1'(\pi) - \tilde{F}_1(\pi))\tau_3. \qquad (46)$$

In arriving at this formula, it has been assumed that pion properties are unchanged in medium up to nuclear matter density. Since pions are almost Goldstone bosons, this assumption seems reasonable. Indeed it is consistent with what is observed in nature. Note that there are no unknown parameters associated with the pion contribution (46): the one-pion-exchange contributions to the Landau parameters $\tilde{F}_1(\pi)$ and $\tilde{F}_1'(\pi)$ are entirely fixed by the chiral effective Lagrangian at any density.

The contributions from the four-Fermi interactions (that is, the vector meson degrees of freedom) are subleading to the pion exchange by the chiral filter [34]. They are given by Fig. 3. Both the ω (isoscalar) and ρ (isovector) channels contribute through the antiparticle intermediate state as shown in Fig. 3*a*. The antiparticle is explicitly indicated in the figure. However, in the heavy-fermion formalism, the backward-going antinucleon line should be shrunk to a point as in Fig. 3*b*, leaving behind an explicit $1/M^*$ dependence folded with a factor of nuclear density indicating a $1/M^*$ cor-

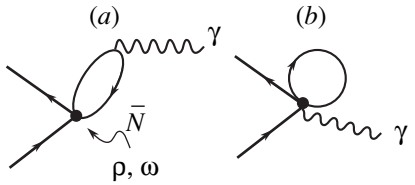

Fig. 3. (*a*) Feynman diagram contributing to the EM convection current from four-Fermi interactions corresponding to all channels of the ω and ρ quantum numbers (contact interaction indicated by the blob) in effective chiral Lagrangian field theory. The $\bar{N}$ denotes the antinucleon state that is given in the chiral Lagrangian as a $1/M$ correction and the one without arrow is a Pauli-blocked or occupied state. (*b*) The equivalent graph in heavy-fermion formalism with the antinucleon line shrunk to a point. The blob represents a four-Fermi interaction coupled to a photon that enters in (3) as a $1/M$ counter term.

rection in the chiral expansion.[9)] One can interpret Fig. 3*a* as saturating the corresponding counter term although this has yet to be verified by writing down the full set of counter terms at the same order. We find

$$\mathbf{J}^{\omega}_{\text{2-body}} = \frac{\mathbf{k}}{M}\cdot\frac{1}{6}\tilde{F}_1(\omega), \tag{47}$$

$$\mathbf{J}^{\rho}_{\text{2-body}} = \frac{\mathbf{k}}{M}\cdot\frac{1}{6}\tilde{F}'_1(\rho)\tau_3, \tag{48}$$

where

$$F_1(\omega) = -C^{*2}_{\omega}\frac{2k_{\text{F}}^3}{\pi^2 M^*} \tag{49}$$

and

$$F'_1(\rho) = -C^{*2}_{\rho}\frac{2k_{\text{F}}^3}{\pi^2 M^*}. \tag{50}$$

The total current given by the sum of (45)–(48) precisely agrees with the Fermi liquid theory result (29) when we identify

$$\tilde{F}_1 = \tilde{F}_1(\omega) + \tilde{F}_1(\pi), \tag{51}$$

$$\tilde{F}'_1 = \tilde{F}'_1(\rho) + \tilde{F}'_1(\pi). \tag{52}$$

If we further assume that the same flavor symmetry as in free space holds in medium, then

$$\tilde{F}'(\rho) = \tilde{F}'(\omega)/9, \tag{53}$$

which uses the nonet symmetry, and

$$\tilde{F}'(\pi) = -\tilde{F}(\pi)/3, \tag{54}$$

which uses the isotopic invariance. The BR-scaling chiral Lagrangian prediction reduces to a one-parameter formula

$$\delta g_l = \frac{1}{6}(\tilde{F}'_1 - \tilde{F}_1)\tau_3 = \frac{4}{9}\left[\Phi^{-1} - 1 - \frac{1}{2}\tilde{F}_1(\pi)\right]\tau_3. \tag{55}$$

Here, $\Phi(\rho)$ is the only parameter in the theory that needs to be determined from theory or experiment. As mentioned, $\tilde{F}_1(\pi)$ is fixed for an arbitrary density from the (assumed) chiral symmetry. It is important that the result is consistent with charge conservation and Galilei invariance.

4.2.3. Axial charge. The axial-charge operator in nuclear matter is protected by the chiral filter in the chiral Lagrangian formalism, so all we need is the soft-pion exchange implemented with BR scaling. We shall continue assuming that pions do not scale in a medium. It was shown in [36] that higher order chiral corrections—such as loops, higher derivative, and four-Fermi terms—to the soft-pion contribution are small. This means that we can limit ourselves to the tree order in the chiral counting and to the pionic range with shorter-range interactions subsumed in the BR scaling.

The procedure for the case at hand will then be identical to that we used for the convection current. The axial charge for a single particle will be identical to that of a particle in free space except that the nucleon mass M is to be replaced by the BR, scaling mass M^*

$$A^a_0 = g_A\frac{\tau^a}{2}\frac{\boldsymbol{\sigma}\cdot\mathbf{k}}{M^*}. \tag{56}$$

Now the leading correction to the single-particle term is given by a diagram similar to Fig. 2*c* with the photon replaced by the weak axial charge. There is no term equivalent to Fig. 2*b* due to *G*-parity invariance. The calculation is straightforward and the result is

$$A^i_{02\text{-body}} = g_A\frac{\boldsymbol{\sigma}\cdot\mathbf{k}}{M^*}\frac{\tau^i}{2}\tilde{\Delta} \tag{57}$$

with

$$\tilde{\Delta} = \frac{f^2 k_{\text{F}} M}{2g_A^2 m_\pi^2 \pi^2}\left(I_0 - I_1 - \frac{m_\pi^2}{2k_{\text{F}}^2}I_1\right), \tag{58}$$

where I_1 is as defined in (42) and I_0 is

$$I_0 = \int_{-1}^{1} dx\frac{1}{1 - x + m_\pi^2/(2k_{\text{F}}^2)} = \ln\left(1 + \frac{4k_{\text{F}}^2}{m_\pi^2}\right). \tag{59}$$

The factor $(1/g_A^2)$ in (37) arose from replacing $1/f_\pi^2$ by $g^2_{\pi NN}/(g_A^2 M^2)$ using the free-space Goldberger–Treiman relation.

Collecting all terms, the chiral Lagrangian prediction is

$$A^a_{0\,\text{chiral}} = g_A\frac{\boldsymbol{\sigma}\cdot\mathbf{k}}{M^*}\frac{\tau^a}{2}(1 + \tilde{\Delta}). \tag{60}$$

[9)] The heavy-baryon formalism must be unreliable once the M^* drops for $\rho \gtrsim \rho_0$. One would then have to resort to a relativistic formulation [35]. We expect, however, that our reasoning will remain qualitatively intact.

For comparison with the Migdal formula $A^i_{0\,\mathrm{Migdal}}$, we reexpress $1/M^*$ in terms of $1/m_N^*$

$$1/M^* = \frac{1}{m_N^*}\left(1-\frac{\Phi}{3}\tilde{F}_1(\pi)\right)^{-1}. \quad (61)$$

Thus

$$A^a_{0\,\mathrm{chiral}} = g_A\frac{\boldsymbol{\sigma}\cdot\mathbf{k}}{m_N^*}\frac{\tau^a}{2}(1+\tilde{\Delta}'), \quad (62)$$

where

$$\tilde{\Delta}' = \left(\tilde{\Delta}+\frac{\Phi}{3}\tilde{F}_1(\pi)\right)\left(1-\frac{\Phi}{3}\tilde{F}_1(\pi)\right)^{-1}. \quad (63)$$

Comparing with the Migdal formula (37), we obtain a formula that expresses a combination of spin–isospin-dependent Landau–Migdal parameters in terms of constants that figure in the chiral Lagrangian with BR scaling:

$$\frac{1}{3}G_1'-\frac{10}{3}H_0'+\frac{4}{3}H_1'-\frac{2}{15}H_2' = \tilde{\Delta}'. \quad (64)$$

Again, the result depends on only one parameter Φ.

There are two points to note here. One is, as noted in the Landau–Migdal formulation, that there is no equivalent to the Kohn theorem for the axial charge. The other is that the soft-pion contribution combined with BR scaling does not lend itself to a direct term-by-term identification on both sides. These are all different from the case of the convection current. In the axial case, both the Landau–Migdal approach and the chiral Lagrangian approach involve complicated relations: on the right-hand side of (64), the factor g_A appears in a nontrivial way and exhibits features that are characteristic of the spontaneously broken axial symmetry and on the left-hand side, this complexity is manifested by the fact that, due to the tensor force, the Migdal parameters involved comprise several multipoles (l = 0, 1, 2) of the quasiparticle interaction.

5. COMPARISON WITH EXPERIMENTS

In confronting our theory with nature, we shall assume that data on heavy nuclei represent nuclear matter. This aspect has been extensively discussed elsewhere so we shall be brief.

5.1. Extracting $\Phi(\rho_0)$

If one assumes BR scaling, then there are several ways to determine Φ at normal nuclear matter density. We shall mention three of them.

(i) The first way is that if pions are taken to be nonscaling, then the in-medium Gell-Mann–Oakes–Renner relation

$$m_\pi^2 f_\pi^{*2} = -(m_u+m_d)\langle\bar{q}q\rangle^* \quad (65)$$

gives

$$\frac{f_\pi^*}{f_\pi}\approx\left(\frac{\langle\bar{q}q\rangle^*}{\langle\bar{q}q\rangle_0}\right)^{1/2}. \quad (66)$$

From the value of quark condensate in nuclear matter estimated from the empirical πN sigma term and using Feynman–Hellmann theorem in the linear density approximation[10] one finds [22]

$$\frac{f_\pi^*}{f_\pi}\approx 0.78. \quad (67)$$

(ii) The second piece of evidence comes from the property of nuclear matter in chiral Lagrangian models with BR scaling. A global fit yields [4]

$$M^*/M\approx 0.78\pm 0.02. \quad (68)$$

(iii) The third piece of evidence comes from QCD sum-rule calculation of the mass of the vector meson ρ in medium [37, 38]. The result is [38]

$$m_\rho^*/m_\rho = 0.78\pm 0.08. \quad (69)$$

All three methods give the same result. We are therefore led to

$$\Phi(\rho_0) = 0.78. \quad (70)$$

As a smooth interpolation, which seems reasonable at least up to $\rho\simeq\rho_0$, we take

$$\Phi(\rho) = (1+0.28\rho/\rho_0)^{-1}. \quad (71)$$

5.2. The Orbital Gyromagnetic Ratio

Given the scaling factor $\Phi(\rho_0)\approx 0.78$ and the pionic contribution (24) which at nuclear matter density yields $\tilde{F}_1(\pi)\approx -0.459$, the anomalous orbital gyromagnetic ratio turns out to be

$$\delta g_l = \frac{4}{9}\left[\Phi^{-1}-1-\frac{1}{2}\tilde{F}_1(\pi)\right]\tau_3 = 0.227\tau_3. \quad (72)$$

This is to be compared[11] with the experimental value for the proton obtained from the giant dipole resonance in the Pb region [39]

$$\delta g_l^p = 0.23\pm 0.03. \quad (73)$$

It is worth commenting at this point which assumptions enter into this calculation and what the possible implications might be. Apart from the BR scaling, we have assumed (1) that pions do not scale, (2) the nonet symmetry for the vector mesons, and (3) the isospin symmetry for the pions. The first is based on the observation that the pion is almost a Goldstone boson and a

[10] The linear-density approximation may be suspect already at nuclear matter density, so it is difficult to assess the uncertainty involved with this estimate.

[11] The precise agreement is probably coincidental.

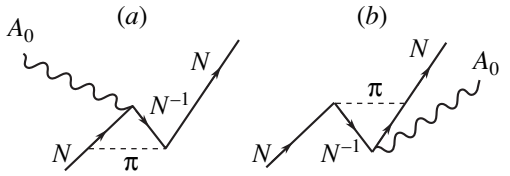

Fig. 4. Particle–hole contribution to the axial charge involving one-pion exchange which is minus the back-flow. Here, A_0 stands for the external field probing axial charge, the backward-going nucleon line N^{-1} denotes a hole and the wiggly line the W boson connected to the axial charge. These graphs vanish in the $q/\omega \longrightarrow 0$ limit.

truly Goldstone boson would preserve its symmetry as density is increased beyond normal nuclear matter density. This assumption needs to be verified. The second is hard to check and remains to be verified. The third is most probably solid. The upshot of the result is that the charge is conserved, the Kohn theorem is satisfied, and the agreement with experiment essentially confirms, on average, the BR scaling for the nucleon mass.

5.3. Landau Mass for the Nucleon

A quantity closely related to δg_l is the Landau effective mass m_N^*. Given Φ and $\tilde{F}_1(\pi)$ for $\rho = \rho_0$, we obtain from Eq. (32) that

$$m_N^* = (1/0.78 + 0.153)^{-1} M \approx 0.70M. \quad (74)$$

There are two sources of information that can be compared with this prediction. One is theoretical, namely, the QCD sum-rule result [40]

$$\left(\frac{m_N^*(\rho_0)}{M}\right)_{\rm QCD} = 0.69^{+0.14}_{-0.07}. \quad (75)$$

The other is an indirect semiempirical indication coming from peripheral heavy-ion collisions at the BEVALAC and the SIS [41]:

$$m_N^{*\rm HI} \simeq 0.68M. \quad (76)$$

The agreement here is essentially a reconfirmation of the gyromagnetic ratio (72).

5.4. Axial-Charge Transitions in Heavy Nuclei

Before confronting the chiral Lagrangian prediction (60) (with (58)) with experiments, we compare the left-hand side of (64) (i.e., Migdal's axial charge) with one-pion exchange only and the right-hand side which is given to next-to-leading order (NLO) chiral perturbation theory with BR-scaling chiral Lagrangian.[12)]

To compute the Migdal charge, it is sufficient to compute the one-pion-exchange graphs of Fig. 4 in the limit $\omega/q \longrightarrow 0$. The negative of this gives the desired quantity, namely, the back-flow. A simple calculation gives

$$\left(\frac{1}{3}G_1' - \frac{10}{3}H_0' + \frac{4}{3}H_1' - \frac{2}{15}H_2'\right)_\pi = \frac{f^2 k_{\rm F} m_N^*}{4m_\pi^2\pi^2}(I_0 - I_1), \quad (77)$$

where the subscript π denotes the pionic contribution. Now since the right-hand side of (64) is valid beyond the leading order in chiral perturbation theory, it contains information that accounts for more than one-pion exchange. In the same vein, Eq. (77) contains a lot more since the mass of the nucleon is given by the Landau mass m_N^*, although the interaction is evaluated with one-pion exchange. Therefore, there is no reason to expect a one-to-one correspondence between the two. Even so, we conjecture that, to the extent that the dynamics is governed by the pion exchange corrected by the BR-scaling Φ, the two must be approximately the same. That is to say that the combination of the Migdal parameters of (64) should be saturated by the pions modulo what corresponds to higher chiral order terms which are argued to be small. This is required if the chiral-filter argument is to hold.

Let us consider how relation (64) fares with the pion for $\rho = \rho_0/2$ and ρ_0. The left-hand side—given by (77)—comes out to be, respectively, 0.42 and 0.50 for $\rho = \rho_0/2$ and ρ_0, while the right-hand side—which is the full contribution from the BR Lagrangian—gives 0.37 and 0.55. Thus the pions are seen to saturate about 90% of the total predicted by the chiral field theory with BR scaling.

Although far from direct, there is a beautiful confirmation of the prediction (60) from axial-charge transitions in heavy nuclei (denoted by the mass number A)

$$A(J^\pm) \longrightarrow A'(J^\mp) + e^-(e^+) + \bar{\nu}(\nu), \quad \Delta T = 1. \quad (78)$$

The quantity we shall look at is Warburton's $\epsilon_{\rm MEC}$ [42] defined by

$$\epsilon_{\rm MEC} = M_{\rm exp}/M_{\rm sp}, \quad (79)$$

where $M_{\rm exp}$ is the measured matrix element for the axial-charge transition and $M_{\rm sp}$ is the theoretical single-particle matrix element for a nucleon without BR scaling. There are theoretical uncertainties in defining the latter, so the ratio is not an unambiguous object but what is significant is Warburton's observation that in heavy nuclei, $\epsilon_{\rm MEC}$ can be as large as two:

$$\epsilon_{\rm MEC}^{\rm Heavy\ Nuclei} = 1.9 \sim 2.0. \quad (80)$$

More recent measurements—and their analyses—in different nuclei [43, 44] quantitatively confirm this result of Warburton.

The theoretical prediction from (60) is

$$\epsilon_{\rm MEC}^{\rm chiral} = \Phi^{-1}(1 + \tilde{\Delta}) \quad (81)$$

[12)] Modulo correction less than 10%, this is valid to next-next-to-leading order (NNLO) in chiral perturbation theory [36].

with $\tilde{\Delta}$ given by (58). For nuclear matter density, we find

$$\epsilon_{\rm MEC}^{\rm chiral} \approx 2.1. \quad (82)$$

The theory therefore correctly describes the large enhancement of the axial-charge matrix element in nuclei in general and the density-dependent enhancement in particular. There are two elements that account for this enhancement. Pions contribute $\tilde{\Delta} \sim 1/2$ with little density dependence and the BR-scaling Φ accounts for the further enhancement for heavier nuclei. This result represents a strong case for the validity of the theory in the normal density regime.

6. GOING TO DENSER MATTER

6.1. Evidence in Dense Matter?

The real strength in effective field theories is that one may be able to describe quantitatively the state of matter that is formed at a high density as one approaches the chiral phase transition. If one assumes that the matter is a Fermi liquid all the way to the phase transition, then one can use the BR-scaling chiral Lagrangian in the mean field. But this means that all degrees of freedom, fermionic as well as bosonic, are treated as quasiparticles. It is established that nucleons are quasiparticles in nuclear matter as Migdal had argued. The shell model for nuclei is justified by the quasiparticle picture. It is also supposed that at asymptotic density where weak coupling of QCD is operative, quarks can be treated as quasiquarks [45]. The presence of a Fermi sea for nucleons and quarks is one of the ingredients for treating them as quasiparticles. In the discussions given above, bosons were not required to be quasiparticles despite that BR scaling is invoked for both fermions and bosons. In addressing heavy-ion processes, however, properties of bosons in medium might play an important role. For instance, in CERN's CERES experiments, it is the property (i.e., mass, width, etc.) of the ρ meson in dense and hot medium that seems to play a key role. So the question arises how bosons behave in extreme conditions.

There are some indirect experimental evidences for vector bosons with dropping masses in dense medium. The effect is usually manifested in spin–isospin-dependent nuclear forces and affect spin–isospin observables [46, 47]. These observables probe off-shell properties of the mesons involved up to nuclear matter density and do not in general give direct information on their physical properties in medium. There are similar indications from tensor forces in heavy nuclei which also can be explained from the exchange of the ρ meson with a reduced mass [48]. A more direct indication comes from dilepton production in heavy-ion collisions at CERN CERES. There, the quasiparticle picture of the vector mesons with dropping mass in hot and dense matter (at a density greater than that of normal nuclear matter) provides a simple and successful explanation of the observed downward shift of the invariant mass of the lepton pair [49]. The approximation used in [49] consists of taking only tree-order graphs with an effective chiral Lagrangian à la BR scaling discussed above that gives a realistic description of nuclear matter: no loop corrections are taken into account in a proper sense although partial account is of course made in the unitarization of the amplitudes involved. The question as to what happens when loop corrections are properly taken into account in this theory so far remains unanswered. It is also not known whether the tree-order (i.e., quasiparticle) treatment correctly describes the excitation of the vector quantum numbers in such dense matter.

6.2. Perturbing from a Zero-Density Vacuum

One might attempt an ambitious program to start from an effective chiral Lagrangian constructed at zero density and do a systematic chiral expansion to arrive at higher density. This is the spirit of [18, 19]. Aided by experiments, this program could be made to work up to nuclear matter density, but it is a completely different matter if one wants to reach a density where the chiral phase transition can occur. Dense matter probes short distances, and chiral perturbation theory (ChPT) cannot access such kinematic regime as is clear from Landau–Migdal Fermi liquid theory. What has been done up to date is a low-order perturbation calculation in a strong-coupling regime. Now, if such a calculation is based on an effective Lagrangian satisfying relevant symmetries (e.g., chiral symmetry), leading-order (tree-order) terms are consistent with low-energy theorems and should give reasonable results at low density, provided the parameters are picked from experiments. See Rapp and Wambach [50] for a review where the relevant references are found. In such low-order calculations, one finds that the mesons, such as the ρ and a_1, get "melted" due to increasing width and lose their particle identities. However, as the density increases away from zero, the tree-order approximations, which are essentially all one can work with, cannot be trusted. Exactly where this discrepancy will become serious is not known. Being in a strong-coupling regime, anomalous dimensions of certain fields (such as scalar fields) grow too big to be natural, signaling that one is fluctuating around the wrong vacuum. We believe this to be the case already at nuclear matter density. Brown–Rho scaling corresponds to shifting to and fluctuating around a vacuum defined at $\rho \gtrsim \rho_0$ where the effective coupling gets weaker in the sense of quasiparticle interactions. As the density approaches the critical for the chiral phase transition, the picture with quasinucleons goes over to the one with quasiquarks. It seems extremely difficult, if not impossible, to arrive at this picture starting from a strong-coupling hadronic theory effective at

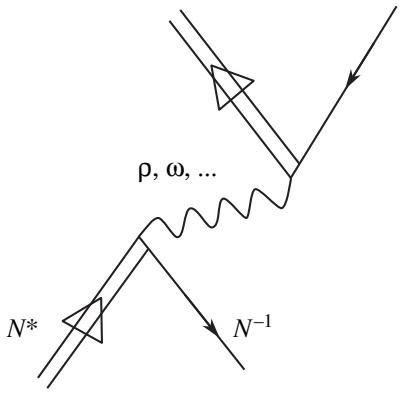

Fig. 5. Particle–hole coherent modes excited by coupling to vector mesons ρ, ω, … .

zero density. See [4, 51] for further discussion on this point.

6.3. Perturbing from the BR-Scaling Ground State

Given a Lagrangian (3) or (5) with BR scaling that gives the ground state of nuclear matter correctly, we would like to know how to make fluctuations around the ground state. As an illustration, consider kaon–nucleon interactions in a medium [22]. This process is relevant for both laboratory experiments and for the structure of compact stars as we will describe below.

For the problem at hand, it is convenient to generalize (5) to the *SU*(3) flavor so as to incorporate kaons in the Lagrangian. The additional term relevant to the process is given by

$$\delta\mathcal{L}_{KN} = \frac{-6i}{8f^{*2}}(\bar{N}\gamma_0 N)\bar{K}\partial_t K + \frac{\Sigma_{KN}}{f^{*2}}(\bar{N}N)\bar{K}K + \ldots \equiv \mathcal{L}_\omega + \mathcal{L}_\phi + \ldots, \quad (83)$$

where $K^T = (K^+K^0)$, f^* is the in-medium Goldstone boson decay constant which, within the approximation adopted here, may be taken to be the pion decay constant, and the ellipses stand for higher order terms in the chiral counting. The structure of the first two leading-order terms of the fluctuating Lagrangian is dictated by current algebras, which implies that Σ_{KN} is the usual *KN* sigma term in free space and also that it may be valid near nuclear matter density.

Within the scheme à la BR, we are to work in the mean-field approximation. Assuming that this is valid up to nuclear matter density, one gets from (83) the potential energy for the scalar (ϕ) field S_{K^-} and the vector (ω) field V_{K^-} that K^- feels in nuclear matter at $\rho = \rho_0$:

$$S_{K^-} + V_{K^-} \approx -192 \text{ MeV}. \quad (84)$$

For this we have used the value for the *KN* sigma term, $\Sigma_{KN} \approx 3.2m_\pi$ and $f_\pi^*/f_\pi \approx \Phi$. The exact value is unknown since the sigma term is not fixed precisely. The attraction (84) is consistent with what is observed in kaonic atoms [52] and also with the K^-/K^+ production ratio in heavy-ion collisions at GSI [53]. When applied to neutron-star matter and extrapolating to higher density, it is more appropriate to adopt the "top–down" approach proposed in [22], in which the kaon field is introduced as a matter field and the relevant fermion field is taken to be the quasiquark rather than the nucleon. With a suitable modification appropriate for the top–down approach of [22] in the Lagrangian (83), one then predicts K^- condensation at a matter density $\rho_c \approx 2 \sim 3\rho_0$ with the intriguing implication that the maximum stable neutron-star mass is 1.5 times the solar mass [53]. These mean-field results with BR-scaling Lagrangians are in agreement with more refined calculations carried out in high-order chiral perturbation theory [54]. If it turned out that condensation occurs at higher density than the range considered so far (due to some higher order effects that cannot be accessed by the effective Lagrangian method used), then the presently available machinery for handling short-distance physics would not be powerful enough to allow us to pin down the critical density [55]. More work is needed in this area.

6.4. Sobar Model

Among Migdal's other major contributions to nuclear physics is his work on pion-nuclear interactions, in particular on pion condensation in dense nuclear matter [6]. It is suggested that the Fermi liquid description à la BR-scaling chiral Lagrangian can be phrased in a form resembling Migdal's description of pion condensation. The initial idea is formulated in a series of recent papers by Kim *et al*. [56].

Consider a vector meson, say ω, which is inserted in a dense medium, and look at the excitation of coherent modes of the ω quantum number. The ω meson will be coupled to particle–hole excitations of the same quantum number as depicted in Fig. 5. Analogous to the treatment of pion condensation, the lowest energy collective particle–hole mode is interpreted as an effective vector meson field operating on the ground state of the nucleus, i.e.,

$$\frac{1}{\sqrt{A}}\sum_i [N_i^* N_i^{-1}]^{1-} \simeq \sum_i [\rho(x_i) \text{ or } \omega(x_i)]|\Psi_0\rangle_s, \quad (85)$$

with the antisymmetrical (symmetrical) sum over neutrons and protons giving the ρ-like (ω-like) nuclear excitation. Here, the "particle" is taken to be *N**, while the "hole" is a nucleon hole. We will ignore the nucleon as a particle since, in the channel we are concerned with, we expect the nucleon to be more weakly coupled than the *N** to the (near on-shell) vector

meson. We call the collective mode (85) sobar, i.e., ρ-sobar, ω-sobar, etc.

The dropping vector meson masses could then be calculated in terms of mixing of the nuclear collective state, Eq. (85), with the elementary vector meson through the mixing matrix elements of Fig. 5. Now building up the collective nuclear mode, the latter can be identified as an analog to the state in the degenerate schematic model of Brown for giant dipole resonance [57]. The fields figuring in a BR-scaling chiral Lagrangian are then to be identified with interpolating fields for the lowest branch modes that emerge from the mixing. An important development which leads to the assumption of Eq. (85) was furnished by Friman, Lutz, and Wolf [58]. From empirical values of the amplitudes such as $\pi + N \longrightarrow \rho + N$, etc., they constructed the ρ-like or ω-like states in agreement with our assumption of Eq. (85). Thus, the input assumption made for the sobar model receives substantial empirical support.

Since the development is at its initial stage and still quite crude, we briefly summarize what we hope to accomplish in the end.

The property of a vector meson, say, ω, in a medium is encoded in the propagator of the meson in interaction with the system. For simplicity, let us consider a two-level schematic model. In (85), we take only one configuration with $N^* = N^*(1520)$ in the ω channel. The starting point is the ω-meson propagator in nuclear matter given by

$$D_\omega(q_0, \mathbf{q}; \rho_N) = \frac{1}{q_0^2 - \mathbf{q}^2 - m_\omega^2 - \Sigma_{\omega N^* N}(q_0, q; \rho_N)}, \quad (86)$$

where we have ignored the ω decay width, and the density-independent real part of the self-energy has been absorbed into the free (physical) mass m_ω. Here, ρ_N is the nucleon-number density. Note that within the low-order approximation made here the entire density dependence resides in the in-medium ω self-energy $\Sigma_{\omega N^* N}$ induced by $N^*(1520)N^{-1}$ excitations. In what follows, we will, for simplicity, concentrate on the limit of a vanishing three-momentum, where the longitudinal and transverse polarization components become identical. Due to the rather high excitation energy of $\Delta E = M_{N^*} - M_N$ =580 MeV, one can safely neglect nuclear Fermi motion to obtain

$$\Sigma_{\omega N^* N}(q_0) \sim g^2_{\omega N^* N} \frac{q_0^2}{m_\omega^2} \frac{\rho_N}{4} \left(\frac{2(\Delta E)}{(q_0 + i\Gamma_{\rm tot}/2)^2 - (\Delta E)^2} \right), \quad (87)$$

where $\Gamma_{\rm tot}$ is the sum of the full width of $N^*(1520)$ in free space and the density-dependent width due to the medium. If the widths of ω and $N^*(1520)$ are sufficiently small, one can invoke the mean-field approximation and determine the quasiparticle excitation energies from the zeros in the real part of the inverse propagator. In particular, for $\mathbf{q} = 0$, the in-medium ω mass is obtained by solving the dispersion relation

$$q_0^2 = m_\omega^2 + \mathrm{Re}\,\Sigma_{\omega N^* N}(q_0). \quad (88)$$

The pertinent spectral weights of the solutions are characterized by Z factors defined by

$$Z = \left(1 - \frac{\partial}{\partial q_0^2} \mathrm{Re}\,\Sigma_{\omega N^* N}\right)^{-1}. \quad (89)$$

The formulas written above are presumably valid for low density since they can be made consistent (by fiat) with low-energy theorems. However, there is no reason to expect that a low-order calculation in strong coupling will be viable at high density. For instance, there is no way that the ω mass will go to zero at any density even in the chiral limit. We are therefore led to make certain assumptions motivated by our objective to model BR scaling. It is clear that with a few-order perturbative calculation in a strong-coupling regime, there is no way to arrive at BR scaling. Lacking a workable scheme to compute systematically, we will simply impose a condition on the model and study the consequence on the model. The simplest condition that we can impose is that $q_0 = 0$ be a solution of (88) at some density ρ_c at which the in-medium pion decay constant f_π^* is to vanish (à la, e.g., in-medium Weinberg sum rule). This is readily achieved if

$$g^{*2}_{\omega N^* N} \frac{q_0^2}{m_\omega^2} \longrightarrow \text{const}, \quad (90)$$

irrespective of density as $\rho \longrightarrow \rho_c$. Note that we have appended a star on the $\omega N^* N$ coupling constant to indicate that higher order corrections will inject a non-linear density dependence into the vertex (as well as into the width, etc.) The limit can be achieved only if the density dependence in f^* cancels the same in q_0 as one approaches the critical density. Now the constant cannot be fixed a priori and what one takes for it will determine at what ρ_c the effective ω-sobar mass will vanish. The basic assumption here is that since the vector mass drops while the pion mass does not, the quasiparticle picture gets restored as ρ approaches ρ_c with the width shrinking due to the decreasing phase space. This is consistent with the general premise of BR scaling.

As stressed in [56], nobody has been able to derive such a sobar description starting from effective field theories defined at zero density. It seems however promising that this is possible in a systematic way in the framework laid down in [56]. How this can come about is sketched in the references [56].

ACKNOWLEDGMENTS

I am very grateful for discussions and collaborations with G.E. Brown, B. Friman, Y. Kim, K. Kubodera, D.-P. Min, T.-S. Park, and Chaejun Song. I particularly thank B. Friman for his insightful advice and comments for this article. Part of this paper was written while I was visiting the Korea Institute for Advanced Study, whose hospitality is acknowledged.

REFERENCES

1. R. Shankar, Rev. Mod. Phys. **66**, 129 (1994); J. Polchinski, *Recent Directions in Particle Theory: From Superstrings and Black Holes to the Standard Model*, Ed. by J. Harvey and J. Polchinski (World Sci., Singapore, 1994), p. 235; T. Chen, J. Fröhlich, and M. Seifert, *"Renormalization Group Methods: Landau Fermi Liquid and BCS Superconductors," Lectures at Les Houches Summer School, August 1994*, cond-mat/9508063; G. Benfatto and G. Gallavotti, J. Stat. Phys. **59**, 541 (1990); Phys. Rev. B **42**, 9967 (1990).
2. A. B. Migdal, *Theory of Finite Fermi Systems and Applications to Finite Nuclei* (Nauka, Moscow, 1982, 2nd ed.; Interscience, London, 1967).
3. B. Friman and M. Rho, Nucl. Phys. A **606**, 303 (1996); C. Song, G. E. Brown, D.-P. Min, and M. Rho, Phys. Rev. C **56**, 2244 (1997); C. Song, D.-P. Min, and M. Rho, B **424**, 226 (1998); B. Friman, M. Rho, and C. Song, Phys. Rev. C **59**, 3357 (1999).
4. C. Song, Phys. Rep. (in press); nucl-th/0006030.
5. See, e.g., T.-S. Park, K. Kubodera, D.-P. Min, and M. Rho, *Effective Field Theories for Nuclei: Confronting Fundamental Questions in Astrophysics* (in press).
6. A. B. Migdal, E. E. Saperstein, M. A. Troitsky, and D. N. Voskresensky, Phys. Rep. **192**, 179 (1990).
7. S. Weinberg, Phys. Lett. B **251**, 288 (1990); Nucl. Phys. B **363**, 3 (1991); Phys. Lett. B **295**, 114 (1992).
8. *Proceedings of the Joint Caltech/INT Workshop: Nuclear Physics with Effective Field Theory I*, Ed. by R. Seki, U. van Kolck and M. J. Savage (World Sci., Singapore, 1998); *Proceedings of the Joint Caltech/INT Workshop: Nuclear Physics with Effective Field Theory II*, Ed. by P. F. Bedaque, M. J. Savage, R. Seki, and U. van Kolck (World Sci., Singapore, 2000).
9. D. B. Kaplan, M. Savage, and M. Wise, Nucl. Phys. B **478**, 629 (1996); Phys. Lett. B **424**, 390 (1998); Nucl. Phys. B **534**, 329 (1998); Phys. Rev. C **59**, 617 (1999).
10. T.-S. Park, K. Kubodera, D.-P. Min, and M. Rho, nucl-th/9904053; Phys. Lett. B **472**, 232 (2000).
11. T.-S. Park, K. Kubodera, D.-P. Min, and M. Rho (in press).
12. J.-W. Chen, G. Rupak, and M. J. Savage, nucl-th/9905002; Phys. Lett. B **464**, 1 (1999).
13. T. Müller, private communication.
14. Y. Fukuda *et al.*, Phys. Rev. Lett. **82**, 2430 (1999); M. B. Smy, hep-ex/9903034.
15. J. N. Bahcall and P. I. Krastev, Phys. Lett. B **436**, 243 (1998).
16. T.-S. Park, D.-P. Min, and M. Rho, Nucl. Phys. A **596**, 515 (1996); Phys. Rev. C **58**, R637 (1998); Nucl. Phys. A **646**, 83 (1999).
17. T.-S. Park, K. Kubodera. D.-P. Min, and M. Rho, Astrophys. J. **507**, 443 (1998).
18. B. W. Lynn, Nucl. Phys. B **402**, 281 (1993).
19. M. Lutz, B. Friman, and Ch. Appel, Phys. Lett. B **474**, 7 (2000); nucl-th/9907078.
20. G. Gelmini and B. Ritzi, Phys. Lett. B **357**, 431 (1995); T.-S. Park, D.-P. Min, and M. Rho, Nucl. Phys. A **596**, 515 (1996).
21. B. D. Serot and J. D. Walecka, Adv. Nucl. Phys. **16**, 1 (1986).
22. G. E. Brown and M. Rho, Nucl. Phys. A **596**, 503 (1996).
23. C. Song, D.-P. Min, and M. Rho, Phys. Lett. B **424**, 226 (1998).
24. T. Matsui, Nucl. Phys. A **370**, 365 (1981).
25. G. E. Brown and M. Rho, Phys. Rev. Lett. **66**, 2720 (1991); Phys. Rep. **269**, 333 (1996).
26. R. J. Furnstahl and B. D. Serot, Nucl. Phys. A **671**, 447 (2000).
27. Y. Kim and H. K. Lee, hep-ph/9905268.
28. S. Beane and U. van Kolck, Phys. Lett. B **328**, 137 (1994); Y. Kim, H. K. Lee, and M. Rho, Phys. Rev. C **52**, R1184 (1995).
29. B. Friman, M. Rho, and C. Song, Phys. Rev. C **59**, 3357 (1999).
30. S.-O. Backman, O. Sjöberg, and A. D. Jackson, Nucl. Phys. A **321**, 10 (1979).
31. W. Kohn, Phys. Rev. **123**, 1242 (1961).
32. A. Houghton, H.-J. Kwon, and J. B. Marston, cond-mat/9810388; Adv. Phys. **49**, 141 (2000).
33. B. Friman and M. Rho, Nucl. Phys. A **606**, 303 (1996).
34. K. Kubodera, J. Delorme, and M. Rho, Phys. Rev. Lett. **40**, 755 (1978); M. Rho, Phys. Rev. Lett. **66**, 1275 (1991).
35. T. Becher and H. Leutwyler, Eur. Phys. J. C **9**, 643 (1999).
36. T.-S. Park, D.-P. Min, and M. Rho, Phys. Rep. **233**, 341 (1993).
37. T. Hatsuda and S. H. Lee, Phys. Rev. C **46**, R34 (1992).
38. X. Jin and D. B. Leinweber, Phys. Rev. C **52**, 3344 (1995).
39. R. Nolte, A. Baumann, K. W. Rose, and M. Schumacher, Phys. Lett. B **173**, 388 (1986).
40. R. J. Furnstahl, X. Jin, and D. B. Leinweber, Phys. Lett. B **387**, 253 (1996).
41. A. B. Larionov, W. Cassing, C. Greiner, and U. Mosel, nucl-th/0006009.
42. E. K. Warburton, Phys. Rev. Lett. **66**, 1823 (1991); Phys. Rev. C **44**, 233 (1991); E. K. Warburton and I. S. Towner, Phys. Lett. B **294**, 1 (1992).
43. P. Baumann *et al.*, Phys. Rev. C **58**, 1970 (1998).
44. T. Minamisono *et al.*, Phys. Rev. Lett. **82**, 1644 (1999).
45. F. Wilczek, hep-ph/0003183; T. Schaefer, nucl-th/9911017; K. Rajagopal, hep-ph/9908360.
46. G. J. Lolos *et al.*, Phys. Rev. Lett. **80**, 241 (1998).
47. E. J. Stephenson *et al.*, Phys. Rev. Lett. **78**, 1636 (1997).
48. G. E. Brown and M. Rho, Phys. Lett. B **237**, 3 (1990).

49. G. Q. Li, C. M. Ko, and G. E. Brown, Phys. Rev. Lett. **75**, 4007 (1995); Nucl. Phys. A **606**, 568 (1996); G. Q. Li, C. M. Ko, G. E. Brown, and H. Sorge, Nucl. Phys. A **611**, 539 (1996).
50. R. Rapp and J. Wambach, Adv. Nucl. Phys. (in press); hep-ph/9909229.
51. G. E. Brown, M. Buballa, and M. Rho, Nucl. Phys. A **609**, 519 (1996).
52. E. Friedman, A. Gal, and C. J. Batty, Phys. Lett. B **308**, 6 (1993); Phys. Lett. A **579**, 519 (1994).
53. G. Q. Li, C.-H. Lee, and G. E. Brown, Phys. Rev. Lett. **79**, 5214 (1997).
54. C.-H. Lee, Phys. Rep. **275**, 256 (1996).
55. J. Carlson, H. Heiselberg, and V. R. Pandharipande, nucl-th/9912043.
56. G. E. Brown, C. Q. Li, R. Rapp, M. Rho, and J. Wambach, Acta Phys. Pol. B **29**, 2309 (1998); Y. Kim, R. Rapp, G. E. Brown, and M. Rho, nucl-th/9902009; nucl-th/9912061; Phys. Rev. C **62**, 015202 (2000).
57. G. E. Brown, in *Unified Theory of Nuclear Models and Forces* (North-Holland, Amsterdam, 1971), Chap. V. 3.
58. B. Friman, M. Lutz, and G. Wolf, nucl-th/9811040; Nucl. Phys. A **661**, 526 (1999); nucl-th/0003012.

Physics of Atomic Nuclei, Vol. 64, No. 4, 2001, pp. 652–669. From Yadernaya Fizika, Vol. 64, No. 4, 2001, pp. 711–728.

90th ANNIVERSARY OF A.B. MIGDAL'S BIRTHDAY
NUCLEI

Soft Modes, Resonances, and Quantum Transport*

Yu. B. Ivanov[1], J. Knoll, H. van Hees, and D. N. Voskresensky[2]
Gesellschaft für Schwerionenforschung mbH, Darmstadt, Germany
Received July 12, 2000

Abstract—Effects of the propagation of particles that have a finite lifetime and an according width in their mass spectrum are discussed in the context of transport description. First, the importance of coherence effects (Landau–Pomeranchuk–Migdal effect) on the production and absorption of field quanta in nonequilibrium dense matter is considered. It is shown that classical diffusion and Langevin results correspond to a resummation of certain field-theory diagrams formulated in terms of full nonequilibrium Green's functions. General properties of broad resonances in dense and hot systems are discussed in the framework of a self-consistent and conserving Φ-derivable method of Baym by considering the examples of the ρ meson in hadronic matter and the pion in dilute nuclear matter. Further, we address the problem of a transport description that properly takes into account the damping width of the particles. The Φ-derivable method generalized to the real-time contour provides a self-consistent and conserving kinetic scheme. We derive a generalized expression for the nonequilibrium kinetic entropy flow, which includes corrections from fluctuations and mass-width effects. In special cases, an *H* theorem is proven. Memory effects in collision terms contribute to the kinetic entropy flow that, in the Fermi liquid case, reproduces the famous bosonic-type $T^3 \ln T$ correction to the specific heat of liquid ^{3}He. For the example of the pion-condensate phase transition in dense nuclear matter, we demonstrate the important role of the width effects within the quantum transport. © *2001 MAIK "Nauka/Interperiodica".*

1. INTRODUCTION

Quasiparticle representations in many-body theory were designed by Landau, Migdal, Galitsky, and others (see [1–4]). This concept was first elaborated for low-lying particle–hole excitations in Fermi liquids. Migdal was the first to apply these methods to description of various nuclear phenomena and construction of a closed semimicroscopic approach that is now usually called the theory of finite Fermi systems [3]. The need for an explicit treatment of soft modes within this approach stimulated him to generalize this concept to include pion and Δ excitations. Migdal suggested a variety of interesting effects like the softening of the pion mode in nuclei, pion condensation in dense nuclear and neutron-star matter, and the possible existence of abnormal nuclei glued by a pion condensate [5–8]. These ideas stimulated further development of pion physics with applications to many phenomena in nuclei, neutron stars, and heavy-ion collisions (see [8–10] and references therein). In this paper, we would like to review briefly recent developments of some of the above ideas as applied to heavy-ion physics.

With the aim of describing a collision of two nuclei at intermediate and high energies, one is confronted with the fact that dynamics has to include particles like the in-medium excitation with the pion quantum numbers, as well as the delta and ρ-meson resonances with lifetimes of less than 2 fm/*c* or, equivalently, with damping widths above 100 MeV. Also, the collision damping rates deduced from currently used transport codes are on the same order, whereas typical mean temperatures range from 50 to 150 MeV, depending on the beam energy. Thus, the damping width of most of the constituents in the system can by no means be treated as a perturbation. As a consequence, the mass spectrum of the particles in dense matter is no longer a sharp delta function, but it rather acquires a width due to collisions and decays. Thus, one arrives at a picture that unifies resonances, which already have a width in vacuum due to decay modes, with the "states" of particles in dense matter, which acquire a width due to collisions (collision broadening). Landau, Pomeranchuk, and Migdal were the first to demonstrate the importance of finite-width effects in multiparticle scattering [11, 12]. Such a coherence scattering effect, known now as the Landau–Pomeranchuk–Migdal effect, was recently observed at the Stanford accelerator [13].

Theoretical concepts for a proper many-body description in terms of a real-time nonequilibrium field theory were devised by Schwinger [14], Kadanoff and Baym [15], and Keldysh [16] in the early 1960s. However, a proper dynamical scheme in terms of a transport concept that deals with unstable particles, such as resonances, is still lacking. Rather ad hoc recipes are in use that sometimes violate basic requirements as given by fundamental symmetries and conservation laws, detailed balance, or thermodynamic consistency. The problem of a conserving approximation has first been addressed by Baym and Kadanoff [17, 18]. They started from an

* This article was submitted by the authors in English.

[1] Permanent address: Russian Research Centre Kurchatov Institute, pl. Kurchatova 1, Moscow, 123182 Russia.
[2] Permanent address: Moscow State Engineering Physics Institute, Kashirskoe sh. 31, Moscow, 115409 Russia.

equilibrium description in the imaginary-time formalism and discussed the response to external disturbances. Baym, in particular, showed [18] that any approximation, in order to be conserving, must be so-called Φ-derivable. It turned out that the Φ functional required is precisely the auxiliary functional introduced by Luttinger and Ward [19] (see also [20]) in connection with the thermodymanic potential. In the nonequilibrium case, the problem of conserving approximations is even more severe than in near-equilibrium linear-response theory [21, 22].

In this review, we discuss recent developments of the transport theory beyond the quasiparticle approximation and consequences of the propagation of particles with short lifetimes in hadron matter. First, we consider few equilibrium systems which clearly indicate that treatment beyond the quasiparticle approximation is really needed. We start with a genuine problem related to the occurrence of broad damping width, i.e., the soft-mode problem (Landau–Pomeranchuk–Migdal effect). This is the direct radiation of quanta from a piece of a dense medium [23]. Classically, this problem is formulated as coupling of a coherent classical field, e.g., the Maxwell field, to a stochastic source described by the Brownian motion of a charged particle. In this case, the classical current–current correlation function can be obtained in closed analytic terms and discussed as a function of the macroscopic transport properties, the friction and diffusion coefficient of the Brownian particle. We show that this result corresponds to a partial resummation of photon self-energy diagrams in the real-time formulation of field theory. Subsequently, properties of particles with broad damping width are illustrated at the examples of the ρ meson in dense matter at a finite temperature [24] and the pion in the limit of a dilute nuclear matter [25]. The question of consistency becomes especially important for a multicomponent system like $\pi N\Delta\rho, \ldots$, where the properties of one species can change due to the presence of interactions with the others and vice versa. The "vice versa" is very important and corresponds to the principle of action = reaction. This implies that the self-energy of one species cannot be changed through the interaction with other species without affecting the self-energies of the latter ones also. The Φ-derivable method of Baym [18] offers a natural and consistent way to account for this principle.

Then we address the question how particles with a broad mass width can be described consistently within a transport picture [21, 22]. We argue that the Kadanoff–Baym equations in the first gradient approximation together with the Φ-functional method of Baym [18] provide a proper self-consistent approach for kinetic description of systems of particles with a broad mass–width. We argue that after gradient expansion the full set of equations describing quantum transport contains two equations, the differential generalized kinetic equation for a distribution function in 8-dimensional (X, p) space and the algebraic equation for the spectral density. Other equations are resolved. We discuss the problems concerning charge and energy–momentum conservation, thermodynamic consistency, memory effects in the collision term and the growth of entropy in specific cases. Finally, we demonstrate finite-width effects in quantum kinetic description at the example of pion condensation, where the width of soft pionic excitations due to their decay into particle–hole pairs governs the dynamics of the phase transition in the isospin-symmetric nuclear matter.

We use the units $\hbar = c = 1$. For simplicity, we treat fermions nonrelativistically, whereas bosons (mesons) are treated as relativistic particles.

2. BREMSSTRAHLUNG FROM CLASSICAL SOURCES

For the clarification of the soft-mode problem, following [23], we first discuss an example in classical electrodynamics. We consider a stochastic source, the hard matter, where the motion of a single charge is described by the diffusion process in terms of the Fokker–Planck equation for the probability distribution f of the position $\mathbf{x}$ and velocity $\mathbf{v}$:

$$\frac{\partial}{\partial t} f(\mathbf{x}, \mathbf{v}, t) = \left(D\Gamma_x^2 \frac{\partial^2}{\partial \mathbf{v}^2} + \Gamma_x \frac{\partial}{\partial \mathbf{v}} \mathbf{v} - \mathbf{v} \frac{\partial}{\partial \mathbf{x}} \right) f(\mathbf{x}, \mathbf{v}, t). \quad (1)$$

Fluctuations also evolve in time according to this equation, or equivalently by the random-walk process [23], and this way determine correlations. This charge is coupled to the Maxwell field. On the assumption of a nonrelativistic source, this case does not suffer from standard pathologies encountered in hard-thermal-loop (HTL) problems of QCD, namely, the collinear singularities, where $\mathbf{v} \cdot \mathbf{q} \approx 1$, and from diverging Bose factors. The advantage of this Abelian example is that damping can be fully included without violating current conservation and gauge invariance. This problem is related to the Landau–Pomeranchuk–Migdal effect of bremsstrahlung in high-energy scattering [11, 12].

The two macroscopic parameters, the spatial diffusion D and friction Γ_x coefficients determine the relaxation rates of velocities. In the equilibrium limit ($t \longrightarrow \infty$), the distribution attains the Maxwell–Boltzmann velocity distribution with the temperature $T = m\langle \mathbf{v}^2 \rangle/3 = mD\Gamma_x$. The correlation function can be obtained in closed form, and one can discuss the resulting time correlations of the current at various values of the spatial photon momentum $\mathbf{q}$, Fig. 1 (details are given in [23]). For the transverse part of the correlation tensor, this correlation decays exponentially as $e^{-\Gamma_x \tau}$ at $\mathbf{q} = 0$, and its width further decreases with increasing momentum $q = |\mathbf{q}|$. The in-medium production rate is given by the time Fourier transform $\tau \longrightarrow \omega$ (right part of Fig. 1).

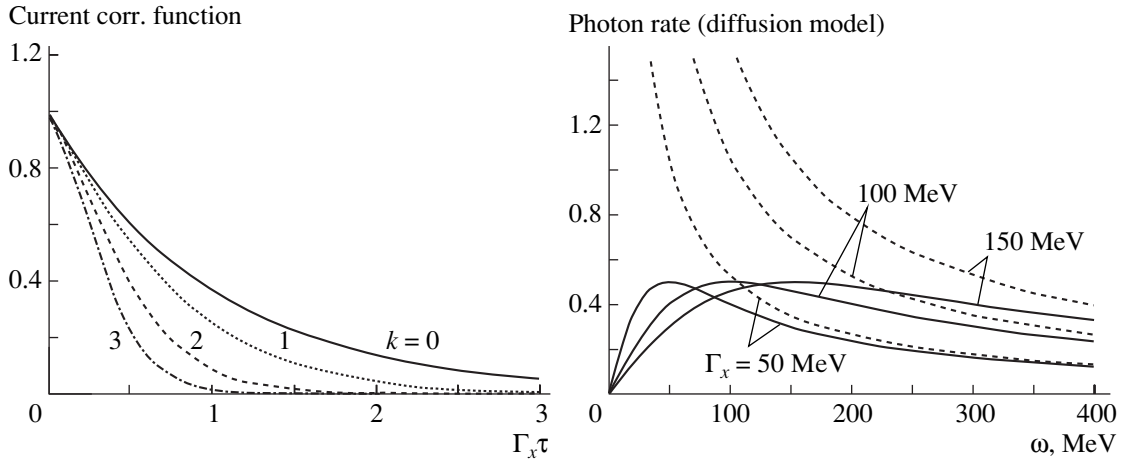

Fig. 1. Left: Current–current correlation function (in units of $e^2\langle v^2\rangle$) as a function of time (in units of $1/\Gamma_x$) for different values of the photon momentum $q^2 = 3k^2\Gamma_x^2/\langle v^2\rangle$ with $k = 0, 1, 2, 3$. Right: Rate of real photons $d^2N/(d\omega dt)$ (in units of $4\pi e^2\langle \mathbf{v}^2\rangle/3$) for a nonrelativistic source for $\Gamma_x = 50, 100, 150$ MeV; for comparison, the IQF results (dashed curves) are also shown.

The hard part of the spectrum behaves as intuitively expected; namely, it is proportional to the microscopic collision rate expressed through Γ_x (cf. below) and thus can be treated perturbatively by incoherent quasifree (IQF) scattering prescriptions. However, independently of Γ_x the rate saturates at a value of ~1/2 in these units around $\omega \sim \Gamma_x$, and the soft part shows the inverse behavior. That is, with increasing collision rate the production rate is more and more suppressed! This is in line with the picture where photons cannot resolve the individual collisions any more. Since the soft part of the spectrum behaves like ω/Γ_x, it shows a genuine nonperturbative feature which cannot be obtained by any power series in Γ_x. For comparison, the dashed curves show the corresponding IQF yields, which agree with the correct rates for the hard part while completely fail and diverge towards the soft end of the spectrum. For nonrelativistic sources $\langle \mathbf{v}^2\rangle \ll 1$, one can ignore the additional q dependence (dipole approximation; cf. Fig. 1) and the entire spectrum is determined by one macroscopic scale, the relaxation rate Γ_x. This scale provides a quenching factor

$$C_0(\omega) = \frac{\omega^2}{\omega^2 + \Gamma_x^2} \qquad (2)$$

by which the IQF results have to be corrected in order to account for the finite-collision-time effects in dense matter.

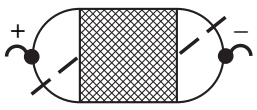

Fig. 2. Self-energy diagrams determining the production and absorption rates.

The diffusion result represents a resummation of the microscopic Langevin multiple-collision picture; altogether, only macroscopic scales are relevant to the form of the spectrum and not the details of microscopic collisions. Note also that the classical result fulfills the classical version ($\hbar \longrightarrow 0$) of the sum rules discussed in [23, 26].

3. RADIATION AT THE QUANTUM LEVEL

We have seen that at the classical level the problem of radiation from dense matter can be solved quite naturally and completely, at least for simple examples, and Fig. 1 displays the main physics. They show that the damping of the particles due to scattering is an important feature, which, in particular, has to be included right from the onset. This not only assures results that no longer diverge but also provides a systematic and convergent scheme. On the quantum level, such problems require techniques beyond the standard repertoire of perturbation theory or the quasiparticle approximation. In terms of nonequilibrium diagrammatic technique in the Keldysh notation, the production or absorption rates are given by the self-energy diagrams of the type presented in Fig. 2 with an in- and out-going radiating particle (e.g., photon) line [23, 27]. The hatched loop area denotes all strong interactions of the source. The latter give rise to a whole series of diagrams. As mentioned, for the particles of the source, e.g., the nucleons, one has to resum the Dyson equation with the corresponding full complex self-energy in order to determine the full Green's functions in dense matter. Once one has these Green's functions together with the interaction vertices at hand, one could in principle calculate the required diagrams. However, both the computational effort to calculate a single diagram and the number of diagrams increase dramatically with

the loop order of the diagrams, such that, in practice, only the lowest order loop diagrams can be considered in the quantum case. In certain limits, some diagrams drop out. We could show that in the classical limit, which in this case implies the hierarchy $\omega, |\mathbf{q}|, \Gamma \ll T \ll m$ together with low phase-space occupations for the source, i.e., $f(x, p) \ll 1$, only the following set of diagrams survives:

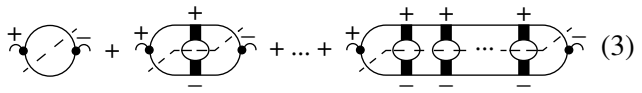

(3)

In these diagrams, the bold lines denote the full nucleon Green's functions which also include the damping width, the black blocks represent the effective nucleon–nucleon interaction in matter, and the full dots denote the coupling vertex to the photon. The thin dashed lines show how the diagrams are to be cut into two interfering amplitudes. This way, each of these diagrams with n interaction loop insertions relates just to the nth term in the corresponding classical Langevin process, where hard scatterings occur at random with a constant mean collision rate Γ. These scatterings consecutively change the velocity of a point charge from $\mathbf{v}_0$ to $\mathbf{v}_1$, to $\mathbf{v}_2$, …. In between scatterings, the charge moves freely. For such a multiple-collision process the space integrated current–current correlation function takes the simple Poisson form

$$i\Pi^{\mu\nu-+} \propto \int d^3x_1 d^3x_2 \left\langle j^\nu\left(\mathbf{x}_1, t-\frac{\tau}{2}\right) j^\mu\left(\mathbf{x}_2, t+\frac{\tau}{2}\right)\right\rangle$$
$$= e^2\langle v^\mu(0) v^\nu(\tau)\rangle = e^2 e^{-|\Gamma\tau|}\sum_{n=0}^{\infty}\frac{|\Gamma\tau|^n}{n!}\langle v_0^\mu v_n^\nu\rangle \quad (4)$$

with $v = (1, \mathbf{v})$. Here, $\langle\ldots\rangle$ denotes the average over the discrete collision sequence. This form, which one writes down intuitively, agrees with the analytic result of the quantum correlation diagrams (3) in the limit $f(x, p) \ll 1$ and $\Gamma \ll T$. Upon the Fourier transformation, it determines the spectrum in completely regular terms (void of any infrared singularities), where each term describes the interference of the photon being emitted at a certain time or n collisions later. In special cases where velocity fluctuations are degraded by a constant fraction α in each collision, such that $\langle \mathbf{v}_0 \cdot \mathbf{v}_n\rangle = \alpha^n\langle \mathbf{v}_0 \cdot \mathbf{v}_0\rangle$, one can resum the whole series in Eq. (4) and thus recover the relaxation result with $2\Gamma_x\langle \mathbf{v}^2\rangle = \Gamma\langle(\mathbf{v}_0 - \mathbf{v}_1)^2\rangle$, at least for $\mathbf{q} = 0$, and the corresponding quenching factor (2). Thus, the classical multiple collision example provides a quite intuitive representation of such diagrams. Further details can be found in [23].

The above example shows that we have to deal with particle transport that explicitly takes account of the particle mass width in order to properly describe soft radiation from the system.

4. THE ρ MESON IN DENSE MATTER

Following the Φ-derivable scheme, we will first discuss two examples within thermoequilibrium systems. First, we will judge properties of the ρ meson and their consequences for the ρ decay into dileptons [24]. In terms of the nonequilibrium diagrammatic technique, the exact production rate of dileptons is given by the formula

$$\frac{dn^{e^+e^-}}{dtdm} = \quad (5)$$

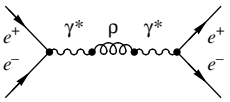

$$= f_\rho(m, \mathbf{p}, \mathbf{x}, t) A_\rho(m, \mathbf{p}, \mathbf{x}, t) 2m\Gamma^{\rho e^+e^-}(m).$$

Here, $\Gamma^{\rho e^+e^-}(m) \propto 1/m^3$ is the mass-dependent electromagnetic decay rate of the ρ into the dilepton pair of invariant mass m. The phase-space distribution $f_\rho(m, \mathbf{p}, \mathbf{x}, t)$ and the spectral function $A_\rho(m, \mathbf{p}, \mathbf{x}, t)$ define the properties of the ρ meson at spacetime point $\mathbf{x}, t$. Both quantities are in principle to be determined dynamically by an appropriate transport model. However, the spectral functions have not yet been treated dynamically in most of the present transport models. Rather one employs on-shell δ functions for all stable particles and spectral functions fixed to the vacuum shape for resonances.

As an illustration, we follow the two-channel example presented by one of us in [28]. There, the ρ meson just strongly couples to two channels, i.e., the $\pi^+\pi^-$ and $\pi N \longleftrightarrow \rho N$ channels, the latter being relevant at finite nuclear densities. The latter component is representative for all channels contributing to the so-called direct ρ in transport codes. For a first orientation, the equilibrium properties[3)] are discussed in simple analytical terms with the aim to discuss the consequences for the implementation of such resonance processes into dynamical transport simulation codes.

Both considered processes add to the total width of the ρ meson

$$\Gamma_{\rm tot}(m, \mathbf{p}) = \Gamma_{\rho\to\pi^+\pi^-}(m, \mathbf{p}) + \Gamma_{\rho\to\pi NN^{-1}}(m, \mathbf{p}), \quad (6)$$

and the equilibrium spectral function then results from the cuts of the two diagrams

$$A_\rho(m, \mathbf{p}) = \quad (7)$$

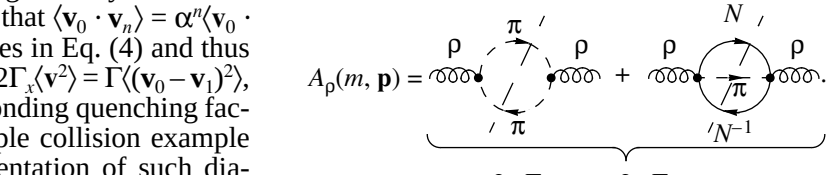

$$\frac{2m\Gamma_{\rho\pi^+\pi^-} + 2m\Gamma_{\rho\pi NN^{-1}}}{(m^2 - m_\rho^2 - {\rm Re}\Sigma^R)^2 + m^2\Gamma_{\rm tot}^2}$$

[3)] Far more sophisticated calculations have already been presented in the literature [29–34]. It is not the point to compete with them at this place.

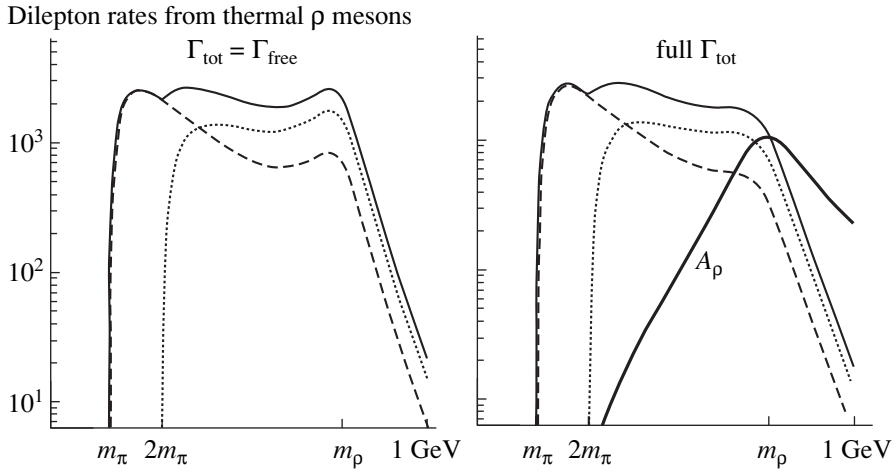

Fig. 3. e^+e^- rates (arb. units) as a function of the invariant pair mass m at $T = 110$ MeV from $\pi^+\pi^-$ annihilation (dotted curve) and direct ρ-meson contribution (dashed curve), the solid curve gives the sum of both contributions. Left part: using the free cross section recipe, i.e., with $\Gamma_{tot} = \Gamma_{\rho\pi^+\pi^-}$; right part: the correct partial rates (7). A_ρ is given by the thick curve. The calculations are done with $\Gamma_{\rho \leftrightarrow \pi\pi}(m_\rho) = 150$ MeV and $\Gamma_{\rho \leftrightarrow \pi N N^{-1}}(m_\rho) = 70$ MeV.

In principle, both diagrams have to be calculated in terms of fully self-consistent propagators, i.e., with corresponding widths for all particles involved. This formidable task has not been done yet. Using microreversibility and the properties of thermal distributions, the two terms in Eq. (7) contributing to the dilepton yield (5) can indeed approximately be reformulated as the thermal average of the $\pi^+\pi^- \longrightarrow \rho \longrightarrow e^+e^-$ annihilation process and the $\pi N \longrightarrow \rho N \longrightarrow e^+e^- N$ scattering process, i.e.,

$$\frac{dn^{e^+e^-}}{dmdt} \propto \langle f_{\pi^+} f_{\pi^-} v_{\pi\pi} \sigma(\pi^+\pi^- \longrightarrow \rho \longrightarrow e^+e^-) + f_\pi f_N v_{\pi N} \sigma(\pi N \longrightarrow \rho N \longrightarrow e^+e^- N)\rangle_T, \quad (8)$$

where f_π and f_N are corresponding particle occupations and $v_{\pi\pi}$ and $v_{\pi N}$ are relative velocities. However, an important fact to be noticed is that, in order to preserve unitarity, the corresponding cross sections are no longer free, as given by the vacuum decay width in the denominator, but rather involve the medium-dependent total width (6). This illustrates in simple terms that rates of broad resonances can no longer simply be added in a perturbative way. Since it concerns a coupled-channel problem, there is a cross talk between the different channels to the extent that the common resonance propagator attains the total width arising from all partial widths feeding and depopulating the resonance. While a perturbative treatment with free cross sections in Eq. (8) would enhance the yield at the resonance mass, $m = m_\rho$, if a channel is added (left part of Fig. 3), the correct treatment (7) even inverts the trend and indeed depletes the yield at the resonance mass (right part in Fig. 3). Furthermore, one sees that only the total yield involves the spectral function, while any partial cross section refers to that partial term with the corresponding partial width in the numerator! Compared to the shape of the spectral function, both thermal components in Fig. 3 show a significant enhancement on the low-mass side and a strong depletion at high masses due to the thermal weight $f \propto \exp(-p_0/T)$ in the rate (5). This kinematical effect related to the broad width also survives in nonequilibrium calculations and is a signature of phase-space restrictions imposed for particles with higher energies. The related question as to how to preserve detailed balance in the case of broad resonances was addressed by Danielewicz and Bertsch [35]. The latter method has then been implemented in transport models mostly applied to the description of the Δ resonance. For the transport description of the ρ meson, only quite recently has a description level been realized that properly includes the width effects discussed above, e.g., in [36], cf. also the comments given in [37]. The transport treatment of broad resonances is discussed further in Sections 5–8.

As an example, we show an exploratory study of the interacting system of π, ρ, and a_1 mesons described by the Φ functional

$$\Phi = \quad (9)$$

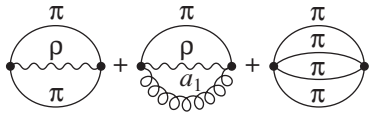

(cf. Section 6 below). The couplings and masses are chosen as to reproduce the known vacuum properties of the ρ and a_1 mesons with nominal masses and widths $m_\rho = 770$ MeV, $m_{a_1} = 1200$ MeV, $\Gamma_\rho = 150$ MeV, and $\Gamma_{a_1} = 400$ MeV. The results of a finite-temperature calculation at $T = 150$ MeV with all self-energy loops resulting from the Φ functional of Eq. (9) computed

[24] with the self-consistent broad-width Green's functions are displayed in Fig. 4 (corrections to the real part of the self-energies were not yet included). The last diagram of Φ with the four-pion self-coupling has been added in order to supply pion with broad mass width as they would result from the coupling of pions to nucleons and the Δ resonance in nuclear matter environment. As compared to first-order one-loop results which drop to zero below the two-pion threshold at 280 MeV, the self-consistent results essentially add in strength at the low-mass side of the dilepton spectrum.

Virial Limit

In the dilute-density limit (virial limit), the corresponding self-energies of the particles and intermediate resonances are entirely determined by two-body scattering properties, in particular, by scattering phase shifts. We illustrate this by example of the interacting system of nucleons, pions, and delta resonances, which have recently been investigated by Weinhold *et al*. [25]. Following their study, we consider a pedagogical example, where the πNN interaction is omitted. Then, with a *p*-wave $\pi N\Delta$-coupling vertex among the three fields the first and only diagram of Φ up to two vertices and the corresponding three self-energies are given by

$\Phi =$ 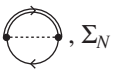 , $\Sigma_N =$  , $\Sigma_\pi =$  , $\Sigma_\Delta =$  . (10)

Here, the solid, dashed, and double lines denote the propagators of N, π, and Δ, respectively. In nonrelativistic approximation for the baryons, we ignore contributions from the baryon Dirac sea. Then, the bare pion mass agrees with its vacuum value, while the nucleon and delta masses require appropriate mass counter terms. The Δ self-energy Σ_Δ attains the vacuum width and position of the delta resonance due to the decay into a pion and a nucleon. The corresponding scattering diagrams are obtained by opening two propagator lines of Φ with the prominent feature that the πN scattering proceeds through the delta resonance. Since in this case a single resonance couples to a single scattering channel, the vacuum spectral function of the resonance can be directly expressed through the scattering T matrix and hence through measured scattering phase shifts

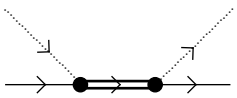 $|T_{33}|^2 = 4\sin^2\delta_{33}(p) = \Gamma_\Delta^{\rm vac}(p)A_\Delta^{\rm vac}(p),$ (11)

where $p = p_N + p_\pi$. Thus, through (11), the vacuum properties of the delta can be obtained from scattering data almost in a model-independent way.

For the multicomponent system the renormalized thermodynamic potential including vacuum counter terms can be written as

$$\Omega\{G_\pi, G_N, G_\Delta\}$$
$$= T\sum_{a\in\{\pi,N,\Delta\}} \mp\kappa\,{\rm tr}\{-\ln[-G_a^R(p_0+i0,\mathbf{p})] + G_a^R\Sigma_a^R\}_{T,\mu} + \Phi_T, \quad (12)$$

$$\kappa = \begin{cases} 1/2 & \text{for neutral bosons} \\ 1 & \text{for charged bosons and fermions.} \end{cases} \quad (13)$$

For any function $f(p)$, the thermodynamic trace ${\rm tr}\{\ldots\}_{T,\mu}$ is defined as

$${\rm tr}\{f(p)\}_{T,\mu} = \mp d\frac{V}{T}\int\frac{d^4p}{(2\pi)^4}n(p_0-\mu)2\,{\rm Im}\,f(p_0+i0,\mathbf{p}), \quad (14)$$

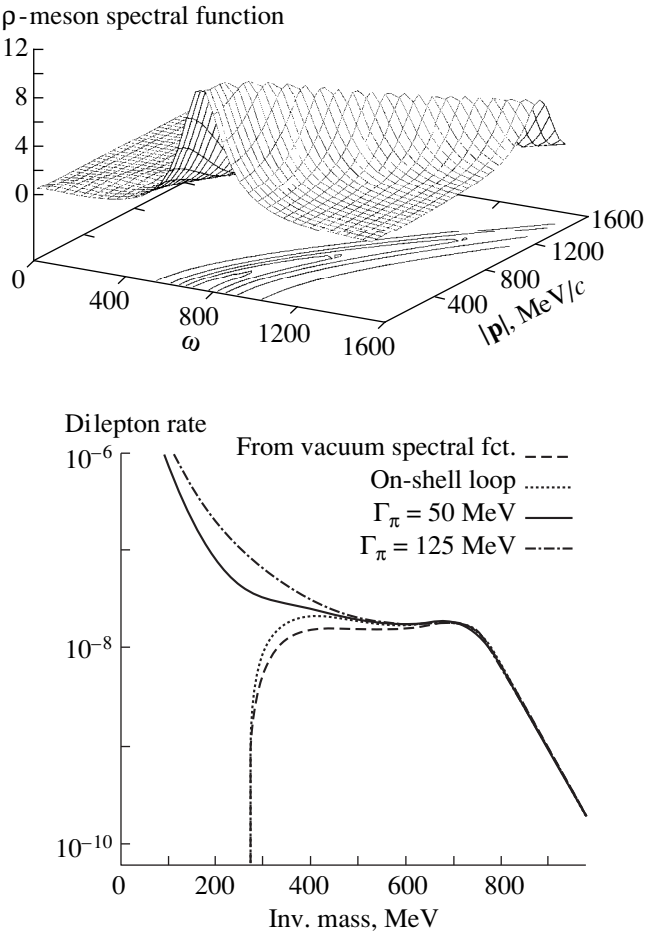

Fig. 4. Upper part: contour plot of the self-consistent spectral function of the ρ meson as a function of energy and spatial momentum, T = 150 MeV; lower part: thermal dilepton rate (arb. units) as a function of invariant mass at $|\mathbf{p}|$ = 300 MeV/c, T = 110 MeV.

an energy integral over thermal occupations $n(\varepsilon) = [\exp(\varepsilon/T) \pm 1]^{-1}$, of Fermi–Dirac or Bose–Einstein type. The upper sign appears for fermions, the lower for bosons, d is the degeneracy in that particle channel, and V denotes the volume. Equation (12) still has the functional property to provide the retarded Dyson's equations for the G_a^R from the stationary condition which we use in order to determine the physical value of Ω. For the particular case here, one can further exploit the property

$$\Phi_T = \pm\kappa T \,\mathrm{tr}\{\Sigma_a G_a\}_{T,\mu},$$
$$\text{for } a \in \{N, \pi, \Delta\} \text{ and } \Phi \text{ of form (10)},$$

valid for Φ_T that depend linearly on all propagators. Compatible with the low-density limit, one can expand the $\mathrm{tr}\ln\{-G\}$ terms for the pion and nucleon around the free propagators and finally obtain

$$\begin{aligned}\Omega_{\pi N\Delta} &= \Omega\{G_\pi, G_N, G_\Delta\}\big|_{\text{stationary}} \\ &= \Omega_N^{\text{free}} + \Omega_\pi^{\text{free}} + T\mathrm{tr}\{\ln[-G_\Delta^R(p_0 + i0, \mathbf{p})]\}_{T,\mu},\end{aligned} \tag{15}$$

$$\begin{aligned}\Omega_{\pi N\Delta} &= \Omega_N^{\text{free}} + \Omega_\pi^{\text{free}} \\ &+ d_\Delta TV\int\frac{d^4p}{(2\pi)^4}\times 2\frac{\partial\delta_{33}(p)}{\partial p_0}\ln[1 - n_\Delta(p_0 - \mu_\Delta)]\end{aligned} \tag{16}$$

for the physical value of Ω. Here, the Ω_a^{free} are the free single-particle thermodynamic potentials,[4)] while μ_Δ and $d_\Delta = 16$ are the chemical potential and degeneracy factor of the Δ resonance, respectively. The last term in (16), obtained through (11), represents a famous result derived by Beth–Uhlenbeck [38, 39], later generalized by Dashen, Ma, and Bernstein [40] and applied to nuclear resonance matter in [25, 41, 42]. It illustrates that the virial corrections of the system's level density due to interactions are entirely given by the energy variation of the corresponding two-body scattering phase shifts $\partial\delta/\partial p_0$.

All thermodynamic properties can be obtained from Ω through partial differentiations with respect to T and the μ. The final form (16) may give the impression that one deals with noninteracting nucleons and pions. This is, however, not the case. For instance, the densities of baryons and pions derived from (16) become

$$\begin{aligned}\rho_B &= \frac{\partial\Omega_{\pi N\Delta}}{\partial\mu_N} = \rho_N^{\text{free}} + \rho_\Delta + \rho_{\text{corr}}, \\ \rho_\pi &= \frac{\partial\Omega_{\pi N\Delta}}{\partial\mu_\pi} = \rho_\pi^{\text{free}} + \rho_\Delta + \rho_{\text{corr}},\end{aligned} \tag{17}$$

with

$$\rho_\Delta = d_\Delta\int\frac{d^4p}{(2\pi)^4}n_\Delta(p_0 - \mu_\Delta)A_\Delta(p), \tag{18}$$

$$\rho_{\text{corr}} = d_\Delta\int\frac{d^4p}{(2\pi)^4}n_\Delta(p_0 - \mu_\Delta)B_{\text{corr}}(p), \tag{19}$$

and $\mu_\Delta = \mu_N + \mu_\pi$.[5)] Here, the density of deltas ρ_Δ is determined by the delta spectral function. The interaction contribution contained in the correlation density ρ_{corr} depends on the difference between the phase-shift variation and the spectral function

$$\begin{aligned}B_{\text{corr}} &= 2\frac{\partial\delta_{33}(p_0)}{\partial p_0} - A_\Delta(p) \\ &= 2\,\mathrm{Im}\left[\frac{\partial\Sigma_\Delta^R(p)}{\partial p_0}G_\Delta^R(p)\right].\end{aligned} \tag{20}$$

Due to the fact that $\Gamma_\Delta(p)$ grows with energy and the real part of G_Δ changes sign at the resonance energy, B_{corr} becomes positive below and negative above resonance, respectively. It leads to an enhancement of both densities at low energies, i.e., below resonance, and also to a further softening of the resulting equation of state compared to the naive spectral function treatment ignoring the B_{corr} terms. This illustrates that an interacting resonance gas cannot consistently be described by a set of free particles (here the pions and nucleons) plus vacuum resonances (here the delta), described by their spectral function. Rather the coupling of a bare resonance to the stable particles determines its width and, thus, its spectral properties in a vacuum. At the same time, the stable particles are modified due to the interaction with the resonance. Only the account of all three self-energies in (10) provides a conserving and thermodynamically consistent approximation.

Alternatively to the picture above, the properties of the system can be discussed entirely in terms of the stable particles, i.e., the pion and the nucleon, thus eliminating the delta. The thermodynamic potential is then still given by (16). This form is valid even without intermediate resonances and the phase shifts just account for the πN-interaction properties. Also, the self-energy of the lightest particle in the system, the pion, can be obtained from phase shifts by means of the optical theorem [43, 44]. To the linear order in the nucleon density ρ_N, one determines the pion self-energy

$$\begin{aligned}\Sigma_\pi(p_{\text{lab}}) &= 4\pi\frac{p_{\text{lab}}}{p_{\text{c.m.}}}\rho_N F_{\pi N}(0) \\ &= -2\pi\frac{p_{\text{lab}}}{p_{\text{c.m.}}^2}\frac{d_\Delta}{d_\pi}\frac{\rho_N}{d_N}\times 2\sin\delta_{33}e^{i\delta_{33}}\end{aligned} \tag{21}$$

[4)] The appropriate cancellation of terms for the result (15) is only achieved if one uses Ω^{free}, i.e., the partition sum of free particles with the free energy–momentum dispersion relation. Within this model, even on the vacuum level the nucleon would acquire loop corrections to its self-energy which would lead to deviations between Ω^{vac} and Ω^{free}, as well as between the corresponding propagators off their mass shell.

[5)] In equilibrium, μ_π has to be put to zero after differentiation.

from the forward πN-scattering amplitude $F_{\pi N}(0)$. Here, $p_{\rm lab}$ and $p_{\rm c.m.}$ refer to the pion 3-momenta in the matter rest frame and the c.m. frame of the πN collisions. The arising kinematical factor $p_{\rm lab}/p_{\rm c.m.} = \sqrt{s}/m_N$ which has mostly escaped notice even in standard references on the low-density theorem, e.g., [45], becomes important for heavier projectiles like kaons, cf. [46]. Here, the degeneracy factors $d_N : d_\pi : d_\Delta = 4 : 3 : 16$ just provide the proper spin–isospin counting. This self-energy, which determines an optical potential or index of refraction, is attractive below the Δ-resonance energy and repulsive above. It agrees with a related effect in optics, where a resonance in the medium causes an anomalous behavior of the real part of the index of refraction, which is larger than 1 below the resonance frequency and less than 1 above the resonance. Thus, absorption, e.g., by exciting a resonance, is always accompanied by a change of the real part of the index of refraction of the scattered particle. The Φ-derivable principle automatically takes care about these features.

As has been discussed in [47], the corrections to the system's level density [last term in (16)] can also be inferred from the time shifts (or time delays) induced by the scattering processes. From ergodicity arguments [47], one obtains, for a single partial wave,

$$\frac{\partial}{\partial p_0}(N_{\rm level}(p_0) - N^{\rm free}_{\rm level}(p_0)) = \tau_{\rm forward} + \tau_{\rm scatt} = \tau_{\rm delay} = 2\frac{\partial}{\partial p_0}[\sin\delta_{33}\cos\delta_{33}] + 4\sin^2\delta_{33}\frac{\partial\delta_{33}}{\partial p_0} = 2\frac{\partial\delta_{33}}{\partial p_0}. \quad (22)$$

These expressions apply to the c.m. frame. Here, the forward delay time $\tau_{\rm forward}$ relates to the change of the group velocity induced by the real part of the optical potential, cf. (21). The scattering time $\tau_{\rm scatt}$ finally results from the delayed reemission of the pion from the intermediate resonance to angles off the forward direction.

5. QUANTUM KINETIC EQUATION

The three above-presented examples unambiguously show that, for consistent dynamical treatment of nonequilibrium evolution of soft radiation and broad resonances, we need a transport theory that takes due account of mass widths of constituent particles. A proper frame for such a transport is provided by Kadanoff–Baym equations. We consider the Kadanoff–Baym equations in the first-order gradient approximation, assuming that the spacetime evolution of a system is smooth enough to justify this approximation.

First of all, it is helpful to avoid all the imaginary factors inherent in the standard Green's function formulation (G^{ij} with $i, j \in \{-+\}$) and introduce quantities which are real and, in the quasihomogeneous limit, positive and therefore have a straightforward physical interpretation [22], much like for the Boltzmann equation. In the Wigner representation, we define

$$F(X,p) = A(X,p)f(X,p) = (\mp)iG^{-+}(X,p), \quad \tilde{F}(X,p) = A(X,p)[1 \mp f(X,p)] = iG^{+-}(X,p), \quad (23)$$

$$A(X,p) \equiv -2\,{\rm Im}\,G^R(X,p) = \tilde{F} \pm F = i(G^{+-} - G^{-+}) \quad (24)$$

for the generalized Wigner functions F and $\tilde{F}$ with the corresponding four-phase-space distribution functions $f(X,p)$ and Fermi (Bose) factors $[1 \mp f(X,p)]$, with the spectral function $A(X,p)$ and the retarded propagator G^R. Here and below, the upper sign corresponds to fermions and the lower one, to bosons. According to relations between the Green's functions G^{ij}, only two independent real functions of all the G^{ij} are required for a complete description. Likewise, the reduced gain and loss rates of the collision integral and the damping rate are defined as

$$\Gamma_{\rm in}(X,p) = (\mp)i\Sigma^{-+}(X,p), \quad \Gamma_{\rm out}(X,p) = i\Sigma^{+-}(X,p), \quad (25)$$

$$\Gamma(X,p) \equiv -2\,{\rm Im}\,\Sigma^R(X,p) = \Gamma_{\rm out}(X,p) \pm \Gamma_{\rm in}(X,p), \quad (26)$$

where Σ^{ij} are contour components of the self-energy and Σ^R is the retarded self-energy.

In terms of this notation and within the first-order gradient approximation, the Kadanoff–Baym equations for F and $\tilde{F}$ (which result from differences of the corresponding Dyson equations with their adjoint ones) take the kinetic form

$$\mathcal{D}F - \{\Gamma_{\rm in}, {\rm Re}\,G^R\} = C, \quad (27)$$

$$\mathcal{D}\tilde{F} - \{\Gamma_{\rm out}, {\rm Re}\,G^R\} = \mp C, \quad (28)$$

with the drift operator and collision term, respectively,

$$\mathcal{D} = \left(2\pi_\mu - \frac{\partial\,{\rm Re}\,\Sigma^R}{\partial p^\mu}\right)\partial^\mu_X + \frac{\partial\,{\rm Re}\,\Sigma^R}{\partial X^\mu}\frac{\partial}{\partial p_\mu}, \quad (29)$$

$$C(X,p) = \Gamma_{\rm in}(X,p)\tilde{F}(X,p) - \Gamma_{\rm out}(X,p)F(X,p); \quad (30)$$

$2\pi^\mu = v^\mu = (1, \mathbf{p}/m)$ for nonrelativistic particles and $\pi^\mu = p^\mu$ for relativistic bosons. Within the same approximation level, there are two alternative equations for F and $\tilde{F}$

$$MF - {\rm Re}\,G^R\Gamma_{\rm in} = \frac{1}{4}(\{\Gamma, F\} - \{\Gamma_{\rm in}, A\}), \quad (31)$$

$$M\tilde{F} - {\rm Re}\,G^R\Gamma_{\rm out} = \frac{1}{4}(\{\Gamma, \tilde{F}\} - \{\Gamma_{\rm out}, A\}) \quad (32)$$

with the "mass" function

$$M(X,p) = \begin{cases} p_0 - \mathbf{p}^2/2m - \mathrm{Re}\,\Sigma^R(X,p) \\ \text{for nonrelativistic particles} \\ -m^2 + p^2 - \mathrm{Re}\,\Sigma^R(X,p) \\ \text{for relativistic bosons.} \end{cases} \tag{33}$$

These two equations result from sums of the corresponding Dyson equations with their adjoint ones. Equations (31) and (32) can be called the mass-shell equations, since in the quasiparticle limit they provide the on-mass-shell condition $M = 0$. Appropriate combinations of the two sets (27), (28) and (31), (32) provide us with the retarded Green's function equations, which are simultaneously solved [15, 48] by

$$G^R = \frac{1}{M(X,p) + i\Gamma(X,p)/2} \longrightarrow \begin{cases} A = \dfrac{\Gamma}{M^2 + \Gamma^2/4} \\ \mathrm{Re}\,G^R = \dfrac{M}{M^2 + \Gamma^2/4}. \end{cases} \tag{34}$$

With solution (34) for G^R, Eqs. (27) and (28) become identical to each other, as well as Eqs. (31) and (32); however, Eqs. (27) and (28) are not yet identical to Eqs. (31) and (32), while they were identical before the gradient expansion. Indeed, one can show [22] that Eqs. (27) and (28) differ from Eqs. (31) and (32) in second-order gradient terms. This is acceptable within the gradient approximation; however, the remaining difference in the second-order terms is inconvenient from the practical point of view. Following Botermans and Malfliet [48], we express $\Gamma_{\mathrm{in}} = \Gamma f + O(\partial_X)$ and $\Gamma_{\mathrm{in}} = \Gamma(1 \mp f) + O(\partial_X)$ from the left-hand side of the mass-shell Eqs. (31) and (32), substitute them into the Poisson-bracketed terms of Eqs. (27) and (28), and neglect all the resulting second-order gradient terms. The so-obtained quantum four-phase-space kinetic equations for $F = fA$ and $\tilde{F} = (1 \mp f)A$ then read

$$\mathcal{D}(fA) - \{\Gamma f, \mathrm{Re}\,G^R\} = C, \tag{35}$$

$$\mathcal{D}((1 \mp f)A) - \{\Gamma(1 \mp f), \mathrm{Re}\,G^R\} = \mp C. \tag{36}$$

These quantum four-phase-space kinetic equations, which are identical to each other in view of retarded relation (34), are at the same time completely identical to the correspondingly substituted mass-shell Eqs. (31) and (32).

The validity of the gradient approximation [22] relies on the overall smallness of the collision term $C = \{\text{gain} - \text{loss}\}$ rather than on the smallness of the damping width Γ. Indeed, while fluctuations and correlations are governed by time scales given by Γ, the Kadanoff–Baym equations describe the behavior of the ensemble mean of the occupation in phase space $F(X, p)$. It implies that $F(X, p)$ varies on spacetime scales determined by C. In cases where Γ is not small enough by itself, the system has to be sufficiently close to equilibrium in order to provide a valid gradient approximation through the smallness of the collision term C. Both the Kadanoff–Baym (27) and the Botermans–Malfliet choice (35) are, of course, equivalent within the validity range of the first-order gradient approximation. Frequently, however, such equations are used beyond the limits of their validity as ad hoc equations, and then the different versions may lead to different results. So far, we have no physical condition to prefer one of the choices. The procedure, where in all Poisson brackets the Γ_{in} and Γ_{out} terms have consistently been replaced by $f\Gamma$ and $(1 \mp f)\Gamma$, respectively, is therefore optional. However, in doing so we gained some advantages. Beside the fact that quantum four-phase-space kinetic equation (35) and the mass-shell equation are then exactly equivalent to each other, this set of equations has particular features with respect to the definition of a nonequilibrium entropy flow in connection with the formulation of an exact H theorem in certain cases. If we omit these substitutions, both these features would become approximate with deviations at the second-order gradient level. A numerical scheme of the BM choice in application to heavy-ion collisions is constructed in [49, 50].

The equations so far presented, mostly with the Kadanoff–Baym choice (27), were the starting point for many derivations of extended Boltzmann and generalized kinetic equations, ever since these equations have been formulated in 1962. Most of those derivations use the equal-time reduction by integrating the four-phase-space equations over energy p_0, thus reducing the description to three-phase-space information (cf. [51–59] and references therein). This can only consistently be done in the limit of small width Γ employing some kind of quasiparticle ansätze for the spectral function $A(X, p)$. Particular attention has been payed to the treatment of the time-derivative parts in the Poisson brackets, which in the four-phase-space formulation still appear time-local, i.e., Markovian, while they lead to retardation effects in the equal-time reduction. Generalized quasiparticle ansätze were proposed, which essentially improve the quality and consistency of the approximation, providing those extra terms to the naive Boltzmann equation (sometimes called additional collision terms) which are responsible for the correct second-order virial corrections and the appropriate conservation of total energy (cf. [53, 56] and references therein). However, all these derivations imply some information loss about the differential mass spectrum due to the inherent reduction to a 3-momentum representation of the distribution functions by some specific ansätze. With the aim to treat cases as those displayed in Figs. 3 and 4, where the differential mass spectrum can be observed by dilepton spectra, within a self-con-

sistent nonequilibrium approach, one has to treat the differential mass information dynamically, i.e., by means of Eq. (34) avoiding any kind of quasiparticle reductions, and work with the full quantum four-phase-space kinetic Eq. (35). In the following section, we discuss the properties of this set of quantum kinetic equations.

6. Φ-DERIVABLE APPROXIMATIONS

The preceding considerations have shown that one needs a transport scheme adapted to broad resonances. Besides the conservation laws, it should comply with requirements of unitarity and detailed balance. A practical suggestion has been given in [35] in terms of cross sections. However, this picture is tied to the concept of asymptotic states and is therefore not well suited for the general case, in particular, if more than one channel feeds into a broad resonance. Therefore, we suggest to revive the so-called Φ-derivable scheme, originally proposed by Baym [18] on the basis of the generating functional, or partition sum, given by Luttinger and Ward [19] and later reformulated in terms of path integrals [60].

With the aim to come to a self-consistent and conserving treatment on the two-point function level, we generalized the Φ-functional method [18, 19] to the real-time contour ($\mathscr{C}$) in [21]. It was based on a decomposition of the generating functional Γ with bilocal sources into a two-particle-reducible part and an auxiliary functional Φ which compiles all two-particle-irreducible (2PI) vacuum diagrams:

$$i\Gamma\{G,\phi,\lambda\} = i\Gamma^0\{G^0\} + \int_{\mathscr{C}} dx \mathscr{L}^0\{\phi, \partial_\mu\phi\}$$

$$+ \Bigg\{ \sum_{n_\Sigma} \frac{1}{n_\Sigma} \Big(-i\Sigma\Big)\cdots\Big(-i\Sigma\Big) - \Big(-i\Sigma\Big) \Bigg\} + \sum_{n_\lambda} \frac{1}{n_\lambda} \Big(\text{2PI}\Big) . \tag{37}$$

$$\pm\ln(1 - \odot G^0 \odot \Sigma) \quad \pm \odot G \odot \Sigma \quad + i\Phi\{G,\phi,\lambda\}$$

Here, $\mathscr{L}^0(\phi)$ is the free classical Lagrangian of the classical field ϕ, G^0 and G denote the free and full-contour Green's functions, while Σ is the full-contour self-energy of the particles. Contrary to the perturbation theory, here the auxiliary functional Φ is given by all two-particle-irreducible closed diagrams in terms of full propagators G, full time-dependent classical fields ϕ, and bare vertices. The upper signs in Eq. (37) relate to fermion quantities, whereas the lower signs, to boson ones, while n_Σ and n_λ count the number of self-energy insertions in the ring diagrams and the number of vertices in the diagrams of Φ, respectively, λ is the scaling factor in each vertex. The stationarity conditions

$$\delta\Gamma\{G,\phi,\lambda\}/\delta G = 0, \quad \delta\Gamma\{G,\phi,\lambda\}/\delta\phi = 0 \tag{38}$$

provide the set of coupled equations of motion for the classical fields ϕ and the Green's functions G (the Dyson equation)

$$\phi(x) = \phi^0(x) - \int_{\mathscr{C}} dy G^0(x,y) J(y), \tag{39}$$

$$G(x,y) = G^0(x,y) + \int_{\mathscr{C}} dz dz' G^0(x,z)\Sigma(z,z')G(z',y), \tag{40}$$

where the superscript "0" marks the free Green's functions and classical fields. The functional $\Phi\{G, \phi\}$ acts as the generating functional for the self-energy Σ and source currents $J(x)$ via the functional variations

$$iJ(x) = \frac{\delta i\Phi}{\delta\phi(x)}, \quad -i\Sigma(x,y) = \frac{\delta i\Phi}{\delta i G(y,x)}. \tag{41}$$

The advantage of this formulation is that Φ can be truncated at any level, thus defining approximation schemes with built-in internal consistency with respect to conservation laws and thermodynamic consistency. For details, we refer to [18, 19] and our previous paper [21]. Note that Φ itself is constructed in terms of the "full" Green's functions, where "full" now takes the sense of solving self-consistently the Dyson equation with the driving term derived from this approximate Φ through relation (41). It means that even restricting ourselves to a single diagram in Φ, in fact, we deal with a whole sub-series of diagrams in terms of free propagators, and "full" takes the sense of the sum of this whole subseries. Thus, restricting the infinite set of diagrams for Φ to either only a few of them or some subseries of them defines a Φ-derivable approximation. Such approximations have the following distinct properties: (a) they are conserving if Φ preserves the invariances and symmetries of the Lagrangian for the full theory; (b) they lead to a consistent dynamics; and (c) they are thermodynamically consistent. These properties originally shown within the imaginary-time formalism with a time-dependent external perturbation [18, 19] also hold in the genuine nonequilibrium case formulated in the real-time field theory [21].

Transport equation (35) weighted either with the charge e or with 4-momentum p^ν, summed over internal degrees of freedomlike spin (tr), and integrated over momentum gives rise to the charge or energy–momentum conservation laws, respectively, with the Noether 4-current and Noether energy–momentum tensor defined by the expressions [22]

$$j^\mu(X) = e\,\mathrm{tr}\int\frac{d^4p}{(2\pi)^4}\times 2\pi^\mu F(X,p), \tag{42}$$

$$\Theta^{\mu\nu}(X) = \mathrm{tr}\int\frac{d^4p}{(2\pi)^4}\times 2\pi^\mu p^\nu F(X,p) + g^{\mu\nu}(\mathscr{E}^{\mathrm{int}}(X) - \mathscr{E}^{\mathrm{pot}}(X)). \tag{43}$$

Here,

$$\mathscr{E}^{\rm int}(X) = \langle -\hat{\mathscr{L}}^{\rm int}(X)\rangle = \frac{\delta\Phi}{\delta\lambda(x)}\bigg|_{\lambda=1} \quad (44)$$

is the interaction energy density, which in terms of Φ is given by a functional variation with respect to a spacetime dependent coupling strength of interaction part of the Lagrangian density $\hat{\mathscr{L}}^{\rm int} \longrightarrow \lambda(x)\hat{\mathscr{L}}^{\rm int}$, cf. [21]. The potential energy density $\mathscr{E}^{\rm pot}$ takes the form

$$\mathscr{E}^{\rm pot} = {\rm tr}\int\frac{d^4p}{(2\pi)^4}\left[{\rm Re}\,\Sigma^R F + {\rm Re}\,G^R\frac{\Gamma}{A}F\right]. \quad (45)$$

Whereas the first term in squared brackets complies with quasiparticle expectations, namely, the mean potential times density, the second term displays the role of fluctuations in the potential energy density.

The conservation laws only hold if all the self-energies are Φ-derivable. In [22], it was shown that this implies the consistency relation,

$$i\,{\rm tr}\int\frac{d^4p}{(2\pi)^4}\left[\{{\rm Re}\,\Sigma^R, F\} - \left\{{\rm Re}\,G^R, \frac{\Gamma}{A}F\right\} + C\right] = 0 \quad (46)$$

and the consistensy relation for the conserved current

$$\partial^\nu(\mathscr{E}^{\rm pot} - \mathscr{E}^{\rm int})$$

$$= {\rm tr}\int\frac{p^\nu d^4p}{(2\pi)^4}\left[\{{\rm Re}\,\Sigma^R, F\} - \left\{{\rm Re}\,G^R, \frac{\Gamma}{A}F\right\} + C\right], \quad (47)$$

for the energy–momentum tensor.

They are obtained after first-order gradient expansion of the corresponding exact relations. The contributions from the Markovian collision term C drop out in both cases, cf. Eq. (50) below. The first term in each of the two relations refers to the change from the free velocity $\mathbf{v}$ to the group velocity $\mathbf{v}_g$ in the medium. It can therefore be associated with a corresponding drag-flow contribution of the surrounding matter to the current or energy–momentum flow. The second (fluctuation) term compensates the former contribution and can therefore be associated with a back-flow contribution, which restores the Noether expressions (42) and (43) to be indeed the conserved quantities. In this compensation, we see the essential role of fluctuations in the quantum kinetic description. Dropping or approximating this term would spoil the conservation laws. Indeed, both expressions (42) and (43) comply with the quantum kinetic equation (35), being approximate (up to the first-order gradient terms) integrals of it.

Expressions (42) and (43) for 4-current and energy–momentum tensor, respectively, as well as self-consistency relations (46) and (47), still need a renormalization. They are written explicitly for the case of nonrelativistic particles whose number is conserved. This follows from the conventional way of nonrelativistic renormalization for such particles based on normal ordering. When the number of particles is not conserved (e.g., for phonons) or a system of relativistic particles is considered, one should replace $F(X, p) \longrightarrow \frac{1}{2}(F(X, p) \mp \tilde{F}(X, p))$ in all the above formulas in order to take proper account of zero-point vibrations (e.g., of phonons) or of the vacuum polarization in the relativistic case. These symmetrized equations, derived from special ($\mp$) combinations of the transport equations (35) and (36), are generally ultraviolet-divergent and, hence, have to be properly renormalized at the vacuum level.

7. COLLISION TERM

To further discuss the transport treatment, we need an explicit form of the collision term (30), which is provided from the Φ functional in the $-+$ matrix notation via the variation rules (41) as

$$C(X, p) = \frac{\delta i\Phi}{\delta\tilde{F}(X, p)}\tilde{F}(X, p) - \frac{\delta i\Phi}{\delta F(X, p)}F(X, p). \quad (48)$$

Here, we assumed Φ to be transformed into the Wigner representation and all $\mp iG^{-+}$ and iG^{+-} to be replaced by the Wigner densities F and $\tilde{F}$. Thus, the structure of the collision term can be inferred from the structure of the diagrams contributing to the functional Φ. To this end, in close analogy to the consideration of [23], we discuss various decompositions of the Φ functional, from which the in- and out-rates are derived. For the sake of physical transparency, we confine our treatment to the local case, where in the Wigner representation all the Green's functions are taken at the same spacetime coordinate X and all nonlocalities, i.e., derivative corrections, are disregarded. Derivative corrections give rise to memory effects in the collision term, which will be analyzed separately for the specific case of the triangle diagram.

Consider a given closed diagram of Φ, at this level specified by a certain number n_λ of vertices and a certain contraction pattern. This fixes the topology of such a contour diagram. It leads to 2^{n_λ} different diagrams in the $-+$ notation from the summation over all $-+$ signs attached to each vertex. Any $-+$ notation diagram of Φ that contains vertices of either sign can be decomposed into two pieces in such a way that each of the two subpieces contains vertices of only one type of sign[6)]

$$i\Phi_{\alpha\beta} = \left(\alpha\right.\!\!\left|\right.\!\!\left.\beta\right) = (\alpha|F_1 \ldots \tilde{F}_1'\ldots|\beta)$$

[6)]To construct the decomposition, just deform a given mixed-vertex diagram of Φ in such a way that all + and – vertices are placed left and, respectively, right from a vertical division line and then cut along this line.

$$\longrightarrow \int \frac{d^4p_1}{(2\pi)^4}\cdots\frac{d^4p_1'}{(2\pi)^4}\cdots(2\pi)^4\delta^4\left(\sum_i p_i - \sum_i p_i'\right) \tag{49}$$

$$\times V_\alpha^* F_1 \ldots \tilde{F}_1' \ldots V_\beta$$

with $F_1 \ldots F_m \tilde{F}_1' \ldots \tilde{F}_{\tilde{m}}'$ linking the two amplitudes. The $V_\alpha^*(X;\, p_1, \ldots p_1', \ldots)$ and $V_\beta(X;\, p_1, \ldots p_1', \ldots)$ amplitudes represent multipoint vertex functions of only one sign for the vertices; i.e., they are either entirely time-ordered (– vertices) or entirely antitime-ordered (+ vertices). Here, we used the fact that adjoint expressions are complex-conjugate to each other. Each such vertex function is determined by normal Feynman diagram rules. Applying the matrix variation rules (48), we find that the considered Φ diagram gives the following contribution to the local part of the collision term (29):

$$C^{\mathrm{loc}}(X, p)$$

$$\longrightarrow \frac{1}{2}\int \frac{d^4p_1}{(2\pi)^4}\cdots\frac{d^4p_1'}{(2\pi)^4}\cdots R\left[\sum_i \delta^4(p_i - p)\right.$$

$$\left. - \sum_i \delta^4(p_i' - p)\right]\{\tilde{F}_1 \ldots F_1' \ldots - F_1 \ldots \tilde{F}_1' \ldots\} \tag{50}$$

$$\times (2\pi)^4\delta^4\left(\sum_i p_i - \sum_i p_i'\right),$$

with the partial process rates

$$R(X;\, p_1, \ldots p_1', \ldots)$$

$$= \sum_{(\alpha\beta)\,\in\,\Phi} \mathrm{Re}\{V_\alpha^*(X;\, p_1, \ldots p_1', \ldots)V_\beta(X;\, p_1, \ldots p_1', \ldots)\}. \tag{51}$$

The restriction to the real part arises, since with $(\alpha|\beta)$ also the adjoint $(\beta|\alpha)$ diagram contributes to this collision term. However, these rates are not necessarily positive. In this point, the generalized scheme differs from the conventional Boltzmann kinetics.

An important example of approximate Φ that we extensively use below is

$i\Phi = \frac{1}{2}$  $+ \frac{1}{4}$  $+ \frac{1}{6}$  , (52)

where logarithmic factors due to the special features of the Φ-diagrammatic technique are written out explicitly, cf. [22]. In this example, we assume a system of fermions interacting via a two-body potential $V = V_0\delta(x - y)$ and, for the sake of simplicity, disregard its spin structure. The Φ functional of Eq. (52) results in the local collision term

$$C^{\mathrm{loc}} = d^2\int \frac{d^4p_1}{(2\pi)^4}\frac{d^4p_2}{(2\pi)^4}\frac{d^4p_3}{(2\pi)^4}$$

$\times \Big($ 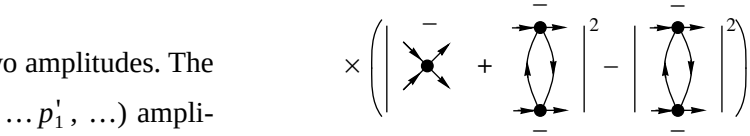 $\Big)$ (53)

$$\times \delta^4(p + p_1 - p_2 - p_3)(F_2F_3\tilde{F}\tilde{F}_1 - \tilde{F}_2\tilde{F}_3FF_1),$$

where d is the spin (and maybe isospin) degeneracy factor. From this example, one can see that the positive definiteness of transition rate is not evident.

The first-order gradient corrections to the local collision term (50) are called memory corrections. Only diagrams of third and higher order in the number of vertices give rise to memory effects. In particular, only the last diagram of Eq. (52) gives rise to the memory correction, which is calculated in [22].

8. ENTROPY

Compared to exact descriptions, which are time-reversible, reduced description schemes in terms of relevant degrees of freedom have access only to some limited information and thus normally lead to irreversibility. In the Green's function formalism presented here, the information loss arises from the truncation of the, exact Martin–Schwinger hierarchy, where the exact one-particle Green's function couples to the two-particle Green's functions, cf. [15, 48], which in turn are coupled to the three-particle level, etc. This truncation is achieved by the standard Wick decomposition, where all observables are expressed in terms of one-particle propagators; therefore, higher order correlations are dropped. This step provides the Dyson equation and the corresponding loss of information is expected to lead to a growth of entropy with time.

We start with general manipulations which lead us to definition of the kinetic entropy flow [22]. We multiply Eq. (35) by $-\ln(F/A)$, Eq. (36) by $(\mp)\ln(\tilde{F}/A)$, take their sum, integrate it over $d^4p/(2\pi)^4$, and finally sum the result over internal degrees of freedom like spin (tr). Then, we arrive at the relation

$$\partial_\mu s^\mu_{\mathrm{loc}}(X) = \mathrm{tr}\int \frac{d^4p}{(2\pi)^4}\ln\frac{\tilde{F}}{F}C(X, p), \tag{54}$$

$$s^\mu_{\mathrm{loc}} = \mathrm{tr}\int \frac{d^4p}{(2\pi)^4}A^\mu_s(X, p)\sigma(X, p), \tag{55}$$

where

$$\sigma(X, p) = \mp[1 \mp f]\ln[1 \mp f] - f\ln f, \tag{56}$$

$$A_s^\mu(X, p) = \frac{A\Gamma}{2}B^\mu, \tag{57}$$

$$B^\mu = A\left[\left(2\pi^\mu - \frac{\partial \operatorname{Re}\Sigma^R}{\partial p_\mu}\right) - M\Gamma^{-1}\frac{\partial\Gamma}{\partial p_\mu}\right], \tag{58}$$

cf. the corresponding drift term [proportional to $\partial_\mu f$ in Eq. (35)]. The zero components of these functions, A_s^0 and B^0, have a meaning of the entropy and flow spectral functions, respectively, and satisfy the same sum rule as A. If the considered particle is a resonance, like the Δ or ρ-meson resonances in hadron physics, the B^0 function relates to the energy variations of scattering phase shift of the scattering-channel coupling to the resonance in the virial limit discussed above. The value $s^0_{\rm loc}$ is interpreted as the local (Markovian) part of the entropy flow. Indeed, the $s^0_{\rm loc}$ has proper thermodynamic and quasiparticle limits [22]. However, to be sure that this is indeed the entropy flow, we must prove the H theorem for this quantity.

First, let us consider the case where memory corrections to the collision term are negligible. Then, we can make use of the form (50) of the local collision term. Thus, we arrive at the relation

$$\operatorname{tr}\int\frac{d^4p}{(2\pi)^4}\ln\frac{\tilde F}{F}C^{\rm loc}(X, p)$$

$$\longrightarrow \operatorname{tr}\frac{1}{2}\int\frac{d^4p_1}{(2\pi)^4}\cdots\frac{d^4p_1'}{(2\pi)^4}\cdots R\{F_1\ldots\tilde F_1'\ldots \tag{59}$$

$$-\tilde F_1\ldots F_1'\ldots\}\ln\frac{F_1\ldots\tilde F_1'\ldots}{\tilde F_1\ldots F_1'\ldots}(2\pi)^4\delta^4\left(\sum_i p_i - \sum_i p_i'\right).$$

If all rates R are nonnegative, i.e., $R \ge 0$, this expression is nonnegative, since $(x - y)\ln(x/y) \ge 0$ for any positive x and y. In particular, $R \ge 0$ takes place for all Φ functionals up to two vertices. Then, the divergence of $s^\mu_{\rm loc}$ is nonnegative:

$$\partial_\mu s^\mu_{\rm loc}(X) \ge 0, \tag{60}$$

which proves the H theorem in this case with (55) as the nonequilibrium entropy flow. However, as has been mentioned above, we are unable to show that R always takes nonnegative values for all Φ functionals.

If memory corrections are essential, the situation is even more involved. Let us consider this situation again at the example of the Φ approximation given by Eq. (52). We assume that the fermion–fermion potential interaction is such that the corresponding transition rate of the corresponding local collision term (53) is always nonnegative, so that the H theorem takes place in the local approximation, i.e., when we keep only $C^{\rm loc}$. Here, we will schematically describe calculations of [22] which, to our opinion, illustrate a general strategy for the derivation of memory correction to the entropy, provided the H theorem holds for the local part.

Now Eq. (54) takes the form

$$\partial_\mu s^\mu_{\rm loc}(X) = \operatorname{tr}\int\frac{d^4p}{(2\pi)^4}\ln\frac{\tilde F}{F}C^{\rm loc} + \operatorname{tr}\int\frac{d^4p}{(2\pi)^4}\ln\frac{\tilde F}{F}C^{\rm mem}, \tag{61}$$

where $s^\mu_{\rm loc}$ is still the Markovian entropy flow defined by Eq. (55). Our aim here is to present the last term on the right-hand side of Eq. (61) in the form of full X derivative

$$\operatorname{tr}\int\frac{d^4p}{(2\pi)^4}\ln\frac{\tilde F}{F}C^{\rm mem} = -\partial_\mu s^\mu_{\rm mem}(X) + \delta c_{\rm mem}(X) \tag{62}$$

of some function $s^\mu_{\rm mem}(X)$, which we then interpret as a non-Markovian correction to the entropy flow of Eq. (55) plus a correction ($\delta c_{\rm mem}$). For the memory induced by the triangle diagram of Eq. (52), the detailed calculations of [22] show that smallness of the $\delta c_{\rm mem}$, originating from small spacetime gradients and small deviation from equilibrium, allows us to neglect this term as compared with the first term on the right-hand side of Eq. (62). Thus, we obtain

$$\partial_\mu(s^\mu_{\rm loc} + s^\mu_{\rm mem}) \simeq \operatorname{tr}\int\frac{d^4p}{(2\pi)^4}\ln\frac{\tilde F}{F}C^{\rm loc} \ge 0, \tag{63}$$

which is the H theorem for the non-Markovian kinetic equation under consideration with $s^\mu_{\rm loc} + s^\mu_{\rm mem}$ as the proper entropy flow. The right-hand side of Eq. (63) is nonnegative, provided that the corresponding transition rate in the local collision term of Eq. (53) is nonnegative.

The explicit form of $s^\mu_{\rm mem}$ is very complicated, see [22]. In equilibrium at low temperatures we get $s^0_{\rm mem} \sim T^3\ln T$ that gives the leading correction to the standard Fermi-liquid entropy. This is the famous correction [61, 62] to the specific heat of liquid ^{3}He. Since this correction is quite comparable (numerically) to the leading term in the specific heat ($\sim T$), one may claim that liquid ^{3}He is a liquid with very strong memory effects from the point of view of kinetics.

9. PION-CONDENSATE PHASE TRANSITION

As a further example for the role of finite-width effects, we consider the phase-transition dynamics into a pion condensate. The possible formation of such a pion condensate in dense nuclear matter was initially suggested by A.B. Migdal in his pioneering work [5]. In realistic treatments of this problem applied to equilibrated isospin-symmetric nuclear matter at low temper-

atures $T \ll m_\pi$, the pion self-energy is determined by nucleon–nucleon–hole and Δ–nucleon–hole contributions corrected by nucleon–nucleon correlations, $\pi\pi$ fluctuations, and a residual interaction [9]. A recent numerical analysis [63] within a variational method with realistic two- and three-nucleon interactions gave $\rho_c \simeq 2\rho_0$ for the critical density of π^+, π^-, π^0 condensation in symmetric nuclear matter and $\rho_c \simeq 1.3\rho_0$ for π^0 condensation in neutron matter, with ρ_0 being nuclear saturation density.

In symmetric nuclear matter, the pion-condesate frequency vanishes while the magnitude of condensate momentum $\mathbf{p}_c$ is approximately given by the nucleon Fermi momentum $|\mathbf{p}_c| \simeq p_F$. The critical behavior of the system is determined by the effective pion gap

$$\tilde{\omega}^2(\mathbf{p}_c) = \min_{\mathbf{p}}\{m_\pi^2 + \mathbf{p}^2 + \mathrm{Re}\,\Sigma_\pi^R(0, \mathbf{p}, \varphi_\pi = 0)\}, \quad (64)$$

where the momentum $\mathbf{p} = \mathbf{p}_c$ corresponds to the minimum of the gap at zero mean field $\varphi_\pi = 0$ [8, 9]. Figure 5 illustrates the behavior of the effective pion gap $\tilde{\omega}^2(\mathbf{p}_c)$ as a function of the baryon density ρ. At low densities, $\mathrm{Re}\Sigma_\pi^R$ is small and one obviously has $\tilde{\omega}^2 > 0$. The dashed curve in Fig. 5 describes the case where the $\pi\pi$ fluctuations are artificially switched off and the phase transition turns out to be of second order. At the critical point of the pion condensation ($\rho = \rho_c$), this value of $\tilde{\omega}^2$ with switched-off $\pi\pi$ fluctuations changes its sign. In reality, the $\pi\pi$ fluctuations are significant in the vicinity of the critical point [64–66]. The corresponding contribution to the pion self-energy behaves as $T/\tilde{\omega}(\varphi_\pi, \mathbf{p}_c)$ at $T > |\tilde{\omega}^2(\varphi_\pi, \mathbf{p}_c)/m_\pi|$, and $\tilde{\omega}^2(\mathbf{p}_c)$ does not cross the zero line at all.[7)] Rather there are two branches (solid curves in Fig. 5) with positive and respectively negative value for $\tilde{\omega}^2(\mathbf{p}_c)$ and the transition becomes of the first order. Calculations of [64–66] demonstrate that at $\rho > \rho_c$ the free energy of the state with $\tilde{\omega}^2(\mathbf{p}_0) > 0$, where the pion mean field is zero, becomes larger than that of the corresponding state with $\tilde{\omega}^2(\mathbf{p}_c) < 0$ and a finite mean field. Thus, at $\rho = \rho_c$ the first-order phase transition to the inhomogeneous pion-condensate state occurs. At $\rho > \rho_c$ the state with $\tilde{\omega}^2(\mathbf{p}_c) > 0$ is metastable and the state with $\tilde{\omega}^2(\mathbf{p}_c) < 0$ and $\tilde{\varphi}_\pi \neq 0$ becomes the ground state.

Before we discuss a self-consistent scheme for a quantitative treatment of this problem, we should qualitatively explain how the instability toward pion condensation develops dynamically. To simplify the treatment, we assume that the pion density is low ($\rho_\pi \ll \rho$) and further use the fact that the pion is much lighter than the nucleon ($m_\pi/m_N \simeq 1/7$). This allows us to consider the pion subsystem as a light admixture in a heavy baryon environment, neglecting the feedback of the pions onto the baryons. It provides the nucleon Green's functions unaffected by the pion distribution. This very approximation was used in the first works exploring the possibility of the pion condensation in dense nuclear matter [5–7]. We will use it for the pion retarded self-energy, thus neglecting the contribution from pion fluctuations (see dashed curve in Fig. 5). Within the above approximations, the quantum kinetic equation (35) for the pion distribution f_π in homogeneous and equilibrated baryon environment becomes

$$\frac{1}{2}\Gamma B_\mu \partial_X^\mu f_\pi = \Gamma_{\mathrm{in}} - \Gamma f_\pi. \quad (65)$$

Here, B_μ is defined in Eq. (58) and all subscripts π are omitted, except for the pion distribution function f_π.

We now illustrate that the second branch in Fig. 5 with negative $\tilde{\omega}^2$ constructed under the assumption of vanishing mean field is indeed unstable and becomes stabilized by a finite mean field. The instability of the system can be discussed considering a weak perturbation δf_π of the pion distribution $f_\pi^{(0)} = [\exp(p_0/T) - 1]^{-1}$, which we assume equilibrated in the rest frame of the system. Linearizing Eq. (65), we find

$$\frac{1}{2}B_\mu \partial_X^\mu \delta f_\pi + \delta f_\pi = 0, \quad (66)$$

with the solution

$$\delta f_\pi(t, p) = \delta f_0(p)\exp[-2t/B_0(p)], \quad (67)$$

where for simplicity the initial fluctuation $\delta f_0(p)$ of the pion distribution is assumed to be space-independent. Let us consider the case where $p_0 \longrightarrow 0$ and $|\mathbf{p}| \simeq p_F$.

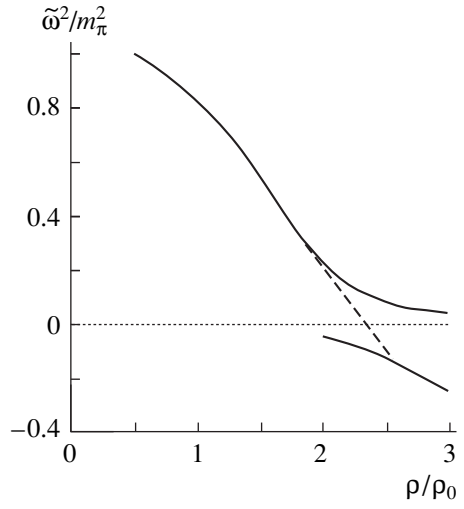

Fig. 5. Effective pion gap (64) versus nuclear density, see [9].

[7)] Here we have used the quantity $\tilde{\omega}^2$, which already takes account of the pion mean field as explained below, cf. Eq. (69) and the definition of $\tilde{\omega}(\varphi_\pi, \mathbf{p}_c)$ after it.

This four-momentum region, being far from the pion mass shell, is right the region where the pion instability is expected in symmetric nuclear matter. Here, the real part of the pion self-energy $\mathrm{Re}\Sigma^R$ is an even function of the pion energy p_0, while the width is an odd function and proportional to p_0 for $p_0 \longrightarrow 0$. Using the results of [8, 9] $2p_0 - \partial \mathrm{Re}\Sigma^R/\partial p_0 \longrightarrow 0$, $\Gamma = \beta(\mathbf{p})p_0$, and $\beta(\mathbf{p}) \sim m_\pi$ for $p_0 \longrightarrow 0$, we get $B_0 = \beta(\mathbf{p})/\tilde{\omega}^2(\mathbf{p})$ from Eq. (58) and therefore

$$\delta f_\pi(t, p_0 = 0, \mathbf{p}) = \delta f_0(p_0 = 0, \mathbf{p}) \exp[-2\tilde{\omega}^2(\mathbf{p})t/\beta(\mathbf{p})]. \quad (68)$$

The above solution shows that for $\tilde{\omega}^2 > 0$ initial fluctuations are damped, whereas they grow in the opposite case. Thus, the change of sign of $\tilde{\omega}^2(\mathbf{p}_c)$ leads to an instability of the virtual pion distribution at low energies and momenta $\simeq \mathbf{p}_c$. The solution (68) illustrates the important role of the width in the quantum kinetic description. If the width had been neglected in the quantum kinetic equation, one would fail to find the above instability.

The growth of the pion distribution δf_π is accompanied by a growth of the condensate field φ_π. Due to the latter, the increase of the virtual pion distribution slows down and finally stops when the mean field reaches its stationary value. Therefore, a consistent treatment of the problem requires the solution of the coupled system of the quantum kinetic equation (35) and the mean-field equation (39). In order to find the behavior of the virtual pion distribution, one also has to include the mean-field contribution to the pion self-energy. Considering only small mean fields, we retain terms of the lowest order in φ_π. Then, Σ^R acquires and additional contribution $\Sigma^R(\varphi_\pi) = \Sigma^R(\varphi_\pi = 0) + \lambda_{\mathrm{eff}}|\varphi_\pi|^2$, where λ_{eff} denotes the total in-medium pion–pion interaction. Within the same order, the mean-field equation becomes

$$\left[\tilde{\omega}^2(\mathbf{p}_c) + \lambda_{\mathrm{eff}}\tilde{\varphi}_\pi^2(t) + \frac{1}{2}\beta(\mathbf{p}_c)\partial_t\right]\tilde{\varphi}_\pi(t) = 0. \quad (69)$$

Here, we have assumed the simplest structure for the condensate field $\varphi_\pi = \tilde{\varphi}_\pi(t)\exp(i\mathbf{p}_c \cdot \mathbf{r})$, where $\tilde{\varphi}_\pi(t)$ is a space-homogeneous real function which varies slowly in time. Also, one should do the replacement $\tilde{\omega}^2(\mathbf{p}_c) \longrightarrow \tilde{\omega}^2(\varphi_\pi, \mathbf{p}_c) \equiv \tilde{\omega}^2(\mathbf{p}_c) + \lambda_{\mathrm{eff}}|\varphi_\pi|^2$ in the above Eqs. (65)–(68) for the pion distribution.

The time dependence of $\tilde{\varphi}$ can qualitatively be understood inspecting the two limits of small and large times. At short times, the mean field is still small and one can neglect the $\lambda_{\mathrm{eff}}\tilde{\varphi}^2(t)$ term in Eq. (69). Then the mean field

$$\tilde{\varphi}_\pi(t) = \tilde{\varphi}_\pi(0)\exp[-2\tilde{\omega}^2(\mathbf{p}_c)t/\beta(\mathbf{p}_c)] \quad (70)$$

grows exponentially with time, just like the distribution function (68). Here, $\tilde{\varphi}_\pi(0)$ is an initial small fluctuation of the field. At later times, the solution of Eq. (69) approaches the stationary limit $\tilde{\varphi}_\pi \longrightarrow \tilde{\varphi}_\pi^{\mathrm{stat}}$ with

$$(\tilde{\varphi}_\pi^{\mathrm{stat}})^2 = -\tilde{\omega}^2(\mathbf{p}_c)/\lambda_{\mathrm{eff}}(\mathbf{p}_c). \quad (71)$$

Since simultaneously $\tilde{\omega}^2(\varphi_\pi, \mathbf{p}_c) = \tilde{\omega}^2(\mathbf{p}_c) + \lambda_{\mathrm{eff}}|\varphi_\pi|^2 \longrightarrow 0$, the change in the pion distribution δf_π will saturate. This stationary solution $\tilde{\varphi}_\pi^{\mathrm{stat}}$ is stable, as can be seen from linearizing Eq. (69) around $\tilde{\varphi}_\pi^{\mathrm{stat}}$,

$$\tilde{\varphi}_\pi(t) = \tilde{\varphi}_\pi^{\mathrm{stat}} - \delta\tilde{\varphi}_0\exp[4\tilde{\omega}^2(\mathbf{p}_c)t/\beta(\mathbf{p}_c)], \quad (72)$$

since the exponential function is negative. Here, $\delta\tilde{\varphi}_0$ denoted an arbitrary initial space-homogeneous fluctuation.

The physics can again be cast into a Φ-derivable form, where the Φ functional should include at least the following diagrams:

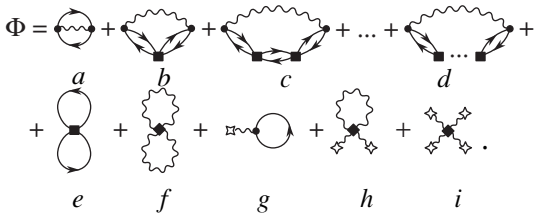

(73)

Here, bold and bold wavy lines represents the baryon and pion Green's functions, respectively, while a wavy line terminated by a cross denotes the pion condensate. Since in the broken phase the mean pion field mixes nucleon with Δ configurations, we adopt the $SU(4)$ formulation of the model, introduced in [67]. There, one deals with a unified description of baryons (N and Δ), based on 20×20 matrix Hamiltonian in the basis of 20 Δ–nucleon spin–isospin states. Thus, the solid lines symbolize a unified propagator matrix for Δ resonance and nucleon. The mixing is provided by condensate-baryon coupling (diagram (*g*)). Numerical symmetry factors are omitted in Eq. (73).

Functional variation of Φ with respect to propagators provides the corresponding self-energies. Diagrammatically, this variation corresponds to cutting and opening the respective propagator lines of the diagrams of Φ in Eq. (73). Thus, diagrams (*a*) to (*d*), (*f*), and (*h*) contribute to the pion self-energy. Diagram (*a*) accounts for the baryon particle–hole contributions to the pion self-energy. It includes NN^{-1}, ΔN^{-1}, $N\Delta^{-1}$, and $\Delta\Delta^{-1}$ terms. The subsequent series of diagrams (*b*) to (*d*) renormalizes baryon–pion vertex including baryon–baryon correlations in terms of the Landau–Migdal parameter g'. Diagram (*f*) accounts for the pion fluctuations. It is proportional to $T/\tilde{\omega}(\varphi_\pi, \mathbf{p}_c)$ and thus causes the transition to be of first order. This becomes espe-

cially important for the case of heated and even nonequilibrium dense matter, where the effective pion gap [65, 66] drops. One should notice that pion fluctuation contributions are also present in the particle–hole diagram (*a*) when opened perturbatively. Diagram (*h*) corresponds to pion interactions with the condensate, which are responsible for the stabilization of the condensate solution (71).

Likewise, cutting and opening the solid lines in Φ determines the baryon self-energy, which describes the feedback of the pions onto the baryonic subsystem. This feedback is required for the conserving and thermodynamically consistent treatment of the problem. Diagrams of the first line correspond to the modification of the baryon motion by the multiple interaction with the pions corrected by correlations. Diagram (*e*) generates a purely local interaction contribution, whereas diagram (*g*) with the coupling of the condensate to baryons leads to the mixing of N and Δ.

Variation of Φ with respect to the condensates (wavy line with a cross) determines the source term J in the equation for the mean field (39). The value λ_{eff} entering Eq. (69) is generated by the last two diagrams (*h*) and (*i*) of Eq. (73).

The kinetic description (35) for the particle distribution together with the equation of motion for the mean field (39) is still insufficient for the numerical simulations of the dynamics of the phase transition. The reason is that the creation of seeds of the new phase, which initiate the growth of the mean field and the particle distribution, is due to fluctuations, cf. Eqs. (68) and (70). However, the scheme of Eqs. (35) and (39) provides no sources of stochastic fluctuations. Thus, it can only simulate the dynamics of one of the phases rather than the transition between them. The required stochastic sources may be introduced into the transport theory in the spirit of the Boltzmann–Langevin approach developed in [68–70] and the stochastic interpretation of the Kadanoff–Baym equations [71]. The stochastic transport approach offers an appropriate framework for the description of the unstable dynamics by means of a stochastic force in the mean-field equation and a stochastic collision term in the transport equation, which both act as a source for a continuous branching of the dynamical trajectories.

The above example shows that we really need the off-mass-shell kinetics to describe the dynamics of the pion-condensate phase transition, since the corresponding instability of the pion distribution function occurs far from the pion mass shell, cf. Eq. (68). Besides the conserving property and thermodynamic consistency of the Φ-derivable approximation, it also leads us to the proper order of the phase transition.

10. SUMMARY AND PROSPECTS

A number of problems arising in different dynamical systems, e.g., in heavy-ion collisions, require an explicit treatment of dynamical evolution of particles with a finite mass width. This was demonstrated for the example of bremsstrahlung from a nuclear source, where the soft part of the spectrum can be reproduced only provided the mass widths of nucleons in the source are taken explicitly into account. In this case, the mass width arises owing to collisional broadening of nucleons. Another example considered concerns propagation of broad resonances (like ρ meson and Δ) in the medium. Decays of ρ mesons are an important source of dileptons radiated by excited nuclear matter. As shown, a consistent description of the invariant-mass spectrum of radiated dileptons can be only achieved if one accounts for the in-medium modification of the ρ meson width (more precisely, its spectral function). The action–reaction principle was demonstrated on a pedagogical example when there is only $\pi N\Delta$ coupling and in the limit of a dilute nuclear matter. We also expect a consistent description of chiral σ-, π-condensates together with fluctuations, as an immediate application of our results to multicomponent systems.

We have argued that the Kadanoff–Baym equation within the first-order gradient approximation, slightly modified to make the set of Dyson's equations exactly consistent (rather than up to the second-order gradient terms), together with algebraic equation for the spectral function provide a proper frame for a quantum four-phase-space kinetic description that applies also to systems of unstable particles. The quantum four-momentum-space kinetic equation proves to be charge and energy–momentum conserving and thermodynamically consistent, provided it is based on a Φ-derivable approximation. The Φ functional also gives rise to a very natural representation of the collision term. Various self-consistent approximations are known since long time which do not explicitly use the Φ-derivable concept like self-consistent Born and T-matrix approximations. The advantage of the Φ-functional method consists in offering a regular way of constructing various self-consistent approximations.

We have also addressed the question as to whether a closed nonequilibrium system approaches the thermodynamic equilibrium during its evolution. We obtained a definite expression for a local (Markovian) entropy flow and were able to explicitly demonstrate the H theorem for some of the common choices of Φ approximations. This expression holds beyond the quasiparticle picture and thus generalizes the well-known Boltzmann kinetic entropy. Memory effects in the quantum four-momentum-space kinetics were discussed and a general strategy to deduce memory corrections to the entropy was outlined.

At the example of pion-condensate phase transition in symmetric nuclear matter we demonstrated important role of the width effects in the dynamics and we formulated a self-consistent Φ-derivable scheme for the transport treatment of this problem. An interesting application of such self-consistent transport description

is possible to dynamics of the phase transition of a neutron star to the pion or kaon condensate state accompanied by the corresponding neutrino burst. In view of the latter, another application concerns description of the neutrino transport in supernovas and hot neutron stars during first few minutes of their evolution. At an initial stage, neutrinos typically of thermal energy, produced outside (in the mantel) and inside the neutron-star core, are trapped within the regions of production. However, coherent effects in neutrino production and their rescattering on nucleons [23] reduce the opacity of the nuclear medium and may allow for soft neutrinos to escape the core and contribute to the heating off the mantle. The extra energy transport may be sufficient to blow off the supernova's mantle in the framework of the shock-reheating mechanism [72]. The description of the neutrino transport in the semitransparent region should therefore be treated with the due account of mass-widths effects.

Further applications concern relativistic plasmas, such as QCD and QED plasmas. The plasma of deconfined quarks and gluons was present in the early Universe; it may exist in cores of massive neutron stars and may also be produced in laboratory in ultrarelativistic nucleus–nucleus collisions. All these systems need a proper treatment of particle transport. Perturbative description of soft-quantum propagation suffers of infrared divergences and one needs a systematic study of the particle mass-width effects in order to treat them, cf. [23]. A thermodynamic Φ-derivable approximation for hot relativistic QED plasmas—a gas of electrons and positrons in a thermal bath of photons—was recently considered in [73]. Their treatment may be also applied to the high-temperature superconductors and the fractional quantum Hall effect [74, 75]. The approach formulated above allows for a natural generalization of such Φ-derivable schemes to the dynamical case.

ACKNOWLEDGMENTS

We are grateful to G. Baym, G.E. Brown, P. Danielewicz, H. Feldmeier, B. Friman, E.E. Kolomeitsev, and P.C. Martin for fruitful discussions. Two of us (Y.B.I. and D.N.V.) highly appreciate the hospitality and support rendered to us at Gesellschaft für Schwerionenforschung.

This work was supported in part by DFG (project 436 Rus 113/558/0). Y.B.I. and D.N.V. were partially supported by RFBR grant NNIO-00-02-04012. Y.B.I. also appreciates partial support of the RFBR under grant 00-15-96590.

REFERENCES

1. L. D. Landau, Zh. Éksp. Teor. Fiz. **30**, 1058 (1956) [Sov. Phys. JETP **3**, 920 (1956)].
2. V. M. Galitskiĭ and A. B. Migdal, Zh. Éksp. Teor. Fiz. **34**, 139 (1958) [Sov. Phys. JETP **7**, 96 (1958)].
3. A. B. Migdal, *Nuclear Theory; the Quasiparticle Method* (Nauka, Moscow, 1967; Benjamin, New York, 1968); *Theory of Finite Fermi Systems and Applications to Atomic Nuclei* (Nauka, Moscow, 1983, 2nd ed.; Wiley, New York, 1967).
4. E. M. Lifshitz and L. P. Pitaevskiĭ, *Course of Theoretical Physics*, Vol. 5: *Statistical Physics* (Nauka, Moscow, 1978; Pergamon, Oxford, 1980), Part 2.
5. A. B. Migdal, Zh. Éksp. Teor. Fiz. **61**, 2209 (1971) [Sov. Phys. JETP **34**, 1184 (1972)].
6. A. B. Migdal, Zh. Éksp. Teor. Fiz. **63**, 1993 (1972) [Sov. Phys. JETP **36**, 1052 (1973)].
7. A. B. Migdal, Phys. Rev. Lett. **31**, 257 (1973); Nucl. Phys. A **210**, 421 (1973); Phys. Lett. B **47B**, 96 (1973); **52B**, 172 (1974); **52B**, 264 (1974).
8. A. B. Migdal, Rev. Mod. Phys. **50**, 107 (1978).
9. A. B. Migdal, E. E. Saperstein, M. A. Troitsky, and D. N. Voskresensky, Phys. Rep. **192**, 179 (1990).
10. D. N. Voskresensky, Nucl. Phys. A **555**, 293 (1993).
11. L. D. Landau and I. Pomeranchuk, Dokl. Akad. Nauk SSSR **92**, 553 (1953); **92**, 735 (1953); in *Collected Papers of Landau*, Ed. by Ter Haar (Gordon and Breach, New York, 1965), Papers 75–77.
12. A. B. Migdal, Phys. Rev. **103**, 1811 (1956); Zh. Éksp. Teor. Fiz. **32**, 633 (1957) [Sov. Phys. JETP **5**, 527 (1957)].
13. P. L. Anthony *et al.*, Phys. Rev. Lett. **75**, 1949 (1995); S. Klein, Rev. Mod. Phys. **71**, 1501 (1999).
14. J. Schwinger, J. Math. Phys. **2**, 407 (1961).
15. L. P. Kadanoff and G. Baym, *Quantum Statistical Mechanics* (Benjamin, New York, 1962).
16. L. P. Keldysh, Zh. Éksp. Teor. Fiz. **47**, 1515 (1964) [Sov. Phys. JETP **20**, 1018 (1965)].
17. G. Baym and L. P. Kadanoff, Phys. Rev. **124**, 287 (1961).
18. G. Baym, Phys. Rev. **127**, 1391 (1962).
19. J. M. Luttinger and J. C. Ward, Phys. Rev. **118**, 1417 (1960).
20. A. A. Abrikosov, L. P. Gor'kov, and I. E. Dzyaloshinskii, *Methods of Quantum Field Theory in Statistical Physics* (Fizmatgiz, Moscow, 1962; Dover, New York, 1975).
21. Yu. B. Ivanov, J. Knoll, and D. N. Voskresensky, Nucl. Phys. A **657**, 413 (1999).
22. Yu. B. Ivanov, J. Knoll, and D. N. Voskresensky, Nucl. Phys. A **672**, 313 (2000).
23. J. Knoll and D. N. Voskresensky, Ann. Phys. (N. Y.) **249**, 532 (1996); Phys. Lett. B **351**, 43 (1995).
24. H. van Hees and J. Knoll, in *Proceedings of the International Workshop XXVIII on Gross Properties of Nuclei and Nuclear Excitations, Hirschegg, 2000*, Ed. by M. Buballa *et al.*, p. 177; hep-ph/0002087; hep-ph/0007070; Nucl. Phys. A (in press).
25. W. Weinhold, B. L. Friman, and W. Nörenberg, Acta Phys. Pol. B **27**, 3249 (1996); Phys. Lett. B **433**, 236 (1998).
26. J. Knoll and C. Guet, Nucl. Phys. A **494**, 334 (1989); M. Durand and J. Knoll, Nucl. Phys. A **496**, 539 (1989).
27. D. N. Voskresensky and A. V. Senatorov, Yad. Fiz. **45**, 657 (1987) [Sov. J. Nucl. Phys. **45**, 411 (1987)].

28. J. Knoll, in *Proceedings of the Erice School on Nuclear Physics, Erice, 1998*; Prog. Part. Nucl. Phys. **42**, 177 (1999).
29. M. Herrmann, B. L. Friman, and W. Nörenberg, Nucl. Phys. A **560**, 411 (1993).
30. R. Rapp, G. Chanfray, and J. Wambach, Nucl. Phys. A **617**, 472 (1997).
31. S. Leupold and U. Mosel, Phys. Rev. C **58**, 2939 (1998).
32. F. Klingl, N. Kaiser, and W. Weise, Nucl. Phys. A **624**, 527 (1997).
33. B. L. Friman and H.-J. Pirner, Nucl. Phys. A **617**, 496 (1997).
34. B. Friman, M. Lutz, and G. Wolf, nucl-th/9811040; in *Proceedings of the "Baryons 98", Bonn, 1998* (World Sci., Singapore, 1999), p. 663; in *Proceedings of the International Workshop XXVIII on Gross Properties of Nuclei and Nuclear Excitations, Hirschegg, 2000*; nucl-th/0003012.
35. P. Danielewicz and G. F. Bertsch, Nucl. Phys. A **533**, 712 (1991).
36. M. Effenberger, E. L. Bratkovskaya, and U. Mosel, Phys. Rev. C **60**, 051901 (1999).
37. M. Effenberger, E. L. Bratkovskaya, W. Cassing, and U. Mosel, Phys. Rev. C **60**, 027601 (1999).
38. E. Beth and G. E. Uhlenbeck, Physica (Amsterdam) **4**, 915 (1937).
39. K. Huang, *Statistical Mechanics* (Wiley, New York, 1963; Mir, Moscow, 1966).
40. R. Dashen, S. Ma, and H. J. Bernstein, Phys. Rev. **187**, 345 (1969).
41. A. Z. Mekjian, Phys. Rev. C **17**, 1051 (1978).
42. R. Venugopalan and M. Prakash, Nucl. Phys. A **546**, 718 (1992).
43. W. Lenz, Z. Phys. **56**, 778 (1929).
44. L. D. Landau and E. M. Lifshitz, *Course of Theoretical Physics*, Vol. 3: *Quantum Mechanics: Non-Relativistic Theory* (Nauka, Moscow, 1989, 4th ed.; Pergamon, Oxford, 1977, 3rd ed.).
45. C. B. Dover, J. Hüfner, and R. H. Lemmer, Ann. Phys. (N. Y.) **66**, 248 (1971).
46. M. Lutz, A. Steiner, and W. Weise, Nucl. Phys. A **574**, 755 (1994).
47. P. Danielewicz and S. Pratt, Phys. Rev. C **53**, 249 (1996).
48. W. Botermans and R. Malfliet, Phys. Rep. **198**, 115 (1990).
49. S. Leupold, Nucl. Phys. A **672**, 475 (2000).
50. W. Cassing and S. Juchem, Nucl. Phys. A **672**, 417 (2000).
51. B. Bezzerides and D. F. DuBois, Ann. Phys. (N. Y.) **70**, 10 (1972).
52. P. Lipavsky, V. Spicka, and B. Velicky, Phys. Rev. B **34**, 6933 (1986).
53. V. Spicka and P. Lipavsky, Phys. Rev. Lett. **73**, 3439 (1994); Phys. Rev. B **52**, 14615 (1995).
54. W. D. Kraeft, D. Kremp, W. Ebelong, and G. Röpke, *Quantum Statistics of Charged Particle Systems* (Akademie-Verlag, Berlin, 1986).
55. M. Bonitz, *Quantum Kinetic Theory* (Teubner, Stuttgart/Leipzig, 1998).
56. Th. Bornath, D. Kremp, W. D. Kraeft, and M. Schlanges, Phys. Rev. E **54**, 3274 (1996).
57. M. Schönhofen, M. Cubero, B. Friman, *et al.*, Nucl. Phys. A **572**, 112 (1994).
58. S. Jeon and L. G. Yaffe, Phys. Rev. D **53**, 5799 (1996).
59. D. N. Voskresensky, D. Blaschke, G. Röpke, and H. Schulz, Int. J. Mod. Phys. E **4**, 1 (1995).
60. J. M. Cornwall, R. Jackiw, and E. Tomboulis, Phys. Rev. D **10**, 2428 (1974).
61. G. Baym and C. Pethick, *Landau Fermi-Liquid Theory* (Wiley, New York, 1991).
62. G. M. Carneiro and C. J. Pethick, Phys. Rev. B **11**, 1106 (1975).
63. A. Akmal, V. R. Pandharipande, and D. G. Ravenhall, Phys. Rev. C **58**, 1804 (1998).
64. A. M. Dyugaev, Pis'ma Zh. Éksp. Teor. Fiz. **22**, 181 (1975) [JETP Lett. **22**, 83 (1975)].
65. D. N. Voskresensky and I. N. Mishustin, Pis'ma Zh. Éksp. Teor. Fiz. **34**, 317 (1981) [JETP Lett. **34**, 303 (1981)]; Yad. Fiz. **35**, 1139 (1982) [Sov. J. Nucl. Phys. **35**, 667 (1982)].
66. A. M. Dyugaev, Pis'ma Zh. Éksp. Teor. Fiz. **35**, 341 (1982) [JETP Lett. **35**, 420 (1982)]; Zh. Éksp. Teor. Fiz. **83**, 1005 (1982) [Sov. Phys. JETP **56**, 567 (1982)]; Yad. Fiz. **38**, 1131 (1983) [Sov. J. Nucl. Phys. **38**, 680 (1983)].
67. D. Campbell, R. Dashen, and J. Manassash, Phys. Rev. D **12**, 979 (1975); **12**, 1010 (1975).
68. S. Ayik and C. Gregoire, Phys. Lett. B **212**, 269 (1988); Nucl. Phys. A **513**, 187 (1990).
69. J. Randrup and B. Remaud, Nucl. Phys. A **514**, 339 (1990).
70. Yu. B. Ivanov and S. Ayik, Nucl. Phys. A **593**, 233 (1995).
71. C. Greiner and S. Leupold, Ann. Phys. (N. Y.) **270**, 328 (1998).
72. H. A. Bethe and J. R. Wilson, Astrophys. J. **295**, 14 (1985).
73. B. Vanderheyden and G. Baym, J. Stat. Phys. **93**, 843 (1998).
74. B. I. Halperin, P. A. Lee, and N. Read, Phys. Rev. B **47**, 7312 (1993).
75. L. B. Ioffe and A. I. Larkin, Phys. Rev. B **39**, 8988 (1989).

Physics of Atomic Nuclei, Vol. 64, No. 4, 2001, pp. 670–690. Translated from Yadernaya Fizika, Vol. 64, No. 4, 2001, pp. 729–749.

90th ANNIVERSARY OF A.B. MIGDAL'S BIRTHDAY
NUCLEI

Semiclassical Approximation and 1/*n* Expansion in Quantum-Mechanical Problems

B. M. Karnakov, V. D. Mur, and V. S. Popov[1)]

Moscow State Engineering Physics Institute (Technical University), Kashirskoe sh. 31, Moscow, 115409 Russia

Received July 6, 2000

Abstract—The semiclassical approximation and the technique of 1/*n* expansion are used to calculate the eigenenergies and the wave functions for the radial Schrödinger equation. It is shown that the expressions that are asymptotically exact in the limit $n = n_r + l + 1 \longrightarrow \infty$ and which describe the above eigenenergies and the asymptotic coefficients at the origin and at infinity ensure a satisfactory precision even for states characterized by modest values of the quantum numbers n_r and l, including the ground state. © *2001 MAIK "Nauka/Interperiodica".*

This article is dedicated to the memory of Arkadiĭ Benediktovich Migdal, who profoundly understood the semiclassical method and successfully used it in various physics problems. His remarkable monograph Qualitative Methods in Quantum Theory had a strong impact on the present authors and aroused their interest in the semiclassical approach.

1. INTRODUCTION

Despite the impressive successes of computational mathematics, qualitative and approximate analytic approaches to solving physics problems are still of heuristic value and appeal [1]. These include the semiclassical approximation, which is also known as the Wentzel–Kramers–Brillouin (WKB) approximation [1–5] and which was developed when quantum mechanics was still in its infancy, and the technique of 1/*N* expansion [6–11]. These methods are both widely used in various realms of theoretical and mathematical physics.

Here, we discuss the application of these methods to calculating the eigenenergies (both for discrete levels and for quasistationary states) and wave functions for the radial Schrödinger equation. Representing the potential in the form

$$V(r) = -g^2\frac{\hbar^2}{2MR^2}v(r/R), \qquad (1.1)$$

where M is the mass of the particle being considered, g is the dimensionless coupling constant, R is the characteristic range of the underlying interaction, and the function $v(r)$ specifies the form of this interaction, we arrive at

$$\frac{d^2\chi_l(r)}{dr^2} + \left[k^2 + g^2 v(r) - \frac{l(l+1)}{r^2}\right]\chi_l(r) = 0. \qquad (1.2)$$

Hereafter, we use the system of units where $\hbar = M = R = 1$, so that the relation between the quantity k and the particle energy E is $E = k^2/2$.

There are many physics problems where it is important to know the value of the normalized wave function at the origin—more precisely, the asymptotic coefficients c_{nl} (as usual, n and l are, respectively, the principal quantum number and the orbital angular momentum of the particle; below, we will also use the radial quantum number n_r specified by the relation $n = n_r + l + 1$),

$$\chi_{nl}(r) = c_{nl}r^{l+1} + \ldots, \quad r \longrightarrow 0 \qquad (1.3)$$

(see, for example, [11] and references therein). In order to calculate the coefficients c_{nl} in the semiclassical approximation, it is necessary to match the wave functions at the boundary between the classically allowed and the subbarrier region. It turns out that the conventional Kramers conditions [12] must be modified in this case [11, 13].

These issues are considered in Section 2, where we obtain analytic formulas that describe the coefficients c_{nl} and which are asymptotically exact in the limit $n_r \longrightarrow \infty$. We also discuss the accuracy of these formulas for modest values of the quantum numbers.

Section 3 is devoted to quantization by means of a procedure where the centrifugal potential is eliminated from the semiclassical momentum. This modified method of quantization makes it possible to extend con-

[1)]Institute of Theoretical Physics and Experimental Physics, Bol'shaya Cheremushkinskaya ul. 25, Moscow, 117218 Russia.

1063-7788/01/6404-0670$21.00 © 2001 MAIK "Nauka/Interperiodica"

siderably the potential of an analytic investigation of the energy spectrum and wave functions.

In Section 4, we consider a 1/*n* expansion, whose zero order corresponds to the classical limit $l \longrightarrow \infty$. In view of this, the technique of 1/*n* expansion is in a sense an alternative to the semiclassical expansion, which is asymptotically exact for $n_r \longrightarrow \infty$. These two approaches supplement each other quite well for finite values of l and n_r.

Finally, a generalization of the Bohr–Sommerfeld quantization rule to the case of quasistationary states is examined in Section 5. By way of example, we discuss a calculation of the positions and widths of Stark resonances in a hydrogen atom placed in a strong electric field.

2. SEMICLASSICAL APPROXIMATION AND CALCULATION OF WAVE FUNCTIONS IN THE SUBBARRIER REGION

2.1. Modified Matching Conditions

It is well known [1–5] that, in the one-dimensional case, the matching of semiclassical wave functions on the two sides of the turning point $x = x_0$,

$$\psi^{\mathrm{WKB}}(x) = \begin{cases} \dfrac{C}{\sqrt{p(x)}}\cos\left(\displaystyle\int_{x_0}^{x} p\,dx - \pi\gamma\right) \text{ for } x > x_0 & (2.1) \\ \dfrac{C'}{\sqrt{|p(x)|}}\exp\left(-\displaystyle\int_{x}^{x_0} |p|\,dx\right) \text{ for } x < x_0, & (2.1') \end{cases}$$

[$p(x; E) = \sqrt{2[E - U(x)]}$ is the semiclassical momentum] for smooth potentials $U(x)$ is determined by the Kramers conditions [12]

$$C'/C = \frac{1}{2}, \quad \gamma = \frac{1}{4}. \tag{2.2}$$

For these conditions to be valid, it is required that the vicinity of the turning point where the linear expansion of the potential

$$U(x) = U(x_0) + F(x - x_0), \quad |x - x_0| \ll 1, \tag{2.3}$$

is valid overlap the region

$$|d(1/p(x))/dx| \ll 1, \tag{2.4}$$

where the use of the semiclassical expansion is justified. It is also well known that, in the three-dimensional case, there arises a complication for states whose orbital angular momentum is nonzero. The point is that, in Eq. (1.2) for the radial wave function $\chi_l(r)$, the potential $V(x)$ is replaced by the effective potential

$$U(r) = V(r) + \frac{l(l+1)}{2r^2}, \tag{2.5}$$

and the condition ensuring the applicability of the semiclassical approximation is violated at small distances because of the presence of the centrifugal potential.

This difficulty was circumvented by Langer [14], who showed that, with the aid of the transformation

$$r = e^x, \quad \psi(x) = e^{-x/2}\chi_l(e^x), \quad -\infty < x < \infty, \tag{2.6}$$

the radial Schrödinger equation is reduced to the form

$$\frac{d^2\psi(x)}{dx^2} + p^2(x)\psi(x) = 0,$$
$$p^2(x) = [k^2 + g^2 v(e^x)]e^{2x} - (l + 1/2)^2, \tag{2.7}$$

for which the subbarrier region $x \longrightarrow -\infty$ is a region where the semiclassical approximation is valid. This ensures, among other things, a correct dependence of the radial function on the orbital angular momentum at small distances. Indeed, it follows from (2.1'), (2.6), and (2.7) that

$$\chi_l^{\mathrm{WKB}}(r) = \frac{C'}{\sqrt{p^{(\mathrm{L})}(r)}}\exp\left\{-\int_{r}^{r_-} |p^{(\mathrm{L})}(r)|\,dr\right\}$$
$$= c_l^{\mathrm{WKB}} r^{l+1} + \ldots, \quad r \longrightarrow 0, \tag{2.8}$$

where $r_- = e^{x_0}$ is a turning point and

$$p^{(\mathrm{L})}(r) = \left[k^2 + g^2 v(r) - \frac{\lambda^2}{r^2}\right]^{1/2}, \quad \lambda = l + \frac{1}{2}. \tag{2.9}$$

Thus, the requirement that the semiclassical approximation be valid for $r \longrightarrow 0$ leads to the substitution $l(l+1) \longrightarrow (l+1/2)^2$ in the centrifugal potential. The corresponding additional term is referred to as the Langer correction [1].

At $\lambda \sim 1$, it would be incorrect, however, to retain only linear terms in expanding the potential at the turning point in matching semiclassical solutions to Eq. (2.7), because the semiclassical approximation is not valid here. This can easily be demonstrated by considering the example of free motion—that is, the case of $g = 0$. In the vicinity of the turning point $x_0 = \ln(\lambda/k)$, we have $p(x) \approx \lambda\sqrt{2(x - x_0)}$, and condition (2.4), which ensures the applicability of the semiclassical approximation, yields

$$\lambda^{-2/3} \ll |x - x_0| \ll 1.$$

These inequalities are satisfied only if $\lambda \gg 1$—that is, if $l \gg 1$, in which case the centrifugal potential becomes semiclassical. At low values of the orbital angular momentum, the matching rules (2.2) must be modified [11, 13, 15, 16].

The semiclassical wave functions can be matched, provided that exact solutions to the Schrödinger equation are known in the region where the semiclassical approximation is not valid. Below, we therefore discuss three typical possibilities, assuming a power-law behavior of the potential for $r \longrightarrow 0$,

$$V(r) = \frac{g^2}{\alpha} r^{\alpha}, \quad \alpha > -2. \tag{2.10}$$

To be more specific, we consider attractive potentials such that collapse into the center does not occur (see [2]).

2.1.1. Matching at high energies. With increasing energy, the turning point r_- approaches zero and x_0 tends to negative infinity. By virtue of (2.10), the term involving the potential can therefore be discarded in Eq. (2.7), whereupon it is solved in terms of Bessel functions. Such a solution makes its possible to pass through the turning point and match [13, 15] the semiclassical asymptotic expressions (2.1), whereby one obtains

$$C'/C = \frac{1}{2}\xi(\lambda), \quad \gamma = \frac{1}{4}, \tag{2.11}$$

$$\xi(\lambda) = \sqrt{2\pi}\lambda^{\lambda - 1/2} e^{-\lambda}/\Gamma(\lambda), \quad \lambda = l + \frac{1}{2}. \tag{2.12}$$

We note that $\xi(1/2) = \sqrt{2/e} = 0.8578$ and $\xi(1) = \sqrt{2\pi}e^{-1} = 0.9221$ and that, with increasing x, the function $\xi(x)$ approaches unity,

$$\xi(x) = 1 - \frac{1}{12x} + \frac{1}{288x^2} + \ldots, \quad x \longrightarrow \infty, \tag{2.12'}$$

so that, for $l \gg 1$, relations (2.11) reduce to the Kramers matching conditions (2.2).

2.1.2. Matching in the case of level condensation. For power-law potentials—that is, in the cases where the dependence given by (2.10) is valid over the entire interval $0 < r < \infty$, it follows from simple scaling considerations and from the Bohr–Sommerfeld quantization rule that

$$E_{n_r} \propto n_r^{2\alpha/(2+\alpha)}, \quad \langle r \rangle \propto n_r^{2/(2+\alpha)}, \quad n_r \gg 1. \tag{2.13}$$

If $\alpha < 0$, then $E_{n_r} \longrightarrow -0$ for $n_r \longrightarrow \infty$; that is, energy levels are condensed at the boundary of the continuum [2]. In Eq. (2.7), the energy can then be disregarded against the potential (this is true for finite energy values as well). As in the preceding case, the resulting equation can be solved exactly, so that we eventually obtain [11, 13]

$$C'/C = \frac{1}{2}\xi(\mu), \quad \gamma = \frac{1}{4}, \quad \mu = \frac{2l+1}{2+\alpha}, \quad -2 < \alpha < 0, \tag{2.14}$$

where the function $\xi(x)$ is given by the same expression as before.

In the cases considered above, it is possible to find a correction to the matching conditions (2.11) and (2.14) [16].

At high energies, the inclusion of the potential yields

$$C'/C = \frac{1}{2}\{1 - b_l^{\mathrm{WKB}}(E)\}\xi(\lambda), \tag{2.15}$$

where

$$b_l^{\mathrm{WKB}}(E) = \frac{g^2\Gamma(\alpha/2)}{4k^{2+\alpha}}\left\{\frac{2^{1+\alpha}\Gamma(1+\alpha/2)\Gamma(1+\lambda+\alpha/2)}{\Gamma(2+\alpha)\Gamma(\lambda-\alpha/2)} - \frac{\sqrt{\pi}\lambda^{1+\alpha}}{\Gamma((3+\alpha)/2)}\right\}. \tag{2.15'}$$

From the last expression, it follows that, at the particular values of $\alpha = -1$ and 0 [the last case corresponds to the logarithmic potential $V(r) = g^2 \ln r$], we have

$$b_l^{\mathrm{WKB}} = 0, \quad b_l^{\mathrm{WKB}} = \left(\frac{g}{k}\right)^2\left[\lambda\psi(\lambda) - \lambda\ln\lambda + \frac{1}{2}\right], \tag{2.15''}$$

where $\psi(z) = \Gamma'(z)/\Gamma(z)$ is a digamma function. Since, for $n_r \gg 1$, it follows from (2.13) and (2.15') that $b_l \propto n_r^{\alpha}$, it is legitimate to retain the above correction to the conditions in (2.11) only for $\alpha \leq 2$.

The inclusion of the potential also yields a correction to the phase [13],

$$\gamma = \frac{1}{4}[1 - 2\beta_l^{\mathrm{WKB}}(E)], \quad \beta_l^{\mathrm{WKB}}(E) = -\frac{1}{\pi}\tan\frac{\pi\alpha}{2} b_l^{\mathrm{WKB}}(E), \quad \alpha < 1. \tag{2.16}$$

At the particular values of $\alpha = -1$ and 0, we have

$$\beta_l^{\mathrm{WKB}} = \frac{g^2}{\pi k}[\ln\lambda - \psi(\lambda + 1/2)], \quad \beta_l^{\mathrm{WKB}} = 0. \tag{2.16'}$$

Under the condition $-2 < \alpha < 0$, in which case the levels condense near the boundary of the continuum, the correction for the energy [see Eq. (2.15')] has the form

$$b_l^{\mathrm{WKB}} = -\frac{\Gamma(2/(2+\alpha))}{(2+\alpha)\lambda}\left(\frac{|\alpha|\lambda^2}{2g^2}\right)^{2/(2+\alpha)} \times \left\{\frac{\sqrt{\pi}}{\Gamma((6+\alpha)/(4+2\alpha))} - \frac{2+\alpha}{2(\lambda-1)}\left(\frac{2+\alpha}{\lambda}\right)^{(2-\alpha)/(2+\alpha)} \times \frac{\Gamma(2/(2+\alpha))\Gamma(2(\lambda+1)/(2+\alpha))}{\Gamma(4/(2+\alpha))\Gamma(2(\lambda-1)/(2+\alpha))}\right\}E. \tag{2.17}$$

By way of example, we indicate that, for the Coulomb potential ($\alpha = -1$), the result is

$$C'/C = \frac{1}{2}\left[1 - \frac{2l+1}{24g^4}E\right]\xi(2l+1). \quad (2.18)$$

2.1.3. Coulomb singularity at the origin. The dependence of the matching conditions on energy over the entire interval of its variation can be obtained in the physically important case of potentials that have a Coulomb singularity at small distances,

$$V(r) = -\frac{Z}{r} + u(r), \quad u(r) = o(r^{-1}). \quad (2.19)$$

No constraints are imposed on $u(r)$ at large distances. If we disregard $u(r)$, the radial Schrödinger equation can be solved in terms of Coulomb functions, whereby one obtains [15]

$$C'/C = \frac{1}{2}\xi(l,\eta), \quad \gamma = \frac{1}{4}[1 - 2\Theta(l,\eta)], \quad (2.20)$$

where

$$\xi(l,\eta) = \xi(\lambda)Q_l(\eta)\exp\{-\lambda f(\lambda/\eta)\}, \quad (2.20')$$

$$\Theta(l,\eta) = \frac{2}{\pi}\left\{\sigma_l(\eta) - \eta\left[\frac{1}{2}\ln\eta^2 - h(-\lambda/\eta)\right]\right\}. \quad (2.20'')$$

Here, $\lambda = l + 1/2$; $\eta = -(\mathrm{sgn}z)/ka_B$ is the Sommerfeld parameter ($\eta < 0$ in the case of Coulomb attraction); $\sigma_l(\eta) = \arg\Gamma(l + 1 + i\eta)$ is the Coulomb phase shift; $a_B = |Z|^{-1}$ is the Bohr radius; and

$$Q_l(\eta) = \exp(\pi|\eta|/2)|\Gamma(l+1+i\eta)|/\Gamma(l+1),$$

$$f(z) = \frac{1}{2}\ln(1+z^{-2}) + (\arctan z)/z, \quad (2.20''')$$

$$h(z) = 1 - \frac{1}{2}\ln(1+z^2) - \mathrm{arccot}\, z.$$

For $E \longrightarrow \infty$ and $E \longrightarrow 0$, the matching conditions (2.20) reduce to (2.11) and (2.14), respectively. By way of example, we indicate that, for $\eta \longrightarrow 0$ ($E \longrightarrow \infty$), the result is

$$\xi(l,\eta) = \xi(\lambda)\left[1 + \frac{a_l}{(ka_B)^2} + \ldots\right], \quad (2.21)$$

where $a_l = \frac{1}{2l+1} - \frac{1}{2}\psi'(l+1)$, so that $a_0 = 0.1775$, $a_1 = 0.0109$, $a_2 = 0.0025$, etc. On the other hand, it can be found that, for $\eta \longrightarrow \infty$ ($E \longrightarrow 0$),

$$\xi(l,\eta) = \xi(2\lambda)\left[1 - \frac{\lambda}{24}(ka_B)^2 + \ldots\right]. \quad (2.22)$$

It can easily be seen that expressions (2.21) and (2.22) comply with (2.15'') and (2.18), respectively.

In these limiting cases, we find for the function $\Theta(l, \eta)$ that

$$\Theta(l,\eta) = \begin{cases} (2/\pi)[\psi(l+1) - \ln\lambda]\eta & \text{for } \eta \longrightarrow 0 \\ (12\pi\eta)^{-1}[1 - (\lambda^2 - 7/120)\eta^{-2}] & \text{for } \eta \longrightarrow \infty \end{cases} \quad (2.23)$$

[compare with expressions (2.16')]. At high orbital angular momenta, we have

$$\xi(l,\eta) = 1 - \frac{1}{8\lambda} + O(\lambda^{-2}),$$
$$\Theta(l,\eta) = \frac{\eta}{12\pi\lambda^2} + O(\lambda^{-4}); \quad (2.24)$$

that is, the conditions in (2.20) reduce, as might have been expected, to the Kramers conditions.

Since the semiclassical phase differs from the conventional value of $\pi/4$, the quantization rule assumes here the form

$$\frac{1}{\pi}\int_{r_-}^{r_+} p^{(L)}(r)dr = n_r + \frac{1}{2}[1 - \Theta(l,\eta)],$$
$$n_r = 0, 1, 2, \ldots, \quad (2.25)$$

where $r_\pm$ are the semiclassical turning points ($0 < r_- < r_+$). Equation (25) generalizes the Bohr–Sommerfeld quantization rule with allowance for the Langer correction. As can be seen from (2.23) and (2.24), the additional term $\Theta(l, \eta)$ in Eq. (2.25) is small and can therefore be taken into account within perturbation theory. The result is

$$\Delta E_{nl} = -\frac{1}{2}\omega_{nl}\Theta(l,\eta), \quad (2.26)$$

where we have used the conventional notation $\omega_{nl} = \partial E_{nl}/\partial n = 2\pi/T_r$, with

$$T_r = 2\int_{r_-}^{r_+} \frac{dr}{p^{(L)}(r)} \quad (2.27)$$

being the period of radial oscillations of the particle between the turning points r_- and r_+.

If, at large distances, the function $u(r)$ introduced in (2.19) behaves as

$$u(r) \propto r^\alpha, \quad r \longrightarrow \infty, \quad \alpha > 0,$$

it can be deduced from (2.23), with allowance for the scaling properties (2.13), that $\Theta \propto n_r^{-\alpha/(2+\alpha)}$, which is parametrically greater than n_r^{-1}. Thus, we conclude that, even for sharply varying potentials with $\alpha \gg 1$, it is legitimate to take into account the correction in (2.25) since it exceeds the $\hbar$ semiclassical correction,

Table 1. Asymptotic coefficients at the origin for the power-law potentials $V(r) = \frac{1}{\alpha} r^{\alpha}$

α	n_r	l	c_{nl}^2	ρ_{nl}^{WKB}	ρ_{nl}^{MQ}	$\rho_{nl}^{(1/n)}$
1	0	0	2	–2.03	0	–0.074
	1	0	2	–0.459	0	–1.98
	0	1	0.85326	–3.94	1.28	–0.040
	1	1	1.45153	–0.88	0.56	–0.79
4	0	0	2.89797	0.29	0.34	–4.24
	1	0	6.78220	0.044	0.046	–17.0
	0	1	3.05888	–2.97	3.59	–1.46
	1	1	12.3423	–0.51	1.18	–7.78

Note: The uncertainties of the calculation of ρ_{nl} are given in percent.

Table 2. Asymptotic coefficients at the origin for the logarithmic potential $V(r) = \ln r$

n_r	l	c_{nl}^2	$\tilde{\rho}_{nl}^{\mathrm{WKB}}$	ρ_{nl}^{WKB}	ρ_{nl}^{MQ}	$\rho_{nl}^{(1/n)}$
0	0	1.951659	–12.6	5.17	17.3	–0.63
1	0	0.995922	–7.36	1.16	7.21	–8.36
2	0	0.678730	–5.85	0.82	5.09	–
0	1	0.339568	–9.14	–5.35	–	–0.17
1	1	0.326674	–4.70	–1.85	–4.49	–3.10
2	1	0.294457	–3.53	–1.12	–3.33	–

Note: A dash instead of the corresponding value means that the uncertainty in this value exceeds 25%.

which translates into an n_r^{-1} correction in the quantization rule.

2.2. Asymptotic Coefficient in the Wave Function at the Origin

The asymptotic coefficients c_{nl} [see Eq. (1.3)], which determine the probability of finding the particles at small distances from one another, are parameters that are especially important for systems governed by interactions featuring two markedly different radii (for example, nuclear and Coulomb interactions).

According to Eqs. (2.8), (2.11), and (2.14), we have

$$c_{nl}^{\mathrm{WKB}} = \xi(\tau) c_{nl}^{(\mathrm{L})} (1 - b_l^{\mathrm{WKB}}),$$
$$c_{nl}^{(\mathrm{L})} = (\lambda T_r)^{-1} r_-^{-\lambda} \exp\left\{ \int_0^{r_-} \left[\frac{\lambda}{r} - \left| p^{(\mathrm{L})}(r) \right| \right] dr \right\} \quad (2.28)$$

($\tau = \lambda$ for $\alpha > 0$ and $\tau = \mu$ for $\alpha < 0$), where we have used the semiclassical normalization condition [1, 2, 17]

$$C = 2 T_r^{-1/2} [1 + O(1/n^2)]. \quad (2.29)$$

Since the coefficients $c_{nl}^{(\mathrm{L})}$ were obtained with the aid of the conventional normalization condition (2.2), a nontrivial point is that the factor $\xi(\tau)$ is present in (2.28).

Let us discuss the accuracy of the semiclassical formula (2.28). We begin by considering the exactly soluble problems of a harmonic oscillator ($\alpha = 2$) and a Coulomb potential ($\alpha = -1$). For those, we have

$$\frac{c_{nl}^{(\mathrm{L})}}{c_{nl}} = \frac{\zeta(n_r + \tau)}{\zeta(n_r)\xi(\tau)}, \quad \tau = \begin{cases} l + 1/2 & \text{for } \alpha = 2 \\ 2l + 1 & \text{for } \alpha = -1, \end{cases} \quad (2.30)$$

where

$$\zeta(x) = \left(1 + \frac{1}{2x}\right)^{1/4} \xi(x) \left[\frac{\xi(x + 1/2)}{\xi(2x)} \right]^{1/2} = 1 + \frac{1}{48x} - \frac{47}{4608x^2} + \ldots. \quad (2.31)$$

From (2.30), it can be seen that, for $n_r \longrightarrow \infty$—that is, for states whose radial wave functions have a large number of nodes—the ratio $c_{nl}^{(\mathrm{L})}/c_{nl}$ has a limit different from unity,

$$\lim_{n_r \to \infty} c_{nl}^{(\mathrm{L})}/c_{nl} = [\xi(\tau)]^{-1}.$$

Thus, the semiclassical approximation that employs the rule in (2.2) for circumventing the turning point is asymptotically exact for $\psi^2(0)$ when $n_r \longrightarrow \infty$ at fixed l (this result was obtained as far back as 1979 [18], but no proper attention was given to it at that time). This contradiction is removed by using modified matching rules such that

$$\left[\frac{c_{nl}^{\mathrm{WKB}}}{c_{nl}} \right]^2 = \left[\frac{\zeta(n_r + \tau)}{\zeta(n_r)} \right]^2 = 1 - \frac{\tau}{24 n_r^2} + O(n_r^{-3}). \quad (2.33)$$

It should be noted that, even in the case of the ground state ($n_r = 0$), this ratio is close to unity, amounting to 0.9679 and 0.9557 for $\alpha = 2$ and –1, respectively.

For the power-law attractive potentials characterized by $\alpha = 1$ and 4 and for the logarithmic potential, the values of the asymptotic coefficients at the origin and of the errors

$$\rho_{nl}^{\mathrm{WKB}} = \left[\frac{c_{nl}^{\mathrm{WKB}}}{c_{nl}} (1 - b_l^{\mathrm{WKB}}(E)) \right]^2 - 1 \quad (2.34)$$

are given in Tables 1 and 2 (for the energy values, the reader is referred to Table 2 of the first study quoted in [13]). Since the scaling relations

$$E_{nl}(g) = g^{4/(2+\alpha)} E_{nl}(1), \quad c_{nl}(g) = g^{(2l+3)/(2+\alpha)} c_{nl}(1) \quad (2.35)$$

hold for the power-law potentials (2.10) [19, 20], it is sufficient to consider only the case of $g = 1$, as was

indeed done in the aforementioned tables. For the logarithmic potential $V(r) = g^2 \ln r$, we have

$$E_{nl}(g) = g^2[E_{nl}(1) - \ln g], \quad c_{nl}(g) = g^{l+3/2} c_{nl}(1). \tag{2.35'}$$

For the example of this potential, the role of the correction in (2.15) in the matching conditions was demonstrated for modest values of n_r and l: the parameter $\tilde{\rho}_{nl}^{\mathrm{WKB}}$ in Table 2 is determined by Eq. (2.34) with $b_l^{\mathrm{WKB}} = 0$.

Table 3 also illustrates the accuracy of the modified matching conditions for the funnel potential [20, 21]

$$V(r) = -\frac{Z}{r} + \frac{1}{2}r, \quad 0 < r < \infty, \tag{2.36}$$

which is written here in the standard form. For the Coulomb parameter $Z = 0.68812$ [Cornell potential, which is used in QCD to describe charmonium ($\bar{c}c$) states], the precise values of the energies and of the coefficients c_{nl} were obtained by numerically solving the Schrödinger equation and were partly reported in [22].

Tables 1–3 demonstrate that the semiclassical approximation with the modified matching conditions for the coefficients c_{nl}, which is asymptotically exact in the limit $n_r \longrightarrow \infty$, remains valid down to values of $n_r \sim 1$. As was shown in [13], the same is true for short-range potentials in all cases with the exception of that of shallow levels.

2.3. States at Zero Energy

This case requires a dedicated consideration, because the asymptotic behavior of the wave function of a bound state (that is, an $l \geq 1$ state since the wave functions for s states are delocalized for $E \longrightarrow 0$) changes: for $r \longrightarrow \infty$, $\chi_l(r, E = 0)$ decreases in proportion to r^{-l} rather than in proportion to an exponential. Therefore, the conventional normalization condition (2.29) must accordingly be modified.

For potentials featuring a power-law tail at infinity,

$$V(r) = -\frac{1}{2}g^2 r^{-\beta}, \quad \beta > 2, \tag{2.37}$$

a finite contribution to the normalization comes from the subbarrier region $r > r_+$ (in contrast to what we have in the case of $E < 0$). At zero energy, the Schrödinger equation with the potential (2.37) is solved in terms of Bessel functions. By using the resulting solution, we find instead of (2.29) that [23]

$$C = 2R_l^{1/2}(\beta) T_r^{-1/2}, \tag{2.38}$$

where

$$R_l(\beta) = \left(\frac{\beta - 2}{2l + 1}\right)^{\frac{\beta+2}{\beta-2}} \frac{\Gamma((2l + 1 + \beta)/(\beta - 2))}{\Gamma((2l - 1)/(\beta - 2))}. \tag{2.39}$$

Table 3. Asymptotic coefficients at the origin and energies of the levels for the funnel potential $V(r) = -0.68812r^{-1} + (1/2)r$

n_r	l	c_{nl}^2	E_{nl}	ρ_{nl}^{WKB}	ρ_{nl}^{MQ}	$\varepsilon_{nl}^{\mathrm{MQ}}$
0	0	4.34022	0.49018	–1.5	8.2	–13
1	0	2.76673	1.61443	–1.4	1.0	–0.50
2	0	2.35982	2.42105	–0.97	0.46	–0.16
0	1	0.80452	1.30557	–6.5	2.3	–3.8
1	1	1.14509	2.14835	–2.5	1.8	–1.4
2	1	1.39408	2.85424	–1.5	1.3	–0.72

Note: The quantity in the last column is $\varepsilon_{nl}^{\mathrm{MQ}} = E_{nl}^{\mathrm{MQ}}/E_{nl} - 1$ (in percent); see Eqs. (3.2) and (3.14).

It can easily be shown that

$$R_l(\beta) = 1 - \frac{\beta(\beta + 2)}{12(\beta - 2)l^2} + \ldots, \quad l \gg 1, \tag{2.40}$$

whence it follows that, at high orbital angular momenta, relation (2.38) reduces to the conventional normalization condition. At the same time, we have

$$R_l(\beta) = \frac{2l - 1}{2l + 1}\left\{1 - \frac{4}{\beta}[\ln(2l + 1) - \mathscr{C}] + \ldots\right\}, \quad \beta \longrightarrow \infty, \tag{2.41}$$

where $\mathscr{C} = 0.5772\ldots$ is the Euler constant.

By way of example, we consider the Tietz potential ($\beta = 3$)

$$V(r) = -\frac{Ze^2}{r(1 + \kappa_0 r)^2}, \tag{2.42}$$

which is extensively used in atomic physics [24–26]. The critical values of the effective coupling constant $g_{nl} = \sqrt{2Z_{nl}/\kappa_0 a_{\mathrm{B}}}$ that correspond to the emergence of the nl level can be found from an exact solution to the Schrödinger equation or from the Bohr–Sommerfeld quantization rule,

$$g_{nl} = \sqrt{(n + l)(n + l + 1)}, \quad g_{nl}^{\mathrm{WKB}} = n + l + \frac{1}{2}. \tag{2.43}$$

For $n \longrightarrow \infty$, we find from (2.43) that

$$\frac{g_{nl}^{\mathrm{WKB}}}{g_{nl}} = 1 + \frac{1}{(2n + 2l + 1)^2} + \ldots \longrightarrow 1. \tag{2.43'}$$

For finite n and l, the semiclassical method ensures a precision for g_{nl} at a level of a few percent.

At the coupling-constant value corresponding to the emergence of a level, we have

$$\chi_{nl}(r) = c_{nl}\frac{n_r!\Gamma(4l+3)}{\Gamma(n_r+4l+3)}\frac{r^{l+1}}{(r+1)^{2l+1}}C_{n_r}^{2l+3/2}\left(\frac{1-r}{1+r}\right), \quad (2.44)$$

where $C_n^{2l+3/2}(x)$ are Gegenbauer polynomials, those at $n = 0$ and 1 being, respectively, $C_0^{2l+3/2}(x) = 1$ and $C_1^{2l+3/2}(x) = (4l+3)x$ (see, for example, [27]), while c_{nl} are the asymptotic coefficients at the origin. Explicitly, these coefficients are given by

$$c_{nl}^2 = \frac{(l+1)(2l+3)\Gamma(n_r+4l+3)}{\Gamma(2l-1)\Gamma(2l+2)\Gamma(n_r+1)\Sigma(n_r,l)}, \quad (2.45)$$

where

$$\Sigma(n_r,l) = \sum_{k=0}^{4}\sigma_k n_r^k,$$

$$\sigma_0 = 4(l+1)^2(2l+1)(2l+3), \quad (2.45')$$

$$\sigma_1 = 4(l+1)(4l+3)^2, \quad \sigma_2 = (4l+3)(16l+13),$$

$$\sigma_3 = 6(4l+3), \quad \sigma_4 = 3.$$

With allowance for (2.28) and (2.38), it can be found in this case that

$$[c_{nl}^{\mathrm{WKB}}]^2 = \xi^2(\mu)R_l(3)[c_{nl}^{(\mathrm{L})}]^2, \quad (2.46)$$

$$[c_{nl}^{(\mathrm{L})}]^2 = \frac{\exp\{\mu[(z+1)\ln(z+1)-(z-1)\ln(z-1)]\}}{4\pi z^2(3z^2-2)}, \quad (2.46')$$

where

$$R_l(3) = \left(1-\frac{1}{\mu^2}\right)\left(1-\frac{4}{\mu^2}\right), \quad z = \frac{2n+\mu}{2\mu}, \quad \mu = 2l+1. \quad (2.46'')$$

As a result, we obtain $R_l(3) = 0.4934$, 0.8082, and 0.8997 at $l = 1$, 2, and 3, respectively. For $n_r \gg 1$, we have

$$\left[\frac{c_{nl}^{\mathrm{WKB}}}{c_{nl}}\right]^2 = 1-\frac{2l-1}{12n^2}+O(n^{-3}), \quad (2.47)$$

which explains the astoundingly high accuracy of the semiclassical approximation in this case (see Table 6 in [13]).

3. MODIFIED QUANTIZATION METHOD

3.1. Elimination of the Centrifugal Potential from the Semiclassical Momentum

Since, for excited states ($n_r \gg 1$), the centrifugal potential at $l \sim 1$ is operative only in the region of small distances and since, over the region where the particle is predominantly localized, this potential appears as a perturbation of order $\hbar^2$ [see also Eq. (2.13)], it can removed from the semiclassical momentum $p^{(\mathrm{L})}(r)$, whereupon the semiclassical radial function can be represented in the form

$$\chi_{El}^{\mathrm{MQ}}(r) = \frac{C}{\sqrt{p(r)}}\cos\left\{\int_0^r p(r)dr - \pi\gamma_l\right\}, \quad (3.1)$$

$$p(r) = [k^2+g^2v(r)]^{1/2}.$$

The parameter γ_l is determined by matching $\chi(r)$ in the form (3.1) with the function that exactly satisfies the Schrödinger equation and the boundary condition (1.3). Obviously, the result depends on the small-distance behavior of the potential. For the energies of the nl levels in the attractive potentials (2.10), we have [28–30]

$$\frac{1}{\pi}\int_0^{r_+} p(r)dr = n_r+\gamma_l, \quad (3.2)$$

where $p(r_+) = 0$, $r_- = 0$ is the left-hand turning point, and

$$\gamma_l = \begin{cases}(2l+3)/4 & \text{for } \alpha > 0\\ (2l+3+\alpha)/2(2+\alpha) & \text{for } -2 < \alpha < 0.\end{cases} \quad (3.3)$$

We note that, in the particular case of the Coulomb potential, the quantization condition (3.2) with $\gamma_l = l+1$ was obtained in the monograph [1].

By means of the modified quantization method, the asymptotic coefficients at origin are found to be [31]

$$c_{nl}^{\mathrm{MQ}} = c_{nl}^{(0)}\{1-b_l^{\mathrm{MQ}}(E)\}, \quad (3.4)$$

where, at high energies, we have

$$[c_{nl}^{(0)}]^2 = \frac{2\pi}{T\Gamma^2(l+3/2)}(E/2)^{(2l+1)/2}, \quad T = 2\int_0^{r_+}\frac{dr}{p(r)} \quad (3.5)$$

and where $b_l^{\mathrm{MQ}}(E)$ coincides with the first term in (2.15'),

$$b_l^{\mathrm{MQ}}(E) = \frac{g^2}{k^{2+\alpha}}\frac{2^{\alpha-2}\alpha\Gamma^2(\alpha/2)\Gamma(1+\lambda+\alpha/2)}{\Gamma(2+\alpha)\Gamma(\lambda-\alpha/2)}, \quad \lambda = l+\frac{1}{2}. \quad (3.6)$$

In the particular cases of the Coulomb and the linear potential ($\alpha = -1$ and $\alpha = 1$, respectively), we have

$$b_l^{\mathrm{MQ}} = -\frac{\pi g^2}{2k}, \quad b_l^{\mathrm{MQ}} = g^2\frac{\pi l(l+1)}{4k^3}. \tag{3.6'}$$

For the cases of power-law potentials and a logarithmic potential, the accuracy of the calculation of c_{nl} on the basis of Eqs. (3.4)–(3.6), which were derived within the modified quantization method, is illustrated in Tables 1 and 2 (see also [31]).

In the case of the condensation of levels ($E \longrightarrow -0$) for $-2 < \alpha < 0$, we obtain

$$[c_{nl}^{(0)}]^2 = \frac{2\pi}{T}\left(\frac{g^2}{|\alpha|}\right)^{\mu}\frac{2^{\mu+1}}{(2+\alpha)^{2\mu+1}\Gamma^2(\mu+1)}, \qquad \mu = \frac{2l+1}{2\alpha}, \tag{3.7}$$

$$b_l^{\mathrm{MQ}} = \frac{\sin\pi(\mu - 2\alpha/(2+\alpha))}{\alpha\sin(\pi\mu)}\left(\frac{(2+\alpha)|\alpha|}{2g^2}\right)^{2/(2+\alpha)} \times \frac{\Gamma(4\alpha/(2+\alpha))\Gamma(1-2\alpha/(2+\alpha))\Gamma(\mu-2\alpha/(2+\alpha))}{\Gamma(2\alpha/(2+\alpha))\Gamma(1+\mu+2\alpha/(2+\alpha))}k^2. \tag{3.8}$$

In particular, the result for the Coulomb potential $V(r) = -Z/r$ is

$$[c_{nl}^{\mathrm{MQ}}]^2 = Z^{2l+3}\frac{4^{l+1}}{[(2l+1)!]^2 n^3}\left\{1 - \frac{l(l+1)(2l+1)}{6n^2}\right\}, \tag{3.8'}$$

which coincides with the expansion of the exact expression for the coefficients c_{nl} [2].

3.2. Funnel Potential

Within the modified quantization method, we further consider the funnel potential (2.36). In this case, the quantization integral (3.2) can be calculated analytically. The result is

$$\nu\, {}_2F_1(1/4, 3/4, 2; -8Z^{-3}\nu^4) = N, \tag{3.9}$$

where $N = n_r + \gamma_l$ and $\nu = Z(-2E)^{-1/2}$. Let us now discuss two extreme cases.

(i) For deep levels, which are determined primarily by the Coulomb potential ($E < 0$ and $N \equiv n$ is the principal quantum number), we find from (3.9) that

$$\frac{1}{\nu_n} = \frac{Z}{n}\left(1 - \frac{3}{4}f - \frac{1}{16}f^2 - \frac{39}{128}f^3 + \ldots\right), \qquad f \longrightarrow 0, \tag{3.10}$$

where $f = n^4/Z^3$ is the effective coupling constant.

A perturbation-theory series for screened Coulomb potentials of the general form

$$V(r) = \frac{Z}{r}\sum_{k=0}^{\infty} v_k r^k$$

was constructed by McEnnan *et al.* [32] and Crant and Lai [33], who showed that

$$\frac{1}{\nu_{nl}} = \frac{Z}{n}\left\{1 - \frac{1}{4}(3-\rho^2)f - \frac{1}{16}\left(1 - 3\rho^2 + 2\rho^4 - \frac{5}{2n^2}\right)f^2 - \frac{1}{128}\left(39 - 20\rho^2 + 11\rho^4 - 14\rho^6 + \frac{60}{n^2} + \frac{5\rho^2}{n^2}\right)f^3 - \ldots\right\}, \tag{3.11}$$

where $\rho = \sqrt{l(l+1)}/n$. A comparison of (3.10) and (3.11) reveals that the semiclassical Eq. (3.9) is a good approximation for $n \gg (1, l)$, especially for *s* states.

(ii) In another extreme case—that where $Z \longrightarrow 0$, $E > 0$, and $N = n - (2l+1)/4$—it is necessary to perform an analytic continuation of Eq. (3.9) to positive energy values $E \equiv \epsilon/2 > 0$ (a similar situation arises in the theory of the Stark effect in a strong electric field [34, 35]):

$$Z(\epsilon^2 + 8Z)^{-1/4}\, {}_2F_1\left(1/2, 5/2, 2; \frac{1}{2}\left[1 + \frac{\epsilon}{(\epsilon^2+8Z)^{1/2}}\right]\right) = N. \tag{3.12}$$

It follows that

$$\epsilon = \epsilon_0\{1 + 2\zeta[\ln\zeta - (2\ln 2 + 1)] + O(\zeta^2\ln\zeta)\}, \tag{3.13}$$

where

$$\epsilon_0 = (3\pi N/2)^{2/3}, \quad \zeta = \frac{1}{2}\frac{Z}{(\pi N)^{4/3}}. \tag{3.13'}$$

At $l = 0$, ϵ_0 coincides with the semiclassical spectrum in the linear potential. The expansion in (3.13) involves the term $\zeta\ln\zeta$, which is nonanalytic in ζ. For potentials featuring a Coulomb singularity at the origin, it can be shown, however, that, in the quantization rule (3.2), it is possible to obtain explicitly [31] a correction associated with taking into account the potential at small distances:

$$\gamma_l \longrightarrow \gamma_l + \gamma_l^{(1)}, \qquad \gamma_l^{(1)} = \frac{1}{\pi k a_{\mathrm{B}}}[\ln(k a_{\mathrm{B}}) + \psi(l+1) + 1], \quad k a_{\mathrm{B}} \gg 1. \tag{3.14}$$

In this case, the introduction of this correction is equivalent to the substitution

$$N \longrightarrow N\left\{1 - \frac{Z}{\pi N\epsilon_0^{1/2}}[\ln(Z/\epsilon_0^{1/2}) - \psi(l+1) - 1]\right\},$$

which compensates the term that is nonanalytic in Z:

$$\epsilon = \epsilon_0\{1 - 2\zeta[\ln(3\pi N) + 2\ln 2 - \psi(l+1)] + O(\zeta^2)\}. \quad (3.15)$$

It can be seen that not only does the correction in (3.14) to the quantization rule lead to the qualitative agreement between the semiclassical and the exact spectrum, but it also ensures a correct analytic dependence of energy levels on the parameters that determine the small-distance behavior of the potential.

For states at high energies $E_{n_r l} > 0$, the asymptotic coefficients at zero can be computed by the formula

$$c_{nl}^{\mathrm{MQ}} \approx c_{nl}^{(0)}\{1 - b_l^{(\mathrm{C})}\}\{1 - b_l^{(\mathrm{L})}\}, \quad (3.16)$$

where the coefficients $c_{nl}^{(0)}$ are specified in (3.5) and where the correction terms $b_l^{(\mathrm{C})}$ and $b_l^{(\mathrm{L})}$ are given by expressions (3.6') and are associated with, respectively, the Coulomb component of the potential (2.36) and its component that is linear in r. As to the energy E_{nl}^{MQ}, it is determined from the quantization condition (3.2) with phase $\gamma_l = (2l+3)/4 + \gamma_l^{(1)}$ [see Eq. (3.14)]. For a potential that has a Coulomb singularity at the origin, it is possible, however, to refine expressions (3.4) and (3.16) by exactly taking into account the effect of this potential at any values of the energy $E = k^2/2 > 0$. It can be shown [31] that, in (3.16), we must then make the substitution

$$1 - b_l^{(\mathrm{C})} \longrightarrow \left\{\frac{2\pi/ka_{\mathrm{B}}}{1 - \exp(-2\pi/ka_{\mathrm{B}})}\prod_{s=1}^{l}(1 + (ska_{\mathrm{B}})^{-2})^{-1}\right\}^{1/2} \approx 1 + \frac{\pi Z}{2k} + \frac{\pi^2 Z^2}{4k^2}\left[\frac{19}{6} + \frac{2}{\pi^2}\psi'(l+1) + \ldots\right] \quad (3.17)$$

(in the case of $l = 0$, the product in the braced expression must be taken to be unity).

In Table 3, the asymptotic coefficients at the origin that were calculated on the basis of the modified quantization method are contrasted against precise values obtained by numerically solving the Schrödinger equation. It can be seen that the semiclassical values c_{nl}^{MQ} are accurate to within a few percent. The same is true for all energies E_{nl}^{MQ}, with the exception of ground-state energy: the point is that, for the ground state, we have $ka_{\mathrm{B}} = 1.44$, but it is necessary, strictly speaking, that $ka_{\mathrm{B}} \gg 1$ for the quantization condition (3.2) and expression (3.14) to be applicable. Thus, we can see that, for the funnel potential (in just the same way as for power-law potentials), the modified quantization method ensures an acceptable accuracy in calculating the relevant energy levels and the asymptotic coefficients at the origin.

3.3. Asymptotic Coefficients at Infinity

Let us consider bound states of a particle for potentials vanishing at infinity,

$$V(r) = -Z/r + o(1/r^2) \quad \text{for} \quad r \longrightarrow \infty, \quad Z \geq 0. \quad (3.18)$$

The asymptotic expression for the normalized radial wave function then takes the form

$$\chi_{\kappa l}(r) \approx C_{\kappa l}\sqrt{\frac{\kappa}{\pi}}(\kappa r)^{\nu}e^{-\kappa r}, \quad (3.19)$$

where $\kappa = \sqrt{-2E}$ is the energy of a level, while $\nu = Z/\kappa$ is the effective principal quantum number, also denoted as n^*. The asymptotic coefficients $C_{\kappa l}$, along with the coefficients at the origin, are extensively used in quantum mechanics and its applications—in particular, applications to peripheral processes. Taking into account the asymptotic expression (3.18), we now express the semiclassical formulas for $C_{\kappa l}$ and the quantization condition in terms of the function $v(r)$ determining the form of the interaction potential (1.1). For the quantization condition, we have [29]

$$gJ(z) = N, \quad N = n_r + \gamma_l, \quad (3.20)$$

where

$$J(z) = \frac{1}{\pi}\int_0^{r_+(z)}\sqrt{v(r) - z^2}\,dr, \qquad v(r_+) = z^2, \quad z = \kappa/g, \quad (3.21)$$

and γ_l is defined in (3.3). Equation (3.20) determines the quantity z and the energies $E_N^{\mathrm{MQ}} = -\frac{1}{2}(gz)^2$ of the levels as functions of the coupling constant. For the asymptotic coefficients, we obtain

$$C_{\kappa l}^{\mathrm{MQ}} = [-8\pi gzJ'(z)]^{-1/2}(gzr_+(z))^{-Z/gz} \times \exp\{g[zr_+(z) - J_1(z) - (l+1/2)^2 J_2(z)]\}, \quad (3.22)$$

where

$$J_1(z) = \int_{r_+(z)}^{\infty}\left[\sqrt{z^2 - v(r)} - z + \frac{Z}{g^2 zr}\right)dr, \quad (3.23)$$

$$J_2(z) = \frac{1}{2}\int_{r_+(z)}^{\infty}\frac{dr}{r^2\sqrt{z^2 - v(r)}}. \quad (3.23')$$

The above formulas make it possible to calculate the energy spectra and the asymptotic coefficients quite straightforwardly. Let us consider a few examples where the calculations can be performed analytically.

(i) For an undistorted attractive Coulomb potential, we have $v(r) = 1/r$, $\gamma_l = l + 1$, $N \equiv n = n_r + l + 1$, $Z = g^2/2$, and

$$J(z) = \frac{1}{2z}, \quad r_+(z) = \frac{1}{z^2}, \quad z = \frac{g}{2n},$$

$$J_1(z) = -\frac{2\ln 2 - 1}{2z}, \quad J_2(z) = \frac{z^2}{g}.$$

It follows that the exact spectrum of Coulomb levels is $E_n = -Z^2/2n^2$ and that the semiclassical formula of the modified quantization method for the asymptotic coefficients has the form

$$C_{nl}^{\mathrm{MQ}} = \frac{1}{4\sqrt{\pi}}\left(\frac{2}{n}\right)^{n+1/2}\exp\left\{n - \frac{(l+1/2)^2}{2n}\right\}. \quad (3.24)$$

A comparison of the results produced by this formula with precise values reveals that its error is at a level of a percent for $n_r = l \geq 1$ states (for the ground state, we have $C_{10}^{\mathrm{MQ}}/C_{10} = 0.906$) and that it fast decreases with increasing n_r at fixed l; that is,

$$C_{nl}^{\mathrm{MQ}}/C_{nl} = 1 - \frac{n}{24[n^2 - (l+1/2)^2]} + \ldots, \quad n \longrightarrow \infty.$$

(ii) For the Hulthén potential $v(r) = (e^r - 1)^{-1}$, we have $\gamma_l = l + 1$; $N \equiv n = n_r + l + 1 = 1, 2, \ldots$ (in just the same way as for the Coulomb potential); $r_+(z) = \ln(1 + z^{-2})$; and $J(z) = \sqrt{1 + z^2} - z$. The quantization condition yields

$$z = \frac{1}{2}\left(\frac{g}{g_n} - \frac{g_n}{g}\right), \quad E_n^{\mathrm{MQ}} = -\frac{(g^2 - n^2)^2}{8n^2}, \quad n < g \quad (3.25)$$

(within the modified quantization method, the values of g that are equal to $g_n = n$ correspond to the conditions under which a bound state emerges). For s levels, this semiclassical spectrum is exact.

(iii) For the exponential potential $v(r) = e^{-r}$, we have

$$\gamma_l = \frac{2l+3}{4}, \quad J(z) = \frac{2}{\pi}(\sqrt{1 - z^2} - 2\arccos z), \quad (3.26)$$

and further calculations are straightforward.

In calculating the energies of shallow levels, the accuracy of the modified quantization method is not very high (in just the same way as the accuracy of the WKB method), but it becomes higher fast for deeper levels (see Fig. 2 in [29]).

3.4. Zero-Energy States

Equation (3.20) determines the quantity z and the energy of the levels together with it. Here, we discuss the case of $E_{nl} = 0$, which is the least favorable for applying the semiclassical approximation. The emergence of a level corresponds to

$$g_{nl}^{\mathrm{MQ}} = \frac{n_r + \gamma_l}{J(0)}. \quad (3.27)$$

For *ns* states in some short-range potentials used in atomic and nuclear physics, Table 4 quotes precise values of g_n and $\delta_n = (g_n^{\mathrm{MQ}} - g_n)/g_n$. In the case of smooth potentials, the constant γ_0 in the quantization condition (3.2) corresponds to expression (3.3); for finite potentials—that is, for potentials such that $V(r) \equiv 0$ for $r > R$—we have

$$\gamma_0 = \begin{cases} 1/2 & \text{for } \alpha > 0 \\ (4+\alpha)/4(2+\alpha) & \text{for } -2 < \alpha < 0, \end{cases}$$
$$\gamma_0 = \begin{cases} 7/12 & \text{for } \alpha > 0 \\ (7+2\alpha)/6(2+\alpha) & \text{for } -2 < \alpha < 0 \end{cases} \quad (3.28)$$

for potentials that are, respectively, discontinuous (nos. 5, 14 in Table 4) and continuous (nos. 6, 15 in Table 4) at $r = R$. A change in the constant γ_0 is associated with the boundary condition $\chi_n'(R) = 0$, which must now be satisfied at $g = g_n$ for s levels.

From the data in Table 4, it can be seen that the error of the modified quantization method in determining the coupling constant g_n does not exceed a few percent and that it decreases fast with increasing n.

The dependence of g_{nl}^{MQ} on the orbital angular momentum l will be analyzed by considering the example of the Tietz potential (2.42) [$v(r) = 1/r(r+1)^2$], in which case we have

$$\gamma_l = l + 1, \quad N = n, \quad r_+ = \infty, \quad J(0) = 1, \quad g_{nl}^{\mathrm{MQ}} = n, \quad (3.29)$$

whence it follows that

$$\delta_{nl}^{\mathrm{MQ}} = g_{nl}^{\mathrm{MQ}}/g_{nl} - 1 = -\frac{2l+1}{n} + \frac{l(l+1) + 3/8}{n^2} + \ldots, \quad n \longrightarrow \infty \quad (3.30)$$

[compare with (2.43')]. With increasing l, the error of the modified quantization method naturally increases. That case, however, can be efficiently investigated by the alternative method of 1/*n* expansion.

Table 4. Accuracy of the modified quantization method for short-range potentials

No.	1	2	3	4	5
$v(x)$	$(e^x-1)^{-1}$	e^{-x}/x	$1/\mathrm{sh}\,x$	$\exp(-x^2)/x$	$x^{-1}\Theta(1-x)$
$n_r=0$	1(0)	1.29607 (–3.3)	0.80088 (5.8)	1.32326 (10)	1.20241 (–2.0)
1	2(0)	2.53915 (–1.3)	1.67636 (1.1)	2.82261 (3.3)	2.76004 (–0.40)
2	3(0)	3.78709 (–0.72)	2.53006 (0.46)	4.29289 (1.8)	4.32686 (–0.17)
5	6(0)	7.53955 (–0.26)	5.07762 (0.11)	8.68001 (0.73)	9.03553 (–0.04)
γ_0	1	1	1	1	3/4
$1/J(0)$	1	$\sqrt{\pi/2}$	0.8472	1.4573	$\pi/2$
No.	6	7	8	9	10
$v(x)$	$(x^{-1}-1)\Theta(1-x)$	$e^{-x}x^{-1/2}$	e^{-x}	$e^{-x}/(1+x)$	$(e^x+1)^{-1}$
$n_r=0$	1.75902 (–5.3)	1.31345 (–3.3)	1.20241 (–2.0)	1.91436 (–6.1)	1.31171 (1.9)
1	3.72572 (–1.6)	2.82127 (–0.94)	2.76004 (–0.40)	4.25959 (–1.6)	3.11034 (0.27)
2	5.71187 (–0.79)	4.33923 (–0.46)	4.32686 (–0.17)	6.63793 (–0.75)	4.89584 (0.11)
5	11.6952 (–0.24)	8.90510 (–0.14)	9.03553 (–0.04)	13.8066 (–0.23)	10.2453 (0.02)
γ_0	5/6	5/6	3/4	3/4	3/4
$1/J(0)$	2	1.5244	$\pi/2$	2.3957	1.7822
No.	11	12	13	14	15
$v(x)$	$\exp(-x^2)$	$1/\mathrm{ch}\,x$	$1/\mathrm{ch}^2 x$	$\Theta(1-x)$	$(1-x^2)\Theta(1-x)$
$n_r=0$	1.63829 (15)	0.87840 (2.3)	1.41421 (6.1)	1.57080 (0)	2.26311 (3.1)
1	4.21849 (4.0)	2.08357 (0.63)	3.46410 (1.0)	4.71239 (0)	6.29769 (0.57)
2	6.75081 (2.1)	3.28633 (0.26)	5.47723 (0.42)	7.85398 (0)	10.3077 (0.25)
5	14.3010 (0.78)	6.88517 (0.06)	11.4891 (0.09)	17.2788 (0)	22.3181 (0.07)
γ_0	3/4	3/4	3/4	1/2	7/12
$1/J(0)$	$\sqrt{2\pi}$	1.1981	2	π	4

Note: The table presents the values of the coupling constant g_n that correspond to the emergence of s levels in short-range potentials. The potentials are represented in the form (1.1). Indicated parenthetically are the values (in percent) of the parameter δ_n characterizing the accuracy of the approximation specified by Eq. (3.27).

4. 1/n EXPANSION

4.1. Energies and Wave Functions

An appealing feature of the 1/N-expansion method is that it is closely related to classical mechanics since the limit $N \longrightarrow \infty$ in quantum mechanics is equivalent to the case of $\hbar \longrightarrow 0$ or $M \longrightarrow \infty$. In this limit, the problem reduces to determining an equilibrium classical configuration; owing to this, the approach in question can be applied to multidimensional problems not admitting a separation of variables and to many-body problems. Various versions of this method are associated with the choice of expansion parameter N. We will consider that version of the method which was proposed in [36] and which can be applied both to discrete and to quasistationary states. In this version, $N \equiv n = n_r + l + 1$; therefore, we will refer to it as a 1/n expansion.

Assuming that $n \gg 1, n_r$, we set

$$E_{nl} = \frac{g^4 \varepsilon_{nl}}{8n^2}, \quad \varepsilon_{nl} = \varepsilon^{(0)} + \frac{\varepsilon^{(1)}}{n} + \frac{\varepsilon^{(2)}}{n^2} + \ldots, \qquad (4.1)$$

$$Q^2(r) \equiv \frac{2}{n^2}[U(r) - E_{nl}] = Q_0^2 + Q_1^2 n^{-1} + Q_2^2 n^{-2} + \ldots,$$

$$Q_0^2 = \frac{1}{r^2} - \frac{2v(r)}{\sigma} - \frac{\varepsilon^{(0)}}{\sigma^2}, \qquad (4.1')$$

$$Q_1^2 = -\frac{2n_r+1}{r^2} - \frac{\varepsilon^{(1)}}{\sigma^2} \equiv -(2n_r+1)P_0(r),$$

where $\sigma = 2n^2/g^2$ is a parameter that is independent of

n. From the Schrödinger equation

$$\chi_l'' - n^2 Q^2 \chi_l = 0 \tag{4.2}$$

it can then be deduced that the particle is localized near the classical equilibrium point determined from the relation [36, 37]

$$r_0^3 v'(r_0) = -\sigma. \tag{4.3}$$

By comparing Eq. (4.2) at $r \approx r_0$ with the Schrödinger equation for a one-dimensional harmonic oscillator, we find that the parameter n plays the role of the ratio $M/\hbar$. Recalling that the amplitude of zero-point oscillations is of order $(\hbar/M\omega)^{1/2} \propto n^{-1/2}$, setting

$$r = r_0(1 + n^{-1/2}x), \tag{4.4}$$

and expanding the wave function χ_l in powers of $n^{-1/2}$, we determine consecutively the coefficients $\varepsilon^{(k)}$ in (4.1) and the corresponding coefficients for the wave function. This yields

$$\begin{aligned} \varepsilon^{(0)} &= (1 + v_0)(\sigma/r_0)^2, \\ \varepsilon^{(1)} &= (2n_r + 1)(\omega - 1)(\sigma/r_0)^2, \end{aligned} \tag{4.5}$$

$$\varepsilon^{(2)} = \left(\frac{\sigma}{2\omega^2 r_0}\right)^2 \{s[2\omega^4 - 12\omega^3 - 8\omega^2 + 6\omega^2 w + 24\omega u - 15u^2] - 6\omega^3 - 4\omega^2 + 6\omega^2 w + 6\omega u - 11u^2\}, \tag{4.5'}$$

where $s = 2n_r(n_r + 1)$,

$$\omega = [3(1 + v_2)]^{1/2} = [3 + r_0 v''(r_0)/v'(r_0)]^{1/2}, \tag{4.6}$$

$$u = 2(1 - v_3), \quad w = \frac{5}{2}(1 + v_4), \tag{4.7}$$

$$v_k = \frac{2}{(k+1)!}\left\{ r^{k-1}\frac{d^k v}{dr^k}/\frac{dv}{dr} \right\}_{r = r_0}. \tag{4.8}$$

We note that $n\omega$ is the frequency of small oscillation about the equilibrium point r_0.

The idea of calculating the wave functions for the entire interval $0 < r < \infty$ is basically the following. In the x region where the particle is predominantly localized, the anharmonic corrections of order $n^{-1/2}x$, $n^{-1/2}x^3$, and $n^{-1}x^4$ in the potential can be taken into account as a perturbation. This region also determines the normalization of the wave function to terms of order $1/n$ inclusive. For the wave function in the subbarrier region, use is made of the WKB approximation including the first-order correction in the parameter of the semiclassical expansion, the quantity $1/n$ playing here the role of the formal expansion parameter $\hbar$. The expressions mentioned immediately above are matched in the overlap region

$$[(2n_r + 1)/\omega]^{1/2} \ll x \ll n^{1/2}, \tag{4.9}$$

whereby the radial function is determined for all values of r. By way of example, we indicate that, in the region containing the equilibrium point r_0 and the turning points $r = r_\pm$, nodeless states are represented by the functions

$$\chi_{n,n-1}(r) = \left(\frac{\omega n}{\pi r_0^2}\right)^{1/4} e^{-\omega x^2/2}\left[1 - \frac{1}{\omega n^{1/2}}\left(\frac{1}{3}ux^3 + \frac{u - \omega}{\omega}x\right)\right], \tag{4.9'}$$

where the bracketed expression takes into account the correction for anharmonicity. In Fig. 1 from [38], the results obtained with the aid of this formula are contrasted against the results of the numerical calculations for the funnel potential.

To terms of order $1/n^2$, the asymptotic coefficients at the origin are given by [11]

$$c_{nl}^{(1/n)} = c_{nl}^{(1/n,0)}\left[1 - \frac{d(n_r)}{n}\right]. \tag{4.10}$$

Here, the first factor is determined from the relation [39]

$$[c_{nl}^{(1/n,0)}]^2 = \frac{1}{n_r!}\left(\frac{n\omega^3}{\pi r_0^2}\right)^{1/2}(2n\omega r_0^2)^{n_r} \times \exp[-2nJ_0 - (2n_r + 1)J_1], \tag{4.11}$$

where

$$\begin{aligned} J_0 &= \ln r_0 + \int_0^{r_0}\left[Q_0(r) - \frac{1}{r}\right]dr, \\ J_1 &= \int_0^{r_0}\left[\frac{r_0}{r(r_0 - r)} - \frac{P_0(r)}{Q_0(r)}\right]dr, \end{aligned} \tag{4.11'}$$

the functions $Q_0(r)$ and $P_0(r)$ being specified by (4.1') and (4.5), respectively. The correction $d(n_r)$ in the bracketed expression on the right-hand side of (4.10) has the form [40, 41]

$$d(n_r) = J_2 + J_3, \tag{4.12}$$

where

$$J_2 = \int_0^{r_0} dr\left\{\frac{1}{8}\left[\frac{1}{r^4} - \frac{v''(r)}{3\sigma} - (1 + 2s)P_0^2(r)\right]Q_0^{-3}(r) + \left(\frac{s}{4r^2} - \frac{2\varepsilon^{(2)}}{\sigma^2}\right)Q_0^{-1}(r) + \frac{1}{12}\frac{(1 + 3s)r_0^2}{\omega(r_0 - r)^3} + \frac{r_0}{\omega^3(r_0 - r)^2}[2(1 + 2s)\omega - (2 + 3s)u]\right\}, \tag{4.12'}$$

$$J_3 = k_0 + k_1\omega^{-1} + k_2\omega^{-2} + k_3\omega^{-3} + k_4 w\omega^{-3} + k_5 u\omega^{-3} + k_6 u\omega^{-4} + k_7\omega^{-5}. \tag{4.12''}$$

Table 5. Coefficients in expression (4.12")

n_r	k_0	k_1	k_2	k_3	k_4	k_5	k_6	k_7
0	–1/24	1/24	13/8	1/2	–61/48	–1/2	–11/4	293/96
1	–13/24	13/24	81/8	9/2	–217/48	–7/2	–63/4	1217/96

The numerical values of the coefficients k_i for nodeless ($n_r = 0$) states and one-node states ($n_r = 1$) are quoted in Table 5.

4.2. Accuracy of the 1/n Expansion

The above expressions for the energy and for the coefficients at the origin are asymptotically exact for $l \longrightarrow \infty$ and fixed n_r. However, the extent to which the $1/n$ expansion can be of use at modest values of the quantum numbers is not obvious from the outset. Let us consider some examples to assess this.

Setting $g = 1$ as before for power-law potentials of the form (2.10), we arrive at

$$v(r) = -\frac{r^\alpha}{\alpha}, \quad v_k = \frac{2(\alpha-1)!}{(k+1)!(\alpha-k)!}, \qquad (4.13)$$
$$r_0 = n^{2/(2+\alpha)}, \quad \omega = (2+\alpha)^{1/2}.$$

In accordance with (4.1) and (4.5), we find for an nl level that the relevant energies can be expanded as

$$E_{nl} = \frac{1}{2}n^{2\alpha/(2+\alpha)}\left(\varepsilon_0 + \frac{\varepsilon_1}{n} + \frac{\varepsilon_2}{n^2} + \ldots\right), \qquad (4.14)$$

where

$$\varepsilon_0 = 1 + \frac{2}{\alpha}, \quad \varepsilon_1 = (2n_r+1)(\omega-1),$$
$$\varepsilon_2 = -\frac{\alpha-2}{2(2+\alpha)}\left[(2n_r+1)\omega + \frac{1}{36}(\alpha^2-15\alpha-52)\right.$$
$$\left. + \frac{1}{6}n_r(n_r+1)(\alpha^2-9\alpha-34)\right].$$

For $-1 \le \alpha \le 4$, the coefficients ε_k decrease fast with increasing k. At $\alpha = -1$ and $\alpha = 2$, all ε_k vanish identically for $k \ge 2$, so that the series in (4.14) is truncated; as a result, the energy spectrum coincides with the exact one.

It should be emphasized that the approximation as simple as that which is given by (4.14) has an astounding precision. By way of example, we indicate that, for $\alpha = 0$–8 and $n_r = 0$, the error is less 1% at $l = 1$ and less than 0.06% at $l = 5$, decreasing fast with increasing l.

For the Coulomb and for the oscillator potential, the accuracy of the approximations in (4.10) and (4.11) for the asymptotic coefficients can be investigated analytically. According to (4.11), we have [39]

$$\left[\frac{c_{nl}^{(1/n,\,0)}}{c_{nl}}\right]^2$$
$$= \begin{cases} 1 - \dfrac{1}{64n^2}\left[\dfrac{1}{36} - 3n_r - 12n_r^2 + 2n_r^3 + 49n_r^4 + \ldots\right] \\ \text{for } \alpha = -1 \\ 1 - \dfrac{1}{24n^2}\left[\dfrac{1}{48} + 2n_r - n_r^2 - 8n_r^3 + 12n_r^4 + \ldots\right] \\ \text{for } \alpha = 2. \end{cases} \qquad (4.15)$$

These expansions show that even the zero-order approximation (4.11) of the $1/n$ expansion has a high accuracy for nodeless states, but this accuracy sharply becomes poorer with increasing n_r. The inclusion of the $1/n$ correction according to (4.10) improves substantially the accuracy not only for nodeless but also for one-node states (see [40, 41] and Tables 1 and 2).

It should be noted that the coefficients c_{nl} change by many orders of magnitude—for example, $c_{nl} \propto [(2n/(2+\alpha))!]^{-1}$ for nodeless states in the potential (2.10). For large values of l, a numerical determination of c_{nl} becomes more complicated because they decrease in proportion to a factorial; at the same time, the $1/n$ expansion becomes ever more precise with increasing l.

For short-range potentials, a similar situation prevails in all cases, with the exception of the case of shallow levels (that is, the case of $g \approx g_{nl}$, where g_{nl} is the coupling-constant value at which an nl level emerges), which calls for a dedicated consideration [11].

4.3. 1/n Expansion for Zero-Energy States

In the case of short-range attractive potentials, the energy of an nl level increases with decreasing coupling constant g, with the result that, as soon as this coupling constant attains a value g_{nl}, the level is expelled into the continuous spectrum, its energy being $E_{nl} = 0$ at this point. By using the $1/n$-expansion method to calculate g_{nl}, we obtain

$$g_{nl}^2 = \frac{2n^2}{\sigma_{cr}}\left[1 + \frac{f_1}{n} + \frac{f_2}{n^2} + \ldots\right]. \qquad (4.16)$$

The parameters of this expansion are determined by the requirement that $\varepsilon^{(k)}$ vanish for all values of $k \ge 0$. From Eq. (4.3) and from the condition $\varepsilon^{(0)} = 0$, we obtain

$$\sigma_{cr} = 2r_0^2 v(r_0), \quad r_0 v'(r_0) + 2v(r_0) = 0. \qquad (4.17)$$

The corrections in the parameter $1/n$ are given by

$$f_1 = (2n_r + 1)(\omega - 1),$$
$$f_2 = \frac{1}{4\omega^4}\{2\omega^6 - 2\omega^5 - 10\omega^4 + 6\omega^2(2u + w) - 11u^2 + 2n_r(n_r + 1)[4\omega^6 - 4\omega^5 - 18\omega^4 + 6\omega^2(4u + w) - 15u^2]\}, \quad (4.18)$$

where the quantities ω, u, and w defined in (4.6)–(4.8) are taken at the value r_0 following from (4.17).

Let us illustrate the application of these formulas by considering the examples of the Tietz and the Yukawa potential. For the former, we have $v(r) = \dfrac{1}{r(1+r)^2}$, $r_0 = 1$, $\omega = 1/2$, $u = 3/8$, and $w = 23/32$; the first three terms of the $1/n$ expansion in (4.16) then yield

$$g_{nl}^2 = 4n^2\left[1 - \frac{2n_r + 1}{2n} + \frac{n_r(n_r + 1)}{4n^2}\right], \quad (4.19)$$

which coincides with the exact value in (2.43).

For the Yukawa potential, $v(r) = e^r/r$, $r_0 = 1$, $\omega = 1/\sqrt{2}$, $u = 2/3$, and $w = 55/48$, so that

$$g_{nl}^2 \approx en^2\left\{1 - \frac{2-\sqrt{2}}{2}\,\frac{2n_r + 1}{n} + \left[\frac{43 - 36\sqrt{2}}{144} + \frac{37 - 24\sqrt{2}}{24}n_r(n_r + 1)\right]\frac{1}{n^2}\right\} \quad (4.20)$$

($e = 2.718...$). Table 6 illustrates the accuracy in calculating the value of g_{nl}^2 corresponding to the emergence of the level. The parameters

$$\rho_{nl}(k) = g_{nl}^2(k)/g_{nl}^2 - 1 \quad (4.21)$$

characterize the accuracy of $1/n$ expansion in the case where k terms are taken into account in expansion (4.20) (for $k = 1, 2, 3$).

When an $l \geq 1$ level arises in a short-range potential, the asymptotic coefficients at infinity, A_{nl}, in the normalized wave function

$$\chi_{nl}(r) = A_{nl}r^{-l} + \ldots, \quad r \longrightarrow \infty, \quad (4.22)$$

determine [42] the effective interaction range

$$r_{nl} = -2^{1-2l}\left[\frac{(2l)!}{l!A_{nl}}\right]^2,$$

which is an important parameter in the theory of low-energy scattering. Following the same line of reasoning as that adopted in calculating the asymptotic coefficients at zero, we obtain

$$[A_{nl}^{(1/n)}]^2 = \frac{1}{n_r!}\left(\frac{n\omega^3}{\pi}\right)^{1/2}\frac{(2n\omega)^{n_r}}{r_0^{2n_r+3}}e^{2nI_0 + (2n_r+1)I_1}\left(1 + \frac{h(n_r)}{n}\right)^2, \quad (4.23)$$

where

$$I_0 = \ln r_0 + \int_{r_0}^{\infty}\left[\frac{1}{r} - Q_0(r)\right]dr,$$
$$I_1 = \int_{r_0}^{\infty}\left[\frac{P_0(r)}{Q_0(r)} - \frac{1}{r - r_0}\right]dr,$$

with

$$Q_0(r) = \frac{1}{r}\left[1 - \frac{r^2 v(r)}{r_0^2 v(r_0)}\right]^{1/2},$$
$$P_0(r) = \frac{1}{r^2}\left[1 + (\omega - 1)\frac{r^2 v(r)}{r_0^2 v(r_0)}\right].$$

The correction of order $1/n$ for nodeless states was calculated in [41].

Table 6

n_r	l	g_{nl}^2	$\rho_{nl}(1)$	$\rho_{nl}(2)$	$\rho_{nl}(3)$
0	0	1.6799	62	14	5.5
	1	9.0820	20	2.2	0.54
	2	21.895	12	0.83	0.18
	5	92.918	5.3	0.18	1.5 (–2)
1	0	6.4472	69	–5.4	3.0
	1	17.745	38	–2.5	0.55
	2	34.420	26	–1.4	0.18
	5	116.99	14	–0.56	2.4 (–2)

Note: Indicated parenthetically for each number less than 0.1 is the negative integral power of this number in the floating-point representation $a(b) \equiv a \times 10^b$.

4.4. Calculation of Energies for Stationary and Quasistationary States

We have presented above the analytic formulas (4.5) for the first three terms of the $1/n$ expansion. The explicit expressions fast become much more complicated with increasing k. However, they can easily be calculated with the aid of recursion relations [43]. For nodeless states, this method admits the simplest imple-

Table 7. Convergence of a $1/n$ expansion

k	$-\varepsilon^{(k)}$	$-\varepsilon_k$, $l = n - 1 = 3$
0	2.2283 (–1)	0.222827
1	8.4564 (–2)	0.243968
2	–1.2496 (–2)	0.243187
3	1.152 (–3)	0.243205
4	3.14 (–4)	0.243206
5	–1.02 (–4)	0.243206
6	–5.89 (–5)	0.243206
7	2.50 (–2)	0.243205
8	7.92 (–1)	0.243193
9	1.21 (+1)	0.243147
10	1.23 (+2)	0.243030
12	–1.14 (3)	0.242918
15	4.44 (8)	0.247577

mentation because one can use logarithmic perturbation theory [44–46].

For a specific example, we consider the Yukawa potential

$$V(r) = -\frac{Ze^2}{r}\exp(-\kappa_0 r),$$

where $\kappa_0 = \sigma/n^2 a_B$ is the screening parameter. In this case, we have

$$\omega = \left(1 - \frac{r_0^2}{1 + r_0}\right)^{1/2}, \quad \varepsilon^{(0)} = (r_0^2 - 1)e^{-2r_0}, \qquad (4.24)$$
$$\varepsilon^{(1)} = -(1 + r_0)(1 - \omega)e^{-2r_0}.$$

As to the quantity $r_0 = r_0(\sigma)$, it is determined from the equation

$$(r_0^2 + r_0)e^{-r_0} = \sigma. \qquad (4.25)$$

For the nodeless $l = 3$ state, the values of $\varepsilon^{(k)}$ and the partial sums $\varepsilon_k = \varepsilon^{(0)} + \varepsilon^{(1)}/n + \ldots + \varepsilon^{(k)}/n^k$ of the series in question are quoted in Table 7 for $\sigma = 0.5$. These values illustrate convergence of the $1/n$ expansion. Since the coefficients $\varepsilon^{(k)}$ first decrease fast, the $1/n$ expansion provides quite accurate results even at $n \sim 1$ [despite the fact that, for $k \geq 7$, the coefficients $\varepsilon^{(k)}$ begin to increase fast, so that the series in (4.1) as a whole is not more than an asymptotic series]. From the data in Table 7, it can be seen that, at $k \approx 4$–6, the partial sums ε_k stabilize, specifying the energy to a precision of about 10^{-6}.

The reduced energies $\varepsilon_{nl} = 2\sigma^2 E_{nl}/n^2$ calculated in this way are quoted in Table 8 for some nodeless states at a few values of the screening parameter σ. Also presented in this table are the results obtained by summing divergent perturbation-theory series [47]. We can see that the two methods produce results that agree to within a high precision.

It should be noted that, at $\sigma = \sigma_* = 0.8399\ldots > \sigma_{cr}$, in which case $\omega = 0$, two classical solutions collide, the coefficients $\varepsilon^{(k)}$ become infinite for $k \geq 2$, and the $1/n$ expansion ceases to be valid. Upon this collision ($\sigma > \sigma_*$), the point of equilibrium $r_0(\sigma)$ goes into the complex plane, whereas the coefficients in the $1/n$ expansion develop an imaginary part. Such a solution is meaningless in classical theory; in quantum mechanics, however, it corresponds to the emergence of the width of a quasistationary level and determines the asymptotic behavior of Breit–Wigner resonances, $E_{nl} = E_r - i\Gamma/2$, characterized by large values of the quantum numbers n and l. Such a situation is prevalent for all short-range potentials, and it is the way in which Breit–Wigner resonances of complex energy can be described within the $1/n$-expansion method.

It should be noted that, for quasistationary states, the asymptotic behavior of higher orders of a $1/n$ expansion is determined by the probability of the tunneling of the relevant particle through the potential barrier and can be calculated by means of the imaginary-time technique. This approach is applicable not only to spherically symmetric potentials but also to cases where the variables in the Schrödinger equations are not separated. This was demonstrated by considering the example of the two-body problem and the example of the hydrogen atom in a constant electric and a constant magnetic field (see [10, p. 149]).

Table 8. Reduced energies ε_{nl} for the Yukawa potential ($n = l + 1$)

σ	$l = 3$	$l = 10$	$l = 30$
0.5	–2.43206 (–1)	–2.30412 (–1)	–2.25542 (–1)
	–2.43206 (–1)	–2.30412 (–1)	–2.25541 (–1)
σ_{cr}	–3.6871 (–2)	–1.40396 (–2)	–5.06734 (–3)
	–3.6872 (–2)	–1.4040 (–2)	–5.07 (–3)
1.25	0.10917 – *i*0.12189	0.15411 – *i*0.13427	0.17142 – *i*0.13768
	0.10917 – *i*0.12189	0.1541 – *i*0.1343	0.1714 – *i*0.1377

Note: At fixed values of l and σ, the upper and the lower line correspond to, respectively, $1/n$ expansion and the result obtained by summing the series of perturbation theory. At $\sigma_{cr} = 2e^{-1} = 0.73575\ldots$, we have $\varepsilon^{(0)}$—that is, the level goes over to the continuous spectrum when $n \longrightarrow \infty$.

5. QUANTIZATION WITH ALLOWANCE FOR BARRIER PENETRABILITY

5.1. Generalization of the Bohr–Sommerfeld Quantization Rule

In many physics problems, the potential possesses a barrier, with the result that the energy levels in this potential prove to be quasistationary, $E = E_r - \frac{i}{2}\Gamma$. If the barrier penetrability is small, it can easily be shown that the generalization of the quantization rule to this case is (see, for example, [48])

$$\frac{1}{\pi}\int_{x_0}^{x_1} p(x)dx \equiv \frac{1}{2\pi}\oint_{C_{01}} p(x)dx = n - \frac{1}{2} - \frac{i}{4\pi}e^{-2a}, \quad (5.1)$$

where $n = 1, 2, \ldots$;

$$a = \frac{1}{\pi}\int_{x_1}^{x_2}[-p^2(x)]^{1/2}dx \equiv \frac{i}{2\pi}\oint_{C_{12}} pdx; \quad (5.2)$$

$x_0 < x < x_1$ is the classically allowed region; $x_1 < x < x_2$ is subbarrier region; for $x > x_2$, the particle goes to infinity; and C_{ik} are integration contours circumventing the corresponding turning points x_i and x_k in the positive direction ($i, k = 1, 2$). Setting $p = \left[2\left(E_r - \frac{i}{2}\Gamma - U(x)\right)\right]^{1/2}$ and assuming that $\Gamma \ll |E_r|$, we arrive at the Gamow formula for the level width:

$$\Gamma = \frac{1}{T}\exp\left(-2\int_{x_1}^{x_2}|p(x)|dx\right), \quad T = 2\int_{x_0}^{x_1}\frac{dx}{p(x)}. \quad (5.3)$$

If the energy of the level is close to the barrier top (or exceeds it), the turning points approach each other, the width is no longer exponentially small, and Eq. (5.1) becomes invalid. Let us now discuss an analytic continuation of the quantization condition to the above-barrier region.

Near the barrier top, $x_1 \approx x_2$, we can make use of the parabolic approximation

$$p(x) = \left(\frac{1}{4}\rho^2 - a\right)^{1/2}, \qquad a = \frac{U_m - E}{\Omega} = \frac{U_m - E_r}{\Omega} + i\frac{\Gamma}{2\Omega}, \quad (5.4)$$

where $\rho = (x - x_m)/\Omega^{1/2}$, $\Omega = [-U''(x_m)]^{1/2}$ being the frequency of the inverted oscillator. The Schrödinger equation then has the exact solution

$$\psi(x) = \text{const} \cdot D_{-1/2-ia}(\rho e^{-i\pi/4}), \quad (5.5)$$

which satisfies the Sommerfeld radiation condition. In (5.5), $D_\nu(z)$ is a parabolic-cylinder function [27]. By matching this solution with the semiclassical solution (2.1) in the overlap region

$$a \ll |\rho| \ll x_m\Omega^{-1/2},$$

we find for $x < x_1$ that [49–51]

$$I(E) \equiv \frac{1}{\pi}\int_{x_0}^{x_1} p(x, E)dx = n - \frac{1}{2} - \frac{1}{2\pi}\varphi(a), \quad (5.6)$$

where

$$\varphi(a) = \frac{1}{2i}\ln\left\{\frac{\Gamma(1/2 + ia)}{\Gamma(1/2 - ia)[1 + \exp(-2\pi a)]}\right\} - a\ln a + a. \quad (5.7)$$

At a complex resonance energy, the turning points and the parameter a defined in (5.2) are complex.

For $|a| \longrightarrow \infty$, the asymptotic expansions for the function $\varphi(a)$ are

$$\varphi(a) = \begin{cases} \frac{1}{24a} + \frac{7}{2880a^3} + \ldots + \frac{i}{2}e^{-2\pi a} \text{ for } -\frac{\pi}{2} < \arg a < \frac{\pi}{2} & (5.8) \\ -2i\pi a + \frac{1}{24a} + \frac{7}{2880a^3} + \ldots \text{ for } \frac{\pi}{2} < \arg a < \pi, & (5.8') \end{cases}$$

the ray $\arg a = \pi/2$ being a Stokes line for this function. By using the expansion in (5.8), it can easily be shown that, for deep levels ($E_r < U_m$, $a \gg 1$), Eq. (5.6) reduces to (5.1).

If $E_r \longrightarrow U_m$, the turning points x_1 and x_2 approach each other, which invalidates the semiclassical approximation near the barrier top. As E_r increases further, these points diverge, however, so that the conditions ensuring the applicability of the WKB method are satisfied again. It is important here that, for above-barrier resonances, the parameter a occurs in the second quadrant of the complex plane. Indeed, we can see from Eq. (5.4) that, in the subbarrier region, $\mathrm{Re}\, a > 0$, while the imaginary part of the parameter a is exponentially small. When the level being considered touches the barrier top ($E_r = U_m$), the point a traverses the positive imaginary axis, so that $\arg a > \pi/2$ at higher energies of the level. Taking into account (5.8'), we find that, for $|a| \gg 1$,

$$\frac{1}{\pi}\int_{x_0}^{x_1} pdx = n - \frac{1}{2} - ia = n - \frac{1}{2} + \frac{i}{\pi}\int_{x_1}^{x_2}(-p^2)^{1/2}dx.$$

Noticing that $(-p^2)^{1/2} = ip(x)$, we recast this equation into the form [52]

$$\frac{1}{2\pi}\oint_C [p^2(x)]^{1/2} dx = n - \frac{1}{2}, \tag{5.9}$$

where the contour of integration circumvents the turning points x_0 and x_2. It is well known from [53] that the Bohr–Sommerfeld quantization condition can also be written in the form (5.9), but the contour C in that case circumvents the turning points x_0 and x_1 both lying on the real axis. Thus, we see that, in going over from the subbarrier to the above-barrier region, the contour of integration is rearranged in such a way that goes around a different pair of the characteristic points.

Equation (5.9) represents an analytic continuation of the quantization rule to the above-barrier region $E_r > U_m$. This analytic continuation can also be implemented by means of the formal substitution

$$a \longrightarrow a\exp(-2\pi i) \tag{5.10}$$

directly in the quantization integral. Since we have [52]

$$I(E) = I_0 + \frac{1}{2\pi} a\ln a - I_1 a + I_2 a^2 + \ldots,$$

substitution (5.10) leads to Eq. (5.6), where use is made of the asymptotic expression (5.8') for the function $\varphi(a)$.

With allowance for the barrier penetrability and the semiclassical correction of order $\hbar^2$, the quantization rule has the form [54]

$$\frac{1}{2\pi\hbar}\oint_{C_{01}}\left(p(x) + \frac{\hbar^2 MU''(x)}{24p^3(x)}\right)dx = n - \frac{1}{2} - \frac{1}{2\pi}\left[\varphi(a) - \frac{1}{24a} - \frac{i}{24}\hbar M\xi(a)\oint_{C_{12}}\frac{U''(x)}{p^3(x)}dx\right], \tag{5.11}$$

where

$$\xi(a) = -\frac{1}{2\pi}\varphi'(a) = \frac{1}{2\pi}[\ln(ia) - \psi(1/2 + ia)] \tag{5.12}$$

and where we have explicitly recovered M and the Planck constant $\hbar$.

If the resonance energy E_r is not very close to the barrier top U_m, so that the turning points can be considered individually, Eq. (5.11) is simplified, as before, to become

$$\frac{1}{2\pi}\oint_C\left(p(x) + \frac{U''(x)}{24p^3(x)}\right)dx = n - \frac{1}{2}, \quad n = 1, 2, \ldots. \tag{5.13}$$

The contour C circumvents the turning points x_0 and x_1 in the case of the discrete spectrum ($E_r < U_m$) or the points x_0 and x_2 in the case of quasistationary states ($E_r > U_m$). (The quantization rule allowing for terms of order $\hbar^6$ inclusive was obtained [52].) Let us now proceed to analyze specific examples.

5.2. Anharmonic Oscillator

Let us consider the potential

$$U(x) = \frac{1}{2}x^2 - \zeta x^N, \tag{5.14}$$

where the exponent N can take odd values of 3, 5, etc. This potential attains a maximum value of U_m at $x = x_m$,

$$x_m = (N\zeta)^{-1/(N-2)}, \quad U_m = \frac{N-2}{2N}(N\zeta)^{-2/(N-2)}. \tag{5.14'}$$

The frequency $\Omega = (N-2)^{1/2}$, which was introduced in (5.4), is independent of the coupling constant ζ. The Schrödinger equation with the potential (5.14) can serve as a reference for the theory of quasistationary states.

The equation $U(x_i) = E(\zeta)$ determines N complex turning points and can be solved explicitly in the limiting cases of $\zeta \longrightarrow 0$ and $\zeta \longrightarrow \infty$. For $\zeta \longrightarrow \infty$, we have

$$x_0 \approx -(E/\zeta)^{1/N}, \quad x_2 \approx (E/\zeta)^{1/N}\exp\left(\frac{i\pi}{N}\right),$$

and Eq. (5.9) assumes the form

$$\frac{1}{\pi}\int_{x_0}^{x_2}[2(E_n + \zeta x^N)]^{1/2}dx = n - \frac{1}{2}, \quad n = 1, 2, \ldots. \tag{5.15}$$

Having calculated the integral, we find that, in the strong-coupling regime, the energy of a quasistationary state is given by

$$E_n(\zeta) \approx \tilde{E}_n(\zeta) \equiv C_N\exp\left(-\frac{i\pi}{N+2}\right)\left[\left(n - \frac{1}{2}\right)^N\zeta\right]^{2/(N+2)}, \tag{5.16}$$

where

$$C_N = \left\{\left(\frac{\pi}{8}\right)^{1/2}(N+2)\Gamma\left(\frac{N+2}{2N}\right)/\Gamma(1/N)\cos(\pi/2N)\right\}^{2N/(N+2)}. \tag{5.16'}$$

In what is concerned with the asymptotic expression (5.16), we would like to note the following:

(i) The dependence $E_n(\zeta) \propto \zeta^{2/(N+2)}$ follows from the scaling considerations alone.

(ii) According to (5.16), the imaginary part of the energy, $\mathrm{Im}E_n(\zeta) = -\Gamma/2$, has a correct sign, the level width being relatively small at large N: $\Gamma/E_r \propto N^{-1}$. This smallness is associated with the fact that the potential (5.14) becomes overly sharp for $N \longrightarrow \infty$.

(iii) For an oscillator featuring only a cubic anharmonicity ($N = 3$), the result given by Eq. (5.16) coincides with expression (5) from [55].

Of particular interest is the structure of the asymptotic expansion of $E_n(\zeta)$ at large ζ. By considering the oscillator term $x^2/2$ in (5.14) as a perturbation, it can be shown [52] that

$$E_n(\zeta) = \tilde{E}_n(\zeta)\sum_{k=0}^{\infty} d_k \tilde{\zeta}_n^{4k/(N+2)}, \qquad (5.17)$$

where

$$d_k = d_k^{(0)} + d_k^{(2)}(n-1/2)^{-2} + d_k^{(4)}(n-1/2)^{-4} + \ldots, \quad (5.18)$$

$d_0^{(0)} = 1$, and $\tilde{\zeta}_n = (n-1/2)^{(N-2)/2}\zeta$ is the effective coupling for highly excited levels. The coefficients $d_k^{(j)}$ can be calculated analytically; in particular, we have

$$d_0^{(2)} = \frac{N(N-1)}{6\pi(N+2)^2}\frac{\cos(\pi/N)}{\tan(\pi/2N)},$$
$$d_1^{(2)} = \frac{\Gamma(3/N)\Gamma((N+2)/2N)}{\Gamma(1/N)\Gamma((N+6)/2N)} \qquad (5.18')$$
$$\times C_N^{-1+2/N}\left(\cos\frac{\pi}{N} - \frac{1}{2}\right)\exp\left(\frac{4i\pi}{N(N+2)}\right).$$

The potential (5.14) at $N = 3$ was considered by Alvarez [55]; by using the method of complex rotations, which is well known in atomic physics (see, for example, [56]), he was able to compute $E_n(\zeta)$ at $n = 1$ and 2 for $\zeta \le 100$ to a very high precision. In this case, the first few coefficients in expansions (5.17) and (5.18) have the following numerical values:

$$C_3 = 1.658602\ldots, \quad d_1^{(0)} = 0,$$
$$d_2^{(0)} = -0.03658\exp(-2i\pi/5),$$
$$d_3^{(0)} = 0.00558\exp(i\pi/5), \quad d_0^{(2)} = 0.01103, \ldots.$$

The coefficients $d_k^{(j)}$ decrease fast with increasing k and j; for this reason, we retain only the first three terms in (5.17); that is, we set

$$E_n(\zeta) = \tilde{E}_n(\zeta)[1 + d_0^{(2)}(n-1/2)^{-2} + d_2^{(0)}\tilde{\zeta}_n^{-8/5}]. \quad (5.19)$$

In Table 9, the results obtained with the aid of this formula are contrasted against the numerical values computed in [55]. It can be seen that the region of applicability of expression (5.19), which is formally valid for $\zeta \gg 1$, extends to $\zeta \sim 1$ even for the ground-state ($n = 1$) level.

A particularly high precision is a achieved for the ratio

$$\xi = -\mathrm{Im}\,E_n(\zeta)/\mathrm{Re}\,E_n(\zeta), \qquad (5.20)$$

Table 9. Energies of quasistationary states in the potential $V(x) = \frac{1}{2}x^2 - \zeta x^N$

ζ	$n = 1$		$n = 2$	
	ReE_n	10ξ	ReE_n	10ξ
100	3.8940	7.26541	13.8388	7.26542
	3.848	7.26534	13.8399	7.26535
10	1.5502	7.2646	5.5093	7.26650
	1.571	7.2620	5.5098	7.2639
5	1.17547	7.2630	4.1751	7.2643
	1.190	7.255	4.1757	7.261
1	0.6165	7.7323	2.1921	7.2502
	0.610	7.128	2.1935	7.206
0.5	0.4664	7.1613	1.6596	7.2182
	0.462	6.84	1.662	7.14

Note: At fixed values of ζ and n, the first and the second line contain, respectively, the results of the numerical calculation from [55] and the results based on the asymptotic expression (5.19). The quantity ξ is defined in (5.20), its limiting value being $\xi_\infty = \tan(\pi/5) = 0.7265425\ldots$.

which, in the limit $\zeta \longrightarrow \infty$, is independent of n and ζ, taking the value of $\xi_\infty = \tan(\pi/(N+2))$. It is astounding that the approximation given by (5.19), which is very simple indeed, provides not only a qualitative but also a quantitative description of resonance energies in the region $\zeta \ge 1$ (for $n \gg 1$ excited levels, its accuracy is still higher).

5.3. Stark Effect in a Hydrogen Atom in a Strong Electric Field

The Schrödinger equation for the hydrogen atom in a uniform electric field $\mathscr{E}$ admits a separation of variables in parabolic coordinates [2]. For $m = 0$ states characterized by specific values of the parabolic quantum numbers n_1 and n_2, the quantization integrals are expressed in terms of a hypergeometric function, so that the condition in (5.9) can be represented in the form [52]

$$(\beta_1/z_1)G(-z_1) = -2\nu_1 F^{1/4},$$
$$(\beta_2/z_2)G(z_2) = 2\nu_2 F^{1/4}, \qquad (5.21)$$

where β_j are the separation constants, $\beta_1 + \beta_2 = 1$; $z_i = 16\beta_i F/\varepsilon^2$;

$$G(z) = z \cdot {}_2F_1(1/4, 3/4, 2; z);$$

and ε, F, and ν_i are reduced variables given by

$$\varepsilon = 2n^2(E_r - i\Gamma/2), \quad F = n^4\mathscr{E},$$
$$\nu_i = (n_i + 1/2)/n, \quad n = n_1 + n_2 + 1. \qquad (5.22)$$

Table 10. Energy positions and widths of the peaks associated with the photoionization of the $m = 0$ Rydberg states of the hydrogen atom in an electric field of strength $\mathscr{E}$ = 16.8 kV/cm

n_1, n_2	E_r, cm^{-1}		$\Gamma/2$, cm^{-1}		F	F_*
	WKB	[57]	WKB	[57]		
16, 1	106.9	103.8	9.0	9.0	0.343	0.265
15, 1	167.8	167.9	0.8	2.1	0.273	0.263
15, 0	196.5	198.5	–	1.1 (–4)	0.214	0.308
14, 2	212.1	210.1	5.4	6.6	0.273	0.236
13, 2	273.6	275.8	–	0.23	0.214	0.233
12, 3	313.3	314.8	–	1.6	0.214	0.214
11, 4	353.8	351.4	2.5	3.0	0.214	0.200
11, 3	384.2	386.3	–	1.8 (–3)	0.165	0.211
10, 4	418.7	419.2	–	3.2 (–2)	0.165	0.197

Note: Here, n_1 and n_2 are the parabolic quantum numbers of a Stark resonance, $F = n^4\mathscr{E}$ is the reduced electric-field strength, and F_* is the classical ionization threshold [58]. The case of $F < F_*$ ($F > F_*$) corresponds to subbarrier (above-barrier) resonances.

The variable z_2 increases monotonically with F; at $z_2 = 1$, the level touches the barrier top in the effective potential $U_2(\eta)$, which includes the Langer correction. The corresponding electric field is that which is equal to the classical ionization threshold $\mathscr{E}_* = n^{-4}F_*$. The parameter a appearing in (5.6) is also calculated analytically. The result is

$$a = \frac{n}{4F}(-\varepsilon/2)^{3/2}G(1-z_2) = na_*(1-z_2) + \ldots, \quad F \longrightarrow F_*. \tag{5.23}$$

In the near-threshold region, the second equation in (5.21) must be modified in accordance with (5.6). This is achieved via the substitution

$$\nu_2 \longrightarrow \tilde{\nu}_2 = \nu_2 - \frac{1}{2\pi n}\varphi(a). \tag{5.24}$$

An analytic continuation of Eqs. (4.21) to the above-barrier region ($F > F_*$) can be performed according to (5.10) and (5.23) with the aid of the substitution

$$1 - z_2 \longrightarrow (1-z_2)e^{-2\pi i}, \tag{5.25}$$

upon which the function $G(z_2)$ appearing in (5.21) is replaced by $\tilde{G}(z_2)$:

$$G(z_2) \longrightarrow \tilde{G}(z_2) = G(z_2) - i\sqrt{2}G(1-z_2). \tag{5.26}$$

Equations (5.21) can be solved numerically [34, 52]. The calculated values of E_r are quoted in Table 10, along with the experimentally measured positions of the peaks in the cross section for the ionization of hydrogen atoms at $\mathscr{E}$ = 16.8 kV/cm. It can be seen that, within the measurement errors (1 to 2 cm^{-1} according to [57]), the semiclassical results agree with experimental data. Since the relevant solutions to Eqs. (5.21) for $F < F_*$ are real, they cannot determine the resonance widths; for this reason, dashes stand for the corresponding entries in this table. For $F > F_*$, the analytically continued quantization rules specify not only the resonance positions but also the resonance widths Γ, which are given in the table.

In order to calculate the widths of subbarrier and above-barrier resonances, it is necessary to use Eqs. (5.21) with substitution (5.24), which take into account a finite barrier penetrability in the effective potential U_2. This is illustrated in Table 11 for $n_1 = n_2$ subbarrier resonances. Since the classical ionization threshold is $F_* = 0.1837$ for such states, the results of the calculations for the effective quantum number $\nu = (-2E_r)^{-1/2}$ and the level widths Γ at moderate fields $F < F_*$, in which case the WKB method cannot determine Γ, are presented in the table.

It was noted above that, in eventual formulas, the semiclassical-expansion parameter $\hbar$ translates into $1/n$; therefore, $\hbar^2$ corrections to the quantization integral are of order $1/n^2$. The quantities ν and Γ were calculated in the semiclassical approximation with allowance for the barrier penetrability both in the $1/n$ approximation [in other words, according to Eqs. (5.21) with

Table 11. Energies of Stark resonances in a hydrogen atom according to calculations based on various methods

$\lvert n_1 n_2, m\rangle$ $\mathscr{E}$ F	$\lvert 2, 2, 0\rangle$ 1.8 (–4) 0.1125		$\lvert 5, 5, 0\rangle$ 1.0 (–5) 0.1464		$\lvert 7, 7, 0\rangle$ 3.0 (–6) 0.1519	
Method	ν	Γ	ν	Γ	ν	Γ
$1/n - A$	4.92385	2.22 (–6)	10.7128	2.82 (–6)	14.5767	1.347 (–6)
$1/n^2 - A$	4.92406	2.19 (–6)	10.7127	2.80 (–6)	14.5766	1.338 (–6)
PHA	4.92402	2.283 (–6)	10.713	2.83 (–6)	14.577	1.35 (–6)
[60]	4.9240	2.282 (–6)	10.688	2.815 (–6)	14.5771	1.338 (–6)

Note: Here, $n_1 = n_2 = (n-1)/2$; the values of $\mathscr{E}$, $\nu = (-2E_r)^{1/2}$, and Γ are presented in a.u.; the classical ionization threshold is $F_* = 0.1837$ for $n_1 = n_2$ states.

substitution (5.24)] and in the $1/n^2$ approximation [59]—that is, with allowance for the $\hbar^2$ correction according to equations similar to those in (5.11). In addition, Table 11 displays the results from [34], which were obtained by summing perturbation-theory series by means of Padé–Hermite approximants (PHA), and the numerical results from [60]. It can be seen that the results of the calculations performed by different methods are consistent and that, with increasing quantum numbers n_1 and n_2 or reduced field F, the accuracy of the semiclassical approximation becomes higher, while the accuracy of the method based on summation of divergent perturbation-theory series deteriorates. Finally, we note that the energies of Stark resonances corresponding to the circular states $|0, 0, n-1\rangle$ can easily be calculated by means of the 1/*n*-expansion technique [34].

6. CONCLUSION

The semiclassical approximation and the 1/*n*-expansion technique have been used to calculate the energies of discrete and quasistationary states and radial wave functions for the Schrödinger equation. It has been shown that not only do these methods provide qualitative estimates for the above quantities, but they are also appropriate for calculating some fine features of the relevant wave functions like the asymptotic coefficients at the origin and at infinity. The resulting analytic formulas for these coefficients, which are important for applications, are asymptotically exact in the limit of large values of the radial quantum number n_r (WKB method) and in the limit of high angular momenta l (1/*n* expansion). It turns out that, as a rule, these formulas are also applicable at modest values of n_r and l, almost completely covering the region of all possible values of these quantum numbers, with the exception of those that correspond to shallow levels in short-range potentials. But for this case, there are simple analytic expressions that determine, to a reasonable precision even for the ground state, coupling-constant values at which a level emerges.

Both the semiclassical approximation and the 1/*n*-expansion technique are especially convenient for solving physics problems where variables in the Schrödinger equation cannot be separated. By way of example, we indicate that, in the case of the Stark effect in a strong electric field, the complex energies of Stark resonances in a hydrogen atom and the positions and widths of peaks in the cross sections for the photoionization of various Rydberg states of arbitrary atoms can be computed by combining these two methods.

ACKNOWLEDGMENTS

We are grateful to V.M. Vaĭnberg, S.G. Pozdnyakov, and A.V. Sergeev for stimulating discussions and for assistance in performing numerical calculations.

This work was supported in part by the Russian Foundation for Basic Research (project nos. 98-02-17007, 00-02-16354, and 01-02-16850).

REFERENCES

1. A. B. Migdal, *Qualitative Methods in Quantum Theory* (Nauka, Moscow, 1975; Benjamin, Reading, 1977).
2. L. D. Landau and E. M. Lifshitz, *Quantum Mechanics: Non-Relativistic Theory* (Nauka, Moscow, 1974; Pergamon, Oxford, 1977).
3. N. Fröman and P. O. Fröman, *JWKB Approximation: Contributions to the Theory* (North-Holland, Amsterdam, 1965; Mir, Moscow, 1967).
4. J. Heading, *An Introduction to Phase-Integral Methods* (Wiley, New York, 1962; Mir, Moscow, 1965).
5. L. I. Schiff, *Quantum Mechanics* (McGraw-Hill, New York, 1955; Inostrannaya Literatura, Moscow, 1957).
6. E. Witten, in *Recent Development in Gauge Theories* (Plenum, New York, 1980).
7. L. G. Jaffe, Rev. Mod. Phys. **54**, 407 (1982).
8. A. Chatterjee, Phys. Rep. **186**, 249 (1990).
9. *Dimensional Scaling in Chemical Physics*, Ed. by D. R. Herschbach, J. Avery, and O. Goscinsky (Kluwer, Dordrecht, 1993).
10. *New Methods in Quantum Theory*, Ed. by C. A. Tsipis, V. S. Popov, D. R. Herschbach, and J. S. Avery (Kluwer, Dordrecht, 1995).
11. B. M. Karnakov, V. D. Mur, and V. S. Popov, Zh. Éksp. Teor. Fiz**. 106**, 976 (1994) [JETP **79**, 534 (1994)].
12. H. A. Kramers, Z. Phys. B **39**, 828 (1926).
13. B. M. Karnakov, V. D. Mur, and V. S. Popov, Zh. Éksp. Teor. Fiz. **107**, 1768 (1995) [JETP **80**, 983 (1995)].
14. R. E. Langer, Phys. Rev. **51**, 669 (1937).
15. V. S. Popov, B. M. Karnakov, and V. D. Mur, Phys. Lett. A **210**, 402 (1996).
16. B. M. Karnakov, V. D. Mur, and V. S. Popov, Yad. Fiz. **61**, 481 (1998) [Phys. At. Nucl. **61**, 420 (1998)].
17. W. H. Furry, Phys. Rev. **71**, 360 (1947).
18. V. L. Eletskiĭ, V. D. Mur, and V. S. Popov, Dokl. Akad. Nauk SSSR **249**, 329 (1979) [Sov. Phys. Dokl. **24**, 906 (1979)].
19. B. Simon, Ann. Phys. (N.Y.) **58**, 76 (1970).
20. C. Quigg and J. L. Rosner, Phys. Rep. **56**, 167 (1979).
21. E. Eichten, K. Gottfried, T. Kinoshita, *et al.*, Phys. Rev. D **17**, 3090 (1978).
22. A. M. Badalyan, D. I. Kitoroage, and D. S. Pariĭskiĭ, Yad. Fiz. **46**, 226 (1987) [Sov. J. Nucl. Phys. **46**, 139 (1987)].
23. B. M. Karnakov, V. D. Mur, and V. S. Popov, Dokl. Akad. Nauk **347**, 466 (1996) [Phys. Dokl. **41**, 139 (1996)].
24. T. Tietz, J. Chem. Phys. **25**, 787 (1956).
25. S. Flügge, *Practical Quantum Mechanics* (Springer-Verlag, Berlin, 1971; Mir, Moscow, 1974), Vol. 2.
26. Yu. N. Demkov and V. N. Ostrovskiĭ, Zh. Éksp. Teor. Fiz. **62**, 125 (1972) [Sov. Phys. JETP **35**, 66 (1972)].
27. *Higher Transcendental Functions (Bateman Manuscript Project)*, Ed. by A. Erdelyi (McGraw-Hill, New York, 1953; Nauka, Moscow, 1974), Vol. 2.

28. *Functional Analysis (Reference Mathematical Library)* (Nauka, Moscow, 1964), Chap. 7.
29. M. S. Marinov and V. S. Popov, Zh. Éksp. Teor. Fiz. **67**, 1250 (1974) [Sov. Phys. JETP **40**, 621 (1975)].
30. M. S. Marinov and V. S. Popov, J. Phys. A **8**, 1575 (1975).
31. B. M. Karnakov, V. D. Mur, and V. S. Popov, Zh. Éksp. Teor. Fiz. **116**, 511 (1999) [JETP **89**, 271 (1999)].
32. J. McEnnan, L. Kissel, and R. H. Pratt, Phys. Rev. A **13**, 532 (1976).
33. M. Grant and C. S. Lai, Phys. Rev. A **20**, 718 (1979).
34. V. M. Vaĭnberg, V. D. Mur, V. S. Popov, and A. V. Sergeev, Zh. Éksp. Teor. Fiz. **93**, 450 (1987) [Sov. Phys. JETP **66**, 258 (1987)].
35. V. S. Popov, V. D. Mur, A. V. Sergeev, and V. M. Weinberg, Phys. Lett. A **149**, 418 (1990).
36. V. S. Popov, V. M. Vaĭnberg, and V. D. Mur, Pis'ma Zh. Éksp. Teor. Fiz. **41**, 439 (1985) [JETP Lett. **41**, 539 (1985)]; Yad. Fiz. **44**, 1103 (1986) [Sov. J. Nucl. Phys. **44**, 714 (1986)].
37. V. D. Mur, V. S. Popov, and A. V. Sergeev, Zh. Éksp. Teor. Fiz. **97**, 32 (1990) [Sov. Phys. JETP **70**, 16 (1990)].
38. V. D. Mur, S. G. Pozdnyakov, and V. S. Popov, Dokl. Akad. Nauk SSSR **303**, 1102 (1988) [Sov. Phys. Dokl. **33**, 899 (1988)].
39. V. D. Mur, S. G. Pozdnyakov, and V. S. Popov, Yad. Fiz. **51**, 390 (1990) [Sov. J. Nucl. Phys. **51**, 249 (1990)].
40. B. M. Karnakov and S. G. Pozdnyakov, Yad. Fiz. **58**, 2201 (1995) [Phys. At. Nucl. **58**, 2088 (1995)].
41. V. S. Popov, B. M. Karnakov, and V. D. Mur, Phys. Lett. A **224**, 15 (1996).
42. V. D. Mur and V. S. Popov, Teor. Mat. Fiz. **27**, 204 (1976).
43. V. M. Vaĭnberg, V. D. Mur, V. S. Popov, *et al.*, Teor. Mat. Fiz. **74**, 399 (1988).
44. A. D. Dolgov and V. S. Popov, Phys. Lett. B **79B**, 403 (1978).
45. A. D. Dolgov and V. S. Popov, Zh. Éksp. Teor. Fiz. **75**, 2010 (1978) [Sov. Phys. JETP **48**, 1012 (1978)].
46. Y. Aharonov and C. K. Au, Phys. Rev. Lett. **42**, 1582 (1979).
47. V. M. Vaĭnberg and V. S. Popov, Dokl. Akad. Nauk SSSR **272**, 335 (1983) [Sov. Phys. Dokl. **28**, 762 (1983)].
48. I. I. Gol'dman and V. D. Krivchenkov, *Problems in Quantum Mechanics* (Gostekhizdat, Moscow, 1957; Academic, New York, 1960).
49. J. N. L. Connor, Mol. Phys. **25**, 1469 (1973).
50. V. D. Mur and V. S. Popov, Pis'ma Zh. Éksp. Teor. Fiz. **51**, 499 (1990) [JETP Lett. **51**, 563 (1990)].
51. V. S. Popov, V. D. Mur, and A. V. Sergeev, Zh. Éksp. Teor. Fiz. **100**, 20 (1991) [Sov. Phys. JETP **73**, 9 (1991)].
52. V. D. Mur and V. S. Popov, Pis'ma Zh. Éksp. Teor. Fiz. **57**, 406 (1993) [JETP Lett. **57**, 418 (1993)]; Zh. Éksp. Teor. Fiz. **104**, 2293 (1993) [JETP **77**, 18 (1993)].
53. J. L. Dunham, Phys. Rev. **41**, 713 (1932).
54. V. D. Mur and V. S. Popov, Yad. Fiz. **58**, 1413 (1995) [Phys. At. Nucl. **58**, 1329 (1995)].
55. G. Alvarez, Phys. Rev. A **37**, 4079 (1988).
56. R. Yaris, J. Bendler, R. A. Lovett, *et al.*, Phys. Rev. A **18**, 1816 (1978).
57. K. Ng, D. Yao, and M. N. Nayfeh, Phys. Rev. A **35**, 2508 (1987).
58. V. S. Popov, V. D. Mur, and A. V. Sergeev, Zh. Éksp. Teor. Fiz. **106**, 1001 (1994) [JETP **79**, 547 (1994)].
59. V. D. Mur, V. S. Popov, A. V. Sergeev, and A. V. Shcheblykin, Zh. Éksp. Teor. Fiz. **96**, 91 (1989) [Sov. Phys. JETP **69**, 49 (1989)].
60. R. J. Damburg and V. V. Kolosov, J. Phys. B **9**, 3149 (1976); **11**, 1921 (1978).

Translated by A. Isaakyan

Physics of Atomic Nuclei, Vol. 64, No. 4, 2001, pp. 691–697. From Yadernaya Fizika, Vol. 64, No. 4, 2001, pp. 750–756.

90th ANNIVERSARY OF A.B. MIGDAL'S BIRTHDAY
ELEMENTARY PARTICLES AND FIELDS

A Meson-Theoretical Explanation of the f_0 (980)-Production Puzzle in the Reaction $\pi^- p \longrightarrow \pi^0\pi^0 n$*

Z. S. Wang, S. Krewald, and J. Speth
Institut für Kernphysik, Forschungszentrum Jülich GmbH, Germany
Received August 19, 2000

Abstract—A meson-theoretical model for the reaction $\pi^- p \longrightarrow \pi^0\pi^0 n$ for large π^- momenta is developed which treats the final-state interaction between the two produced pions microscopically. For small momentum transfers, the squares of the *S*-wave amplitudes of the produced two-pion system show a dip for invariant two-pion masses in the vicinity of the $f_0(980)$ meson, while for momentum transfers $-t > 0.2$ (GeV/c)^2, the $f_0(980)$ meson appears as a bump. The model provides a microscopic explanation of the long-standing puzzle seen by both the GAMS and the BNL experimental collaborations. © *2001 MAIK "Nauka/Interperiodica".*

1. INTRODUCTION

The reaction $\pi N \longrightarrow \pi\pi N$ is one of the major sources of information about pion–pion scattering. For pion beam momenta above approximately 10 GeV/c and for small values of the square $t = (p_N - p_{N'})^2$ of the momentum transfer between the incoming and the outgoing nucleon, the reaction is peripheral and is therefore dominated by one-pion exchange. During the last decade, there has been significant experimental progress due to new detector developments which allow high-statistics studies of two-pion production [1, 2]. In this work, we concentrate on the charge-exchange reaction $\pi^- p \longrightarrow \pi^0\pi^0 n$. This reaction eliminates the odd angular momenta from the partial-wave analysis of the two-pion system and is selective to the isospin $I = 0$ and $I = 2$.

The GAMS collaboration employs a π^--beam momentum of 38 GeV/c [1], while the BNL-E852 collaboration uses an incident beam momentum of 18.3 GeV/c [2]. The experimental results can be summarized as follows. For momentum transfers $-t <$ 0.2 (GeV/c)^2, the squares of the *S*-wave amplitudes show a broad enhancement above the threshold with a sharp dip near the invariant two-pion mass $m_{\pi\pi}$ = 980 MeV. This dip corresponds to the excitation of the $f_0(980)$. A similar dip has been seen in the reaction $\bar{p}p \longrightarrow 3\pi^0$ by the Crystal Barrel collaboration [3, 4]. For momentum transfers above $-t < 0.4$ (GeV/c)^2, however, a puzzle emerges: at $m_{\pi\pi}$ = 1 GeV, a distinct peak is seen. In the GAMS data, the peak is taller than in the corresponding BNL data.

Despite a large body of experimental and theoretical work, the structure of the $f_0(980)$ meson remains a controversial issue (see, e.g., the recent review by Godfrey and Napolitano [5]). Since at least three scalar–isoscalar mesons have been established to date, i.e., $f_0(980)$, $f_0(1370)$, and $f_0(1500)$, and since the low-lying scalar–isoscalar strength can be summarized as a meson $f_0(400–1200)$, there is no obvious single candidate for the scalar member of the $q\bar{q}$ nonet. The $f_0(980)$ meson was interpreted as a multiquark state [6], a $K\bar{K}$ molecule [7–9], or as a unitarized $q\bar{q}$ state [10, 11]. The issue could not be decided by analyses of the $\gamma\gamma \longrightarrow \pi\pi$ reaction [12, 13].

The earliest theoretical model that specifically addresses the GAMS data is the *K*-matrix analysis by Anisovich *et al*. [14, 15]. In that model, the transition amplitude $A(\pi N \longrightarrow Nb)$ is given by the product of a pionic vertex for the proton-to-neutron transition, a standard pion propagator, and a unitarized $\pi\pi \longrightarrow b$ transition amplitude which is parameterized as a sum of Breit–Wigner terms with momentum-dependent coupling constants. A suitable multiplicative factor ensures that the amplitude vanishes at the two-pion production threshold.

An alternative model was suggested by Achasov and Shestakov [16, 17], who point out that one-pion exchange dies out rapidly as the momentum transfer $-t$ is increased. For large momentum transfers, the reaction mechanism has to be generalized to include mesons of larger mass. In addition to pion exchange, Achasov and Shestakov therefore include the a_1 exchange. The necessity to include a_1 exchange in the extraction of pion–pion phase shifts was emphasized by Kaminski, Lesniak, and Rubicki [18, 19]. The $\pi\pi \longrightarrow \pi\pi$ and the $a_1\pi \longrightarrow \pi\pi$ transition amplitudes are parameterized by generalized Breit–Wigner-like amplitudes and background terms with parameters directly adjusted to the GAMS data. A good fit to the GAMS data is obtained [16].

* This article was submitted by the authors in English.

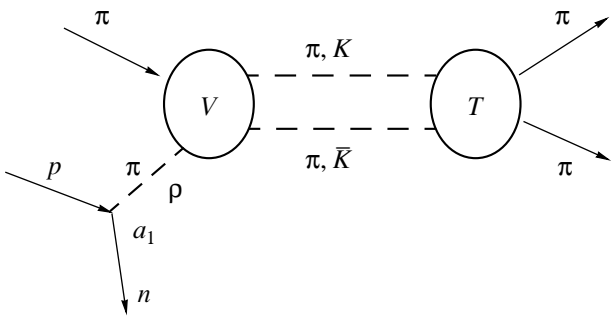

Fig. 1. Meson-exchange model for the reaction $\pi N \longrightarrow \pi\pi N$.

In our work, we present a meson-theoretical model for the reaction $\pi^- p \longrightarrow \pi^0\pi^0 n$. The advantage of a microscopic approach like the present one is that one does not have to rely on assumptions concerning the background amplitude because the background is explicitly generated by the meson–meson scattering dynamics. In a meson-theoretical approach, one is straightforwardly led to include both the pion and the a_1 in the reaction mechanism.

2. THE MODEL

The reaction mechanism considered in the present work is shown in Fig. 1. In addition to the pion, we also include the exchange of the a_1 meson. In principle, one also has to consider the exchange of the ρ meson, which may contribute via *G*-parity violating couplings. At a quantitative level, however, this contribution turns out to be entirely negligible. The incoming pion and the virtual meson can interact via meson exchanges and can couple to both $\pi\pi$ and $K\bar{K}$ intermediate states which undergo final-state interactions.

First, we have to choose an effective Lagrangian for the meson dynamics. By imposing *SU*(3)-flavor symmetry, one can reduce the number of triple meson couplings [8, 9]. But the *SU*(3) symmetry does not yet constrain the couplings of the a_1 meson. Since the a_1 meson is chirally related to the pion, chiral symmetry helps to reduce the number of independent coupling constants. We start from an underlying effective-quark Lagrangian which respects chiral symmetry and derive the required meson interactions by integrating out the quark degrees of freedom using known techniques [20–24]. We employ the simplest such Lagrangian available, i.e., the one due to Nambu and Jona-Lasinio [25].

The following three-meson couplings result.

The pseudoscalar–pseudoscalar–scalar coupling is a typical *D* coupling which reads

$$\mathcal{L}_{pps0} = -\frac{1}{4}G_{pps}\mathrm{tr}(\{P, P\}S)$$

$$-\frac{1}{4}F_{pps}\mathrm{tr}(\{\partial^\mu P, \partial_\mu P\}S) + \frac{1}{2}F_{pps}\mathrm{tr}(\{P, P\}\partial_\alpha^2 S) \quad (1)$$

$$+ 2F_{pps}\mathrm{tr}(\{P, \partial_\alpha^2 P\}S) + \frac{3}{2}F_{pps}\mathrm{tr}(\{P, \partial^\mu P\}\partial_\mu S),$$

with the following relation between scalar and derivative coupling constants:

$$F_{pps} = \frac{G_{pps}}{9M_s^2\left(1 + 2\ln\dfrac{\Lambda^2}{M_s^2}\right)}. \quad (2)$$

The coupling constant of the pseudoscalar–pseudoscalar–scalar interaction is denoted by G_{pps}, Λ is a cutoff parameter, and M_s is the scalar mass; M_s and Λ are defined within the NJL model.

In the actual calculations, we use the experimental scalar mass and the corresponding cutoff parameters given in the end of the section.

The pseudoscalar–pseudoscalar–vector coupling interaction is

$$\mathcal{L}_{ppv1} = \frac{i}{4}G_{ppv}\mathrm{tr}([P, \partial_\mu P]V^\mu), \quad (3)$$

where G_{ppv} is a pseudoscalar–pseudoscalar–vector coupling constant.

The pseudovector–vector–pseudoscalar interaction may be expressed as

$$\mathcal{L}_{Avp0} = -\frac{i}{4}G_{Avp}\,\mathrm{tr}([A_\mu, V^\mu]P)$$

$$+\frac{3}{4}iF_{Avp}\,\mathrm{tr}([\partial^\mu A^\nu - \partial^\nu A^\mu, \partial_\mu V_\nu - \partial_\nu V_\mu]P)$$

$$+\frac{3}{2}iF_{Avp}\,\mathrm{tr}([A^\mu, \partial_\alpha^2 V_\mu]P) + \frac{1}{2}iF_{Avp} \quad (4)$$

$$\times\,\mathrm{tr}([\partial_\alpha^2 A_\mu, V^\mu]P) + \frac{3}{2}iF_{Avp}\,\mathrm{tr}([\partial_\mu A^\mu, \partial_\nu V^\nu]P)$$

$$-iF_{Avp}\,\mathrm{tr}([\partial_\nu A^\mu, V^\nu]\partial_\mu P) + iF_{Avp}\,\mathrm{tr}([A^\mu, \partial_\nu V^\nu]\partial_\mu P),$$

with the following relation between scalar and derivative coupling constants:

$$F_{Avp} = \frac{G_{Avp}}{3M_s^2\left(1 + 2\ln\dfrac{\Lambda^2}{M_s^2}\right)}, \quad (5)$$

where G_{Avp} is a coupling constant of the pseudovector–vector–pseudoscalar interaction.

The pseudovector–pseudoscalar–scalar interaction is

$$\mathcal{L}_{Aps1} = -\frac{1}{4}G_{Aps}\mathrm{tr}(\{A^\mu, \partial_\mu P\}S) + \frac{1}{4}G'_{Aps}\mathrm{tr}(\{A^\mu, P\}\partial_\mu S) - \frac{1}{4}G''_{Aps}\mathrm{tr}(\{\partial_\mu A^\mu, P\}S), \quad (6)$$

with the coupling constant G_{Aps} and the related constants

$$G'_{Aps} = \frac{3\ln\dfrac{\Lambda^2}{M_s^2}}{2\left(1+\dfrac{3}{2}\ln\dfrac{\Lambda^2}{M_s^2}\right)}G_{Aps}, \qquad G''_{Aps} = \frac{1}{\left(1+\dfrac{3}{2}\ln\dfrac{\Lambda^2}{M_s^2}\right)}G_{Aps}. \quad (7)$$

The vector–vector–pseudoscalar coupling has the form

$$\mathcal{L}_{vvp2} = \frac{1}{2}iG_{vvp}\epsilon^{\mu\nu\rho\lambda}\mathrm{tr}(\{\partial_\nu V_\rho, V_\lambda\}\partial_\mu P) + \frac{1}{4}iG_{vvp}\epsilon^{\mu\nu\rho\lambda}\mathrm{tr}(\{\partial_\mu V_\rho, \partial_\nu V_\lambda\}P), \quad (8)$$

which is a pure *D*-type coupling with the coupling constant G_{vvp}. Here, $\epsilon^{\mu\nu\rho\lambda}$ denotes the totally antisymmetric four-tensor. The pseudovector–pseudovector–pseudoscalar coupling is

$$\mathcal{L}_{AAp2} = iG_{AAp}\epsilon^{\mu\nu\rho\lambda}\mathrm{tr}([\partial_\mu P, \partial_\nu A_\rho]A_\lambda) + \frac{i}{2}G_{AAp}\epsilon^{\mu\nu\rho\lambda}\mathrm{tr}(\{\partial_\mu A_\rho, \partial_\nu A_\lambda\}P), \quad (9)$$

with the coupling constant G_{AAp}. The pseudoscalar–pseudoscalar–tensor coupling is

$$\mathcal{L}_{ppt} = \frac{i}{4}G_{ppt}\mathrm{tr}([\partial_\mu P, \partial_\nu P]f^{\mu\nu}), \quad (10)$$

with the coupling constant G_{ppt}.

For the nucleon–nucleon meson interaction, we follow Aitchison and Fraser [21, 22]. The resulting total effective Lagrangian reads

$$\mathcal{L}_{\mathrm{eff}} = \bar{N}[\gamma^\mu(i\partial_\mu - g_v(V_\mu + \gamma_5 A_\mu)) - g_s(S + i\gamma_5 P) - g_t\sigma_{\mu\nu}f^{\mu\nu}]N + \frac{1}{2}(\partial_\mu S\partial^\mu S + \partial_\mu P\partial^\mu P) - \frac{1}{4}(F^V_{\mu\nu}F^{V\mu\nu} + F^A_{\mu\nu}F^{A\mu\nu}) - \frac{1}{2}\mu_s^2(S^2+P^2) + \frac{1}{2}\mu_v^2(V_\mu^2 + A_\mu^2) + \frac{1}{2}\partial_\lambda f^{\mu\nu}\partial^\lambda f_{\mu\nu} - \frac{1}{2}\mu_s^2 f_{\mu\nu}^2 + \mathcal{L}_{\mathrm{int}}, \quad (11)$$

where μ_s and μ_v are the experimental masses of the scalar and vector mesons and $\mathcal{L}_{\mathrm{int}}$ is the sum of the three-meson-interaction Lagrangians displayed above.

The meson–meson scattering amplitudes are obtained by solving the Blankenbecler–Sugar reduction of the Bethe–Salpeter equation.

As a numerical value of the pion–nucleon coupling constant, we take $g_s^2/4\pi$ =13.8 which is close to the value determined in [26] from new experimental data, $g^2_{NN\pi}/4\pi$ = 14.5. For the rho-meson–nucleon coupling constant, we take $g_v^2/4\pi$ = 0.9, which corresponds to the value employed in the Bonn meson-exchange model of the nucleon–nucleon interaction, $g^2_{NN\rho}/4\pi$ = 0.92. According to the construction of our Lagrangian, this number directly fixes the a_1–nucleon coupling constant. In [27], the experimental tests of time-reversal asymmetry give an upper limit of 0.9 for $g^2_{NNa_1}/4\pi$ assuming maximal symmetry violation.

In our model, we assume that the chiral partner of the pion can be identified with the $f_0(1370)$ meson which fixes the required coupling constants of the $f_0(1370)$.

We take the following three-meson couplings in our calculation: $G^2_{pps}/4\pi = G^2_{ppv}/4\pi = 5.5$, $G^2_{Aps}/4\pi = G^2_{Avp}/4\pi = 0.6$, and $G^2_{vvp}/4\pi = 3.3$. For regularization purposes, standard form factors of the dipole type are employed [9]. For the *t*-channel and *u*-channel interactions, we take (in MeV) $\Lambda^{(t)}_{\pi\pi\rho} = \Lambda^{(t)}_{a_1\pi\rho} = 1355$, $\Lambda^{(t)}_{KK\rho} = 3080$, $\Lambda^{(t)}_{KK\omega} = 1000$, and $\Lambda^{(t)}_{KK\phi} = 1400$. For the *s*-channel, the values are (in MeV) $\Lambda^{(s)}_{\pi\pi\rho} = \Lambda^{(s)}_{a_1\pi\rho} = 2355$, $\Lambda^{(s)}_{KK\rho} = 2000$, $\Lambda^{(s)}_{\pi\pi f_0(1370)} = \Lambda^{(s)}_{a_1\pi f_0(1370)} = 1500$, $\Lambda^{(s)}_{\pi\pi f_2(1400)} = \Lambda^{(s)}_{a_1\pi f_2(1400)} = 2320$, and $\Lambda^{(s)}_{KKf_2(1400)} = 2800$. For the meson–nucleon form factors, we use $\Lambda_{\pi NN}$ = 1300 MeV and Λ_{a_1NN} = 1800 MeV.

These values were determined from a fit to the $\pi\pi$ phase shifts. The theoretical phase shifts obtained with the present model are virtually identical to the ones already published in [9]. The $f_0(980)$ is reproduced as a quasibound $K\bar{K}$ molecule. We now proceed to discuss the results of the model for the reaction $\pi^- p \longrightarrow \pi^0\pi^0 n$.

3. RESULTS

We first analyze the BNL-E852 data. In Fig. 2, the experimental events are shown as a function of the square of the momentum transfer $|t|$ summed over the interval of invariant two-pion masses $0.98 < m_{\pi\pi} < 1.08$ GeV. Gunter *et al*. point out that the experimental distribution cannot be characterized by a single expo-

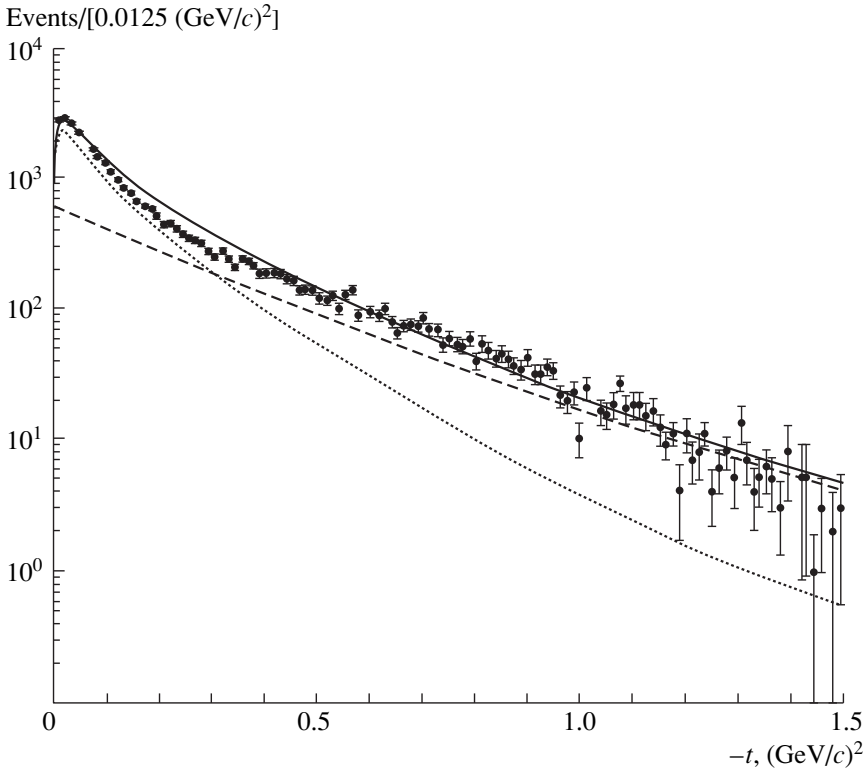

Fig. 2. The two-pion events obtained in the $\pi^- p \longrightarrow \pi^0\pi^0 n$ reaction at a pion beam momentum of 18.3 GeV/c by the BNL-E852 collaboration [2] are shown as a function of the square $-t$ of the momentum transferred between the proton and the neutron. The invariant two-pion masses have been averaged over the interval $0.98 < m_{\pi\pi} < 1.08$ GeV. The dotted curve shows the results obtained by assuming a pure one-pion exchange as a reaction mechanism, the dashed curve shows the corresponding result for a pure a_1 exchange. The full model is given by the solid curve.

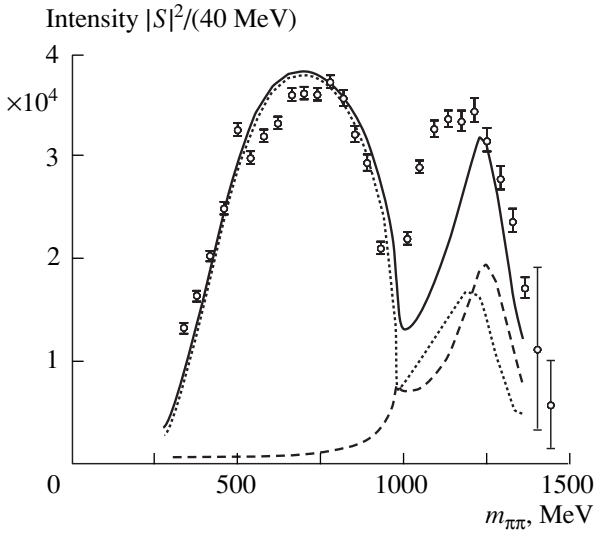

Fig. 3. The squares of the absolute values of the S-wave partial wave amplitude are shown as a function of the invariant two-pion mass for events in the region $0.01 < -t < 0.10$ (GeV/c)^2. The present ($\pi + a_1$) calculation is given by the solid curve. The contribution due to pion exchange is displayed by the dotted curve, while the contribution due to a_1 exchange is given by the dashed curve. Circles represent the BNL-E852 data.

nential. In order to fit the distribution, a sum of two exponentials was required, which suggests more than one production mechanism [2]. We identify the rapidly decreasing amplitude with the one-pion exchange mechanism and the slowly decreasing amplitude with the a_1 exchange, as was done already in [16]. The amplitudes are multiplied by reduction factors $C_\pi^{1/2} e^{b_\pi t/2}$ and $C_{a_1}^{1/2} e^{b_{a_1} t/2}$. The corresponding slope parameters $b_\pi = 3.80$ (GeV/c)$^{-2}$ and $b_{a_1} = 1.20$ (GeV/c)$^{-2}$, as well as the amplitudes $C_\pi = 0.970$ and $C_{a_1} = 0.004$, are phenomenological parameters which are chosen to reproduce the data displayed in Fig. 2. As pointed out by Achasov and Shestakov[17], the parameterization of [14] predicts a rapid variation of the distribution with t which is not confirmed by the data [2]. This finding supports the assumption that the a_1 exchange plays an important role in the reaction mechanism.

The square of the S-wave partial wave amplitude is shown in Fig. 3 as a function of the invariant two-pion mass for values of the momentum transfer summed over $0.01 < -t < 0.10$ (GeV/c)^2. The data show a broad strength distribution above the threshold which is interrupted by a sharp dip in the vicinity of $m_{\pi\pi} = 1$ GeV. For

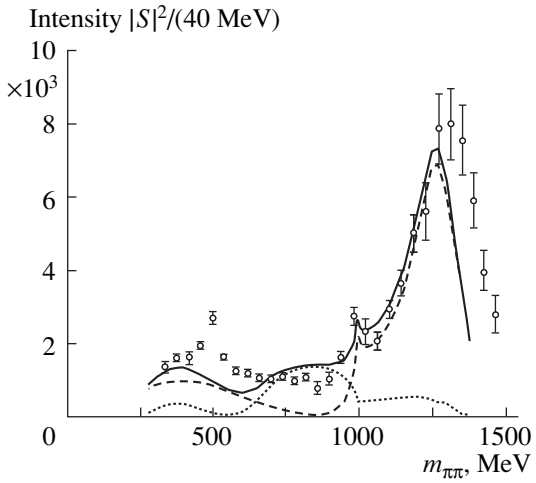

Fig. 4. The squares of the absolute values of the *S*-wave partial wave amplitude are shown as a function of the invariant two-pion mass for events in the region $0.4 < -t < 1.5$ (GeV/c)^2. The present calculation is given by the solid curve. The contribution due to pion exchange is displayed by the dotted curve, while the contribution due to a_1 exchange is given by the dashed curve. Circles represent the BNL-E852 data.

these small momentum transfers, the reaction mechanism is dominated by one-pion exchange. The a_1 exchange becomes noticeable only above 1 GeV. The appearance of a dip can be understood microscopically in meson-exchange models: the exchange of a ρ meson in the *t* channel of the two-pion system leads to a strong attraction between the two interacting pions. The pion–pion phase shift consequently rises rapidly to 90°, and therefore interferes destructively with the amplitude generated by the opening of the $K\bar{K}$ channel. Detailed discussions on the structure of the δ_0^0 partial-wave amplitude as generated by meson-exchange models can be found in [8, 9].

In our model, we have only considered those f_0 mesons above 1 GeV that are listed in the Particle Data Group [28] and fitted the pion–pion phase shifts, but not the BNL-E852 data. Now, we note that the present calculation misses some *S*-wave strength above $m_{\pi\pi}$ = 1 GeV. A straightforward possible method for reproducing the BNL-E852 data would be to follow Anisovich and Sarantsev and postulate that the $f_0(1370)$ resonance summarizes two scalar resonances, namely, a $f_0(1300)$ and a broad $f_0(1550)$ [29].

Figure 4 shows the squares of the *S*-wave amplitudes summed over the interval $0.4 < -t < 1.5$ (GeV/c)^2. For these large momentum transfers, the pionic contribution to the reaction mechanism almost disappears. The data is reproduced satisfactorily. The peak at $m_{\pi\pi}$ = 500 MeV is due to a K^- contamination in the pion beam which generates a small signal due to the decay $K_S^0 \longrightarrow \pi\pi$ which survives despite the presence of a veto detector [2]. The enhancement near the threshold is mainly produced by the a_1-exchange mechanism. In the vicinity of 1 GeV, the theoretical calculation produces a clear peak. This is the major result of the present investigation. The meson-exchange model straightforwardly produces the $f_0(980)$ meson as a peak in the cross section, provided the momentum transfer is sufficiently large. For large momentum transfers, there

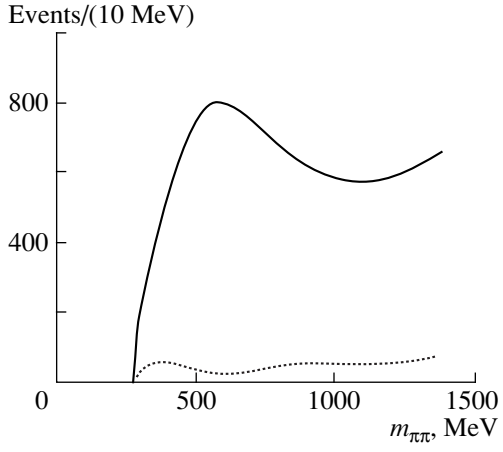

Fig. 5. Theoretical two-pion mass distributions for the $\pi^- p \longrightarrow \pi^0\pi^0 n$ reaction at a pion beam momentum of 18.3 GeV/c obtained in a calculation without a $K\bar{K}$ channel are shown for two ranges of the square of the momentum transfer: $|t| < 0.2$ (GeV/c)^2 (solid curve) and $|t| > 0.4$ (GeV/c)^2 (dotted curve).

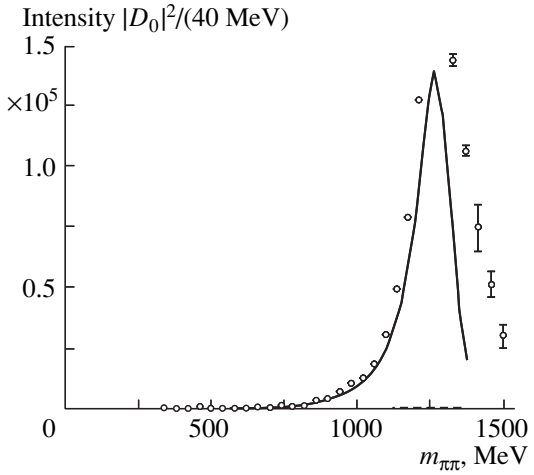

Fig. 6. The squares of the absolute values of the D_0 partial-wave amplitude are shown as a function of the invariant two-pion mass for events in the region $0.01 < -t < 0.10$ (GeV/c)^2. The contribution due to pion exchange is given by the solid curve, while the contribution due to a_1 exchange is given by the dashed curve; the latter is negligible here. Circles represent the BNL-E852 data.

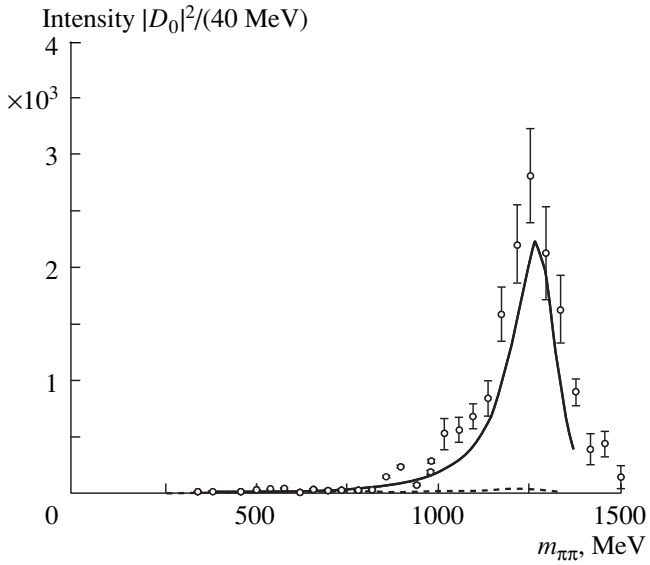

Fig. 7. The squares of the absolute values of the D_0 partial-wave amplitude are shown as a function of the invariant two-pion mass for events in the region $0.4 < -t < 1.5$ (GeV/c)^2. For a description of the theoretical curves and the experimental data, see Fig. 6.

is no missing strength between 1 and 1.3 GeV, in contrast to the situation at smaller momentum transfers.

In Fig. 5, we show the results obtained after switching off the coupling to the $K\bar{K}$ channel. For small momentum transfers ($|t| < 0.2$ (GeV/c)^2), the dip disappears. Likewise, for large momentum transfers ($|t| > 0.4$ (GeV/c)^2), there is no peak near 1 GeV. We have to conclude that, in the present model, the description of the $f_0(980)$ meson as a quasibound $K\bar{K}$ state is the major ingredient that produces the strong variation of the $f_0(980)$ production as a function of the momentum transfer.

The partial wave D_0 is dominated by the $f_2(1270)$, which is included as a pole diagram in our model. We find, indeed, a fair agreement with the experimental data for both small (Fig. 6) and large (Fig. 7) momentum transfers.

The slope parameters b_π and b_{a_1} and the amplitudes C_π and C_{a_1} summarize absorption effects and are expected to change with the total available energy. For analysis of the GAMS data, which were taken with a beam momentum of 38 GeV/c, we employ $C_\pi = 0.77$,

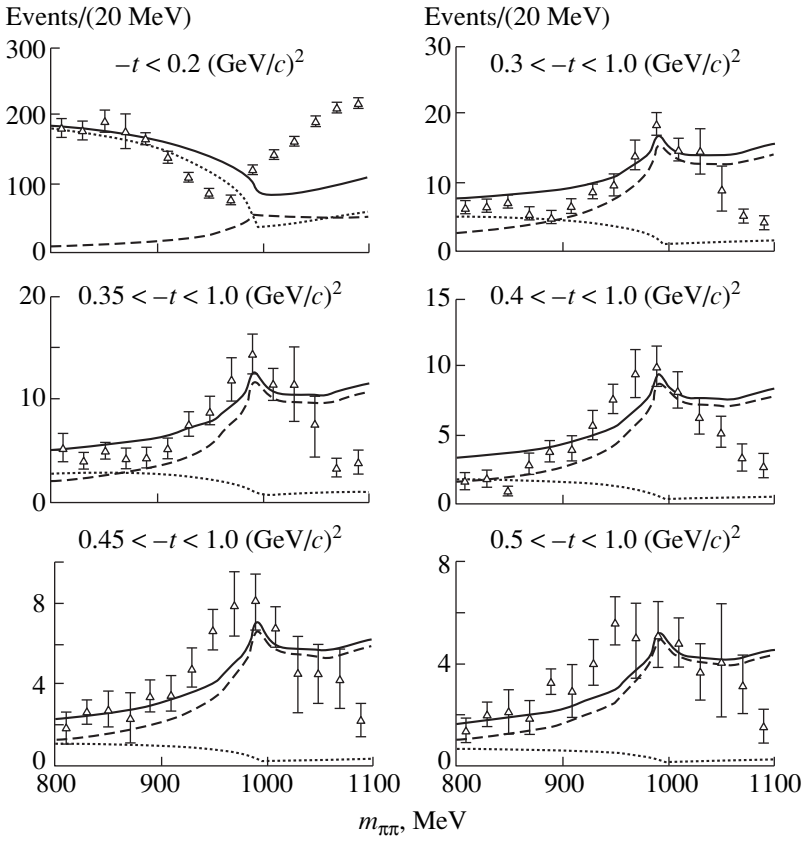

Fig. 8. The squares of the absolute values of the S partial-wave amplitude obtained in the reaction $\pi^- p \longrightarrow \pi^0\pi^0 n$ at a pion beam momentum of 38 GeV/c by the GAMS collaboration [1] are shown as a function of the invariant two-pion mass for events averaged over different t intervals. For a description of the theoretical curves, see Fig. 2.

$C_{a_1} = 0.001$, $b_\pi = 7.20$ (GeV/c)$^{-2}$, and $b_{a_1} = 3.50$ (GeV/c)$^{-2}$. With this choice, the model can reproduce a dip in the S-wave amplitudes for small momentum transfers and a peak at large momentum transfers, see Fig. 8. One notices that the bump at $m_{\pi\pi} \sim 1$ GeV can be seen even more clearly than in the case of the BNL-E852 data.

4. CONCLUSIONS

The present microscopic model shows that the $f_0(980)$-production puzzle in the reaction $\pi^- p \longrightarrow \pi^0\pi^0 n$ can be explained by meson dynamics. The a_1 meson plays a crucial role in the reaction mechanism, as was pointed out already by Achasov and Shestakov [16]. The present meson-exchange model does not include an explicit $f_0(980)$ resonance, but reproduces the experimental scalar–isoscalar phase shifts by the coupling to the $K\bar{K}$ channel, where the attractive vector–meson exchange in the t channel generates a quasibound state, as was already found in [8, 9]. The findings of both the GAMS [1] and the BNL-E852 [2] collaborations are therefore compatible with the assumption that the $f_0(980)$ meson is a $K\bar{K}$ molecule.

ACKNOWLEDGMENTS

Discussions with Prof. J. Durso and Prof. E. Klempt are gratefully acknowledged. Z.S.W. wishes to acknowledge the financial support extended to him by the Graduiertenkolleg “Die Erforschung der subnuklearen Strukturen der Materie” of the University of Bonn and by the Forschungszentrum Jülich.

REFERENCES

1. D. Alde *et al.*, Z. Phys. C **66**, 375 (1995).
2. J. Gunter *et al.*, hep-ex/0001038.
3. C. Amsler, Rev. Mod. Phys. **70**, 1293 (1998).
4. C. Amsler *et al.*, Phys. Lett. B **355**, 425 (1995).
5. S. Godfrey and J. Napolitano, Rev. Mod. Phys. **71**, 1411 (1999).
6. R. L. Jaffe, Phys. Rev. D **15**, 267 (1977).
7. J. Weinstein and N. Isgur, Phys. Rev. D **41**, 2236 (1990).
8. D. Lohse *et al.*, Nucl. Phys. A **516**, 513 (1990).
9. G. Janssen *et al.*, Phys. Rev. D **52**, 2690 (1995).
10. N. A. Tornqvist, Phys. Rev. Lett. **49**, 624 (1982).
11. N. A. Tornqvist, Phys. Rev. Lett. **76**, 1575 (1996).
12. T. Barnes, Phys. Lett. B **165B**, 434 (1985).
13. A. Antreasyan, Phys. Rev. D **33**, 1847 (1986).
14. V. V. Anisovich, Yu. D. Prokoshkin, and A. V. Sarantsev, Phys. Lett. B **389**, 388 (1996).
15. V. V. Anisovich, Yu. D. Prokoshkin, and A. V. Sarantsev, Phys. Lett. B **355**, 363 (1995).
16. N. N. Achasov and G. N. Shestakov, Phys. Rev. D **58**, 054011 (1998).
17. N. N. Achasov and G. N. Shestakov, Yad. Fiz. **62**, 548 (1999) [Phys. At. Nucl. **62**, 505 (1999)].
18. R. Kaminski, L. Lesniak, and K. Rybicki, Z. Phys. C **74**, 79 (1997).
19. R. Kaminski, L. Lesniak, and K. Rybicki, Phys. Lett. B **413**, 130 (1997).
20. D. Ebert and H. Reinhardt, Nucl. Phys. B **271**, 188 (1986).
21. I. J. R. Aitchison and C. M. Fraser, Phys. Rev. D **31**, 2605 (1985).
22. I. J. R. Aitchison and C. M. Fraser, Phys. Lett. B **146B**, 63 (1984).
23. C. M. Fraser, Z. Phys. C **28**, 101 (1985).
24. Zisheng Wang *et al.*, Z. Phys. A **358**, 451 (1997); Phys. Rev. C **55**, 3159 (1997).
25. Y. Nambu and G. Jona-Lasinio, Phys. Rev. **124**, 246 (1961).
26. J. Rahm *et al.*, Phys. Rev. C **57**, 1077 (1998).
27. R. Bryan, Phys. Rev. C **12**, 1968 (1975).
28. C. Caso *et al.*, Eur. Phys. J. C **3**, 1 (1998).
29. V. V. Anisovich and A. V. Sarantsev, Phys. Lett. B **413**, 137 (1997).

Physics of Atomic Nuclei, Vol. 64, No. 4, 2001, pp. 698–726. From Yadernaya Fizika, Vol. 64, No. 4, 2001, pp. 757–785.

90th ANNIVERSARY OF A.B. MIGDAL'S BIRTHDAY
ELEMENTARY PARTICLES AND FIELDS

Meson-Loop Effects in the NJL Model at Zero and Nonzero Temperature*

M. Oertel, M. Buballa, and J. Wambach

Institut für Kernphysik, TU Darmstadt, Schlossgartenstrasse 9, 64289 Darmstadt, Germany

Received August 23, 2000

Abstract—We compare two different possibilities of including meson-loop corrections in the Nambu–Jona-Lasinio model: a strict $1/N_c$ expansion in the next-to-leading order and a nonperturbative scheme corresponding to a one-meson-loop approximation to the effective action. Both schemes are consistent with chiral symmetry, in particular, with the Goldstone theorem and the Gell-Mann–Oakes–Renner relation. The numerical part at zero temperature focuses on the pion and the ρ-meson sector. For the latter, meson-loop corrections are crucial in order to include the dominant $\rho \longrightarrow \pi\pi$-decay channel, while the standard Hartree + RPA approximation only contains unphysical $q\bar{q}$-decay channels. We find that m_π, f_π, $\langle \bar{\psi}\psi \rangle$, and quantities related to the ρ-meson self-energy can be described reasonably with one parameter set in the $1/N_c$-expansion scheme, whereas we did not succeed in obtaining such a fit in the nonperturbative scheme. We also investigate the temperature dependence of the quark condensate. Here, we find consistency with the chiral perturbation theory to the lowest order. Similarities and differences of both schemes are discussed. *© 2001 MAIK "Nauka/Interperiodica".*

1. INTRODUCTION

During the last few years, one of the principal goals in nuclear physics has been to explore the phase structure of QCD. Along with this comes the investigation of hadron properties in a vacuum, as well as in hot or dense matter. In principle, all properties of strongly interacting particles should be derived from QCD. However, at least in the low-energy regime, where perturbation theory is not applicable, this is presently limited to a rather small number of observables that can be studied on a lattice, while more complex processes can either be addressed by chiral perturbation theory or within effective model calculations that try to incorporate the relevant degrees of freedom.

So far, the best descriptions of hadronic spectra, decays, and scattering processes have been obtained within phenomenological hadronic models. For instance, the pion electromagnetic form factor in the timelike region can be reproduced rather well within a simple-vector dominance model with a dressed ρ meson, which is constructed by coupling a bare ρ meson to a two-pion intermediate state [1, 2]. Models of this type have been successfully extended to investigate medium modifications of vector mesons and to calculate dilepton production rates in hot and dense hadronic matter [3].

In this situation, one might ask how the phenomenologically successful hadronic models emerge from the underlying quark structure and the symmetry properties of QCD. Since this question cannot be answered at present from first principles, it has to be addressed within quark models. For light hadrons, chiral symmetry and its spontaneous breaking in a physical vacuum through instantons play a decisive role in describing the two-point correlation functions [4], with confinement being much less important. This feature is captured by the Nambu–Jona-Lasinio (NJL) model, in which the four-fermion interactions can be viewed as being induced by instantons. Furthermore, the model allows a study of the chiral phase transition, as well as an examination of the influence of (partial) chiral-symmetry restoration on the properties of light hadrons.

The study of hadrons within the NJL model has, of course, a long history. In fact, mesons of various quantum numbers have already been discussed in the original papers by Nambu and Jona-Lasinio [5] and by many authors thereafter (for reviews, see [6–8]).

In most of these works, quark masses are calculated in the mean-field approximation (Hartree or Hartree–Fock), while mesons are constructed as correlated quark–antiquark states [random-phase approximation (RPA)]. This corresponds to a leading-order approximation in $1/N_c$, the inverse number of colors. With the appropriate choice of parameters, chiral symmetry, which is an (approximate) symmetry of the model Lagrangian, is spontaneously broken in the vacuum and pions emerge as (nearly) massless Goldstone bosons. While this is clearly one of the successes of the model, the description of other mesons is more problematic. One reason is the fact that the NJL model does not confine quarks. As a consequence, a meson can decay into free constituent quarks if its mass is larger than twice the constituent quark mass m. Hence, for a typical value of $m \sim 300$ MeV, the ρ meson with a mass of 770 MeV, for instance, would be unstable against decay into quarks.

* This article was submitted by the authors in English.

On the other hand, the physical decay channel of the ρ meson into two pions is not included in the standard approximation. Hence, even if a large constituent quark mass is chosen in order to suppress the unphysical decays into quarks, one obtains a poor description of the ρ-meson propagator and related observables, like the pion electromagnetic form factor.

Similar problems arise if one wants to study the phase structure of strongly interacting matter within a mean-field calculation for the NJL model, although this has been done by many authors (see, e.g., [7–10]). In these calculations, the thermodynamics is entirely driven by unphysical unconfined quarks even at low temperatures and densities, whereas the physical degrees of freedom, in particular the pion, are missing.

This and other reasons have motivated several authors to go beyond the standard approximation scheme and to include mesonic fluctuations. In [11], a quark–antiquark ρ meson is coupled via a quark triangle to a two-pion state. Also, higher order corrections to the quark self-energy [12] and to the quark condensate [13] have been investigated. However, as the most important feature of the NJL model is chiral symmetry, one should use an approximation scheme which conserves the symmetry properties in order to ensure the existence of massless Goldstone bosons.

A nonperturbative symmetry-conserving approximation scheme was discussed in [14, 15]. In [14], a correction term to the quark self-energy is included in the gap equation. The authors find a consistent scheme to describe mesons and show the validity of the Goldstone theorem and the Goldberger–Treiman relation in that scheme. The authors of [15] use a one-meson-loop approximation to the effective action in a bosonized NJL model. The structure of the meson propagators turns out to be the same as in the approach of [14]. Based on this scheme, various authors have investigated the effect of meson-loop corrections on the pion electromagnetic form factor [16] and on ππ scattering in the vector [17] and the scalar channel [18]. However, since the numerical evaluation of the multiloop diagrams is rather involved, the exact expressions are approximated by low-momentum expansions in these references.

Another possible method for constructing a symmetry-conserving approximate scheme beyond the Hartree approximation and RPA is a strict $1/N_c$ expansion up to the next-to-leading order. Whereas, in the approximation scheme mentioned above, the gap equation is modified in a self-consistent way, the corrections in the $1/N_c$-expansion scheme are perturbative. The consistency of the $1/N_c$-expansion scheme with chiral symmetry was shown in [14]. It was studied in more detail in [19, 20]. Recently, such an expansion was also discussed in the framework of a nonlocal generalization of the NJL model [21].

In the present paper, we compare the results obtained in the nonperturbative scheme with those obtained in the $1/N_c$-expansion scheme. In vacuum, we focus our discussion on the pion and the ρ meson calculated with the full momentum dependence of all expressions. Within the $1/N_c$-expansion scheme, the influence of mesonic fluctuations on the pion propagator was examined closely in [19]. This was mainly motivated by the recent works of Kleinert and Van den Bossche [22], who claim that chiral symmetry is not spontaneously broken in the NJL model as a result of strong mesonic fluctuations. In [19], we argued that because of the nonrenormalizability of the NJL model, new divergences and, hence, new cutoff parameters emerge if one includes meson loops. Following [14, 15], we regularize meson loops by an independent cutoff parameter Λ_M. The results are, of course, strongly dependent on this parameter. Whereas, for moderate values of Λ_M, the pion properties change only quantitatively, strong instabilities are encountered for larger values of Λ_M. In [19], we suggested that this might hint to instability of the spontaneously broken vacuum state. It turns out that instabilities of the same type also emerge in the nonperturbative scheme. This allows for an analysis of the vacuum structure and, therefore, for a more decisive answer to the question of whether chiral symmetry indeed gets restored due to strong mesonic fluctuations within this approximation.

In any case, in the $1/N_c$-expansion scheme, the region of parameter values where instabilities emerge in the pion propagator is far away from the realistic parameter set [20]. We used m_π, f_π, $\langle\bar{\psi}\psi\rangle$, and the ρ-meson spectral function to fix the parameters. The last one is particularly suited to fix the parameters, as it cannot be described realistically without taking into account pion loops. An important result of the analysis in [20] was that such a fit can be achieved with a constituent quark mass that is large enough such that the unphysical $q\bar{q}$ threshold opens above the ρ-meson peak. Since the constituent quark mass is not an independent input parameter, this was not clear a priori. In this paper, we will try the same for the self-consistent scheme. It turns out that it is not possible to find a parameter set where the constituent quark mass comes out to be large enough to describe the properties of the ρ meson reasonably. In fact, we encounter instabilities in the ρ-meson propagator that are similar to those we found in the pion propagator for large Λ_M.

The inclusion of meson-loop effects should also improve the thermodynamics of the model considerably. A first insight into the influence of mesonic fluctuations on the thermodynamics can be obtained via the temperature dependence of the quark condensate. It was shown in [23] that, in the self-consistent scheme, the low-temperature behavior is dominated by pionic degrees of freedom, which is a considerable improvement on calculations in the Hartree approximation, where quarks are the only degrees of freedom. Within this scheme, the results obtained in lowest order chiral perturbation theory can be reproduced. This is also the

Fig. 1. The Dyson equation for the quark propagator in the Hartree approximation (solid lines). The dashed lines denote the bare quark propagator.

case for the $1/N_c$-expansion scheme, which will be demonstrated in the last part of this paper. The nonperturbative scheme also allows for an examination of the chiral phase transition [23], whereas this is not possible within the $1/N_c$-expansion scheme.

The paper is organized as follows. In Section 2, we begin with a brief summary of the standard approximation scheme used in the NJL model to describe quarks and mesons and afterward present the scheme for describing quantities in the next-to-leading order in $1/N_c$. In Section 3, we discuss the nonperturbative approximation scheme. The consistency of these schemes with the Goldstone theorem and with the Gell-Mann–Oakes–Renner (GOR) relation will be shown in Section 4. The numerical results at zero temperature will be presented in Section 5. The temperature dependence of the quark condensate at nonzero temperature within the above-mentioned approximation schemes will be studied in Section 6. Finally, our conclusions are drawn in Section 7.

2. THE NJL MODEL IN LEADING ORDER AND IN THE NEXT-TO-LEADING ORDER IN $1/N_c$

2.1. The Standard Approximation Scheme: Hartree + RPA

We consider the generalized NJL-model Lagrangian

$$\begin{aligned}\mathcal{L} &= \bar\psi(i\hat\partial - m_0)\psi + g_s[(\bar\psi\psi)^2 + (\bar\psi i\gamma_5\boldsymbol{\tau}\psi)^2] \\ &\quad - g_v[(\bar\psi\gamma^\mu\boldsymbol{\tau}\psi)^2 + (\bar\psi\gamma^\mu\gamma_5\boldsymbol{\tau}\psi)^2],\end{aligned} \tag{2.1}$$

where ψ is a quark field with $N_f = 2$ flavors and $N_c = 3$ colors and g_s and g_v are coupling constants of dimension length^2. In contrast to QCD, color is not related to gauge symmetry in this model, but it is only related to the counting of degrees of freedom. However, if one defines the coupling constants to be of order $1/N_c$, the large-N_c behavior of the model agrees with that of QCD [14, 15]. Although we are not interested in the behavior of the model for arbitrary numbers of colors in the present article, the $1/N_c$ expansion is introduced for the purpose of book-keeping. This will allow us to take into account mesonic fluctuations in a symmetry-conserving way. In order to establish the expansion scheme, the number of colors will be formally treated as a variable. All numerical calculations will be performed, however, with the physical value of $N_c = 3$.

In the limit of vanishing current quark masses m_0 ("chiral limit"), the above Lagrangian is invariant under global $SU(2)_L \times SU(2)_R$ transformations. For a sufficiently large scalar attraction, this symmetry is spontaneously broken. This has mostly been studied within the Bogolyubov–Hartree approximation.[1)]

The Dyson equation for the quark propagator in the Hartree approximation is diagrammatically shown in Fig. 1. The self-consistent solution of this equation leads to a momentum-independent quark self-energy Σ_H and, therefore, only gives a correction to the quark mass:

$$\begin{aligned} m &= m_0 + \Sigma_H(m) \\ &= m_0 + \sum_M 2ig_M\int\frac{d^4p}{(2\pi)^4}\mathrm{tr}[\Gamma_M S(p)].\end{aligned} \tag{2.2}$$

Usually, m is called the "constituent quark mass." Here, $S(p) = (\hat p - m)^{-1}$ is the (Hartree) quark propagator and "tr" denotes a trace in color, flavor, and Dirac space. The sum runs over all interaction channels $M = \sigma, \pi, \rho, a_1$ with $\Gamma_\sigma = \mathbb{1}$, $\Gamma_\pi^a = i\gamma_5\tau^a$, $\Gamma_\rho^{\mu a} = \gamma^\mu\tau^a$, and $\Gamma_{a_1}^{\mu a} = \gamma^\mu\gamma_5\tau^a$. The corresponding coupling constants are $g_M = g_s$ for $M = \sigma$ or $M = \pi$ and $g_M = g_v$ for $M = \rho$ or $M = a_1$. Of course, only the scalar channel ($M = \sigma$) contributes in a vacuum. One gets

$$m = m_0 + 2ig_s 4N_cN_f\int\frac{d^4p}{(2\pi)^4}\frac{m}{p^2 - m^2 + i\epsilon}. \tag{2.3}$$

In a $1/N_c$ expansion of the quark self-energy, the Hartree approximation corresponds to the leading order. Since g_s is of order $1/N_c$, the constituent quark mass m and, hence, the quark propagator are about unity.

For sufficiently large couplings g_s, Eq. (2.3) allows for a finite constituent quark mass m even in the chiral limit. In the mean-field approximation, this solution minimizes the ground-state energy. Because of the related gap in the quark spectrum, one usually refers to this equation as the gap equation, in analogy to BCS theory.

A closely related quantity is the quark condensate, which is generally given by

$$\langle\bar\psi\psi\rangle = -i\int\frac{d^4p}{(2\pi)^4}\mathrm{tr}\,S(p). \tag{2.4}$$

In a Hartree approximation, one immediately gets from the gap equation

$$\langle\bar\psi\psi\rangle^{(0)} = -\frac{m - m_0}{2g_s}, \tag{2.5}$$

[1)]Because of the local 4-fermion interaction in the Lagrangian, exchange diagrams can always be cast in the form of direct diagrams via a Fierz transformation. This is well known from zero-range interactions in nuclear physics. In particular, the Hartree–Fock approximation is equivalent to the Hartree approximation with appropriately redefined coupling constants. In this sense, we call the Hartree approximation the "standard approximation" to the NJL model, although, in several references, the Hartree–Fock approximation was performed.

where we have used the superscript (0) to indicate that this corresponds to a Hartree approximation.

Mesons are described via a Bethe–Salpeter equation. Here, the leading order in $1/N_c$ is given by an RPA without Pauli exchange diagrams. This is diagrammatically shown in Fig. 2. The elementary building blocks of this scheme are the quark–antiquark polarization functions

$$\Pi_M(q) = -i\int\frac{d^4p}{(2\pi)^4}\mathrm{tr}\left[\Gamma_M iS\left(p+\frac{q}{2}\right)\Gamma_M iS\left(p-\frac{q}{2}\right)\right], \quad (2.6)$$

with Γ_M, $M = \sigma, \pi, \rho, a_1$, as defined above. Again, the trace has to be taken in color, flavor, and Dirac space. Iterating the scalar (pseudoscalar) part of the four-fermion interaction, one obtains for the sigma meson (pion)

$$D_\sigma(q) = \frac{-2g_s}{1-2g_s\Pi_\sigma(q)},$$
$$D_\pi^{ab}(q) \equiv D_\pi(q)\delta_{ab} = \frac{-2g_s}{1-2g_s\Pi_\pi(q)}\delta_{ab}. \quad (2.7)$$

Here, a and b are isospin indices and we have used the notation $\Pi_\pi^{ab}(q) \equiv \Pi_\pi(q)\delta_{ab}$.

In the vector channel, this can be done in a similar way. Using the transverse structure of the polarization loop in the vector channel,

$$\Pi_\rho^{\mu\nu,ab}(q) = \Pi_\rho(q)T^{\mu\nu}\delta_{ab},$$
$$T^{\mu\nu} = \left(-g^{\mu\nu}+\frac{q^\mu q^\nu}{q^2}\right), \quad (2.8)$$

one obtains for the ρ meson

$$D_\rho^{\mu\nu,ab}(q) \equiv D_\rho(q)T^{\mu\nu}\delta_{ab} = \frac{-2g_v}{1-2g_v\Pi_\rho(q)}T^{\mu\nu}\delta_{ab}. \quad (2.9)$$

Analogously, a_1 can be constructed from the transverse part of the axial polarization function Π_{a_1}. As discussed, e.g., in [24], $\Pi_{a_1}^{\mu\nu}$ also contains a longitudinal part, which contributes to the pion. Although there is no conceptional problem in including this mixing, we will neglect it in the present paper in order to keep the structure of the model as simple as possible.

It follows from Eqs. (2.6)–(2.9) that the functions $D_M(q)$ are of order $1/N_c$. Their explicit forms are given in Appendix B. For simplicity, we will call them "propagators," although, strictly speaking, they should be interpreted as the product of a renormalized meson propagator and a squared quark–meson coupling constant. The latter is given by the inverse residue of the function $D_M(q)$, while the pole position determines the meson mass:

$$D_M^{-1}(q)|_{q^2=m_M^{2(0)}} = 0, \quad g_{Mqq}^{-2(0)} = \left.\frac{d\Pi_M(q)}{dq^2}\right|_{q^2=m_M^{2(0)}}. \quad (2.10)$$

Again, the superscript (0) indicates that $m_M^{2(0)}$ and $g_{Mqq}^{-2(0)}$ are quantities in RPA. One easily verifies that they are of order unity and $1/\sqrt{N_c}$, respectively.

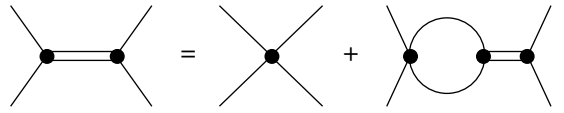

Fig. 2. The Bethe–Salpeter equation for the meson propagator in the RPA (double line). The solid lines indicate quark propagators.

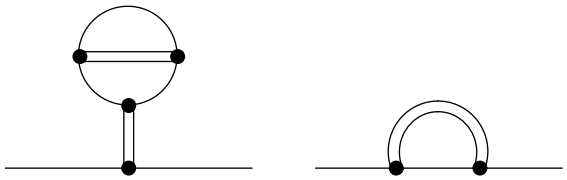

Fig. 3. The $1/N_c$ corrections $\delta\Sigma^{(a)}$ (left) and $\delta\Sigma^{(b)}$ (right) to the quark self-energy.

2.2 Next-to-Leading Order Corrections

With the help of the gap equation, Eq. (2.3), one can show that the "standard scheme," i.e., Hartree approximation + RPA, is consistent with chiral symmetry. For instance, in the chiral limit, pions are massless, as required by the Goldstone theorem. Of course, one would like to preserve this feature when one goes beyond the standard scheme. One way to accomplish this is to perform a strict $1/N_c$ expansion systematically including higher order corrections. In this subsection, we want to construct the quark self-energy and the mesonic polarization functions in next-to-leading order in $1/N_c$.

The correction terms to the quark self-energy,

$$\delta\Sigma(p) = \delta\Sigma^{(a)} + \delta\Sigma^{(b)}(p), \quad (2.11)$$

are shown in Fig. 3. In these diagrams, the single lines and the double lines correspond to quark propagators in the Hartree approximation (order unity) and to meson propagators in the RPA (order $1/N_c$), respectively. Recalling that one obtains a factor N_c for a closed quark loop, one finds that both diagrams are of order $1/N_c$. One can also easily convince oneself that there are no other self-energy diagrams of that order.

According to Eq. (2.4), the $1/N_c$ correction to the quark condensate is given by

$$\delta\langle\bar\psi\psi\rangle = -i\int\frac{d^4p}{(2\pi)^4}\mathrm{tr}\delta S(p), \quad (2.12)$$

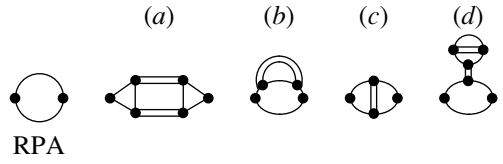

Fig. 4. Contributions to the mesonic polarization function in the leading (RPA) and the next-to-leading order in $1/N_c$.

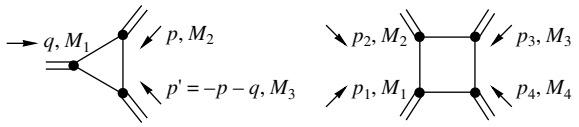

Fig. 5. (Left) The quark triangle vertex $-i\Gamma_{M_1, M_2, M_3}(q, p)$. (Right) The quark box vertex $-i\Gamma_{M_1, M_2, M_3, M_4}(p_1, p_2, p_3)$.

with

$$\delta S(p) = S(p)\delta\Sigma(p)S(p) \tag{2.13}$$

being the $1/N_c$ correction to the Hartree quark propagator $S(p)$. Since we are interested in a strict $1/N_c$ expansion, the self-energy correction must not be iterated.

The $1/N_c$-corrected mesonic polarization diagrams read

$$\tilde{\Pi}_M(q) = \Pi_M(q) + \sum_{k = a, b, c, d} \delta\Pi_M^{(k)}(q). \tag{2.14}$$

The four correction terms $\delta\Pi_M^{(a)}$ to $\delta\Pi_M^{(d)}$, together with the leading-order term Π_M, are shown in Fig. 4. Again, the lines in this figure correspond to Hartree quarks and RPA mesons. Since the correction terms consist of either one RPA propagator and one quark loop or two RPA propagators and two quark loops, they are of order unity, whereas the leading-order term is of order N_c.

In analogy to Eqs. (2.7), (2.9), and (2.10), the corrected meson propagators are given by

$$\tilde{D}_M(q) = \frac{-2g_M}{1 - 2g_M\tilde{\Pi}_M(q)}, \tag{2.15}$$

while the corrected meson masses are defined by the pole positions of the propagators:

$$\tilde{D}_M^{-1}(q)\big|_{q^2 = m_M^2} = 0. \tag{2.16}$$

As we will see in Subsection 4.1, this scheme is consistent with the Goldstone theorem; i.e., in the chiral limit, it leads to massless pions. Note, however, that, because of its implicit definition, m_M contains terms of arbitrary orders in $1/N_c$, although we start from a strict expansion of the inverse meson propagator up to the next-to-leading order. This will be important in the context of the GOR relation.

For a more explicit evaluation of the correction terms, it is advantageous to introduce the quark triangle and box diagrams, which are shown in Fig. 5. The triangle diagrams entering into $\delta\Sigma^{(a)}$, $\delta\Pi_M^{(a)}$, and $\delta\Pi_M^{(d)}$ can be interpreted as effective three-meson vertices. For external mesons M_1, M_2, and M_3, they are given by

$$\begin{aligned} &-i\Gamma_{M_1, M_2, M_3}(q, p) \\ &= -\int\frac{d^4k}{(2\pi)^4}\{\mathrm{tr}[\Gamma_{M_1}iS(k)\Gamma_{M_2}iS(k-p)\Gamma_{M_3}iS(k+q)] \\ &\quad + \mathrm{tr}[\Gamma_{M_1}iS(k-q)\Gamma_{M_3}iS(k+p)\Gamma_{M_2}iS(k)]\} \end{aligned} \tag{2.17}$$

with the operators Γ_M as defined below Eq. (2.2). We have summed over both possible orientations of the quark loop. For later convenience, we also define the constant

$$\Delta = \frac{1}{2}\int\frac{d^4p}{(2\pi)^4}\sum_M(-iD_M(p))(-i\Gamma_{M, M, \sigma}(p, -p)), \tag{2.18}$$

which corresponds to a quark triangle coupled to an external scalar vertex and a closed meson loop.

The quark box diagrams are effective four-meson vertices and are needed for the evaluation of $\delta\Pi_M^{(b)}$ and $\delta\Pi_M^{(c)}$. If one again sums over both orientations of the quark loop, they are given by

$$\begin{aligned} &-i\Gamma_{M_1, M_2, M_3, M_4}(p_1, p_2, p_3) \\ &= -\int\frac{d^4k}{(2\pi)^4}(\mathrm{tr}[\Gamma_{M_1}iS(k)\Gamma_{M_2}iS(k-p_2) \\ &\quad \times\Gamma_{M_3}iS(k-p_2-p_3)\Gamma_{M_4}iS(k+p_1)] \\ &\quad + \mathrm{tr}[\Gamma_{M_1}iS(k-p_1)\Gamma_{M_4}iS(k+p_2+p_3) \\ &\quad \times\Gamma_{M_3}iS(k+p_2)\Gamma_{M_2}iS(k)]). \end{aligned} \tag{2.19}$$

With these definitions, the various diagrams can be written in a relatively compact form. For the momentum-independent correction term to the quark self-energy, we get

$$\begin{aligned} \delta\Sigma^{(a)} &= -\frac{1}{2}D_\sigma(0)\sum_M\int\frac{d^4p}{(2\pi)^4}D_M(p)\Gamma_{M, M, \sigma}(p, -p) \\ &= D_\sigma(0)\Delta. \end{aligned} \tag{2.20}$$

In principle, there should also be a sum over the quantum numbers of the meson that connects the quark loop with the external quark legs, but all contributions from mesons other than the σ meson vanish. The factor of 1/2 is a necessary symmetry factor because, otherwise, the sum over the two orientations of the quark propagators [which is contained in the definition of the quark triangle vertex (Eq. (2.7))] would lead to double counting.

The evaluation of the momentum-dependent correction term $\delta\Sigma^{(b)}$ is straightforward:

$$\delta\Sigma^{(b)}(k) = i\sum_M \int \frac{d^4p}{(2\pi)^4} D_M(p)\Gamma_M S(k-p)\Gamma_M. \quad (2.21)$$

Inserting these expressions for $\delta\Sigma^{(a)}$ and $\delta\Sigma^{(b)}$ into Eq. (2.13), we can recast the $1/N_c$-correction term to the quark condensate, Eq. (2.12), into the form

$$\delta\langle\bar\psi\psi\rangle = -\frac{D_\sigma(0)\Delta}{2g_s}. \quad (2.22)$$

For the mesonic polarization diagrams, we get

$$\delta\Pi_M^{(a)}(q) = \frac{i}{2}\int\frac{d^4p}{(2\pi)^4}\sum_{M_1M_2}\Gamma_{M,M_1,M_2}(q,p)D_{M_1}(p)$$
$$\times\Gamma_{M,M_1,M_2}(-q,-p)D_{M_2}(-p-q),$$

$$\delta\Pi_M^{(b)}(q)$$
$$= -i\int\frac{d^4p}{(2\pi)^4}\sum_{M_1}\Gamma_{M,M_1,M_1,M}(q,p,-p)D_{M_1}(p),$$

$$\delta\Pi_M^{(c)}(q) \quad (2.23)$$
$$= -\frac{i}{2}\int\frac{d^4p}{(2\pi)^4}\sum_{M_1}\Gamma_{M,M_1,M,M_1}(q,p,-q)D_{M_1}(p),$$

$$\delta\Pi_M^{(d)}(q) = \frac{i}{2}\Gamma_{M,M,\sigma}(q,-q)D_\sigma(0)$$
$$\times\int\frac{d^4p}{(2\pi)^4}\sum_{M_1}\Gamma_{M_1,M_1,\sigma}(p,-p)D_{M_1}(p)$$
$$= -i\Gamma_{M,M,\sigma}(q,-q)D_\sigma(0)\Delta.$$

The symmetry factor of 1/2 for $\delta\Pi_M^{(c)}$ and $\delta\Pi_M^{(d)}$ has the same origin as in Eq. (2.20). Similarly, in $\delta\Pi_M^{(a)}$, we had to correct for the fact that the exchange of M_1 and M_2 leads to identical diagrams.

For the further evaluation of Eqs. (2.20) to (2.23), we proceed in two steps. In the first step, we calculate the intermediate RPA meson propagators. We can simultaneously calculate the quark triangles and box diagrams. One is then left with a meson loop, which has to be evaluated in a second step.

The various sums in Eqs. (2.20) to (2.23) are, in principle, over all quantum numbers of the intermediate mesons. However, for most applications, we expect that the most important contributions come from the pion, which is the lightest particle in the game. For instance, the change of the quark condensate at low temperatures should be dominated by thermally excited pions. Also, for a proper description of the ρ-meson width in a vacuum, we only need the two-pion intermediate state in diagram $\delta\Pi_M^{(a)}$. Other contributions to this diagram, i.e., πa_1, $\rho\sigma$, $\rho\rho$, and a_1a_1 intermediate states, are much less important since the corresponding decay channels open far above the ρ-meson mass and—in the NJL model—also above the unphysical two-quark threshold. Hence, from a purely phenomenological point of view, it should be sufficient for many applications to restrict the sums in Eq. (2.23) to intermediate pions. However, in order to stay consistent with chiral symmetry, we have to include intermediate σ mesons as well. On the other hand, vector and axial-vector mesons can be neglected without violating chiral symmetry. Since this leads to an appreciable simplification of the numerics, we have restricted the intermediate degrees of freedom to scalar and pseudoscalar mesons in the present paper. Of course, in order to describe a ρ meson, we have to take vector couplings at the external vertices of the diagrams shown in Fig. 4.

3. NONPERTURBATIVE SYMMETRY-CONSERVING SCHEMES

3.1. Axial Ward identities

The disadvantage of the $1/N_c$-expansion scheme is that it is perturbative. Although we have constructed the $1/N_c$ corrections to the Hartree quark self-energy (Fig. 3), we did not self-consistently include such diagrams in the gap equation. Since the iteration would produce terms of arbitrary orders in $1/N_c$, one is not allowed to do so in a strict expansion scheme. Therefore, all correction diagrams we have discussed in the previous section consist of "Hartree" quark propagators. This perturbative treatment should work rather well as long as the $1/N_c$ corrections to the quark self-energy are small compared with the leading order, i.e., the constituent quark mass. On the other hand, it is clear that the scheme must fail to describe the chiral phase transition, e.g., at finite temperatures. Here, a nonperturbative treatment is mandatory.

Therefore, in this section, we want to follow a different strategy, exploiting the fact that the Goldstone theorem is basically a consequence of Ward identities. Consider an external axial current $j^a_{\mu5}$ coupled to a quark. Then, in the chiral limit, the corresponding vertex function $\Gamma^a_{\mu5}$ is related to the quark propagator $S(p)$ via the axial Ward–Takahashi identity:

$$q^\mu\Gamma^a_{\mu5}(p,q) = S^{-1}(p+q)\gamma_5\tau^a + \gamma_5\tau^a S^{-1}(p), \quad (3.1)$$

where p and $p+q$ are the 4-momenta of the incoming and the outgoing quark, respectively. Obviously, for a nonvanishing constituent quark mass, the right-hand side of this equation remains finite even for $q \longrightarrow 0$. Consequently, $\Gamma^a_{\mu5}(p,q)$ must have a pole in this limit that can be identified with the Goldstone boson. More-

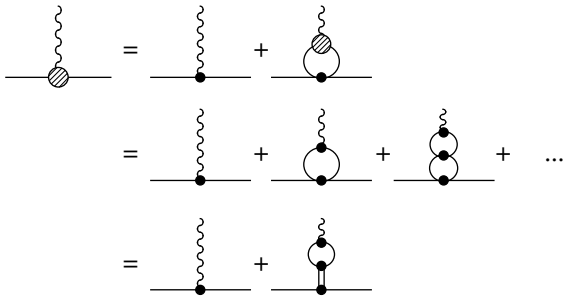

Fig. 6. Vertex function for an external axial current coupled to a "Hartree" quark.

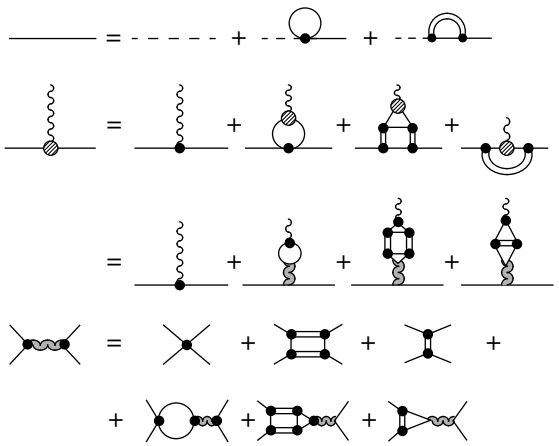

Fig. 7. Self-consistent scheme with a nonlocal self-energy term: gap equation (upper part), equation for the vertex function of an external current (middle), and the corresponding equation for the quark–antiquark T matrix (lower part). The double line denotes an RPA meson propagator (see Fig. 2), which is self-consistently constructed from the dressed-quark propagators of the present equation (solid line).

over, the explicit structure of the Goldstone boson can be constructed from the structure of the axial vertex function.

As a first example, let us start again from the Hartree gap equation [Eq. (2.2), Fig. 1] and construct the axial vertex function by coupling the propagator to an external axial current. This is illustrated in Fig. 6. In the upper line, the first term on the right-hand side describes the coupling to the bare quark corresponding to the bare vertex $\gamma_\mu\gamma_5\tau^a$. In the second term, however, the current is coupled to a dressed quark; therefore, we have to use the same vertex function as on the left-hand side of the equation

$$\Gamma^a_{\mu 5}(p,q) = \gamma_\mu\gamma_5\tau^a + \sum_M 2ig_M\Gamma_M\int\frac{d^4k}{(2\pi)^4}\mathrm{tr}[\Gamma_M S(k+q)\Gamma^a_{\mu 5}(k,q)S(k)]. \quad (3.2)$$

Here, $S(k)$ denotes the quark propagator in the Hartree approximation. As in Eq. (2.2), the sum runs over all interaction channels, but, of course, only the pseudoscalar and the axial vector contributions do not vanish. Contracting Eq. (3.2) with q_μ, one obtains a linear equation for $q_\mu\Gamma^a_{\mu 5}$. One can easily verify that, in the chiral limit, the solution of this equation is given by the axial Ward–Takahashi identity, Eq. (3.1). To this end, we replace $q_\mu\Gamma^a_{\mu 5}$ on both sides of the equation by the expressions given by Eq. (3.1) and check whether the results agree. On the right-hand side, the insertion of Eq. (3.1) basically amounts to removing one of the quark propagators from the loop. In this way, the loop receives the structure of the quark self-energy and we can use the gap equation, Eq. (2.2), to simplify the expression. For $m_0 = 0$, the result turns out to be equal to the left-hand side of the equation, which proves the validity of the axial Ward–Takahashi in this scheme.

We have seen above that this implies the existence of a massless Goldstone boson in the chiral limit. As illustrated in the second and the third line of Fig. 6, the self-consistent structure of Eq. (3.2) for the dressed vertex $\Gamma^a_{\mu 5}$ leads to an iteration of the quark loop and an RPA pion emerges. Hence, we can identify the Goldstone boson with an RPA pion.

Obviously, the above procedure can be generalized to other cases. Starting from any given gap equation for the quark propagator, we construct the vertex function to an external axial current by coupling the current in all possible ways to the right-hand side of the equation. As long as the gap equation does not violate chiral symmetry, this automatically guarantees the validity of the axial Ward–Takahashi identity and, therefore, the existence of a massless pion in the chiral limit. The structure of this pion can then be obtained from the structure of the vertex correction.

As an example, we start from the extended gap equation depicted in the upper part of Fig. 7. There, in addition to the Hartree term, the quark is dressed by RPA mesons. These are defined in the same way as before (Fig. 2), but now self-consistently using the quark propagator which results from the extended gap equation. Therefore, the RPA pions are no longer massless in the chiral limit. However, following the strategy described above, we can construct the consistent pion propagator. To that end, we again couple an external axial current to both sides of the gap equation. The resulting equation for the vertex function is also shown in Fig. 7 (middle part). The additional term in the gap equation leads to two new diagrams, which were not present in Fig. 6. In the first, the current couples to a quark–antiquark loop of the RPA meson, while, in the second, it couples to the quark inside of the meson loop. Again, one can easily check that the vertex function and the quark propagator fulfill the axial Ward–Takahashi identity, Eq. (3.1), in the chiral limit.

In principle, one can construct the corresponding massless Goldstone boson from the quark–antiquark T

matrix given in the lower part of Fig. 7. In practice, however, this is very difficult. In fact, even solving the extended gap equation is difficult, since the additional self-energy term is nonlocal, leading to a nontrivial 4-momentum dependence of the quark propagator. Note that this propagator has to be self-consistently used for the calculation of the RPA-meson propagator. Therefore, the authors of [14] suggested droping the nonlocal terms, but retaining a particular class of local diagrams that arises from the combined iteration of the quark loop and the meson loop. This gap equation is shown in Fig. 8. Because of the restriction to local self-energy insertions, we will call this scheme the "local self-consistent scheme" (LSS). It will be discussed in the next subsection.

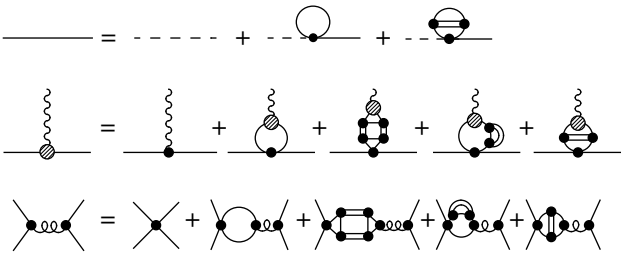

Fig. 8. The "local self-consistent scheme": gap equation (upper part), equation for the vertex function of an external current (middle), and the corresponding equation for the consistent meson propagator (lower part). The double curve denotes an RPA meson propagator (see Fig. 2) that is self-consistently constructed from the dressed-quark propagators of the present equation (solid curve).

3.2. The Local Self-Consistent Scheme

The gap equation for the constituent quark mass in the LSS (upper part of Fig. 8) reads

$$m = m_0 + \tilde{\Sigma}(m) = m_0 + \Sigma_{\mathrm{H}}(m) + \delta\tilde{\Sigma}(m). \qquad (3.3)$$

Here, Σ_{H} is the Hartree contribution to the self-energy as defined in Eq. (2.2). The correction term $\delta\tilde{\Sigma}$ corresponds to the third diagram on the right-hand side of Fig. 8. We have explicitly indicated that the self-energy diagrams have to be evaluated self-consistently at the quark mass m, which comes out of the equation. Because of the new diagram $\delta\tilde{\Sigma}$, this mass is, in general, different from the Hartree mass. However, since all diagrams in the LSS are constructed from the constituent quarks of Eq. (3.3), we prefer not to introduce a new symbol for this mass. This has the advantage that we can also keep the notation for the quark propagator $S(p) = (\hat{p} - m)^{-1}$, quark–antiquark loops, triangles, etc. that we introduced earlier. The general structure of these diagrams is the same in all schemes we discuss in this article. Therefore, we introduce the convention that, in the $1/N_c$-expansion scheme, m denotes the Hartree mass, while it denotes the solution of Eq. (3.3) in the LSS, and all diagrams should be evaluated at that mass, unless otherwise stated.

The self-energy term $\delta\tilde{\Sigma}$ consists of a quark loop dressed by an RPA-meson loop. The quark loop is coupled to the external quark propagators via the NJL point interaction. It can again be shown that only the scalar interaction contributes. Hence, $\delta\tilde{\Sigma}$ is given by

$$\delta\tilde{\Sigma} = -2g_s\Delta, \qquad (3.4)$$

where Δ is the constant defined in Eq. (2.18).

Because of this additional self-energy diagram in the gap equation, the RPA is not the consistent scheme to describe mesons: in the chiral limit, RPA pions are no longer massless. Hence, in order to find the consistent meson propagators, we proceed in the way discussed in the previous subsection.

The equation for the axial vertex function is shown in the middle part of Fig. 8. Compared with the corresponding equation that follows from the Hartree approximation (Fig. 6), there are three extra terms. This leads to three additional polarization diagrams, which have to be iterated in the Bethe–Salpeter equation for the consistent meson propagator (lower part of Fig. 8).

Obviously, these diagrams are identical to $\delta\Pi_M^{(a)}$, $\delta\Pi_M^{(b)}$, and $\delta\Pi_M^{(c)}$, which we defined in Subsection 2.2 [Fig. 4, Eq. (2.23)]; i.e., the new meson propagators are given by

$$\tilde{D}_M(q) = \frac{-2g_M}{1 - 2g_M\tilde{\Pi}_M(q)}, \qquad (3.5)$$

with

$$\tilde{\Pi}_M(q) = \Pi_M(q) + \sum_{k=a,b,c} \delta\Pi_M^{(k)}(q). \qquad (3.6)$$

This structure agrees with the result of [14]. In that reference, the scheme was motivated by a $1/N_c$ expansion. However, one should again stress that the self-consistent solution of the gap equation mixes all orders in $1/N_c$. Moreover, the next-to-leading-order self-energy correction term $\delta\Sigma^{(b)}$ (cf. Fig. 3) is not contained in the gap equation of Fig. 8. Therefore, the consistency of the scheme cannot be explained by $1/N_c$ arguments. In fact, our discussion shows that the structure of the consistent pion propagator can be derived from the gap equation without any reference to $1/N_c$ counting.

On the other hand, if one performs a strict $1/N_c$ expansion of the mesonic polarization diagrams up to the next-to-leading order, one exactly recovers the diagrams shown in Fig. 4 [14]. This is quite obvious for the diagrams $\delta\Pi_M^{(a)}$ to $\delta\Pi_M^{(c)}$, which are explicitly contained in poltilde. The diagram $\delta\Pi_M^{(d)}$, which seems to be missing, is implicitly contained in the quark–antiquark loop via the next-to-leading-order terms in the

quark propagator, which arise from the extended gap equation.

In this sense, the LSS may be viewed as the simplest nonperturbative extension of the standard scheme which is consistent with the Goldstone theorem and which contains all mesonic polarization diagrams up to next-to-leading order in $1/N_c$. However, since the diagram $\delta\Sigma^{(b)}$ is not contained in the gap equation, this is not true for the quark condensate: if we evaluate Eq. (2.4) with the quark propagator of the present scheme, we obtain

$$\langle\bar{\psi}\psi\rangle = -\frac{\Sigma_{\mathrm{H}}}{2g_s} = -\frac{m-m_0}{2g_s} - \Delta. \tag{3.7}$$

Performing a strict $1/N_c$ expansion of this expression and only keeping the next-to-leading order term, one does not recover Eq. (2.22) but only the contribution of $\delta\Sigma^{(a)}$. This might be the reason why the authors of [14] determine the quark condensate as

$$\langle\bar{\psi}\psi\rangle = -\frac{\tilde{\Sigma}}{2g_s} = -\frac{m-m_0}{2g_s}. \tag{3.8}$$

In contrast to Eq. (3.7), this expression reduces to the perturbative result in a strict $1/N_c$ expansion. Moreover, as we will discuss in Subsection 4.2, it is consistent with the GOR relation. On the other hand, Eq. (3.8) obviously does not follow from Eq. (2.4) with the quark propagator of the present scheme. A possible resolution to this problem was given in [15], where the LSS was derived using functional methods. The meson propagators obtained in this way are identical to Eqs. (3.5) and (3.6), while the quark condensate is given by Eq. (3.8). This will be briefly discussed in the following subsection.

Finally, we would like to comment on the name "local self-consistent scheme," which we have introduced in order to distinguish this scheme from the perturbative $1/N_c$ expansion. We call this scheme "self-consistent" because the quark propagator which is determined by the gap equation is self-consistently used in the loops and the RPA-meson propagator on the right-hand side of the equation. However, as we have seen, the scheme is not self-consistent with respect to the mesons: the improved meson propagators given by Eqs. (3.5) and (3.6) are different from the RPA mesons which are used in the gap equation and hence as intermediate states in the mesonic polarization functions $\delta\Sigma^{(a)}$ to $\delta\Sigma^{(c)}$. On the other hand, if we had used the improved mesons already in the gap equation, our method of Subsection 3.1 would have led to further mesonic polarization diagrams in order to be consistent with chiral symmetry. Obviously, the construction of an expansion scheme which is self-consistent for quarks and mesons is an extremely difficult task.

3.3 One-Meson-Loop Order in the Effective Action Formalism

Both the nonlocal self-consistent scheme, which we briefly discussed in Subsection 3.1 (Fig. 7), and the local self-consistent scheme can be derived from functional methods: the nonlocal self-consistent scheme can be obtained as a Φ-derivable theory [25, 26] if one includes the "ring sum" in the generating functional. The present section is devoted to a brief discussion on how the local self-consistent scheme can be derived from a one-meson-loop approximation to the effective action. The interested reader is referred to [15, 27]. Here, we will basically follow [15].

In this section, we drop the vector and the axial-vector interaction and start from a Lagrangian which contains only scalar and pseudoscalar interaction terms:

$$\mathcal{L} = \bar{\psi}(i\hat{\partial} - m_0)\psi + g_s[(\bar{\psi}\psi)^2 + (\bar{\psi}i\gamma_5\boldsymbol{\tau}\psi)^2]. \tag{3.9}$$

The partition function of the system can be expressed in terms of the path integral

$$Z = e^{-W} = \int\mathcal{D}(\psi^\dagger)\mathcal{D}(\psi)e^{-I(\psi^\dagger,\psi)}, \tag{3.10}$$

with the Euclidean action

$$\begin{aligned} I(\psi^\dagger,\psi) = \int d^4x_{\mathrm{E}}\{&\psi^\dagger\gamma_0(\partial_\tau\gamma_0 - i\boldsymbol{\gamma}\cdot\boldsymbol{\nabla} + m_0)\psi \\ &- g_s((\psi^\dagger\gamma_0\psi)^2 + (\psi^\dagger\gamma_0 i\gamma_5\boldsymbol{\tau}\psi)^2)\}. \end{aligned} \tag{3.11}$$

The integration here is over a Euclidean spacetime volume d^4x_{E}, where ∂_τ corresponds to $i\partial_t$. The standard procedure is now to bosonize the action by introducing auxiliary fields Φ'_a, $a = \{0, 1, 2, 3\}$:

$$\begin{aligned} Z = &\int\mathcal{D}(\psi^\dagger)\mathcal{D}(\psi)\mathcal{D}(\Phi'_a) \\ &\times\exp\left\{-I(\psi^\dagger,\psi) - \frac{1}{4g_s}\int d^4x_{\mathrm{E}}(\Phi'_a + 2g_s\psi^\dagger\gamma_0\Gamma_a\psi)^2\right\}, \end{aligned} \tag{3.12}$$

with $\Gamma_a = (1, i\gamma_5\boldsymbol{\tau})$. Then, the action contains only bilinear terms in the quark fields, so that they can be integrated out. After performing a shift of the auxiliary fields, $\Phi_a = \Phi'_a + (m_0, \mathbf{0})$, one finally arrives at the bosonized action

$$I(\Phi) = -\mathrm{tr}\ln S^{-1} + \frac{1}{4g_s}\int d^4x_{\mathrm{E}}(\Phi^2 - 2m_0\Phi_0 + m_0^2), \tag{3.13}$$

where S^{-1} is the Dirac operator

$$S^{-1} = \gamma_0\partial_\tau - i\boldsymbol{\gamma}\cdot\boldsymbol{\nabla} + \Gamma_a\Phi_a. \tag{3.14}$$

The symbol tr in Eq. (3.13) is to be understood as a functional trace and a trace over internal degrees of freedom like flavor, color, and spin; $\mathrm{tr}\ln S^{-1}$ is the quark-

loop contribution. The imaginary part of this term vanishes for the $SU(2)$ case and we can rewrite the action as

$$I(\Phi) = -\frac{1}{2}\mathrm{tr}\ln S^{-1\dagger}S^{-1} + \frac{1}{4g_s}\int d^4x_{\mathrm{E}}(\Phi^2 - 2m_0\Phi_0 + m_0^2). \quad (3.15)$$

The effective action $\Gamma(\Phi)$ is defined as a Legendre transform of the generating functional $W(j)$. Its stationary point $\langle\Phi_a\rangle$, i.e.,

$$\left.\frac{\delta\Gamma(\Phi)}{\delta\Phi_a}\right|_{\Phi_a = \langle\Phi_a\rangle} = 0, \quad (3.16)$$

represents the vacuum expectation values of the fields.

The quark condensate can be expressed via the expectation value of Φ_0. It is given as

$$\langle\bar{\psi}\psi\rangle = \frac{\partial W}{\partial m_0} = -\frac{1}{2g_s}(\langle\Phi_0\rangle - m_0). \quad (3.17)$$

Another important feature of the effective action is that the inverse propagators of the fields (in our case, the propagators for π and σ mesons) can be generated in a symmetry-conserving way by second-order derivatives:

$$D^{-1}_{ab} = \frac{\delta^2\Gamma(\Phi)}{\delta\Phi_a\delta\Phi_b}. \quad (3.18)$$

To obtain an expression for the effective action, the path integral is evaluated using the saddle-point approximation. The lowest order contribution to the effective action is

$$\Gamma^{(0)}(\Phi) = I(\Phi). \quad (3.19)$$

This corresponds to the mean-field (Hartree) approximation [27]. The vacuum expectation values of the fields in the mean-field approximation coincide with the stationary point of the action $I(\Phi)$. This is obvious if one combines Eqs. (3.16) and (3.19). Including quadratic mesonic fluctuations leads to the following expression for the effective action [27]:

$$\Gamma(\Phi) = I(\Phi) + \frac{1}{2}\mathrm{tr}\ln\left(\frac{\delta^2 I(\Phi)}{\delta\Phi_a\delta\Phi_b}\right). \quad (3.20)$$

The second term in the above expression contains the mesonic fluctuations. As discussed in [27], the method is only meaningful if the second-order functional derivative which enters into this term is positive definite. Otherwise, severe problems arise due to an ill-defined logarithm, which would then be complex. We will come back to this point in Subsection 5.2.

Determining the stationary point of the effective action in Eq. (3.20) leads to the following "gap equation" [15]:

$$\langle\Phi_0\rangle - m_0 - \Sigma_{\mathrm{H}}(\langle\Phi_0\rangle) - \delta\tilde{\Sigma}(\langle\Phi_0\rangle) = 0. \quad (3.21)$$

Here, Σ_{H} and $\delta\tilde{\Sigma}$ are the same functions we already defined in Eqs. (2.2) and (3.4) in the context of the Hartree and the LSS gap equation. In fact, Eq. (3.21) is identical to the LSS gap equation, Eq. (3.3), if we identify $\langle\Phi_0\rangle$ with the LSS-constituent quark mass m.

In the same way, we exactly recover the meson structure of the LSS if we evaluate Eq. (3.18) at the stationary point. This means that the "local self-consistent scheme" which was constructed from a somewhat arbitrary starting point in Subsection 3.2 can be derived in a systematic way in the effective action formalism. However, the interpretation is different: as emphasized in [15], the solution of the gap equation is only the expectation value of the Φ_0 field and does not correspond to the pole of the quark propagator. This becomes clear if we look at the quark condensate, which is given by Eq. (3.17). The right-hand side of this equation is identical to Eq. (3.8) and is therefore different from Eq. (3.7), which was derived by taking the trace over what we called the "quark propagator" in Subsection 3.2.

Hence, within the effective-action formalism, Eq. (3.8) is the correct expression for the quark condensate (in that approximation scheme), whereas the gap equation should not be interpreted as an equation for the corresponding inverse quark propagator. In the following, we will adopt this point of view. For simplicity, however, we will still call m a "constituent quark mass" and $(\hat{p} - m)^{-1}$ a "quark propagator," although this is not entirely correct.

4. CONSISTENCY WITH CHIRAL SYMMETRY

By construction, the LSS is consistent with axial Ward–Takahashi identities and hence—as discussed in Section 1—with the Goldstone theorem. Since the mesonic polarization functions of the LSS contain all diagrams up to the next-to-leading order of the $1/N_c$-expansion scheme and since the various contributions to the pion mass have to cancel order by order in the chiral limit, this implies that the $1/N_c$ scheme discussed in Subsection 2.2 is also consistent with the Goldstone theorem.

Nevertheless, for numerical implementation, it is instructive to show the consistency of the different schemes with chiral symmetry on a less formal level. Since most of the integrals that have to be evaluated are divergent and must be regularized, one has to ensure that the various symmetry relations are not destroyed by the regularization. To this end, it is important to know how these relations emerge in detail. This will also enable us to perform approximations without violating chiral symmetry. As we will see in Subsection 5.2, this is very important for practical calculations within the LSS, which cannot be applied as it stands.

For both the $1/N_c$ expansion and the LSS, we begin our discussion with the explicit proof of the Goldstone theorem. This was given first by Dmitrašinović *et al.* [14]. After that, we discuss the GOR relation. This is of particular interest in the context of the proper definition

of the quark condensate in the LSS [cf. Eqs. (3.7) and (3.8)].

4.1. $1/N_c$ Expansion

We begin with the $1/N_c$ expansion scheme. For the Goldstone theorem, one has to show that, in the chiral limit, the inverse pion propagator vanishes at zero momentum:

$$2g_s\tilde{\Pi}_\pi(0) = 1 \quad \text{for} \quad m_0 = 0. \tag{4.1}$$

As before, we use the notation $\tilde{\Pi}_\pi^{ab} = \delta_{ab}\tilde{\Pi}_\pi$. The function $\tilde{\Pi}_\pi^{ab}$ has been defined in Eq. (2.14). It consists of the RPA-polarization loop Π_π^{ab} and the four $1/N_c$-correction diagrams $\delta\Pi_\pi^{(k)ab}$, $k = a, b, c, d$. Restricting the calculation to the chiral limit and to zero momentum simplifies the expressions considerably, and Eq. (4.1) can be proven analytically.

For the RPA loop, one obtains

$$2g_s\Pi_\pi(0) = \frac{\Sigma_H}{m}. \tag{4.2}$$

This is the relation that guarantees the consistency of the Hartree + RPA scheme: in the Hartree approximation, we have $m = m_0 + \Sigma_H$; hence, Eq. (4.1) is fulfilled by Eq. (4.2). Since the gap equation is not changed in the perturbative $1/N_c$ expansion, this remains true if we include the next-to-leading order. Therefore, we have to show that the contributions of the correction terms add up to zero:

$$\sum_{k = a, b, c, d} \delta\Pi_\pi^{(k)}(0) = 0 \quad \text{for} \quad m_0 = 0. \tag{4.3}$$

The correction terms $\delta\Pi_\pi^{(k)}$ are defined in Eq. (2.23). Let us begin with the diagram $\delta\Pi_\pi^{(a)}$. As mentioned above, we neglect the ρ and a_1 subspace for intermediate mesons. Then, one can easily see that the external pion can only couple to a $\pi\sigma$ intermediate state. Evaluating the trace in Eq. (2.17) for zero external momentum, one gets for the corresponding triangle diagram

$$\Gamma_{\pi,\pi,\sigma}^{ab}(0, p) = -\delta_{ab}4N_cN_f2mI(p), \tag{4.4}$$

with a and b being isospin indices and the elementary integral

$$I(p) = \int\frac{d^4k}{(2\pi)^4}\frac{1}{(k^2 - m^2 + i\varepsilon)((k+p)^2 - m^2 + i\varepsilon)}. \tag{4.5}$$

Inserting this into Eq. (2.23), we find

$$\delta\Pi_\pi^{(a)ab}(0) = i\delta_{ab}\int\frac{d^4p}{(2\pi)^4}(4N_cN_fI(p))^2 4m^2D_\sigma(p)D_\pi(p). \tag{4.6}$$

Now, the essential step is to realize that the product of the RPA-sigma and pion propagators can be converted into a difference [14],

$$D_\sigma(p)D_\pi(p) = i\frac{D_\sigma(p) - D_\pi(p)}{4N_cN_f2m^2I(p)}, \tag{4.7}$$

to finally obtain

$$\delta\Pi_\pi^{(a)ab}(0) = -\delta_{ab}4N_cN_f\int\frac{d^4p}{(2\pi)^4}2I(p)\{D_\sigma(p) - D_\pi(p)\}. \tag{4.8}$$

The next two diagrams can be evaluated straightforwardly. One finds

$$\delta\Pi_\pi^{(b)ab}(0) = -\delta_{ab}4N_cN_f \times\int\frac{d^4p}{(2\pi)^4}\{D_\sigma(p)(I(p) + I(0) - (p^2 - 4m^2)K(p)) + D_\pi(p)(3I(p) + 3I(0) - 3p^2K(p))\}, \tag{4.9}$$

$$\delta\Pi_\pi^{(c)ab}(0) = -\delta_{ab}4N_cN_f\int\frac{d^4p}{(2\pi)^4}I(p)\{-D_\sigma(p) - D_\pi(p)\}.$$

The elementary integral $K(p)$ is of the same type as the integral $I(p)$ and is defined in Appendix A.

Finally, we have to calculate $\delta\Pi_\pi^{(d)}(0)$. According to Eq. (2.23), it can be written in the form

$$\delta\Pi_\pi^{(d)ab}(0) = -i\Gamma_{\pi,\pi,\sigma}^{ab}(0, 0)D_\sigma(0)\Delta. \tag{4.10}$$

For the constant Δ defined in Eq. (2.18), one obtains

$$\Delta = 4N_cN_fm\int\frac{d^4p}{(2\pi)^4}\{D_\sigma(p)(2I(p) + I(0) - (p^2 - 4m^2)K(p)) + D_\pi(p)(3I(0) - 3p^2K(p))\}. \tag{4.11}$$

Evaluating $D_\sigma(0)$ in the chiral limit and comparing the result with Eq. (4.4), one finds that the product of the first two factors in Eq. (4.10) is simply δ_{ab}/m; i.e., one gets

$$\delta\Pi_\pi^{(d)ab}(0) = \delta_{ab}\frac{\Delta}{m}. \tag{4.12}$$

With these results it can be easily checked that Eq. (4.3) indeed holds in this scheme.

As already pointed out, most of the integrals we have to deal with are divergent and have to be regularized. Therefore, one has to make sure that all steps that lead to Eq. (4.3) remain valid in the regularized model. One important observation is that the cancellations occur already at the level of the p integrand, i.e., before performing the meson-loop integral. This means that

there is no restriction on the regularization of this loop. We also do not need to perform the various quark loop integrals explicitly, but we have to make use of several relations between them. For instance, in order to arrive at Eq. (4.12) we need the similar structure of the quark triangle $\Gamma_{\pi,\pi,\sigma}(0, 0)$ and the inverse RPA propagator $D_\sigma(0)^{-1}$. Therefore, all quark loops, i.e., RPA polarizations, triangles, and box diagrams, should be consistently regularized within the same scheme, whereas the meson loops can be regularized independently.

Going away from the chiral limit, the pion receives a finite mass. To lowest order in the current quark mass, it is given by the GOR relation

$$m_\pi^2 f_\pi^2 = -m_0\langle\bar\psi\psi\rangle. \tag{4.13}$$

However, in the $1/N_c$-expansion scheme, we cannot expect that the GOR relation holds in this form. In Section 2, we calculated the quark condensate in the leading order and the next-to-leading order in $1/N_c$. Hence, to be consistent, we should also expand the left-hand side of the GOR relation up to the next-to-leading order in $1/N_c$:

$$\begin{aligned} &m_\pi^{2(0)} f_\pi^{2(0)} + m_\pi^{2(0)}\delta f_\pi^2 + \delta m_\pi^2 f_\pi^{2(0)} \\ &\quad = -m_0(\langle\bar\psi\psi\rangle^{(0)} + \delta\langle\bar\psi\psi\rangle). \end{aligned} \tag{4.14}$$

Here, similar to the notation we already introduced for the quark condensate, $m_\pi^{2(0)}$ and $f_\pi^{2(0)}$ denote the leading-order and δm_π^2 and δf_π^2 the next-to-leading-order contributions to the squared pion mass and the squared pion decay constant, respectively. Since the GOR relation holds only in the lowest order in m_0, Eq. (4.14) corresponds to a double expansion: m_π^2 has to be calculated in the linear order in m_0, f_π^2, and $\langle\bar\psi\psi\rangle$, in the chiral limit.

The leading-order and next-to-leading-order expressions for the quark condensate are given in Eqs. (2.5) and (2.22). The pion decay constant f_π is calculated from the one-pion to vacuum axial-vector matrix element. Basically, this corresponds to evaluating the mesonic polarization diagrams, Fig. 4, coupled to an external axial current and to a pion. This leads to expressions similar to Eqs. (2.6) and (2.23), but with one external vertex equal to $\gamma^\mu\gamma_5\tau^a/2$, corresponding to the axial current, and the second external vertex equal to $g_{\pi qq} i\gamma_5\tau^b$, corresponding to the pion. Here, the $1/N_c$-corrected pion–quark coupling constant is defined as

$$g_{\pi qq}^{-2} = g_{\pi qq}^{-2(0)} + \delta g_{\pi qq}^{-2} = \left.\frac{d\tilde\Pi_\pi(q)}{dq^2}\right|_{q^2 = m_\pi^2}, \tag{4.15}$$

analogously to Eq. (2.10). Now, we take the divergence of the axial current and then use the relation

$$\gamma_5\hat p = 2m\gamma_5 + \gamma_5 S^{-1}(k+p) + S^{-1}(k)\gamma_5 \tag{4.16}$$

to simplify the expressions [14]. One finds

$$\begin{aligned} f_\pi = g_{\pi qq}\Bigg(&\frac{\tilde\Pi_\pi(q) - \tilde\Pi_\pi(0)}{q^2} m \\ &+ \frac{\Pi_\pi(q) - \Pi_\pi(0)}{q^2} D_\sigma(0)\Delta\Bigg)\Bigg|_{q^2 = m_\pi^2}. \end{aligned} \tag{4.17}$$

In the chiral limit, $q^2 = m_\pi^2 \longrightarrow 0$, Eqs. (2.10) and (4.15) can be employed to replace the difference ratios on the right-hand side by pion–quark coupling constants. When we square this result and only keep the leading order and the next-to-leading order in $1/N_c$, we finally obtain

$$\begin{aligned} &f_\pi^{2(0)} + \delta f_\pi^2 \\ &= m^2 g_{\pi qq}^{-2(0)} + (m^2\delta g_{\pi qq}^{-2} + 2mD_\sigma(0)\Delta g_{\pi qq}^{-2(0)}). \end{aligned} \tag{4.18}$$

For the pion mass, we start from Eqs. (2.15) and (2.16) and expand the inverse pion propagator around $q^2 = 0$:

$$\begin{aligned} &1 - 2g_s\tilde\Pi_\pi(0) \\ &- 2g_s\left(\frac{d}{dq^2}\tilde\Pi_\pi(q)\right)\Bigg|_{q^2=0} m_\pi^2 + O(m_\pi^4) = 0. \end{aligned} \tag{4.19}$$

To find m_π^2 in the lowest nonvanishing order in m_0, we have to expand $1 - 2g_s\tilde\Pi_\pi(0)$ up to the linear order in m_0, while the derivative has to be calculated in the chiral limit, where it can be identified with the inverse squared pion–quark coupling constant, Eq. (4.15). The result can be written in the form

$$m_\pi^2 = \frac{m_0}{m}\frac{g_{\pi qq}^2}{2g_s}\left(1 - \frac{D_\sigma(0)\Delta}{m}\right) + O(m_0^2). \tag{4.20}$$

Finally, one has to expand this equation in powers of $1/N_c$. This amounts to expanding $g_{\pi qq}^2$, which is the only term in Eq. (4.20) which is not of a definite order in $1/N_c$. One gets

$$\begin{aligned} m_\pi^{2(0)} + \delta m_\pi^2 &= m_0\frac{m}{2g_s}\frac{g_{\pi qq}^{2(0)}}{m^2} \\ &- m_0\frac{m}{2g_s}\frac{g_{\pi qq}^{2(0)}}{m^2}\left(g_{\pi qq}^{2(0)}\delta g_{\pi qq}^{-2} + \frac{D_\sigma(0)\Delta}{m}\right). \end{aligned} \tag{4.21}$$

It can be seen immediately that the leading-order term is exactly equal to $-m_0\langle\bar\psi\psi\rangle^{(0)}/f_\pi^{2(0)}$, as required by the GOR relation. Moreover, combining Eqs. (2.22), (4.18), and (4.21), one finds that the GOR relation in next-to-leading order, Eq. (4.14), holds in this scheme.

However, one should emphasize that this result is obtained by a strict $1/N_c$ expansion of the various prop-

erties which enter into the GOR relation and of the GOR relation itself. If one takes f_π and m_π as they result from Eqs. (4.17) and (4.20) and inserts them into the left-hand side of Eq. (4.13), one will in general find deviations from the right-hand side which are due to higher order terms in $1/N_c$. In this sense, one can take the violation of the GOR relation as a measure for the importance of these higher order terms [19].

4.2. Local Self-Consistent Scheme

The proof of the Goldstone theorem in the LSS is very similar to that in the $1/N_c$-expansion scheme. Therefore, we can be brief, concentrating on the steps which are different.

Again, we have to show the validity of Eq. (4.1). In the LSS, the function $\tilde{\Pi}_\pi$ is given by Eq. (3.6); i.e., it differs from the corresponding function in the $1/N_c$-expansion scheme (Eq. (2.14)) by the fact that the diagram $\delta\Pi_\pi^{(d)}$ is (formally) missing. (As we already discussed, it is implicitly contained in the RPA diagram.) The other diagrams have the same structure as before, and we can largely use the results of the previous subsection. However, we should keep in mind that the constituent quark mass is now given by the extended gap equation, Eq. (3.3). Therefore, the right-hand side of Eq. (4.2) is different from unity in the chiral limit and RPA pions are not massless. This has important consequences for the practical calculations within this scheme, which will be discussed in greater detail in Subsection 5.2.

Using Eqs. (4.8), (4.9), and (4.11), as well as Eq. (3.4), we get for the correction terms to the pion polarization function

$$\sum_{k=a,b,c} \delta\Pi_\pi^{(k)}(0) = -\frac{\Delta}{m} = \frac{\delta\tilde{\Sigma}}{2g_s m}. \tag{4.22}$$

Hence, together with the modified gap equation (3.3), we find

$$2g_s\tilde{\Pi}_\pi(0) = 1 - \frac{m_0}{m} \tag{4.23}$$

in agreement with Eq. (4.1).

The discussion concerning the regularization procedure can be repeated here. The structure of the proof again leads to the conclusion that we have to regularize all quark loops in the same way, whereas we have the freedom to choose the regularization for the meson loops independently.

Another important observation is that we do not need the explicit form of the RPA propagators; $D_\sigma(p)$ and $D_\pi(p)$ only need to fulfill Eq. (4.7). Thus, approximations to the RPA propagators can be made as long as Eq. (4.7) remains valid.

For a nonvanishing current quark mass, the pion mass is given by the GOR relation (Eq. (4.13)). To the linear order in m_0, this relation holds exactly in the LSS, if we choose the appropriate definition of the quark condensate. This will be demonstrated in the following.

For the pion decay constant f_π, we follow the same steps as in the $1/N_c$-expansion scheme to arrive at the following expression:

$$f_\pi = g_{\pi qq} m \left.\frac{\tilde{\Pi}_\pi(q) - \tilde{\Pi}_\pi(0)}{q^2}\right|_{q^2 = m_\pi^2}. \tag{4.24}$$

Here, the modified pion–quark coupling constant is defined as

$$g_{\pi qq}^{-2} = \left.\frac{d\tilde{\Pi}_\pi(q)}{dq^2}\right|_{q^2 = m_\pi^2}. \tag{4.25}$$

In the chiral limit, $m_\pi^2 \longrightarrow 0$, the difference ratio on the right-hand side of Eq. (4.24) can be replaced by the pion–quark coupling constant [Eq. (4.25)]. This leads to the Goldberger–Treiman relation

$$f_\pi g_{\pi qq} = m. \tag{4.26}$$

Following the analogous steps which led us to Eq. (4.20), we find for the pion mass

$$m_\pi^2 = \frac{m_0}{m}\frac{g_{\pi qq}^2}{2g_s} + O(m_0^2). \tag{4.27}$$

Multiplying this by f_π^2 as given by Eq. (4.26), we get to the linear order in m_0:

$$m_\pi^2 f_\pi^2 = m_0 \frac{\tilde{\Sigma}}{2g_s}. \tag{4.28}$$

Obviously, this is consistent with the GOR relation (Eq. (4.13)) if the quark condensate is given by Eq. (3.8), but not if it is given by Eq. (3.7). In Subsection 3.3, we saw that, within the effective action formalism, the quark condensate is given by Eq. (3.8). Therefore, at this point, we clearly see that the interpretation of m as a constituent quark mass, which would mean that we have to calculate the quark condensate according to Eq. (3.7), leads to a contradiction with the GOR relation. Therefore, in the numerical part, we will calculate the quark condensate according to Eq. (3.8).

5. NUMERICAL RESULTS AT ZERO TEMPERATURE

In this section, we present our numerical results at zero temperature. We begin with a brief description of the regularization scheme and then discuss peculiarities related to the solution of the gap equation in the LSS. After that, we study the influence of mesonic fluctuations on quantities in the pion sector, thereby focusing on possible instabilities. Finally, we perform a refit of

these quantities within the $1/N_c$-expansion scheme and the LSS and apply the model to observables in the ρ-meson sector.

5.1. Regularization

Before we begin with the explicit calculation, we have to fix our regularization scheme. As discussed in Section 4, all quark loops, i.e., the RPA polarization diagrams, the quark triangles, and the quark box diagrams, must be regularized in the same way in order to preserve chiral symmetry. We use Pauli–Villars regularization with two regulators; i.e., we replace

$$\int \frac{d^4k}{(2\pi)^4} f(k; m) \longrightarrow \int \frac{d^4k}{(2\pi)^4} \sum_{j=0}^{2} c_j f(k; \mu_j) \qquad (5.1)$$

with

$$\mu_j^2 = m^2 + j\Lambda_q^2; \quad c_0 = 1, \quad c_1 = -2, \quad c_2 = 1. \qquad (5.2)$$

Here, Λ_q is a cutoff parameter.

The regularization of the meson loop (integration over d^4p in Eq. (2.23)) is not constrained by chiral symmetry and is independent of the quark-loop regularization. For practical reasons, we choose a three-dimensional cutoff Λ_M in momentum space. In order to obtain a well-defined result, we work in the rest frame of the "improved" meson. The same regularization scheme was already used in [19, 20].

5.2. Solution of the Gap Equation in the LSS

In contrast to the $1/N_c$-expansion scheme, where all diagrams are constructed from "Hartree" quarks, the LSS is based on the extended gap equation, Eq. (3.3). In Subsection 3.2, this equation was the starting point to find a consistent set of diagrams for the description of mesons. In fact, in Subsection 4.2, we have shown that various symmetry relations, namely, the Goldstone theorem, the Goldberger–Treiman relation, and the GOR relation, hold in this scheme. It is not surprising that the structure of the extended gap equation was needed to prove these relations. So far, all this has been done on a rather formal level. This section is now devoted to the explicit solution of the modified gap equation in the LSS. We will see that this cannot be done in a straightforward manner, and we are forced to a slight modification of the scheme.

In addition to the Hartree term Σ_H, Eq. (3.3) contains the term $\delta\tilde{\Sigma}$, which is a quark loop dressed by RPA mesons (see Fig. 8). As already pointed out, these RPA mesons consist of quarks with self-consistent mass m, which is in general different from the "Hartree" mass m_H. Hence, the masses of these mesons are also different from the meson masses in the Hartree + RPA scheme. On the left-hand side of Fig. 9, we have plotted

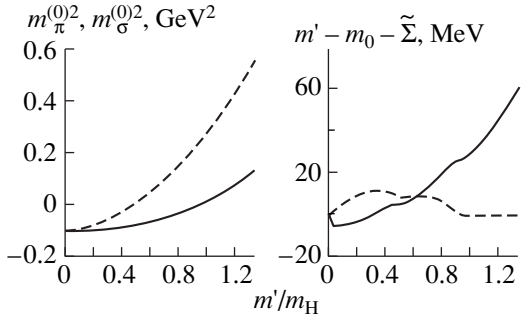

Fig. 9. (Left) Squared pole masses of the pion (solid) and the σ meson (dashed) in RPA as functions of a trial constituent quark mass m' in units of the Hartree quark mass. (Right) Difference $m' - m_0 - \tilde{\Sigma}(m')$ between the left-hand side and the right-hand side of the LSS gap equation, Eq. (3.3), as a function of the trial constituent quark mass m'. The real part is denoted by the solid curve; the imaginary part, by the dashed curve.

the squared masses $m_M^{(0)2}$ of the RPA pion (solid) and the RPA σ meson (dashed) as functions of a trial constituent quark mass m'. An important observation is that the pion becomes tachyonic; i.e., $m_\pi^{(0)2}$ becomes negative for quark masses smaller than the Hartree quark mass. Strictly speaking, this is only the case in the chiral limit, whereas for nonvanishing current quark masses, $m_\pi^{(0)2}$ becomes negative slightly below the Hartree quark mass. A similar observation can be made for $m_\sigma^{(0)2}$, but only for m' much smaller than the Hartree mass. This observation of tachyonic RPA mesons is related to the point discussed in Subsection 3.3 that the meson-loop term in the effective action [second term of Eq. (3.20)] is no longer positive definite.

Tachyonic RPA mesons lead to a complex correction to the quark self-energy. Therefore, the solution of the extended gap equation can only be real if it is larger than the Hartree mass. Otherwise, it must be complex. To investigate this point, we plot the difference between the left-hand side and the right-hand side of Eq. (3.3) as a function of the (real) trial quark mass m'. This is shown in the right panel of Fig. 9. The solid curve denotes the real part; the dashed curve shows the imaginary part of $m' - m_0 - \tilde{\Sigma}(m')$. Obviously, below the Hartree quark mass, the self-energy indeed gets complex. Moreover, we see that there is no solution of the gap equation for real constituent quark masses. Hence, in principle, one should search for solutions of the gap equation in the complex plane. However, this would mean that the RPA mesons would also consist of quarks with complex masses. In this case, e.g., a reasonable description of the ρ meson would be completely impossible, because its properties are mainly determined by intermediate pions.

Therefore, we prefer to perform the approximation that was introduced in [15]. As discussed in Subsection 4.2,

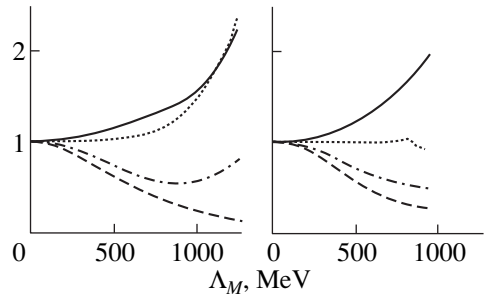

Fig. 10. The ratios $m_\pi^2/m_\pi^{2(0)}$ (solid), $f_\pi^2/f_\pi^{2(0)}$ (dashed), $\langle\bar\psi\psi\rangle/\langle\bar\psi\psi\rangle^{(0)}$ (dash-dotted), and the combination $-m_0\langle\bar\psi\psi\rangle/m_\pi^2 f_\pi^2$ (dotted) as functions of the meson-loop cutoff Λ_M. Left: $1/N_c$-expansion scheme. Right: LSS.

the symmetry properties of the LSS are not affected by approximations to the RPA-meson propagators which preserve the validity of Eq. (4.7). The authors of [15] simply replace the RPA-pion propagator in the extended gap equation

$$D_\pi(p) = -2g_s\Big[1 - 2ig_s 4N_cN_f \times\int\frac{d^4k}{(2\pi)^4}\frac{1}{k^2-m^2+i\varepsilon} + 2ig_s(2N_cN_f)p^2I(p)\Big]^{-1} \quad (5.3)$$

by

$$D_\pi(p) = -2g_s\Big[\frac{m_0}{m} + 2ig_s 2N_cN_f p^2 I(p)\Big]^{-1} \quad (5.4)$$

and, analogously, for the σ propagator. The same replacements are performed for the RPA-meson propagators in the correction terms $\delta\Pi_M^{(k)}$ to the mesonic polarization diagrams. The RPA contribution Π_M itself, however, is not changed. In this way, the solution of the gap equation and the masses of the intermediate mesons remain real. Moreover, in the chiral limit, the intermediate pions are massless, as one can immediately see from Eq. (5.4).

The above replacements would be exact in the Hartree approximation (cf. Eq. (A.13)). The authors of [15] argue that the correction terms are suppressed because they are of higher orders in $1/N_c$ (beyond the next-to-leading order). In the LSS, this is a questionable argument because the self-consistent solution of the gap equation mixes all orders of $1/N_c$ anyway. Nevertheless, this approximation preserves the validity of the various symmetry relations we checked in Subsection 4.2.

In the following, we will call this scheme, including the above replacements, the "local self-consistent scheme," although it is, strictly speaking, only an approximation to the LSS as it was originally introduced in Subsection 3.2.

5.3. Meson-Loop Effects on Quantities in the Pion Sector

In this subsection, we want to study the influence of mesonic fluctuations on the quark condensate, the pion mass, and the pion decay constant, both within the $1/N_c$-expansion scheme and within the LSS. Since the strength of the fluctuations is controlled by the meson cutoff Λ_M, we first keep all other parameters fixed and investigate how the above quantities change when Λ_M is varied. For the $1/N_c$-expansion scheme, this has been done in more detail in [19]. Later, in the next subsection, we will perform a refit of the parameters to reproduce the empirical values of $\langle\bar\psi\psi\rangle$, m_π, and f_π.

Our starting point is the Hartree + RPA scheme, which corresponds to $\Lambda_M = 0$. Here, we obtain a reasonable fit ($\langle\bar\psi\psi\rangle^{(0)} = -2(241.1\ \text{MeV})^3$, $m_\pi^{(0)} = 140.0$ MeV, and $f_\pi^{(0)} = 93.6$ MeV) with the parameters $\Lambda_q = 800$ MeV, $g_s\Lambda_q^2 = 2.90$, and $m_0 = 6.13$ MeV. These parameters correspond to a relatively small "Hartree" constituent quark mass of 260 MeV.

Now, we turn on the mesonic fluctuations by taking a nonzero meson cutoff Λ_M. All other parameters are kept constant at the values given above. The resulting behavior of m_π^2, f_π^2, and the quark condensate as functions of Λ_M is displayed in Fig. 10. The left panel corresponds to the $1/N_c$-expansion scheme and the right panel, to the LSS. As one can see, in both schemes, the mesonic fluctuations lead to a reduction of f_π (dashed curves), while m_π (solid) is increased. At smaller values of Λ_M, the absolute value of the quark condensate decreases but goes up again for $\Lambda_M \gtrsim 900$ MeV. This is also an effect that is found in both schemes.

In the Hartree + RPA scheme, the quantities $m_\pi^{2(0)}$, $f_\pi^{2(0)}$, and $\langle\bar\psi\psi\rangle^{(0)}$ are in almost perfect agreement with the GOR relation, Eq. (4.13). As discussed in Subsection 4.1, the $1/N_c$-expansion scheme is consistent with the GOR relation up to the next-to-leading order in $1/N_c$, but the relation is violated by higher order terms. We therefore expect a less perfect agreement in this scheme becoming worse with increasing values of Λ_M. In the LSS, on the other hand, the quantities should be in good agreement with the GOR relation (see Subsection 4.2).

These expectations are more or less confirmed by the results. In Fig. 10, the ratio of the right-hand side and the left-hand side of Eq. (4.13) is displayed by the dotted curves. In the $1/N_c$-expansion scheme (left panel), the relation holds within 30% for $\Lambda_M \le 900$ MeV. However, when the meson cutoff is further increased, the deviation grows rapidly. This indicates that higher order corrections in $1/N_c$ become important in this regime and this perturbative scheme should no longer be trusted. In the LSS, the agreement with the GOR relation is almost perfect.

In Fig. 10, the various curves are only shown up to $\Lambda_M = 1250$ MeV for the $1/N_c$-expansion scheme and up to $\Lambda_M = 950$ MeV for the LSS. For larger values of Λ_M, a second, unphysical pole with a residue of the "wrong" sign emerges in the pion propagator. This would correspond to an imaginary pion–quark coupling constant and hence an imaginary pion decay constant. Upon further increasing Λ_M, the two poles merge and finally disappear from the positive real axis.

For the $1/N_c$-expansion scheme, this has been discussed in more detail in [19]. In that reference, we suggested that the instabilities of the pion propagator might indicate an instability of the underlying ground state against mesonic fluctuations. In fact, it has been claimed by Kleinert and Van den Bossche [22] that there is no spontaneous chiral-symmetry breaking in the NJL model as a consequence of strong mesonic fluctuations. Although this cannot be true in general if the strength of the mesonic fluctuations is controlled by an independent cutoff parameter Λ_M [19], this phenomenon might very well occur for large values of Λ_M. In other words, there could be some kind of "chiral-symmetry restoration" at a certain value of the parameter Λ_M.

Clearly, this could not be studied within the $1/N_c$-expansion scheme, where the mesonic fluctuations are built perturbatively on the Hartree ground state. In the LSS, however, where we encounter the same type of instabilities in the pion propagator, this question can be investigated more closely. To that end, we consider the effective action Eq. (3.20), which describes the energy density of the system. It is explicitly given by

$$\Gamma(m') = 2iN_cN_f\int\frac{d^4p}{(2\pi)^4}\ln\left(\frac{m'^2-p^2}{m_0^2-p^2}\right)+\frac{(m'-m_0)^2}{4g_s} \tag{5.5}$$

$$-\frac{i}{2}\int\frac{d^4p}{(2\pi)^4}\{\ln(1-2g_s\Pi_\sigma(p))+3\ln(1-2g_s\Pi_\pi(p))\}$$

$$+\text{ const.}$$

The irrelevant constant can be chosen in such a way that $\Gamma(0) = 0$. The positions of the extrema of $\Gamma(m')$ correspond to the solutions of the gap equation (3.3). In particular, the vacuum expectation value m is given by the value of m' at the absolute minimum of Γ. Note that, according to Eq. (3.8), m is proportional to the quark condensate, i.e., to the order parameter of chiral symmetry breaking. Hence, for a given value of Λ_M, chiral symmetry is spontaneously broken if the absolute minimum of Γ is located at a nonzero value of m' and it is unbroken ("restored") otherwise.

We perform the calculations in the chiral limit.[2)] Our results for $\Gamma(m')$ as a function of m'/m_H for different values of Λ_M are displayed in Fig. 11. For $\Lambda_M = 0$, we find, of course, the minimum at $m' = m_H = 260$ MeV, while there is a maximum at $m' = 0$. If there was indeed a "phase transition" due to mesonic fluctuations, this maximum should eventually convert to a minimum when Λ_M is increased. In fact, for $\Lambda_M \lesssim 900$ MeV, the results seem to point in this direction: in this regime, the constituent quark mass m is reduced to about 30% of the Hartree mass. At the same time, the "bag constant" $B = \Gamma(0) - \Gamma(m)$ decreases from 48.7 MeV/fm^3 at $\Lambda_M = 0$ to 0.8 MeV/fm^3 at $\Lambda_M = 900$ MeV. However, upon further increasing Λ_M, both m and B go up again. In particular, the point $\Gamma(0)$ always remains a local maximum: in the LSS, we do not observe a "phase transition" due to strong mesonic fluctuations.

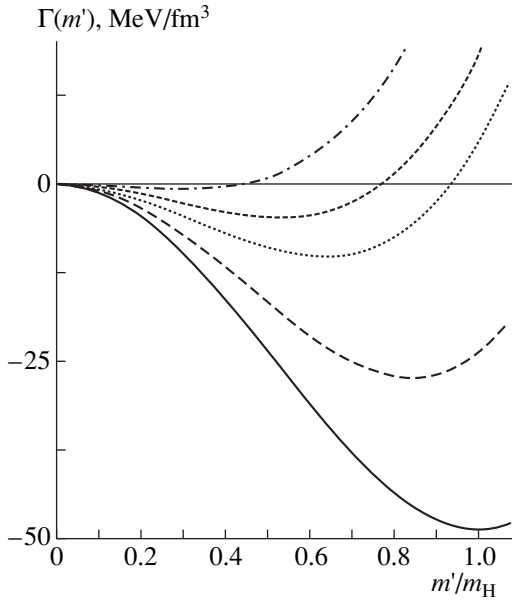

Fig. 11. Effective action $\Gamma(m')$ as a function of m'/m_H in the LSS for different values of the meson cutoff Λ_M: 0 MeV (solid), 300 MeV (long-dashed), 500 MeV (dotted), 900 MeV (dash-dotted), and 1200 MeV (short-dashed).

Here we should remark that, according to the conjecture by Kleinert and Van den Bossche [22], the mesonic fluctuations do not restore the trivial vacuum in the NJL model, but they lead to a so-called pseudogap phase. (See also [28] for a critical discussion of that article.) In that phase, the quarks still have a nonvanishing constituent mass, if the latter is identified with the vacuum expectation value of the modulus of the scalar field Φ (cf. Subsection 3.3). Nevertheless, chiral symmetry is not broken as the phase of the Φ field is strongly fluctuating. An analogous phenomenon is well known from strong-coupling superconductors above T_c [29, 30], where Cooper pairs are formed but do not condense. Obviously, our above investigations, which focused on the change in m assuming a uniform phase factor, cannot exclude a transition into a phase of this type. Here, more refined investigations are needed to give a conclusive answer.

[2)]To be precise, we proceed as follows: starting from the parameters given above, we keep the Hartree constituent quark mass, $m_H = 260$ MeV, fixed, while m_0 is reduced from 6.1 MeV to zero. Therefore, the coupling constant is slightly enhanced from $g_s\Lambda_q^2 = 2.90$ to $g_s\Lambda_q^2 = 2.96$.

Another type of vacuum instability which is caused by unphysical poles of the RPA-meson propagators has recently been discussed by Ripka [31]. Here, "unphysical" means that these poles are located in regions of the complex plane where they are forbidden by microcausality. Ripka stated that they are induced by the regulator scheme, in his case, a 4-momentum cutoff or a Gaussian form factor. In fact, the RPA-meson propagators have this unphysical feature for most of the known regulator schemes, such as proper-time regularization, subtracted dispersion relations, dimensional regularization, or, as mentioned above, a 4-momentum cutoff. A 3-momentum cutoff and the Pauli–Villars regularization in the form we use (cf. Appendix B) are exceptions. On the other hand, due to Pauli–Villars regulators, the imaginary part of the quark loops can have the wrong sign in some kinematical regions and we cannot rule out that the instabilities we find for the pion propagator are related to this. This supposition is corroborated by the fact that these instabilities could be traced back to the imaginary part of the diagram $\delta\Pi^{(b)}$ (see Fig. 4), which has the "wrong" sign and which becomes large at large values of Λ_M [19]. Further investigations are needed, however, to clarify this point.

Recently, a second (unphysical) pole in the pion propagator was also found in a nonlocal generalization of the NJL model [21]. The calculations indicate that these instabilities could probably be removed by including vector and axial-vector intermediate states. This point is certainly worth closer examination. In any case, at least in the $1/N_c$-expansion scheme, we found [20] that, with a reasonable fit of all parameters, we are far away from the region where these instabilities occur. We will come back to this point in Subsection 5.5.

5.4 Parameter Fit in the Pion Sector

In the previous subsection, we did not change the parameters which were determined in the Hartree + RPA scheme by fitting $f_\pi^{(0)}$, $m_\pi^{(0)}$, and $\langle\bar\psi\psi\rangle^{(0)}$. Of course, if one wants to apply the model to describe physical processes, a refit of these observables should be performed that includes the mesonic fluctuations. In [20], this was already done for the $1/N_c$-expansion scheme, and we will now try to perform an analogous fit within the LSS. Of course, by fitting the above three observables, we cannot conclusively fix the five parameters of our model, g_s, g_v, Λ_q, Λ_M, and m_0. Therefore, we try to proceed in a similar way as in [20]: for various values of Λ_M, we fix the scalar coupling constant g_s, the current quark mass m_0, and the quark-loop cutoff Λ_q to reproduce the empirical values of the pion mass, f_π, and $\langle\bar\psi\psi\rangle$. Then, in the next subsection, we will try to fix the two remaining parameters, i.e., the vector coupling constant g_v and the meson cutoff Λ_M, by fitting the pion electromagnetic form factor in the timelike region, which is related, via vector-meson dominance, to the ρ-meson propagator. Roughly speaking, this amounts to fitting the ρ-meson mass and its width. Since, in our model, the latter is due to intermediate RPA pions, we decided to fix the empirical value of $m_\pi^{(0)}$, not m_π, in order to get the correct threshold behavior. In [20], we found for the $1/N_c$-expansion scheme that the deviation is about 10%. As we will see below, the difference is somewhat larger in the LSS.

Of course, the ρ meson can only be described reasonably if the unphysical $q\bar q$ threshold lies well above the peak in the ρ-meson spectral function; i.e., the constituent quark mass m should be larger than about 400 MeV. For that reason, we try to increase the constituent quark mass as much as possible. Here, we have some freedom as the empirical value of the quark condensate is not known very precisely. {Its absolute value is probably less than $2(260\ \text{MeV})^3$, which roughly corresponds to the upper limit extracted in [32] from sum rules at a renormalization scale of 1 GeV. Recent lattice results give $\langle\bar\psi\psi\rangle = -2(231 \pm 4 \pm 8 \pm 6\ \text{MeV})^3$ [33].} On the other hand, since the correction term $\delta\tilde\Sigma$ in the LSS gap equation, Eq. (3.3), contributes negatively to m, it is much more difficult to obtain sufficiently large quark masses in the LSS than in the $1/N_c$-expansion scheme.

Our results for the LSS are given in Table 1. For comparison, we also summarize the results obtained in [20] within the $1/N_c$-expansion scheme (Table 2). In both tables, we list five parameter sets (corresponding to five different meson cutoffs Λ_M), together with the constituent quark mass m, the values of m_π, f_π, and $\langle\bar\psi\psi\rangle$ and the corresponding RPA quantities. In the LSS, the "RPA quantities" are calculated with the constituent quark mass m in order to represent the properties of the intermediate pion states. For completeness, we also give the value of the Hartree mass m_H in Table 1 and the value of the quark condensate according to Eq. (3.7). We also show the ratio $-m_0\langle\bar\psi\psi\rangle/m_\pi^2 f_\pi^2$, which would be equal to 1 if the GOR relation was exactly fulfilled. Note that the deviations in the $1/N_c$-expansion scheme are less than 10% (for $\Lambda_M \le 600$ MeV, they are even less than 3%), indicating that higher order corrections in $1/N_c$ are small. In the LSS, the deviations are considerably smaller, as already discussed in the previous subsection.

In both schemes, we find that the constituent quark mass increases with increasing meson cutoff Λ_M. In the $1/N_c$-expansion scheme for $\Lambda_M \ge 500$ MeV, the value of m is large enough to shift the $q\bar q$ threshold above the ρ-meson peak. Moreover, it turns out that we can only stay below the limit of $-2(260\ \text{MeV})^3$ for the quark condensate and simultaneously reproduce the empirical value of f_π if the cutoff is not too large ($\Lambda_M \lesssim 700$ MeV). In the LSS, the region of values for Λ_M where, on one hand, the constituent quark mass is large enough and,

Table 1. The model parameters (Λ_M, Λ_q, m_0, and g_s); the resulting values of m_π, f_π, and $\langle\bar\psi\psi\rangle$ (together with the corresponding leading-order quantities); and the constituent quark mass m for the LSS. [The quantity $-m_0\langle\bar\psi\psi\rangle/m_\pi^2 f_\pi^2$ is also given; the quantity $\langle\bar\psi\psi\rangle'$ denotes the quark condensate calculated according to Eq. (3.7)]

Λ_M [MeV]	0	300	500	600	700
Λ_q [MeV]	800	800	810	820	835
m_0 [MeV]	6.13	6.47	7.02	7.30	7.90
$g_s\Lambda_q^2$	2.90	3.08	3.44	3.71	4.52
$m_{\rm H}$ [MeV]	260	305	390	450	600
m [MeV]	260	278.2	320.0	355.7	468.4
$m_\pi^{(0)}$ [MeV]	140.0	139.9	140.0	139.7	140.0
m_π [MeV]	140.0	145.1	156.3	164.5	182.7
$f_\pi^{(0)}$ [MeV]	93.6	96.7	103.6	108.4	120.0
f_π [MeV]	93.6	93.2	92.9	92.9	92.8
$\langle\bar\psi\psi\rangle'$ [MeV^3]	$-2(241.1)^3$	$-2(244.7)^3$	$-2(254.3)^3$	$-2(261.9)^3$	$-2(277.3)^3$
$\langle\bar\psi\psi\rangle$ [MeV^3]	$-2(241.1)^3$	$-2(241.7)^3$	$-2(246.2)^3$	$-2(250.8)^3$	$-2(260.9)^3$
$-m_0\langle\bar\psi\psi\rangle/m_\pi^2 f_\pi^2$	1.001	1.001	1.006	1.01	1.02

Table 2. The same as in Table 1, but in the $1/N_c$-expansion scheme

Λ_M [MeV]	0	300	500	600	700
Λ_q [MeV]	800	800	800	820	852
m_0 [MeV]	6.13	6.40	6.77	6.70	6.54
$g_s\Lambda_q^2$	2.90	3.07	3.49	3.70	4.16
m [MeV]	260	304	396	446	550
$m_\pi^{(0)}$ [MeV]	140.0	140.0	140.0	140.0	140.0
m_π [MeV]	140.0	143.8	149.6	153.2	158.1
$f_\pi^{(0)}$ [MeV]	93.6	100.6	111.1	117.0	126.0
f_π [MeV]	93.6	93.1	93.0	93.1	93.4
$\langle\bar\psi\psi\rangle^{(0)}$ [MeV^3]	$-2(241.1)^3$	$-2(249.3)^3$	$-2(261.2)^3$	$-2(271.3)^3$	$-2(287.2)^3$
$\langle\bar\psi\psi\rangle$ [MeV^3]	$-2(241.1)^3$	$-2(241.7)^3$	$-2(244.1)^3$	$-2(249.5)^3$	$-2(261.4)^3$
$-m_0\langle\bar\psi\psi\rangle/m_\pi^2 f_\pi^2$	1.001	1.007	1.018	1.023	1.072

on the other hand, the quark condensate stays below the limit is much narrower. This can be seen from the values listed in Table 1. For a meson cutoff of Λ_M = 600 MeV, m is still too small, and for Λ_M = 700 MeV, the quark condensate lies already slightly above the limit. The reason for this is obvious: in the LSS, m and the quark condensate are directly related by Eq. (3.8); therefore, the mesonic fluctuations, which lower the quark condensate, also decrease the constituent quark mass. In the $1/N_c$-expansion scheme, on the contrary, the meson-loop effects only contribute to the quark condensate and lower its value, whereas m is kept fixed at its Hartree value.

5.5. *Description of the* ρ *Meson*

As already pointed out, the parameter fit in the pion sector was not complete. It is clear, e.g., that the meson-loop cutoff Λ_M cannot be determined just by fitting the pion mass, f_π, and $\langle\bar\psi\psi\rangle$, since these observables can already be reproduced in the Hartree + RPA scheme, i.e., without any meson-loop effects. We only found an

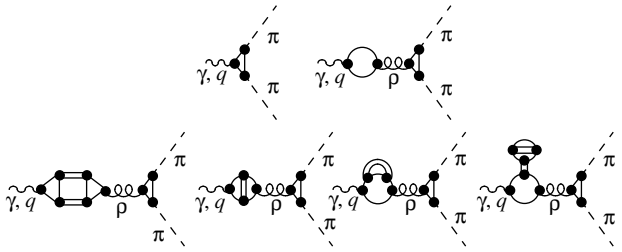

Fig. 12. Contributions to the pion electromagnetic form factor in the $1/N_c$-expansion scheme. The propagator denoted by the curly line corresponds to the $1/N_c$-corrected ρ meson, while the double lines indicate RPA pions and sigmas.

upper limit of $\Lambda_M \sim 700$ MeV in both schemes (see Tables 1 and 2). In [20], we therefore fixed the remaining parameters g_v and Λ_M for the $1/N_c$-expansion scheme in the ρ-meson sector. In this subsection, we want to give a short summary of these results and then try to perform a similar fit for the LSS.

According to Eqs. (2.14) and (3.6), the polarization function of the ρ meson reads

$$\tilde{\Pi}_\rho^{\mu\nu,ab}(q) = \Pi_\rho^{\mu\nu,ab}(q) + \sum_k \delta\Pi_\rho^{(k)\mu\nu,ab}(q). \quad (5.6)$$

Here, k runs over $\{a, b, c, d\}$ in the $1/N_c$-expansion scheme and only over $\{a, b, c\}$ in the LSS. Because of vector-current conservation, the polarization function has to be transverse; i.e.,

$$q_\mu \tilde{\Pi}_\rho^{\mu\nu,ab}(q) = q_\nu \tilde{\Pi}_\rho^{\mu\nu,ab}(q) = 0. \quad (5.7)$$

With the help of Ward identities, it can be shown that these relations hold in both schemes, if we assume that the regularization preserves this property. This is the case for the Pauli–Villars regularization scheme, which was employed to regularize the RPA part Π_ρ. Together with Lorentz covariance, this leads to Eq. (2.8) for the tensor structure of Π_ρ. On the other hand, since we use a three-dimensional sharp cutoff for the regularization of the meson loops, the correction terms $\delta\Pi_\rho^{(k)\mu\nu,ab}$ are, in general, not transverse. However, as mentioned in Subsection 5.1, we work in the rest frame of the ρ meson, i.e., $\mathbf{q} = 0$. In this particular case, Eq. (5.7) is not affected by the cutoff and the entire function $\tilde{\Pi}_\rho$ can be written in the form of Eq. (2.8):

$$\begin{aligned}\tilde{\Pi}_\rho^{\mu\nu,ab}(q) &= \tilde{\Pi}_\rho(q) T^{\mu\nu}\delta_{ab} \\ &= \left(\Pi_\rho(q) + \sum_k \delta\Pi_\rho^{(k)}(q)\right) T^{\mu\nu}\delta_{ab};\end{aligned} \quad (5.8)$$

i.e., instead of evaluating all tensor components separately, we only need to calculate the scalar functions $\Pi_\rho = -(1/3) g_{\mu\nu}\Pi_\rho^{\mu\nu}$ and $\delta\Pi_\rho^{(k)} = -(1/3) g_{\mu\nu}\delta\Pi_\rho^{(k)\mu\nu}$.

A second consequence of vector-current conservation is that the polarization function should vanish for $q^2 = 0$. For the correction terms, this is violated by the sharp cutoff. We cure this problem by performing a subtraction:

$$\sum_k \delta\Pi_\rho^{(k)}(q) \longrightarrow \sum_k (\delta\Pi_\rho^{(k)}(q) - \delta\Pi_\rho^{(k)}(0)). \quad (5.9)$$

Note, however, that, already at the RPA level, a subtraction is required, although the RPA part is regularized by Pauli–Villars regulators. This is due to a rather general problem that is discussed in detail in Appendix B.

In [20], we have fixed g_v and Λ_M in the $1/N_c$-expansion scheme by fitting the pion electromagnetic form factor, $F_\pi(q)$, in the timelike region, which is dominated by the ρ meson. The diagrams we included in these calculations are shown in Fig. 12. The two diagrams in the upper part correspond to the standard NJL description of the form factor [34] if the full ρ-meson propagator (curly line) is replaced by the RPA one. Hence, the first improvement is the use of the $1/N_c$-corrected ρ-meson propagator in the $1/N_c$-expansion scheme. Since, in the standard scheme, the photon couples to the ρ meson via a quark–antiquark polarization loop, in the $1/N_c$-expansion scheme, we should also take into account the $1/N_c$-corrections to the polarization diagram for consistency. This leads to the diagrams in the lower part of Fig. 12. On the other hand, the external pions are taken to be RPA pions (i.e., the mass is $m_\pi^{(0)}$ and the pion–quark–quark coupling constant is $g_{\pi qq}^{(0)}$). This is more consistent with the fact that the ρ meson is also dressed by RPA pions and, as discussed above, we have fitted $m_\pi^{(0)}$ to the experimental value.

The numerical results for $|F_\pi|^2$ as a function of the center-of-mass energy squared are displayed in the left panel of Fig. 13 together with the experimental data from [35]. The theoretical curve was calculated with a meson cutoff of $\Lambda_M = 600$ MeV; a vector coupling constant $g_v = 1.6 g_s$; and other parameters, Λ_q, g_s, and m_0, as listed in Table 2. This roughly corresponds to a best fit to the data [20]. Since we assumed exact isospin symmetry, we can, of course, not reproduce the detailed structure of the form factor around 0.61 GeV^2, which is due to ρ–ω mixing. The high-energy part above the peak is somewhat underestimated, mainly due to the subthreshold attraction in the ρ-meson channel below the $q\bar{q}$ threshold at $s = 0.80$ GeV^2. Probably, the fit can be somewhat improved if we take a slightly larger meson cutoff, but we are not interested in fine tuning here.

A closely related quantity is the charge radius of the pion, which is defined as

$$\langle r_\pi^2 \rangle = 6 \left.\frac{dF_\pi}{dq^2}\right|_{q^2=0}. \quad (5.10)$$

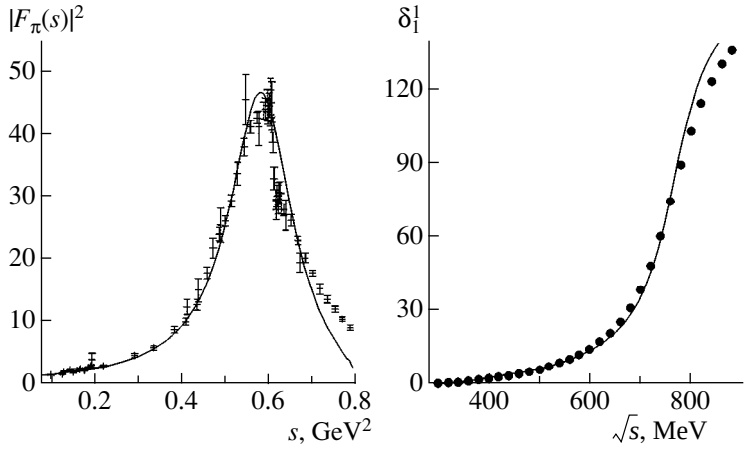

Fig. 13. The pion electromagnetic form factor (left panel) and the ππ-phase shifts in the vector–isovector channel (right panel) for $\Lambda_M = 600$ MeV and $g_V = 1.6g_s$. The other parameter values are taken from Table 2. The data points are taken from [35] and [36], respectively.

With the above parameter set, we obtain a value of $\langle r_\pi^2 \rangle^{1/2} = 0.61$ fm. It lies slightly below the experimental value $\langle r_\pi^2 \rangle^{1/2} = (0.663 \pm 0.006)$ fm [37].

One can also look at the ππ-phase shifts in the vector–isovector channel. We include the diagrams shown in Fig. 14, i.e., the *s*-channel ρ-meson exchange and the direct ππ-scattering via a quark box diagram. The latter has to be projected onto spin and isospin 1, which is a standard procedure. (For example, the analogous projection onto spin and isospin 0 can be found in [38, 39].) The result, together with the empirical data [36], is displayed in the right panel of Fig. 13. Since the main contribution comes from the *s*-channel ρ-meson exchange, it more or less confirms our findings for the form factor: below the ρ-meson peak, a good description of the data is obtained, while, at higher energies, where $q\bar{q}$-threshold effects start to play a role, we slightly overestimate the data.

Let us now turn to the LSS. As already discussed in the last paragraph of Subsection 5.4, there is not much room to vary the meson cutoff Λ_M in this scheme: on the one hand, Λ_M is restricted to values $\lesssim 700$ MeV by the fit to f_π and $\langle \bar{\psi}\psi \rangle$ (see Table 1). On the other hand, we only have a chance to get a realistic description of the ρ meson if the constituent quark mass m is larger than at least 400 MeV. To achieve this, the meson cutoff cannot be much smaller than 700 MeV. This means that Λ_M is more or less fixed to this value, so that the only remaining parameter is the vector-coupling constant g_V.

It turns out, however, that with $\Lambda_M \gtrsim 700$ MeV, we already run into instabilities in the ρ-meson channel. These instabilities are of the same type as the instabilities in the pion channel (see Subsection 5.3), but unfortunately emerge already at lower values of Λ_M. This can be seen in Fig. 15, where the real part of the ρ-meson polarization function $\tilde{\Pi}_\rho$ multiplied by $2g_V$ is plotted as a function of the energy $\sqrt{s}$ in the rest frame of the meson. The LSS result corresponds to the solid curve.

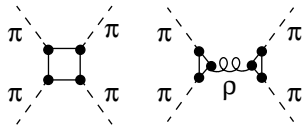

Fig. 14. Diagrams contributing to the ππ-scattering amplitude: quark box diagram (left) and *s*-channel ρ-meson exchange (right).

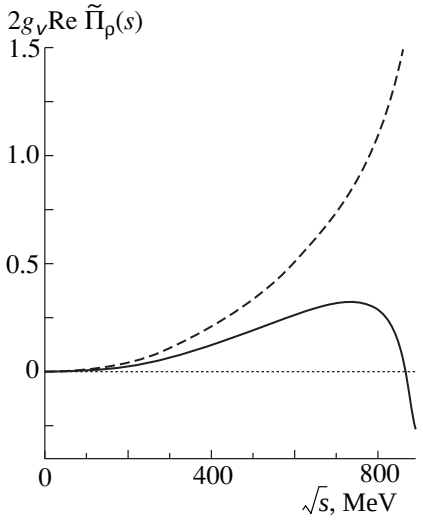

Fig. 15. Real part of the ρ-meson polarization function $\tilde{\Pi}_\rho$ multiplied by $2g_V = 17.6$ GeV^{-2} as a function of the energy $\sqrt{s}$ in the rest frame of the meson. The dashed line corresponds to the $1/N_c$-expansion scheme with $\Lambda_M = 600$ MeV; the solid curve corresponds to the LSS with $\Lambda_M = 700$ MeV. The other parameters are given in Tables 2 and 1, respectively.

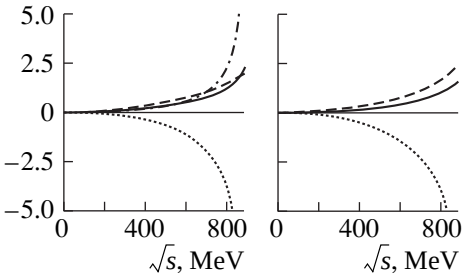

Fig. 16. RPA contribution $2g_V\Pi_\rho$ (solid) and the various correction terms to $2g_V\tilde{\Pi}_\rho$: $2g_V\delta\Pi_\rho^{(a)}$ (dashed), $2g_V(\delta\Pi_\rho^{(b)} + \delta\Pi_\rho^{(c)})$ (dotted), and $2g_V\delta\Pi_\rho^{(d)}$ (dash-dotted). For all contributions, we performed a subtraction such that they vanish at $\sqrt{s} = 0$. The left panel corresponds to the $1/N_c$-expansion scheme; the right panel corresponds to the LSS. The model parameters are the same as in Fig. 15.

For comparison, we also show this function in the $1/N_c$-expansion scheme using the "best-fit parameters" given above (dashed curve).

According to Eqs. (2.15) and (3.5), the function $2g_V\mathrm{Re}\tilde{\Pi}_\rho$ has to become equal to 1 for $\sqrt{s} \simeq m_\rho$, crossing the line $2g_V\mathrm{Re}\tilde{\Pi}_\rho = 1$ from below. This is obviously the case in the $1/N_c$-expansion scheme. In this scheme, $\mathrm{Re}\tilde{\Pi}_\rho$ is a rising function and the above condition can be easily fulfilled with the appropriate choice of g_V. The situation is quite different in the LSS. Here, $\mathrm{Re}\tilde{\Pi}_\rho$ has a maximum at $\sqrt{s} \sim 740$ MeV and then steeply drops. Hence, if g_V is too small, the equation $2g_V\mathrm{Re}\tilde{\Pi}_\rho = 1$ has no solution at all (see Fig. 15). On the other hand, for large values of g_V, we get a "physical" solution at lower energies and an "unphysical" solution at higher energies. It is clear that neither of these two scenarios would lead to a realistic description of the ρ meson.

One might wonder why the results in the $1/N_c$-expansion scheme and in the LSS are so different. To answer this question, we have separately plotted the various contributions to the polarization function in Fig. 16. The left panel corresponds to the results in the $1/N_c$-expansion scheme and the right panel, to the LSS. One immediately sees that the unphysical behavior in the LSS is due to the sum of the diagrams $\delta\Pi_\rho^{(b)}$ and $\delta\Pi_\rho^{(c)}$ (dotted), which is the only negative contribution. In the $1/N_c$-expansion scheme, these diagrams behave very similarly. However, in this scheme, their contribution is almost cancelled by the contribution of the diagram $\delta\Pi_\rho^{(d)}$, which is not present in the LSS.

We should note that the diagram $\delta\Pi_\rho^{(a)}$, which describes the two-meson intermediate state, is well-behaved in both schemes. On the other hand, the momentum dependence of all other diagrams is a pure quark effect, which could be related to the imaginary part of these diagrams above the (unphysical) two-quark threshold via dispersion relations. Hence, if we could manage to further push up the constituent quark mass, the momentum dependence of these contributions should become smaller and the instabilities should eventually vanish. Perhaps this is possible if further intermediate mesons, like ρ and a_1, are included in the model.

6. QUARK CONDENSATE AT $T \neq 0$

It is expected that, at sufficiently large temperatures, chiral symmetry, which is spontaneously broken in vacuum, gets restored. The quark condensate as an order parameter of chiral symmetry is well suited to study indications of (partial) chiral-symmetry restoration. At low temperatures, model-independent results for the changes of the quark condensate can be obtained from considering a gas of pions, which are the lightest particles and, therefore, the main degrees of freedom in this range. Approaching the phase transition, we have to rely on model calculations or lattice data because we do not have any fundamental knowledge of the quark condensate at higher temperatures. Most of the results show a phase transition at a temperature of $T_c \sim 150$ MeV.

Among others, the NJL model has been used to examine the behavior of the quark condensate as a function of temperature. Most of these investigations were performed in the mean-field approximation [7–10]. There, one finds a second-order phase transition with $T_c \sim$ 150–200 MeV. However, one has to mention that these calculations suffer from the severe problem that the thermodynamics is generated exclusively by a gas of quarks. One consequence is that the low-temperature behavior, which is driven mainly by pions, is completely missed. Although we cannot bypass the fundamental problem of lack of confinement in the NJL model, which, in any case, leads to the existence of a quark gas at nonzero temperature, we can hope to improve the situation at least at low temperatures via the inclusion of mesonic degrees of freedom in a calculation beyond mean field.

Therefore, we begin with a closer look at the low-temperature behavior of the quark condensate at $T \neq 0$. After that, we will discuss our numerical results within the $1/N_c$-expansion scheme and within the LSS.

6.1. Low-Temperature Behavior

In the chiral limit and at vanishing baryon density, a strict low-temperature expansion in chiral perturbation theory leads to the following expression for the quark condensate [40]:

$$\langle\bar{\psi}\psi\rangle_T = \langle\bar{\psi}\psi\rangle\left(1 - \frac{T^2}{8f_\pi^2} - \frac{T^4}{384f_\pi^4} + \ldots\right). \qquad (6.1)$$

Here, $\langle\bar{\psi}\psi\rangle$ denotes the quark condensate at zero temperature. The T^2 term represents the contributions from

a pure pion gas, whereas the higher order terms are due to interactions between the pions. It has been shown [40] that the T^2 and the T^4 term of this expansion are model-independent results which follow from chiral symmetry alone. Thus, in principle, every chirally symmetric model, including the NJL model, should reproduce these terms. However, as f_π is of order $\sqrt{N_c}$, we can see that they are of order $1/N_c$ and $1/N_c^2$, respectively. Therefore, a mean-field calculation, which corresponds to a restriction to leading order in $1/N_c$, will not be able to reproduce these terms [23]. Indeed, NJL-model calculations in mean field show a much flatter behavior at low temperatures [10, 27]:

$$\langle\bar\psi\psi\rangle_T^{(0)} = \langle\bar\psi\psi\rangle^{(0)}\left(1-\frac{(2mT)^{3/2}}{\pi^{3/2}\langle\bar\psi\psi\rangle^{(0)}}e^{-m/T}+\ldots\right). \quad (6.2)$$

Extending the calculations to next-to-leading order in $1/N_c$ will allow us to reproduce the T^2 term. This will be demonstrated in the following.

Our calculations at nonzero temperature are performed within imaginary-time formalism. Basically, this amounts to replacing the energy integration in the various n-point functions by a sum over Matsubara frequencies. The explicit expressions are listed in Appendix D. As there exists a preferred frame of reference in the heat bath, all dynamical quantities depend separately on energy and three-momentum. Hence, in the following, a finite-temperature RPA propagator, for instance, will be denoted as $D_M(\omega, \mathbf{p})$. For scalar quantities, like masses or condensates at nonzero temperature, we use a suffix T in order to distinguish them from the analogous quantities in a vacuum (cf. Eqs. (6.1) and (6.2)).

In analogy to the vacuum expressions (Eqs. (2.5) and (2.22)), the quark condensate in the next-to-leading order of the $1/N_c$-expansion scheme is given by

$$\begin{aligned}\langle\bar\psi\psi\rangle_T &= \langle\bar\psi\psi\rangle_T^{(0)} + \delta\langle\bar\psi\psi\rangle_T \\ &= -\frac{m_T-m_0}{2g_s}-\frac{D_\sigma(0,0)\Delta_T}{2g_s}.\end{aligned} \quad (6.3)$$

As shown in Eq. (6.2), the leading-order term $\langle\bar\psi\psi\rangle_T^{(0)}$ does not contribute to the change of the quark condensate to order T^2. Similarly, thermal effects in the σ-meson propagator can be neglected at low temperatures. Therefore, we only need to consider the temperature dependence of Δ_T. If standard techniques are used, the sum over the Matsubara frequencies in Eq. (A.30) can be converted into a contour integral [41]:

$$\Delta_T = 4iN_cN_f m_T\frac{1}{2\pi i}\int\frac{d^3p}{(2\pi)^3}\int_C\frac{dz}{e^{z/T}-1}$$

$$\times\{D_\pi(z,\mathbf{p})(3I(0,0)-3(z^2-\mathbf{p}^2)K(z,\mathbf{p})) \quad (6.4)$$

$$+D_\sigma(z,\mathbf{p})(2I(z,\mathbf{p})+I(0,0)-(z^2-\mathbf{p}^2-4m_T^2)K(z,\mathbf{p}))\}.$$

At low temperatures, the main contribution to the temperature-dependent part of this integral comes from the lowest lying pion pole, as the other contributions are exponentially suppressed. In the chiral limit, we can therefore approximate this part for low temperatures by

$$\Delta_T-\Delta = 4N_cN_f m\int\frac{d^3p}{(2\pi)^3}\frac{2}{e^{|\mathbf{p}|/T}-1}\left\{\frac{3}{2|\mathbf{p}|2N_cN_f}\right\}. \quad (6.5)$$

This integral can be evaluated analytically and we obtain

$$\Delta_T-\Delta = m\frac{T^2}{2}. \quad (6.6)$$

The last step is to realize that, in the chiral limit, the vacuum σ-meson propagator can be expressed through the leading-order pion decay constant as

$$D_\sigma(0) = -\frac{1}{4f_\pi^{2(0)}} \quad (6.7)$$

(see Eqs. (A.16) and (A.21)). We finally obtain for the quark condensate in the next-to-leading order at low temperatures

$$\langle\bar\psi\psi\rangle_T = \langle\bar\psi\psi\rangle-\langle\bar\psi\psi\rangle^{(0)}\frac{T^2}{8f_\pi^{2(0)}}. \quad (6.8)$$

Comparing this with the chiral-perturbation-theory result, Eq. (6.1), we see that we can, in principle, reproduce the T^2 term. Note, however, that the coefficient is given by the quark condensate and the pion decay constant in the leading order in $1/N_c$ according to a strict expansion of Eq. (6.1) up to the next-to-leading order in $1/N_c$. The physical reason for this behavior is the fact that the $1/N_c$ corrections to the quark condensate correspond to fluctuating RPA mesons; hence, the thermal corrections at low temperatures are due to thermally excited RPA pions in this model.

For the LSS, a similar result was derived in [23]. In the chiral limit, the authors find

$$\langle\bar\psi\psi\rangle_T = \langle\bar\psi\psi\rangle\left(1-\frac{T^2}{8f_\pi^{2(0)}}\right). \quad (6.9)$$

Here, $f_\pi^{2(0)}$ is understood as the RPA pion decay constant, Eq. (A.21), but evaluated at the quark mass m which follows from the LSS gap equation, Eq. (3.3). This corresponds to the fact that, in the LSS, the thermal corrections to the quark condensate at low temperatures are due to RPA pions which consist of LSS quarks.

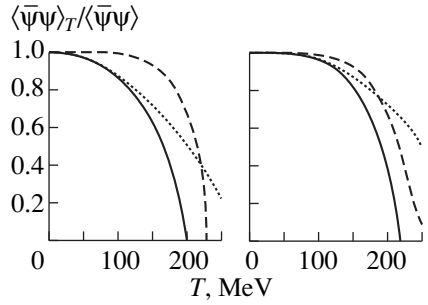

Fig. 17. Quark condensate as a function of temperature, normalized to the vacuum value, in the chiral limit (left) and with $m_\pi^{(0)} = 140$ MeV (right): leading order in $1/N_c$ (dashed curve), next-to-leading order (solid curve), and free pion gas (dotted curve).

6.2. Numerical Results within the $1/N_c$-Expansion Scheme

Our numerical results for the temperature behavior of the quark condensate within the $1/N_c$-expansion scheme are displayed in Fig. 17. The right-hand side corresponds to a realistic parameter set with $m_\pi^{(0)} = 140$ MeV (Table 2 with $\Lambda_M = 600$ MeV) and the left-hand side, to the chiral limit. The solid curves indicate the results obtained in the next-to-leading order. For comparison, we also show the leading order (dashed curve) and the pure pion-gas result (dotted).

We begin our discussion with the chiral limit. At low temperatures ($T \lesssim 100$ MeV), our results show the behavior discussed in the previous subsection: the next-to-leading-order result is in very good agreement with the pion-gas result (Eq. (6.8)), whereas the leading-order result remains almost constant. Therefore, in this regime, the extension of the NJL model to the next-to-leading order in $1/N_c$ leads to a considerable improvement. Since the unphysical quark degrees of freedom, which are in principle always present in the NJL model, are exponentially suppressed, the system is dominated by the (physical) pion degrees of freedom, which come about in the next-to-leading order.

However, because of the much larger degeneracy factor (24 as compared to 3), we cannot avoid the fact that effects due to thermally excited quarks become important at some temperature. In our present calculation, this happens at about $T \sim 100$ MeV. In a free-gas approximation, this roughly corresponds to the temperature at which the quark pressure becomes equal to the pion pressure.

At this point, one might raise a question as to the physical meaning of quark effects at these temperatures. In nature, quark degrees of freedom can only be excited above the deconfinement phase transition. In the NJL model, there is no confinement and, hence, no deconfinement transition. However, lattice calculations [42] indicate that the deconfinement phase transition at finite temperature coincides with the chiral phase transition. One should therefore compare the temperature at which thermally excited quarks become important with the critical temperature for the chiral phase transition. Unfortunately, as already pointed out in Section 3, the perturbative treatment of the mesonic fluctuations does not allow for a description of the chiral phase transition. Although the quark condensate vanishes at $T \sim 200$ MeV, this does not correspond to a true phase transition. (Note that the slope of the curve does not diverge at this point.) In any case, the perturbative-expansion scheme probably breaks down much earlier. Therefore, we cannot give a definite answer to the question of whether the thermally excited quarks become important near the phase transition or much below.

Our results with $m_0 \neq 0$ are shown on the right-hand side of Fig. 17. Since the RPA pions are now massive and therefore exponentially suppressed, the quark condensate as a function of T stays much flatter than in the chiral limit. Nevertheless, at low temperatures, pions can still be most easily excited as they are the lightest particles. Therefore, the next-to-leading-order result (solid curve) can be approximated quite well, albeit not perfectly, by the pure pion-gas result (dotted) in this regime. The latter was calculated from the pressure p_π of a massive pion gas as

$$\langle\bar\psi\psi\rangle_T = \langle\bar\psi\psi\rangle + \langle\bar\psi\psi\rangle^{(0)} \frac{m_0}{f_\pi^{2(0)}} \frac{dp_\pi(T)}{dm_\pi^{2(0)}}, \qquad (6.10)$$

which can be easily derived with the help of the GOR relation.

Quark effects become important at almost the same temperature as in the chiral limit, at $T \sim 100$ MeV.

6.3. Local Self-Consistent Scheme

Let us now compare the results of the previous subsection with the analogous calculations in the LSS. A study of the temperature dependence of the quark condensate within the LSS can also be found in [23]. Here, we restrict ourselves to the chiral limit.

Our results are shown on the left-hand side of Fig. 18. The calculations have been performed using the parameters of Table 1 for $\Lambda_M = 700$ MeV, but $m_0 = 0$. As discussed in Subsection 6.1, at low temperatures, the model behaves again like a free pion gas (dotted curve). Deviations from this behavior become visible at $T \sim 100$ MeV, which is quite similar to our observations in the $1/N_c$-expansion scheme.

In contrast to the $1/N_c$-expansion scheme, the treatment of the mesonic fluctuations in the LSS also allows examination of the phase transition. With the present parameters, this takes place at $T_c = 164.5$ MeV, which is considerably lower than in the Hartree approximation, where we have $T_c = 266.1$ MeV. Note, however, that about one third of this reduction can be attributed to the fact that the constituent quark mass $m = 468.4$ MeV in

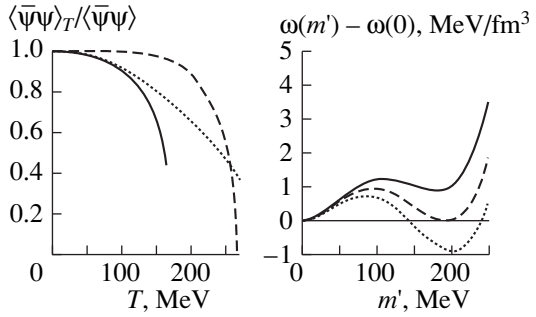

Fig. 18. Left: quark condensate in the chiral limit as a function of temperature, normalized to the vacuum value, Hartree approximation (dashed), LSS (solid), and free pion gas (dotted). Right: thermodynamic potential per volume as a function of the constituent quark mass in the self-consistent scheme with T = 163.9 (dotted), 164.5 (dashed), and 165.3 MeV (solid).

the LSS is lower than the corresponding Hartree mass m_{H} = 600.0 MeV. For m_{H} = 468 MeV, we would get a critical temperature of about 236 MeV in the Hartree approximation. (It is also interesting to note that the critical temperature in the LSS calculation almost coincides with the critical temperature T_c^{RPA} = 164.4 MeV one obtains in the Hartree approximation for the parameters fitted in the RPA; i.e., $m = m_{\mathrm{H}}$ = 260 MeV.)

Whereas in the Hartree approximation, the phase transition is of second order, in the LSS, the system undergoes a first-order phase transition, as already reported in [23]. This can be inferred from the thermodynamic potential ω, which is displayed on the right-hand side of Fig. 18 for different temperatures as a function of the constituent quark mass m'. At T = 164.5 MeV, one can clearly identify two degenerate minima at $m' = 0$ and $m' \neq 0$ corresponding to a first-order phase transition at that temperature. One can ask the question of whether this phenomenon depends on the strength of the mesonic fluctuations that can be controlled by the cutoff Λ_M. Varying this parameter, we find that the discontinuity decreases with decreasing Λ_M, but, even for very small values of the cutoff, we encounter a first-order phase transition.

Let us come back to the questions on the relevance of the unphysical quark degrees of freedom. As already mentioned, deviations from the pure pion-gas result become visible at $T \sim 100$ MeV, which corresponds to about $0.6T_c$. At this temperature, one would not expect quark effects to be present in nature. Furthermore, according to universality arguments, it is generally believed that the finite-temperature chiral phase transition in QCD with two massless quarks is of second order [43]. This is based on the assumption that, at T_c, there are four massless bosonic degrees of freedom (three pions and one σ) which determine the infrared behavior of the system. In this case, QCD—and also the NJL model—should lie in the same universality class as the $O(4)$ model, which is known to have a second-order phase transition. Although some time ago it was claimed that this argument might not hold if the boson fields are not elementary but composite [44], it is probably more likely that the first-order phase transition we observe is an artifact of the approximation scheme. In this context, the application of renormalization-group techniques to the NJL model would be extremely interesting.

7. CONCLUSIONS

We have investigated quark and meson properties within the NJL model, including meson-loop corrections. These were generated in two different ways. The first method is a systematic expansion of the self-energies in powers of $1/N_c$ up to the next-to-leading order [14, 19, 20]. In the second scheme, a local correction term to the standard Hartree self-energy is self-consistently included in the gap equation [14]. We therefore call it the "local self-consistent scheme." This scheme can also be derived as the one-meson-loop approximation to the effective action [15]. Both schemes, the $1/N_c$-expansion scheme and the LSS, are consistent with chiral symmetry, leading to massless pions in the chiral limit. For nonvanishing current quark masses, the pion mass is consistent with the GOR relation in the LSS. This is also true in the $1/N_c$-expansion scheme if one carefully expands both sides of the relation up to next-to-leading order in $1/N_c$.

The relative importance of the mesonic fluctuations is controlled by a parameter Λ_M, which cuts off the three-momenta of the meson loops. In both schemes, we encounter instabilities in the pion propagator if the meson effects become too strong. In order to find out whether these instabilities are related to an unstable ground state [19, 22] leading to a "chiral restoration phase transition" at some critical value of Λ_M, we calculated the effective action of the LSS for increasing values of Λ_M. (Note that such investigations are not possible within the $1/N_c$-expansion scheme, where mesonic fluctuations are included only perturbatively.) It turned out that, up to a certain value of Λ_M, the system indeed seems to move toward a "phase transition." However, when Λ_M is further increased, the nontrivial ground state becomes again more stable and no phase transition takes place.

Of course, at the end, the value of Λ_M, together with the other parameters, has to be determined by fitting physical observables. The ρ meson and related quantities are very well suited for this purpose, since the meson loops are absolutely crucial in order to include the dominant $\rho \longrightarrow \pi\pi$-decay channel, while the Hartree + RPA approximation contains only unphysical $q\bar{q}$-decay channels. Here, another problem, which constraints the possible choice of parameter values, becomes obvious: a priori, it is not clear to what extent

these unphysical decay modes, which are an unavoidable consequence of the missing confinement mechanism in the NJL model, are still present in the region of the ρ-meson peak.

For the $1/N_c$-expansion scheme, the parameters have already been fixed in [20]. We obtained a reasonable fit of f_π, $\langle\bar{\psi}\psi\rangle$, and the pion electromagnetic form factor with a constituent quark mass of $m = 446$ MeV. This means that the unphysical $q\bar{q}$-decay channel opens at 892 MeV, about 120 MeV above the maximum of the ρ-meson peak. Furthermore, the parameters of that fit are far away from the region where the instabilities in the pion propagator emerge. In fact, we found only moderate changes in the pion and quark sector: f_π and $\langle\bar{\psi}\psi\rangle$ are lowered by about 20% by the meson-loop corrections, while the pion mass is increased by about 10%. This indicates that the $1/N_c$ expansion converges rapidly and higher order terms in the $1/N_c$ expansion are small.

Unfortunately, we did not succeed in obtaining a similar fit within the LSS. Since, in this scheme, the meson-loop effects lower the constituent quark mass as compared to the Hartree mass, it is much more difficult to evade the problem of unphysical $q\bar{q}$-decay channels in the vicinity of the ρ-meson peak. We found that a relatively large meson cutoff, $\Lambda_M \sim 700$ MeV, is needed in order to get the quark mass large enough and, at the same time, to get a fit for f_π. However, to our surprise, for this cutoff, the ρ-meson self-energy already suffers from stability problems, similar to those already discussed for the pion. As a result, we are not able to get a reasonable description of the ρ-meson propagator and, hence, of the pion electromagnetic form factor within the LSS. It remains to be checked whether these problems can be cured by taking into account additional intermediate states, like vector mesons and axial vector mesons, or by different methods of regularization.

In the last part of this article, we investigated the temperature dependence of the quark condensate. In both schemes, the low-temperature behavior is consistent with lowest order chiral perturbation theory, i.e., the temperature dependence arising from a free pion gas. This is a considerable improvement over the mean-field result, where the temperature dependence is entirely due to thermally excited quarks, i.e., unphysical degrees of freedom. At higher temperatures, however, thermal quark effects also become visible in the two extended schemes. We argued that this could be tolerable near the chiral phase boundary, which is, according to lattice results, identical to the deconfinement phase boundary at nonzero temperatures.

Whereas the perturbative treatment of the mesonic fluctuations within the $1/N_c$-expansion scheme does not allow an examination of the chiral phase transition, this is possible in the LSS. For our model parameter set, we found a critical temperature of 164.5 MeV. On the other hand, quark effects are visible already at a temperature of ~100 MeV. Obviously, this is still too early to be realistic. Maybe here the model can be improved by including additional intermediate meson states.

In agreement with [23], we found a first-order phase transition in that scheme. This contradicts the general belief that the nonzero-temperature chiral phase transition in a model with two light flavors should be of second order and is probably an artifact of the approximation. Here, further investigations, e.g., applying renormalization-group techniques, would be very interesting.

ACKNOWLEDGMENTS

We are indebted to G.J. van Oldenborgh for his assistance in questions related to his program package FF (see http://www.xs4all.nl/~gjvo/FF.html), which was used in parts of our numerical calculations. We also thank G. Ripka, B.-J. Schaefer, and M. Urban for illuminating discussions.

This work was supported in part by the BMBF and NSF grant NSF-PHY98-00978.

APPENDIX A

Definition of Elementary Integrals

It is possible to reduce the expressions for the quark loops to some elementary integrals [45], see Appendices B and C. In this section, we give the definitions of these integrals.

$$I_1 = \int\frac{d^4k}{(2\pi)^4}\frac{1}{k^2-m^2+i\varepsilon}, \tag{A.1}$$

$$I(p) = \int\frac{d^4k}{(2\pi)^4}\frac{1}{(k^2-m^2+i\varepsilon)((k+p)^2-m^2+i\varepsilon)}, \tag{A.2}$$

$$K(p) = \int\frac{d^4k}{(2\pi)^4}\frac{1}{(k^2-m^2+i\varepsilon)^2((k+p)^2-m^2+i\varepsilon)}, \tag{A.3}$$

$$M(p_1,p_2) = \int\frac{d^4k}{(2\pi)^4}\frac{1}{(k^2-m^2+i\varepsilon)(k_1^2-m^2+i\varepsilon)(k_2^2-m^2+i\varepsilon)}, \tag{A.4}$$

$$L(p_1,p_2,p_3) = \int\frac{d^4k}{(2\pi)^4} \times\frac{1}{(k^2-m^2+i\varepsilon)(k_1^2-m^2+i\varepsilon)(k_2^2-m^2+i\varepsilon)(k_3^2-m^2+i\varepsilon)}, \tag{A.5}$$

$$p_1^\mu M_1(p_1,p_2) + p_2^\mu M_1(p_2,p_1) = \int\frac{d^4k}{(2\pi)^4}\frac{k^\mu}{(k^2-m^2+i\varepsilon)(k_1^2-m^2+i\varepsilon)(k_2^2-m^2+i\varepsilon)}, \tag{A.6}$$

with $k_i = k + p_i$. The function $M_1(p_1, p_2)$ can be expressed in terms of the other integrals:

$$M_1(p_1, p_2) = \frac{p_1 \cdot p_2 I(p_1) - p_2^2 I(p_2) + (p_2^2 - p_1 \cdot p_2) I(p_1 - p_2) + p_2^2 (p_1^2 - p_1 \cdot p_2) M(p_1, p_2)}{2((p_1 \cdot p_2)^2 - p_1^2 p_2^2)}. \quad \text{(A.7)}$$

All integrals in Eqs. (A.1) to (A.6), are understood to be regularized. As described in Subsection 5.1, we use Pauli–Villars regularization with two regulators, i.e., we replace

$$\int \frac{d^4k}{(2\pi)^4} f(k; m) \longrightarrow \int \frac{d^4k}{(2\pi)^4} \sum_{j=0}^{2} c_j f(k; \mu_j)$$

with

$$\mu_j^2 = m^2 + j\Lambda_q^2; \quad c_0 = 1, \quad c_1 = -2, \quad c_2 = 1$$

(see Eqs (5.1) and (5.2)).

One then gets the following relatively simple analytic expressions for the integrals I_1, $I(p)$, and $K(p)$:

$$I_1 = \frac{-i}{16\pi^2} \sum_j c_j \mu_j^2 \ln(\mu_j^2), \quad \text{(A.8)}$$

$$I(p) = \frac{-i}{16\pi^2} \sum_j c_j (x_{j1} \ln(x_{j1}) + x_{j2} \ln(-x_{j2}) + x_{j1} \ln(-p^2 x_{j1}) + x_{j2} \ln(p^2 x_{j2})), \quad \text{(A.9)}$$

$$I(p = 0) = \frac{-i}{16\pi^2} \sum_j c_j \ln(\mu_j^2), \quad \text{(A.10)}$$

$$K(p) = \frac{-i}{16\pi^2} \sum_j c_j \frac{1}{2p^2(x_{j1} - x_{j2})} (-\ln(x_{j1}) - \ln(-x_{j1}) + \ln(x_{j2}) + \ln(-x_{j2})), \quad \text{(A.11)}$$

with

$$x_{j1,2} = \frac{1}{2} \pm \frac{1}{2} \sqrt{1 - \frac{4\mu_j^2}{p^2}}. \quad \text{(A.12)}$$

An analytic expression for the three-point function (A.4) can be found in [46, 47]. In certain kinematical regions, the four-point function (A.5) is also known analytically [46, 47].

APPENDIX B

RPA Propagators

By using the definitions given in the previous section, the gap equation (Eq. (2.2)) can be reduced to the form

$$m = m_0 + 2ig_s 4N_c N_f m I_1. \quad \text{(A.13)}$$

Similarly, one can evaluate the quark–antiquark polarization diagrams (Eq. (2.6)) and calculate the RPA meson propagators. The results for the σ meson and pion read

$$D_\sigma(p) = \frac{-2g_s}{1 - 2ig_s 2N_c N_f (2I_1 - (p^2 - 4m^2) I(p))}, \quad \text{(A.14)}$$

$$D_\pi(p) = \frac{-2g_s}{1 - 2ig_s 2N_c N_f (2I_1 - p^2 I(p))}. \quad \text{(A.15)}$$

If we evaluate these propagators with the constituent quark mass in Hartree approximation, we can simplify the above expressions with the help of the gap equation (Eq. (A.13)) to obtain

$$D_\sigma(p) = \frac{-2g_s}{m_0/m + 2ig_s 2N_c N_f (p^2 - 4m^2) I(p)}, \quad \text{(A.16)}$$

$$D_\pi(p) = \frac{-2g_s}{m_0/m + 2ig_s 2N_c N_f p^2 I(p)}. \quad \text{(A.17)}$$

As discussed in Subsection 5.2, this form is also used for the internal meson propagators in the LSS.

A straightforward evaluation of the vector and axial-vector polarization diagrams gives

$$\Pi_\rho(p) = -i\frac{4}{3} N_c N_f (-2I_1 + (p^2 + 2m^2) I(p)), \quad \text{(A.18)}$$

$$\Pi_{a_1}(p) = -i\frac{4}{3} N_c N_f (-2I_1 + (p^2 - 4m^2) I(p)). \quad \text{(A.19)}$$

Because of vector-current conservation, Π_ρ should vanish for $p^2 = 0$. This is only true if

$$m^2 I(0) = I_1, \quad \text{(A.20)}$$

which is not the case if we regularize $I(p)$ and I_1 as described in Appendix A. This corresponds to the standard form of Pauli–Villars regularization in the NJL model [7]. Alternatively, one could perform the replacement of Eq. (5.1) for the entire polarization loop. In fact, this is more in the original sense of Pauli–Villars regularization [48]. Then, the factor m^2 in Eq. (A.18) should be replaced by a factor μ_j^2 inside the sum over regulators and one can easily show that Eq. (A.20) holds (see Eqs. (A.8) and (A.10)). However, this scheme would lead to even more severe problems: from the gap equation (A.13), we conclude that iI_1 should be positive. On the other hand, the pion decay constant in the chiral limit and in leading order in $1/N_c$ is given by [7]

$$f_\pi^{2(0)} = -2iN_c N_f m^2 I(0), \quad \text{(A.21)}$$

which implies that $im^2I(0)$ should be negative. Thus, irrespective of the regularization scheme, Eq. (A.20) cannot be fulfilled if we want to get reasonable results for m and $f_\pi^{(0)}$ at the same time. Therefore, we choose the standard form of Pauli–Villars regularization in the NJL model [7] and replace the term I_1 in Eq. (A.18) by hand by $m^2I(0)$. For consistency, a_1 is treated in an analogous manner. This leads to the following ρ- and a_1-meson propagator:

$$D_\rho(p) = \frac{-2g_v}{1 + 2ig_v\frac{4}{3}N_cN_f(-2m^2I(0) + (p^2 + 2m^2)I(p))}, \quad \text{(A.22)}$$

$$D_{a_1}(p) = \frac{-2g_v}{1 + 2ig_v\frac{4}{3}N_cN_f(-2m^2I(0) + (p^2 - 4m^2)I(p))}. \quad \text{(A.23)}$$

APPENDIX C

Explicit Expressions for the Meson–Meson Vertices

In this section, we list the explicit formulas for the meson–meson vertices. We restrict ourselves to those combinations that are needed for the calculations presented in this article.

We begin with the three-meson vertices $\Gamma_{M_1, M_2, M_3}(q, p)$ (see Fig. 5):

$$-i\Gamma_{\sigma,\sigma,\sigma}(q, p) = i2mN\Big(I(p') + I(q) + I(p) + \Big(4m^2 - \frac{1}{2}(p'^2 + p^2 + q^2)\Big)M(p, -q)\Big),$$

$$-i\Gamma^{ab}_{\pi,\pi,\sigma}(q, p) = i2mN\delta_{ab}(I(p') + p\cdot qM(p, -q)),$$

$$-i\Gamma^{\mu\lambda, ab}_{\rho,\rho,\sigma}(q, p) = \delta_{ab}h(q, p)\Big(g^{\mu\lambda} - \frac{p^2q^\mu q^\lambda + q^2p^\mu p^\lambda - p\cdot q(p^\mu q^\lambda + q^\mu p^\lambda)}{p^2q^2 - (p\cdot q)^2}\Big), \quad \text{(A.24)}$$

$$h(q, p) = imN(I(q) + I(p) - 2I(p') + (4m^2 - 2p\cdot q - p'^2)M(p, -q)),$$

$$-i\Gamma^{\mu, abc}_{\pi,\pi,\rho}(q, p) = \varepsilon_{abc}(q^\mu f(q, p) - p^\mu f(p, q)),$$

$$f(q, p) = N(-I(q) + p^2M(p, -q) + 2p\cdot qM_1(q, -p)),$$

with $p' = -p - q$ and $N = 4N_cN_f$.

For the four-meson vertices, we only need to consider the special cases needed for diagrams (*b*) and (*c*) in Fig. 5:

$$-i\Gamma_{\sigma,\sigma,\sigma,\sigma}(q, p, -q) = -N\Big\{\frac{I(p-q) + I(p+q)}{2} + 4m^2(M(p, q) + M(p, -q)) + 2\Big(m^2(4m^2 - p^2 - q^2) - \frac{p^2q^2}{4}\Big)L(p, -q, p-q)\Big\},$$

$$-i\Gamma_{\sigma,\sigma,\sigma,\sigma}(q, p, -p) = -N\Big\{I(p+q) + I(0) + 4m^2(K(p) + K(q) + 2M(p, -q)) + 2p\cdot qM(p, -q) - q^2K(q) - p^2K(p) + m^2\Big(16m^2 - 4p^2 - 4q^2 + \frac{p^2q^2}{m^2}\Big)L(p, -q, 0)\Big\},$$

$$-i\Gamma^{ab}_{\sigma,\pi,\sigma,\pi}(q, p, -q) = \delta_{ab}N\{I(p+q) + I(p-q) + p^2(4m^2 - q^2)L(p, -q, p-q)\},$$

$$-i\Gamma^{ab}_{\sigma,\pi,\pi,\sigma}(q, p, -p) = \delta_{ab}N\{-I(p+q) - I(0) - (4m^2 - q^2)(K(q) - p^2L(p, -q, 0)) + p^2K(p) - 2p\cdot qM(p, -q)\},$$

$$-i\Gamma^{abcd}_{\pi,\pi,\pi,\pi}(q, p, -q) = -N\kappa_{abcd}\{I(p+q) + I(p-q) - p^2q^2L(p, -q, p-q)\},$$

$$-i\Gamma^{abcd}_{\pi,\pi,\pi,\pi}(q, p, -p) = -N\kappa_{abcd}\{I(p+q) + I(0) - p^2K(p) - q^2K(q) + 2p\cdot qM(p, -q) + p^2q^2L(p, -q, 0)\}, \quad \text{(A.25)}$$

$$-i\Gamma^{ab}_{\rho,\sigma,\rho,\sigma}(q, p, -q) = -2\delta_{ab}N\Big\{I(p+q) + I(p-q) + 2I(q) - p\cdot q(M(p, -q) - M(p, q)) + (4m^2 - 2p^2)(M(p, q) + M(p, -q)) m^2\Big(8m^2 - 6p^2 + 4q^2 + \frac{p^4 - (p\cdot q)^2}{m^2}\Big)L(p, -q, p-q)\Big\},$$

$$-i\Gamma^{ab}_{\rho,\sigma,\sigma,\rho}(q, p, -q) = -2\delta_{ab}N\Big\{-I(p+q) - I(0)$$

$$+ (p^2 - 4m^2)K(p) + (q^2 + 2m^2)K(q)$$
$$+ (4m^2 - 2p\cdot q)M(p,-q)$$
$$+ m^2\left(8m^2 - 2p^2 + 4q^2 - \frac{p^2q^2}{m^2}\right)L(p,-q,0)\Big\},$$

$$-i\Gamma^{abcd}_{\rho,\pi,\rho,\pi}(q,p,-q) = 2N\kappa_{abcd}\{-I(p+q)$$
$$- I(p-q) - 2I(q) + 2p^2(M(p,q) + M(p,-q))$$
$$+ p\cdot q(M(p,-q) - M(p,q))$$
$$+ (2m^2p^2 - p^4 + (p\cdot q)^2)L(p,-q,p-q)\},$$

$$-i\Gamma^{abcd}_{\rho,\pi,\pi,\rho}(q,p,-q) = 2N\kappa_{abcd}\{I(p+q) + I(0)$$
$$- p^2K(p) - (q^2 + 2m^2)K(q) + 2p\cdot qM(p,-q)$$
$$+ p^2(2m^2 + q^2)L(p,-q,0)\},$$

with $\Gamma_{\rho,M,M,\rho}(q,\ p,\ -q) = g_{\mu\nu}\Gamma^{\mu\nu}_{\rho,M,M,\rho}(q,\ p,\ -q)$, $\Gamma_{\rho,M,\rho,M}(q,p,-p) = g_{\mu\nu}\Gamma^{\mu\nu}_{\rho,M,\rho,M}(q,p,-p)$, and $\kappa_{abcd} = \delta_{ab}\delta_{cd} + \delta_{ad}\delta_{bc} - \delta_{ac}\delta_{bd}$.

APPENDIX D

Expressions at Nonzero Temperature

To determine the temperature dependence of various quantities we need, for the calculation of the quark condensate at nonzero temperature in Section 6, to adopt the imaginary-time or Matsubara formalism (see, e.g., [41]). In principle, this amounts to replacing the integration over energy in the zero-temperature expressions by a sum over fermionic or bosonic Matsubara frequencies ω_n:

$$i\int\frac{d^4k}{(2\pi)^4}f(k) \longrightarrow -T\sum_n\int\frac{d^3k}{(2\pi)^3}f(i\omega_n,\mathbf{k}). \quad \text{(A.26)}$$

With this replacement prescription, we can define the temperature analogue to the elementary integrals; e.g.,

$$I(p) = \int\frac{d^4k}{(2\pi)^4}\frac{1}{(k^2 - m^2 + i\varepsilon)((k+p)^2 - m^2 + i\varepsilon)}$$
$$\longrightarrow I(i\omega_l,\mathbf{p}) = iT\sum_n\int\frac{d^3k}{(2\pi)^3} \quad \text{(A.27)}$$
$$\times\frac{1}{((i\omega_n)^2 - \mathbf{k}^2 - m^2)((i\omega_n + i\omega_l)^2 - (\mathbf{k}+\mathbf{p})^2 - m^2)}.$$

This example also illustrates our notation: at nonzero temperature, the integral depends on energy and three-momentum separately, which is indicated via a second argument. In this way, it can be clearly distinguished from its vacuum counterpart with only one argument. A similar notation is used for other momentum-dependent integrals. The nonzero-temperature analog to the integral I_1 will be denoted by I_{1T}.

We will now summarize the explicit expressions for various temperature dependent quantities which are related to the determination of the quark condensate at nonzero temperature. The temperature analog to the gap equation (A.13) is given by

$$m_T = m_0 - 2g_s4N_cN_fm_TT\sum_n\int\frac{d^3k}{(2\pi)^3}\frac{1}{(i\omega_n)^2 - E^2}$$
$$= m_0 + 2g_s4N_cN_fm_TI_{1T}, \quad \text{(A.28)}$$

with $E = \sqrt{\mathbf{k}^2 + m_T^2}$ and $\omega_n = (2n+1)\pi T$ being fermionic Matsubara frequencies.

The polarization functions for the RPA mesons read

$$\Pi_\sigma(i\omega_l,\mathbf{p}) = 4iN_cN_fI_{1T}$$
$$- 2iN_cN_f((i\omega_l)^2 - \mathbf{p}^2 - 4m_T^2)I(i\omega_l,\mathbf{p}), \quad \text{(A.29)}$$
$$\Pi_\pi(i\omega_l,\mathbf{p}) = 4iN_cN_fI_{1T}$$
$$- 2iN_cN_f((i\omega_l)^2 - \mathbf{p}^2)I(i\omega_l,\mathbf{p}),$$

with $\omega_l = 2l\pi T$ being bosonic Matsubara frequencies. Below the phase transition, the integral I_{1T} can again be replaced with the help of the gap equation (A.28) (cf. Eqs. (A.16) to (A.17)).

Finally, the constant Δ_T is given by

$$\Delta_T = 4iN_cN_fm_TT\int\frac{d^3p}{(2\pi)^3}\sum_l\{D_\sigma(i\omega_l,\mathbf{p})(2I(i\omega_l,\mathbf{p})$$
$$+ I(0,0) - ((i\omega_l)^2 - \mathbf{p}^2 - 4m_T^2)K(i\omega_l,\mathbf{p})) \quad \text{(A.30)}$$
$$+ D_\pi(i\omega_l,\mathbf{p})(3I(0,0) - 3((i\omega_l)^2 - \mathbf{p}^2)K(i\omega_l,\mathbf{p}))\},$$

where ω_l are again bosonic Matsubara frequencies.

REFERENCES

1. G. E. Brown, Nucl. Phys. A **446**, 12 (1985); G. E. Brown, M. Rho, and W. Weise, Nucl. Phys. A **454**, 669 (1986).
2. M. Herrmann, B. Friman, and W. Nörenberg, Nucl. Phys. A **560**, 411 (1993).
3. R. Rapp and J. Wambach, hep-ph/9909229; Adv. Nucl. Phys. **25**, 1 (2000).
4. T. Schafer and E. V. Shuryak, Rev. Mod. Phys. **70**, 323 (1998).
5. Y. Nambu and G. Jona-Lasinio, Phys. Rev. **122**, 345 (1961); **124**, 246 (1961).
6. U. Vogl and W. Weise, Prog. Part. Nucl. Phys. **27**, 195 (1991).
7. S. P. Klevansky, Rev. Mod. Phys. **64**, 649 (1992).
8. T. Hatsuda and T. Kunihiro, Phys. Rep. **247**, 221 (1994).
9. S. Klimt, M. Lutz, and W. Weise, Phys. Lett. B **249**, 386 (1990).

10. M. Lutz, S. Klimt, and W. Weise, Nucl. Phys. A **542**, 521 (1992).
11. S. Krewald, K. Nakayama, and J. Speth, Phys. Lett. B **272**, 190 (1991).
12. E. Quack and S.P. Klevansky, Phys. Rev. C **49**, 3283 (1994).
13. D. Blaschke, Yu. L. Kalinovsky, G. Röpke, *et al.*, Phys. Rev. C **53**, 2394 (1996).
14. V. Dmitrašinovič, H.-J. Schulze, R. Tegen, and R. H. Lemmer, Ann. Phys. (N. Y.) **238**, 332 (1995).
15. E. N. Nikolov, W. Broniowski, C. V. Christov, *et al.*, Nucl. Phys. A **608**, 411 (1996).
16. R. H. Lemmer and R. Tegen, Nucl. Phys. A **593**, 315 (1995).
17. Y. B. He, J. Hüfner, S. P. Klevansky, and P. Rehberg, Nucl. Phys. A **630**, 719 (1998).
18. M. Huang, P. Zhuang, and W. Chao, Phys. Lett. B **465**, 55 (1999); hep-ph/9903304.
19. M. Oertel, M. Buballa, and J. Wambach, Phys. Lett. B **477**, 77 (2000).
20. M. Oertel, M. Buballa, and J. Wambach, Nucl. Phys. A **676**, 247 (2000).
21. R.S. Plant and M.C. Birse, hep-ph/0007340.
22. H. Kleinert and B. van den Bossche, Phys. Lett. B **474**, 336 (2000); hep-ph/9908284.
23. W. Florkowski and W. Broniowski, Phys. Lett. B **386**, 62 (1996).
24. S. Klimt, M. Lutz, U. Vogl, and W. Weise, Nucl. Phys. A **516**, 429 (1990).
25. L. M. Luttinger and J. C. Ward, Phys. Rev. **118**, 1417 (1960).
26. G. Baym and L.P. Kadanoff, Phys. Rev. **124**, 287 (1961); G. Baym, Phys. Rev. **127**, 1391 (1962).
27. G. Ripka, *Quarks Bound by Chiral Fields* (Clarendon Press, Oxford, 1997).
28. E. Babaev, hep-ph/0006087; Phys. Rev. D **62**, 074020 (2000).
29. P. Nozieres and S. Schmitt-Rink, J. Low Temp. Phys. **59**, 195 (1985).
30. C. A. R. Sá de Melo, M. Randeria, and J. R. Engelbrecht, Phys. Rev. Lett. **71**, 3202 (1993).
31. G. Ripka, hep-ph/0003201; (to be published in Nucl. Phys. A); hep-ph/0007250.
32. H. G. Dosch and S. Narison, Phys. Lett. B **417**, 173 (1998).
33. L. Giusti, F. Rapuano, M. Talevi, and A. Vladikas, Nucl. Phys. B **538**, 249 (1999).
34. M. Lutz and W. Weise, Nucl. Phys. A **518**, 156 (1990).
35. L. M. Barkov *et al.*, Nucl. Phys. B **256**, 365 (1985); S. R. Amendolia *et al.*, Phys. Lett. B **138B**, 454 (1984).
36. C. D. Frogatt and J. L. Petersen, Nucl. Phys. B **129**, 89 (1977).
37. S. R. Amendolia *et al.*, Nucl. Phys. B **277**, 168 (1986).
38. D. Davesne, Y. J. Zhang, and G. Chanfray, nucl-th/9909032.
39. V. Bernard, U.-G. Meißner, A. H. Blin, and B. Hiller, Phys. Lett. B **253**, 443 (1991).
40. J. Gasser and H. Leutwyler, Phys. Lett. B **184**, 83 (1987); Phys. Lett. B **188**, 477 (1987); Nucl. Phys. B **307**, 763 (1988).
41. A. L. Fetter and J. D. Walecka, *Quantum Theory of Many-Particle Systems* (McGraw-Hill, New York, 1971).
42. F. Karsch and E. Laermann, Phys. Rev. D **50**, 6954 (1994); S. Digal, E. Laermann, and H. Satz, hep-ph/0007175.
43. R. D. Pisarski and F. Wilczek, Phys. Rev. D **29**, 338 (1984).
44. A. Kocič and J. Kogut, Phys. Rev. Lett. **74**, 3109 (1995); Nucl. Phys. B **455**, 229 (1995).
45. G. Passarino and M. Veltman, Nucl. Phys. B **160**, 151 (1979).
46. G. J. van Oldenborgh and J. A. M. Vermaseren, Z. Phys. C **46**, 425 (1990).
47. G. 't Hooft and M. Veltman, Nucl. Phys. B **153**, 365 (1979).
48. C. Itzykson and J.-B. Zuber, *Quantum Field Theory* (McGraw-Hill, New York, 1980).

Physics of Atomic Nuclei, Vol. 64, No. 4, 2001, pp. 727–752. Translated from Yadernaya Fizika, Vol. 64, No. 4, 2001, pp. 786–812.

90th ANNIVERSARY OF A.B. MIGDAL'S BIRTHDAY
ELEMENTARY PARTICLES AND FIELDS

Transition Form Factors and Probabilities of the Semileptonic Decays of *B* and *D* Mesons within Covariant Light-Front Dynamics

L. A. Kondratyuk and D. V. Tchekin[1)]

Institute of Theoretical and Experimental Physics, Bol'shaya Cheremushkinskaya ul. 25, Moscow, 117259 Russia

Received July 28, 2000

Abstract—Electroweak form factors for the decays of heavy *B* and *D* mesons are considered within the covariant formulation of light-front dynamics. With the aid of this approach, it is possible to separate the physical and unphysical contributions to the form factors. An analytic expression is obtained for gluon corrections to the electroweak vertex of the vector and the vector-axial quark current, and it is shown that, for constructing a quantitative description of available experimental data, it is important to take into account such corrections to the decay widths of heavy hadrons. The effect of contact interaction on the transition form factors is analyzed, and the importance of taking into account contact interaction for $0^- \longrightarrow 1^-$ transitions is demonstrated numerically. The elements $|V_{bc}|$, $|V_{bu}|$, $|V_{cs}|$, and $|V_{cd}|$ of the Cabibbo–Kobayashi–Maskawa matrix are determined from an analysis of the entire body of data on $0^- \longrightarrow 0^-$ and $0^- \longrightarrow 1^-$ semileptonic decays. Within the experimental errors, the results obtained in this way are intrinsically consistent and comply with world-averaged data. © *2001 MAIK "Nauka/Interperiodica".*

1. INTRODUCTION

The semileptonic decays of heavy *B* and *D* mesons furnish important information about the elements $|V_{bu}|$, $|V_{bc}|$, $|V_{cs}|$, and $|V_{cd}|$ of the Cabibbo–Kobayashi–Maskawa (CKM) matrix. Since the differential and partial widths with respect to hadronic decays depend both on the CKM-matrix elements and on the transition form factors, theoretical models that describe adequately the soft (nonperturbative) interaction of quarks within hadrons are necessary for extracting, from experimental data, reliable information about the quark transition amplitude, which is proportional to the CKM-matrix elements. Theoretical approaches that are used to describe the semileptonic decays of hadrons employ, in addition to QCD lattice calculations, calculations based on QCD sum rules, calculations within various effective theories, and calculations relying on relativistic quark models. Weak-decay form factors calculated on the basis of lattice QCD make it possible to confirm or disprove one idea or another of the internal structure of hadrons and to test relevant models. Unfortunately, present-day lattice calculations involve significant uncertainties. Therefore, quark models, whose applicability range is comparatively wide, play an important role in such investigations.

That light-front dynamics (LFD) is one of the viable approaches to describing quark bound states is suggested by many arguments. In relation to various quark models used to treat quark bound states, the LFD approach stands out for a number of reasons. For an arbitrary system quantized on a hypersurface specified by the light-front equation $\omega x = \sigma$, there always exists a kinematical subgroup of the total group of Poincaré transformations. It follows that, within the LFD approach, constructing a state characterized by a specific value of the total 4-momentum reduces to solving a purely kinematical problem. At the same time, the diagram technique developed within the LFD approach is essentially an analog of chronological perturbation theory and makes it possible to describe correctly relativistic spin effects. It should also be recalled that, within this approach, vacuum diagrams that correspond to the production of a few particles from a vacuum are forbidden from the outset.

In this connection, it is highly desirable to apply the LFD approach to two and three-quark systems and to perform a detailed analysis of heavy-hadron decays within this scheme. This is the reason why the LFD approach has recently been used in many studies to analyze inclusive and exclusive hadronic transitions (see [1–17]).

Within this approach, *B*-meson and Λ_b-hyperon decays associated with transitions of a heavy quark into another heavy quark were considered in our previous studies [18, 19]. Here, we analyze *B*- and *D*-meson decays caused by a transition of a heavy quark into a light one. Of particular interest in this connection are the transitions $B \longrightarrow \pi l\nu_l$ and $B \longrightarrow \rho l\nu_l$, which make it possible to explore the CKM-matrix element V_{bu}, which has not yet received adequate study—at present,

[1)] Institute of Theoretical and Experimental Physics, Bol'shaya Cheremushkinskaya ul. 25, Moscow, 117259 Russia, and Moscow Institute for Physics and Technology, Institutskiĭ pr. 9, Dolgoprudnyĭ, Moscow oblast, 141700 Russia.

measurement of this matrix element is an important problem in heavy-quark physics. Yet another novel element in the present analysis is that we take into account contact interaction, which inevitably arises in LFD, and gluon corrections (Sudakov form factor) to the vector and the axial-vector current.

The ensuing exposition is organized as follows. In Section 2, we give an account of the formalism for constructing matrix elements of the vector and the axial-vector current within the covariant formulation of LFD, taking into account contact interaction. In Section 3, we discuss gluon corrections. In Section 4, we present our basic results and compare them with available data. The conclusions are summarized in Section 5.

2. MATRIX ELEMENTS OF THE VECTOR AND THE AXIAL-VECTOR CURRENT IN LIGHT-FRONT DYNAMICS

Following the covariant formulation of LFD [20], we introduce the required definitions. Within the LFD approach, vectors that characterize the states of the system are defined on the hypersurface specified by the equations $\omega x = \sigma$ and $\omega^2 = 0$. The conventional choice of the 4-vector ω_μ is

$$\omega_\mu = (\omega_0, \omega_x, \omega_y, \omega_z) = (1, 0, 0, 1), \qquad \omega_\pm = \omega_0 \pm \omega_z. \tag{1}$$

The equation of the hypersurface is then written as $x_+ =$ const. The evolution of the system along the time axis on the light front [x_+ for the conventional choice of ω_μ according to (1)] is controlled by the Hamilton equation on the light front. Transformations of the Poincaré group that do not change the orientation of the light-front hypersurface and which map this hypersurface onto itself are kinematical transformations—namely, the transformation properties of a state vector under kinematical transformations do not depend on interaction and do not require knowing the Hamiltonian of the system. The generators of the transformations that do not change the orientation of the hypersurface $\omega x = \sigma$ are kinematical transformations forming a subgroup of the Poincaré group. Owing to this, a system having an arbitrary 4-momentum can be transformed into a system having a preset 4-momentum by using only kinematical transformations.

The diagram technique on the light front (see [20] and references therein) is similar to old chronological perturbation theory, the only distinction being that the variable $\tau = t + z$, an analog of time on the light front, appears to be the evolution parameter along the time axis τ. In LFD, all particles are on their mass shells, the momentum conservation law being violated for the minus component $P_- = P_0 - P_3$ (for the conventional choice of ω_μ)—more generally, for the 4-momentum component proportional to ω_μ.

In the LFD diagram technique, vectors characterizing states of an arbitrary bound system can be expanded in a series in Fock components with an increasing number of particles, $|H\rangle = \sum_i \phi^{(i)} |q^{(1)} \ldots q^{(i)}\rangle$. In this expression, the index i labels the Fock component involving i particles, $\phi^{(i)}$ being the wave function of the ith state. The physical matrix elements of the current are obtained by summing the matrix elements of the current between the individual Fock states of the expansion. We assume that the main contribution to the transitions in question comes from the sector featuring the minimum number of particles. Therefore, mesons will be considered as quark–antiquark bound states.

For a two-particle state that is pure in 4-momentum and in mass, $\{P_\mu, M\}$, and which is formed by a quark q_1 and an antiquark $\bar{q}$, their 4-momenta and masses being $\{p_{1\mu}, m_1\}$ and $\{p_{2\mu}, m_2\}$, respectively, the 4-momentum conservation law can be written as

$$\mathcal{P}_\mu \equiv p_{1\mu} + p_{2\mu} = P_\mu + \omega_\mu \tau. \tag{2}$$

Since the spatial component of 4-momentum is not conserved, the rest frame of the composite particle does not coincide with the c.m. frame of the $(p_1 p_2)$ state, where $\boldsymbol{\mathcal{P}} = 0$: at $\boldsymbol{\mathcal{P}} = 0$, the spatial component of the 4-momentum does not vanish—that is, $\mathbf{P} \neq 0$.

Within the LFD approach, the $(q_1 q) \longrightarrow (q_2 q)$ transition amplitude is represented as the sum of the contributions from the one-body current (Fig. 1) and the contributions of diagrams corresponding to contact interaction in LFD (Figs. 2–4).

According to general rules of diagram technique (for details, see [20]), the contribution of the one-body current (Fig. 1) for a transition between states characterized by specific values of momentum and spin (we denote these quantum numbers by P_1 and j_1 for the initial state and by P_2 and j_2 for the final state) has the form

$$J_\mu^{\mathrm{OBC}} = \int \theta(\omega(P_1 - p))\delta((P_1 + \omega\tau_1 - p)^2 - m_1^2) \times \theta(\omega(P_2 - p))\delta((P_2 + \omega\tau_2 - p)^2 - m_2^2)\theta(\omega p) \times \delta(p^2 - m^2)\mathrm{tr}[\Gamma_2^{j_2}\Gamma_\mu\Gamma_1^{j_1}]\frac{d\tau_1}{(\tau_1 - i0)}\frac{d\tau_2}{(\tau_2 - i0)}\frac{d^4p}{(2\pi)^4}, \tag{3}$$

where $\Gamma_{1,2}^{j_i} = \Gamma_{1,2}^{j_i}(p_{1,2}, p, P, \omega\tau_{1,2})$ are vertex functions that are related to the wave functions by the equations [20]

$$\Phi^{j_i}(p_1, p_2, P, \omega\tau) = \frac{\Gamma^{j_i}(p_1, p_2, P, \omega\tau)}{(p_1 + p_2)^2 - M^2} \tag{4}$$

and $\Gamma_\mu = \bar{u}(p_2)\{\gamma_\mu, \gamma_\mu\gamma_5\}u(p_1)$ is the quark vertex for the one-body current. Integration with respect to τ_1 and τ_2 in expression (3) corresponds to spurions describing 4-momentum nonconservation in the intermediate state (see Fig. 1).

Integration with respect to τ_1, τ_2, and k_0 is performed with the aid of delta functions. The result is (recall that the abbreviation OBC in the superscript indicated that we are dealing here with the one-body-current contribution)

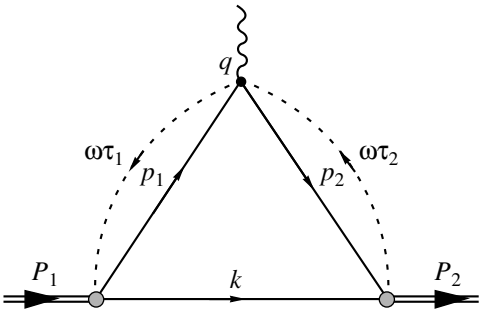

Fig. 1. One-body current in light-front dynamics.

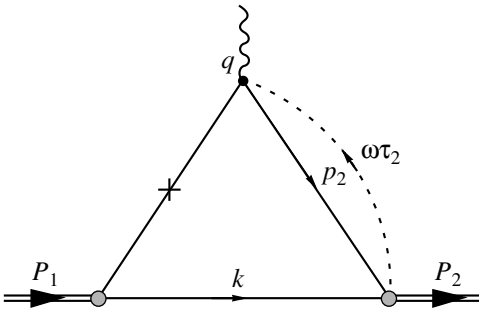

Fig. 2. Contact interaction of the m_1 particle.

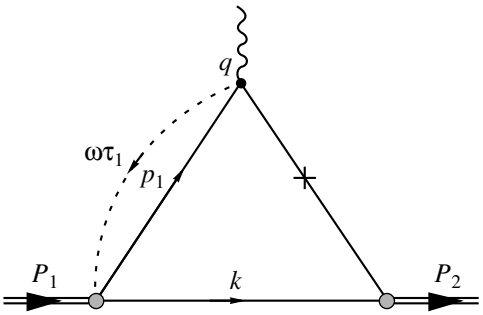

Fig. 3. Contact interaction of the m_2 particle.

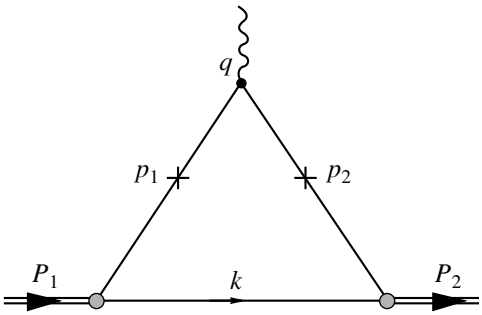

Fig. 4. Double contact interaction.

$$J_\mu^{(\mathrm{OBC})} = \int \frac{\mathrm{tr}[(\hat{p}_2 + \hat{\omega}\tau_2^* + m_2)\Gamma_\mu(\hat{p}_1 + \hat{\omega}\tau_1^* + m_1)\phi_1^{(J_1)}(-\hat{p} + m)\phi_2^{(J_2)*}]}{(1-x)(1-x')(M_1^2 - M_{10}^2)(M_2^2 - M_{20}^2)}\theta(\omega(P_1 - p_1))\frac{d^3\mathbf{p}}{2(2\pi)^3\varepsilon_\mathbf{p}}$$
$$= \frac{1}{2(2\pi)^3}\int_0^y \frac{dx}{x(1-x)(1-x')}\int d^2\mathbf{k}_\perp \mathrm{tr}[(\hat{p}_2 + \hat{\omega}\tau_2^* + m_2)\Gamma_\mu(\hat{p}_1 + \hat{\omega}\tau_1^* + m_1)\phi_1^{(J_1)}(-\hat{p} + m)\phi_2^{(J_2)*}], \quad (5)$$

where

$$x = \frac{p_+}{P_{1+}}, \quad x' = \frac{p_+}{P_{2+}}, \quad y = \frac{P_{2+}}{P_{1+}},$$
$$p_+ = xP_{1+} \quad \mathbf{p}_\perp = x\mathbf{P}_{1\perp} + \mathbf{k}_\perp,$$
$$\mathbf{p}_{1\perp} = (1-x)\mathbf{P}_{1\perp} - \mathbf{k}_\perp, \quad \mathbf{p}_{2\perp} = (1-x')\mathbf{P}_{2\perp} - \mathbf{k}'_\perp, \quad (6)$$
$$M_{10}^2 = \frac{m^2 + \mathbf{k}_\perp^2}{x} + \frac{m_1^2 + \mathbf{k}_\perp^2}{1-x},$$
$$M_{20}^2 = \frac{m^2 + \mathbf{k}_\perp'^2}{x'} + \frac{m_2^2 + \mathbf{k}_\perp'^2}{1-x'},$$
$$\tau_1^* = [m_1^2 - (P_1 - p)^2]/(2\omega(P_1 - p)),$$
$$\tau_2^* = [m_2^2 - (P_2 - p)^2]/(2\omega(P_2 - p)). \quad (7)$$

In transforming the integral in Eq. (5), we have made use of the relations

$$\frac{d^3\mathbf{p}}{\varepsilon_\mathbf{p}} = \frac{dp_+}{p_+}d^2\mathbf{p}_\perp = \frac{dx}{x}d^2\mathbf{p}_\perp = \frac{dx}{x}d^2\mathbf{k}_\perp. \quad (8)$$

Having constrained the integration domain by the inequality $0 \le x \le y$ (or $0 \le p_+ \le P_{2+}$), we took into account the so-called parton contribution. The contribution from the region $P_{2+} < p_+ < P_{1+}$ corresponds to that configuration of particles in the intermediate state in which the valence quark in the final state is on the mass shell. The spacetime pattern corresponding to this configuration can be represented as follows: a pair $q_2\bar{q}_2$ is produced from a vacuum, whereupon the quark q_2 recombines with the spectator antiquark $\bar{q}$, forming the final meson; the remaining pair $q_1\bar{q}_2$ annihilates into W^-. This configuration can be described only if one takes into account the relevant components of the vertex function, which are not considered here.

In Eq. (5), the form factor is expressed in terms of the wave functions dependent on 3-momentum. From the point of view of the instantaneous form of dynamics, these functions are specified in the infinite-momentum frame. We will use the approximation where they are independent of the direction in which a transition to the infinite-momentum frame occurs. In general, such a dependence arises in LFD when one is dealing with

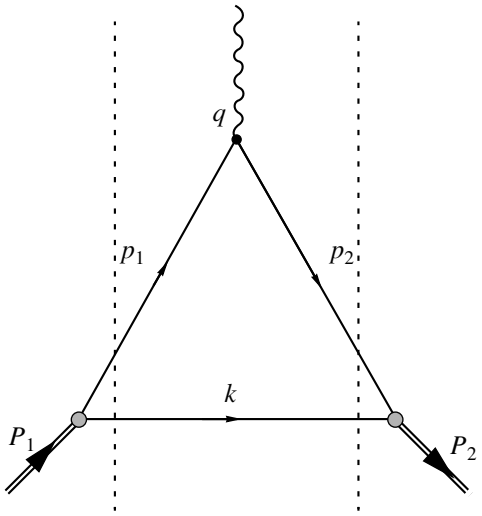

Fig. 5. Parton contribution to the triangle diagram.

particles having a nonzero spin. It is important to note that the problem of two particles treated on the basis of field theory always involves relative time. A reduction to an expression of the type in (5) is equivalent to eliminating the relative time in LFD.

The problem of eliminating the relative time in the theory of a QCD string with quarks was discussed in [22]. In principle, this theory provides a basis for constructing hadron wave functions and diagonal and off-diagonal form factors in the QCD string model. In what is concerned with constructing wave functions, our approach is equivalent to the use of the relativistic-quark-model limit, which is obtained in string dynamics at $l = 0$ {see Eq. (73) in [22a]}. Formally, expression (5) then involves the relativistic-quark wave functions taken in the infinite-momentum frame. However, these wave functions depend on the relative momentum; therefore, it may seem, at first glance, that they are taken in the rest frame, but, in fact, this is not so. The example of a relativistic oscillator on the light cone reveals (see [23]) that the wave functions defined in the infinite-momentum frame cannot be obtained directly by determining the eigenfunctions of the Hamiltonian on the light cone, since the angular-momentum operators depend on interaction in this representation.

Within LFD, the wave function $\Phi^{J=0}_{\sigma_1\sigma_2}$ of the $J = 0$ state ($\{p_1, m_1\}$, $\{p_2, m_2\}$) is generally parametrized in terms of two scalar functions:

$$\Phi^{J=0}_{\sigma_1\sigma_2} = \bar{u}(p_1, \sigma_1)[\phi^{(J=1)}]v(p_2, \sigma_2),$$
$$\phi^{(J=1)} = \gamma_5 h_1 + \gamma_5 \hat{\omega} h_2. \tag{9}$$

In the quark–antiquark c.m. frame, this expression can be represented in the form

$$\Psi^{J=0}_{\sigma_1\sigma_2} = \rho(\mathbf{k}^2)\chi^*_1(\sigma_1)[\psi_1 + \left(\frac{\mathbf{n}\cdot\mathbf{k}}{k}\,\frac{(m_1-m_2)}{M_0} + i\frac{\boldsymbol{\sigma}\cdot[\mathbf{k}\times\mathbf{n}]}{k}\right)\psi_2\Big]\chi_2(\sigma_2), \tag{10}$$

where $\rho(\mathbf{k}^2)$ is given by

$$\rho = \frac{\varepsilon_1\varepsilon_2}{\varepsilon_1+\varepsilon_2} = \frac{M_0}{4}\left(1 - \frac{(m_1-m_2)^2}{M_0^4}\right), \tag{11}$$

with $\varepsilon_i = \sqrt{\mathbf{p}^2 + m_i^2}$.

Only the functions h_1 and ψ_1 survive in the nonrelativistic approximation. They describe a $q\bar{q}$ bound state in the S wave. The functions h_2 and ψ_2 have no nonrelativistic analogs. Their origin is associated with the fact that, within the covariant LFD formalism, two invariant functions h_1 and h_2 must be introduced in order to construct a unified description of the $0^- \longrightarrow (1/2)^+(1/2)^-$ bound state (Fig. 5) and the $(1/2)^- \longrightarrow 0^-(1/2)^+$ fragmentation (Fig. 6). Taking into account relativistic effects in a minimal way, we will henceforth disregard the functions h_2 and ψ_2 and the dependence of the functions h_1 and ψ_1 on the direction of the unit vector $\mathbf{n}$ specifying a transition to the infinite-momentum frame. We then have

$$h_1 = \frac{\sqrt{\varepsilon_1+m_1}\sqrt{\varepsilon_2+m_2}}{(\varepsilon_1+m_1)(\varepsilon_2+m_2)+\mathbf{k}^2}\rho\psi_S = \frac{1}{\sqrt{M_0^2-(m_1-m_2)^2}}\rho\psi_S, \tag{12}$$

where ψ_S is the wave function of the S-wave bound state of the $q\bar{q}$ system.

Let us now consider the case of $J = 1$. Within LFD, the wave function $\Phi^{J=1\lambda}_{\sigma_1\sigma_2}$ of the $J = 1$ state formed by two particles $\left\{j_{1,2} = \frac{1}{2},\ p_{1,2},\ m_{1,2}\right\}$ can be parametrized as

$$\Phi^{J=1\lambda}_{\sigma_1\sigma_2}(p_1, p_2, P, \omega\tau) = \bar{u}(p_1, \sigma_1)\phi^{(J=1)}_\mu(p_1, p_2)v(p_2, \sigma_2)\epsilon^\lambda_\mu(P, M), \tag{13}$$

where we generally have six independent terms:

$$\phi^{(J=1)}_\mu = \tilde{f}_1\gamma_\mu + \tilde{f}_2(p_1-p_2)_\mu + \tilde{f}_3\frac{\omega_\mu}{\omega P} + \tilde{f}_4\frac{\hat{\omega}}{\omega P}(p_1-p_2)_\mu + \tilde{f}_5\frac{i}{\omega P}\gamma_5\epsilon_{\mu\nu\lambda\sigma}p_{1\nu}p_{2\lambda}\omega_\sigma + \tilde{f}_6\frac{\omega_\mu\hat{\omega}}{(\omega P)^2}. \tag{14}$$

Here, $\epsilon_\mu(P, M)$ is the polarization 4-vector in the spin-1 state.

In the quark–antiquark c.m. frame, the wave function (13) can be parametrized in terms of six scalar functions appearing as coefficients of independent spin structures composed from the vectors **k** and **n**:

$$\Psi^{J=1\lambda}_{\sigma_1\sigma_2}(p_1, p_2, P, \omega\tau)$$

$$= \rho(\mathbf{k}^2)\chi_1^*(\sigma_1)[\psi_{ij}(\mathbf{k}, \mathbf{n})]\sigma_i\chi_2(\sigma_2)\epsilon_j^\lambda,$$

$$\psi_{ij}(\mathbf{k}, \mathbf{n}) = \psi_1\delta_{ij} + \psi_2\left(\delta_{ij} - 3\frac{k_ik_j}{\mathbf{k}^2}\right) + \psi_3 n_i n_j \quad (15)$$

$$+ \psi_4\frac{1}{2k}(3n_ik_j + 3k_in_j - 2(\mathbf{k}\cdot\mathbf{n})\delta_{ij})$$

$$+ \psi_5\frac{1}{k}i\varepsilon_{jlm}k_ln_m\sigma_i + \psi_6\frac{1}{k}\varepsilon_{ijl}[\mathbf{k}\times\mathbf{n}]_l.$$

Here, ϵ_j^λ is the polarization 3-vector in the c.m. frame. In general, $\psi_1, \psi_2, ..., \psi_6$ depend on the scalars $\mathbf{k}^2$ and $\mathbf{k}\cdot\mathbf{n}$; that is, $\psi_n = \psi_n(\mathbf{k}^2, \mathbf{k}\cdot\mathbf{n})$. The functions $\tilde{f}_3, ..., \tilde{f}_6$ and $\psi_3, ..., \psi_6$ have no nonrelativistic analogs. They are associated with the covariant description of the $(1/2)^- \longrightarrow 1^+(1/2)^-$ fragmentation process (Fig. 6). In just the same way as in the case of zero spin ($J = 0$), we disregard these functions. The functions $\tilde{f}_1$ and $\tilde{f}_2$ or ψ_1 and ψ_2 correspond to the *S*- and *D*-wave functions of the bound quark–antiquark state. In [18], we took into account *S*- and *D*-wave contributions. The *D* wave was introduced in order to improve the description of the decay $B \longrightarrow Dl\nu_l$. In [18], we neglected, however, the contact contributions, which are of importance, as will be shown here—their inclusion makes it possible to describe experimental data without taking into account the *D* wave. If we consider only the *S* wave, the $1^- \longrightarrow (1/2)^+(1/2)^-$ wave function in the c.m. frame has the form

$$\Phi^{J=1\lambda}_{\sigma_1\sigma_2} = \bar{u}(p_1, \sigma_1)\frac{\sqrt{\varepsilon_1 + m_1}\sqrt{\varepsilon_2 + m_2}}{(\varepsilon_1 + m_1)(\varepsilon_2 + m_2) + \mathbf{k}^2} \quad (16)$$

$$\times\rho\left[\gamma_j - \frac{(p_1 - p_2)_j}{(\varepsilon_1 + \varepsilon_2 + m_1 + m_2)}\right]v(p_2, \sigma_2)\tilde{\epsilon}_j^\lambda\psi_S.$$

As in the case of zero spin, we neglect the dependence of ψ_S on the vector **n**.

According to the LFD diagram technique, the one-body hadronic current $J_\mu^{(\mathrm{OBC})}$ must be supplemented with the contributions corresponding to the contact interaction of p_1 and p_2 particles with the weak-current vertex. Each of the contact contributions is associated with a diagram where the quark lines contactly interact with the current $q_1\Gamma_\mu\bar{q}_2$ (see Figs. 2, 3). A crossed quark line then corresponds to the quantity $-\frac{\hat{\omega}}{2\omega P}$, where *P* is the sum of the momenta flowing into the vertex (for more details, see [20]).

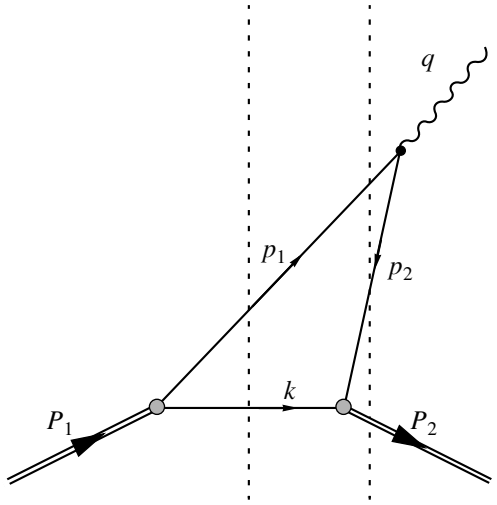

Fig. 6. Fragmentation contribution to the triangle diagram.

Exact expressions for the contact terms can be obtained if the vertex functions in (3) are taken to be constant. In this approximation, the sum of the three diagrams in Figs. 1–3 has the form

$$J_\mu = J_\mu^{(\mathrm{OBC})} + J_\mu^{\mathrm{c.t.1}} + J_\mu^{\mathrm{c.t.2}}$$

$$= \int\frac{\mathrm{tr}[(\hat{p}_2 + m_2)\Gamma_\mu(\hat{p}_1 + m_1)\phi_1^{(J_1)}(-\hat{p} + m)\phi_2^{(J_2)*}]}{(1-x)(1-x')(M_1^2 - M_{10}^2)(M_2^2 - M_{20}^2)}$$

$$\times\theta(\omega(P_1 - p_1))\frac{d^3\mathbf{p}}{2(2\pi)^3\varepsilon_\mathbf{p}} \quad (17)$$

$$= \frac{1}{2(2\pi)^3}\int_0^y\frac{dx}{x(1-x)(1-x')}\int d^2\mathbf{k}_\perp$$

$$\times\mathrm{tr}[(\hat{p}_2 + m_2)\Gamma_\mu(\hat{p}_1 + m_1)\phi_1^{(J_1)}(-\hat{p} + m)\phi_2^{(J_2)*}],$$

where

$$p_{1\mu} = P_{1\mu} - p_\mu, \quad p_{2\mu} = P_{2\mu} - p_\mu. \quad (18)$$

The double contact interaction corresponding to the crossed lines of the two quarks p_1 and p_2 appears to be proportional to ω_μ and does not contribute to the components J_+ and $\mathbf{J}_\perp$ of the current. Expression (17) will be used below to calculate the spin structure of the matrix elements of the current.

Thus, the contact interaction has no effect on the vertex functions in the most general parametrization given by Eqs. (13) and (14), but, according to (18), it changes the momenta of the m_1 and m_2 particles involved in the spin structure of expression (5). Gener-

ally speaking, this conclusion is valid only for LFD diagrams where vertex functions do not depend on the variables of integration. However, even this approximate inclusion of the contact interaction affects significantly the results of the calculations for the $0^- \longrightarrow 1^-$ off-diagonal transition (see Section 5).

3. SELF-CONSISTENCY OF THE MODEL AND DETERMINATION OF PHYSICAL FORM FACTORS

An exact calculation of the form factors in field theory—in particular, in LFD treated as a field theory on the light-front hypersurface—must lead to covariant expressions for current matrix elements. In the approximate scheme where we restrict ourselves to the contributions of the sector featuring a fixed number of particles, the matrix elements of the current operator appear to be dependent on the orientation of the vector ω.

This problem was discussed in [18, 19], where a regular method for separating physical form factors from unphysical structures was considered. In the majority of studies, this problem is usually sidestepped by indicating a reliable choice of matrix elements. As a rule, quantities calculated with the current component J_+, which possesses "good" properties, are taken for such matrix elements. However, the number of matrix elements corresponding to this good current component is usually insufficient for determining all physical form factors for a given transition.

In the covariant formulation of LFD, physical form factors can be self-consistently determined by eliminating the unphysical ω_μ dependence of the transition form factors. To illustrate the general approach to the covariant LFD parametrization, we first consider $0^- \longrightarrow 0^-$ transitions.

In the matrix elements of the current, we introduce, apart from the vectors $P_{1\mu}$ and $P_{2\mu}$, an explicit ω_μ dependence; that is,

$$\begin{aligned} J_\mu^{(\mathrm{L.F.})} &= F_1(q^2, y)(P_1 + P_2)_\mu \\ &+ (F_0(q^2, y) - F_1(q^2, y))\frac{M_1^2 - M_2^2}{q^2} q_\mu \\ &+ B_0(q^2, y)\frac{\omega_\mu}{\omega(P_1 + P_2)}, \end{aligned} \tag{19}$$

where $y = (P_2\omega)/(P_1\omega)$, F_0 and F_1 are physical form factors; B_0 is a form factor that parametrizes the unphysical contribution; and superscript L.F. explicitly indicates that the left-hand side was calculated approximately within the LFD approach. For the standard choice of ω_μ, we have $y = P_{2+}/P_{1+}$. In (19), we have considered that, within this approach, form factors can involve ω only in the form $\omega_\mu/(P_i\omega)$, because the calculations on the light front depend only on the orientation of the vector $\mathbf{n} = \boldsymbol{\omega}/\omega_0$, undergoing no changes upon the multiplication of ω_μ by an arbitrary integer. As a matter of fact, the ω dependence of the matrix elements can be taken into account through the quantity y. All the remaining dimensionless combinations of ω_μ can be reduced to this expression. Thus, the form factors depend not only on q^2 but also on y, which is reflected in the form of (19).

In the two-body approximation, the matrix element of the $0^- \longrightarrow 0^-$ transition current can be represented in the form

$$\begin{aligned} \langle P_2|J_\mu^{\mathrm{LFD}}|P_1\rangle &= \frac{1}{2(2\pi)^3}\int_0^y \frac{dx}{x(1-x)(1-x')} \\ &\times \int d^2\mathbf{k}_\perp h_1^{(i)}(x, \mathbf{k}^2) h_1^{(f)}(x', \mathbf{k}'^2) \\ &\times \mathrm{tr}[(\hat{p}_2 + m_2)\gamma_\mu(1-\gamma_5)(\hat{p}_1 + m_1)\gamma_5(-\hat{p} + m)\gamma_5], \end{aligned} \tag{20}$$

where, in accord with the statements of Section 2, $p_{(i)\mu} = P_{(i)\mu} - p_\mu$ and $p_i^2 \neq m_i^2$. If ω is chosen in a standard way, the unphysical form factor does not contribute to the good and the transverse component of the matrix elements of the current. In order to determine two physical form factors, we must therefore consider the matrix elements of J_+ and $\mathbf{J}_\perp$.

We will use a reference frame where the momenta of the initial and the final meson have small components along the x axis. In this configuration, the square of the 4-momentum transfer is given by

$$q^2 = (1-y)\left(M_1^2 - \frac{M_2^2}{y}\right) - y\left(\mathbf{P}_{1\perp} - \frac{1}{y}\mathbf{P}_{2\perp}\right)^2. \tag{21}$$

If $\mathbf{P}_\perp$ is chosen to be sufficiently small, almost all kinematically possible values in the region $0 \le q^2 \le q^2_{\max} = (M_1 - M_2)^2$ can be realized. By using the current components J_+ and $\mathbf{J}_\perp$, we find that the form factors F_1 and F_2 satisfy the set of two equations

$$\begin{aligned} F_1(P_{1+} + P_{2+}) + (F_0 - F_1)\frac{M_1^2 - M_2^2}{q^2} q_+ &= J_+^{(\mathrm{L.F.})}, \\ F_1(\mathbf{P}_{1\perp} + \mathbf{P}_{2\perp}) + (F_0 - F_1)\frac{M_1^2 - M_2^2}{q^2}\mathbf{q}_\perp &= \mathbf{J}_\perp^{(\mathrm{L.F.})}. \end{aligned} \tag{22}$$

In order to take into account the Sudakov form factor (see below), the integrand on the right-hand side of (20) [it determines the matrix elements of the current in Eq. (22)] must be multiplied by $S(q^2, x, \mathbf{k}_\perp)$,

$$\int d^2\mathbf{k}_\perp dx I(x, \mathbf{k}_\perp) \longrightarrow \int d^2\mathbf{k}_\perp dx I(x, \mathbf{k}_\perp) S(q^2, x, \mathbf{k}_\perp). \tag{23}$$

The dependence of the Sudakov form factor on x and $\mathbf{k}_\perp$, which are the variables of integration in the relevant diagram, is a consequence of the fact that particles in the intermediate state (quarks in our case) are on the

mass shell. In this case, the 4-momentum is not conserved in the weak-current vertex, so that the quantity $\tilde{q}^2$ in the timelike region is not equal to the physical momentum transfer squared, $(p_{q_1} - p_{q_2})^2 \equiv \tilde{q}^2 \neq q^2 = (P_1 - P_2)^2$.

In the set of Eqs. (22), P_+ is a parameter that is canceled in each of the equalities and can be chosen arbitrarily. In the case of $\mathbf{P}_{1\perp} = \mathbf{P}_{2\perp} = \mathbf{P}_\perp$, this set of equations is further simplified to become

$$F_1(1+y) + (F_0 - F_1)\frac{M_1^2 - M_2^2}{q^2}(1-y) = \frac{J_+^{(\mathrm{L.F.})}}{P_+},$$
$$2F_1 = \frac{J_\perp^{(\mathrm{L.F.})}}{P_\perp}. \tag{24}$$

At $y = 1$—we then have $q^2 = 0$ ($P_\perp \longrightarrow 0$)—the left-hand side of the set of equations in question becomes degenerate; on the right-hand side, the matrix elements of the current components J_+ and $J_\perp$ concurrently become proportional to each other, apart from the factors P_+ and $\mathbf{P}_\perp$. Formulas (24) express the physical $0^- \longrightarrow 0^-$ transition form factors F_0 and F_1 in terms of the matrix elements of the good and the transverse current components as given by Eq. (20).

For the $0^- \longrightarrow 1^-$ transition, the general LFD expression for the matrix element of the current has the more complicated form

$$\langle P_2(\epsilon)|J_\mu^{\mathrm{LFD}}|P_1\rangle = \frac{1}{2(2\pi)^3}\int_0^y \frac{dx}{x(1-x)(1-x')}$$
$$\times \int d^2\mathbf{k}_\perp f_1^{(i)}(x,\mathbf{k}^2) f_2^{(f)}(x',\mathbf{k}'^2)$$
$$\times \mathrm{tr}\Big[\gamma_\mu(1-\gamma_5)(\hat{p}_1 + m_1)\gamma_5(-\hat{p} + m)$$
$$\times\left(\gamma_\nu - \frac{(p_2 - p)_\nu}{M_{20} + m_2 + m}\right)\tilde{\epsilon}_\nu^*(\hat{p}_2 + m_2)\Big], \tag{25}$$

where $\tilde{\epsilon}$ is the polarization 4-vector specified in the c.m. frame of the constituent quarks; in an arbitrary reference frame, it is given by

$$\tilde{\epsilon}_\mu^{J_3=\pm1}(P_\mu) = \left[0, \boldsymbol{\epsilon}_\perp(\pm1), \frac{2}{P_+}\boldsymbol{\epsilon}_\perp\mathbf{P}_\perp\right],$$
$$\tilde{\epsilon}_\mu^{J_3=0}(P_\mu) = \frac{1}{M_0}\left[P_+, \mathbf{P}_\perp, -\frac{M_{0+}P_\perp^2}{P_+}\right], \tag{26}$$
$$\boldsymbol{\epsilon}_\perp(\pm1) = \mp\left(\frac{1}{\sqrt{2}}, \pm\frac{i}{\sqrt{2}}\right).$$

The momenta $p_{1\mu}$ and $p_{2\mu}$ in (25) are defined as $p_{1\mu} = P_{1\mu} - p_\mu$ and $p_{2\mu} = P_{2\mu} - p_\mu$. The functions $f_1^{(i)}$ and $f_2^{(f)}$ correspond to the *S*-wave states of the initial and the final meson.

The spin structures of the contributions from the vector and the axial-vector current to the trace tr[…] on the right-hand side of (25) are given by

$$\mathrm{tr}[\,]_A = \mathrm{tr}\Big[\gamma_\mu\gamma_5(\hat{p}_1 + m_1)\gamma_5(-\hat{p} + m)$$
$$\times\left(\gamma_\nu - \frac{(p_2 - p)_\nu}{M_{20} + m_2 + m}\right)(\hat{p}_2 + m_2)\Big]\epsilon_\nu^*$$
$$= [4m_2(p_{1\mu}p_\nu - p_\mu p_{1\nu}) - m_1(p_\mu p_{2\nu} + p_{2\mu}p_\nu)$$
$$- m(p_{1\mu}p_{2\nu} + p_{2\mu}p_{1\nu}) + g_{\mu\nu}(m_2 pp_1 + m_1 pp_2$$
$$+ m_1 pp_2 + mm_1m_2)]\epsilon_\nu^* \tag{27}$$

and

$$\mathrm{tr}[\,]_V = \mathrm{tr}\Big[\gamma_\mu(\hat{p} + m_1)\gamma_5(-\hat{p} + m)$$
$$\times\left(\gamma_\nu - \frac{(p_2 - p)_\nu}{M_0 + m_2 + m}\right)(\hat{p} + m_2)\Big]\epsilon_\nu^*$$
$$= 4(-i)\varepsilon_{\mu\lambda\alpha\beta}\Big[(mp_{1\alpha}p_{2\beta} + m_1p_\alpha p_{2\beta} + m_2p_{1\alpha}p_\beta)\epsilon_\lambda^*$$
$$+ \frac{(p - p_2)_\nu\epsilon_\nu^*}{M_{20} + m_2 + m}p_{1\alpha}p_{2\beta}(-p_\lambda)\Big]. \tag{28}$$

We note that the transverse component of the meson polarization vector ϵ_μ coincides with that of the polarization vector $\tilde{\epsilon}_\mu$ of the $q\bar{q}$ system.

Equations (27) and (28) represent the fullest LFD parametrization that describes the transformation properties of the matrix elements of the current.

Thus, the most general parametrization of the $0^- \longrightarrow 1^-$ transition current in the covariant LFD approach can be represented as

$$V_\mu^{\mathrm{LFD}} = \frac{2i}{M_1 + M_2}V(q^2)\epsilon_{\mu\nu\alpha\beta}\epsilon_\nu P_{1\alpha}P_{2\beta}$$
$$+ B_1\varepsilon_{\mu\nu\alpha\beta}\epsilon_\nu^* P_{1\alpha}\frac{\omega_\beta}{\omega(P_1 + P_2)}$$
$$+ B_2\varepsilon_{\mu\nu\alpha\beta}\epsilon_\nu^* P_{2\alpha}\frac{\omega_\beta}{\omega(P_1 + P_2)} \tag{29}$$
$$+ B_3(S_\mu P_{1\nu} + P_{1\mu}S_\nu)\epsilon_\nu^* + B_4(S_\mu P_{2\nu} + P_{2\mu}S_\nu)\epsilon_\nu^*$$
$$+ B_5\left(S_\mu\frac{\omega_\nu}{\omega(P_1 + P_2)} + \frac{\omega_\mu}{\omega(P_1 + P_2)}S_\nu\right)\epsilon_\nu^*,$$

$$A_\mu^{\rm LFD} = A_1(M_1+M_2)\left(\epsilon_\mu^* - \frac{\epsilon^* q}{q^2}q_\mu\right) - A_2\frac{\epsilon^* q}{M_1+M_2}\left((P_1+P_2)_\mu - \frac{M_1^2-M_2^2}{q^2}q_\mu\right) + A_0 2M_2\frac{\epsilon^* q}{q^2}q_\mu + H_1\left(\frac{\epsilon^*\omega}{\omega P_1}\right)P_{1\mu} + H_2\left(\frac{\epsilon^*\omega}{\omega P_2}\right)P_{2\mu} + H_3\left(\frac{\epsilon^* P_1}{\omega P_1}\right)\omega_\mu + H_4\frac{\epsilon^*\omega}{(\omega(P_1+P_2))^2}\omega_\mu, \quad (30)$$

where $S_\mu = \dfrac{i\epsilon_{\mu\nu\alpha\beta}\omega_\nu P_{1\alpha}P_{2\beta}}{\omega(P_1+P_2)}$. The matrix elements of the vector and the axial-vector current involve four physical form factors, V for the former and A_1, A_2, and A_0 for the latter; they also contain five (B_1, …, B_5) and four (H_1, …, H_4) unphysical form factors for the former and the latter, respectively.

Let us choose the reference frame where

$$P_{1\mu} = \left[P_+, \mathbf{P}_\perp, \frac{M_1^2+\mathbf{P}_\perp^2}{P_+}\right], \quad P_{2\mu} = \left[yP_+, \mathbf{0}, \frac{M_2^2}{yP_+}\right]. \quad (31)$$

In this frame, the final vector meson moves along the z axis, which is singled out for the standard choice of ω [see (1)]. In numerical calculations, the parton contribution is maximized by choosing a reference frame where the initial-meson transverse momentum is small in relation to the masses of particles participating in the reaction (see [18, 19]). We further consider only the matrix elements of the good and the transverse current component, whereby the unphysical form factors H_3, B_1, and B_2 are eliminated from the outset. In order to eliminate H_1 and H_2, we consider only the transverse polarization of the final meson. In this meson-momentum configuration, the vector ϵ_μ is orthogonal to the z-axis direction and to the final-vector-meson momentum, so that ϵ_μ has only transverse components. In order to eliminate the remaining unphysical form factors B_1 and B_2, we introduce the auxiliary tensor [24]

$$G_{\mu\nu} = \sqrt{M_1M_2}(ig\varepsilon_{\mu\nu\alpha\beta}P_{1\alpha}P_{2\beta} + B_1\varepsilon_{\mu\nu\alpha\beta}P_{1\alpha}\omega_\beta + B_2\varepsilon_{\mu\nu\alpha\beta}P_{2\alpha}\omega_\beta) + \sqrt{M_1M_2}(B_3(S_\mu P_{1\nu}+P_{1\mu}S_\nu) + B_4(S_\mu P_{2\nu}+P_{2\mu}S_\nu) + B_5(S_\mu\omega_\nu+\omega_\mu S_\nu)). \quad (32)$$

The current calculated within LFD can then be represented as (see also [24])

$$J_\mu = G_{\mu\nu}\epsilon_\nu^*. \quad (33)$$

For the transverse polarization vector, this can be done, in the momentum configuration being considered, for $J_\mu^{(\rm OBC)}$ as well, since $\epsilon_\perp^*$ does not involve, in this case, quantities that depend on the integration variables x and $\mathbf{k}_\perp$ (in general, this is incorrect). Upon antisymmetrization with respect to the indices μ and ν, $G_{\mu\nu} \longrightarrow \bar{G}_{\mu\nu} = \frac{1}{2}(G_{\mu\nu} - G_{\nu\mu})$, the covariant structures at B_3, B_4, and B_5 vanish. For the remaining nonvanishing matrix elements of the current, we arrive at a set of equations that, in terms of the form factors appearing at the 4-velocities $V_1 = P_1/M_1$ and $V_2 = P_2/M_2$ (this representation is chosen for the sake of convenience), has the form

$$A_+(\epsilon_x) = \sqrt{M_1M_2}[b_1V_{1+} + b_2V_{2+}](-\epsilon_\perp V_{1\perp}),$$
$$A_x(\epsilon_x) = \sqrt{M_1M_2}(f + b_1V_{1\perp}(-\epsilon_\perp V_{1\perp})), \quad (34)$$
$$A_y(\epsilon_y) = \sqrt{M_1M_2}f,$$

where the form factors b_1, b_2, and f are defined via the relation

$$\langle 1^-|\bar{q}_2\gamma_\mu q_1|0^-\rangle = \sqrt{M_1M_2}(f(\eta)\epsilon_\mu^* + [b_1(\eta)V_{1\mu} + b_2(\eta)V_{2\mu}](\epsilon^* V_1)). \quad (35)$$

They can be expressed in terms of the form factors A_1, A_2, and V as given by Eqs. (29) and (30). In the configuration being considered, the remaining matrix elements vanish.

Thus, relations (34) solve the problem of self-consistently determining physical form factors for the $0^- \longrightarrow 1^-$ electroweak transition within the covariant LFD approach.

4. RADIATIVE CORRECTIONS FOR THE VECTOR AND THE AXIAL-VECTOR CURRENT

In this section, we calculate the Sudakov form factor, which corresponds to radiative corrections to the electroweak vertex of the quark current $\langle q_2|J_\mu|q_1\rangle$. Within QCD, the Sudakov form factor has been considered by many authors (see, for example, [25–29] and references therein). In our case, the momentum transfer squared q^2 is positive and is constrained by the condition $q^2 \le (m_1 - m_2)^2$; therefore, attention is given here primarily to a self-consistent analysis of radiative corrections to the first order in α_s in this region. The resulting formulas have a unified analytic structure both at positive and at negative q^2 values.

Since, within the covariant LFD scheme, intermediate-state particles are on the mass shell, we set $p_i^2 = m_i^2$ (for quark lines as well) in calculating radiative corrections that correspond to the total contribution of the triangle diagram (Fig. 7) and the total contribution of diagrams that describe the renormalization of external

photon lines (Fig. 8) and the emission of soft gluons (Fig. 9).

For the gluon field, we choose the Feynman gauge, so that the gluon propagator is written in the form

$$D^{ab}_{\mu\nu}(k^2) = \frac{-i\delta^{ab}}{k^2 - \lambda^2 - i0} g_{\mu\nu},$$

where λ is the gluon mass introduced formally.

Let us calculate the contribution of the triangle diagram that corresponds to virtual-gluon exchange between the m_1 and the m_2 quark. We have

$$\begin{aligned} -ie\bar{u}(p_2)\Gamma^{(1)}_\mu(q^2)u(p_1) &= (-ie)^3 C_F \bar{u}(p_2) \\ &\times \int \frac{d^4k}{(2\pi)^4}\gamma_\nu i\frac{\hat{p}_2 + \hat{k} + m_2}{(p_2+k)^2 - m_2^2}\gamma_\mu(1-\gamma_5) \\ &\times i\frac{\hat{p}_1 + \hat{k} + m_1}{(p_1+k)^2 - m_1^2}\gamma_\nu\frac{(-i)}{k^2-\lambda^2}u(p_1), \end{aligned} \tag{36}$$

where $C_F = 4/3$. Thus, the vector and the axial-vector vertex function are determined in the form of integrals as

$$\begin{aligned} \Gamma^{(1)V}_\mu(q^2) &= i\left(-\frac{\alpha_s(k^2)}{4\pi^3}\right)C_F \\ &\times \int d^4k\gamma_\nu\frac{\hat{p}_2 + \hat{k} + m_2}{(p_2+k)^2 - m_2^2}\gamma_\mu\frac{\hat{p}_1 + \hat{k} + m_1}{(p_1+k)^2 - m_1^2}\gamma_\nu\frac{1}{k^2-\lambda^2}, \end{aligned} \tag{37}$$

$$\begin{aligned} \Gamma^{(1)A}_\mu(q^2) &= i\left(-\frac{\alpha_s(k^2)}{4\pi^3}\right)C_F \\ &\times \int d^4k\gamma_\nu\frac{\hat{p}_2 + \hat{k} + m_2}{(p_2+k)^2 - m_2^2}\gamma_\mu\gamma_5\frac{\hat{p}_1 + \hat{k} + m_1}{(p_1+k)^2 - m_1^2}\gamma_\nu\frac{1}{k^2-\lambda^2}. \end{aligned} \tag{38}$$

The Sudakov form factor for the vector and the axial-vector vertex can be parametrized as

$$\begin{aligned} &\Gamma^{(1)V}_\mu(q^2) \\ &= \bar{u}(p_2)\left[F_0^{(V)}\gamma_\mu\gamma_5 - i\frac{q_\mu}{m_1+m_2}\sigma_{\mu\nu}F_1^{(V)} - q_\mu F_2^{(V)}\right]u(p_1), \end{aligned} \tag{39}$$

$$\begin{aligned} &\Gamma^{(1)A}_\mu(q^2) \\ &= \bar{u}(p_2)\left[F_0^{(A)}\gamma_\mu\gamma_5 - i\frac{q_\mu}{m_1+m_2}\sigma_{\mu\nu}F_1^{(A)} - q_\mu F_2^{(A)}\right]u(p_1). \end{aligned} \tag{40}$$

In order to transform Eq. (37), we make use of the Feynman relation

$$\begin{aligned} &\frac{1}{a_1a_2\cdots a_n} \\ &= (n-1)!\int_0^1 dx_1 \cdots \int_0^{x_{n-1}} dx_n \frac{\delta(x_1 + x_2 + \ldots + x_{n-1})}{(a_1x_1 + a_2x_2 + \ldots + a_nx_n)^n} \end{aligned} \tag{41}$$

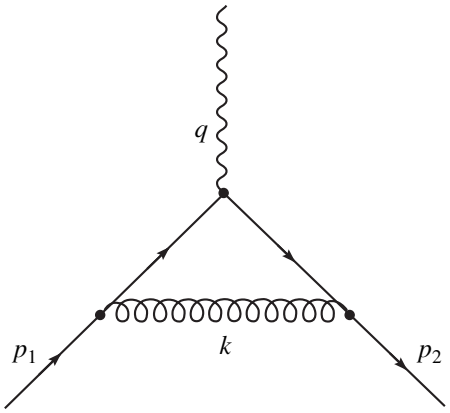

Fig. 7. Diagram involving virtual-gluon exchange.

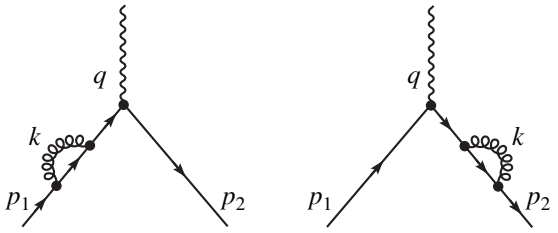

Fig. 8. Diagrams renormalizing external quark lines.

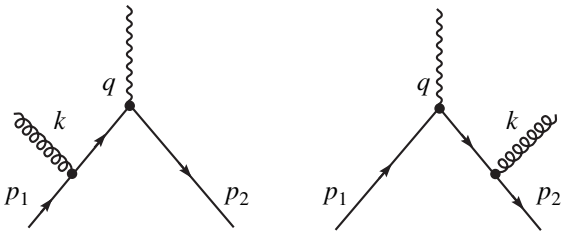

Fig. 9. Diagrams involving soft-gluon emission.

and introduce the following notation for the spin structure of the amplitude in (36):

$$\begin{aligned} &\mathrm{Spin}_\mu[k, x_1, x_2] \\ &= \gamma_\nu(\hat{p}_2 + \hat{k} + m_2)\gamma_\mu(1-\gamma_5)(\hat{p}_1 + \hat{k} + m_1)\gamma_\nu. \end{aligned} \tag{42}$$

In performing four-dimensional integration with respect to k, the right-hand side of (37) can be written as

$$\begin{aligned} &2\int_0^1 dx_1\int_0^{x_1} dx_2 d^4k[k^2 + 2[p_2x_2 + p_1(x_1 - x_2)]k \\ &- \lambda^2(1-x_1)]^{-3}\mathrm{Spin}_\mu[k, x_1, x_2] \\ &= 2\int_0^1 dx_1\int_0^{x_1} dx_2 d^4k[(k^2)^2 - A^2 - \lambda^2(1-x_1)]^{-3} \end{aligned} \tag{43}$$

$$\times \mathrm{Spin}_\mu[k - A_\mu, x_1, x_2],$$

where $A_\mu = x_2 p_{2\mu} + (x_1 - x_2)p_{1\mu}$.

Further, the integration with respect to this four dimensional variable reduces to evaluating integrals of the two types

$$\int \frac{d^4k}{(2\pi)^4}\frac{1}{[k^2 - A_\lambda^2 - i0]^3}, \quad \int \frac{d^4k}{(2\pi)^4}\frac{k^2}{[k^2 - A_\lambda^2 - i0]^3}, \quad (44)$$

where $A_\lambda^2 \equiv A^2 + \lambda^2(1 - x_1)$.

The ultraviolet divergence in the second integral is removed by the dimensional-regularization method,

$$\int \frac{d^4k}{(2\pi)^4}\frac{1}{[k^2 + A_\lambda^2]^3} = (-i)\frac{\pi^2}{(2\pi)^4}\frac{1}{2A_\lambda^2},$$

$$\int \frac{d^4k}{(2\pi)^4}\frac{k^2}{[k^2 + A_\lambda^2]^3} \quad (45)$$

$$\xrightarrow{\text{reg}} (-i)\frac{\pi^2}{(2\pi)^4}\left[C + \frac{1}{2} - \ln(4\pi) + \ln\left(\frac{A_\lambda^2}{\mu^2}\right)\right].$$

We then proceed to perform integration with respect to x_1 and x_2; there, an infrared divergence in the limit $\lambda \longrightarrow 0$ arises only in the integral $2\int_0^1 dx_1 \int_0^{x_1} dx_2 \frac{1}{A^2 + \lambda^2(1 - x_1)}$ and stems from the region $\{x_1, x_2\} \longrightarrow 0$. In the limit $\lambda^2 \longrightarrow 0$, we can set $A_\lambda^2 = A^2 + \lambda^2$ over the entire integration domain $0 \le x_2 \le x_1 \le 1$ without changing the structure of the infrared singularity.

For further integration, it is convenient to introduce, instead of the Feynman variables x_1 and x_2, the variables

$$x = x_1, \qquad \zeta = x_2 - \alpha_1 x_1, \quad (46)$$

where

$$\alpha_1 = \frac{1}{2}\left(1 + \frac{m_1^2 - m_2^2}{q^2}\right), \quad \alpha_2 = \frac{1}{2}\left(1 - \frac{m_1^2 - m_2^2}{q^2}\right). \quad (47)$$

The integrals with respect to x_1 and x_2 then transform as

$$2\int_0^1 dx_1 \int_0^{x_1} dx_2 F[x_1, x_2] \longrightarrow 2\int_0^1 dx \int_{-\alpha_1 x}^{-|\alpha_2|x} d\zeta F[x, \zeta]. \quad (48)$$

The vector A_μ is expressed in terms of the new variables as

$$A_\mu = x_2 p_{2\mu} + (x_1 - x_2)p_{1\mu} = q_\mu \zeta + (\alpha_1 p_{2\mu} + \alpha_2 p_{1\mu})x, \qquad A^2 = q^2[\zeta^2 - \beta^2 x^2], \quad (49)$$

where

$$\beta = \frac{1}{2}\sqrt{1 - 2\frac{m_1^2 + m_2^2}{q^2} + \frac{(m_1^2 - m_2^2)^2}{(q^2)^2}}. \quad (50)$$

The above auxiliary variables $\alpha_1(q^2)$, $\alpha_2(q^2)$, and $\beta(q^2)$ have the following physical meaning: $\sqrt{q^2}\alpha_1(q^2)$ and $\sqrt{q^2}|\alpha_2(q^2)|$ are the energies of, respectively, the m_1 and the m_2 particle ($\mathbf{q} = 0$) in the c.m. frame, while $\sqrt{q^2}\beta(q^2)$ is the absolute value of the 3-momentum of each particle in this frame. In the region corresponding to the decay process $m_1 \longrightarrow Wm_2$, the energy conservation law has the form

$$\sqrt{q^2}\alpha_1(q^2) = \sqrt{q^2} + \sqrt{q^2}|\alpha_2(q^2)|, \qquad (\sqrt{q^2}\alpha_i)^2 - m_i^2 = (\sqrt{q^2}\beta)^2. \quad (51)$$

Upon four-dimensional integration with respect to k, the integrand [see Eq. (45)] involves the following structures:

$$\int \frac{d^4k}{(2\pi)^4}\mathrm{Spin}_\mu^{A,V}[x, \zeta]\frac{1}{[k^2 + A_\lambda^2]^3} \quad (52)$$

$$\longrightarrow \left\{1, \ln\left[\frac{A_\lambda^2}{\mu^2}\right], x\frac{1}{A_\lambda^2}, \zeta\frac{1}{A_\lambda^2}, x^2\frac{1}{A_\lambda^2}, \zeta x\frac{1}{A_\lambda^2}, \zeta^2\frac{1}{A_\lambda^2}, \frac{1}{A_\lambda^2}\right\}.$$

Presented immediately below are integrals that are taken of these functions $F[x, \zeta]$ and which arise upon integrating (52) with respect to x and ζ:

$$2\int_0^1 dx \int_{-\alpha_1 x}^{-|\alpha_2|x} d\zeta 1 = 1,$$

$$2\int_0^1 dx \int_{-\alpha_1 x}^{-|\alpha_2|x} d\zeta \ln\left(\frac{A^2}{\mu^2}\right) = -3 + (\alpha_1 - \beta)\ln\left(\frac{m_1^2}{\mu^2}\right) - (|\alpha_2 - \beta|)\ln\left(\frac{m_2^2}{\mu^2}\right) + 2\beta\ln\left(\frac{\alpha_1 + \beta}{|\alpha_2| + \beta}\right),$$

$$2\int_0^1 dx \int_{-\alpha_1 x}^{-|\alpha_2|x} d\zeta \zeta\frac{1}{A^2} = (q^2)^{-1}\ln\left(\frac{m_2^2}{m_1^2}\right), \quad (53)$$

$$2\int_0^1 dx \int_{-\alpha_1 x}^{-|\alpha_2|x} d\zeta x\frac{1}{A^2} = (q^2)^{-1}\frac{1}{\beta}\ln\left(\frac{\alpha_1 - \beta}{\alpha_1 + \beta}\frac{|\alpha_2| + \beta}{|\alpha_2| - \beta}\right),$$

$$2\int_0^1 dx \int_{-\alpha_1 x}^{-|\alpha_2|x} d\zeta x^2\frac{1}{A^2} = \frac{1}{2\beta q^2}\ln\left(\frac{\alpha_1 - \beta}{\alpha_1 + \beta}\frac{|\alpha_2| + \beta}{|\alpha_2| - \beta}\right),$$

$$2\int_0^1 dx \int_{-\alpha_1 x}^{-|\alpha_2|x} d\zeta x\zeta \frac{1}{A^2} = \frac{(-1)}{q^2}\ln\left(\frac{m_1}{m_2}\right),$$

$$2\int_0^1 dx \int_{-\alpha_1 x}^{-|\alpha_2|x} d\zeta \zeta^2 \frac{1}{A^2} = \frac{1}{q^2}\left[1 + \frac{1}{2}\beta\ln\left(\frac{\alpha_1-\beta}{\alpha_1+\beta}\frac{|\alpha_2|+\beta}{|\alpha_2|-\beta}\right)\right].$$

Since the integrals in (53) do not involve infrared divergences, we everywhere set $\lambda^2 = 0$ ($A^2 + \lambda^2 = A^2$) in the above equations. The most important (doubly logarithmic) term $DL(q^2) = 2\int_0^1 dx \int_{-\alpha_1 x}^{-|\alpha_2|x} d\zeta \frac{1}{A^2+\lambda^2}$ can be represented in the form

$$DL[q^2] = (q^2)^{-1}\int_0^1 \frac{dx}{x}\frac{1}{\left[\beta^2 - \frac{\lambda^2}{q^2x^2}\right]^{1/2}} \times \ln\left(\frac{\alpha_1 - \left[\beta^2 - \frac{\lambda^2}{q^2x^2}\right]^{1/2}}{\alpha_1 + \left[\beta^2 - \frac{\lambda^2}{q^2x^2}\right]^{1/2}} \frac{|\alpha_2| + \left[\beta^2 - \frac{\lambda^2}{q^2x^2}\right]^{1/2}}{|\alpha_2| - \left[\beta^2 - \frac{\lambda^2}{q^2x^2}\right]^{1/2}}\right) = (q^2)^{-1}\int_\gamma^{i\infty} \frac{dz}{(z^2-\beta^2)}\ln\left(\frac{\alpha_1+z}{\alpha_1+z}\frac{|\alpha_2|+z}{|\alpha_2|-z}\right), \quad (54)$$

where $\gamma(q^2) = [\beta^2(q^2) - \lambda^2/q^2]^{1/2}$.

This doubly logarithmic term can be written in a unified form for $q^2 < 0$ and for $0 < q^2 < (m_1 - m_2)^2$:

$$DL[q^2] = \frac{1}{2\beta q^2}\left(\left\{F\left[\frac{\alpha_1-\beta}{\beta+\gamma}\right] + F\left[\frac{\alpha_1-\beta}{\beta-\gamma}\right] - F\left[\frac{\alpha_1+\beta}{-\beta+\gamma}\right] - F\left[\frac{-\alpha_1-\beta}{\beta+\gamma}\right]\right\} - \{\alpha_1 \longleftrightarrow |\alpha_2|\}\right). \quad (55)$$

The function $F[x] = \int_0^x \frac{d\zeta}{\zeta}\ln[1+\zeta]$ is real for $x > -1$.

For positive q^2 values, we have $\alpha_1, |\alpha_2| > \beta > \gamma$ and the doubly logarithmic term can be represented in the form

$$DL[q^2] = (q^2)^{-1}\frac{1}{2\beta}Z[q^2], \quad (56)$$

where

$$Z[q^2] = \ln\left[\frac{\alpha_1+\beta}{\alpha_1-\beta}\frac{|\alpha_2|-\beta}{|\alpha_2|+\beta}\right]\ln\left[\frac{\lambda^2}{m_1m_2}\right] + \ln\left[\frac{\alpha_1+\beta}{\alpha_1-\beta}\frac{|\alpha_2|+\beta}{|\alpha_2|-\beta}\right]\ln\left[\frac{|\alpha_2|+\beta}{\alpha_1+\beta}\right] + 2F\left[-\frac{2\beta}{\alpha_1+\beta}\right] - 2F\left[-\frac{2\beta}{|\alpha_2|+\beta}\right]. \quad (57)$$

Since the inequalities $q^2 > 0$ hold for $-\frac{2\beta}{\alpha_1+\beta}$, $-\frac{2\beta}{|\alpha_2|+\beta} > -1$, all functions in (57) are real-valued. In (57), we set $\lambda \longrightarrow 0$ ($\gamma \longrightarrow \beta$) in all expressions where no divergence arises in this limit.

In the spacelike region $q^2 < 0$, the relations $\gamma > \beta > |\alpha_1|, |\alpha_2|$ hold and the doubly logarithmic term can be recast into the form

$$Z[q^2] = -\left\{\frac{\pi^2}{6} - \frac{1}{2}\ln^2\left[\frac{\gamma-\beta}{\beta+\alpha_1}\right] + \frac{1}{2}\ln^2\left[\frac{\gamma-\beta}{\beta-\alpha_1}\right] + \ln\left[\frac{\beta-\alpha_1}{2\beta}\right]\ln\left[\frac{\beta+\alpha_1}{2\beta}\right] - 2F\left[\frac{\beta+\alpha_1}{2\beta}\right]\right\} + \{\alpha_1 \longleftrightarrow \alpha_2\} = -\frac{\pi^2}{3} - \frac{1}{2}\left(\ln^2\left[\frac{\gamma-\beta}{\beta+\alpha_1}\right] + \ln^2\left[\frac{\gamma-\beta}{\beta+\alpha_2}\right]\right) + \frac{1}{2}\left(\ln^2\left[\frac{\gamma-\beta}{\beta-\alpha_1}\right] + \ln^2\left[\frac{\gamma-\beta}{\beta+\alpha_2}\right]\right) + \ln\left[\frac{\beta-\alpha_1}{2\beta}\right]\ln\left[\frac{\beta+\alpha_1}{2\beta}\right] + \ln\left[\frac{\beta-\alpha_2}{2\beta}\right]\ln\left[\frac{\beta+\alpha_2}{2\beta}\right] - 2\left(F\left[\frac{\beta+\alpha_1}{2\beta}\right] + F\left[\frac{\beta+\alpha_2}{2\beta}\right]\right). \quad (58)$$

We note that the quantity $Z[q^2]$ determined by expression (58) is invariant under the interchange of the m_1 and the m_2 particle and under the substitution $\alpha_1 \longleftrightarrow \alpha_2$.

Finally, the expressions for the gluon corrections (Fig. 7) are obtained by substituting (53), (56), (57), and (58) into Eqs. (52) and (42).

In order to take into account all gluon corrections to the first order in the strong-interaction constant α_s, the expression for the renormalized weak vertex must be supplemented with the contributions of the diagrams (Fig. 8) that renormalize the external quark propagators and of the diagrams involving the emission of soft gluons (Fig. 9).

The contributions (Fig. 8) that renormalize the external quark propagators are independent of q^2 and can be expressed in terms of the contributions of the corresponding diagrams in Fig. 7 that are diagonal in the quark flavor. Indeed, we consider the diagram in Fig. 7 that is diagonal in the flavor of the m_i quark and denote by $F[q^2, m_1, m_2]$ its contribution and by $Z[m_i]$ the constant corresponding to the contribution of one of the diagrams in Fig. 8. By virtue of vector-current conservation, the relation $F[q^2 = 0, m_i, m_i] + 2Z[m_i] = 0$ must hold in the first order in α_s, whence it follows that

$$Z[m_i] = -\frac{1}{2}F[q^2 = 0, m_i, m_i]. \quad (59)$$

Thus, the total contribution of the diagrams in Fig. 7 and 8 can be represented as

$$F[q^2, m_1, m_2] - \frac{1}{2}(F[q^2 = 0, m_1, m_1] + F[q^2 = 0, m_2, m_2]). \quad (60)$$

Since $Z[m_i]$ in (59) is associated with the vector vertex, we then have

$$Z[m_i] = F_1^V[m_i, m_i, q^2 = 0]. \quad (61)$$

The form factors F_1^V and F_1^A transform as

$$F_0^V(q^2) \longrightarrow F_1^V(q^2) - \frac{1}{2}[F_0^V[q^2 = 0, m_1, m_1] + F_0^V[q^2 = 0, m_2, m_2]], \quad (62)$$

$$F_0^A(q^2) \longrightarrow F_1^A(q^2) - \frac{1}{2}[F_0^V[q^2 = 0, m_1, m_1] + F_0^V[q^2 = 0, m_2, m_2]]. \quad (63)$$

As a result, $Z[m_i]$ does not contribute to the form factors F_1^V, F_2^V, F_1^A, and F_2^A.

At $q^2 = q^2_{\max} = (m_1 - m_2)^2$, the form factors F_i^V and F_i^A are normalized as [gluon-emission diagrams, which will be considered in the next section, do not contribute at this $q^2 = (m_1 - m_2)^2$ value] (see also [25])

$$F_0^V(q^2_{\max}) = 1 + 2\frac{4}{3}\frac{\alpha_s}{4\pi}\left[-2 + \frac{m_1 + m_2}{m_1 - m_2}\ln\left(\frac{m_1}{m_2}\right)\right],$$

$$F_1^V(q^2_{\max}) = \frac{4}{3}\frac{\alpha_s}{4\pi}\frac{m_1 + m_2}{m_1 - m_2}\ln\left(\frac{m_1}{m_2}\right),$$

$$F_2^V(q^2_{\max}) = 2\frac{4}{3}\frac{\alpha_s}{4\pi}\left[2 - \frac{m_1 + m_2}{m_1 - m_2}\ln\left(\frac{m_1}{m_2}\right)\right]\frac{1}{m_1 - m_2},$$

$$F_0^A(q^2_{\max}) = 1 + 2\frac{4}{3}\frac{\alpha_s}{4\pi}\left[-3 + \frac{m_1 + m_2}{m_1 - m_2}\ln\left(\frac{m_1}{m_2}\right)\right], \quad (64)$$

$$F_1^A(q^2_{\max}) = \frac{4}{3}\frac{\alpha_s}{4\pi}\frac{m_1 + m_2}{m_1 - m_2}\left[2 - \ln\left(\frac{m_1}{m_2}\right)\right],$$

$$F_2^A(q^2_{\max}) = \frac{4}{3}\frac{\alpha_s}{4\pi}\left[4(m_1 + m_2) + \frac{m_1^2 + m_2^2 - 10m_1m_2}{m_1 - m_2}\ln\left(\frac{m_1}{m_2}\right)\right]\frac{1}{(m_1 - m_2)^2}.$$

The ultraviolet divergence is independent of the quark masses m_1 and m_2 and of q^2 and is canceled in (60). The numerical procedure applied in (45) within the dimensional-regularization method is validated in (60). The functions $F[q^2, m_i, m_j]$ involve an infrared divergence in the form of a logarithmic dependence on the soft-gluon mass λ. The infrared divergence is canceled upon taking into account soft-gluon-emission diagrams. (While there are no free gluons in nature, the principle of quark–hadron duality treats a color-singlet hadron as a system formed by constituent quarks and a collinear hadron jet where the particle momenta can be projected onto the hadron wave function.)

Let us consider radiative corrections to external quark lines. In order to eliminate infrared divergences in the total cross section, we must take into account soft-gluon-emission diagrams (see Fig. 9).The expression for the cross section characterizing the emission of soft gluons with a nonvanishing mass is well known (see, for example, [30]). In the Feynman gauge, it can be represented as

$$d\sigma^{(1)}(q^2) = -\alpha_s C_F\left(\frac{p_1}{(p_1k)} - \frac{p_2}{(p_2k)}\right)^2\frac{d^3\mathbf{k}}{4\pi^2\omega(\mathbf{k}^2)}\sigma_{\rm el}, \quad (65)$$

where $d\sigma_{\rm el}$ is the differential cross section for the one-body quark current $\bar{u}_2\gamma_\mu(1 - \gamma_5)u_1$. As can be seen directly from (65), the equality $d\sigma(q^2_{\max}) = 0$ holds at $q^2 = q^2_{\max} = (m_1 - m_2)^2$.

Here, the gluon energy $\omega(\mathbf{k}^2) = \sqrt{\mathbf{k}^2 + \lambda^2}$ takes into account the fictitious gluon mass λ. Upon restricting the limit of integration with respect to $\omega(\mathbf{k}^2)$ by the condition $0 \le \omega(\mathbf{k}^2) \le \omega_{\max}$, we obtain

$$\sigma^{(1)}(q^2) = -\frac{\alpha_s C_F}{4\pi^2}\sigma_{\rm el}(-2G[q^2, m_1, m_2, \lambda] + G[q^2 = 0, m_1, m_1, \lambda] + G[q^2 = 0, m_2, m_2, \lambda]), \quad (66)$$

where

$$G[q^2, m_1, m_2, \lambda] = \int_0^{\omega_{\max}}\frac{d\Omega\mathbf{k}^2d\mathbf{k}}{\sqrt{\mathbf{k}^2 + \lambda^2}}\frac{p_1p_2}{(p_1k)(p_2k)} = 4\pi(p_1p_2)\int_0^1 dx\frac{1}{P^2}\left[\int_0^{\omega_{\max}/\lambda}\frac{d\xi}{\sqrt{\xi^2 + 1}} + \int_0^{+\infty}\frac{P_0^2d\xi}{\sqrt{\xi^2 + 1}(\xi^2P^2 + P_0^2)}\right]. \quad (67)$$

The last term is taken in the limit $\lambda \longrightarrow 0$ (we then have $\omega_{\max}/\lambda \longrightarrow +\infty$). The first term can be reduced to the form

$$\int_0^{\omega_{\max}/\lambda}\frac{d\xi}{\sqrt{\xi^2 + 1}} = \ln\left(\frac{\omega_{\max}}{\lambda} + \sqrt{1 + \frac{\omega^2_{\max}}{\lambda^2}}\right)\Bigg|_{\lambda \to 0} \longrightarrow \ln\left(\frac{2\omega_{\max}}{\lambda}\right). \quad (68)$$

Thus, we have

$$G[q^2, m_1, m_2, \lambda] = (p_1p_2)\int_0^{\omega_{max}} \frac{d^3\mathbf{k}}{\sqrt{\mathbf{k}^2+\lambda^2}}\frac{1}{(p_1k)(p_2k)}$$

$$= 4\pi(p_1p_2)\left(\frac{1}{2\beta q^2}\ln\left[\frac{\alpha_1-\beta|\alpha_2|+\beta}{\alpha_1+\beta|\alpha_2|-\beta}\right]\ln\left[\frac{2\omega_{max}}{\lambda}\right]\right. \quad (69)$$

$$\left. -\int_0^1 dx\frac{1}{P^2(1-r(x))^{1/2}}\ln\left[\frac{1+(1-r(x))^{1/2}}{r^{1/2}(x)}\right]\right),$$

where

$$r(x) = \frac{P^2(x)}{P_0^2(x)}, \quad P_\mu(x) = p_{1\mu}x + p_{2\mu}(1-x). \quad (70)$$

Expressions (67)–(69) specify gluon-emission-induced corrections to the weak vertex for the quark current.

Let us now consider the q^2 dependence of regular contributions to $\sigma^{(1)}(q^2)$. The quantity $\sigma^{(1)}(q^2)$ is not invariant under Lorentz transformations, since integration in Eq. (67) is defined in a specific reference frame where the gluon energy is constrained by the noninvariant condition $0 \le \omega(\mathbf{k}^2) \le \omega_{max}$. In order to define $\sigma^{(1)}(q^2)$, it is therefore necessary to fix a reference frame where the 4-vector A_μ is specified. It seems that the quasi-Breit frame, where the velocities of the initial and the final quark are equal in magnitude and opposite in direction (see, for example, [31]), is the most convenient for computing off-diagonal form factors. Thus, we define the quantity $P_0(x)$ in (67) in the quasi-Breit frame as

$$P_0^2(x) = \frac{(m_1+m_2)^2-q^2}{4m_1m_2}[x_2m_2 + (x_1-x_2)m_1]^2. \quad (71)$$

The Sudakov form factor is specified in the region $-\infty \le \tilde{q}^2 \le (m_1-m_2)^2$, where $\tilde{q}^2 = (p_1-p_2)^2$, p_1 and p_2 being the quark momenta ($p_i^2 = m_i^2$); the boundaries of the physical region are specified by the meson masses, $0 \le q^2 \le (M_1 - M_2)^2$. The square of the momentum transfer is given by

$$q^2 = (P_1-P_2)^2$$
$$= (1-y)\left[M_1^2 - \frac{1}{y}M_2^2\right] - y\left[\mathbf{P}_{1\perp} - \frac{1}{y}\mathbf{P}_{2\perp}\right]^2, \quad (72)$$

$$\tilde{q}^2(q^2, x, \mathbf{k}_\perp^2) = (1-y)\left[M_{01}^2(x, \mathbf{k}_\perp^2) - \frac{1}{y}M_{02}^2(x', \mathbf{k}_\perp'^2)\right]$$
$$-y\left[\mathbf{P}_{1\perp} - \frac{1}{y}\mathbf{P}_{2\perp}\right]^2. \quad (73)$$

By way of example, we indicate that, for $0^- \longrightarrow 0^-$, the physical region of q^2 is not covered by the region $-\infty \le \tilde{q}^2 \le (m_1-m_2)^2$.

In the spacelike region $q^2 \le 0$, one can always choose a reference frame where $q_+ = 0$. In this case, we have $\tilde{q}^2(q^2, x, \mathbf{k}_\perp^2) = q^2$, since $\tilde{q}^2 = (q_\mu + \omega_\mu(\tau_1^* - \tau_1^*))^2$ and $\omega^2 = 0$. The condition $q^2 = \tilde{q}^2$ makes it possible to factorize the relevant diagram into the hadronic-current diagram and the W^--meson propagator [20]. In the timelike region $q^2 > 0$, there is no such possibility; for this reason, the Sudakov form factor is calculated for a given configuration of quarks (not mesons). Since integration over the intermediate quark configurations is then performed for each meson configuration, the Sudakov form factor, which now depends on $\tilde{q}^2(q^2, x, \mathbf{k}_\perp^2)$, is also integrated in accordance with Eq. (23).

5. TRANSITIONS FORM FACTORS AND PROBABILITIES OF SEMILEPTONIC DECAYS

Meson wave functions are determined by solving the relativistic wave equation

$$(\hat{M}_0(\mathbf{k}^2) + \hat{V})\Psi^{J\lambda} = M\Psi^{J\lambda}. \quad (74)$$

As was indicated above, the dependence of the wave functions on the variable $(\mathbf{n}\cdot\mathbf{k})$ is disregarded in our calculations.

We relied on the potential proposed by Godfrey and Isgur [32]. The computational procedure used and the choice of parameter values are given in [18]. For various quark pairs, the parameter σ that specifies the smearing of the potential was set to $\sigma_{\pi(\rho)} = \sigma_{K(K^*)} = 0.8$ GeV, $\sigma_{D(D^*)} = 1.0$ GeV, and $\sigma_{B(B^*)} = 1.2$ GeV. For the transitions $B \longrightarrow D(D^*)$, we also employed wave functions obtained as solutions to the Schrödinger equation (74) with the potential V_0 and the confining potential V_{red},

$$V_{red} = c + br, \quad V_0 = c + br - \frac{4\alpha_s}{3r}. \quad (75)$$

In order to take into account the difference between the wave functions of the vector and the pseudoscalar $(q_1\bar{q}_2)$ bound state, the potential used in Eq. (74) was supplemented with the spin-dependent potential $V_{spin}(\mathbf{k}^2)$ parametrized as

$$V_{spin}(\mathbf{k}^2) = -\frac{\tilde{c}}{m_1m_2}\mathbf{S}_i\cdot\mathbf{S}_j\exp(-\mathbf{k}^2/\sigma^2), \quad (76)$$

where the parameter $\tilde{c}$ was determined for the (m_1, m_2) quark system in such a way that the difference between the masses of the corresponding 1^- vector meson and the corresponding 0^- scalar meson was equal to its

Table 1. Observables of the decays $B \longrightarrow Dl\bar{\nu}_l$ and $B \longrightarrow D^*l\bar{\nu}_l$ (partial decay widths are expressed in units of $|V_{bc}|^2 \times 10^{12}$ s^{-1}; $|V_{bc}|$ was set to 0.037; and $\tau_B = 1.60 \times 10^{-12}$ s)

	$\Gamma(D)$	$\mathcal{B}(D)$, %	$\Gamma(D^*)$	$\mathcal{B}(D^*)$, %	Γ_L/Γ_T	$\Gamma(D^*)/\Gamma(D)$
Model I(S)	9.78	2.14	22.4	4.90	1.16	2.16
Model I	10.14	2.22	26.5	5.78	1.24	2.61
Model II(S)	8.58	1.88	20.4	4.48	1.06	2.38
Model II	8.87	1.94	24.2	5.28	1.16	2.73
QM:						
WSB [2]	8.08	1.77	21.9	4.80		2.71
ISGW2 [6]	11.9	2.61	24.8	5.43	1.04	2.08
Jaus [4]	9.6	2.10	25.3	5.55	1.04	2.08
Faustov [8]	13.2	2.89	22.5	4.93		1.71
Melikhov [12]	8.7	1.90	23.2	5.08	1.28	2.65
DNKO [14]	9.09	1.99	23.1	5.06	1.15	2.54
SR:						
Narison 92 [33]	9 ± 3	2.0 ± 0.6	17 ± 6	3.7 ± 1.3	$0.98^{+0.14}_{-0.12}$	$1.9^{+0.4}_{-0.3}$
Experiment [34, 35]		1.95 ± 0.27		5.05 ± 0.25	1.24 ± 0.16	

physical value. To a high precision, this condition is met at $\tilde{c} = 0.25$ GeV^3.

With the Godfrey–Isgur potential, the partial widths were calculated at $m_b = 5.1$ GeV, $m_c = 1.70$ GeV, $m_s = 0.45$ GeV, and $m = 0.33$ GeV. For each of the transitions $b \longrightarrow c$, $b \longrightarrow u$, $c \longrightarrow s$, and $c \longrightarrow d$, the form factors were calculated for (a) the wave functions as obtained by solving the wave equation and (b) the model Gaussian wave functions with parameters set to the values from [3].

The calculations were performed with allowance for the Sudakov form factor (explicit expressions for it are given in Section 4) and also without it, $S(q^2) \longrightarrow 1$. The integrals that determine the Sudakov form factor are dominated by the contribution from the region where the gluon virtualities μ^2 are modest; for this reason, α_s was set to 0.30 for all types of quark transitions (see also [25]).

In a calculation of the Sudakov form factor, the parameter $\omega_{\max}$ has the meaning of the maximum possible energy of the emitted gluon or, what is the same, of characteristic parton virtualities in a meson. For quark states to be color-singlet (hadronic) both in the initial and in the final state, it is necessary to project the emitted gluon onto the wave function of the initial or the final meson; otherwise, a hard gluon with a characteristic virtuality μ^2 in excess of $\langle \mathbf{k}_\perp^2 \rangle$ will lead, in the initial or in the final state, to the formation of a hadronic jet. Hence, the quantity $\omega_{\max}$ must be determined by characteristic parton virtualities in a meson. If spin interaction is taken into account, the wave function of the initial meson may differ from the wave function of the final meson; however, our numerical calculations were performed with the parameter $\omega_{\max}$ set to the same value for the scalar and for the vector meson ($\omega_{\max} = 0.5$ GeV).

Tables 1–10 display the results of our calculations performed with various wave functions of the initial and the final meson and with or without allowance for the Sudakov form factor. Listed immediately below are further details on the models used in these calculations.

(i) Model I: The wave functions for the initial and the final meson were determined as solutions to the wave equation for the potential, the smearing parameters, and the potential of spin–spin interaction as specified by the above formulas; no account was taken of the Sudakov form factor.

(ii) Model I(S): The wave functions were determined as solutions to the wave equation; the Sudakov form factor was included.

(iii) Model II: Use was made of model wave functions in the Gaussian parametrization $\psi(\mathbf{k}) = N\exp\left[-\dfrac{\mathbf{k}^2}{2\beta^2}\right]$ with the parameters $\beta = \beta_{m_1, m_2, J}$ from [6]; no account was taken of the Sudakov form factor.

(iv) Model II(S): Use was made of model wave functions; the Sudakov form factor was included.

In the tables, we also quote relevant experimental data and results obtained by other authors. The theoretical approaches against which we contrast our results include those that are based on quark models (QM), sum rules (SR), and lattice calculations (Lattice). In Tables 1, 5, 7, and 9, we present the results of the calculations for the partial widths and branching fractions

Table 2. Form factors for the decay processes $B \longrightarrow Dl\bar{\nu}_l$ and $B \longrightarrow D^*l\bar{\nu}_l$ at $q^2 = 0$

	$F_1(0)$	$V(0)$	$A_1(0)$	$A_2(0)$	$V(0)/A_1(0)$	$A_2(0)/A_1(0)$
Model I(*S*)	0.69	0.73	0.62	0.54	1.19	0.88
Model I	0.73	0.74	0.70	0.59	1.06	0.84
Model II(*S*)	0.63	0.67	0.56	0.52	1.20	0.92
Model II	0.67	0.68	0.64	0.55	1.07	0.87
QM:						
WSB [2]	0.71				1.09	1.06
Jaus [4]	0.69	0.81	0.69	0.64	1.17	0.93
Melikhov [12]	0.684	1.12	0.68		1.08	0.89
DNKO [14]	0.683	0.677	0.623	0.556	1.08	0.89
SR:						
Narison 92 [33]	0.62 ± 0.06	0.58 ± 0.03	0.46 ± 0.02	0.53 ± 0.09	1.26 ± 0.08	1.15 ± 0.20
Experiment [36]					$1.18^{+0.30+0.12}_{-0.30-0.12}$	$0.71^{+0.20+0.07}_{-0.20-0.07}$

Table 3. Observables of the decays $B \longrightarrow Dl\bar{\nu}_l$ and $B \longrightarrow D^*l\bar{\nu}_l$ (*A*) with and (*B*) without allowance for contact interaction (the calculation of the branching fractions employed the parameter values of $|V_{bc}| = 0.037$ and $\tau_B = 1.60 \times 10^{-12}$ s; no account was taken of the Sudakov form factor)

	$\mathcal{B}(D)$, %	$\mathcal{B}(D^*)$, %	Γ_L/Γ_T	$\Gamma(D^*)/\Gamma(D)$	$V(0)/A_1(0)$	$A_2(0)/A_1(0)$
Model I *A*	2.22	5.78	1.24	2.61	1.06	0.84
Model I *B*	2.22	8.43	1.41	3.79	0.91	0.72
Model II *A*	1.94	5.28	1.16	2.73	1.07	0.87
Model II *B*	1.95	6.99	1.28	3.58	0.95	0.77
$V = c + br - 4\alpha_s/3r$ (*B*)	2.21	9.02	1.49	1.96	0.69	0.92
$V = c + br$ (*B*)	4.08	6.61	1.26	3.37	0.83	1.02

Table 4. Observables of the decays $B \longrightarrow Dl\bar{\nu}_l$ and $B \longrightarrow D^*l\bar{\nu}_l$ without allowance for contact interaction in models *B* and *C* (the calculations employed the parameter values of $|V_{bc}| = 0.037$and $\tau_B = 1.60 \times 10^{-12}$ s)

	$\mathcal{B}(D)$, %	$\mathcal{B}(D^*)$, %	Γ_L/Γ_T	$\Gamma(D^*)/\Gamma(D)$	$V(0)/A_1(0)$	$A_2(0)/A_1(0)$
Model I *B*	2.22	8.43	1.49	3.79	0.91	0.72
Model I *C*	2.22	7.33	1.45	3.30	0.91	1.12
Model II *B*	1.95	6.99	1.35	3.58	0.95	0.77
Model II *C*	1.94	6.32	1.32	3.26	0.95	0.81

for transitions into pseudoscalar and vector mesons and the observable values of Γ_L/Γ_T and $\Gamma(1^-)/\Gamma(0^-)$.

In the first column of Tables 1, 5, 7, and 9, we quote a reference to a theoretical or an experimental study. In the second and the fourth column, we give partial widths (in $|V_{if}|^2$ units) with respect to semileptonic decays into a pseudoscalar and a vector meson, respectively. It is convenient to compare these quantities with the results of other theoretical studies. The third and the fifth column contain the branching fractions for transitions into a pseudoscalar and a vector meson, respectively. The theoretical branching fractions $\mathcal{B}$ were obtained by multiplying the widths in the second and the fourth column by $|V_{if}|^2\tau_{M_i}$, where the CKM-matrix elements for the relevant transitions were taken to be $|V_{bc}| = 0.037$, $|V_{bu}| = 0.003$, $|V_{cs}| = 0.975$, and $|V_{cd}| = 0.24$. In the sixth and the seventh column, we quote the ratios Γ_L/Γ_T and $\Gamma(0^- \longrightarrow 1^-)/\Gamma(0^- \longrightarrow 0^-)$, respectively. These quantities are independent of the CKM-matrix elements; therefore, they can be directly compared with experimental data.

In Tables 2, 6, 8, and 10, we give the values of the form factors $F_1(0)$, $V(0)$, $A_1(0)$, and $A_2(0)$, as well as the

Table 5. Observables of the decays $B \longrightarrow \pi l \bar{\nu}_l$ and $B \longrightarrow \rho e \bar{\nu}_e$ (partial decay widths are expressed in units of $|V_{bu}|^2 \times 10^{12}$ s^{-1}; $|V_{bu}|$ was set to 0.003)

	$\Gamma(\pi)$	$\mathcal{B}(\pi)$, 10^{-4}	$\Gamma(\rho)$	$\mathcal{B}(\rho)$, 10^{-4}	Γ_L/Γ_T	$\Gamma(\rho)/\Gamma(\pi)$
Model I(S)	13.8	1.94	21.1	2.97	1.16	1.53
Model I	14.8	2.07	23.7	3.32	1.33	1.60
Model II(S)	8.93	1.26	15.1	2.16	0.90	1.69
Model II	9.18	1.29	16.5	2.31	1.02	1.80
QM:						
WSB [2]	7.43	1.04	26.1	3.66	1.34	3.51
ISGW2 [6]	9.6	1.35	14.2	1.99	0.3	1.48
Jaus [4]	10.0	1.40	19.1	2.68	0.82	1.91
Faustov [10]	3.0 ± 0.6	0.42 ± 0.08	5.4 ± 1.2	0.76 ± 0.17	0.5 ± 0.3	1.8 ± 0.4
Melikhov [12]	7.2	1.01	9.64	1.36	1.13	1.34
DNKO [14]	8.72	1.22	13.2	1.85		1.51
SR:						
Narison 92 [33]	3.0 ± 0.1	0.42 ± 0.01	33 ± 3	4.6 ± 0.5	$0.88^{+0.39}_{-0.20}$	11 ± 1
Ball 93 [37]	5.1 ± 1.1	0.72 ± 0.16	12 ± 4	1.7 ± 0.6	0.06 ± 0.02	2.4 ± 0.8
Yang 97 [38]	$5.4^{+1.6}_{-1.4}$	$0.76^{+0.22}_{-0.20}$	$3.1^{+0.9}_{-0.5}$	$0.44^{+0.12}_{-0.7}$	$0.48^{+0.46}_{-0.26}$	0.57 ± 0.17
Lattice:						
ELC 94 [39]	12 ± 8	1.7 ± 1.2	13 ± 12	1.8 ± 1.7		1.1 ± 1.0
APE 96 [40]	8 ± 4	1.2 ± 0.6				2.0 ± 0.9
UKQCD 98 [41]	$8.5^{+3.3}_{-1.4}$	$1.19^{+0.46}_{-0.20}$	$16.5^{+3.5}_{-2.3}$	$2.3^{+0.5}_{-0.3}$	$0.80^{+0.04}_{-0.03}$	$1.9^{+0.9}_{-0.7}$
Experiment B^0 [34]		1.8 ± 0.6		$2.5^{+0.8}_{-1.0}$		1.39

ratios $V(0)/A_1(0)$ and $A_2(0)/A_1(0)$. A comparison with experimental data is somewhat difficult here because the form factors are not measured directly in experiments. In view of this, they cannot be determined without resort to some additional model assumptions.

The value of $q^2 = 0$ stands out in describing various hadronic processes within LFD. From the point of view of the diagrammatic approach within the covariant LFD scheme, there are no contact terms at $q^2 = 0$, so that LFD calculations are the most reliable there. Moreover, it turns out that, in the LFD diagram technique, the hadronic current and the W-meson propagator can be factorized at $q^2 = 0$. For negative q^2 far from the analytic singularities of the form factors, sum rules represent a good approximation to nonperturbative QCD. For the semileptonic decays of hadrons, sum rules can therefore be used in the region of small positive q^2. On the other hand, lattice calculations yield reliable results for configurations in which the final meson has a small recoil. In a sense, lattice calculations therefore supplement calculations on the basis of sum rules. As to results of lattice calculations for the form factors at the point $q^2 = 0$, they involve a large uncertainty, since the form factors are continued in a model-dependent way over the entire region of q^2 allowed in the decay process. In all cases where there are results of lattice calculations over the entire interval of q^2, the form factors obtained within the covariant LFD formalism are contrasted against lattice results in the graphs.

5.1. Transitions $B \longrightarrow Dl\nu_l$ and $B \longrightarrow D^*l\nu_l$ (Contributions of the One-Body Current and of Contact Interaction)

At present, the $B \longrightarrow D(D^*)$ transitions have been best understood since the effective theory of heavy quarks [48] is applicable to them. This makes it possible to determine many parameters of $B \longrightarrow D$ decays in a model-independent way. Corrections to the effective theory of heavy quarks are proportional to Λ/m_b or Λ/m_c, where $\Lambda \sim \Lambda_{\rm QCD}$ is the expansion parameter in the effective theory of heavy quarks. According to the Luke theorem [49], corrections of order $\Lambda/m_{b,c}$ to the predictions of the effective theory of heavy quarks for form factors at the point $q^2 = 0$ vanish, so that the expansion begins from $(\Lambda/m_{b,c})^2$ terms. Nonetheless, corrections to the effective theory of heavy quarks of order Λ/m_c may prove to be significant for integrated quantities like the decay width.

Table 6. Form factors for the decay processes $B \longrightarrow \pi l \bar{\nu}_l$ and $B \longrightarrow \rho l \bar{\nu}_l$ at $q^2 = 0$

	$F_1(0)$	$V(0)$	$A_1(0)$	$A_2(0)$	$V(0)/A_1(0)$	$A_2(0)/A_1(0)$
Model I(S)	0.392	0.278	0.227	0.179	1.23	0.79
Model I	0.380	0.321	0.273	0.217	1.18	0.79
Model II(S)	0.252	0.197	0.160	0.134	1.23	0.84
Model II	0.305	0.236	0.200	0.169	1.18	0.84
QM:						
WSB [2]	0.33	0.33	0.28	0.28	1.2	1.0
ISGW2 [6]	0.09	0.27	0.05	0.02	5.4	0.4
Jaus [4]	0.27	0.35	0.26	0.24	1.35	0.92
Faustov [10]	0.20 ± 0.02	0.29 ± 0.03	0.26 ± 0.03	0.31 ± 0.03	1.1	1.2
Melikhov [12]	0.293	0.215	0.169	0.154	1.27	0.91
DNKO [14]	0.293	0.216	0.170	0.155	1.27	0.91
SR:						
Narison 92 [33]	0.23 ± 0.02	0.47 ± 0.14	0.35 ± 0.16	0.42 ± 0.12	1.3 ± 0.6	1.2 ± 0.5
Ball 93 [37]	0.26 ± 0.02	0.6 ± 0.2	0.5 ± 0.1	0.4 ± 0.2	1.2 ± 0.4	0.8 ± 0.4
Yang 97 [38]	0.29 ± 0.04	0.19 ± 0.01	0.07 ± 0.01	0.16 ± 0.01	2.7 ± 0.4	2.3 ± 0.3
Ball 98 [42]	0.305 ± 0.05	0.34 ± 0.05	0.26 ± 0.04	0.22 ± 0.03	1.20 ± 0.15	0.85 ± 0.13
Lattice:						
ELC 94 [39]	0.28 ± 0.14	0.37 ± 0.14	0.24 ± 0.06	0.39 ± 0.24	1.4 ± 0.5	1.5 ± 0.8
APE 96 [40]	0.29 ± 0.06	0.45 ± 0.22	0.29 ± 0.16	0.24 ± 0.56	1.6 ± 0.8	0.8 ± 1.5
UKQCD 98 [41]	0.27 ± 0.11	$0.35^{+0.06}_{-0.05}$	$0.46^{+0.02}_{-0.01}$	$0.26^{+0.05}_{-0.03}$	1.3 ± 0.2	0.96 ± 0.20

Table 7. Observables of the decays $D \longrightarrow Kl\bar{\nu}_l$ and $D \longrightarrow K^*l\bar{\nu}_l$ (partial decay widths are expressed in units of $|V_{cs}|^2 \times 10^{10}$ s^{-1}; the calculations were performed at $|V_{cs}| = 0.975$)

	$\Gamma(K)$	$\mathcal{B}(K)$, %	$\Gamma(K^*)$	$\mathcal{B}(K^*)$, %	Γ_L/Γ_T	$\Gamma(K^*)/\Gamma(K)$
Model I(S)	10.44	4.12	5.63	2.22	1.26	0.54
Model I	9.77	3.85	6.14	2.42	1.32	0.63
Model II(S)	10.05	3.97	5.74	2.27	1.20	0.57
Model II	9.38	3.70	6.25	2.47	1.26	0.67
QM:						
WSB [2]	7.95	3.14	8.13	3.21	1.34	1.02
ISGW2 [6]	10.5	4.14	5.7	2.25	0.94	0.54
Jaus [4]	9.6	3.79	5.5	2.17	1.33	0.57
Faustov [8]	7.43	2.93	4.83	1.91	1.05	0.65
Melikhov [12]	9.15	3.6	5.66	2.2	1.31	0.62
DNKO [14]	9.88	3.90	6.70	2.64	1.30	0.68
SR:						
BBD 91 [43]	6.8 ± 1.4	2.68 ± 0.55	3.9 ± 1.3	1.54 ± 0.51	0.86 ± 0.06	0.57 ± 0.15
Yang 97 [38]	$8.6^{+3.0}_{-2.5}$	$3.4^{+1.2}_{-1.0}$	4.0 ± 0.8	1.58 ± 0.32	0.87 ± 0.20	0.47 ± 0.16
Lattice:						
Lubicz 92 [44]	6.1 ± 1.6	2.41 ± 0.62	5.3 ± 0.9	2.08 ± 0.37	1.51 ± 0.27	0.85 ± 0.22
ELC 94 [39]	6.8 ± 3.4	2.68 ± 1.34	6.0 ± 2.2	2.37 ± 0.87	1.27 ± 0.29	0.92 ± 0.55
UKQCD 95 [45]	$7.4 \pm 1.7 \pm 0.4$	2.91 ± 0.71	$6.0^{+0.8}_{-1.6}$	2.37 ± 0.67	1.06 ± 0.16	0.86 ± 0.28
APE 96 [40]	9.6 ± 2.1	9.1 ± 2.0	7.3 ± 1.9	6.9 ± 0.18	1.2 ± 0.3	0.76 ± 0.20
Experiment [46] D^0		$3.78 \pm 0.12 \pm 0.25$		2.37 ± 0.29		0.62 ± 0.08

Table 8. Form factors for the decay processes $D \longrightarrow Kl\bar{\nu}_l$ and $D \longrightarrow K^*l\bar{\nu}_l$ at $q^2 = 0$

	$F_1(0)$	$V(0)$	$A_1(0)$	$A_2(0)$	$V(0)/A_1(0)$	$A_2(0)/A_1(0)$
Model I(S)	0.82	0.88	0.61	0.44	1.44	0.73
Model I	0.81	0.84	0.65	0.45	1.30	0.70
Model II(S)	0.77	0.87	0.60	0.45	1.46	0.75
Model II	0.77	0.83	0.63	0.46	1.31	0.72
QM:						
WSB [2]	0.76	1.27	0.88	1.15	1.36	1.48
ISGW2 [6]	0.76	1.10	0.80	0.80	1.37	1.0
Jaus [4]	0.78	1.04	0.66	0.43	1.58	0.65
Faustov [8]	0.73	0.62	0.63	0.43	0.98	0.68
Melikhov [12]	0.78	0.77	0.64	0.46	1.2	0.72
DKNO [14]	0.78	0.777	0.633	0.464	1.23	0.73
SR:						
BBD 91 [43]	$0.60^{+0.15}_{-0.10}$	1.10 ± 0.25	0.50 ± 0.15	0.60 ± 0.15	2.2 ± 0.2	1.2 ± 0.2
Yang 97 [38]	0.75 ± 0.12	1.1 ± 0.1	0.54 ± 0.04	0.67 ± 0.08	2.04 ± 0.19	1.24 ± 0.15
Lattice:						
Lubicz 92 [44]	0.63 ± 0.08	0.86 ± 0.10	0.53 ± 0.03	0.19 ± 0.21	0.62 ± 0.07	0.36 ± 0.40
ELC 94 [39]	0.65 ± 0.18	0.95 ± 0.34	0.63 ± 0.14	0.45 ± 0.33	1.5 ± 0.28	0.7 ± 0.4
APE 96 [40]	0.78 ± 0.08	1.08 ± 0.22	0.67 ± 0.11	0.49 ± 0.34	1.6 ± 0.3	0.7 ± 0.4
UKQCD 95 [45]	$0.67^{+0.07}_{-0.08}$	$1.01^{+0.30}_{-0.13}$	$0.70^{+0.07}_{-0.10}$	$0.66^{+0.10}_{-0.15}$	$1.4^{+0.055}_{-0.02}$	0.9 ± 0.2
Gupta 96 [47]	0.71 ± 0.04	1.28 ± 0.07	0.72 ± 0.03	0.84 ± 0.03	1.78 ± 0.07	0.68 ± 0.11
Experiment [34] D^0	0.76 ± 0.03	1.07 ± 0.09	0.58 ± 0.03	0.41 ± 0.05		

Table 9. Observables of the decays $D \longrightarrow \pi l\bar{\nu}_l$ and $D \longrightarrow \rho l\bar{\nu}_l$ (partial decay widths are expressed in units of $|V_{cd}|^2 \times 10^{10}$ s^{-1}; the calculations were performed at $|V_{cd}| = 0.24$)

	$\Gamma(\pi)$	$\mathcal{B}(\pi)$, 10^{-3}	$\Gamma(\rho)$	$\mathcal{B}(\rho)$, 10^{-3}	Γ_L/Γ_T	$\Gamma(\rho)/\Gamma(\pi)$
Model I(S)	15.6	3.73	6.54	1.56	1.29	0.42
Model I	14.4	3.44	6.83	1.62	1.34	0.47
Model II(S)	16.0	3.83	6.34	1.52	1.19	0.40
Model II	14.5	3.47	6.57	1.57	1.24	0.46
QM:						
WSB [2]	14.0	3.35	13.8	3.30	0.91	0.98
ISGW2 [6]	9.8	2.34	4.9	2.89	0.67	0.5
Jaus [4]	8.0	1.91	3.3	0.79	1.22	0.41
Melikhov [12]	12.8	3.06	5.37	1.28	1.27	0.41
DKNO [14]	15.3	3.66	7.85	1.88		0.51
SR:						
Ball 93 [37]	8.0 ± 1.7	1.91 ± 0.04	2.4 ± 0.7	0.57 ± 0.17	0.3 ± 0.1	0.31 ± 0.11
Yang 97 [38]	$13.4^{+4.4}_{-3.8}$	$3.2^{+0.11}_{-0.09}$	$2.8^{+1.5}_{-0.8}$	$0.67^{+0.36}_{-0.19}$	$0.35^{+0.37}_{-0.24}$	0.21 ± 0.10
Lattice:						
Lubicz 92 [44]	10 ± 4	0.24 ± 0.10	8 ± 2	0.19 ± 0.05	1.86 ± 0.56	0.8 ± 0.3
APE 96 [40]	16.2 ± 4.1	0.39 ± 0.10	12.2 ± 4.1	0.29 ± 0.10		
UKQCD 95 [45]	$10.6 \pm 3.7 \pm 1.0$	0.39 ± 0.10	8.7 ± 2.2	0.21 ± 0.05	$1.05^{+0.29}_{-0.20}$	0.82 ± 0.31
Experiment [34] D^0		3.1 ± 1.5		2.2 ± 0.8		

Table 10. Form factors for the decays $D \longrightarrow \pi l \bar{\nu}_l$ and $D \longrightarrow \rho l \bar{\nu}_l$ at $q^2 = 0$

	$F_1(0)$	$V(0)$	$A_1(0)$	$A_2(0)$	$V(0)/A_1(0)$	$A_2(0)/A_1(0)$
Model I(S)	0.76	0.79	0.54	0.37	1.46	0.68
Model I	0.75	0.76	0.57	0.38	1.34	0.68
Model II(S)	0.72	0.75	0.51	0.37	1.46	0.73
Model II	0.71	0.72	0.53	0.39	1.34	0.73
QM:						
WSB [2]	0.69	1.23	0.78	0.92	1.58	1.18
Jaus [4]	0.67	0.93	0.58	0.42	1.60	0.72
Melikhov [12]	0.68	0.66	0.50	0.37	1.32	0.74
DKNO [14]	0.681	0.663	0.502	0.366	1.32	0.73
SR:						
Ball 93 [37]	0.5 ± 0.1	1.0 ± 0.2	0.5 ± 0.2	0.4 ± 0.1	2.0 ± 0.8	0.8 ± 0.3
Yang 97 [38]	0.65 ± 0.10	0.98 ± 0.11	0.34 ± 0.08	0.57 ± 0.08	2.88 ± 0.68	1.68 ± 0.39
Lattice:						
Lubicz 92 [44]	0.58 ± 0.09	0.78 ± 0.12	0.45 ± 0.04	0.02 ± 0.26	1.7 ± 0.3	0.04 ± 0.50
UKQCD 95 [45]	$0.61^{+0.12}_{-0.11}$	$0.95^{+0.29}_{-0.14}$	$0.63^{+0.6}_{-0.9}$	$0.51^{+0.10}_{-0.15}$	1.5 ± 0.5	0.81 ± 0.25
Gupta 96 [47]	0.56 ± 0.08	1.18 ± 0.15	0.67 ± 0.07	0.44 ± 0.24	1.77 ± 0.16	0.67 ± 0.31

Tables 1 and 2 show the results of the calculations for $B \longrightarrow D$ and $B \longrightarrow D^*$ transitions. For $B \longrightarrow D$ transitions, the partial decay width calculated within the covariant LFD scheme is $\Gamma(B \longrightarrow D) = 9.78 \times 10^{12}|V_{bc}|^2\ s^{-1}$ (see Table 1). By using this result together with the experimental value of $\mathcal{B}(B \longrightarrow D)_{expt} = (1.95 \pm 0.27)\%$ [34], we obtain $|V_{bc}| = 0.0353 \pm 0.0024$. A calculation within the covariant LFD approach yields $\Gamma(B \longrightarrow D^*) = 22.4 \times |V_{bc}|^2$ (see Table 1). From this result and from the experimental value of $\mathcal{B}(B \longrightarrow D^*)_{expt} = (5.05 \pm 0.25)\%$, we deduce that $|V_{bc}| = 0.0387 \pm 0.0009$.

The tables quote the experimental branching fractions $\mathcal{B}(D)$ and $\mathcal{B}(D^*)$ averaged over the decays of B^0, B^+, and B_s mesons. Accordingly, the calculation of the theoretical branching fractions relied on the value of $\tau_B = 1.60 \times 10^{-12}$ s. Although the value quoted by the Particle Data Group for the branching fraction of the transition $B^0 \longrightarrow D^-(2010)^* l \bar{\nu}_l$ is $\mathcal{B}(D^-(2010)^*) = (4.60 \pm 0.27)\%$ [34], the latest experimental data yield, on average, $\mathcal{B}(D^-(2010)^*) \approx 5.5\%$: $(5.08 \pm 0.21 \pm 0.66)\%$ [50], $(5.53 \pm 0.26 \pm 0.52)\%$ [51], and $(5.52 \pm 0.17 \pm 0.68)\%$ [52]. The value of $\Gamma_L/\Gamma_T = 1.16$ (see Table 1) agrees with the experimental result 1.24 ± 0.16 [35] within the errors. The partial transition width calculated as a function of q^2 is displayed in Fig. 10, along with available experimental data [53]. The quantity $|V_{bc}|$ was set to 0.037. We can see that the theoretical curve faithfully reproduces the experimental data.

The effect of the Sudakov form factor is quite significant for B-meson decays (more significant than in the case of D-meson decays—see below), because the width of the interval of physical q^2 values is much greater than the final-meson (quark) mass: $q^2_{max} \approx 11\ GeV^2$ for $B \longrightarrow D(D^*)$ transitions and $q^2_{max} \approx 25\ GeV^2$ for $B \longrightarrow \pi(\rho)$ transitions. It can be seen from Tables 1, 2, 5, and 6, however, that this effect is compensated in part by the normalization of the Sudakov for factor at $q^2 = q^2_{max}$. Since the probability of the $B \longrightarrow D^*$ transitions is three times as great as the probability of the $B \longrightarrow D$ transition, the accuracy of an experimental determination of $\mathcal{B}(B \longrightarrow D^*)$ is higher.

The values obtained for $|V_{bc}|$, $|V_{bc}|_{(D)} = 0.0387 \pm 0.0031$ and $|V_{bc}|_{(D^*)} = 0.0394 \pm 0.0050$, comply with the results of the calculations from [12, 14] and with the values quoted in [34]. Within quark models, the value determined for $|V_{bc}|$ from data on inclusive decays are somewhat greater than the value extracted from an analysis of exclusive decays.

Figure 11 displays the calculated pseudoscalar and axial-vector form factors (ξ^{F_1} and ξ^{A_1}, respectively), which were obtained from F_1 and A_1 by the formulas

$$\xi^{A_1}(\eta) = \frac{M_1 + M_2}{2\sqrt{M_1 M_2}}\left(1 - \frac{q^2}{(M_1 + M_2)^2}\right)^{-1} A_1(\eta),$$
$$\xi^{F_1}(\eta) = \frac{M_1 + M_2}{2\sqrt{M_1 M_2}} F_1(\eta). \quad (77)$$

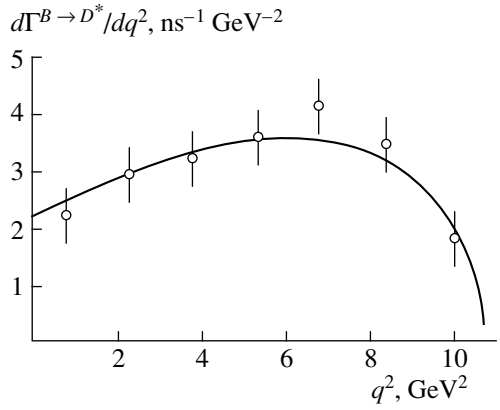

Fig. 10. Differential width $d\Gamma/dq^2$ with respect to the decay $B \longrightarrow D^*l\nu_l$. Experimental data were borrowed from [53]. The parameter $|V_{bc}|$ was set to 0.037.

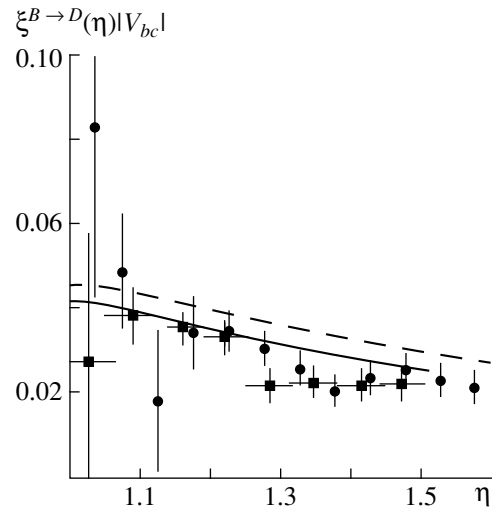

Fig. 11. Form factors (solid curve) $\xi^{A_1}(\eta)$ and (dashed curve) $\xi^{F_1}(\eta)$ as functions of $\eta = V_1V_2$. Points corresponding to the Isgur–Wise function $\xi(\eta)$ were obtained by processing experimental data on the decays (closed circles) $B \longrightarrow D^*l\nu_l$ [54] and (closed boxes) $B \longrightarrow Dl\nu_l$ [55]. The matrix element $|V_{bc}|$ was taken to be 0.037.

The form factors ξ^{A_1} and ξ^{F_1} are represented by, respectively, the solid and the dashed curve. The figure also shows experimental values (points) obtained by processing data for the differential width $d\Gamma^{D^*}/dq^2$ [54] with respect to the transition $B \longrightarrow D^*l\nu_l$ and the differential width $d\Gamma^{D}/dq^2$ [55] with respect to the transition $B \longrightarrow Dl\nu_l$. It can be seen that $b \longrightarrow c$ quark transitions are described reasonably well in the limit of the effective theory of heavy quarks and that the results in this limit comply with the results of the calculations within the covariant LPD approach.

In general, a correct comparison of the results of the calculations for $B \longrightarrow D^*$ transitions with experimental data is that which is performed directly for the differential width $d\Gamma/dq^2$ (see Fig. 10).

The problem of assessing the degree to which the physical form factors obtained by taking into account only the one-body current $J^{(\mathrm{OBC})}$ make it possible to reproduce experimental data and the degree to which these form factors comply with other models deserves a dedicated consideration. Since, in the proposed approach, the physical form factors are determined in terms of the matrix elements of the currents J_+ and $\mathbf{J}_\perp$, such an analysis would enable us to estimate the contribution of the contact interaction to LFD diagrams. It is convenient to perform this analysis for a transition of a heavy quark into a heavy one by considering the example of $B \longrightarrow D$ and $B \longrightarrow D^*$ transitions, where the results can be compared with the predictions of the effective theory of heavy quarks.

Table 3 displays observables of the decays $B \longrightarrow Dl\bar{\nu}_l$ and $B \longrightarrow D^*l\bar{\nu}_l$ for various options of potential in Eq. (74). The calculations were performed (*A*) with and (*B*) without allowance for contact interaction. In these calculations, the wave functions were determined as solutions to the wave equation (model I) for the confining potentials $V_{\mathrm{red}}(r) = c + br$ and $V_0 = c + br - 4\alpha_s/3r$ (75). Model II relies on model wave functions. The partial widths with respect to the decays $B \longrightarrow Dl\bar{\nu}_l$ and $B \longrightarrow D^*l\bar{\nu}_l$ were computed at $|V_{bc}| = 0.037$.

It can be seen from the tables that, for a transition of a pseudoscalar meson into a pseudoscalar one, the inclusion of contact interaction has virtually no effect on the results of the calculations: $\mathcal{B}(B \longrightarrow Dl\bar{\nu}_l) \approx 2.22\%$ in model I and $\mathcal{B}(B \longrightarrow Dl\bar{\nu}_l) \approx 1.94\%$ in model II, the experimental value being $(1.95 \pm 0.27)\%$. The results of the calculations with and without allowance for contact interaction differ significantly for a transition that is off-diagonal in spin, in which case the branching fractions $\mathcal{B}(D^*)$ in models *A* and *B* differ by a factor of about 1.5: $\mathcal{B}(D^*)(A) = 5.78\%$ in model *A* and $\mathcal{B}(D^*)(B) = 8.43\%$ in model *B*. In addition, the ratio Γ_L/Γ_T in model B is greater by about 15%. These effects are due primarily to the fact that, without allowance for the contact interaction, the form factor A_1, which determines the behavior of the differential width, is significantly overestimated, which can be seen from a comparison of the data in the last two columns of Table 3, which contain the form-factor ratios $V(0)/A_1(0)$ and $A_2(0)/A_1(0)$. The use of a linear potential leads to close values for integrated quantities. The results obtained with the potential V_0 are less satisfactory, because the term $4\alpha_s/3r$ leads to an overly slow decrease of the wave function in the momentum representation.

One of the problems in the approach based on model *B*, where use is made of only the one-body current and where the contact interaction is disregarded, is that it

yields a slightly exaggerated value for the branching fraction of the decay $B \longrightarrow D^* l\bar{\nu}_l$. At the most reasonable values of the potential parameters and $|V_{bc}| = 0.037$, we have $\mathcal{B}(B \longrightarrow D^*) = 8.43\%$, which exceeds considerably the experimental value of $(5.05 \pm 0.25)\%$. Obviously, the inclusion of the Sudakov form factor cannot reconcile the results of the calculations with the experimental value. The theoretical value of $\mathcal{B}(B \longrightarrow D^*)$ can be reduced by introducing a D-wave admixture in the D^*-meson wave function. For a spin-1 particle, the wave function is given by expression (16). The magnitude of the D-wave admixture depends on the coefficient c in the vertex function of the 1^- meson:

$$\left(\gamma_\nu - c\frac{(p_1 - p_2)_\nu}{M_0 + m_1 + m_2}\right)\epsilon_\nu. \tag{78}$$

In the case of the S wave, $c = 1$. Zero value of c corresponds to the presence of a D-wave admixture. We have additionally calculated the branching fraction of the $B \longrightarrow D^*$ decay under the assumption of γ_ν dominance in the $D^* \longrightarrow c\bar{q}$ vertex function—that is, at $c = 0$. The results of this calculation are quoted in Table 4. By model C, we mean that which assumes $c = 0$. The results in Table 4 were obtained without allowance for the Sudakov form factor. At the most reasonable values of the parameters in a potential of the Godfrey–Isgur type (model I C), we have $\mathcal{B}(B \longrightarrow D^* l\bar{\nu}_l) = 7.33\%$, which is in better agreement with the experimental value, but which is still considerably exaggerated. Thus, a description of the branching fraction in the model employing only the one-body current requires the presence of a D wave in the D^* meson. In the case of $c = 0$, this admixture is 0.5%. The expressions for the partial widths and branching fractions, whose values are quoted in Table 4, were obtained without allowance for the Sudakov form factor. Even upon the introduction of a D-wave admixture in the wave function of the 1^--meson, we have obtained exaggerated partial-width values not complying with experimental data.

Model B takes into account only the S wave in the final D^* meson, while model C corresponds to γ_ν dominance in the spin structure [see Eq. (78)].

Similarly, the introduction of D-wave admixtures in the wave functions of the final-state ρ and K^* mesons for the transitions $b \longrightarrow u$, $c \longrightarrow s$, and $c \longrightarrow d$ leads to the reduction of the relevant form factors and branching fractions. However, contact-interaction-induced changes in the transition form factors are sufficient in the sense that the form factors and widths obtained within the covariant LFD formalism become consistent with experimental data. In view of this, it is not necessary to introduce a D-wave admixture in the vector-meson wave function.

5.2. Transitions $B \longrightarrow \pi l\bar{\nu}_l$ and $B \longrightarrow \rho l\bar{\nu}_l$

The decays of B mesons into light π and ρ mesons make it possible to analyze the poorly known CKM-matrix element $|V_{bu}|$. Presently, measurement of this matrix element is one of the most important problems in heavy-quark physics.

The results of the calculations with the various wave functions (model I, model II) are quoted in Tables 5 and 6, along with the results from other theoretical studies. The parameters of the Sudakov form factor were taken to be $\alpha_s = 0.30$ and $\omega_{\max} = 0.5$ GeV. From these tables, we can see that the inclusion of the Sudakov form factor and the choice of model wave functions affects the results of the calculations to a degree below that which might have been expected for this quark transition.

The partial width calculated within the covariant LFD scheme for the transition $B^0 \longrightarrow \pi^- l^+ \nu_l$ into a pseudoscalar state is $\Gamma(B^0 \longrightarrow \pi^-) = 13.8 \times 10^{12}|V_{bu}|^2\ \mathrm{s}^{-1}$ (Table 5), the corresponding branching fraction being $\mathcal{B}(B^0 \longrightarrow \pi^-) = 22.1 \times |V_{bu}|^2$. Using this result together with the experimental value of $\mathcal{B}(B^0 \longrightarrow \pi^-) = (1.8 \pm 0.6) \times 10^{-4}$, we obtain $|V_{bu}| = (2.9 \pm 0.5) \times 10^{-3}$. The partial width with respect to the transition into a vector state is $\Gamma(B^0 \longrightarrow \rho^-) = 21.1 \times 10^{12}|V_{bu}|^2\ \mathrm{s}^{-1}$. On this basis, $|V_{bu}|$ can be estimated at $|V_{bu}| = (2.8 \pm 0.4) \times 10^{-3}$. Within the experimental errors, the predictions of the covariant LFD approach for $|V_{bu}|$ on the basis of data on the transitions $B \longrightarrow \pi$ and $B \longrightarrow \rho$ are consistent.

The results of our calculations for the $B \longrightarrow \pi$ and $B \longrightarrow \rho$ form factors are presented in Figs. 12–14, along with the results of the lattice calculations reported in [56, 45, 39] (see also [57]). It can be seen that, within the errors, our results agree with those lattice data.

In Figs. 15 and 16, the normalized form factors $V(q^2)/V(0)$ and $A_1(q^2)/A_1(0)$ for the $B^0 \longrightarrow \rho^-$ transition are contrasted against the pole parametrization

$$\frac{1}{(1 - q^2/M_{\mathrm{pole}})^n}, \tag{79}$$

which is traditionally used in the literature to continue form factors to the region of positive q^2 (see the review article of Stech [58]). The solid curves represent the normalized form factors $V(q^2)/V(0)$ and $A_1(q^2)/A_1(0)$ calculated in the present study, while the dashed curves correspond to the pole parametrization (79) at $n = 1$ and 2. The parameter M_{pole} is the minimum mass of a resonance that can be formed from the $b\bar{d}$ system, $M_{\mathrm{pole}} = M_B \approx M_{B^*} = 5.28$ GeV. Since the region of momentum transfers squared q^2 is wide for $B \longrightarrow \pi(\rho)$ transitions, the applicability of the pole approximation over the entire region $0 \le q^2 \le (M_1 - M_2)^2$ is questionable. Indeed, the form-factor slope with increasing q^2 is determined, in quark models, by the integrated overlap

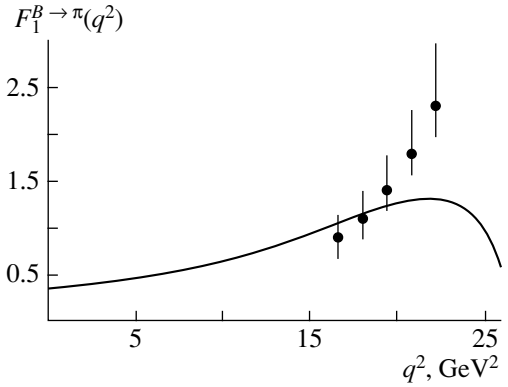

Fig. 12. Form factor $F_1(q^2)$ for the $B^0 \longrightarrow \pi^-$ transition. The results of lattice calculations were borrowed from [56].

of the wave functions of the initial and the final meson; therefore, it is directly governed by the parameters of the wave functions.

It can be seen from the figures that only at q^2 values in the vicinity of zero is it possible to obtain reasonable agreement with the model parametrization of the form factors at $n_A = 1$ (lower dashed curves in Figs. 15, 16) and $n_V = n_A + 1 = 2$ (upper dashed curves in Figs. 15, 16).

5.3. Transitions $D \longrightarrow Kl\nu_l$ and $D \longrightarrow K^*l\nu_l$

The CKM-matrix element $|V_{cs}|$ is related to $|V_{cd}|$ by the unitarity condition (see the review article of Caso *et al.* [34]) and is one of the most accurately measured ones, which is associated, among other things, with the proximity of $|V_{cs}|$ to unity and with the fact that the transitions $D \longrightarrow Kl\nu_l$ and $D \longrightarrow K^*l\nu_l$ are not suppressed by the Cabibbo selection rule.

The $D^0 \longrightarrow \bar{K}^-(K^{*-})l^+\nu_l$ semileptonic partial widths and branching fractions are quoted in Table 7. Table 8 gives the form factors $F_1(0)$, $V(0)$, $A_1(0)$, and $A_2(0)$ calculated here for model wave functions and for wave functions determined as solutions to the wave equation. The parameters of the Sudakov form factor were chosen to be $\alpha_s^{\text{eff}} = 0.30$ and $\omega_{\max} = 0.5$ GeV.

Tables 7 and 8 also display relevant experimental values and the results obtained in other theoretical studies based on lattice calculations, sum rules, and quark models. Within the errors, there is agreement with the entire body of experimental data. The inclusion of the Sudakov form factor has a modest effect (of 5 to 10%) on the $D \longrightarrow K$ partial widths $\Gamma(D \longrightarrow K)$: $\Gamma(K) = 9.77 \times 10^{10}|V_{cs}|^2$ and $10.44 \times 10^{10}|V_{cs}|^2$ s^{-1} in model I without and with allowance for the Sudakov form factor, respectively. This is explained by a relatively slow variation of the Sudakov form factor in the region $0 \le q^2 \le (M_D - M_{K,K^*}) \approx 1$ GeV^2.

The $D \longrightarrow K$ branching fraction predicted in our model is $\mathcal{B}(D \longrightarrow K) = 4.12 \times 10^{-2}|V_{cs}|^2$. By using the experimental value of $\mathcal{B}(D^0 \longrightarrow \bar{K}^- l\nu_l) = (3.78 \pm 0.12 \pm 0.25)\%$, which was obtained by the CLEO collaboration [46], we obtain $|V_{cs}| = 0.934 \pm 0.015 \pm 0.030$.

For the transition to the $\bar{K}^{*-}$ final state, the experimental errors are somewhat greater, $\mathcal{B}(D^0 \longrightarrow \bar{K}^{*-}) = (2.37 \pm 0.29) \times 10^{-2}$ (see Table 7). A comparison with the theoretical result $\mathcal{B}(D^0 \longrightarrow \bar{K}^{*-}) = 2.22 \times 10^{-2}|V_{cs}|^2$ yields $|V_{cs}| = 1.01 \pm 0.06$.

The form factors $F_1(q^2)$ and $A_1(q^2)$ as functions of q^2 are shown in Figs. 17 and 18, respectively, along with

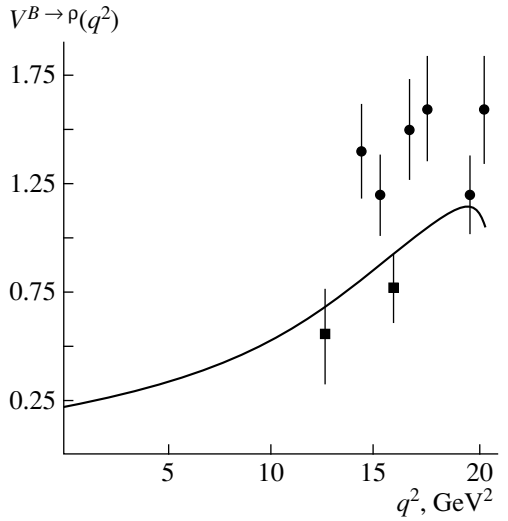

Fig. 13. Form factor $V(q^2)$ for the $B^0 \longrightarrow \rho^-$ transition. The results of lattice calculations were borrowed from (closed boxes) [45] and (closed circles) [39].

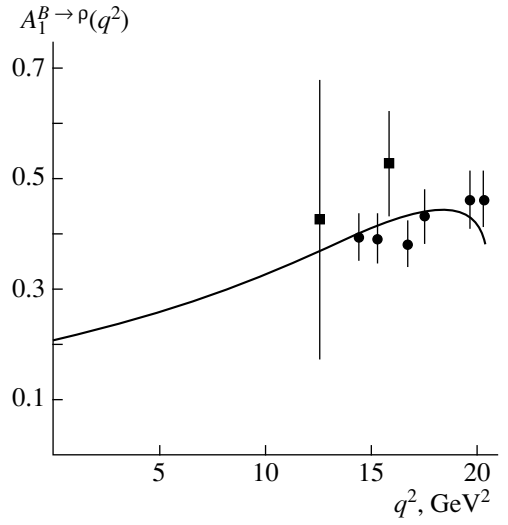

Fig. 14. Form factor $A_1(q^2)$ for the $B^0 \longrightarrow \rho^-$ transition. The results of lattice calculations were borrowed from (closed boxes) [45] and (closed circles) [39].

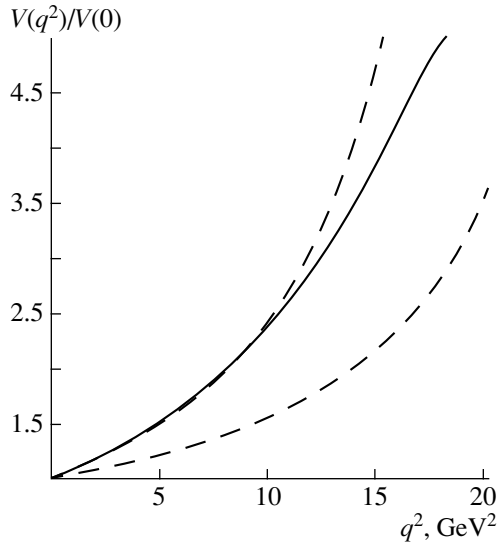

Fig. 15. Normalized form factor $V(q^2)/V(0)$ for the transition $B^0 \longrightarrow \rho^-$ (solid curve). Also shown in this figure is the pole approximation according to Eq. (79) at $n = 1$ and 2 (lower and upper dashed curves, respectively).

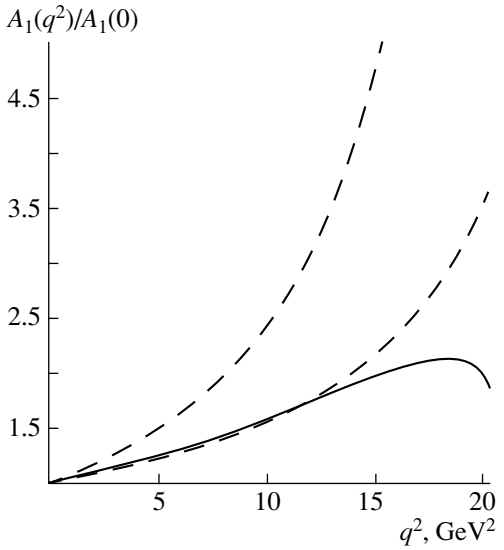

Fig. 16. Normalized form factor $A_1(q^2)/A_1(0)$ for the transition $B^0 \longrightarrow \rho^-$ (solid curve). Also shown in this figure is the pole approximation according to Eq. (79) at $n = 1$ and 2 (lower and upper dashed curves, respectively).

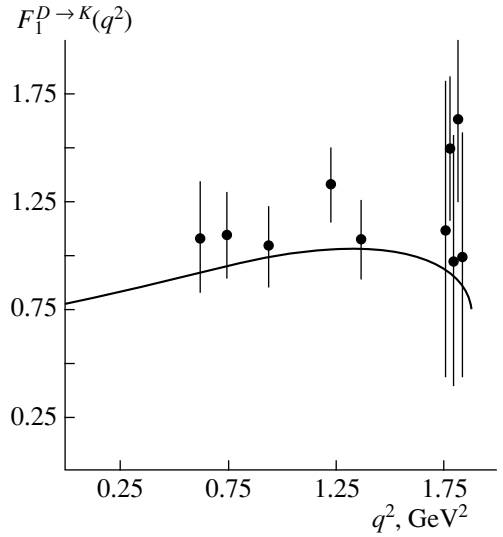

Fig. 17. Form factor $F_1(q^2)$ for the transition $D \longrightarrow Kl\nu_l$. Points represent the results of lattice calculations from [59].

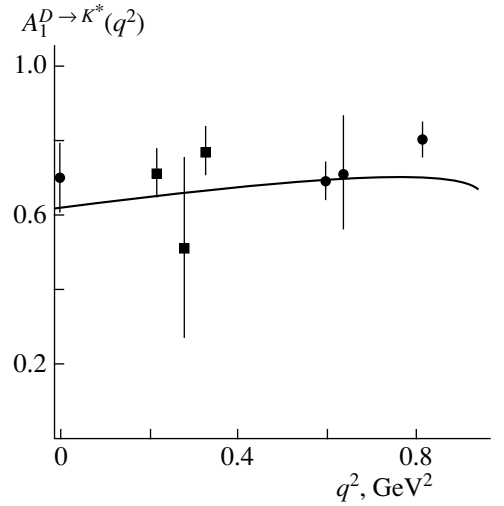

Fig. 18. Form factor $A_1(q^2)$ for the transition $D \longrightarrow K^*l\nu_l$. Points represent the results of lattice calculations from (closed boxes) [40] and (closed circles) [59].

the results of lattice calculations performed for these decays in [40, 59].

It can be stated that, by and large, the form factors calculated here are in good agreement with available experimental data and with the results of lattice calculations. For $c \longrightarrow s$ transitions, both the inclusion of the Sudakov form factor and the choice of wave functions affect the results of the calculations only slightly. The latter is associated above all with the fact that the final meson has a low recoil over the entire interval of physical q^2 values. As a consequence, the form factors are calculated predominantly in the region of the maximum overlap of the wave functions, so that they are unaffected by a decrease in the overlap of the wave functions of the initial and the final meson with increasing q^2. Within LFD, the center of mass of a bound system does not coincide with the rest frame of a composite particle; therefore, the overlap of the wave functions of the initial and the final meson is maximal in the $q^2 = (m_1 - m_2)^2$ frame and not in the frame where the initial and the final meson are at rest [$q^2 = q^2_{\max} = (M_1 - M_2)^2$].

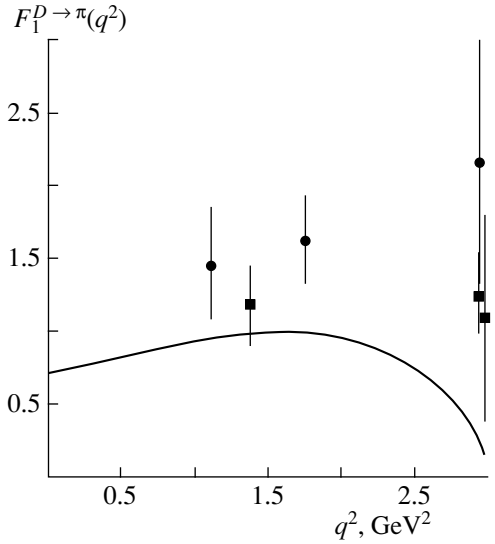

Fig. 19. Form factor $F_1(q^2)$ for the transition $D^0 \longrightarrow \pi^- l\nu_l$. Points represent the results of lattice calculations from [59].

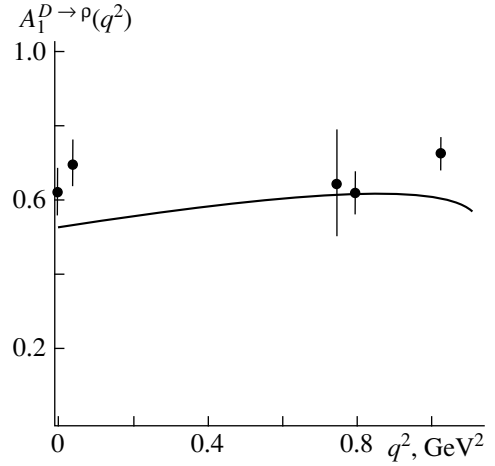

Fig. 20. Form factor $A_1(q^2)$ for the transition $D^0 \longrightarrow \rho^- l\nu_l$. Points represent the results of lattice calculations from [45].

A few comments on the value of $|f_1^K(0)|_{\exp} = 0.70$, which is quoted by the Particle Data Group [34] as an experimental value, and on the value of $|V_{cs}| = 1.04 \pm 0.16$, which follows from the former, are in order here. The value of $f_1^K(0)$ presented in [34] was obtained under the assumption that the form factor obeys the model dependence $f_1^K(q^2) = f_1^K(0)\dfrac{M_{\text{pole}}^2}{M_{\text{pole}}^2 - q^2}$, where $M_{\text{pole}} = 2.1$ GeV, in which case the $D \longrightarrow \bar{K} l\nu_l$ decay width is expressed in terms of $|V_{cs}|$ and $|f_1^K(0)|$ as

$$\Gamma(D \longrightarrow \bar{K} l\nu_l) = \left|f_1^K(0)\right|^2 |V_{cs}|^2 (1.54 \times 10^{11}\ \text{s}^{-1}). \quad (80)$$

Along with the parameter M_{pole}, the product $|V_{cs}| \times |f_1^K(0)| = 0.531 \pm 0.027$ is determined from a fit to experimental data. If one uses the value of $f_1^K(0) = 0.7 \pm 0.1$ from [2, 60, 61], the prediction for $|V_{cs}|$ appears to be $|V_{cs}| = 1.04 \pm 0.16$. It is rather difficult to assess the model uncertainty in this determination of $|V_{cs}|$. In [34], the uncertainty in determining the ratio $\left|\dfrac{V_{cd}}{V_{cs}}\right|$ was estimated at ±14%(theor). Thus, the values of $|V_{cs}|$ and $f_1^K(0)$ from [34] may serve only as guidelines.

5.4. Transitions $D \longrightarrow \pi l\bar{\nu}_l$ and $D \longrightarrow \rho l\bar{\nu}_l$

For some observables of the $D \longrightarrow \pi$ and $D \longrightarrow \rho$ transitions, including their partial widths and branching fractions, as well as for the relevant form factors at the point $q^2 = 0$, Tables 9 and 10 display the results of the calculations performed within the covariant LFD formalism on the basis of models I and II. These results are contrasted against available experimental data and against the results of lattice calculations and calculations relying on sum rules and quark models. In calculating the branching fractions quoted in Table 9, use was made of the value of $|V_{cd}| = 0.24$. The parameters of the Sudakov form factor were chosen to be $\alpha_s = 0.30$ and $\omega_{\max} = 0.5$ GeV. The inclusion of the Sudakov form factor reduces the $D \longrightarrow \rho$ branching fractions by about 10% and increases the $D \longrightarrow \pi$ branching fractions by nearly the same value. In just the same way as for $D \longrightarrow K(K^*)$ transitions, the dependence on the choice of model wave functions is insignificant.

The $D^0 \longrightarrow \pi^- l^+\nu_l$ partial width calculated within the covariant LFD formalism is $\Gamma(D^0 \longrightarrow \pi) = 15.6 \times 10^{10}|V_{cd}|^2\ \text{s}^{-1}$ (see Table 9). If one considers that the D^0-meson lifetime is $\tau_{D^0} = (0.415 \pm 0.004) \times 10^{-12}$ s, the $|V_{cd}|$ value predicted in our model is $|V_{cd}| = 0.219 \pm 0.047$. The value of $|V_{cd}| = 0.28 \pm 0.10$ is obtained by using the model prediction $\Gamma(\rho) = 6.54 \times 10^{10}|V_{cd}|^2\ \text{s}^{-1}$ (see Table 9) together with the experimental $D^0 \longrightarrow \rho^-$ branching fraction $\mathcal{B}(\rho^-) = (2.2 \pm 0.8) \times 10^{-3}$.

The $D \longrightarrow \pi$ transition form factor $F_1(q^2)$ is shown in Fig. 19, along with the results of the relevant calculations from [59]. The results of the calculations for the form factor $A_1(q^2)$ are illustrated in Fig. 20, which also displays the predictions of the lattice calculations from [45] for this form factor. We can see that the agreement with the lattice calculations for the form factor $A_1(q^2)$ is quite reasonable over the entire accessible region of q^2.

6. CONCLUSION

The semileptonic decays $B \longrightarrow D(D^*)l\bar{\nu}_l$, $B \longrightarrow (\pi)\rho l\bar{\nu}_l$, $D \longrightarrow K(K^*)l\bar{\nu}_l$, and $D \longrightarrow \pi(\rho)l\bar{\nu}_l$ have been analyzed within the covariant LFD approach. The use of the covariant LFD parametrization has enabled us to separate self-consistently physical and unphysical contributions to the form factors under study. For the above decays, we have calculated some important observables and performed a comparison with available experimental data.

The meson wave functions have been determined as solutions to the relativistic wave equation for two quarks with allowance for spin–spin interaction and for the relativistic smearing of the interaction potential. The inclusion of spin–spin interaction in solving the wave equation has led to wave functions that behave differently for the pseudoscalar and the vector meson.

For the case of different quark masses m_1 and m_2, an analytic expression for gluon corrections to the electroweak vertices for the vector and the axial-vector quark current has been obtained in the region $-\infty < q^2 \leq (m_1 - m_2)^2$. A cancellation of the infrared divergence is achieved upon summation of all diagrams involving gluon corrections in the first order in α_s. It has been shown that the inclusion of such corrections to the decay widths of heavy mesons is of importance for quantitatively describing experimental data.

By considering the example of the $B \longrightarrow D(D^*)l\nu_l$ transition form factors, we have analyzed the effect of contact interaction, as well as the effect of introducing a D-wave admixture in the vector-meson wave function. The statement that the inclusion of contact interaction is more important for $0^- \longrightarrow 1^-$ transitions than for spin-diagonal $0^- \longrightarrow 0^-$ transitions has been verified numerically. For each type of semileptonic decays, we have investigated the effect of the Sudakov form factor and the effect of the choice of meson wave functions on the results of the calculations. Our results have been compared with the results of other theoretical studies based on relativistic quark models, sum rules, and lattice calculations.

It has been shown that the semileptonic decays of mesons featuring b and c quarks can be reasonably described within the covariant LFD approach, provided that the Sudakov form is taken into account. From an analysis of the entire body of data on the $0^- \longrightarrow 0^-$ and $0^- \longrightarrow 1^-$ semileptonic decays of B and D mesons, we have determined the CKM-matrix elements $|V_{bc}|$, $|V_{bu}|$, $|V_{cs}|$, and $|V_{cd}|$. Within the experimental errors, the resulting values are intrinsically consistent and comply with available world-averaged data.

ACKNOWLEDGMENTS

We are grateful to V.A. Karmanov, I.M. Narodetskiĭ, Yu.A. Simonov, K.A. Ter-Martirosyan, and R.N. Faustov for stimulating discussions.

REFERENCES

1. M. B. Voloshin and M. A. Shifman, Yad. Fiz. **45**, 463 (1987) [Sov. J. Nucl. Phys. **45**, 292 (1987)]; **47**, 801 (1988) [**47**, 511 (1988)].
2. M. Bauer, B. Stech, and M. Wirbel, Z. Phys. C **34**, 103 (1987); **29**, 637 (1985); M. Bauer and M. Wirbel, Z. Phys. C **42**, 671 (1989).
3. N. Isgur, D. Scora, B. Grinstein, and M. B. Wise, Phys. Rev. D **39**, 799 (1989).
4. W. Jaus, Phys. Rev. D **41**, 3394 (1990).
5. R. Singleton, Phys. Rev. D **43**, 2939 (1991).
6. D. Scora and N. Isgur, Phys. Rev. D **52**, 2783 (1995).
7. V. L. Morgunov and K. A. Ter-Martirosyan, Yad. Fiz. **59**, 1279 (1996) [Phys. At. Nucl. **59**, 1221 (1996)].
8. R. N. Faustov, V. O. Galkin, and A. Y. Mishurov, Phys. Rev. D **53**, 1391 (1996).
9. R. N. Faustov, V. O. Galkin, and A. Y. Mishurov, Phys. Lett. B **356**, 316 (1995).
10. R. N. Faustov, V. O. Galkin, and A. Y. Mishurov, Phys. Rev. D **53**, 6302 (1996).
11. D. Melikhov, Phys. Rev. D **53**, 2460 (1996); Phys. Lett. B **380**, 363 (1996).
12. D. Melikhov, Phys. Lett. B **394**, 385 (1997).
13. I. L Grach, I. M. Narodetskii, and S. Simula, Phys. Lett. B **385**, 317 (1996); N. B. Demchuk, I. L. Grach, I. M. Narodetskii, and S. Simula, Yad. Fiz. **59**, 2235 (1996) [Phys. At. Nucl. **59**, 2152 (1996)].
14. N. B. Demchuk, P. Yu. Kulikov, I. M. Narodetskii, and P. J. O'Donnell, Yad. Fiz. **60**, 1429 (1997) [Phys. At. Nucl. **60**, 1292 (1997)].
15. B. Konig, J. G. Korner, M. Kramer, and P. Kroll, Phys. Rev. D **56**, 4282 (1997).
16. D. Ebert, R. N. Faustov, V. O. Galkin, *et al*., Z. Phys. C **76**, 111 (1997); D. Ebert, R. N. Faustov, and V. O. Galkin, Phys. Rev. D **56**, 312 (1997); Phys. Lett. B **434**, 365 (1998); hep-ph/9906415; hep-ph/9912357.
17. A. Yu. Anisimov, P. Yu. Kulikov, I. M. Narodetskii, and K. A. Ter-Martirosyan, Yad. Fiz. **62**, 1868 (1999) [Phys. At. Nucl. **62**, 1739 (1999)]; A. Yu. Anisimov, I. M. Narodetskii, C. Semay, and B. Silvestre-Brac, Phys. Lett. B **452**, 129 (1999).
18. L. A. Kondratyuk and D. V. Tchekin, Yad. Fiz. **61**, 337 (1998) [Phys. At. Nucl. **61**, 285 (1998)].
19. L. A. Kondratyuk and D. V. Tchekin, Yad. Fiz. **61**, 355 (1998) [Phys. At. Nucl. **61**, 302 (1998)].
20. J. Carbonell, B. Desplanques, V. A. Karmanov, and J.-F. Mathiot, Phys. Rep. **300**, 215 (1998).
21. B. Desplanques, V. A. Karmanov, and J.-F. Mathiot, Few-Body Syst., Suppl. **8**, 419 (1995).
22. A. Yu. Dubin, A. B. Kaĭdalov, and Yu. A. Simonov, Yad. Fiz. **56** (12), 213 (1993) [Phys. At. Nucl. **56**, 1745 (1993)]; A. Yu. Dubin, A. B. Kaidalov, and Yu. A. Simonov, Yad. Fiz. **58**, 348 (1995) [Phys. At. Nucl. **58**, 300 (1995)].
23. L. A. Kondratyuk, Few-Body Syst., Suppl. **6**, 512 (1992).
24. B. Desplanques, V. A. Karmanov, and J.-F. Mathiot, Nucl. Phys. A **589**, 697 (1995).
25. F. E. Close, G. J. Gounaris, and J. E. Paschalis, Phys. Lett. B **149B**, 209 (1984).

26. A. Czarnecki and K. Melnikov, hep-ph/9806258.
27. M. Neubert, Nucl. Phys. B **371**, 149 (1992).
28. U. Aglietti, G. Corbo, and L. Trentadue, Int. J. Mod. Phys. A **14**, 1769 (1999).
29. E. Bagan, P. Ball, and V. M. Braun, Phys. Lett. B **417**, 154 (1998); hep-ph/9709243.
30. V. B. Berestetskiĭ, E. M. Lifshitz, and L. P. Pitaevskiĭ, *Quantum Electrodynamics* (Nauka, Moscow, 1980; Pergamon, Oxford, 1982).
31. L. A. Kondratyuk, Yad. Fiz. **4**, 825 (1966) [Sov. J. Nucl. Phys. **4**, 587 (1966)].
32. S. Godfrey and N. Isgur, Phys. Rev. D **32**, 189 (1985).
33. S. Narison, Phys. Lett. B **283**, 384 (1992).
34. C. Caso *et al.*, Eur. Phys. J. C **3**, 1 (1998).
35. S. Sanghera *et al.*, Phys. Rev. D **47**, 791 (1993).
36. J. E. Duboscq *et al.*, Phys. Rev. Lett. **76**, 3898 (1996).
37. P. Ball, Phys. Rev. D **48**, 3190 (1993).
38. K. Yang and W. Y. Hwang, Z. Phys. C **73**, 275 (1997).
39. A. Abada *et al.*, Nucl. Phys. B **416**, 675 (1994).
40. C. Allton, Nucl. Phys. B (Proc. Suppl.) **47**, 31 (1996).
41. L. Del Debbio *et al.*, Phys. Lett. B **416**, 392 (1998).
42. P. Ball and V. M. Braun, Phys. Rev. D **58**, 094016 (1998); P. Ball, JHEP **9**, 5 (1999).
43. P. Ball, V. M. Braun, and H. G. Dosch, Phys. Rev. D **44**, 3567 (1991).
44. V. Lubicz, G. Martinelli, M. McCarthy, and C. T. Sachrajda, Phys. Lett. B **274**, 415 (1992).
45. K. C. Bowler *et al.*, Phys. Rev. D **51**, 4905 (1995).
46. A. Bean *et al.*, Phys. Lett. B **317**, 647 (1993).
47. T. Bhattacharya and R. Gupta, Nucl. Phys. B (Proc. Suppl.) **42**, 935 (1995); **47**, 481 (1996).
48. N. Isgur and M. Wise, Phys. Lett. B **232**, 113 (1989); **237**, 527 (1990).
49. M. E. Luke, Phys. Lett. B **252**, 447 (1990); C. G. Boyd and D. E. Brahm, Phys. Lett. B **257**, 393 (1991).
50. K. Ackerstaff *et al.*, Phys. Lett. B **395**, 128 (1997).
51. D. Buskulic *et al.*, Phys. Lett. B **395**, 373 (1997).
52. P. Abreu *et al.*, Z. Phys. C **71**, 539 (1996).
53. B. Barish *et al.*, Phys. Rev. D **51**, 1014 (1995).
54. M. Athanas *et al.*, Phys. Rev. Lett. **79**, 2208 (1997).
55. H. Albrecht *et al.*, Z. Phys. C **57**, 249 (1993).
56. D. R. Burford *et al.*, Nucl. Phys. B **447**, 425 (1995).
57. C. R. Allton *et al.*, Phys. Lett. B **345**, 513 (1995).
58. B. Stech, Z. Phys. C **75**, 245 (1997).
59. C. W. Bernard, A. X. El-Khadra, and A. Soni, Phys. Rev. D **43**, 2140 (1991); **45**, 869 (1992).
60. T. M. Aliev, V. L. Eletskiĭ, and Ya. I. Kogan, Yad. Fiz. **40**, 823 (1984) [Sov. J. Nucl. Phys. **40**, 527 (1984)].
61. B. Grinstein, N. Isgur, and M. B. Wise, Phys. Rev. Lett. **56**, 298 (1986).

Translated by A. Isaakyan

Physics of Atomic Nuclei, Vol. 64, No. 4, 2001, pp. 753–774. From Yadernaya Fizika, Vol. 64, No. 4, 2001, pp. 813–835.

90th ANNIVERSARY OF A.B. MIGDAL'S BIRTHDAY
ELEMENTARY PARTICLES AND FIELDS

Deep-Inelastic Scattering in κ Factorization and the Anatomy of the Differential Gluon Structure Function of the Proton*

I. P. Ivanov[1), 2), 3), **] and N. N. Nikolaev[1), 4), *]**

Received 18 July, 2000

Abstract—The differential gluon structure function of the proton, $\mathcal{F}(x, Q^2)$, introduced by Fadin, Kuraev, and Lipatov in 1975 is extensively used in small-x QCD. We report here the first determination of $\mathcal{F}(x, Q^2)$ from experimental data on the small-x proton structure function $F_{2p}(x, Q^2)$. We give convenient parametrizations for $\mathcal{F}(x, Q^2)$ based partly on the available DGLAP evolution fits (GRV, CTEQ, and MRS) to parton distribution functions and on realistic extrapolations into the soft region. We discuss the impact of soft gluons on various observables. The x dependence of the so-determined $\mathcal{F}(x, Q^2)$ varies strongly with Q^2 and does not exhibit simple Regge properties. Nonetheless, the hard-to-soft diffusion is found to give rise to a viable approximation of the proton structure function $F_{2p}(x, Q^2)$ by the soft and hard Regge components with intercepts $\Delta_{\text{soft}} = 0$ and $\Delta_{\text{hard}} \sim 0.4$. © *2001 MAIK "Nauka/Interperiodica".*

1. INTRODUCTION: WHY UNINTEGRATED GLUON STRUCTURE FUNCTIONS?

The familiar objects from the Gribov–Lipatov–Dokshitzer–Altarelli–Parisi (DGLAP) evolution description of deep-inelastic scattering (DIS) are the quark, antiquark, and gluon distribution functions $q_i(x, Q^2)$, $\bar{q}_i(x, Q^2)$, $g(x, Q^2)$ (hereafter, x and Q^2 are the standard DIS variables). At small x, they describe the integral flux of partons with light-cone momentum x in units of the target momentum and transverse momentum squared $\leq Q^2$ and form the basis of the highly sophisticated description of hard scattering processes in terms of collinear partons [1]. On the other hand, the object of the Balitsky–Fadin–Kuraev–Lipatov (BFKL) evolution equation at very small x is the differential gluon structure function (DGSF) of the target [2],

$$\mathcal{F}(x, Q^2) = \frac{\partial G(x, Q^2)}{\partial \log Q^2} \qquad (1)$$

(evidently, the related unintegrated distributions can be defined for charged partons as well). For instance, it is precisely the DGSF of the target proton that emerges in the familiar color-dipole picture of inclusive DIS at small x [3] and diffractive DIS into dijets [4]. Another familiar example is the QCD calculation of helicity amplitudes for diffractive DIS into a continuum [5, 6] and the production of vector mesons [7, 8]. Differential gluon structure functions are custom-tailored for a QCD treatment of hard processes when one needs to keep track of the transverse momentum of gluons neglected in the standard collinear approximation [9].

Over the past two decades, the DGLAP phenomenology of DIS has become a big industry and several groups—notably, GRV [10], CTEQ [11], MRS [12], and some others [13]—keep continuously incorporating new experimental data and providing the high-energy community with updates of the parton distribution functions supplemented with the interpolation routines facilitating practical applications. On the other hand, there are several pertinent issues—the onset of the purely perturbative QCD treatment of DIS and the impact of soft mechanisms of photoabsorption on the proton structure function in the large-Q^2 region are top ones on the list—that cannot be answered within the DGLAP approach itself because DGLAP evolution is obviously hampered at moderate-to-small Q^2. The related issue is that of assessing the extent to which the soft mechanisms of photoabsorption can bias the Q^2 dependence of the proton structure function and, consequently, the determination of the gluon density from scaling violations. We recall here the recent dispute [14] on the applicability of the DGLAP analysis at $Q^2 \lesssim 2$–4 GeV^2 triggered by the so-called Caldwell's plot [15]. Arguably, the κ-factorization formalism of DGSF in which the interesting observables are expanded in interactions of gluons of transverse momentum κ changing from soft to hard values is better suited to look into the issue of the soft–hard interface. Last but not least, neglecting the transverse momentum κ of gluons is a questionable approximation in evaluating cross sections for the production of jets or hadrons with high transverse momenta. It is dis-

* This article was submitted by the authors in English.

[1)] Institut für Kernphysik (Theorie), Forschungszentrum Jülich, Germany.
[2)] Sobolev Institute for Mathematics, Siberian Division, Russian Academy of Sciences, Universitetskiĭ pr. 4, Novosibirsk, 630090 Russia.
[3)] Novosibirsk State University, Novosibirsk, Russia.
[4)] Landau Institute for Theoretical Physics, Russian Academy of Sciences, ul. Kosygina 2, Moscow, 117924 Russia.
** e-mail: i.ivanov@fz-juelich.de
*** e-mail: n.nikolaev@fz-juelich.de

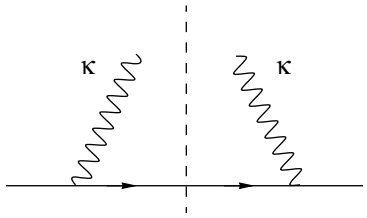

Fig. 1. The Fermi–Weizsäcker–Williams diagram for calculation of the flux of equivalent photons.

tressing, then, that convenient parametrizations of DGSF are not yet available in the literature.

In this article, we report on a simple phenomenological determination of the DGSF of the proton at small x. We analyze x and Q^2 dependences of the proton structure function $F_{2p}(x, Q^2)$ in the framework of the κ-factorization approach, which is closely related to the color-dipole factorization. In the formulation of our ansatz for $\mathcal{F}(x, \boldsymbol{\kappa}^2)$, we take advantage of a large body of early work on color-dipole factorization [3, 16, 17] and follow a very pragmatic strategy first applied in [5, 6]: (i) For hard gluons with large κ, we make as much use as possible of the existing DGLAP parametrizations of $G(x, \boldsymbol{\kappa}^2)$. (ii) For the extrapolation of hard-gluon densities to small $\boldsymbol{\kappa}^2$, we use an ansatz [4] that correctly describes the color-gauge-invariance constraints on the radiation of soft perturbative gluons by color singlet targets. (iii) As suggested by color-dipole phenomenology, we supplement the density of gluons with small $\boldsymbol{\kappa}^2$ with a nonperturbative soft component. (iv) As suggested by soft–hard diffusion inherent in BFKL evolution, we allow for the propagation of the predominantly hard-interaction-driven small-x rise of DGSF into the soft region, invoking plausible soft-to-hard interpolations. The last two components of the DGSF are parametrized on the basis of the modern knowledge of the infrared (IR) freezing of the QCD coupling and the short propagation radius of perturbative gluons. Having specified the IR regularization, we can apply the resulting $\mathcal{F}(x, \boldsymbol{\kappa}^2)$ to the evaluation of the photoabsorption cross section in the whole range of small-to-hard Q^2.

The practical realization of the above strategy is expounded as follows. The subject of Section 2 is a pedagogical introduction to the concept of DGSF by considering the example of Fermi–Weizsäcker–Williams photons in QED. Taking electrically neutral positronium as a target, we explain important constraints imposed by gauge invariance on DGSF at small κ^2. In Section 3, we present the κ-factorization approach, which forms a basis of our analysis of small-x DIS in terms of DGSF. We also comment on the connection between the standard DGLAP analysis of DIS and κ factorization and property of soft-to-hard and hard-to-soft diffusion inherent in κ factorization. In Section 4, we formulate our ansatz for DGSF. The results obtained by determining DGSF from the experimental data on the proton structure function $F_{2p}(x, Q^2)$ and on the real-photoabsorption cross section are presented in Section 5. In Section 6, we discuss the anatomy of the so-determined DGSF in the momentum space and comment on the interplay of soft and hard components in the DGSF, the integrated gluon structure function (GSF), and the proton structure function $F_{2p}(x, Q^2)$. In Section 7, we focus on the effective intercepts of x dependence and the systematics of their change from DGSF to integrated GSF to $F_{2p}(x, Q^2)$, which illustrates nicely the gross features of soft-to-hard and hard-to-soft diffusion pertinent to BFKL physics. The subject of Section 8 is a comparison of integrated gluon distributions from κ factorization and conventional DGLAP analysis of the proton structure function. As anticipated, the two distributions diverge substantially at very small x and small to moderate Q^2. In Section 9, we discuss in more detail how different observables—the scaling violations $\partial F_{2p}(x, Q^2)/\partial \log Q^2$, the longitudinal structure function $F_L(x, Q^2)$, and charm structure function $F_{2p}^{c\bar{c}}(x, Q^2)$—probe the DGSF. In Section 10, we summarize our major findings.

2. DIFFERENTIAL DENSITY OF GAUGE BOSONS: A QED EXAMPLE

For a pedagogical introduction, we recall the celebrated Fermi–Weizsäcker–Williams approximation in QED, which is the well-known precursor of the parton model (for a review, see [18]). Here, high-energy reactions in the Coulomb field of a charged particle are treated as collisions with equivalent transversely polarized photons—partons of a charged particle (Fig. 1). The familiar flux of comoving equivalent transverse soft photons carrying a light-cone fraction $x_\gamma \ll 1$ of the momentum of a relativistic particle, let it be the electron, is given by

$$dn_e^\gamma = \frac{\alpha_{\rm em}}{\pi}\frac{\boldsymbol{\kappa}^2 d\boldsymbol{\kappa}^2}{(\boldsymbol{\kappa}^2+\kappa_z^2)^2}\frac{dx_\gamma}{x_\gamma} \approx \frac{\alpha_{\rm em}}{\pi}\frac{d\boldsymbol{\kappa}^2}{\boldsymbol{\kappa}^2}\frac{dx_\gamma}{x_\gamma}. \qquad (2)$$

Here, $\boldsymbol{\kappa}$ is the photon transverse momentum and $\kappa_z = m_e x_\gamma$ is the photon longitudinal momentum in the electron Breit frame. The origin of $\boldsymbol{\kappa}^2$ in the numerator is associated with current conservation—that is, with gauge invariance. By definition, the unintegrated photon structure function of the electron is then given by

$$\mathcal{F}_\gamma(x_\gamma, \boldsymbol{\kappa}^2) = \frac{\partial G_\gamma}{\partial \log \boldsymbol{\kappa}^2} = x_\gamma \frac{dn_e^\gamma}{dx_\gamma d\log\boldsymbol{\kappa}^2} = \frac{\alpha_{\rm em}}{\pi}\left(\frac{\boldsymbol{\kappa}^2}{\boldsymbol{\kappa}^2+\kappa_z^2}\right)^2. \qquad (3)$$

If the relativistic particle is a positronium P (Fig. 2), we must take into account the destructive interference

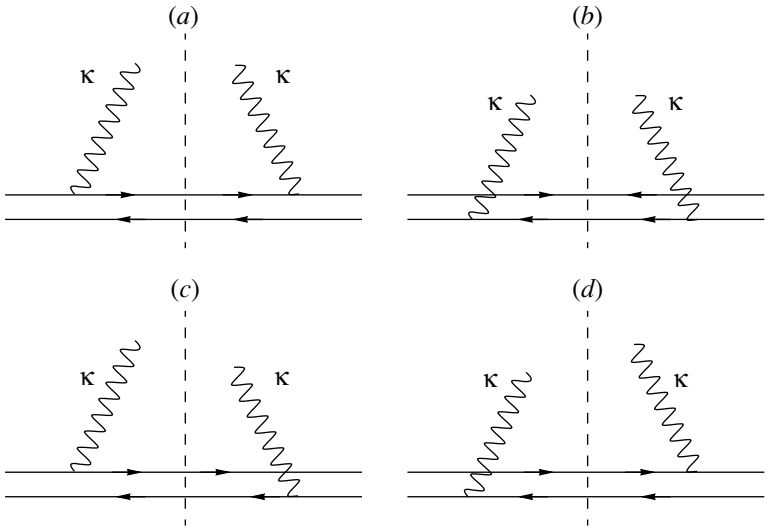

Fig. 2. The Fermi–Weizsäcker–Williams diagrams for calculating the flux of equivalent photons in positronium.

between the electromagnetic fields of the electron and positron. Specifically, the electromagnetic fields of the electron and positron cancel each other for soft photons with wavelength $\lambda = 1/\kappa \gg a_P$, where a_P is the positronium Bohr radius, and the flux of photons vanishes; for $\lambda \ll a_P$, the flux of photons will be twice as large as that for a single electron. The above properties are quantified by the formula

$$\mathcal{F}_\gamma^P(x_\gamma, \boldsymbol{\kappa}^2) = 2\frac{\alpha_{\rm em}}{\pi}\left(\frac{\boldsymbol{\kappa}^2}{\boldsymbol{\kappa}^2 + \kappa_z^2}\right)^2 V(\kappa), \tag{4}$$

where the factor of 2 is the number of charged particles in the positronium and corresponds to the Feynman diagrams in Figs. 2*a* and 2*b*. The vertex function $V(\kappa)$ is expressed in terms of the two-body form factor of the positronium as

$$\begin{aligned} V(\kappa) &= 1 - F_2(\boldsymbol{\kappa}, -\boldsymbol{\kappa}) \\ &= 1 - \langle P|\exp(i\boldsymbol{\kappa}\cdot(\mathbf{r}_- - \mathbf{r}_+))|P\rangle, \end{aligned} \tag{5}$$

where $\mathbf{r}_- - \mathbf{r}_+$ is the spatial separation of e^+ and e^- in the positronium. The two-body form factor $F_2(\boldsymbol{\kappa}, -\boldsymbol{\kappa})$ describes the destructive interference between the electromagnetic fields of the electron and positron and corresponds to the Feynman diagrams in Figs. 2*c* and 2*d*. It vanishes for sufficiently large $\kappa \gtrsim a_P^{-1}$, leaving us with $V(\kappa) = 2$, whereas, for soft gluons, one has

$$V(\kappa) \propto \boldsymbol{\kappa}^2 a_P^2. \tag{6}$$

One can say that the law in (6) is driven by electromagnetic gauge invariance, which guarantees that long-wave photons decouple from the neutral system.

Finally, we recall that the derivation of the differential flux of transversely polarized photons would apply to the case of massive vector bosons interacting with a conserved current, the only change being in the propagator. For instance, for the neutral source, one finds

$$\mathcal{F}_V^P(x_V, \boldsymbol{\kappa}^2) = \frac{\alpha_{\rm em}}{\pi}\left(\frac{\boldsymbol{\kappa}^2}{\boldsymbol{\kappa}^2 + m_V^2}\right)^2 V(\kappa). \tag{7}$$

Recall that the massive vector fields are Yukawa–Debye-screened, with the screening radius being given by

$$R_c = m_V^{-1}. \tag{8}$$

To the lowest order in QED perturbation theory, the two exchanged photons in Figs. 1 and 2 do not interact, and we will often refer to (7) as the Born approximation for the differential vector-boson structure function. One can regard (7) as a minimal model for soft-κ behavior of the differential structure function for Yukawa–Debye-screened vector bosons.

3. INSIGHT INTO THE DIFFERENTIAL DENSITY OF GLUONS

3.1. Modeling Virtual Photoabsorption in QCD

The quantity that is measured in deep inelastic leptoproduction is the total cross section of photo-absorption $\gamma_\mu^* p \longrightarrow X$ summed over all hadronic final states X, where $\mu, \nu = \pm 1, 0$ are the helicities of (T) transverse and (L) longitudinal virtual photons. One usually starts with the imaginary part of the amplitude $A_{\mu\nu}$ for the forward Compton scattering $\gamma_\mu^* p \longrightarrow \gamma_\nu^* p'$, which, by optical theorem, gives the total cross section for the photo-absorption of virtual photons,

$$\sigma_T^{\gamma^* p}(x_{\rm Bj}, Q^2) = \frac{1}{\sqrt{(W^2 + Q^2 - m_p^2)^2 + 4Q^2 m_p^2}}\,{\rm Im}\,A_{\pm\pm}, \tag{9}$$

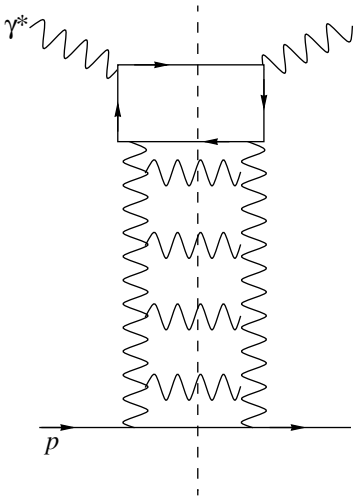

Fig. 3. The pQCD modeling of DIS in terms of multiproduction of parton final states.

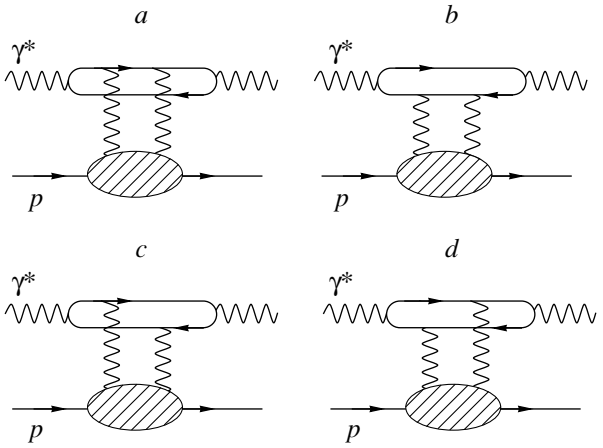

Fig. 4. The κ-factorization representation for DIS at small x.

$$\sigma_L^{\gamma^* p}(x_{\rm Bj}, Q^2) = \frac{1}{\sqrt{(W^2+Q^2-m_p^2)^2+4Q^2m_p^2}}\,{\rm Im}\,A_{00}, \qquad (10)$$

where W is the total energy in the $\gamma^* p$ c.m.s., m_p is the proton mass, Q^2 is the virtuality of the photon, and $x_{\rm Bj} = Q^2/(Q^2 + W^2 - m_p^2)$ is the Bjorken variable.

In perturbative QCD (pQCD), one models virtual photoabsorption in terms of the multiple production of gluons, quarks, and antiquarks (Fig. 3). Experimental integration over the full phase space of hadronic states X is substituted in the pQCD calculation by integration over the whole phase space of QCD partons:

$$\int |M_X|^2 d\tau_X \Rightarrow \sum_n |M_n|^2 \prod \int_0^1 \frac{dx_i}{x_i} d^2\boldsymbol{\kappa}_i, \qquad (11)$$

where the integration with respect to the longitudinal Sudakov variables x_i and the transverse momenta $\boldsymbol{\kappa}_i$ of partons goes over the whole allowed region

$$0 \le \kappa_i^2 \le \frac{1}{4}W^2 = \frac{Q^2(1-x)}{4x}. \qquad (12)$$

The core of the so-called DGLAP approximation [1] is an observation that, at finite x, the dominant contribution to the multiparton production cross sections comes from a tiny part of the phase space

$$\begin{aligned} 1 \ge x_1 \ge x_2 \ge \ldots \ge x_{n-1} \ge x_n \ge x, \\ 0 \le \kappa_1^2 \ll \kappa_2^2 \ll \ldots \ll \kappa_{n-1}^2 \ll k^2 \ll Q^2, \end{aligned} \qquad (13)$$

in which the upper limit of integration with respect to the transverse momenta of partons is much smaller than the kinematical limit (12). At very small x, this limitation of the transverse phase space becomes much too restrictive and the DGLAP approximation is doomed to failure.

Hereafter, we focus on how lifting the restrictions on the transverse phase space changes our understanding of the gluon structure function of the nucleon at very small x, that is, very large $1/x$. In this kinematical region, the gluon density $g(x, Q^2)$ is much higher than the density of charged partons $q(x, Q^2)$ and $\bar{q}(x, Q^2)$. Fadin, Kuraev, and Lipatov [2] showed that, to the leading $\log\frac{1}{x}$ $\left({\rm LL}\frac{1}{x}\right)$ approximation, the dominant contribution to photoabsorption comes from multigluon final states of Fig. 3; alternatively, to the LL$1/x$, the splitting of gluons into gluons dominates the splitting of gluons into $q\bar{q}$ pairs. As a matter of fact, we do not need the full BFKL dynamics for the purposes of the present analysis; in the κ factorization, only the $q\bar{q}$ loop is treated explicitly to the LL$1/x$ approximation. In this regime, the Compton scattering can be viewed as an interaction of the nucleon with the light-cone $q\bar{q}$ Fock states of the photon via the exchange of gluons (Fig. 4), and the Compton scattering amplitude takes the form

$$A_{\nu\mu} = \Psi^*_{\nu,\lambda\bar{\lambda}} \otimes A_{q\bar{q}} \otimes \Psi_{\mu,\lambda\bar{\lambda}}. \qquad (14)$$

Here, $\Psi_{\mu,\lambda\bar{\lambda}}$ is the light-cone photon wave function dependent on Q^2 and on the q and $\bar{q}$ helicities λ and $\bar{\lambda}$, while the QCD Pomeron-exchange $q\bar{q}$-proton scattering kernel $A_{q\bar{q}}$ does not depend on the q and $\bar{q}$ helicities and conserves them exactly, summation over these helicities being implied in (14).

The resummation of the diagrams in Fig. 3 defines the unintegrated GSF of the target, which is represented in the diagrams of Fig. 4 as the striped oval. The calculation of the forward Compton scattering amplitudes ($\boldsymbol{\Delta} = 0$) is straightforward and gives the κ-factorization formulas for photoabsorption cross sections [19, 20]

$$\sigma_T(x_{\rm Bj}, Q^2)$$

$$= \frac{\alpha_{em}}{\pi}\sum_f e_f^2 \int_0^1 dz \int d^2\mathbf{k} \int \frac{d^2\boldsymbol{\kappa}}{\boldsymbol{\kappa}^4}\alpha_S(q^2)\mathcal{F}(x_g, \boldsymbol{\kappa}^2)$$
$$\times\left\{[z^2 + (1-z)^2]\left(\frac{\mathbf{k}}{\mathbf{k}^2+\varepsilon^2} - \frac{\mathbf{k}-\boldsymbol{\kappa}}{(\mathbf{k}-\boldsymbol{\kappa})^2+\varepsilon^2}\right)^2\right. \quad (15)$$
$$\left. + m_f^2\left(\frac{1}{\mathbf{k}^2+\varepsilon^2} - \frac{1}{(\mathbf{k}-\boldsymbol{\kappa})^2+\varepsilon^2}\right)^2\right\},$$

$$\sigma_L(x_{Bj}, Q^2)$$
$$= \frac{\alpha_{em}}{\pi}\sum_f e_f^2 \int_0^1 dz \int d^2\mathbf{k} \int \frac{d^2\boldsymbol{\kappa}}{\boldsymbol{\kappa}^4}\alpha_S(q^2)\mathcal{F}(x_g, \boldsymbol{\kappa}^2) \quad (16)$$
$$\times 4Q^2z^2(1-z)^2\left(\frac{1}{\mathbf{k}^2+\varepsilon^2} - \frac{1}{(\mathbf{k}-\boldsymbol{\kappa})^2+\varepsilon^2}\right)^2.$$

Here, $\boldsymbol{\kappa}$ is the transverse momentum of the gluon; $\mathbf{k}$ is the transverse momentum in the quark–antiquark loop; z and $1 - z$ are the fractions of the light-cone momentum of the proton that are carried by the quark and the antiquark, respectively; m_f and e_f are the mass and charge of the quark $f = u, d, s, c, b, \ldots$;

$$\varepsilon^2 = z(1-z)Q^2 + m_f^2; \quad (17)$$

the QCD running coupling constant $\alpha_S(q^2)$ enters into the integrand at the largest relevant virtuality;

$$q^2 = \max\{\varepsilon^2 + \mathbf{k}^2, \boldsymbol{\kappa}^2\}; \quad (18)$$

and the density of gluons is taken at

$$x_g = \frac{Q^2 + M_t^2}{W^2 + Q^2} = x_{Bj}\left(1 + \frac{M_t^2}{Q^2}\right). \quad (19)$$

Here, M_t is the transverse mass of the produced $q\bar{q}$ pair in the photon–gluon fusion $\gamma^* g \longrightarrow q\bar{q}$:

$$M_t^2 = \frac{m_f^2 + \mathbf{k}^2}{1-z} + \frac{m_f^2 + (\mathbf{k}-\boldsymbol{\kappa})^2}{z}. \quad (20)$$

For longitudinal photons, only the transitions $\gamma_L \longrightarrow q_\lambda \bar{q}_{\bar{\lambda}}$ into states with $\lambda + \bar{\lambda} = 0$ are allowed. In σ_T, the terms $\propto m_f^2$ are the contribution of states with $\lambda + \bar{\lambda} = \mu$, whereas the dominant contribution in the scaling regime of $Q^2 \gg m_f^2$ comes from the transitions $\gamma_T \longrightarrow q_\lambda \bar{q}_{\bar{\lambda}}$ into states $\lambda + \bar{\lambda} = 0$, when the helicity of the photon is transferred to the angular momentum of the quark–antiquark pair. The corresponding transition amplitudes are $\propto \mathbf{k}$, $\mathbf{k} \pm \boldsymbol{\kappa}$ (for more discussion see [7]).

No restrictions on the transverse momentum in the $q\bar{q}$ loop, $\mathbf{k}$, and gluon momentum $\boldsymbol{\kappa}$ are imposed in the representation (15) and (16). This representation was contained essentially in the classic Fadin, Kuraev, and Lipatov papers [2] of the mid-1970s; in recent literature, it is sometimes referred to as the κ factorization.

We note that Eqs. (15) and (16) are for forward diagonal Compton scattering, but similar representation in terms of the unintegrated GSF holds also for the off-forward Compton scattering at finite momentum transfer $\boldsymbol{\Delta}$, off-diagonal Compton scattering when the virtualities of the initial and final-state photons are different, $Q_f^2 \neq Q_i^2$, including the timelike photons and vector mesons, $Q_f^2 = -m_V^2$, in the final state.

The photoabsorption cross sections define the dimensionless structure functions

$$F_{T,L}(x_{Bj}, Q^2) = \frac{Q^2}{4\pi^2\alpha_{em}}\sigma_{T,L} \quad (21)$$

and $F_2 = F_T + F_L$, which admit the familiar pQCD parton model interpretation

$$F_T(x_{Bj}, Q^2)$$
$$= \sum_{f = u, d, s, c, b, \ldots} e_f^2[q_f(x_{Bj}, Q^2) + \bar{q}_f(x_{Bj}, Q^2)], \quad (22)$$

where $q_f(x_{Bj}, Q^2)$ an $\bar{q}_f(x_{Bj}, Q^2)$ are the integrated densities of quarks and antiquarks carrying the fraction x_{Bj} of the light-cone momentum of the target and with transverse momenta $\leq Q$. Hereafter, we suppress the subscript Bj.

3.2. Where κ Factorization Meets DGLAP Factorization

Recall the familiar DGLAP equation [1] for scaling violations at small x,

$$\frac{dF_2(x, Q^2)}{d\log Q^2}$$
$$= \sum_f e_f^2 \frac{\alpha_S(Q^2)}{2\pi}\int_x^1 dy[y^2 + (1-y)^2]G\left(\frac{x}{y}, Q^2\right) \quad (23)$$
$$\approx \frac{\alpha_S(Q^2)}{3\pi}G(2x, Q^2)\sum_f e_f^2,$$

where for the sake of simplicity we only consider light flavors. Upon integration, we find

$$F_2(x, Q^2) \approx \sum_f e_f^2 \int_0^{Q^2} \frac{d\bar{Q}^2}{\bar{Q}^2}\frac{\alpha_S(\bar{Q}^2)}{3\pi}G(2x, \bar{Q}^2). \quad (24)$$

In order to see the correspondence between the κ factorization and DGLAP factorization, it is instructive to follow the derivation of (24) from the κ representation (15).

First, separate the $\boldsymbol{\kappa}^2$ integration in (15) into the DGLAP part of the gluon phase space $\boldsymbol{\kappa}^2 \lesssim \bar{Q}^2 = \varepsilon^2 + \mathbf{k}^2$ and the beyond-DGLAP region $\boldsymbol{\kappa}^2 \gtrsim \bar{Q}^2$. One readily finds

$$\left(\frac{\mathbf{k}}{\mathbf{k}^2+\varepsilon^2} - \frac{\mathbf{k}-\boldsymbol{\kappa}}{(\mathbf{k}-\boldsymbol{\kappa})^2+\varepsilon^2}\right)^2 = \begin{cases} \left(\dfrac{2z^2(1-z)^2Q^4}{\bar{Q}^8} - \dfrac{2z(1-z)Q^2}{\bar{Q}^6} + \dfrac{1}{\bar{Q}^4}\right)\boldsymbol{\kappa}^2 \\ \text{if} \quad \boldsymbol{\kappa}^2 \lesssim \bar{Q}^2 \\ \left(\dfrac{1}{\bar{Q}^2} - \dfrac{z(1-z)Q^2}{\bar{Q}^4}\right) \quad \text{if} \quad \boldsymbol{\kappa}^2 \gtrsim \bar{Q}^2. \end{cases} \tag{25}$$

Consider first the contribution from the DGLAP part of the phase space $\boldsymbol{\kappa}^2 \lesssim \bar{Q}^2$. Notice that because of the factor $\boldsymbol{\kappa}^2$ in (25), the straightforward $\boldsymbol{\kappa}^2$ integration of the DGLAP component yields $G(x_g, \bar{Q}^2)$ and $\bar{Q}^2$ is precisely the pQCD hard scale for the gluonic transverse momentum scale:

$$\int_0^{\bar{Q}^2} \frac{d\boldsymbol{\kappa}^2}{\boldsymbol{\kappa}^2}\alpha_S(q^2)\mathcal{F}(x_g, \boldsymbol{\kappa}^2)\left(\frac{\mathbf{k}}{\mathbf{k}^2+\varepsilon^2} - \frac{\mathbf{k}-\boldsymbol{\kappa}}{(\mathbf{k}-\boldsymbol{\kappa})^2+\varepsilon^2}\right)^2 = \left(\frac{2z^2(1-z)^2Q^4}{\bar{Q}^8} - \frac{2z(1-z)Q^2}{\bar{Q}^6} + \frac{1}{\bar{Q}^4}\right)G(x_g, \bar{Q}^2). \tag{26}$$

The contribution from the beyond-DGLAP region of the phase space can be evaluated as

$$\begin{aligned} &\int_{\bar{Q}^2}^{\infty} \frac{d\boldsymbol{\kappa}^2}{\boldsymbol{\kappa}^4}\alpha_S(q^2)\mathcal{F}(x_g, \boldsymbol{\kappa}^2)\left(\frac{1}{\bar{Q}^2} - \frac{z(1-z)Q^2}{\bar{Q}^4}\right) \\ &= \left(\frac{1}{\bar{Q}^4} - \frac{z(1-z)Q^2}{\bar{Q}^6}\right)\mathcal{F}(x_g, \bar{Q}^2)I(x_g, \bar{Q}^2) \\ &= \left(\frac{2z^2(1-z)^2Q^4}{\bar{Q}^8} - \frac{2z(1-z)Q^2}{\bar{Q}^6} + \frac{1}{\bar{Q}^4}\right) \\ &\quad \times \mathcal{F}(x_g, \bar{Q}^2)\log C_2(x_g, \bar{Q}^2, z). \end{aligned} \tag{27}$$

The latter form of (27) allows us to combine conveniently (26) and (27) by rescaling the hard scale in the GSF:

$$G(x_g, \bar{Q}^2) + \mathcal{F}(x_g, \bar{Q}^2)\log C_2(x_g, \bar{Q}^2, z) = G(x_g, C_2(x_g, \bar{Q}^2, z)\bar{Q}^2). \tag{28}$$

Here, the exact value of $I(x_g, \bar{Q}^2) \geq 1$ depends on the rate of the $\boldsymbol{\kappa}^2$ rise of $\mathcal{F}(x_g, \boldsymbol{\kappa}^2)$. At small x_g and small to moderate $\bar{Q}^2$, one finds $I(x_g, \bar{Q}^2)$ substantially larger than 1 and $C_2(x_g, \bar{Q}^2, z) \gg 1$ (for extended discussion, see Section 9 below).

Now change from $d\mathbf{k}^2$ integration to $d\bar{Q}^2$ and again split the z, Q^2 integration into the DGLAP part of the phase space $\bar{Q}^2 \ll \frac{1}{4}Q^2$, where either $z < \bar{Q}^2/Q^2$ or $1 - z < \bar{Q}^2/Q^2$, and the beyond-DGLAP region $\bar{Q}^2 \gtrsim \frac{1}{4}Q^2$, where $0 < z < 1$. As a result, one finds

$$\int dz[z^2 + (1-z)^2]\left(\frac{2z^2(1-z)^2Q^4}{\bar{Q}^8} - \frac{2z(1-z)Q^2}{\bar{Q}^6} + \frac{1}{\bar{Q}^4}\right) = \begin{cases} \dfrac{4}{3\bar{Q}^2Q^2} \quad \text{if} \quad \bar{Q}^2 \ll \dfrac{1}{4}Q^2 \\ \left(2A_2\dfrac{Q^4}{\bar{Q}^8} - 2A_1\dfrac{Q^2}{\bar{Q}^6} + A_0\dfrac{1}{\bar{Q}^4}\right) \quad \text{if} \quad \bar{Q}^2 \gtrsim \dfrac{1}{4}Q^2, \end{cases} \tag{29}$$

where

$$A_m = \int_0^1 dz[z^2 + (1-z)^2]z^m(1-z)^m. \tag{30}$$

Let $\bar{C}_2$ be $C_2(x_g, \bar{Q}^2, z)$ at a mean point. Notice also that $M_t^2 \sim Q^2$, so that $x_g \sim 2x$. Then the contribution from the DGLAP phase space of $\bar{Q}^2$ can be cast precisely in the form (24)

$$F_2(x, Q^2)\big|_{\text{DGLAP}} \approx \sum_f e_f^2 \int_0^{\frac{\bar{C}_2}{4}Q^2} \frac{d\bar{Q}^2}{\bar{Q}^2}\frac{\alpha_S(\bar{Q}^2)}{3\pi}G(2x, \bar{Q}^2). \tag{31}$$

The beyond-DGLAP region of the phase space gives an extra contribution of the form

$$\Delta F_2(x, Q^2)\big|_{\text{non-DGLAP}} \sim \sum_f e_f^2 \frac{\alpha_S(Q^2)}{3\pi}\int_{Q^2}^{\infty} \frac{d\bar{Q}^2}{\bar{Q}^2}\frac{Q^2}{\bar{Q}^2}G(2x, \bar{Q}^2) \sim \sum_f e_f^2 \frac{\alpha_S(Q^2)}{3\pi}G(2x, Q^2). \tag{32}$$

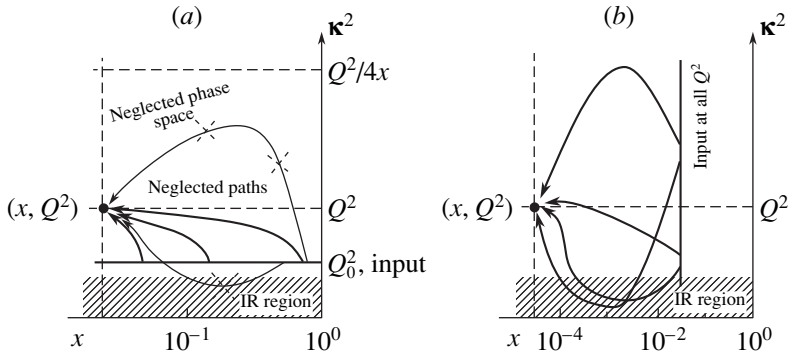

Fig. 5. Huygens principle for Q^2, x evolution of DIS structure functions with (*a*) DGLAP-restricted transverse phase space and (*b*) for the BFKL x evolution without restrictions on the transverse phase space and hard-to-soft and soft-to-hard diffusion. The "IR region" label refers to the domain of nonperturbative soft transverse momenta.

Equations (31) and (32) immediately reveal the phenomenological consequences of lifting the DGLAP restrictions in the transverse momentum integration. Indeed, the DGLAP approach respects the following strict inequalities

$$\boldsymbol{\kappa}^2 \ll \mathbf{k}^2 \quad \text{and} \quad \mathbf{k}^2 \ll Q^2. \tag{33}$$

As we just saw, removing the first limitation effectively shifted the upper limit in the $\bar{Q}^2$ integral to $\frac{\bar{C}_2}{4}Q^2 \neq Q^2$, while lifting the second constraint led to an additional, purely non-DGLAP contribution. Although both of these corrections lack one leading $\log Q^2$ factor, they are numerically substantial. As a matter of fact, in Section 9, we show that $\bar{C}_2 \approx 8$.

The above analysis suggests that the DGLAP and κ-factorization schemes converge logarithmically at large Q^2. However, in order to reproduce the results (31) and (32) for the full phase space by the conventional DGLAP contribution (24) from the restricted phase space (13), one has to ask for DGLAP gluon density $G_{\text{pt}}(x, Q^2)$ larger than the integrated GSF in the κ-factorization scheme and the difference may be quite substantial in the domain of strong scaling violations.

3.3. Different Evolution Paths: Soft-to-Hard Diffusion, and Vice Versa

The above discussion of the contributions to the total cross section from the DGLAP and non-DGLAP parts of the phase space can conveniently be cast in the form of Huygens principle. To the standard DGLAP leading $\log Q^2$ (LLQ^2) approximation, one only considers the contribution from the restricted part of the available transverse phase space (13). The familiar Huygens principle for the homogeneous DGLAP LLQ^2 evaluation of parton densities in the x_{Bj}–Q^2 plane is illustrated in Fig. 5*a*: one starts with the boundary condition $p(x, Q_0^2)$ as a function of x at fixed Q_0^2, the evolution paths $(z, \tilde{Q}^2)$ for the calculation of $p(x, Q^2)$ shown in Fig. 5*a* are confined to a rectangle $x \le z \le 1$, $Q_0^2 \le \tilde{Q}^2 \le Q^2$, the evolution is unidirectional in the sense that there is no feedback on the x dependence of $p(x, Q_1^2)$ from the x dependence of $p(x, Q_2^2)$ at $Q_2^2 \ge Q_1^2$. In Fig. 5*a*, we show some examples of evolution paths which are kinematically allowed but neglected in the DGLAP approximation. Starting with about flat or slowly rising $G(x, Q_0^2)$, one finds that the larger Q^2, the steeper the small-x rise of $G(x, Q^2)$.

At $x \ll 1$, the DGLAP contribution from the restricted transverse phase space (13) no longer dominates the multiparton production cross sections, the restriction (13) must be lifted, and the contribution to the cross section from small $\boldsymbol{\kappa}_i^2$ and large $\boldsymbol{\kappa}_i^2 \gtrsim Q^2$ can no longer be neglected. Huygens principle for the homogeneous BFKL evolution is illustrated in Fig. 5*b*: one starts with the boundary condition $\mathcal{F}(x_0, Q^2)$ as a function of Q^2 at fixed $x_0 \ll 1$, and the evolution paths $(z, \tilde{Q}^2)$ for the calculation of $p(x, Q^2)$ are confined to a stripe $x \le z \le x_0$. In contrast to the unidirectional DGLAP evolution, one can say that, under BFKL evolution, the small-x behavior of $p(x, Q^2)$ at large Q^2 is fed partly by the x dependence of soft $p(x, Q^2)$ at larger x and vice versa. The most dramatic consequence of this soft-to-hard and hard-to-soft diffusion, which cannot be eliminated, is that, at very small x, the x dependence of the gluon structure in the soft and hard regions will eventually be the same:

$$\lim_{1/x \to \infty} G(x, Q^2) = G(Q^2)\left(\frac{1}{x}\right)^{\Delta_{\text{IP}}}, \tag{34}$$

Parameters of the DGSF for various DGLAP inputs

DGSF	D-GRV	D-MRS	D-CTEQ
LO DGLAP input	GRV98LO [10]	MRS-LO-1998 [12]	CTEQ4L (v.4.6) [11]
Q_c^2, GeV^2	0.895	1.37	3.26
κ_h^2, GeV^2	$(1 + 0.0018\log^4\frac{1}{x})^{1/2}$	$(1 + 0.038\log^2\frac{1}{x})^{1/2}$	$(1 + 0.047\log^2\frac{1}{x})^{1/2}$
μ_{soft}, GeV	0.1	0.07	0.1

where Δ_{IP} is the intercept of the rightmost BFKL singularity. The rate of such hard-to-soft diffusion is evidently sensitive to the IR regularization of pQCD; the model estimates show that it is very slow in the HERA range of x [16, 21, 22].

4. ANSATZ FOR DIFFERENTIAL GLUON STRUCTURE FUNCTION

The major insight into the parametrization of DGSF comes from early experience with color-dipole phenomenology of small-x DIS. In the color-dipole approach, which is closely related to κ factorization, the principal quantity is the total cross section of interaction of the $q\bar{q}$ color dipole $\mathbf{r}$ with the proton target [3, 20, 23]

$$\sigma(x, r) = \frac{\pi^2 r^2}{3}\int\frac{d\boldsymbol{\kappa}^2}{\boldsymbol{\kappa}^2}\frac{4[1 - J_0(\kappa r)]}{(\kappa r)^2} \times \alpha_S\left(\max\left\{\boldsymbol{\kappa}^2, \frac{A}{r^2}\right\}\right)\mathcal{F}(x, \boldsymbol{\kappa}^2), \quad (35)$$

which for very small color dipoles can be approximated by

$$\sigma(x, r) = \frac{\pi^2 r^2}{3}\alpha_S\left(\frac{A}{r^2}\right)G\left(x, \frac{A}{r^2}\right), \quad (36)$$

where $A \approx 10$ comes from properties of the Bessel function $J_0(z)$. The phenomenological properties of the dipole cross section are well understood (for extraction of $\sigma(x, r)$ from the experimental data, see [24, 25]). The known dipole-size dependence of $\sigma(x, r)$ serves as a constraint on the possible $\boldsymbol{\kappa}^2$ dependence of $\mathcal{F}(x, \boldsymbol{\kappa}^2)$.

As we argued in Subsection 3.2, DGLAP fits are likely to overestimate $\mathcal{F}_{hard}(x, \boldsymbol{\kappa}^2)$ at moderate $\boldsymbol{\kappa}^2$. Still, approximation (36) does a good job when the hardness A/r^2 is very large, and at large Q^2 we can arguably approximate the DGSF by the direct differentiation of available fits (GRV, CTEQ, MRS, …) to the integrated GSF $G_{pt}(x, Q^2)$:

$$\mathcal{F}_{pt}(x, \boldsymbol{\kappa}^2) \approx \frac{\partial G_{pt}(x, \boldsymbol{\kappa}^2)}{\partial\log\boldsymbol{\kappa}^2}. \quad (37)$$

Hereafter, the subscript "pt" serves as a reminder that these gluon distributions were obtained from the pQCD evolution analyses of the proton structure function and cross sections of related hard processes.

The available DGLAP fits are only applicable at $\boldsymbol{\kappa}^2 \geq Q_c^2$ (see table for the values of Q_c^2); in the extrapolation to soft region $\boldsymbol{\kappa}^2 \leq Q_c^2$, we are bound to an educated guess. To this end, we recall that perturbative gluons are confined and do not propagate over large distances; recent fits [26] to the lattice QCD data suggest Yukawa–Debye screening of perturbative color fields with a propagation/screening radius $R_c \approx 0.27$ fm. Incidentally, precisely this value of R_c for Yukawa screened color fields has been used since 1994 in the very successful color-dipole phenomenology of small-x DIS [16, 17]. Furthermore, the important finding of [17] is a good quantitative description of the rising component of the proton structure function starting with the Yukawa-screened perturbative two-gluon exchange as a boundary condition for the color-dipole BFKL evolution.

The above suggests that, to the Born approximation, the $\boldsymbol{\kappa}^2$ dependence of perturbative hard $\mathcal{F}_{hard}(x, \boldsymbol{\kappa}^2)$ in the soft region $\boldsymbol{\kappa}^2 \leq Q_c^2$ is similar to the Yukawa-screened flux of photons in the positron [cf. Eq. (4)] with α_{em} replaced by the running strong coupling of quarks $C_F\alpha_S(\boldsymbol{\kappa}^2)$ and with factor N_c instead of two leptons in the positronium (for the early discussion, see [4])

$$\mathcal{F}_{pt}^{(B)}(\boldsymbol{\kappa}^2) = C_F N_c\frac{\alpha_S(\boldsymbol{\kappa}^2)}{\pi}\left(\frac{\boldsymbol{\kappa}^2}{\boldsymbol{\kappa}^2 + \mu_{pt}^2}\right)^2 V_N(\kappa). \quad (38)$$

Here, $\mu_{pt} = 1/R_c = 0.75$ GeV is the inverse Yukawa screening radius and must not be interpreted as a gluon mass; more sophisticated forms of screening can be considered. Following [16, 17, 19, 21], we also impose the IR freezing of strong coupling: $\alpha_S(\boldsymbol{\kappa}^2) \leq 0.82$; recently, the concept of freezed coupling has become very popular (for a review, see [27]).

The vertex function $V_N(\kappa)$ describes the decoupling of soft gluons, $\kappa \ll 1/R_p$, from color-neutral proton and has the same structure as in Eq. (5). In the nonrelativis-

tic oscillator model for the nucleon, one can relate the two-quark form factor of the nucleon to the single-quark form factor,

$$F_2(\boldsymbol{\kappa}, -\boldsymbol{\kappa}) = F_1\left(\frac{2N_c}{N_c-1}\boldsymbol{\kappa}^2\right). \quad (39)$$

To the extent that $R_c^2 \ll R_p^2$, the detailed functional form of $F_2(\boldsymbol{\kappa}, -\boldsymbol{\kappa})$ is not crucial, and the simple relation (39) will be used also for a more realistic dipole approximation

$$F_1(\boldsymbol{\kappa}^2) = \frac{1}{(1+\boldsymbol{\kappa}^2/\Lambda^2)^2}. \quad (40)$$

The gluon probed radius of the proton and the charge radius of the proton can be somewhat different and $\Lambda \sim 1$ GeV must be regarded as a free parameter. Anticipating the forthcoming discussion of the diffraction slope in vector-meson production, we put $\Lambda = 1$ GeV.

As discussed above, the hard-to-soft diffusion makes the DGSF rise at small x even in the soft region. We model this hard-to-soft diffusion by matching the $\boldsymbol{\kappa}^2$ dependence (38) to the DGLAP fit $\mathcal{F}_{\rm pt}(x, Q_c^2)$ at the soft-hard interface Q_c^2 and assigning to $\mathcal{F}_{\rm hard}(x, \boldsymbol{\kappa}^2)$ in the region of $\boldsymbol{\kappa}^2 \le Q_c^2$ the same x dependence as shown by the DGLAP fit $\mathcal{F}_{\rm pt}(x, Q_c^2)$; i.e.,

$$\mathcal{F}_{\rm hard}(x, \boldsymbol{\kappa}^2) = \mathcal{F}_{\rm pt}^{(\rm B)}(\boldsymbol{\kappa}^2)\frac{\mathcal{F}_{\rm pt}(x, Q_c^2)}{\mathcal{F}_{\rm pt}^{(\rm B)}(Q_c^2)}\theta(Q_c^2-\boldsymbol{\kappa}^2) + \mathcal{F}_{\rm pt}(x, \boldsymbol{\kappa}^2)\theta(\boldsymbol{\kappa}^2 - Q_c^2). \quad (41)$$

Because the accepted propagation radius $R_c \sim 0.3$ fm for perturbative gluons is short compared to a typical range of strong interaction the dipole cross section (35) evaluated with the DGSF (41) would miss an interaction strength in the soft region, for large color dipoles.

In [16, 17], the interaction of large dipoles has been modeled by the nonperturbative soft mechanism with an energy-independent dipole cross section, whose specific form [16, 8] has been driven by the early analysis [19] of the exchange of two nonperturbative gluons. More recently, several closely related models for $\sigma_{\rm soft}(r)$ have appeared in the literature (see, for instance, models for dipole–dipole scattering via polarization of nonperturbative QCD vacuum [28] and the model of soft–hard two-component Pomeron [29]). In order to reproduce the required interaction strength for large dipoles, we introduce the genuinely soft, nonperturbative component of DGSF which we parametrize as

$$\mathcal{F}_{\rm soft}^{(\rm B)}(x, \boldsymbol{\kappa}^2) = a_{\rm soft}C_F N_c\frac{\alpha_S(\boldsymbol{\kappa}^2)}{\pi}\left(\frac{\boldsymbol{\kappa}^2}{\boldsymbol{\kappa}^2+\mu_{\rm soft}^2}\right)^2 V_N(\kappa). \quad (42)$$

The principal point about this nonperturbative component of DGSF is that it must not be subjected to pQCD evolution. Thus, the arguments about the hard-to-soft diffusion-driven rise of perturbative DGSF even at small $\boldsymbol{\kappa}^2$ do not apply to the nonperturbative DGSF and we take it as the energy-independent one. Such a nonperturbative component of the DGSF would have a certain high-$\boldsymbol{\kappa}^2$ tail which should not extend too far. The desired suppression of soft DGSF at large $\boldsymbol{\kappa}^2$ and of hard DGSF (41) at moderate and small $\boldsymbol{\kappa}^2$ can be achieved by the extrapolation of the form suggested in [5, 6]:

$$\mathcal{F}(x, \boldsymbol{\kappa}^2) = \mathcal{F}_{\rm soft}^{(\rm B)}(x, \boldsymbol{\kappa}^2)\frac{\kappa_s^2}{\boldsymbol{\kappa}^2+\kappa_s^2} + \mathcal{F}_{\rm hard}(x, \boldsymbol{\kappa}^2)\frac{\boldsymbol{\kappa}^2}{\boldsymbol{\kappa}^2+\kappa_h^2}. \quad (43)$$

The above-described ansatz for DGSF must be regarded as a poor man's approximation, and the parameters entering into Eqs. (42) and (43) will be discussed below in Section 5.1. The separation of small-$\boldsymbol{\kappa}^2$ DGSF into the genuine nonperturbative component and small-$\boldsymbol{\kappa}^2$ tail of the hard perturbative DGSF is not unique. Specifically, we attributed to the latter the same small-x rise as in the DGLAP fits at Q_c^2, while one cannot exclude that the hard DGSF has a small x-independent component. The issue of soft–hard separation must be addressed in dynamical models for IR regularization of perturbative QCD. As we shall see below, in Section 5.1, the soft component of the above-described ansatz is about twice as large as the soft component used in the early color-dipole phenomenology [16, 17].

The κ-factorization formulas (15) and (16) correspond to the full-phase space extension of the LO DGLAP approach at small x. For this reason, our ansatz for $\mathcal{F}_{\rm hard}(x, Q^2)$ will be based on LO DGLAP fits to the GSF of the proton $G_{\rm pt}(x, Q^2)$. We consider the GRV98LO [10], CTEQ4L, version 4.6 [11], and MRS-LO-1998 [12] parametrizations. We take the liberty of referring to our ansatz for DGSF based on those LO DGLAP input as D-GRV, D-CTEQ, and D-MRS parametrizations, respectively.

Our formulas (15) and (16) describe the sea component of the proton structure function. Arguably, these LL1/x formulas are applicable at $x \lesssim x_0 = (1\text{–}3)\times 10^{-2}$. At large Q^2, the experimentally attainable values of x are not so small. In order to give a crude idea of the finite-energy effects at moderately small x, we stretch our fits to $x \gtrsim x_0$, multiplying the above ansatz for DGSF by the purely phenomenological factor $(1-x)^5$ motivated by the familiar large-x behavior of DGLAP parametrizations of the GSF of the proton. We also add to the sea components (15) and (16), the contribution from DIS on valence quarks borrowing the parametrizations from the respective GRV, CTEQ, and MRS fits.

The latter are only available for $Q^2 \geq Q_c^2$. At $x \lesssim 10^{-2}$, this valence contribution is small and fades away rapidly with decreasing x (for instance, see [17]).

5. DETERMINATION OF THE DIFFERENTIAL GLUON STRUCTURE FUNCTION OF THE PROTON

5.1. Parameters of DGFS for Different DGLAP Inputs

Our goal is a determination of the small-x DGSF in the whole range of $\boldsymbol{\kappa}^2$ by adjusting the relevant parameters to the experimental data on small-x $F_{2p}(x, Q^2)$ in the whole available region of Q^2 as well as the real photoabsorption cross section. The theoretical calculation of these observables is based on Eqs. (15), (16), and (43).

The parameters which we did not try adjusting but borrowed from early work in the color-dipole picture are $R_c = 0.27$ fm, i.e., $\mu_{\rm pt} = 0.75$ GeV, and the frozen value of the LO QCD coupling with $\Lambda_{\rm QCD} = 0.2$ GeV:

$$\alpha_S(Q^2) = \min\left\{0.82, \frac{4\pi}{\beta_0 \log(Q^2/\Lambda^2_{\rm QCD})}\right\}. \qquad (44)$$

We recall that the GRV, MRS, and CTEQ fits to GSF start the DGLAP evolution at quite a different soft-to-hard interface Q_c^2 and diverge quite a lot, especially at moderate and small $\boldsymbol{\kappa}^2$. The value of Q_c^2 is borrowed from these fits and is not a free parameter.

The adjustable parameters are $\mu_{\rm soft}$, $a_{\rm soft}$, $m_{u,d}$, κ_s^2, and κ_h^2. We take $m_s = m_{u,d} + 0.15$ GeV and $m_c = 1.5$ GeV. The role of these parameters is as follows. The quark mass $m_{u,d}$ defines the transverse size of the $q\bar{q} = u\bar{u}, d\bar{d}$ Fock state of the photon, whereas $\mu_{\rm soft}^{-2}$ controls the r dependence of, and in conjunction with $a_{\rm soft}$ sets the scale for, the dipole cross section for large-size $q\bar{q}$ dipoles in the photon. The both $m_{u,d}$ and $\mu_{\rm soft}$ have clear physical meaning and we have certain insight into their variation range from the early work on color-dipole phenomenology of DIS. The magnitude of the dipole cross section at large and moderately small dipole size depends also on the soft-to-hard interpolation of DGSF, which is somewhat different for different LO DGLAP inputs for $G_{\rm pt}(x, Q^2)$. This difference of DGLAP inputs can be corrected for by adjusting $\mu_{\rm soft}^2$ and the value of κ_h^2. Because of soft-to-hard and hard-to-soft diffusion, the DGLAP fits are expected to fail at small x; therefore, we allow for the x dependence of κ_h^2.

Evidently, roughly equal values of $F_{2p}(x, Q^2)$ can be obtained for somewhat smaller $\mathcal{F}(x, Q^2)$ at the expense of taking smaller $m_{u,d}$ and vice versa. Therefore, though the quark mass does not explicitly enter into the parametrization for $\mathcal{F}(x, \boldsymbol{\kappa}^2)$, the preferred value of $m_{u,d}$ turns out to be correlated with the ansatz for DGSF; i.e., each particular parametrization of DGSF implies a certain $m_{u,d}$. In what follows, we set $a_{\rm soft} = 2$, $\kappa_s^2 = 3.0\ {\rm GeV}^2$, and $m_{u,d} = 0.22$ GeV, so that only κ_h^2 and $\mu_{\rm soft}$ varied from one DGLAP input to another (see table). The soft components of the D-GRV and D-CTEQ parametrizations turn out to be identical. The eyeball fits are sufficient for the purposes of the present exploratory study. The parameters found are similar to those used in [5, 6], where the focus has been on the description of diffractive DIS.

One minor problem encountered in numerical differentiation of all three parametrizations for $G_{\rm pt}(x, Q^2)$ was the seesaw $\boldsymbol{\kappa}^2$ behavior of the resulting DGSF (37), which was an artifact of the grid interpolation routines. Although this seesaw behavior of DGSF is smoothed out in integral observables like $G(x, Q^2)$ or $F_{2p}(x, Q^2)$, we still preferred to remove the unphysical seesaw cusps and have smooth DGSF. This was achieved by calculation of DGSF from (37) at the center of each interval of the Q^2 grid and further interpolation of the results between these points. by integration of the so-smoothed $\mathcal{F}_{\rm pt}(x, Q^2)$ one recovers the input $G_{\rm pt}(x, Q^2)$. The values of Q_c^2 cited in the table correspond to centers of the first bin of the corresponding Q^2 grid.

5.2. Description of the Proton Structure Function $F_{2p}(x, Q^2)$

We focus on the sea dominated LL1/x region of $x < 10^{-2}$. The practical calculation of the proton structure function involves the two running arguments of DGSF: x_g and $\boldsymbol{\kappa}^2$. We recall that in the standard collinear DGLAP approximation, one has $\boldsymbol{\kappa}^2 \ll k^2 \ll Q^2$ and $x_g \approx 2x$ [see Eq. (23)]. Within the κ factorization, one finds that the dominant contribution to $F_{2p}(x, Q^2)$ comes from $M_t^2 \sim Q^2$ with little contribution from $M_t^2 \gtrsim Q^2$. Because at small x_g, the x_g dependence of $\mathcal{F}(x_g, Q^2)$ is rather steep, we take into account the x_g–$x_{\rm Bj}$ relationship (19).Anticipating the results on effective intercepts to be reported in Section 7, we notice that for all practical purposes one can neglect the impact of $\boldsymbol{\kappa}$ on relationship (19), which simplifies greatly the numerical analysis. Indeed, the x_g dependence of $\mathcal{F}(x_g, \boldsymbol{\kappa}^2)$ is important only at large $\boldsymbol{\kappa}^2$, which contribute to $F_{2p}(x, Q^2)$ only at large Q^2; but the larger Q^2, the better holds the DGLAP ordering $\boldsymbol{\kappa}^2 \ll k^2, Q^2$. Although at small to moderate Q^2, the DGLAP ordering breaks down, the x_g dependence of $\mathcal{F}(x_g, \boldsymbol{\kappa}^2)$ is negligibly weak here.

As we shall discuss in more detail below, achieving a good agreement from small to moderate to large Q^2 is a highly nontrivial task, because strong modification of

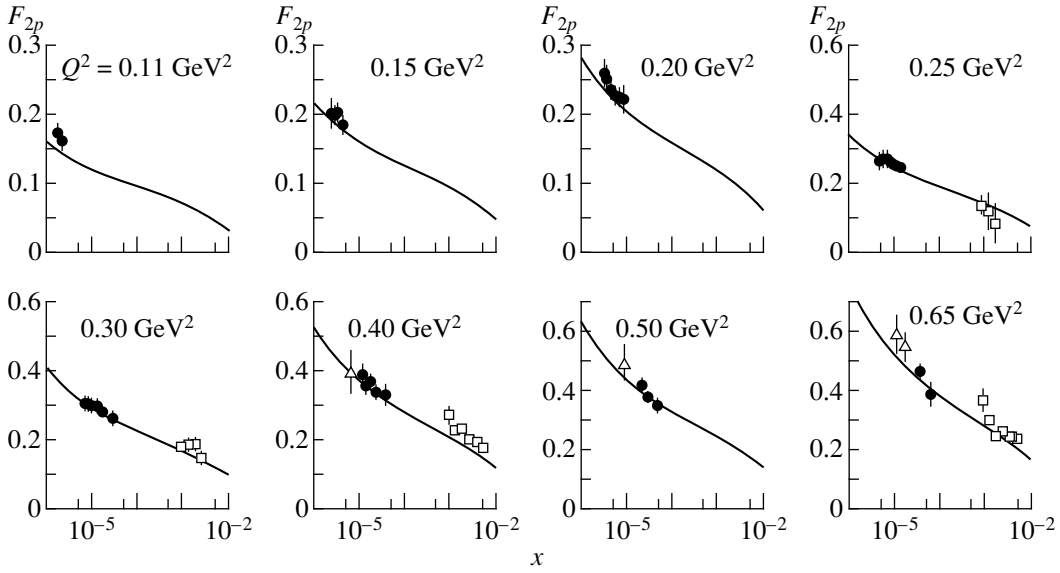

Fig. 6. The κ-factorization description of the experimental data on $F_{2p}(x, Q^2)$ in the low-Q^2 region: open squares are E665 data [30], closed circles are ZEUS BPC data [31], open triangles denote H1 shifted vertex data [32]. The solid curve represents κ-factorization results based on the D-GRV parametrization of the DGSF $\mathcal{F}(x, \boldsymbol{\kappa}^2)$.

the soft contribution to $\mathcal{F}(x, Q^2)$ unavoidably echoes in the integral quantity $G_D(x, Q^2)$ throughout the whole range of Q^2 and shall affect the calculated structure function from small to moderate to large Q^2.

The quality of the achieved description of the experimental data on the small-x proton structure function is illustrated in Figs. 6 and 7. The data shown include recent FNAL E665 experiment [30], HERA data (ZEUS BPC [31], H1 shifted vertex [32], ZEUS [33], ZEUS shifted vertex [34], H1 [35]), and CERN NMC experiment [36]. When plotting the E665 and NMC data, we took the liberty of shifting the data points from the reported values of Q^2 to the closest Q^2 boxes for which the HERA data are available. For $Q^2 < Q_c^2 = 0.9$ GeV^2, the parametrizations for valence distributions are not available and our curves show only the sea component of $F_{2p}(x, Q^2)$, at larger Q^2 the valence component is included.

At $x < 10^{-2}$, the accuracy of our D-GRV description of the proton structure function is commensurate to that of the accuracy of standard LO GRV fits. In order not to cram the figures with nearly overlapping curves, we show the results for D-GRV parametrization. The situation with D-CTEQ and D-MRS is very similar, which is seen in Fig. 8, where we show on a larger scale simultaneously the results from the D-GRV, D-CTEQ, and D-MRS DGSFs for several selected values of Q^2. Here, at large Q^2 we show separately the contribution from valence quarks. The difference between the results for $F_{2p}(x, Q^2)$ for different DGLAP inputs is marginal for all the practical purposes (see also a comparison of the results for $\sigma^{\gamma p}$ for different DGLAP inputs in Fig. 9).

5.3. Cross Section for Real Photoabsorption

In the limiting case of $Q^2 = 0$, the relevant observable is the real photoabsorption cross section $\sigma^{\gamma p}$. Although the Bjorken variable is meaningless at very small Q^2, the gluon variable x_g remains well defined at $Q^2 = 0$ [see Eq. (19)]. In Fig. 9, we present our results alongside with the results of the direct measurements of $\sigma^{\gamma p}$ and the results of extrapolation of virtual photoabsorption cross sections to $Q^2 = 0$ (for the summary of the experimental data, see [31]). We emphasize that we reproduce the observed magnitude and pattern of the energy dependence of $\sigma^{\gamma p}$ in an approach with the manifestly energy-independent soft contribution to the total cross section (which is shown separately in Fig. 9). We recall that our parametrizations for $\mathcal{F}(x, Q^2)$ give identical soft cross sections for the GRV and CTEQ inputs (see table). The barely visible decrease of $\sigma_{\text{soft}}^{\gamma p}$ towards small W is a manifestation of the $(1 - x)^5$ large-x behavior of gluon densities. The extension to lower energies requires introduction of the secondary Reggeon exchanges, which goes beyond the subject of this study.

In our scenario, the energy dependence of $\sigma^{\gamma p}$ is entirely due to the x_g-dependent hard component $\mathcal{F}_{\text{hard}}(x_g, Q^2)$ and as such this rise of the total cross section for soft reaction can be regarded as driven entirely by very substantial hard-to-soft diffusion. Such a scenario has repeatedly been discussed earlier [16, 17, 37]. Time and again, we shall see similar effects of hard-to-soft diffusion and vice versa. Notice that hard-to-soft diffusion is a straightforward consequence of full phase-space calculation of partonic cross sections and we do not see any possibility for decoupling of hard-

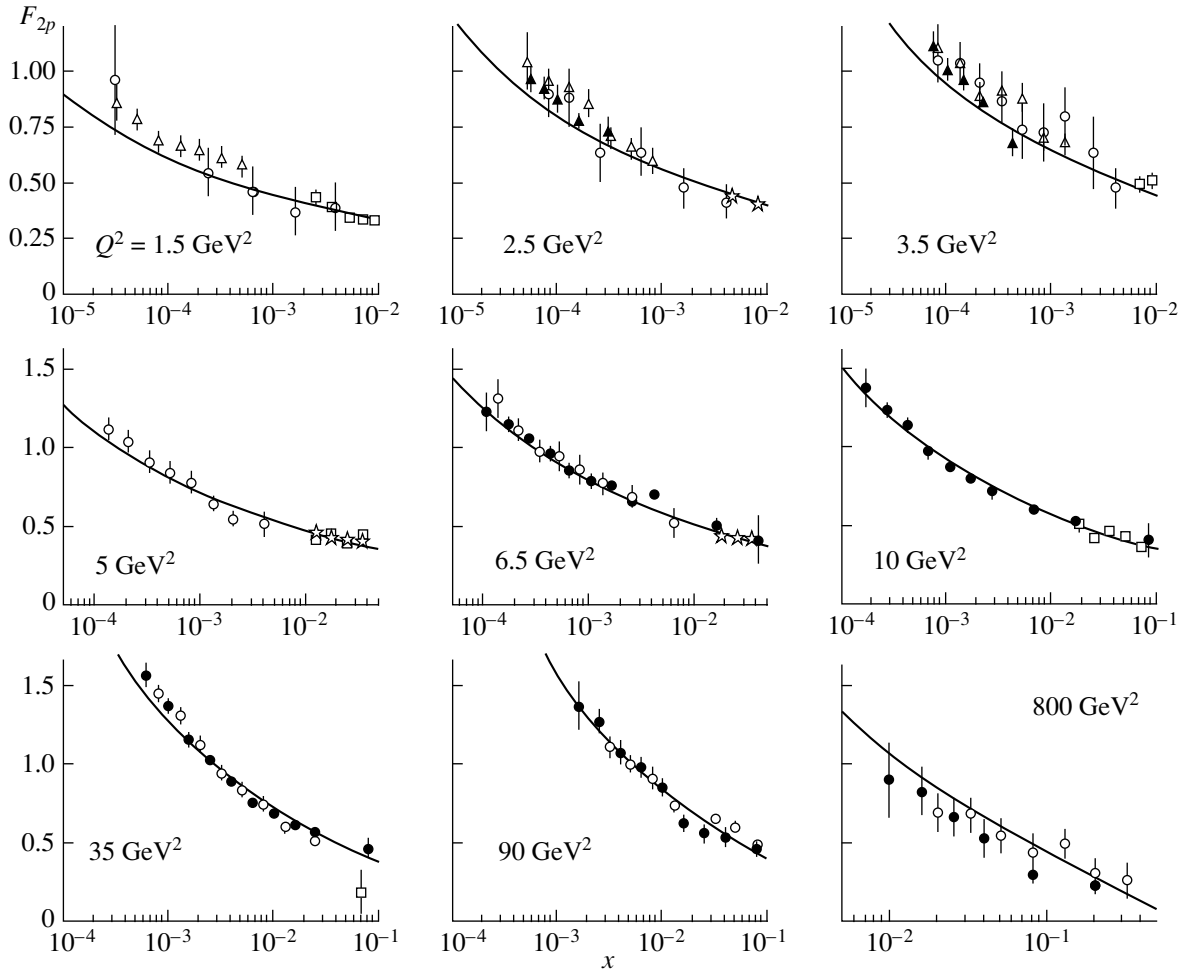

Fig. 7. The κ-factorization description of the experimental data on $F_{2p}(x, Q^2)$ in the moderate and high Q^2 region: close circles and triangles are ZEUS data [33, 34], open circles and triangles show H1 data [32, 35], open squares are E665 data [30], stars refer to NMC results [36]. The solid curve represents κ-factorization results based on the D-GRV parametrization of the DGSF $\mathcal{F}(x, \boldsymbol{\kappa}^2)$.

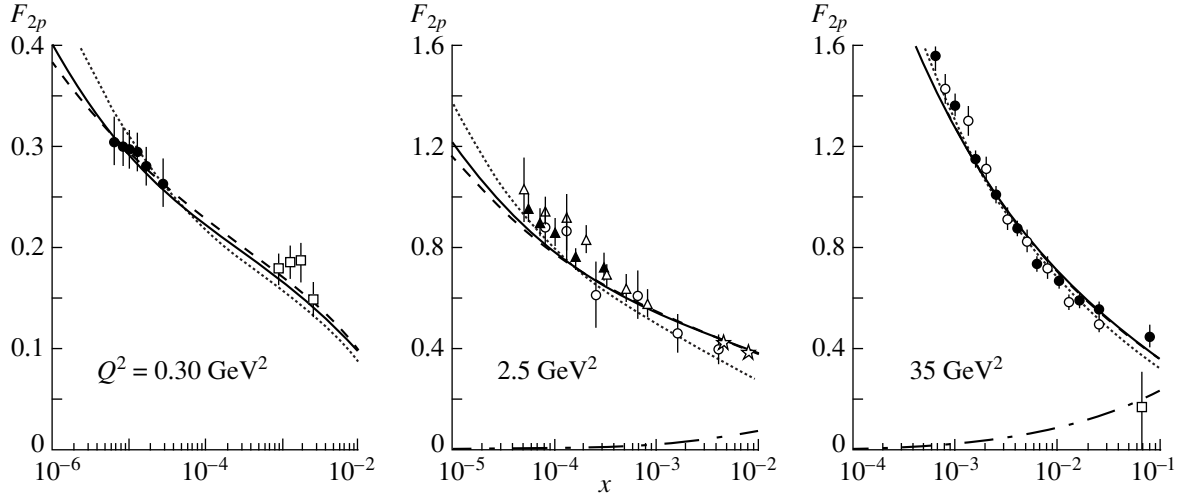

Fig. 8. A comparison of the κ-factorization description of the experimental data on $F_{2p}(x, Q^2)$ for several values of Q^2 based on the three parametrizations of the DGSF $\mathcal{F}(x, \boldsymbol{\kappa}^2)$. The solid, dashed, and dotted curves represent κ-factorization calculations with the D-GRV, D-MRS, and D-CTEQ parametrizations of $\mathcal{F}(x, \boldsymbol{\kappa}^2)$, respectively. For larger Q^2, the dash-dotted curve shows the contribution to $F_{2p}(x, Q^2)$ from DIS off valence quarks. Closed circles and triangles are the experimental data from ZEUS, open circles and triangles show H1 data, open squares are E665 data, stars refer to NMC results.

gluon contribution from the total cross sections of any soft interaction, whose generic example is the real photoabsorption.

6. PROPERTIES OF DIFFERENTIAL GLUON STRUCTURE FUNCTION IN THE MOMENTUM SPACE

6.1. Soft–Hard Decomposition of DGSF

Now we focus on the x and $\boldsymbol{\kappa}^2$ behavior of the so-determined DGSF starting for the reference with the D-GRV parametrization. The same pattern hods for DGSF based on CTEQ and MRS DGLAP inputs, see below. In Figs. 10 and 11, we plot the DGSF $\mathcal{F}(x_g, \boldsymbol{\kappa}^2)$, while in Fig. 12 we show the integrated GSF

$$G_D(x, Q^2) = \int_0^{Q^2} \frac{d\boldsymbol{\kappa}^2}{\boldsymbol{\kappa}^2} \mathcal{F}(x, \boldsymbol{\kappa}^2). \quad (45)$$

Here, the subscript D is a reminder that the integrated $G_D(x, Q^2)$ is derived from DGSF. As such, it must not be confused with the DGLAP parametrization $G_{\rm pt}(x, Q^2)$ supplied with the subscript pt.

Figures 10 and 11 illustrate the interplay of the nonperturbative soft component of DGSF and perturbative hard contribution supplemented with the above described continuation into $\boldsymbol{\kappa}^2 \le Q_c^2$ at various x and $\boldsymbol{\kappa}^2$. The soft and hard contributions are shown by the dashed and dotted curves, respectively; their sum is given by the solid curve.

Apart from the large-x suppression factor $(1 - x)^5$, our nonperturbative soft component does not depend on x. At a not so small $x = 10^{-2}$, it dominates the soft region of $\boldsymbol{\kappa}^2 \lesssim 1$–2 GeV^2, and the hard component takes over at higher $\boldsymbol{\kappa}^2$. The soft–hard crossover point is close to $\mu_{\rm pt}^2$ but because of the hard-to-soft diffusion it moves with decreasing x to a gradually smaller Q^2.

6.2. Soft–Hard Decomposition of the Integrated Gluon Structure Function

The role of the soft component is further illustrated by Fig. 12, where we show by the solid curve the integrated GSF (45) and by the dashed curve its soft component $G_{\rm soft}(x, Q^2)$. The soft contribution $G_{\rm soft}(x, Q^2)$ is a dominant feature of the integrated GSF $G_D(x, Q^2)$ for $Q^2 \lesssim 1$ GeV^2. It builds up rapidly with Q^2 and receives the major contribution from the region $\boldsymbol{\kappa}^2 \sim 0.3$–0.5 GeV^2. Our ansatz for $\mathcal{F}_{\rm soft}(x, \boldsymbol{\kappa}^2)$ is such that it starts decreasing already at $\boldsymbol{\kappa}^2 \sim 0.2$ GeV^2 and vanishes rapidly beyond $\boldsymbol{\kappa}^2 \gtrsim \boldsymbol{\kappa}_{\rm soft}^2$ (see Figs. 10, 11). Still, the residual rise of the soft gluon density beyond $Q^2 \sim 0.5$ GeV^2 is substantial: $G_{\rm soft}(x, Q^2)$ rises by about the factor of two before it flattens at large Q^2. We emphasize that $G_{\rm soft}(Q^2)$ being finite at large Q^2 is quite natural—a decrease of $G_{\rm soft}(Q^2)$ at large Q^2 is possible only if $\mathcal{F}_{\rm soft}(Q^2)$ becomes negative-valued at large Q^2, which does not seem to be a viable option.

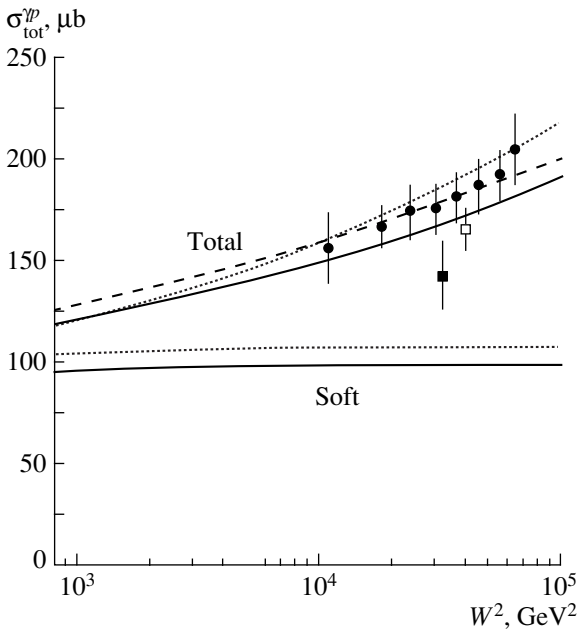

Fig. 9. A comparison of the κ-factorization description of the experimental data on real photoabsorption cross section based on the D-GRV, D-MRS, and D-CTEQ parametrizations of the DGSF $\mathcal{F}(x, \boldsymbol{\kappa}^2)$. The squares show the experimental data from 1992–1993 direct measurements, the bullets are the results of extrapolation of virtual photoabsorption to $Q^2 = 0$ ([31] and references therein). The solid, dashed, and dotted curves represent κ-factorization calculations with the D-GRV, D-MRS, and D-CTEQ parametrizations of $\mathcal{F}(x, \boldsymbol{\kappa}^2)$, respectively. The soft component of photoabsorption cross section is shown separately; it is identical for D-GRV (solid) and D-CTEQ-based calculations (dotted).

At moderately small $x \sim 10^{-2}$, the scaling violations are still weak and the soft contribution $G_{\rm soft}(x, Q^2)$ remains a substantial part, about one half, of the integrated GSF $G_D(x, Q^2)$ at all Q^2. At very small $x \lesssim 10^{-3}$, the scaling violations in the GSF are strong and $G_{\rm hard}(x, Q^2) = G_D(x, Q^2) - G_{\rm soft}(x, Q^2) \gg G_{\rm soft}(x, Q^2)$ starting from $Q^2 \sim 1$–2 GeV^2.

6.3. Soft–Hard Decomposition of the Proton Structure Function $F_2(x, Q^2)$

Equations (15) and (16) define the soft–hard decomposition of the proton structure function. In Fig. 13, we show $F_{2p}^{\rm hard}(x, Q^2)$ and $F_{2p}^{\rm soft}(x, Q^2)$ as functions of Q^2 for the two representative values of x. Notice how the significance of soft component as a function of Q^2 rises from the fully differential $\mathcal{F}(x, Q^2)$ to the integrated $G_D(x, Q^2)$ to doubly integrated $F_{2p}^{\rm soft}(x, Q^2)$. At a moderately small $x \sim 10^{-3}$, the soft contribution is a dominant

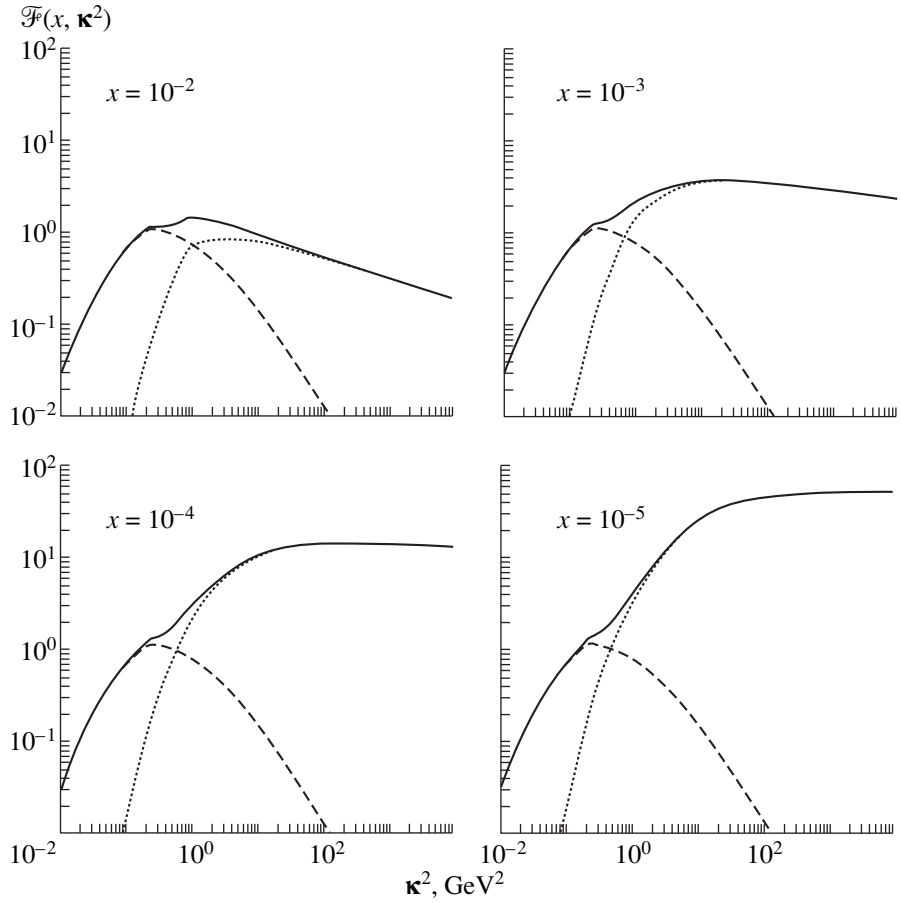

Fig. 10. D-GRV DGSF $\mathcal{F}(x, \boldsymbol{\kappa}^2)$ as a function of $\boldsymbol{\kappa}^2$ at several values of x. The dashed and dotted curves represent the soft and hard components, respectively; the total unintegrated gluon density is shown by the solid curve.

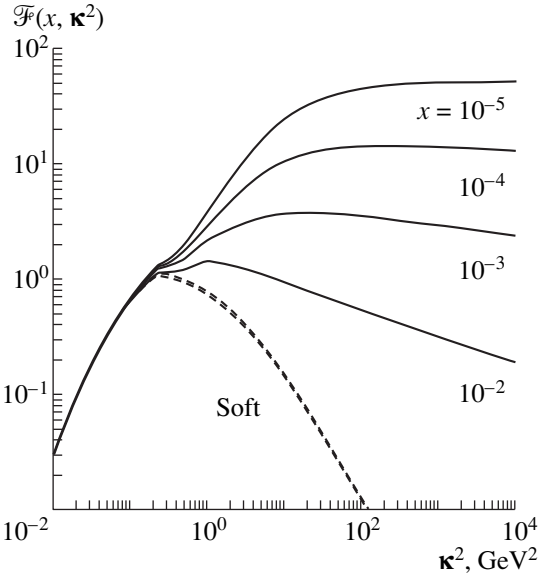

Fig. 11. The same as in Fig. 10, but overlaid onto one graph for illustration of the x dependence of $\mathcal{F}(x, \boldsymbol{\kappa}^2)$. The dashed curves show the soft component $\mathcal{F}_{\text{soft}}(x, \boldsymbol{\kappa}^2)$ and its slight rise with x from $x = 10^{-2}$ to $x = 10^{-5}$ is due to the finite-x factor $(1 - x)^5$.

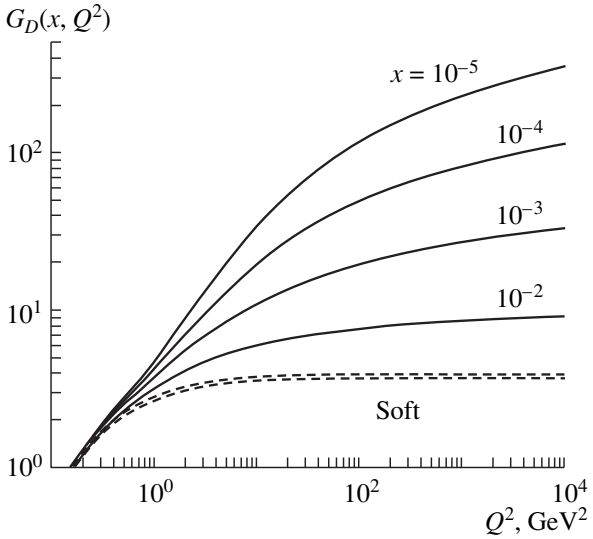

Fig. 12. The same as in Fig. 11, but for integrated GSF $G_D(x, Q^2)$ as given by the D-GRV parametrization of the DGSF $\mathcal{F}(x, \boldsymbol{\kappa}^2)$ (for the discussion, see Section 6.2).

part of $F_{2p}(x, Q^2)$, although the rapidly rising hard component $F_{2p}^{\text{hard}}(x, Q^2)$ gradually takes over at smaller x.

Notice that not only does $F_{2p}^{\text{soft}}(x, Q^2)$ not vanish at large Q^2, but also it rises slowly with Q^2 as

$$F_{2p}^{\text{soft}}(x, Q^2) \sim \sum e_f^2 \frac{4G_{\text{soft}}(Q^2)}{3\beta_0} \log \frac{1}{\alpha_S(Q^2)}. \quad (46)$$

Again, the decrease of $F_{2p}^{\text{soft}}(x, Q^2)$ with Q^2 would only be possible at the expense of unphysical negative valued $G_{\text{soft}}(Q^2)$ at large Q^2.

7. DGSF IN THE x SPACE: EFFECTIVE INTERCEPTS AND HARD-TO-SOFT DIFFUSION

It is instructive to look at the change of the x dependence from the DGSF $\mathcal{F}(x, Q^2)$ to integrated GSF $G_D(x, Q^2)$ to proton structure function $F_{2p}(x, Q^2)$. It is customary to parametrize the x dependence of various structure functions by the effective intercept. For instance, for the effective intercept τ_{eff} the DGSF structure function is defined by the parametrization

$$\mathcal{F}(x, \boldsymbol{\kappa}^2) \propto \left(\frac{1}{x}\right)^{\tau_{\text{eff}}(\boldsymbol{\kappa}^2)}. \quad (47)$$

One can define the related intercepts τ_{hard} for the hard component $\mathcal{F}_{\text{hard}}(x, Q^2)$. Notice that in our ansatz $\tau_{\text{soft}} \equiv 0$.

The power law (47) is only a crude approximation to the actual x dependence of DGSF and the effective intercept τ_{eff} will evidently depend on the range of fitted x. To be more definite, for the purposes of the present discussion, we define the effective intercept as

$$\tau_{\text{eff}}(\boldsymbol{\kappa}^2) = \frac{\log[\mathcal{F}(x_2, \boldsymbol{\kappa}^2)/\mathcal{F}(x_1, \boldsymbol{\kappa}^2)]}{\log(x_1/x_2)}, \quad (48)$$

taking $x_2 = 10^{-5}$ and $x_1 = 10^{-3}$. The effective intercept $\tau_{\text{hard}}(Q^2)$ is defined by (48) in terms of $\mathcal{F}_{\text{hard}}(x, Q^2)$.

One can define the related intercepts λ_{eff} and λ_{hard} for the integrated GSF $G_D(x, Q^2)$:

$$G_D(x, Q^2) \propto \left(\frac{1}{x}\right)^{\lambda_{\text{eff}}(Q^2)}. \quad (49)$$

In the case of $F_{2p}(x, Q^2)$, we define the intercept $\Delta(Q^2)$ in terms of the variable $\bar{x}$ defined as

$$\bar{x} = \frac{Q^2 + M_V^2}{W^2 + Q^2} \sim x_g, \quad (50)$$

where M_V is the mass of the ground state vector meson in the considered flavor channel. Such a replacement allows one to treat on equal footing $Q^2 \lesssim 1\ \text{GeV}^2$, where the formally defined Bjorken variable x_{Bj} can no longer be interpreted as a light-cone momentum carried by charged partons. For the purposes of the direct comparison with $\tau(Q^2)$ and $\lambda(Q^2)$ and in order to avoid biases caused by the valence structure function, here we focus on intercepts Δ_{eff} and Δ_{hard} for the sea component of the proton structure function $F_{2p}^{\text{sea}}(x, Q^2)$:

$$F_{2p}^{\text{sea}}(x, Q^2) \propto \left(\frac{1}{\bar{x}}\right)^{\Delta_{\text{eff}}(Q^2)}. \quad (51)$$

The results for the effective intercepts are shown in Figs. 14–16.

In our simplified hard-to-soft extrapolation of $\mathcal{F}_{\text{hard}}(x, Q^2)$, we attribute to $\mathcal{F}_{\text{hard}}(x, Q^2)$ at $Q^2 \le Q_c^2$ the same x dependence as at $Q^2 = Q_c^2$ modulo to slight modifications for the x dependence of κ_h^2. This gives

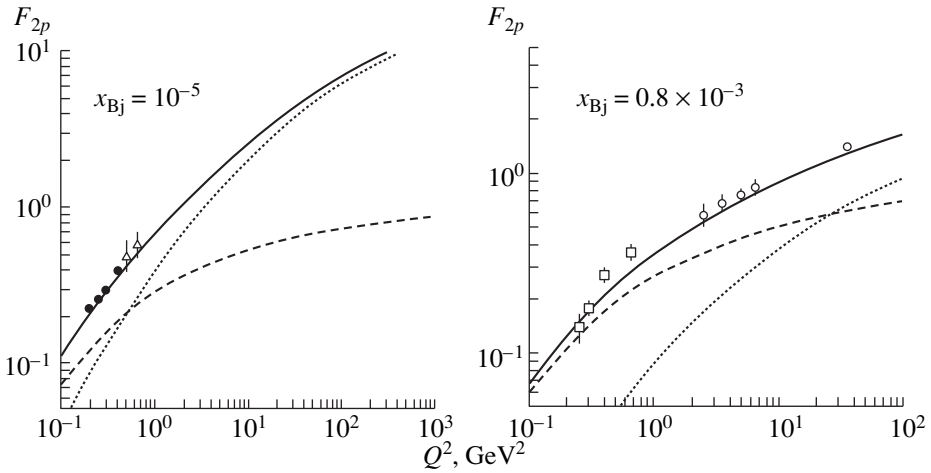

Fig. 13. The soft–hard decomposition of κ-factorization results for the proton structure function $F_{2p}(x, Q^2)$ evaluated with the D-GRV parametrization of the DGSF $\mathcal{F}(x, \boldsymbol{\kappa}^2)$. The soft and hard contributions are shown with the dashed and dotted curves, respectively; their sum is given in the solid curve. Closed circles show the ZEUS BPC data [31], open triangles and circles are H1 data [32, 35], and open squares refer to E665 results [30].

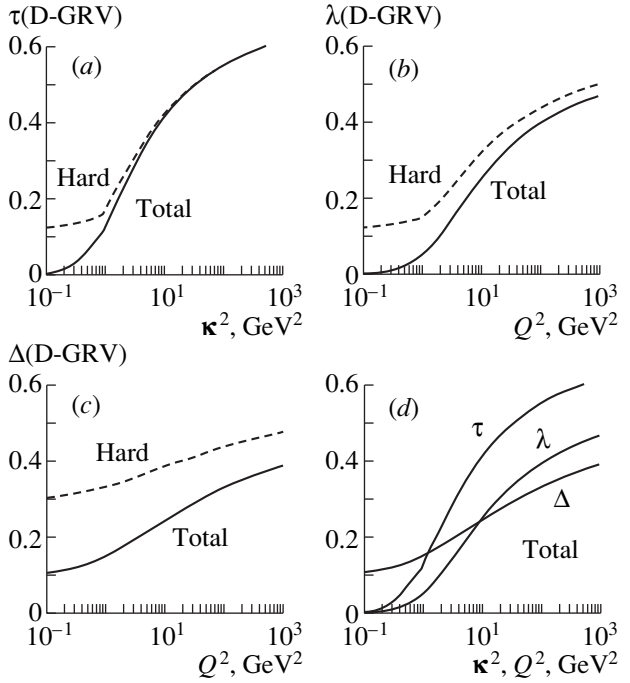

Fig. 14. Effective intercepts for total and hard components of (*a*) the DGSF $\mathcal{F}(x, \boldsymbol{\kappa}^2)$, (*b*) integrated GSF $G_D(x, Q^2)$, and (*c*) proton structure function $F_{2p}(x, Q^2)$ evaluated with the D-GRV parametrization of the DGSF $\mathcal{F}(x, \boldsymbol{\kappa}^2)$. In (*d*) we compare the effective intercepts $\tau_{\text{eff}}(\boldsymbol{\kappa}^2)$, $\lambda_{\text{eff}}(Q^2)$, and $\Delta_{\text{eff}}(Q^2)$ for $\mathcal{F}(x, Q^2)$, $G_D(x, Q^2)$, and $F_{2p}(x, Q^2)$, respectively.

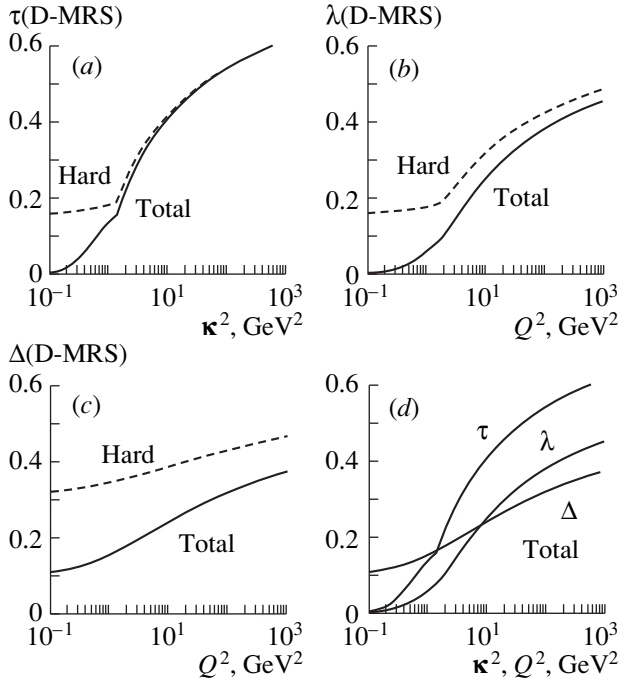

Fig. 15. Effective intercepts for total and hard components of (*a*) the DGSF $\mathcal{F}(x, \boldsymbol{\kappa}^2)$, (*b*) integrated GSF $G_D(x, Q^2)$, and (*c*) proton structure function $F_{2p}(x, Q^2)$ evaluated with the D-MRS parametrization of $\mathcal{F}(x, \boldsymbol{\kappa}^2)$. In (*d*) we compare the effective intercepts $\tau_{\text{eff}}(\boldsymbol{\kappa}^2)$, $\lambda_{\text{eff}}(Q^2)$, and $\Delta_{\text{eff}}(Q^2)$ for $\mathcal{F}(x, Q^2)$, $G_D(x, Q^2)$, and $F_{2p}(x, Q^2)$, respectively.

the cusp in $\tau_{\text{hard}}(Q^2)$ at $Q^2 = Q_c^2$, i.e., the first derivative of $\tau_{\text{hard}}(Q^2)$ is discontinuous at $Q^2 = Q_c^2$.

A comparison of Fig. 11 with Fig. 12 and further with Fig. 13 shows clearly that only in DGSF $\mathcal{F}(x, Q^2)$ is the effect of the soft component concentrated at small Q^2; in integrated $G_D(x, Q^2)$ and especially in the proton structure function $F_{2p}(x, Q^2)$ is the impact of the soft component extends to much larger Q^2. The larger the soft contribution, the stronger is the reduction of τ_{eff} from τ_{hard} and so forth, this pattern is evident from Fig. 14*a* to Fig. 14*b* to Fig. 14*c* (see also Figs. 15 and 16).

The change of effective intercepts from differential $\mathcal{F}(x, Q^2)$ to integrated $G_D(x, Q^2)$ is straightforward, the principal effect is that $\lambda_{\text{hard}}(Q^2) < \tau_{\text{hard}}(Q^2)$ and $\lambda_{\text{eff}}(Q^2) < \tau_{\text{eff}}(Q^2)$, which reflects the growing importance of soft component in $G_D(x, Q^2)$. The change of effective intercepts from $\mathcal{F}(x, Q^2)$ and $G_D(x, Q^2)$ to $F_{2p}(x, Q^2)$ is less trivial and exhibits two dramatic consequences of the hard-to-soft and soft-to-hard diffusion. If the standard DGLAP contribution (24) were all, then the change from the intercept $\lambda(Q^2)$ for integrated gluon density to the intercept $\Delta(Q^2)$ for the proton structure function $F_{2p}(x, Q^2)$ would have been similar to the change from $\tau(Q^2)$ to $\lambda(Q^2)$; i.e., the effective intercept $\Delta_{\text{eff}}(Q^2)$ would have been close to zero for $Q^2 \lesssim 1$ GeV^2. However, by virtue of the hard-to-soft diffusion phenomenon inherent to the κ factorization, $F_{2p}(x, Q^2)$ receives a contribution from gluons with $\boldsymbol{\kappa}^2 > Q^2$, which enhances substantially $\Delta_{\text{hard}}(Q^2)$ and $\Delta_{\text{eff}}(Q^2)$. The net result is that, at small to moderately large Q^2, we find $\Delta_{\text{hard}}(Q^2) > \lambda_{\text{hard}}(Q^2)$ and $\Delta_{\text{eff}}(Q^2) > \lambda_{\text{eff}}(Q^2)$. As we emphasized above in Section 5.3, the rise of the real-photoabsorption cross section is precisely of the same origin.

The second effect is a dramatic flattening of the effective hard intercept $\Delta_{\text{hard}}(Q^2)$ over the whole range of Q^2. For all three DGLAP inputs, $\Delta_{\text{hard}}(Q^2)$ flattens at approximately the same $\Delta_{\text{hard}} \approx 0.4$.

The set of Figs. 14–16 also shows that the systematics of intercepts in the hard region of $Q^2 > Q_c^2$ is nearly identical for all three DGLAP inputs. In the soft region, we have a slight inequality $\tau_{\text{hard}}(\boldsymbol{\kappa}^2)|_{\text{D-MRS}} > \tau_{\text{hard}}(\boldsymbol{\kappa}^2)|_{\text{D-GRV}}$, which can be readily attributed to the slight inequality $Q_c^2(\text{MRS}) > Q_c^2(\text{GRV})$. In the case of CTEQ4L (v.4.6) input, the value of $Q_c^2(\text{CTEQ})$ is substantially larger than $Q_c^2(\text{MRS})$, $Q_c^2(\text{GRV})$. In the range $Q_c^2(\text{MRS}) < \boldsymbol{\kappa}^2 < Q_c^2(\text{CTEQ})$, the effective intercept

$\tau_{hard}(\boldsymbol{\kappa}^2)$ rises steeply with $\boldsymbol{\kappa}^2$. This explains why in the soft region $\tau_{hard}(\boldsymbol{\kappa}^2)|_{CTEQ}$ is significantly larger than for the D-GRV and D-MRS parametrization. The difference among intercepts for the three parametrizations decreases gradually from the differential $\mathcal{F}(x, \boldsymbol{\kappa}^2)$ to the integrated $G_D(x, Q^2)$ gluon density to the proton structure function $F_{2p}(x, Q^2)$.

Finally, in Fig. 17 we compare our results for $\Delta_{eff}(Q^2)$ with the recent experimental data from the ZEUS collaboration [34]. In the experimental fit, the range of $x = [x_{max}, x_{min}]$ varies from point to point; in our evaluation of Δ_{eff} from Eq. (48), we mimicked the experimental procedure, taking $\bar{x}_2 = x_{max}$ and $\bar{x}_1 = x_{min}$. This explains the somewhat irregular Q^2 dependence. The experimental data include both sea and valence components. At $Q^2 > Q_c^2(\text{GRV}) = 0.9$ GeV^2, we included the valence component of the structure function taking the GRV98LO parametrization. For CTEQ4L (v.4.6) and MRS-LO-1998, the values of Q_c^2 are substantially larger. However, the valence component is a small correction and we took the liberty of evaluating the valence contribution $F_{2p}^{val}(x, Q^2)$ for $Q_c^2(\text{GRV}) < Q^2 < Q_c^2(\text{MRS}), Q_c^2(\text{CTEQ})$. The overall agreement with the experiment is good. Difference among the three parametrizations is marginal and can of course be traced back to Figs. 14–16.

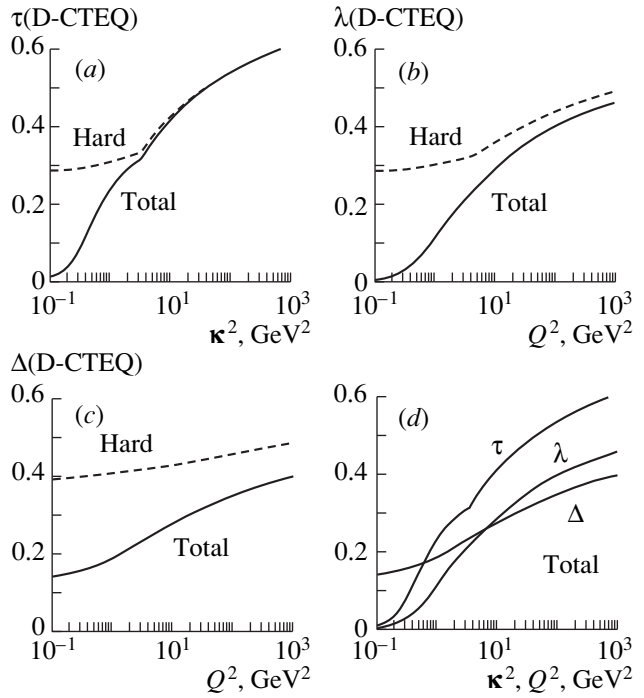

Fig. 16. Effective intercepts fort total and hard components of (*a*) the DGSF $\mathcal{F}(x, \boldsymbol{\kappa}^2)$, (*b*) integrated GSF $G_D(x, Q^2)$, and (*c*) proton structure function $F_{2p}(x, Q^2)$ evaluated with the D-CTEQ parametrization of $\mathcal{F}(x, \boldsymbol{\kappa}^2)$. In (*d*) we compare the effective intercepts $\tau_{eff}(\boldsymbol{\kappa}^2)$, $\lambda_{eff}(Q^2)$, and $\Delta_{eff}(Q^2)$ for $\mathcal{F}(x, Q^2)$, $G_D(x, Q^2)$, and $F_{2p}(x, Q^2)$, respectively.

8. HOW THE GLUON DENSITIES OF κ FACTORIZATION DIFFER FROM DGLAP GLUON DENSITIES

It is also instructive to compare our results for integrated GSF (45) with the conventional DGLAP fit $G_{pt}(x, Q^2)$. In Fig. 18, we present such a comparison between our integrated D-GRV distribution (solid curves) and the GRV98LO distribution (dashed curves). As was anticipated in Subsection 3.2, at very large Q^2, the two gluon distributions converge. We also anticipated that, at small x and moderate Q^2, the DGLAP gluon structure functions $G_{pt}(x, Q^2)$ are substantially larger than the result of integration of DGSF [see Eq. (45)]. At $x = 10^{-5}$, they differ by as much as a factor of two to three over a broad range of $Q^2 \lesssim 100$ GeV^2. The difference between integrated DGSF and the DGLAP fit decreases gradually at large x and is only marginal at $x = 10^{-2}$.

Recall the substantial divergence of the GRV, MRS, and CTEQ GSF of DGLAP approximation $G_{pt}(x, Q^2)$ at small and moderate Q^2. Contrary to that, the κ-factorization D-GRV, D-CTEQ, and D-MRS GSF $G_D(x, Q^2)$ are nearly identical. We demonstrate this property in Fig. 19, where we show integrated $G_D(x, Q^2)$ and their DGLAP counterparts $G_{pt}(x, Q^2)$ for the three parametri-

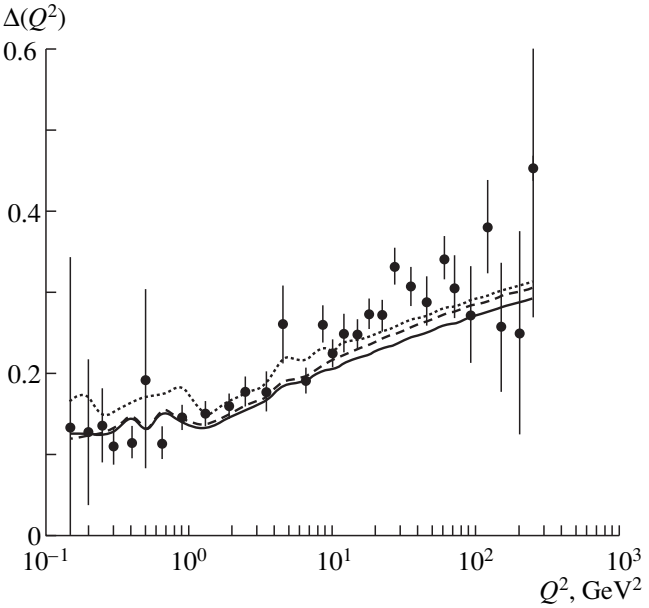

Fig. 17. Effective intercepts $\Delta(Q^2)$ of the proton structure function $F_{2p}(x, Q^2)$ in the HERA domain evaluated for the D-GRV, D-MRS, and D-CTEQ parametrizations for the DGSF $\mathcal{F}(x, \boldsymbol{\kappa}^2)$, shown in solid, dashed, and dotted curves, respectively. The experimental data points are from ZEUS [34].

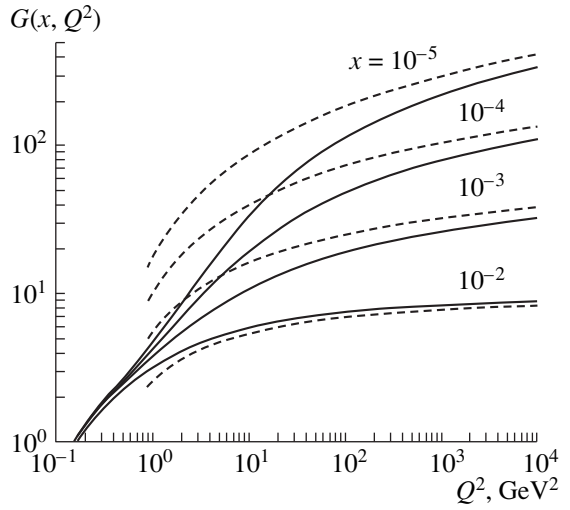

Fig. 18. Comparison of our results for integrated GSF $G_D(x, Q^2)$ (solid curves) evaluated with the D-GRV parametrization of the DGSF $\mathcal{F}(x, \boldsymbol{\kappa}^2)$ with the GRV98LO DGLAP input parametrization $G_{\rm pt}(x, Q^2)$ (dashed curves).

zations at two typical values of x. Because of an essentially unified treatment of the region of $\boldsymbol{\kappa}^2 \le Q_c^2$ and strong constraint on DGSF in this region from the experimental data at small Q^2, such a convergence of D-GRV, D-CTEQ, and D-MRS DGSFs is not unexpected.

One can also compare the effective intercepts for our integrated GSF $G_D(x, Q^2)$ with those obtained from DGLAP gluon distributions $G_{\rm pt}(x, Q^2)$. Figure 20 shows large scattering of $\lambda_{\rm eff}^{\rm (pt)}(Q^2)$ from one DGLAP input to another. At the same time, this divergence of different DGLAP input parametrizations is washed out to a large extent in the κ-factorization description of physical observables (see also Fig. 17).

9. HOW DIFFERENT OBSERVABLES PROBE THE DGSF $\mathcal{F}(x, Q^2)$

The issue we address in this section is how different observables map the $\boldsymbol{\kappa}^2$-dependence of $\mathcal{F}(x_g, \boldsymbol{\kappa}^2)$. We expand on the qualitative discussion in Section 3.2 and corroborate it with numerical analysis following the discussion in [20]. We start with two closely related quantities—longitudinal structure function $F_L(x, Q^2)$ and scaling violations $\partial F_2(x, Q^2)/\partial \log Q^2$—and proceed to $F_{2p}(x, Q^2)$ and the charm structure function of the proton, $F_{2p}^{c\bar{c}}(x, Q^2)$. This mapping is best studied if, in (15) and (16), we first integrate with respect to $\mathbf{k}$ and z. In order to focus on the $\boldsymbol{\kappa}^2$ dependence, we prefer pre-

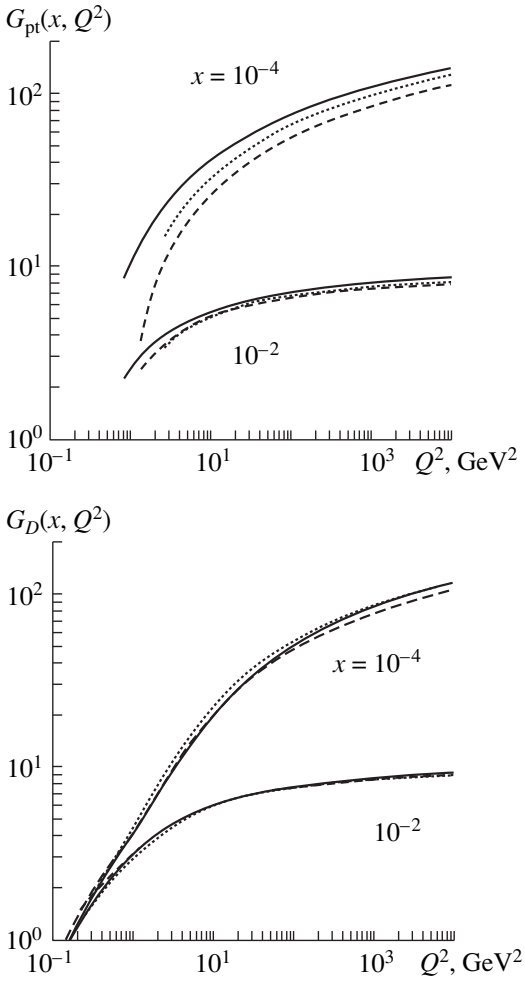

Fig. 19. A comparison of the divergence of GRV98LO, CTEQ4L(v.4.6), and MRS-LO-1998 GSF $G_{\rm pt}(x, Q^2)$ (top) with the divergence of our integrated gluon structure functions $G_D(x, Q^2)$ (bottom) evaluated for the D-GRV, D-CTEQ, and D-MRS parametrizations for differential gluon structure function $\mathcal{F}(x, Q^2)$ at two typical values of x. The solid, dashed, and dotted curves refer to GRV, MRS, and CTEQ ansatz, respectively.

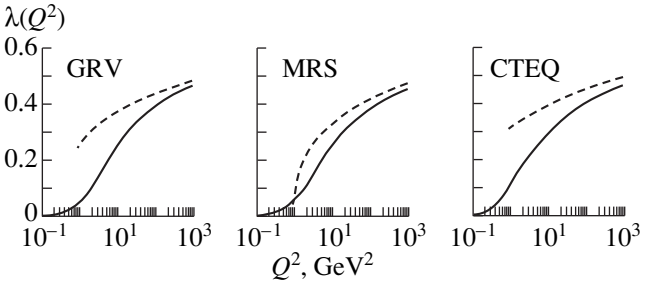

Fig. 20. A comparison of the intercept $\lambda_{\rm eff}^{\rm (pt)}(Q^2)$ of the x dependence of the GRV98LO, CTEQ4L(v.4.6), and MRS-LO-1998 GSF $G_{\rm pt}(x, Q^2)$ (dashed curves) with their counterpart $\lambda_{\rm eff}(Q^2)$ for integrated $G_D(x, Q^2)$ evaluated with D-GRV, D-CTEQ, and D-MRS parametrizations for differential gluon structure function $\mathcal{F}(x, Q^2)$ (solid curves).

senting different observables in terms of $\mathcal{F}(2x, \boldsymbol{\kappa}^2)$ and $G_D(2x, \boldsymbol{\kappa}^2)$:

$$F_L(x, Q^2) = \frac{\alpha_S(Q^2)}{3\pi}\sum e_f^2 \int \frac{d\boldsymbol{\kappa}^2}{\boldsymbol{\kappa}^2}\Theta_L^{(f\bar{f})}(Q^2, \boldsymbol{\kappa}^2)\mathcal{F}(2x, \boldsymbol{\kappa}^2), \quad (52)$$

$$\frac{\partial F_2(x, Q^2)}{\partial \log Q^2} = \frac{\alpha_S(Q^2)}{3\pi}\sum e_f^2 \int \frac{d\boldsymbol{\kappa}^2}{\boldsymbol{\kappa}^2}\Theta_2^{(f\bar{f})}(Q^2, \boldsymbol{\kappa}^2)\mathcal{F}(2x, \boldsymbol{\kappa}^2). \quad (53)$$

In the numerical calculation of $F_L(x, Q^2)$ starting from Eq. (16), we have x_g and $\boldsymbol{\kappa}^2$ as the two running arguments of $\mathcal{F}(x_g, \boldsymbol{\kappa}^2)$. As discussed above, the mean value of x_g is close to $2x$, but the exact relationship depends on $\boldsymbol{\kappa}^2$. The $\mathbf{k}, z$ integration amounts to the averaging of $\mathcal{F}(x_g, \boldsymbol{\kappa}^2)$ over a certain range of x_g. The result of this averaging is for the most part controlled by the effective intercept $\tau_{\text{eff}}(\boldsymbol{\kappa}^2)$:

$$\langle \mathcal{F}(x_g, \boldsymbol{\kappa}^2)\rangle = \langle \mathcal{F}(2x, \boldsymbol{\kappa}^2)(2x/x_g)^{\tau_{\text{eff}}(\boldsymbol{\kappa}^2)}\rangle = r(\boldsymbol{\kappa}^2)\mathcal{F}(2x, \boldsymbol{\kappa}^2). \quad (54)$$

Because the derivative of $\tau_{\text{eff}}(\boldsymbol{\kappa}^2)$ changes rapidly around $\boldsymbol{\kappa}^2 = Q_c^2$, the rescaling factor $r(\boldsymbol{\kappa}^2)$ also has a rapid variation of the derivative at $\boldsymbol{\kappa}^2 = Q_c^2$. As far as the mapping of differential $\mathcal{F}(2x, \boldsymbol{\kappa}^2)$ is concerned, this is an entirely marginal effect. However, let us consider the mapping of the integrated GSF $G_D(x, Q^2)$, which is derived from Eqs. (52) and (53) by integration by parts:

$$F_L(x, Q^2) = -\frac{\alpha_S(Q^2)}{3\pi}\sum e_f^2 \int \frac{d\boldsymbol{\kappa}^2}{\boldsymbol{\kappa}^2}\frac{\partial \Theta_L^{(f\bar{f})}(Q^2, \boldsymbol{\kappa}^2)}{\partial \log \boldsymbol{\kappa}^2} G_D(2x, \boldsymbol{\kappa}^2), \quad (55)$$

$$\frac{\partial F_2(x, Q^2)}{\partial \log Q^2} = -\frac{\alpha_S(Q^2)}{3\pi}\sum e_f^2 \int \frac{d\boldsymbol{\kappa}^2}{\boldsymbol{\kappa}^2}\frac{\partial \Theta_2^{(f\bar{f})}(Q^2, \boldsymbol{\kappa}^2)}{\partial \log \boldsymbol{\kappa}^2} G_D(2x, \boldsymbol{\kappa}^2). \quad (56)$$

Then, because of rapid variation of the derivative of the rescaling factor $r(\boldsymbol{\kappa}^2)$ around $\boldsymbol{\kappa}^2 = Q_c^2$, the weight functions $\partial\Theta_{2,L}^{(f\bar{f})}(Q^2, \boldsymbol{\kappa}^2)/\partial\log\boldsymbol{\kappa}^2$ will exhibit a slightly irregular behavior around $\boldsymbol{\kappa}^2 = Q_c^2$. Evidently, such an irregularity appears in any region of fast variation of $\tau_{\text{eff}}(\boldsymbol{\kappa}^2)$; in our simplified model, it is somewhat amplified by the cusp-like $\boldsymbol{\kappa}^2$ dependence of $\tau_{\text{eff}}(\boldsymbol{\kappa}^2)$.

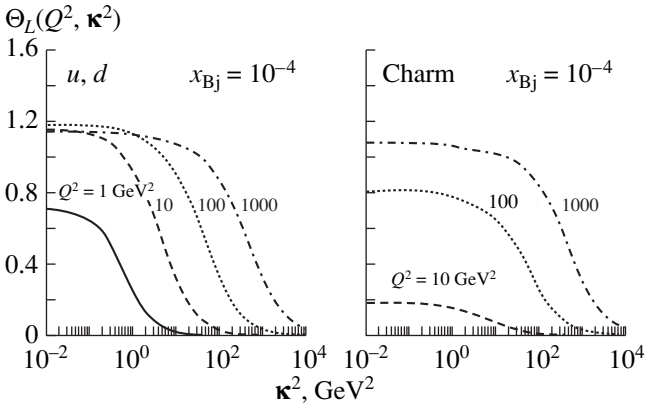

Fig. 21. The weight function Θ_L for mapping (52) of the DGSF $\mathcal{F}(x, \boldsymbol{\kappa}^2)$ as a function of $\boldsymbol{\kappa}^2$ for several values of Q^2. We show separately the results for light flavors, *u*, *d*, and charm.

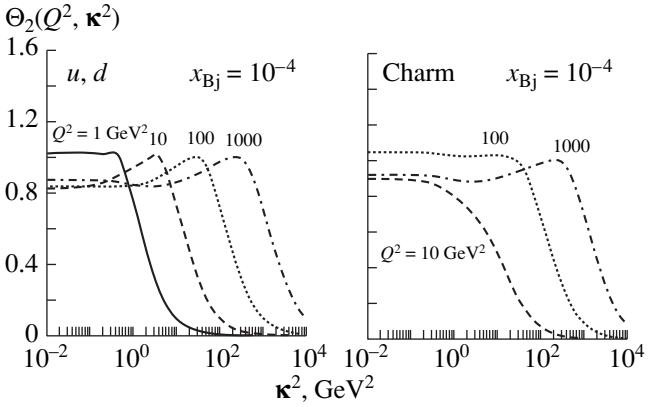

Fig. 22. The weight function Θ_2 for mapping (53) of the DGSF $\mathcal{F}(x, \boldsymbol{\kappa}^2)$ as a function of $\boldsymbol{\kappa}^2$ for several values of Q^2. We show separately the results for light flavors, *u*, *d*, and charm.

Finally, starting from (56), one obtains a useful representation for how the proton structure function $F_{2p}(x, Q^2)$ maps the integrated GSF:

$$F_{2p}(x, Q^2) = -\int_0^{Q^2}\frac{dq^2}{q^2}\frac{\alpha_S(q^2)}{3\pi} \times \sum e_f^2 \int \frac{d\boldsymbol{\kappa}^2}{\boldsymbol{\kappa}^2}\frac{\partial \Theta_2^{(f\bar{f})}(q^2, \boldsymbol{\kappa}^2)}{\partial \log \boldsymbol{\kappa}^2} G_D(2x, \boldsymbol{\kappa}^2) = \frac{1}{3\pi}\sum e_f^2 \int \frac{d\kappa^2}{\kappa^2} W_2^{(f\bar{f})}(Q^2, \kappa^2)\alpha_S(\kappa^2) G_D(2x, \kappa^2). \quad (57)$$

In Figs. 21 and 22, we show the weight functions Θ_L and Θ_2. Evidently, for light flavors and very large Q^2, they can be approximated by step-functions

$$\Theta_{L,2}^{(f\bar{f})}(Q^2, \boldsymbol{\kappa}^2) \sim \theta(C_{L,2}Q^2 - \boldsymbol{\kappa}^2), \quad (58)$$

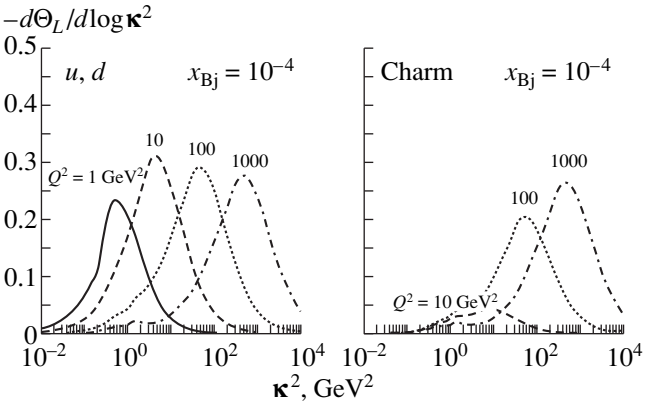

Fig. 23. The same as Fig. 21, but for mapping (55) of the integrated GSF $G_D(x, \boldsymbol{\kappa}^2)$ as a function of $\boldsymbol{\kappa}^2$ for several values of Q^2. We show separately the results for light flavors and charm.

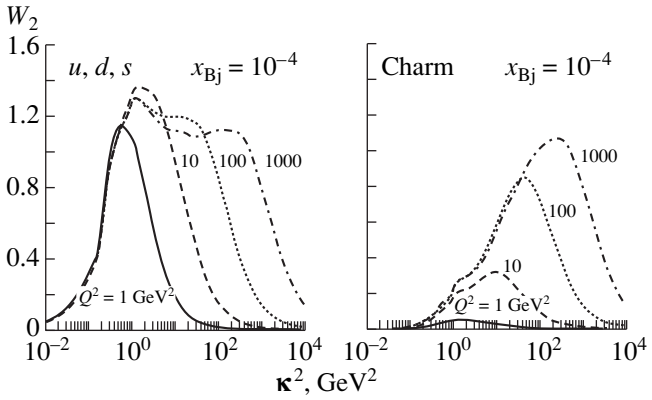

Fig. 24. The weight function W_2 for mapping of the integrated GSF $G_D(x, \boldsymbol{\kappa}^2)$ as a function of $\boldsymbol{\kappa}^2$ for several values of Q^2. We show separately the results for light flavors and charm.

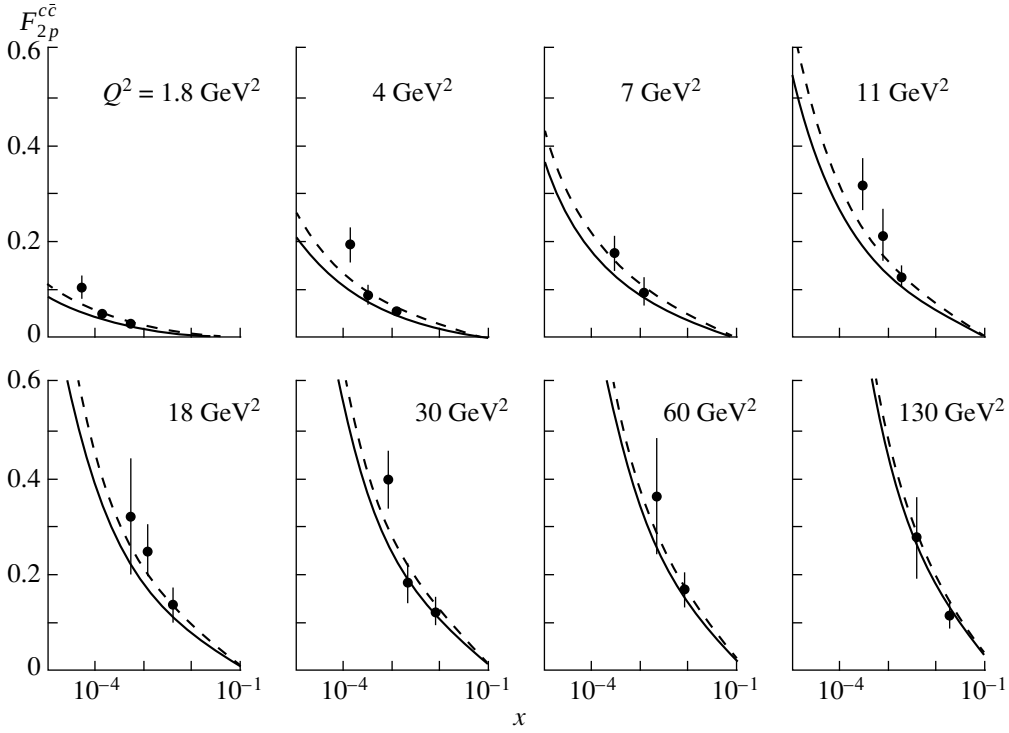

Fig. 25. A comparison of the experimental data from ZEUS [38] on the charm structure function of the proton with κ-factorization results for $F_{2p}^{c\bar{c}}(x, Q^2)$ based on the D-GRV parametrization of the DGSF $\mathcal{F}(x, Q^2)$. Predictions, given in solid and dashed curves, refer to charmed quark mass m_c = 1.5 GeV and m_c = 1.3 GeV, respectively.

where the scale factors $C_L \sim 1/2$ and $C_2 \sim 2$ can be readily read from the figures (for the related discussion, see [20]). Note that the value $C_2 \sim 2$ corresponds to $\bar{C}_2 \sim 8$ introduced in Section 3.2. Recall that the development of the plateau-like behavior of Θ_L and Θ_2, which extends to $\boldsymbol{\kappa}^2 \sim Q^2$, signals the onset of the LLQ^2 approximation. For large Q^2 in approximation (58), the $\boldsymbol{\kappa}^2$ integration can be carried out explicitly and $F_L(x, Q^2) \propto G_D(2x, C_L Q^2)$. Similarly, we have $\partial F_2(x, Q^2)/\partial \log Q^2 \propto G_D(2x, C_2 Q^2)$, cf. Eq. (28).

A still better idea on how F_L and scaling violations map the integrated GSF is shown in Figs. 23 and 24, where we show results for $-\partial\Theta_L^{(f\bar{f})}/\partial\log\boldsymbol{\kappa}^2$ and $W_2^{(f\bar{f})}$. The first quantity is sharply peaked at $\boldsymbol{\kappa}^2 \sim C_L Q^2$. The second quantity visibly develops a plateau at large Q^2.

As can be easily seen, scaling violations do receive a substantial contribution from the beyond-DGLAP region of $\boldsymbol{\kappa}^2 > Q^2$.

Because of the heavy mass, the case of the charm structure function $F_{2p}^{c\bar{c}}(x, Q^2)$ is somewhat special. Figures 23 and 24 show the weak sensitivity of $F_{2p}^{c\bar{c}}(x, Q^2)$ to the soft component of $\mathcal{F}(x_{\mathrm{Bj}}, \boldsymbol{\kappa}^2)$, which has an obvious origin: long-wavelength soft gluons with $\kappa \lesssim m_c$ decouple from the color-neutral $c\bar{c}$ Fock state of the photon which has a small transverse size $\lesssim 1/m_c$. Our results for $F_{2p}^{c\bar{c}}(x, Q^2)$ are shown in Fig. 25 and the agreement with the recent precision experimental data from ZEUS [38] is good.

10. SUMMARY

We present the first parametrization of DGSF $\mathcal{F}(x, Q^2)$ of the proton inherent to the κ-factorization approach to small-x DIS. The form of the parametrization is driven by color gauge invariance constraints for soft Q^2, early ideas from color-dipole phenomenology on the necessity of the nonperturbative soft mechanism for the interaction of large color dipoles and by matching to the derivative of familiar DGLAP fits $G_{\mathrm{pt}}(x, Q^2)$. The latter condition is not imperative, though, and can be relaxed; in this exploratory study, we simply wanted to take advantage of the insight on $G_{\mathrm{pt}}(x, Q^2)$ from early DGLAP approximation studies on scaling violations. The parameters of $\mathcal{F}(x, Q^2)$ have been tuned to the experimental data on F_{2p} in the low-x ($x \lesssim 0.01$) domain and throughout the entire Q^2 region, as well as on the real-photoabsorption cross section $\sigma_{\mathrm{tot}}^{\gamma p}$. The DGSF $\mathcal{F}(x, Q^2)$ is the principal input for pQCD calculation of many diffractive processes and we anticipate that the consistent use of our parametrizations shall reduce the uncertainties of calculations of cross sections of such processes as diffractive DIS into vector mesons and continuum.

Our results allow us to address several interesting issues. First, our ansatz for $\mathcal{F}(x, Q^2)$ have been constructed so as to ensure the convergence of $G_D(x, Q^2)$—the integral of $\mathcal{F}(x, Q^2)$—to the corresponding large Q^2 DGLAP input $G_{\mathrm{pt}}(x, Q^2)$. We notice that both gluon distributions provide a comparable description of the same set of experimental data on the proton structure function, the only difference being that, in the κ factorization, we lift the DGLAP limitation on the transverse phase space of quarks and antiquarks. We find very slow convergence of and a numerically very large difference between the κ-factorization distribution $G_D(x, Q^2)$ and the DGLAP fit $G_{\mathrm{pt}}(x, Q^2)$. As anticipated, the divergence of the two distributions is especially large at small-x and persists even in the hard region up to $Q^2 \sim$ 10–100 GeV^2 at $x = 10^{-5}$. We interpret this divergence as a signal of breaking of the DGLAP approximation, which arguably becomes poorer at smaller x. The second finding is a numerically very strong impact of soft gluons on the integrated GSF $G_D(x, Q^2)$ and the proton structure function $F_{2p}(x, Q^2)$. It is not unexpected in view of the early work on color-dipole phenomenology of small-x DIS, but the evaluation of the soft component of the integrated GSF is reported here for the first time. In conjunction with the strong departure of the κ-factorization distribution $G_D(x, Q^2)$ from the DGLAP fit $G_{\mathrm{pt}}(x, Q^2)$ it serves as a warning against the unwarranted application of DGLAP evolution at Q^2 in the range of several GeV^2.

The phenomenologically most interesting find is the anatomy of the rising component of the proton structure function from the Regge theory point of view. We notice that the effective intercepts $\tau_{\mathrm{hard}}(Q^2)$ and $\lambda_{\mathrm{hard}}(Q^2)$ for hard components of the differential and integrated gluon distributions are lively functions of Q^2 which vary quite rapidly with Q^2 from ≈ 0.1 at small Q^2 to ≈ 0.6 at $Q^2 \sim 10^3$ GeV^2. In the language of Regge theory, this evidently implies that the hard component of neither $\mathcal{F}(x, Q^2)$ nor $G_D(x, Q^2)$ is dominated by a single Regge-pole exchange and a contribution from several hard Regge poles with broad spacing of intercepts is called upon. However, an approximately flat Q^2 dependence of $\Delta_{\mathrm{hard}}(Q^2)$ shows that the hard component of the proton structure function can be approximated by a single Regge pole with an intercept of $\Delta_{\mathrm{hard}} \approx 0.4$. Such a scenario in which a contribution of subleading BFKL-Regge poles to $F_{2p}(x, Q^2)$ is suppressed dynamically because of the nodal properties of gluon distributions for subleading BFKL-Regge poles has been encountered earlier in the color-dipole BFKL approach [17]. The intercept $\Delta_{\mathrm{hard}}(Q^2)$ found in the present analysis is remarkably close to the intercept of the leading BFKL-Regge pole $\Delta_{\mathrm{IP}} = 0.4$ found in the color-dipole approach in 1994 [16, 17, 21] (or the related two-Pomeron phenomenology of DIS, see also [29]). From the point of view of κ factorization, the hard-to-soft diffusion is a unique mechanism by which an approximate constancy of $\Delta_{\mathrm{hard}}(Q^2)$ derives from a very rapidly changing $\tau_{\mathrm{hard}}(Q^2)$. Fourth, the same hard-to-soft diffusion provides a mechanism for the rise of the real photoabsorption cross section $\sigma^{\gamma p}$ in a model with the manifestly energy-independent soft cross section. We emphasize that the hard-to-soft diffusion is a generic phenomenon and we do not see any possibility for the decoupling of hard contribution from photoabsorption at $Q^2 = 0$.

We restricted ourselves to a purely phenomenological determination of differential gluon distributions from the experimental data on $F_{2p}(x, Q^2)$, which is sufficient for major applications of the κ-factorization technique. Whether the so-determined hard components of $\mathcal{F}(x, Q^2)$ and $G_D(x, Q^2)$ do satisfy the dynamical evolution equations and what is the onset of DGLAP regime will be addressed elsewhere.

One of the authors (N.N.N.) had the privilege of belonging to the A.B. Migdal's Nuclear Theory Divi-

sion at the L.D. Landau Institute for Theoretical Physics. This paper is a humble tribute to the memory of Arkadiĭ Benediktovich, who was a great physicist, teacher, artist, sportsman, a sparkling source of inspiration, and a bull of a man with exemplary lust for life in all its facets.

ACKNOWLEDGMENTS

I.P. Ivanov wishes to thank Prof. J. Speth for the hospitality at Forschungszentrum Jülich.

This work was supported in part by the INTAS (grant no. INTAS 97-30494).

REFERENCES

1. V. N. Gribov and L. N. Lipatov, Yad. Fiz. **15**, 781 (1972) [Sov. J. Nucl. Phys. **15**, 438 (1972)]; L. N. Lipatov, Yad. Fiz. **20**, 340 (1974) [Sov. J. Nucl. Phys. **20**, 94 (1975)]; Yu. L. Dokshitser, Zh. Éksp. Teor. Fiz. **73**, 1216 (1977) [Sov. Phys. JETP **46**, 641 (1977)]; G. Altarelli and G. Parisi, Nucl. Phys. B **126**, 298 (1977); for the review, see R. G. Roberts, *The Structure of the Proton* (Cambridge Univ. Press, Cambridge, 1990).
2. V. S. Fadin, E. A. Kuraev, and L. N. Lipatov, Phys. Lett. B **60B**, 50 (1975); E. A. Kuraev, L. N. Lipatov, and V. S. Fadin, Zh. Éksp. Teor. Fiz. **71**, 840 (1976) [Sov. Phys. JETP **44**, 443 (1976)]; **72**, 377 (1977) [**45**, 199 (1977)].
3. N. N. Nikolaev and B. G. Zakharov, Zh. Éksp. Teor. Fiz. **105**, 1117 (1994) [JETP **78**, 598 (1994)]; Z. Phys. C **64**, 631 (1992).
4. N. N. Nikolaev and B. G. Zakharov, Phys. Lett. B **332**, 177 (1994); Z. Phys. C **53**, 331 (1992).
5. N. N. Nikolaev, A. V. Pronyaev, and B. G. Zakharov, Phys. Rev. D **59**, 091501 (1999).
6. M. Bertini, M. Genovese, N. N. Nikolaev, *et al.*, Phys. Lett. B **422**, 238 (1998).
7. E. V. Kuraev, N. N. Nikolaev, and B. G. Zakharov, Pis'ma Zh. Éksp. Teor. Fiz. **68**, 667 (1998) [JETP Lett. **68**, 696 (1998)]; I. P. Ivanov and N. N. Nikolaev, Pis'ma Zh. Éksp. Teor. Fiz. **69**, 268 (1999) [JETP Lett. **69**, 294 (1999)].
8. J. Nemchik, N. N. Nikolaev, E. Predazzi, *et al.*, Zh. Éksp. Teor. Fiz. **113**, 1930 (1998) [JETP **86**, 1054 (1998)].
9. N. N. Nikolaev, in *Proceedings of the Workshop on Monte Carlo Generators for HERA Physics, Hamburg 1998–1999*, p. 377; hep-ph/9905562.
10. M. Glueck, E. Reya, and A. Vogt, Eur. Phys. J. C **5**, 461 (1998).
11. H. L. Lai and W. K. Tung, Z. Phys. C **74**, 463 (1997).
12. A. D. Martin, R. G. Roberts, W. J. Stirling, and R. S. Thorne, Phys. Lett. B **443**, 301 (1998).
13. V. Barone, C. Pascaud, and F. Zomer, Eur. Phys. J. C **12**, 243 (2000).
14. N. N. Nikolaev and V. R. Zoller, Zh. Éksp. Teor. Fiz. **69**, 92 (1999) [JETP Lett. **69**, 103 (1999)]; E. Gotsman, E. Levin, U. Maor, and E. Naftali, Nucl. Phys. B **539**, 535 (1999).
15. H. Abramowicz and A. Caldwell, Rev. Mod. Phys. **71**, 1275 (1999).
16. N. N. Nikolaev and B. G. Zakharov, Phys. Lett. B **327**, 157 (1994).
17. N. N. Nikolaev, B. G. Zakharov, and V. R. Zoller, Pis'ma Zh. Éksp. Teor. Fiz. **66**, 134 (1997) [JETP Lett. **66**, 138 (1997)]; N. N. Nikolaev, J. Speth, and V. R. Zoller, Phys. Lett. B **473**, 157 (2000).
18. V. M. Budnev, I. F. Ginzburg, G. V. Meledin, and V. G. Serbo, Phys. Rep. **15**, 181 (1974).
19. N. N. Nikolaev and B. G. Zakharov, Z. Phys. C **49**, 607 (1991).
20. N. N. Nikolaev and B. G. Zakharov, Phys. Lett. B **332**, 184 (1994).
21. N. N. Nikolaev, B. G. Zakharov, and V. R. Zoller, Zh. Éksp. Teor. Fiz. **105**, 1498 (1994) [JETP **105**, 1498 (1994)].
22. N. N. Nikolaev and B. G. Zakharov, KFA-IKP-TH-1994-5; hep-ph/9401312.
23. V. Barone, M. Genovese, N. N. Nikolaev, *et al.*, Phys. Lett. B **326**, 161 (1994).
24. J. Nemchik, N. N. Nikolaev, E. Predazzi, and B. G. Zakharov, Phys. Lett. B **374**, 199 (1996).
25. J. Nemchik, N. N. Nikolaev, E. Predazzi, and B. G. Zakharov, Z. Phys. C **75**, 71 (1997).
26. E. Meggiolaro, Phys. Lett. B **451**, 414 (1999).
27. V. N. Gribov, Eur. Phys. J. C **10**, 71 (1999); D. V. Shirkov, Yad. Fiz. **62**, 2082 (1999) [Phys. At. Nucl. **62**, 1928 (1999)]; Yu. L. Dokshitzer, G. Marchesini, and B. R. Webber, JHEP **07**, 012 (1999).
28. P. V. Landshoff and O. Nachtmann, Z. Phys. C **35**, 405 (1987); H. G. Dosch, T. Gousset, G. Kulzinger, and H. J. Pirner, Phys. Rev. D **55**, 2602 (1997).
29. A. Donnachie and P. V. Landshoff, Phys. Lett. B **437**, 408 (1998).
30. E665 Collab. (M. R. Adams *et al.*), Phys. Rev. D **54**, 3006 (1996).
31. ZEUS Collab. (J. Breitweg *et al.*), Phys. Lett. B **407**, 432 (1997).
32. H1 Collab. (C. Adloff *et al.*), Nucl. Phys. B **497**, 3 (1997).
33. ZEUS Collab. (M. Derrick *et al.*), Z. Phys. C **72**, 399 (1996).
34. ZEUS Collab. (J. Breitweg *et al.*), Eur. Phys. J. C **7**, 609 (1999).
35. H1 Collab. (S. Aid *et al.*), Nucl. Phys. B **470**, 3 (1996).
36. NMC Collab. (M. Arneodo *et al.*), Nucl. Phys. B **483**, 3 (1997).
37. J. Nemchik, N. N. Nikolaev, and B. G. Zakharov, Phys. Lett. B **341**, 228 (1994).
38. ZEUS Collab. (J. Breitweg *et al.*), Eur. Phys. J. C **12**, 35 (2000).

Physics of Atomic Nuclei, Vol. 64, No. 4, 2001, pp. 775–786. Translated from Yadernaya Fizika, Vol. 64, No. 4, 2001, pp. 836–848.

90th ANNIVERSARY OF A.B. MIGDAL'S BIRTHDAY
ELEMENTARY PARTICLES AND FIELDS

Kinetic Description of Vacuum Particle Production in Collisions of Ultrarelativistic Nuclei

D. V. Vinnik[1)], V. A. Mizerny[1)], A. V. Prozorkevich[1)], S. A. Smolyansky[1)], and V. D. Toneev

Bogolyubov Laboratory for Theoretical Physics, Joint Institute for Nuclear Research, Dubna, Moscow oblast, 141980 Russia

Received July 28, 2000

Abstract—The dynamics of partons that emerge as the result of quantum tunneling in a spatially uniform time-dependent field is studied under conditions prevalent in ultrarelativistic heavy-ion collisions. A self-consistent set of coupled equations that consists of the renormalized Maxwell equation and the Vlasov kinetic equation that involves a source and which is derived on a dynamical basis is solved numerically. The time dependence of the distributions of internal fields and currents for bosons and fermions is investigated within this back-reaction mechanism, and their momentum spectra are constructed. Clear evidence that oscillations in the time dependence of parton distributions in phase-space cells are of a stochastic character is obtained, and a significant irregularity in the momentum distribution on large time scales is found. If the influence of the back reaction is disregarded, these effects disappear completely, the oscillations becoming regular. A possible thermalization scenario for such a quasiparticle plasma is considered in the relaxation-time approximation. A locally equilibrium state is described within the two-component thermodynamics of particles and antiparticles. The possibility of introducing temperature under conditions of a strong vacuum polarization is discussed. © *2001 MAIK "Nauka/Interperiodica".*

1. INTRODUCTION

A.B. Migdal made a decisive contribution to the development of quasiparticle concepts in many-body theory, which were used as a basis for evolving methods for describing various phenomena in nuclear physics and the physics of neutron stars [1, 2]. In particular, he predicted the softening of pion modes and pion condensation in dense nuclei as a general corollary of physical-vacuum instability in strong fields [3]. These predictions gave impetus to subsequent intensive investigations into the properties of the equation of state of hot and compressed nuclear matter and, in particular, into possible phase transitions in nuclei; in a sense, Migdal's ideas served as a motivation and a precursor to experimental heavy-ion studies that are being presently performed over a wide interval of projectile energies. That one can vary, in this way, the temperature and the baryon density of the system formed in a nuclear collision opens a unique possibility of seeking and exploring various phase transitions in nuclei like liquid–gas phase transitions, chiral-symmetry restoration, and the phase transition through which hadrons transform into a quark–gluon plasma.

In the present study, we develop a dynamical approach to describing the evolution of quark–gluon plasma, heavily relying on the concept of quasiparticles. The conditions under which a quark–gluon plasma can be formed are considered only to the extent that is required by the purposes pursued here. Models of the nonequilibrium evolution of the system and of its thermalization differ by the degree of roughening and by the underlying interaction mechanisms. Here, we decide on a kinetic method for describing nonequilibrium matter and on the unsteady-state Schwinger mechanism for vacuum particle production in strong fields. Alternative models will be discussed precisely from this point of view.

In accordance with general ideas of ultrarelativistic heavy-ion collisions, it is assumed that, in each nucleus that has suffered a collision, there arise color charges generating chromoelectric fields between disklike nuclear residues flying apart (flux-tube model [4, 5]). These stringlike fields can prove to be sufficiently strong (supercritical) to ensure intense vacuum tunneling of partons, which enrich the quark–gluon plasma formed. If the density of such partons is sufficiently high, parton collisions become operative, leading to thermalization and local equilibration. Fast motion of charges in a quark–gluon plasma induces a color field, thereby affecting the vacuum production and annihilation of partons. This scenario corresponds to the so-called back-reaction problem; obviously, the evolution of all field components of the system must be considered self-consistently in this case.

A quantum-field model of a system of massive partons occurring in a preset spatially uniform time-dependent classical electromagnetic field that is sufficiently strong for inducing noticeable vacuum tunneling of particles represents one of the possible realizations of the flux-tube model. The assumption that the field in question is of a semiclassical character is supported by the result obtained in the leading $1/N$ approximation

[1)] Saratov State University, Saratov, 410071 Russia.

(here, N is the number of identical copies of charged matter fields) [6–11]. In conformity with the flux-tube model, it would also be reasonable to assume, for a first step, that the direction of the chromoelectric field is fixed and that there is no chromomagnetic field.

This system of model assumptions, which leads to the Abelian version of the theory, was extensively used at the semiphenomenological level to construct a kinetic description of quark–gluon plasmas. The role of the Schwinger mechanism [10] of vacuum parton production in strong fields was first realized within time-independent models (see, for example, [11]). A further step in describing the dynamics of vacuum particle production consisted in introducing a kinetic equation for the time-dependent momentum distribution of partons [12–15],

$$\frac{\partial f(\mathbf{p}, t)}{\partial t} eE(t) \frac{\partial}{\partial p_\parallel} f(\mathbf{p}, t) = C(\mathbf{p}, t) + S(\mathbf{p}, t), \quad (1)$$

where $f(\mathbf{p}, t)$ is the relevant distribution function. In addition to the collision integral $S(\mathbf{p}, t)$, which ensures redistribution of particles in energy and momentum as the result of binary collisions, the right-hand side of this equation involves a source $C(\mathbf{p}, t)$ describing the change in the number of charged particles as the result of vacuum tunneling in an electric field of strength $E(t)$. Originally, the two terms on the right-hand side of the kinetic Eq. (1) were constructed phenomenologically on the basis of the simplest physical considerations. For example, the Schwinger source was chosen in the form

$$S(\mathbf{p}, t) = |eE(t)| \ln\left[1 \pm \exp\left(-\frac{\pi E_{\text{cr}}}{|E(t)|}\right)\right] \times [1 \pm 2 f(\mathbf{p}, t)] \delta(p_\parallel), \quad (2)$$

where the critical field is $E_{\text{cr}} = m^2/e$ and where a plus (minus) sign corresponds to Bose–Einstein (Fermi–Dirac) statistics. The form of the source was specified differently in different studies; the statistical factor $(1 \pm 2f)$ was first introduced in [16]. As a rule, the relaxation-time approximation was adopted for the collision integral [17, 18].

Later, the Schwinger source in the kinetic Eq. (1) was derived, for some simple cases, on a dynamical basis as an exact solution to the equations of motion [19, 20]. This derivation relied on the circumstance that gauge-invariant theories (like QED and QCD) have much in common, especially in the formulation of problems peculiar to the flux-tube model. In particular, the theory of vacuum particle production in strong time-dependent electromagnetic fields was studied in [21–25]. Some tricks devised in those studies and based on a transition to the semiclassical representation will be used in Section 2 to derive a kinetic equation of the type in (1) in the collision-free approximation. On the basis of these exact equations, the dynamics of partons originating from a vacuum in a strong field was investigated in [20, 26] (see also Section 3 in the present study). The supercritical values of the amplitudes of (chromo)electric fields are chosen in accordance with estimates based on the flux-tube model. We will show that the results obtained in Section 3 are in qualitative agreement with the results produced by semiphenomenological approaches.

In Section 4, we investigate the back-reaction problem in the collision-free regime. Here, the role of an external field reduces to the generation of a plasma consisting of particles and antiparticles that have originated from a vacuum via tunneling. Upon switching the external field off, the plasma formed undergoes self-consistent evolution governed by the back-reaction mechanism. As will be shown in the present study, a transition to a self-consistent field generates sources of nonlinearity in the description of the dynamics of massless and massive fields, whereby there arise dynamical singularities and large-scale plasma oscillations against the background of small-scale instabilities [27]. These oscillations are quickly damped as soon as one switches on the thermalization mechanism associated with binary collisions. In Section 5, this mechanism is considered in the relaxation-time approximation for a two-component thermodynamic system.

2. KINETIC EQUATION

In accordance with the ideology of the flux-tube model, the vector potential of a semiclassical vector field satisfying the gauge condition $A^0 = 0$ is chosen here in the form

$$A^\mu(t) = (0, 0, 0, -A(t)). \quad (3)$$

Let us first consider the case of scalar electrodynamics, which describes the vacuum production of scalar bosons in such a field [19, 20, 28].

Solutions to the wave equation in the spatially uniform field (3) are sought in the form

$$\phi_{\mathbf{k}}^{(\pm)}(x) = (2\pi)^{-3/2} [2\omega_-(\mathbf{k})]^{-1/2} e^{i\mathbf{k}\cdot\mathbf{x}} g^{(\pm)}(\mathbf{k}, t), \quad (4)$$

where the functions $g^{(\pm)}(\mathbf{k}, t)$ satisfy the oscillatory-type differential equation

$$\ddot{g}^{(\pm)}(\mathbf{k}, t) + \omega^2(\mathbf{k}, t) g^{(\pm)}(\mathbf{k}, t) = 0. \quad (5)$$

Here, $\omega^2(\mathbf{k}, t) = \varepsilon_\perp^2 + [k_3 - eA(t)]^2$ is the quasiparticle energy with $\varepsilon_\perp^2 = m^2 + k_\perp^2$. In Eq. (4), $\omega_-(\mathbf{k}) = \lim_{t \to -\infty} \omega(\mathbf{k}, t)$. Positive- and negative-frequency solutions are established by considering their asymptotic behavior for $t \longrightarrow -\infty$ [21, 22, 24],

$$\phi^{(\pm)}(\mathbf{k}, t) \underset{t \to -\infty}{\sim} \exp[\pm i\omega_-(\mathbf{k}) t]. \quad (6)$$

The expansion of field operators in the orthonormalized basis (4) has the form

$$\phi(x) = \int d^3k [\phi_{\mathbf{k}}^{(+)}(x) a_{-\mathbf{k}}^{(+)} + \phi_{\mathbf{k}}^{(-)}(x) a_{\mathbf{k}}^{(-)}]. \quad (7)$$

The condition in (6) defines the operators $a_{\mathbf{k}}^{(-)}$ and $\overset{*}{a}_{\mathbf{k}}^{(-)}$ as the operators annihilating particles and antiparticles, respectively, in the initial (in) state and obeying a conventional set of commutation relations.

The solutions given by Eqs. (4) and (7) make it possible to diagonalize the Hamiltonian and to go over to the quasiparticle representation by means of the time-dependent canonical Bogolyubov transformation

$$\begin{aligned} b_{\mathbf{k}}^{(-)}(t) &= \alpha_{\mathbf{k}}(t)a_{\mathbf{k}}^{(-)} + \beta_{\mathbf{k}}(t)a_{-\mathbf{k}}^{(+)}, \\ b_{-\mathbf{k}}^{(+)}(t) &= \alpha_{\mathbf{k}}^{*}(t)a_{-\mathbf{k}}^{(+)} + \beta_{\mathbf{k}}^{*}(t)a_{\mathbf{k}}^{(-)}, \end{aligned} \tag{8}$$

which is valid under the condition $|\alpha_{\mathbf{k}}(t)|^2 - |\beta_{\mathbf{k}}(t)|^2 = 1$. On the basis of the equations of motion as given by (5), we can find, with the aid of the Lagrange method, that the coefficients in the Bogolyubov transformation (8) satisfy the equations [24, 25, 29, 30]

$$\begin{aligned} \dot{\alpha}_{\mathbf{k}}(t) &= \frac{\dot{\omega}(t)}{2\omega(t)}\beta_{\mathbf{k}}^{*}(t)e^{2i\Theta(t)}, \\ \dot{\beta}_{\mathbf{k}}(t) &= \frac{\dot{\omega}(t)}{2\omega t}\alpha_{\mathbf{k}}^{*}(t)e^{2i\Theta(t)}, \end{aligned} \tag{9}$$

where the dynamical phase factor is given by

$$\Theta(\mathbf{k}, t) = \int_{-\infty}^{t} d\tau\omega(\mathbf{k}, \tau). \tag{10}$$

For the quasiparticle creation and annihilation operators, Eqs. (9) in turn lead to the equations of motion (of the Heisenberg type)

$$\frac{dc_{\mathbf{k}}^{(\pm)}(t)}{dt} = \frac{\dot{\omega}(t)}{2\omega(t)}c_{-\mathbf{k}}^{(\mp)}(t) + i[H(t), c_{\mathbf{k}}^{(\pm)}(t)], \tag{11}$$

where we have introduced the operators

$$c_{\mathbf{k}}^{(\pm)}(t) = b_{\mathbf{k}}^{(\pm)}(t)\exp[\pm i\Theta(t)],$$

which also obey the canonical commutation relations. In the quasiparticle representation, the Hamiltonian assumes the diagonal form

$$H(t) = \sum_{\mathbf{k}} \omega(t)\{\overset{*}{c}_{\mathbf{k}}^{(+)}(t)c_{\mathbf{k}}^{(-)}(t) + \overset{*}{c}_{-\mathbf{k}}^{(-)}(t)c_{-\mathbf{k}}^{(+)}(t)\}. \tag{12}$$

The unusual form of the equations of motion in (11) is associated with nonunitarity of the transition from the original to the quasiparticle representation.

In the new representation, one can define the instantaneous value of the number of particles produced from a vacuum,

$$\begin{aligned} f(\mathbf{k}, t) &= \langle 0_{\text{in}}|\overset{*}{b}_{\mathbf{k}}^{(+)}(t)b_{\mathbf{k}}^{(-)}(t)|0_{\text{in}}\rangle \\ &= \langle 0_{\text{in}}|\overset{*}{c}_{\mathbf{k}}^{(+)}(t)c_{\mathbf{k}}^{(-)}(t)|0_{\text{in}}\rangle, \end{aligned} \tag{13}$$

and, in the same way, the analogous value for antiparticles, $\bar{f}(\mathbf{k}, t)$; obviously, we have $\bar{f}(\mathbf{k}, t) = f(-\mathbf{k}, t)$.

Differentiating this definition with respect to time with allowance for Eq. (11), we obtain

$$\frac{df(\mathbf{k}, t)}{dt} = -\frac{e\varepsilon_{\perp}E(t)}{2\omega^2(t)}[\Phi^{(+)}(\mathbf{k}, t) + \Phi^{(-)}(\mathbf{k}, t)]. \tag{14}$$

The functions $\Phi^{(\pm)}(\mathbf{k}, t)$ describe the production and annihilation of a particle and an antiparticle as the result of vacuum tunneling:

$$\begin{aligned} \Phi^{(-)}(\mathbf{k}, t) &= \langle 0_{\text{in}}|\overset{*}{c}_{-\mathbf{k}}^{(-)}(t)c_{\mathbf{k}}^{(-)}(t)|0_{\text{in}}\rangle, \\ \Phi^{(+)}(\mathbf{k}, t) &= \langle 0_{\text{in}}|\overset{*}{c}_{\mathbf{k}}^{(+)}(t)c_{-\mathbf{k}}^{(+)}(t)|0_{\text{in}}\rangle. \end{aligned}$$

For these functions, we can easily derive equations. From the outset, it is convenient to represent them in the integral form

$$\begin{aligned} \Phi^{(\pm)}(\mathbf{k}, t) &= \frac{\varepsilon_{\perp}}{2}\int_{-\infty}^{t} dt'\frac{eE(t')}{\omega^2(\mathbf{k}, t')}[2f(\mathbf{k}, t') - 1] \\ &\times \exp\{\pm 2i[\Theta(t) - \Theta(t')]\}, \end{aligned} \tag{15}$$

where it is assumed that $\lim_{t \to -\infty} \Phi^{(\pm)}(\mathbf{k}, t) = 0$.

Substituting (15) into (14) and going over to the distribution with respect to the kinetic momentum, $f(\mathbf{p}, t)$ with $\mathbf{p} = \mathbf{k} - e\mathbf{A}(t)$, we arrive at a kinetic equation in the above form (1), but without a collision integral and with the source given by

$$\begin{aligned} S(\mathbf{p}, t) &= \frac{eE(t)p_3}{2(p^0)^2}\int_{-\infty}^{t} dt'\frac{eE(t')p_3(t, t')}{\omega^2(t, t')} \\ &\times [1 + 2f(\mathbf{p}, t')]\cos\left(2\int_{t'}^{t} d\tau\omega(t, \tau)\right), \end{aligned} \tag{16}$$

where

$$\begin{aligned} (p^0)^2 &= \varepsilon_{\perp}^2 + p_3^2, \quad \omega(t, t') = \sqrt{\varepsilon_{\perp}^2 + p_3^2(t, t')}, \\ \mathbf{p}(t, t') &= \mathbf{p} - e\int_{t'}^{t} \mathbf{E}(\tau)d\tau. \end{aligned}$$

In a similar way, one can derive a kinetic equation for spin-1/2 fermions produced from a vacuum [19, 20]. Combining the two cases, we can write the source in the kinetic Eq. (1) as

$$\begin{aligned} S^{\pm}(\mathbf{p}, t) &= W(\mathbf{p}, t)\int_{-\infty}^{t} dt' W(\mathbf{p}(t, t'), t') \\ &\times [1 \pm 2f(\mathbf{p}, t')]\cos\left(2\int_{t'}^{t} d\tau\omega(t, \tau)\right), \end{aligned} \tag{17}$$

where the transition amplitude $W(\mathbf{p}, t)$ has the form

$$W(\mathbf{p}, t) = \frac{eE(t)p_3}{(p^0)^2}\left(\frac{\varepsilon_\perp}{p_3}\right)^{g-1}, \tag{18}$$

the degeneracy factor being $g = 1$ for spinless bosons and $g = 2$ for spin-1/2 fermions.

The kinetic Eq. (1) with the source given by (17) is a linear integro-differential equation of the non-Markov type. The analytic structure of the source in (17) is very intricate because of the quickly oscillating factor that involves the dynamical phase (10) and which describes the effect of an external field on vacuum oscillations of charged particles [27].

In order to investigate the kinetic equation, it is therefore convenient to represent it as a set of ordinary differential equations. This can be done, for example, by introducing two auxiliary real-valued functions [31]

$$\begin{aligned} v(\mathbf{k}, t) &= \int_{-\infty}^{t} dt' W(\mathbf{k} - e\mathbf{A}(t'), t') \\ &\times [1 \pm 2f(\mathbf{k}, t')]\cos\left(2\int_{t'}^{t} d\tau\omega(t, \tau)\right), \\ z(\mathbf{k}, t) &= \int_{-\infty}^{t} dt' W(\mathbf{k} - e\mathbf{A}(t'), t') \\ &\times [1 \pm 2f(\mathbf{k}, t')]\sin\left(2\int_{t'}^{t} d\tau\omega(t, \tau)\right). \end{aligned} \tag{19}$$

Differentiating Eq. (19) with respect to time and using the kinetic Eq. (1) with $C(\mathbf{p}, t) = 0$, we arrive at the set of ordinary linear differential equations

$$\begin{aligned} \dot{f} &= \frac{1}{2}Wv, \\ \dot{v} &= W(1 \pm 2f) - 2\omega z, \\ \dot{z} &= 2\omega v \end{aligned} \tag{20}$$

with zero initial conditions and a parametric dependence on the canonical momentum $\mathbf{k}$. It should be noted that the set of Eq. (20) has the obvious first integral

$$\mp(1 \pm f)^2 + v^2 + u^2 = \text{const}. \tag{21}$$

Going over to observable momenta, we can represent the set of Eqs. (20) as the set of partial differential equations

$$\begin{aligned} \frac{\partial f(\mathbf{p}, t)}{\partial t} + eE(t)\frac{\partial f(\mathbf{p}, t)}{\partial p_3} &= \frac{1}{2}W(\mathbf{p}, t)v(\mathbf{p}, t), \\ \frac{\partial v(\mathbf{p}, t)}{\partial t} + eE(t)\frac{\partial v(\mathbf{p}, t)}{\partial p_3} &= W(\mathbf{p}, t)[1 \pm 2f(\mathbf{p}, t)] - 2p^0 z(\mathbf{p}, t), \\ \frac{\partial z(\mathbf{p}, t)}{\partial t} + eE(t)\frac{\partial z(\mathbf{p}, t)}{\partial p_3} &= 2p^0 v(\mathbf{p}, t). \end{aligned} \tag{22}$$

The set of Eqs. (20) or (22) or its subsequent modifications served as a basis for numerically simulating the processes under investigation [20, 26, 32].

In the model being considered, Eqs. (20) and (22) can also be derived without resort to kinetic theory [25, 31]. However, the realization of the theory in the form of a kinetic equation is preferable for further developing relativistic kinetics with allowance for vacuum particle production.

3. DYNAMICS OF VACUUM PARTON PRODUCTION IN AN EXTERNAL FIELD

The application of the kinetic Eq. (1), which was obtained on a dynamical basis and which involves a source in the form (17), to the physics of quarks and gluons (partons)[2)] leads to some new effects that could not be obtained within phenomenological approaches.

A nontrivial momentum distribution of partons [20, 26, 36] seems to be the most important of these. In contrast to the majority of phenomenological approaches, where it is assumed that particles are produced at rest [compare, for example, with relation (2)], the source given by (17) generates particles of any momentum, the relevant spectrum showing a power-law decrease. For the parameter values typical of the flux-tube model [14, 37–40], Fig. 1 shows the momentum distributions of bosons and fermions generated from a vacuum by the electric field specified by the Narozhnyĭ–Nikishov potential [21]

$$\begin{aligned} A_{\text{ext}}(t) &= E_0 b[\tanh(t/b) + 1], \\ E_{\text{ext}}(t) &= E_0 \cosh^{-2}(t/b). \end{aligned} \tag{23}$$

The scale of the variables is specified by the parton mass, which serves as a natural measurement unit for them: $t \longrightarrow tm$, $p \longrightarrow p/m$, $E_0 \longrightarrow eE_0/m^2$, and $b \longrightarrow bm$. Hereafter, the above quantities are given precisely in these units, unless stated otherwise. Upon the substitution of these variables reduced to a dimensionless form into dynamical equations, the characteristic scale of observables is also determined by the parton mass. In particular, the field energy density then transforms as $\varepsilon \longrightarrow e^2\varepsilon/m^4$. Owing to this, one can study, at the same values of the external-field potential (23), systems having markedly different energy densities—for example, QED and QCD. In some cases, it is convenient to go over to dimensionless variables with the aid of the quantity $\varepsilon_\perp$.

Once the external field is switched on, the momentum distribution of bosons develops a valley in the region of zero longitudinal momenta, while the distri-

[2)] We emphasize once again that many aspects of nonequilibrium dynamics in QED are similar to those in QCD [33–35].

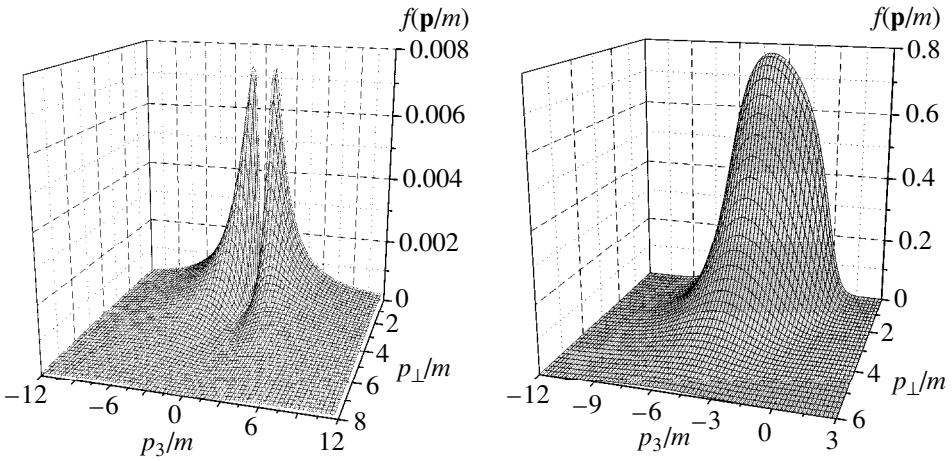

Fig. 1. Momentum spectra of product (left panel) bosons and (right panel) fermions for $eE_0/m^2 = 7$, $bm = 0.5$, and $e^2 = 4$ at the instant $tm = 0.05$.

bution of fermions develops a hill. These distributions are concentrated within finite momentum regions and are shifted with time toward higher longitudinal momenta; the boson valley is filled, while the fermion hill is stabilized (saturation effect). If the external field is operative for a sufficiently long time, oscillations in the longitudinal momentum can arise in the momentum spectrum (see Fig. 2); this is in qualitative agreement with the results obtained in other studies under the assumption that the external field is constant [28, 41].

We note that the effect of statistics in the source manifests itself both through the amplitude $W(\mathbf{p}, t)$ (18) and through the statistical factor $(1 \pm 2f)$. The former determines primarily the shape of the momentum distribution, while the latter is responsible either for the Fermi suppression or for the Bose enhancement of the particle-production rate. The last effect is nonnegligible only if the parton density is sufficiently high.

The time dependence of the distribution function also exhibits new singularities associated with a non-Markov character of the source given by (17) [26]. In the case of sufficiently weak and slowly varying fields, the statistical factor $(1 \pm 2f)$ can be removed outside the integral sign in (17), whereupon the kinetic equation can be solved explicitly. The result has the form

$$f^M(\mathbf{p}, t) = \mp\frac{1}{2}\left\{1 - \exp\left[\pm 2\int\limits_{-\infty}^{t} dt' S_0(\mathbf{k}, t')\right]\right\}, \quad (24)$$

where

$$S_0(\mathbf{p}, t) = W(\mathbf{p}, t)\int\limits_{-\infty}^{t} dt' \frac{eE(t')p_3(t, t')}{2\omega^2(t, t')} \times \cos\left(2\int\limits_{t'}^{t} d\tau\omega(t, \tau)\right)\left[\frac{\varepsilon_\perp^2}{p_3(t, t')}\right]^{g-1} \quad (25)$$

is the source function in the low-density approximation. From (24), it follows that, in the low-density limit, the distribution function assumes the form

$$f_0(\mathbf{p}, t) = \int\limits_{-\infty}^{t} dt' S_0(\mathbf{p}, t'). \quad (26)$$

This relation can also be rewritten as [24]

$$f_0(\mathbf{p}, t) = \frac{1}{4}\left|\int\limits_{-\infty}^{t} dt' \frac{eE(t')p_3(t, t')}{2\omega^2(t, t')} \times \left[\frac{\varepsilon_\perp^2}{p_3(t, t')}\right]^{g-1} \exp[2i\Theta(\mathbf{p}, t')]\right|^2, \quad (27)$$

whence it follows that $f_0(\mathbf{p}, t)$ is always nonnegative.

In the Markov approximation, it is more convenient to perform numerical calculations not on the basis of expressions (24)–(27) but on the basis of the relevant set of differential equations, which is derived by applying a procedure similar to that which has led to Eqs. (20). Specifically, we obtain

$$\dot{f} = \frac{1}{2}W(1 \pm 2f)v, \quad \dot{v} = W - 2\omega z, \quad \dot{z} = 2\omega v. \quad (28)$$

In contrast to the set of Eqs. (20), this set of equations is nonlinear.

In order to assess non-Markov effects, it is convenient to make use of two time scales characterizing vacuum particle production [20, 28, 42]. The first of these is the tunneling time $\tau_{qu} \sim 1/\omega$, while the second is the pair-production time

$$\tau_{prod} \sim \{\int [dp] S(\mathbf{p}, t)\}^{-1}, \quad [dp] = g\frac{d\mathbf{p}}{(2\pi)^3}. \quad (29)$$

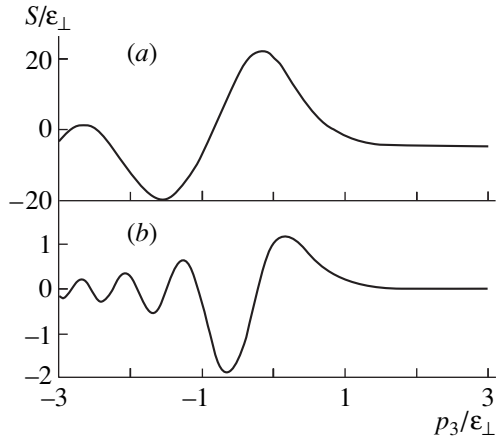

Fig. 2. Fermion-production rate as a function of longitudinal momentum in a constant field of strength (*a*) $eE/\varepsilon_\perp^2 = 1.5$ and (*b*) 0.5.

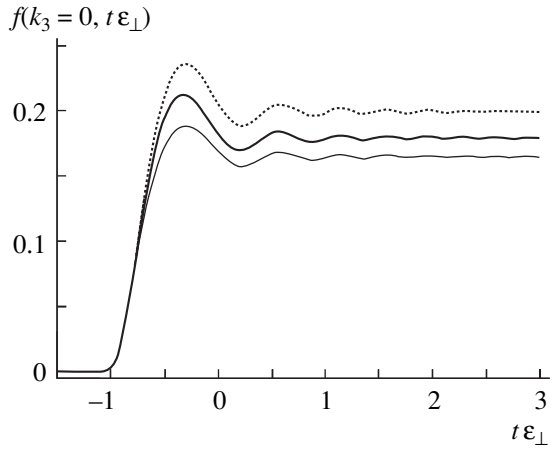

Fig. 3. Precise solution to the kinetic equation for fermions (thick solid curve) along with solutions in the Markov approximation (thin solid curve) and in the low-density limit (dotted curve) at $p_\parallel = 0$ and $eE/\varepsilon_\perp^2 = 3$.

To state it otherwise, τ_{prod}^{-1} represents the mean pair-production rate. In the Markov approximation, we have $\tau_{\text{prod}} \gg \tau_{\text{qu}}$.

In supercritical fields, memory effects become operative, so that phenomenological constructions of the type in (2) can lead to sizable inconsistencies, as can be seen in Fig. 3. In this figure, we can also observe oscillations of the distribution function, which decay with time and which were previously suggested by the results of other studies (see, for example, [28, 37]). The distribution functions themselves tend asymptotically to constant values that are determined by the amplitude of the external field, the effects of Fermi suppression and of Bose enhancement being leveled out in this case. It can easily be verified, however, that, when $E \longrightarrow \infty$, the Fermi distribution function tends to its limiting value of unity, while the Bose distribution function grows indefinitely.

4. DYNAMICS OF VACUUM PARTON PRODUCTION IN THE MEAN-FIELD APPROXIMATION

Let us now assume that the role of the external field A_{ex}^μ reduces to triggering the generation of parton–antiparton pairs, which in turn produce the internal massless field A_{in}^μ. As soon as the external field is switched off, the parton plasma becomes an isolated self-consistent system. For a first approximation, it is reasonable to consider its dynamics in the mean-field approximation. The kinetic Eq. (1) with the source given by (17) (in the collision-free version for the time being) must be supplemented with the Maxwell equation

$$\dot{E}(t) = -j(t), \tag{30}$$

which renders the total field $E(t) = -\dot{A}_{\text{ex}}(t) - \dot{A}_{\text{in}}(t)$ consistent with the total current $j(t) = j_{\text{ex}}(t) + j_{\text{in}}(t)$ in the system. The internal current is the sum of the conduction current and the vacuum polarization current,

$$j_{\text{int}}(t) = j_{\text{cond}}(t) + j_{\text{pol}}(t), \tag{31}$$

$$j_{\text{cond}}(t) = 2e\int [dp]\frac{p_3}{\omega} f(\mathbf{p}, t), \tag{32}$$

$$j_{\text{pol}}(t) = e\int [dp]\frac{p_3}{\omega} v(\mathbf{p}, t)\left(\frac{\varepsilon_\perp}{p_3}\right)^{g-1}, \tag{33}$$

where $v(\mathbf{p}, t)$ is given by (19), while the momentum-space element $[dp]$ is defined in (29).

In order to eliminate the ultraviolet divergences in the currents given by (32) and (33), we will make use of the procedure of *n*-wave regularization [24, 31, 43]. In order to construct counterterms according to the prescription of this procedure, it is necessary to expand the functions f, v, and z (19) in asymptotic series in inverse powers of ω. Having implemented this procedure in the set of Eqs. (20), we obtain the leading contributions

$$f_4 = \left[eE(t)\frac{p_3}{4\omega^3}\left(\frac{\varepsilon_\perp}{p_3}\right)^{g-1}\right]^2,$$

$$v_3 = e\dot{E}(t)\frac{p_3}{4\omega^4}\left(\frac{\varepsilon_\perp}{p_3}\right)^{g-1}, \tag{34}$$

$$z_2 = eE(t)\frac{p_3}{2\omega^3}\left(\frac{\varepsilon_\perp}{p_3}\right)^{g-1}.$$

From a comparison with expressions (32) and (33), we can see that the current j_{cond} is finite, while the current j_{pol} diverges logarithmically. In order to regularize the currents, it is therefore sufficient to make the formal

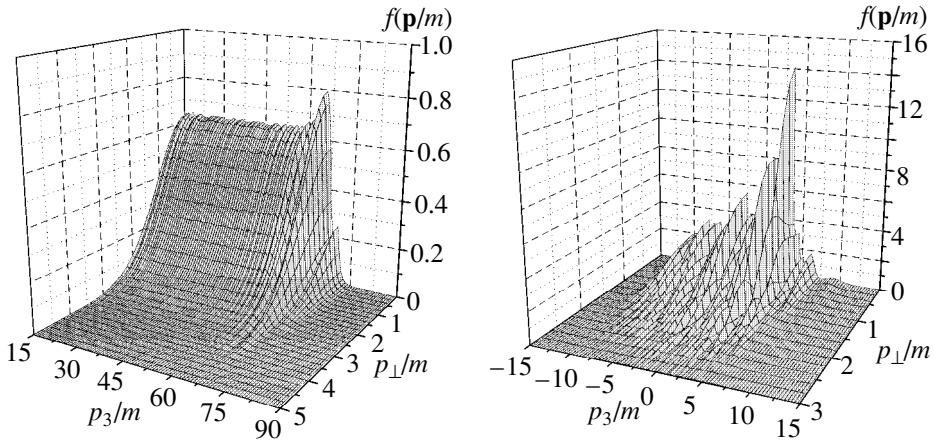

Fig. 4. Boson distribution (left panel) without and (right panel) with allowance for the back-reaction mechanism at the instant $tm = 10$ for $eE_0/m^2 = 7$.

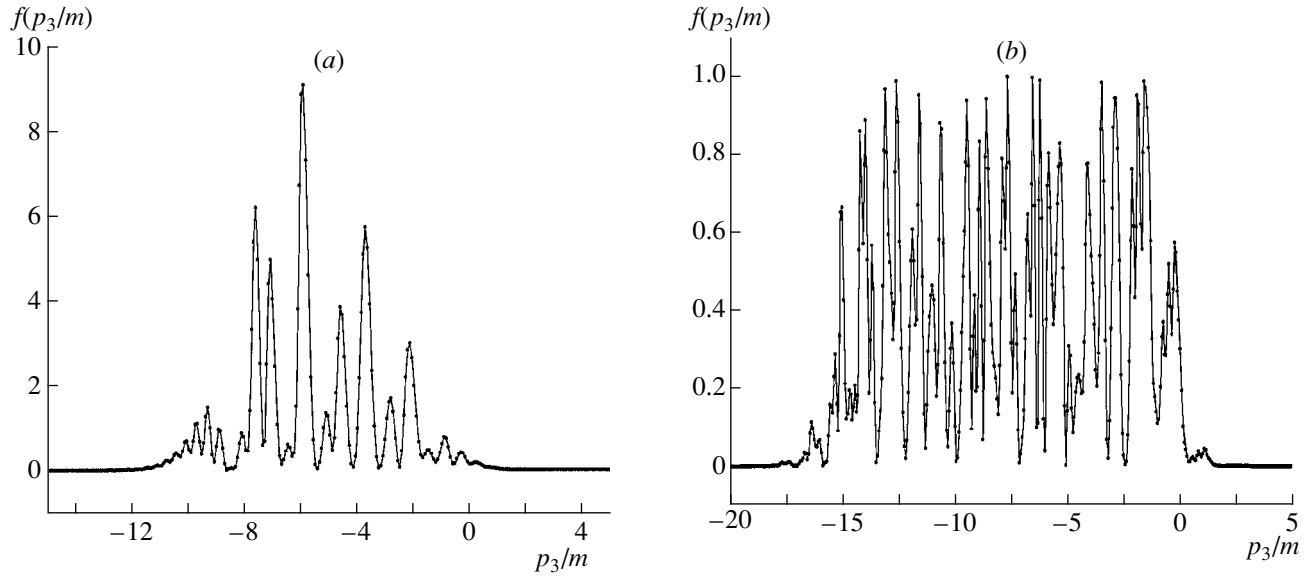

Fig. 5. Longitudinal-momentum (p_3/m) distribution of (*a*) bosons and (*b*) fermions at the instant $tm = 25$ ($p_\perp = 0$).

substitution $v \longrightarrow v - v_3$ in (33). We write the regularized Maxwell equation as [44]

$$\dot{E}_{\text{in}} = -2e\int [dp]\frac{p_3}{\omega}\left[f + \frac{v}{2}\left(\frac{\varepsilon_\perp}{p_3}\right)^{g-1} - e\dot{E}\frac{p_3}{8\omega^4}\left(\frac{\varepsilon_\perp}{p_3}\right)^{2(g-1)}\right]. \tag{35}$$

The Maxwell equation (35), in conjunction with the kinetic Eq. (1) with the source given by (17) [or the set of Eqs. (20)], forms a basis for studying the back-reaction problem within the approach developed here. This problem was solved by numerical methods in [32, 36] for various versions of triggering external-field pulse.

Basic features of the dynamics of the system being considered are associated with the essentially nonlinear character of the self-consistent set of equations describing the back-reaction problem. This is reflected primarily in the irregular dynamical behavior of the system, most spectacularly in the evolution of the distribution function. In Fig. 4, one can see how the smooth distribution of bosons (see also Fig. 1) ceases to be regular as soon as the back-reaction mechanism is included [for the triggering pulse, we have chosen the potential (23) with the parameter values corresponding to those in Fig. 1].

Irregularities can be seen both in the momentum distribution (comb in Fig. 5) and in the time scan of the distribution function (Fig. 6). Figure 6, which shows the fermion distribution function versus time and longitudinal momentum, exhibits a small smooth fragment that corresponds in time to the action of the external pulse. After this pulse is switched off, the system undergoes a self-consistent evolution, which is characterized by an ever growing instability of multimode

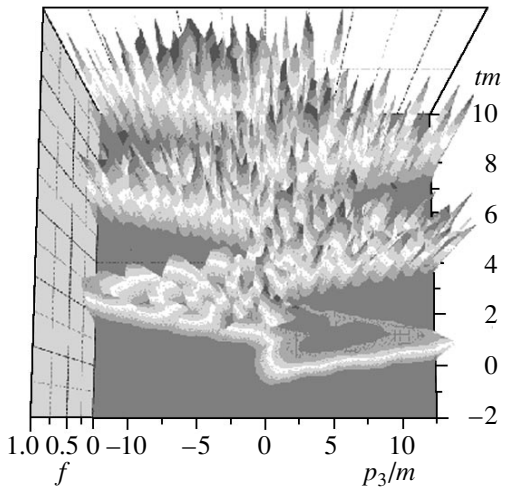

Fig. 6. Fermion distribution function versus time and longitudinal momentum at $eE_0/m^2 = 7$.

oscillations on small time scales (about τ_{qu}) and by the emergence of large-scale plasma oscillations of characteristic time τ_{pl} (within the semiphenomenological approach, results similar to those in Fig. 6 were previously obtained in [37]).

On the basis of the above results, it can be conjectured that a stochastic process is developed in the self-consistent dynamics of vacuum particle production in strong fields. Below, we present arguments in support of this conjecture. Figure 7 displays the correlation coefficient

$$C(\tau) = \frac{K(\tau)}{K(0)}, \quad K(\tau) = \frac{1}{T}\int_0^T \hat{f}(t)\hat{f}(t+\tau)dt, \quad (36)$$

where

$$\hat{f}(t) = f(t) - \frac{1}{T}\int_0^T f(t)dt,$$

and the power spectrum

$$P(\omega) = \int dt e^{i\omega t} C(t) \quad (37)$$

for the distribution function $f(t) \equiv f(0, t)$, which were constructed for the $d = 1 + 1$ version of the approach proposed here. The results shown in this figure are peculiar to systems that exhibit stochastic behavior (for example, a Lorenz system [45]): a continuous spectrum and virtually no correlations. The presence of small irregular oscillations in the vicinity of the origin following the exponential decay has no bearing on this conclusion—they may be due to scanning the process within a bounded time interval.

From the point of view of the theory of dynamical systems, the problem being considered belongs to the

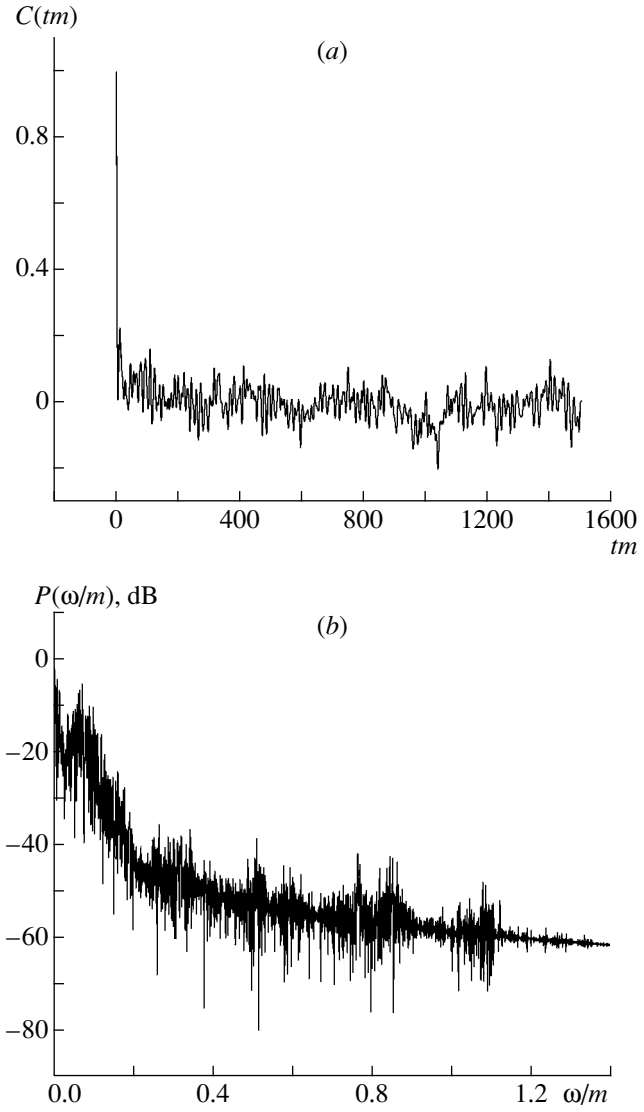

Fig. 7. (*a*) Correlation coefficient and (*b*) power spectrum for the distribution function at $eE_0/m^2 = 7$.

class of nonlinear distributed quantum-mechanical problems. Here, nonintegrability is one of the general criteria of the existence of stochasticity [46]. For the basic set of equations studied here for the back-reaction problem, this criterion is obviously satisfied.

In contrast to the distribution function, other observables that are expressed in terms of its moments (current, internal field, energy density, etc.) behave quite regularly (Fig. 8). In the absence of dissipative mechanisms, these variables undergo undamped oscillations whose character is weakly dependent on the shape of the external-field pulse. The amplitude and frequency of these oscillations depend strongly on statistics: they are much greater for fermions than for bosons. The presence of small ripples in the vicinities of extremal points of the current corresponds to the time scale τ_{qu}.

In all probability, a stochastic behavior of parton plasmas in the mean-field approximation exemplifies the emergence of stochasticity in high-energy physics [47] and can lead to observable effects. Finally, we note that the very existence of large-scale plasma oscillations (Fig. 6) can be interpreted in terms of self-organization effects [48].

5. THERMALIZATION

A consideration of plasma dynamics in the collision-free approximation has a significant drawback associated with mean-field oscillations against the background of particle density values $n(t)$ close to the Compton value. As soon as the field strength E is reduced to values below $en^{2/3}$, pair interaction becomes dominant, so that the mean-field approximation ceases to be valid in this case. At the same time, there are data suggesting that, at an early stage of an ultrarelativistic heavy-ion collision, partons interact strongly, whereby matter is thermalized on the time scale $t_e < 1$ fm/c, which is commensurate with the period of field oscillations.

Since solving the relevant self-consistent problem requires performing very involved computations, binary collisions are usually taken into account in the relaxation-time approximation. In this case, the right-hand side of the Vlasov equation is supplemented with the model collision integral [17],

$$C(\mathbf{p}, t) = -\frac{f(\mathbf{p}, t) - f_{\mathrm{eq}}(\mathbf{p}, t)}{\tau_c(\mathbf{p}, t)}. \qquad (38)$$

The quasiequilibrium distribution function f_{eq} depends on thermodynamic parameters whose number is equal to the number of conservation laws that must be satisfied in simulating collision events. The relaxation time τ_c can be estimated as the ratio of the mean free path to the mean velocity, $\tau_c \sim n^{-1/3}/u$, or expressed in terms of the total cross section as $\tau_c \sim [\sigma n]^{-1}$ [17]. Usually, the system is assumed to be one-component and to be governed by a single thermodynamic parameter, the temperature $T(t)$, which is determined from the condition requiring that the instantaneous energy densities in a nonequilibrium and in a quasiequilibrium state be equal [49]:

$$\int [dp]\omega f(\mathbf{p}, t) = \int [dp]\omega f_{\mathrm{eq}}(\mathbf{p}, t). \qquad (39)$$

In this case, thermalization is described in the rest frame of one of the components of the system, while the relative hydrodynamic flows of the components are disregarded.

This scheme was used in many studies [13, 49–51] to describe QED and quark–gluon plasmas with a model source.

There arises a serious problem when the scheme specified by Eq. (39) is used in an exact kinetic equation featuring a non-Markov source. In this case, the matter energy density is negative at early plasma-formation stages because of vacuum polarization by a supercritical field, so that the scheme that introduces the temperature according to Eq. (39) is not applicable directly. The presence of the collision term in the kinetic equation changes the asymptotic behavior of $f(p \longrightarrow \infty)$ in such a way that this effect is partly compensated, but this does not solve the problem completely.

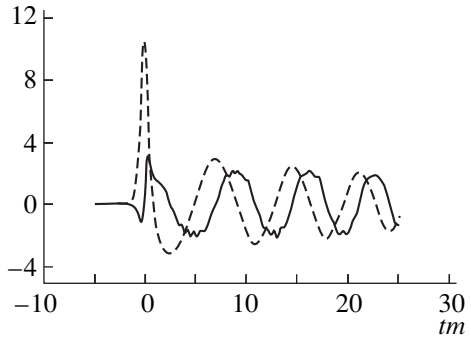

Fig. 8. Electric-current density $j(tm)/m^3$ (solid curve) and electric field $E(tm)/m^2$ (dashed curve) in the system of bosons produced from a vacuum in the external field (23) at $eE_0/m^2 = 10$, $bm = 0.5$, and e^2 versus time.

A simple trick that makes it possible to sidestep this difficulty consists in that only after a lapse of some delay time τ_d from the application of the external-field pulse is the collision integral included in the kinetic equation, whereby yet another phenomenological parameter τ_d, which can be interpreted as the lifetime of a strongly nonequilibrium state, appears in the system.

The system of particles f and antiparticles $\bar{f}$, which is considered here, is a thermodynamically two-component system, but, because of high symmetry of the problem and of the initial conditions, there are only two independent thermodynamic parameters, the temperature $T(t)$ and the longitudinal hydrodynamic velocity $u^\mu = \gamma(1, 0, 0, u(t))$, where $\gamma = (1 - u^2)^{-1/2}$. The chemical potential is zero because of the electric neutrality of the system, whence it follows that the equilibrium distribution function has the form [52]

$$f_{\mathrm{eq}}(\mathbf{p}, t) = \left\{ \exp\left[\frac{u^\mu p_\mu}{T(t)}\right] + (-1)^g \right\}^{-1}. \qquad (40)$$

Since we have $f(\mathbf{p}, t) = \bar{f}(-\mathbf{p}, t)$ in view of the symmetry of the problem, particles and antiparticles have oppositely directed mean velocities equal in magnitude and identical temperatures. Thus, the antiparticle distribution function $\bar{f}_{\mathrm{eq}}(\mathbf{p}, t)$ is obtained from expression (40) upon the substitution $u \longrightarrow -u$, so that it is sufficient to use only one kinetic equation for particles. The mean velocity is determined from the momentum conservation law

$$\int [dp]\mathbf{p}C(\mathbf{p}, t) = 0. \qquad (41)$$

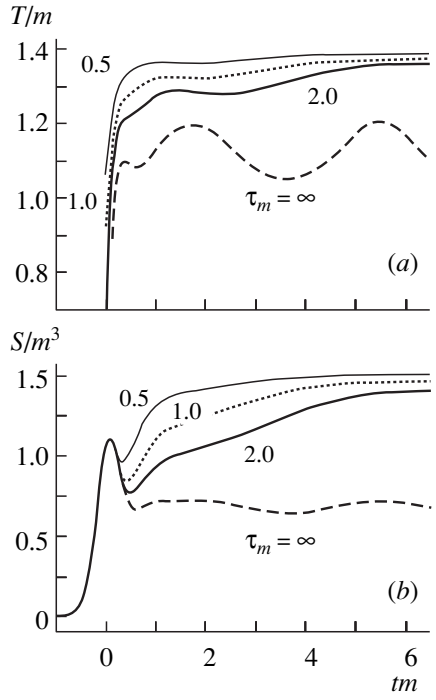

Fig. 9. (*a*) Temperature in parton-mass units and (*b*) entropy density at various values of $\tau_m = \tau_c m$ (numbers on the curves) versus time (time delay is equal to half the pulse duration $\tau_d m = 1$; the pulse is applied at $t_0 m = -2$).

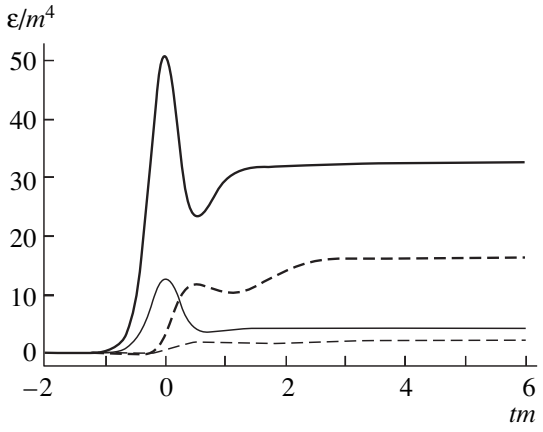

Fig. 10. Energy density (solid curves) with and (dashed curves) without allowance for the external-field energy at $eE_0/m^2 = 1.5$ for eE_0/m^2 = (thick curves) 20 and (thin curves) 10. The product $\tau_i m$ was set to 1.5 here.

In this approximation, the model collision integral can be represented as

$$C(\mathbf{p}, t) = \frac{-2f(\mathbf{p}, t) + f_{\rm eq}(\mathbf{p}, t) + \bar{f}_{\rm eq}(\mathbf{p}, t)}{\tau_c}\theta(t - t_0 - \tau_d). \quad (42)$$

The presence of the collision integral (42) in the kinetic Eq. (1) does not induce qualitative changes in the asymptotic behavior of $f(\mathbf{p}, t)$ for $p \longrightarrow \infty$—in particular, all singularities survive. Only the expression for the leading term f_4 changes, developing a non-Markov term:

$$f_4 = \left(\frac{W}{4\omega}\right)^2\left\{1 - \frac{1}{\tau_c E^2}\int_{t_0}^{t}[E(t')\exp((t' - t)/\tau_c)]^2 dt'\right\}. \quad (43)$$

Since the integrand on the right-hand side of (43) is positive definite, collisions only reduce the negative contribution of vacuum polarization to the particle energy density. This is, however, insufficient for the scheme specified by Eq. (39) to become valid. In the collision integral, we therefore introduce the factor $\theta(t - t_0 - \tau_d)$, which ensures that collisions become operative after a lapse of the delay time τ_d from the instant t_0 at which the external pulse was applied. Figure 9 illustrates the time evolution of the temperature and the entropy at various values of τ_c. As might have been expected, the inclusion of collisions leads to an additional growth of the entropy and temperature, each of which approaches a plateau with time, demonstrating equilibration in the system.

The evolution of the energy density in the system is shown in Fig. 10. At the values chosen here for the field parameters, the relevant conditions reproduce those that are prevalent in ultrarelativistic nuclear collisions [51]. In just the same way as the temperature, $\varepsilon(t)$ reaches a plateau as soon as tm exceeds unity—that is, almost immediately after the instant at which the external field is switched off; this is consistent with a very fast decay of fluctuations (see also Fig. 7). The doubling of the external-field strength leads to a sixfold increase in the equilibrium quark density; concurrently, the temperature changes from about 280 MeV (see Fig. 9) to 500 MeV at $m = 200$ MeV.

6. CONCLUSION

The present investigation has been performed on the basis of the kinetic Eq. (1) featuring a source in the form (17) and describing, in the collision-free approximation, the dynamics of vacuum particle production in a strong spatially uniform time-dependent field of fixed orientation in space [19, 20]. It is of importance that the kinetic equation has been obtained on a dynamical nonperturbative basis. This has enabled us to consider an essentially nonperturbative region of a nonequilibrium parton–antiparton plasma and to analyze the effect of various factors on process dynamics. In the simplest situation where the external field is preset, the evolution of our quantum system is of a regular character; at the same time, the assumption (3) of an external (background) field has shown natural conformity to the flux-tube model. The inclusion of the back-reaction mechanism via a self-consistent description of the dynamics

of a parton plasma that has originated from a vacuum and of its intrinsic field has led to the emergence of a significant irregularity in parton distribution functions. This is indicative of a change in the character of evolution from regular oscillations to stochastic behavior. The additional inclusion of the dissipation mechanism due to collisions at the phenomenological level contributes to thermodynamic equilibration in the system. All these models make it possible to fit a theoretical description to conditions expected in ultrarelativistic nuclear collisions. A more detailed application of the proposed approach to specific nuclear systems at RHIC and LHC will be developed elsewhere. It would be of great interest to elaborate further on the model by going, for example, beyond the $1/N$-expansion technique within some nonperturbative scheme.

ACKNOWLEDGMENTS

S.A. Smolyansky is grateful to V.V. Voronov and V.K. Lukyanov for the hospitality extended to him at the Bogolyubov Laboratory for Theoretical Physics at the Joint Institute for Nuclear Research (Dubna).

This work was supported in part by the State Committee of the Russian Federation for Higher Education (grant no. 97-0-6.1-4) and the Russian Foundation for Basic Research (project no. 00-02-04012).

REFERENCES

1. A. B. Migdal, Rev. Mod. Phys. **50**, 107 (1978).
2. A. B. Migdal, E. E. Saperstein, M. A. Troitsky, and D. N. Voskresensky, Phys. Rep. **192**, 179 (1990).
3. A. B. Migdal, *Fermions and Bosons in Strong Fields* (Nauka, Moscow, 1972).
4. F. E. Low, Phys. Rev. D **12**, 163 (1975).
5. S. Nussinov, Phys. Rev. Lett. **34**, 1286 (1975).
6. F. Cooper and E. Mottola, Phys. Rev. D **36**, 3114 (1987).
7. F. Cooper and E. Mottola, Phys. Rev. D **40**, 456 (1989).
8. Y. Kluger, J. M. Eisenberg, B. Svetitsky, *et al.*, Phys. Rev. Lett. **67**, 2427 (1991).
9. F. Cooper, J. M. Eisenberg, Y. Kluger, *et al.*, Phys. Rev. D **48**, 190 (1993).
10. J. Schwinger, Phys. Rev. **82**, 664 (1951).
11. E. G. Gurvich, Phys. Lett. B **87B**, 386 (1979).
12. K. Kajantie and T. Matsui, Phys. Lett. B **164B**, 373 (1985).
13. G. Gatoff, A. K. Kerman, and T. Matsui, Phys. Rev. D **36**, 114 (1987).
14. A. Białas and W. Czyż, Phys. Rev. D **31**, 198 (1985); **30**, 2371 (1984); Z. Phys. C **28**, 225 (1985); Nucl. Phys. B **267**, 242 (1986); Acta. Phys. Pol. B **17**, 635 (1986).
15. A. B. Białas, W. Czyż, A. Dyrek, and W. Florkowski, Nucl. Phys. B **296**, 611 (1988).
16. Y. Kluger, J. M. Eisenberg, B. Svetitsky, *et al.*, Phys. Rev. D **45**, 4659 (1992).
17. G. Baym, Phys. Lett. B **138B**, 18 (1984).
18. J. L. Anderson and H. R. Witting, Physica **74**, 466 (1974).
19. S. A. Smolyansky, G. Röpke, S. M. Schmidt, *et al.*, hep-ph/9712377; GSI-Preprint-97-92 (Darmstadt, 1997).
20. S. M. Schmidt, D. Blaschke, G. Röpke, *et al.*, Int. J. Mod. Phys. E **7**, 709 (1998).
21. N. B. Narozhnyĭ and A. I. Nikishov, Yad. Fiz. **11**, 1072 (1970) [Sov. J. Nucl. Phys. **11**, 596 (1970)].
22. A. I. Nikishov, Tr. Fiz. Inst. Akad. Nauk SSSR **111**, 152 (1979).
23. M. I. Shirokov, Yad. Fiz. **7**, 672 (1968) [Sov. J. Nucl. Phys. **7**, 411 (1968)].
24. A. A. Grib, S. G. Mamaev, and V. M. Mostepanenko, *Vacuum Quantum Effects in Strong Fields* (Énergoatomizdat, Moscow, 1988).
25. V. S. Popov and M. S. Marinov, Yad. Fiz. **16**, 809 (1972) [Sov. J. Nucl. Phys. **16**, 449 (1973)].
26. S. M. Schmidt, D. Blaschke, G. Röpke, *et al.*, Phys. Rev. D **59**, 094005 (1999).
27. E. Brezin and C. Itzykson, Phys. Rev. D **2**, 1191 (1970).
28. Y. Kluger, E. Mottola, and J. M. Eisenberg, Phys. Rev. D **58**, 125015 (1998).
29. V. S. Popov, Zh. Éksp. Teor. Fiz. **62**, 1248 (1972) [Sov. Phys. JETP **35**, 659 (1972)].
30. M. S. Marinov and V. S. Popov, Fortschr. Phys. **25**, 373 (1977).
31. S. G. Mamaev and N. N. Trunov, Yad. Fiz. **30**, 1301 (1979) [Sov. J. Nucl. Phys. **30**, 677 (1979)].
32. J. C. R. Bloch, V. A. Mizerny, A. V. Prozorkevich, *et al.*, Phys. Rev. D **60**, 116011 (1999).
33. V. V. Klimov, Yad. Fiz. **33**, 1734 (1981) [Sov. J. Nucl. Phys. **33**, 934 (1981)]; Zh. Éksp. Teor. Fiz. **82**, 336 (1982) [Sov. Phys. JETP **55**, 199 (1982)].
34. H. A. Weldon, Phys. Rev. D **26**, 1394, 2789 (1982); **40**, 2410 (1989).
35. G. E. Braaten and P. D. Pisarski, Nucl. Phys. B **337**, 569 (1990); **339**, 310 (1990).
36. S. A. Smolyansky, V. A. Mizerny, D. V. Vinnik, *et al.*, in *Progress in Nonequilibrium Green's Functions*, Ed. by M. Bonitz (World Sci., Singapore, 2000), p. 375.
37. Y. Kluger, J. M. Eisenberg, and B. Svetitsky, Int. J. Mod. Phys. E **2**, 333 (1993).
38. A. Casher, H. Neuberger, and S. Nussinov, Phys. Rev. D **20**, 179 (1979).
39. A. Casher, H. Neuberger, and S. Nussinov, Phys. Rev. D **21**, 1966 (1980).
40. H. Neuberger, Phys. Rev. D **20**, 2936 (1979).
41. J. Rau, Phys. Rev. D **50**, 6911 (1994).
42. J. Rau and B. Müller, Phys. Rep. **272**, 1 (1996).
43. Ya. B. Zel'dovich and A. A. Starobinskiĭ, Zh. Éksp. Teor. Fiz. **61**, 2161 (1971) [Sov. Phys. JETP **34**, 1159 (1971)].
44. D. V. Vinnik, V. A. Mizernyĭ, A. V. Prozorkevich, *et al.*, Preprint No. R2-2000-85, OIYaI (Joint Institute for Nuclear Research, Dubna, 2000).

45. H. G. Schuster, *Deterministic Chaos* (Physik-Verlag, Weinheim, 1984; Mir, Moscow, 1988).
46. V. A. Bunakov, Yad. Fiz. **62**, 5 (1999) [Phys. At. Nucl. **62**, 1 (1999)].
47. T. S. Biro, S. G. Matinyan and B. Müller, *Chaos and Gauge Field Theory* (World Sci., Singapore, 1994).
48. H. Haken, *Springer Series in Synergetics*, Vol. 20: *Advanced Synergetics* (Springer-Verlag, Berlin, 1983).
49. J. M. Eisenberg, in *Hot and Dense Nuclear Matter*, Ed. by W. Greiner *et al.* (Plenum, New York, 1994), p. 333; Found. Phys. **27**, 1213 (1997).
50. G. C. Nayak and V. Ravishankar, Phys. Rev. D **55**, 6877 (1997); Phys. Rev. C **58**, 356 (1998); R. S. Bhalerao and V. Ravishankar, Phys. Lett. B **409**, 38 (1997).
51. J. C. R. Bloch, C. D. Roberts, and S. M. Schmidt, Phys. Rev. D **61**, 117502 (2000).
52. R. D. Tenreiro and R. Hakim, Physica A (Amsterdam) **133**, 477 (1982).

Translated by A. Isaakyan